Transactions of the ASME®

Transactions of the ASME, Journal of Fluids Engineering (ISSN 0098-2202) is published bimonthly (Jan., Mar., May, July, Sept., Nov.) by The American Society of Mechanical Engineers, Three Park Avenue, New York, NY 10016. Periodicals postage paid at New York, NY and additional mailing offices.
POSTMASTER: Send address changes to Transactions of the ASME, Journal of Fluids Engineering, c/o THE AMERICAN SOCIETY OF MECHANICAL ENGINEERS, 22 Law Drive, Box 2300, Fairfield, NJ 07007-2300.
CHANGES OF ADDRESS must be received at Society headquarters seven weeks before they are to be effective. Please send old label and new address.
STATEMENT from By-Laws. The Society shall not be responsible for statements or opinions advanced in papers or ... printed in its publications (B7.1, Par. 3).

INDEXED by Applied Mechanics Reviews and Engineering Information, Inc. Canadian Goods & Services Tax Registration #126148048.

Journal of Fluids Engineering

Published Bimonthly by The American Society of Mechanical Engineers

VOLUME 125 • NUMBER 5 • SEPTEMBER 2003

TECHNICAL PAPERS

(Contents continued on inside back cover)

This journal is printed on acid-free paper, which exceeds the ANSI Z39.48-1992 specification for permanence of paper and library materials. ♾™
♻ 85% recycled content, including 10% post-consumer fibers.

Journal of Fluids Engineering Volume 125, Number 5 SEPTEMBER 2003

TECHNICAL BRIEFS

BOOK REVIEW

ANNOUNCEMENTS AND SPECIAL NOTES

The ASME Journal of Fluids Engineering is abstracted and indexed in the following:

Applied Science & Technology Index, AMR Abstracts Database, Chemical Abstracts, Chemical Engineering and Biotechnology Abstracts (Electronic equivalent of Process and Chemical Engineering), Civil Engineering Abstracts, Computer & Information Systems Abstracts, Corrosion Abstracts, Current Contents, Ei EncompassLit, Electronics & Communications Abstracts, Engineered Materials Abstracts, Engineering Index, Environmental Engineering Abstracts, Environmental Science and Pollution Management, Excerpta Medica, Fluidex, Index to Scientific Reviews, INSPEC, International Building Services Abstracts, Mechanical & Transportation Engineering Abstracts, Mechanical Engineering Abstracts, METADEX (The electronic equivalent of Metals Abstracts and Alloys Index), Petroleum Abstracts, Process and Chemical Engineering, Referativnyi Zhurnal, Science Citation Index, SciSearch (The electronic equivalent of Science Citation Index), Shock and Vibration Digest, Solid State and Superconductivity Abstracts, Theoretical Chemical Engineering

Numerical Analysis of Cavitating Flow of Liquid Helium in a Converging-Diverging Nozzle

Jun Ishimoto
Associate Professor,
Department of Intelligent Machines
and System Engineering,
Hirosaki University,
3, Bunkyo-cho,
Hirosaki 036-8561, Japan
e-mail: ishimoto@cc.hirosaki-u.ac.jp

Kenjiro Kamijo
Professor,
Institute of Fluid Science,
Tohoku University,
Sendai 980-8577, Japan

The fundamental characteristics of the two-dimensional cavitating flow of liquid helium through a horizontal converging-diverging nozzle near the lambda point are numerically investigated to realize the further development and high performance of new multiphase superfluid cooling systems. First, the governing equations of the cavitating flow of liquid helium based on the unsteady thermal nonequilibrium multifluid model with generalized curvilinear coordinates system are presented, and several flow characteristics are numerically calculated, taking into account the effect of superfluidity. Based on the numerical results, the two-dimensional structure of the cavitating flow of liquid helium though a horizontal converging-diverging nozzle is shown in detail, and it is also found that the generation of superfluid counterflow against normal fluid flow based on the thermomechanical effect is conspicuous in the large gas phase volume fraction region where the liquid to gas phase change actively occurs. Furthermore, it is clarified that the mechanism of the He I to He II phase transition caused by the temperature decrease is due to the deprivation of latent heat for vaporization from the liquid phase.
[DOI: 10.1115/1.1601253]

1 Introduction

Recently, the importance of the development of high-performance cooling systems which can be employed under severe conditions, such as low temperature, microgravity, or the environment in space, has markedly increased, and fluid machinery systems using cryogenic refrigerant are widely used in LNG (liquefied natural gas) plants and aerospace technology, [1–3]. In general, cryogenic fluids are characterized by large compressibility compared with fluids at room temperature such as water, as well as by a small difference in density between the gas and liquid phases, and a small latent heat of vaporization. These unique characteristics of cryogenic fluids can be utilized to realize high performance in fluid apparatuses, such as the cavitating operation of inducers, [4].

Among such fluids, liquid helium, which is known as the ultimate low-temperature cryogen which possesses high functionality of zero viscosity with λ transition, is effectively utilized as a cooling device for superconducting magnets or infrared space telescopes and many other engineering applications, [1]. When liquid helium is employed for cooling, cavitation frequently occurs in the flow duct, and the flow pattern consists of two phases. Thus, investigation of the cavitating flow characteristics of cryogenic fluids such as liquid helium is very interesting and important not only in the basic study of the hydrodynamics of cryogenic fluids, [3], but also for providing solutions to problems related to new practical engineering applications.

However, the cryogenic system presently employed generally uses a refrigerant for the undercooling condition, and its cooling performance depends only on the single-phase region. Thus, few attempts have been made to positively apply the extensive heat transfer and fluid acceleration characteristics of cryogenic two-phase flow to low-temperature cooling systems, [5,6]. In recent research on two-phase flow or cavitating flow with liquid helium, numerical analysis of two-phase flow of liquid helium through an orifice, [7], observation of cavitating flow in a converging-diverging pipe, [8], and cavitation of saturated liquid helium through a venturi channel, [9], have been conducted and the special characteristics of liquid helium cavitation near the λ point have been partially clarified.

Numerical study has also partially clarified the He I to He II phase transition and the superfluid counterflow generation at the time of cavitation, [7]. Moreover, since the numerical model assumed the production method for cavitation based on the flow passing through the orifice, a local increase of the pressure loss resulting from the sudden decrease of the passage cross-sectional area led to the demerit of decreasing heat transfer efficiency of whole cooling system. Numerical and experimental study to date on two-phase flow of liquid helium has yielded only limited information on the basic multiphase hydrodynamic characteristics of cavitation in liquid helium, [5–9], and results directly related to the development of a superfluid cooling system utilizing the peculiarity of liquid helium multiphase flows have not yet been obtained.

Under the above-mentioned conditions, we contrived a new concept of a multiphase superfluid cooling system using liquid helium cavitating flow. The system can realize extensive low temperature cooling by utilizing the two-phase superfluid counterflow generated by He I to He II phase transition based on the occurrence of cavitation of the normal fluid, without the direct use of He II. Additionally, it is expected that the concept of multiphase super-fluid cooling can be utilized for further development of available microcooling systems, such as MEMS (micro-electro-mechanical systems) technology using microbubbles, [10], because the unique characteristics of zero viscosity of superfluid working refrigerant prevents the frictional dissipation of capillary channels in microdevices. The direct use of He II flow entails very difficult problems because of the ultra low-temperature field in which it is produced or due to super-leak phenomena in fluid transfer systems, etc. Thus, the application of cavitating flow of He I as a refrigerant is a very useful and effective method for low-temperature cooling or cryogenic heat exchange systems.

In order to develop a new type of superfluid cooling system and to estimate cooling performance numerically, we herein develop a new method for analyzing cavitating flow based on an advanced mathematical model, which takes the effect of superfluidity of the cavitating cryogenic flow state in the low-temperature field into consideration.

Contributed by the Fluids Engineering Division for publication in the JOURNAL OF FLUIDS ENGINEERING. Manuscript received by the Fluids Engineering Division October 7, 2002; revised manuscript received April 1, 2003. Associate Editor: J. Katz.

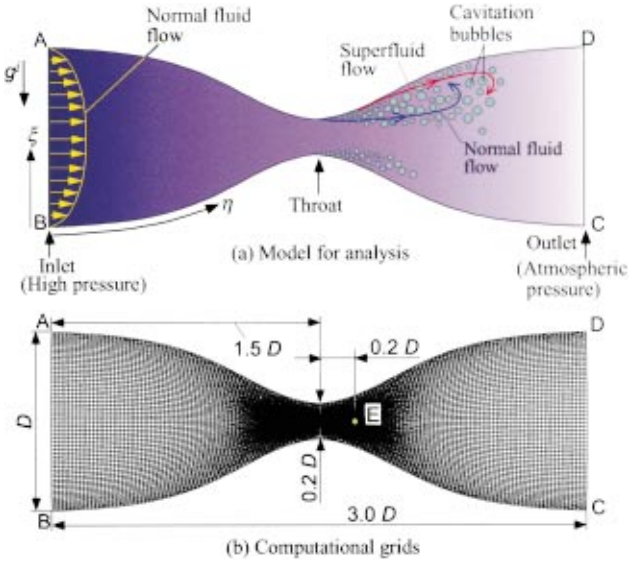

Fig. 1 Schematic of computational system used in numerical analysis

In the present study, the two-dimensional thermal fluid characteristics of cavitating flow of liquid helium with phase change through the converging-diverging nozzle are numerically investigated. First, the governing equations of the cavitating flow of liquid helium based on the unsteady multifluid model are presented, and then several flow characteristics are numerically calculated, taking into account the effect of superfluidity.

2 Numerical Method

In the present study on the cavitating flow of liquid helium, we developed a new model for analysis, which is based on the unsteady thermal nonequilibrium multifluid model, [11], in the generalized curvilinear coordinates system. Furthermore, to consider the effects of evaporation and condensation on the vapor bubbles, we apply the rapid phase change model to the cavitating flow of liquid helium with superfluidity. The system used in the numerical analysis is schematically depicted in Fig. 1. Applications using cryogenic fluid generally encounter obstacles, or complex pipe shapes such as those of an orifice or a converging-diverging section. Additionally, the transfer tube for cryogenic fluids generally has many horizontal passage sections. Thus, the model used for analysis simulates the cavitating flow of liquid helium passing through a horizontal converging-diverging nozzle. The duct is filled with pressurized liquid helium. Flow immediately occurs when the outlet D-C is opened. Liquid helium is continuously introduced via the inlet section A-B, the flow is accelerated at the point of the nozzle throat, and cavitation or liquid-to-vapor phase change is induced by a decrease of pressure.

2.1 Governing Equations. In the present numerical formulation of the cavitating flow characteristics of liquid helium, we extend the old two-fluid model, [3], to a new cryogenic vapor-liquid multiphase fluid model for analysis which is based on the unsteady thermal nonequilibrium multifluid model of Kataoka [11] and Harlow and Amsden [12]. In the numerical model, the cryogenic cavitating flow state can be approximated to that of a homogeneous bubbly flow because the differences in the physical properties, such as density, viscosity, and surface tension of the cryogenic fluid between the gas and liquid phases, are very small compared with those of the fluid at room temperature. The small difference in the properties between the gas and liquid phases is unique to cryogenic fluids. Accordingly, it seems reasonable to assume that the cryogenic cavitating flow pattern is easily formed in the bubbly two-phase flow. In the process of modeling, we consider the effects of superfluidity in two-phase liquid helium, namely, superfluid in He II and normal fluid in He I are treated as a perfect fluid and meta-viscous fluid, respectively. In the calculation, we assume that the property of superfluidity appears when the fluid temperature becomes less than the λ point (temperature at normal fluid to superfluid transition, about 2.17 K); however, in the case of temperatures above the λ point, we assume that the superfluid behaves in the same manner as the normal fluid. Here, we consider only the temperature dependence of the superfluid and normal fluid densities; thus, the normal fluid-superfluid transition rate based on quantum theory is not strictly considered. Furthermore, to consider the effects of the rapid evaporation and condensation of cryogenic fluid, we apply the rapid phase change model of Yamamoto et al. [13] and Young [14] to the cavitating flow of liquid helium.

The calculation is carried out using the two-dimensional generalized curvilinear coordinate system (ξ, η), with ξ and η denoting the transverse coordinate and the longitudinal coordinate, respectively. The model for analysis simulates the cavitating flow of liquid helium passing through the nozzle throat of the duct. In the numerical modeling under this condition, the following assumptions are employed to formulate the governing equations.

1. The cavitating flow is a two-dimensional unsteady duct flow.
2. The vapor gas phase is produced by the phase change of the normal fluid.
3. The energy exchange between the liquid and gas phases is taken into account.

For construction of the cavitating flow characteristics in the present numerical model, it is assumed that the gas phase is homogeneously dispersed in the surrounding liquid phase and that the flow structure will form a bubbly flow.

Under the above conditions, the governing equations of the cavitating flow, taking into account the effect of superfluidity based on the unsteady two-dimensional multifluid model, are derived as follows.

The mass conservation equation for the gas phase is

$$\frac{\partial}{\partial t}(\alpha_g \rho_g) + \nabla_j(\alpha_g \rho_g u_g^j) = \Gamma_g \,. \tag{1}$$

The mass conservation equation for the liquid phase is

$$\frac{\partial}{\partial t}(\alpha_l \rho_l) + \nabla_j(\alpha_l J_l^j) = \Gamma_l \,, \tag{2}$$

where the relationship $(\alpha_g + \alpha_l = 1)$ is assumed, and the liquid phase density, ρ_l, must be comprised of a linear combination of the two components. The density is expressed by the sum of the normal fluid and superfluid components, and ρ_l is defined as follows:

$$\rho_l = \rho_{l(n)} + \rho_{l(s)} \,. \tag{3}$$

For the two-fluid model, it is assumed that the entire temperature dependence of liquid helium densities enters through the variation of the normal fluid density. It is therefore possible to write

$$\frac{\rho_{l(n)}}{\rho_l} = \begin{cases} \left(\dfrac{T_l}{T_{l\lambda}}\right)^{5.6} & \text{for } T_l \leqslant T_{l\lambda} \\ 1 & \text{for } T_l > T_{l\lambda} \,, \end{cases} \tag{4}$$

as the temperature dependence of the normal fluid density, [3]. Because of this strong temperature dependence, the He II constitutes about 99% of the superfluid component at 1.0 K. The total densities of the two components, namely, the superfluid and the normal fluid densities in control volume are conservative in the numerical calculation process. Also, the liquid-phase momentum

flux density $J_l^j(=\rho_l u_l^j)$ can be written as the sum of each normal fluid and superfluid momentum flux density component, defined as follows:

$$J_l^j=\rho_{l(s)}u_{l(s)}^j+\rho_{l(n)}u_{l(n)}^j. \tag{5}$$

The combined equation of motion for a total gas and normal fluid is

$$\frac{\partial}{\partial t}(\alpha_g\rho_g u_g^i+\alpha_l\rho_l u_{l(n)}^i)+\nabla_j(\alpha_g\rho_g u_g^i u_g^j+\alpha_l\rho_l u_{l(n)}^i u_{l(n)}^j)$$
$$=-g^{ij}\nabla_j p_l-\alpha_l\frac{\rho_l\rho_{l(s)}}{\rho_{l(n)}}S_l g^{ij}\nabla_j T_l-\alpha_l\frac{\rho_{l(s)}}{2}g^{ij}\nabla_j(u_{l(n)}^j-u_{l(s)}^j)^2$$
$$+\mu_T g^{jk}\nabla_j\nabla_k u_{l(n)}^i+\frac{1}{3}(\mu_T\nabla_j\nabla_k u_{l(n)}^k)g^{ij}+\alpha_l\rho_l g_r^i-\alpha_l F_{l(sn)}^i. \tag{6}$$

The combined equation of motion for a total gas and superfluid is

$$\frac{\partial}{\partial t}(\alpha_g\rho_g u_g^i+\alpha_l\rho_l u_{l(s)}^i)+\nabla_j(\alpha_g\rho_g u_g^i u_g^j+\alpha_l\rho_l u_{l(s)}^i u_{l(s)}^j)$$
$$=-g^{ij}\nabla_j p_l+\alpha_l\rho_l S_l g^{ij}\nabla_j T_l+\alpha_l\frac{\rho_{l(n)}}{2}g^{ij}\nabla_j(u_{l(n)}^j-u_{l(s)}^j)^2$$
$$+\alpha_l\rho_l g_r^i+\alpha_l F_{l(sn)}^i, \tag{7}$$

where the second terms on the right-hand side of Eqs. (6) and (7) denote the thermomechanical effect of the force based on the product of the entropy by the temperature gradient, and the third terms denote the effect of the momentum energy gradient based on the two-phase superfluid-normal fluid relative velocity caused by counterflow of the superfluid against the normal fluid. The terms mentioned above are peculiar to liquid helium with superfluidity, [3]. The signs of these terms in Eq. (6) are opposite those in Eq. (7); thus, the forces based on the superfluidity of Eq. (6) act in the direction opposite those of Eq. (7). In this calculation, because the vapor phase is assumed to be produced by the phase change of the normal fluid, the cavitating flow of the superfluid consists of the mixture flow of the vapor phase produced by the normal fluid and the superfluid. The term $F_{l(sn)}^i$ denotes the two-phase superfluid-normal fluid mutual friction interaction term based on the generation of vortex filaments in the superfluid, [7,15–17]. Additionally, μ_T in Eq. (6) denotes the viscosity of the two-phase mixture flow that includes small dispersed bubbles. μ_T was evaluated using the following formula by the viscosity of a suspension, [18,19]:

$$\mu_T=\left[1-\left(\frac{\alpha_g}{0.680}\right)\right]^{-2}\cdot\mu_{l(n)},\quad(\alpha_g<0.5), \tag{8}$$

Eq. (8) being mainly applicable in the small gas phase volume fraction region. Concerning the viscosity, the present numerical model assumes that superfluid viscosity $\mu_{l(s)}=0$ and that the dissipative interaction is due only to the normal fluid. This assumption corresponds to the physical fact that the superfluid experiences no resistance to flow and therefore no turbulence. The superfluid can flow through a duct without viscous drag along the boundaries. Equations (6) and (7) above are derived by complying the equations of momentum for both the gas and liquid phases.

To consider the effects of additional forces that act on the bubbles and radial expansion of the bubbles, the equation of motion for the gas phase is here replaced with the translational motion of a single bubble, [20]. Therefore, the Eulerian-Lagrangian two-way coupling model, [21], is applied to predict the two-dimensional cavitating flow characteristics. The viscous drag forces that act on the bubbles in the He II fluids are partially neglected because of the superfluidity.

The equation of motion for the gas phase is

$$\frac{4}{3}\pi\rho_g R_g^3\frac{du_g^i}{dt}=-F_p^i+F_g^i-F_D^i-F_{VM}^i-F_B^i+F_{LM}^i+F_{LS}^i, \tag{9}$$

where each additional force term is derived as follows:

$$F_p^i=\frac{4}{3}\pi R_g^3 g^{ij}\nabla_j p_l \tag{10}$$

$$F_g^i=\frac{4}{3}\pi R_g^3\rho_g g_r^i \tag{11}$$

$$F_D^i=\frac{1}{2}\rho_l C_D|u_g^i-u_l^i|(u_g^i-u_l^i)\pi R_g^2 \tag{12}$$

$$F_{VM}^i=C_{VM}\cdot\rho_l\frac{4}{3}\pi R_g^3\left[\frac{d}{dt}(u_g^i-u_l^i)+\frac{3}{R_g}(u_g^i-u_l^i)\frac{dR_g}{dt}\right] \tag{13}$$

$$F_B^i=6R_g^2\sqrt{\pi\rho_l\mu_l}\int_0^t\frac{\frac{d}{d\tau}(u_g^i-u_l^i)}{\sqrt{t-\tau}}d\tau \tag{14}$$

$$F_{LM}^i=\pi R_g^3\rho_l e^{ijk}(\Omega_{gj}-\Omega_{lj})(u_{gk}-u_{lk}) \tag{15}$$

$$F_{LS}^i=6.46\frac{\mu_l R_g^2}{\sqrt{|(\Omega_g^i-\Omega_l^i)|\,\nu_l}}e^{ijk}(\Omega_{gj}-\Omega_{lj})(u_{gk}-u_{lk}) \tag{16}$$

$$\Omega_l^i=\frac{1}{4}e^{ijk}(\nabla_j u_{lk}-\nabla_k u_{lj}), \tag{17}$$

where $u_l^i=J_l^i/\rho_l$, R_g is the equivalent bubble diameter, F_P^i is the force due to the liquid phase pressure gradient, F_g^i is the gravitational acceleration force, F_D^i is the drag force, F_{VM}^i is the virtual mass force considering the expansion of a bubble, and F_B^i is the Basset history term which takes into account the effect of the deviation in flow pattern from the steady state. F_{LM}^i is the Magnus lift force caused by the rotation of the bubble as reported by Auton et al. [22]. F_{LS}^i is Saffman's lift force, [23], caused by the velocity gradient of the liquid phase. C_D is the drag coefficient and C_{VM} is the virtual mass coefficient. d/dt denotes the substantial derivative.

The equation for the angular velocity of a bubble is derived as follows, [23]:

$$\frac{d\Omega_g^i}{dt}=\frac{15\mu_l}{R_g^2\cdot\rho_g}(\Omega_l^i-\Omega_g^i). \tag{18}$$

The energy equation for the gas phase is

$$\frac{\partial}{\partial t}(\alpha_g\rho_g e_g)+\nabla_j(\alpha_g\rho_g e_g u_g^j)=-p_g\frac{\partial\alpha_g}{\partial t}-\nabla_j(\alpha_g p_g u_g^j)+\Gamma_g h_g^{(i)}$$
$$+q_g^{(i)}a^{(i)}-\nabla_j(\alpha_g q_g^j)+\alpha_g\Phi_g. \tag{19}$$

The energy equation for the liquid phase is

$$\frac{\partial}{\partial t}(\alpha_l\rho_l e_l)+\nabla_j(\alpha_l\rho_l e_l u_l^j)=-p_l\frac{\partial\alpha_l}{\partial t}-\nabla_j(\alpha_l p_l u_l^j)+\Gamma_l h_l^{(i)}$$
$$+q_l^{(i)}a^{(i)}-\nabla_j(\alpha_l q_l^j)+\alpha_l\Phi_l. \tag{20}$$

In the above equations, $h_g^{(i)}$ and $h_l^{(i)}$ are the enthalpy of the gas phase and the liquid phase at the interface, respectively. $a^{(i)}$ is the interfacial area concentration. $\Gamma_g h_g^{(i)}$ and $\Gamma_l h_l^{(i)}$ are the interfacial energy transfer terms due to the liquid-vapor phase change. $q_g^{(i)}$ and $q_l^{(i)}$ are the heat transfer terms of mutual interaction between

the vapor and liquid interface. q^j is the contravariant heat flow vector and Φ is the energy dissipation function, as described below:

$$\begin{cases} q_m^i = -\lambda_m g^{ij} \nabla_j T_m, \\ \Phi_m = -\dfrac{2}{3}\mu_m (\nabla_i u_m^i)^2 + 2\mu_m s_{jm}^i s_{im}^j, \\ s_{jm}^i = \dfrac{1}{2}(\nabla_j u_m^i + \nabla_i u_m^j), \end{cases} \tag{21}$$

where subscript m denotes the gas phase ($m=g$) or liquid phase ($m=l$). In the condition of the He II state, Gorter-Mellink 1/3 power law, [3,6], is considered to formulate the expression for λ_l in Eq. (21) by the following equation.

$$\lambda_l = \left(\frac{f^{-1}(T_l)}{|\nabla_j T_l|^2} \right)^{1/3}, \tag{22}$$

where $f(T_l)$ is the He II heat conductivity function which exhibits strong temperature dependence, [3]. In Eqs. (19) and (20), the mutual friction dissipation term is neglected because the energy transfer terms between the gas and liquid phases become dominant to the mutual friction dissipation term.

Assuming that the mass of each vapor bubble and condensed liquid droplet in each computational cell is constant results in the following mass conservation equation for number density, N_k:

$$\frac{\partial}{\partial t}\left(\frac{4}{3}\pi R_k^3 N_k \rho_k \right) + \nabla_j \left(\frac{4}{3}\pi R_k^3 N_k \rho_k u_k^j \right) = \Gamma_k, \tag{23}$$

$$\begin{cases} k=e: & R_k = R_g, & N_k = N_g, & \rho_k = \rho_g, & u_k^i = u_g^i, & \Gamma_k = \Gamma_g \\ k=c: & R_k = R_l, & N_k = N_l, & \rho_k = \rho_l, & u_k^i = u_l^i, & \Gamma_k = \Gamma_l, \end{cases}$$

where subscript k denotes evaporation ($k=e$) or condensation ($k=c$).

These present governing equations of cavitating flow mentioned above are constructed by Eulerian-type equations for the liquid phase and Lagrangian-type equations for the gas phase.

2.2 Constitutive Equations. The drag coefficient, C_D, and the virtual mass coefficient, C_{VM}, are defined as follows, [23]:

$$C_D = \frac{24}{R_B}(1 + 0.15 R_B^{0.687}) + \frac{0.42}{1 + 42500 R_B^{-1.16}} \tag{24}$$

$$C_{VM} = 0.5 \tag{25}$$

$$R_B = \frac{\rho_l |u_g^i - u_l^i| D}{\mu_l}. \tag{26}$$

The energy balance condition through the gas and liquid phases interface is expressed by the following equation:

$$\Gamma_g h_g^{(i)} + q_g^{(i)} + \Gamma_l h_l^{(i)} + q_l^{(i)} = 0, \tag{27}$$

where the detailed constitutive equations for interfacial transfer terms in Eq. (27) are given by an empirical formula that is taken from the work of Dobran [24]. It is assumed that the energy transfer is caused by the heat transfer between the isothermal spherical bubble and the surrounding liquid. With an assumption of a spherical bubble with equivalent radius R_g, the expression of interfacial area concentration, [11], is obtained by $a^{(i)} = 3\alpha_g / R_g$. Assuming that the vapor gas phase follows an ideal gas law and that the relationship between gas phase pressure, p_g, and density, ρ_g, obeys polytropic change, the following equation by Hirt and Romero [25] results:

$$\rho_g(\kappa_g - 1) e_g = [p_g - c_0^2 \rho_l (\alpha_g^* - \alpha_g)] \alpha_g^*, \tag{28}$$

$$\begin{cases} \alpha_g \geqslant \alpha_{gc}: & \alpha_g^* = \alpha_g \\ \alpha_g < \alpha_{gc}: & \alpha_g^* = \alpha_{gc}, \end{cases}$$

where c_0 is the first sound velocity in liquid helium at the initial state ($c_0 = 236.1$ m/s) and α_{gc} denotes the threshold of void fraction ($\alpha_{gc} = 0.005$). The tables of the thermophysical properties of liquid helium by Maynard [26], Brooks and Donnelly [27], and McCarty [28] give the required physical properties of the liquid phase.

The constitutive equation for gas-phase generation density, Γ_g, is defined by the following equation:

$$\Gamma_g = \Gamma_{ge} - \Gamma_{gc}, \tag{29}$$

where Γ_{ge} and Γ_{gc} denote the gas-phase evaporation density and gas-phase condensation density, respectively. By introducing constitutive equations for Γ_{ge} and Γ_{gc}, we extend the classical nucleation theory for water droplets from subcooled vapor to cryogenic fluid. Namely, Γ_{ge} and Γ_{ge} are assumed to be proportional to the degree of subcooling and superheat and are expressed by the sum of the nucleation rate of the evaporated bubble or the condensed liquid droplet, [13,14]. The classical nucleation theory without quantum effect can be applied to the present numerical model because the temperature range which has been dealt with this calculation is about $T_l = 2.1$ to 2.3 K (near the λ point), [29,30].

2.3 Numerical Conditions and Procedure. To construct the numerical conditions for cavitating liquid helium flow, we refer to the previous experimental research on the cryogenic cavitating internal flow condition of liquid helium, [8,9]. The computational grid is generated referring to the geometry of a converging-diverging flow pipe which was used in a previous visualization measurement, [8]. The finite difference method is used to solve the set of governing equations mentioned above. In the present calculation, the discrete forms of these equations are semi-implicitly obtained using a staggered grid. The grid is concentrated at the nozzle wall to capture the cavitation inception precisely. Then a modified SOLA (numerical SOLution Algorithm for transient fluid flow) method of Tomiyama et al. [31], which is superior for the formulation and solution of a gas liquid two-phase flow problem, is applied for the numerical calculation. The Neumann-type boundary condition is considered in the iteration process of the pressure correction equation, and the effect of void fraction is implicitly taken into account in each iteration process, [21]. The liquid phase velocity, u_l^i, at the location of bubbles is calculated using an area-weighting interpolation method which was used in the SMAC algorithm by Amsden and Harlow [32].

To determine the boundary conditions, nonslip conditions for prescribed normal fluid velocities and free-slip conditions for prescribed superfluid velocities are applied to the sidewalls, A-D and B-C, in Fig. 1. Also, a fully developed velocity profile is applied for normal fluid velocities to the inlet cross-sectional area of the flow duct, A-B. A convective outflow condition is applied for normal fluid and superfluid velocities to the exit section of the duct, D-C. Adiabatic conditions are applied for thermal boundary conditions at the duct wall surface. The initial stationary condition of the liquid phase is assumed to be the pressurized He I state. Also, the initial conditions at the inlet section of the flow duct are as given in Table 1. For other physical properties used in constitutive equations, μ_l and S_l are given as functions of temperature, [26–28]. The constitutive equation for the two-phase heat transfer coefficient is given as a function of temperature based on the previous experimental results in Ref. [6].

The interval of each time-step is automatically adjusted during the computation to satisfy the CFL condition. We actually calcu-

Table 1 Conditions for numerical analysis

Inlet pressure	$p_{l(\mathrm{in})}$	0.20	MPa
Outlet pressure	$p_{l(\mathrm{ex})}$	0.101	MPa
Internal energy	$e_{l(\mathrm{in})}$	6.021	kJ/kg
Inlet width of duct	D	10.0	mm

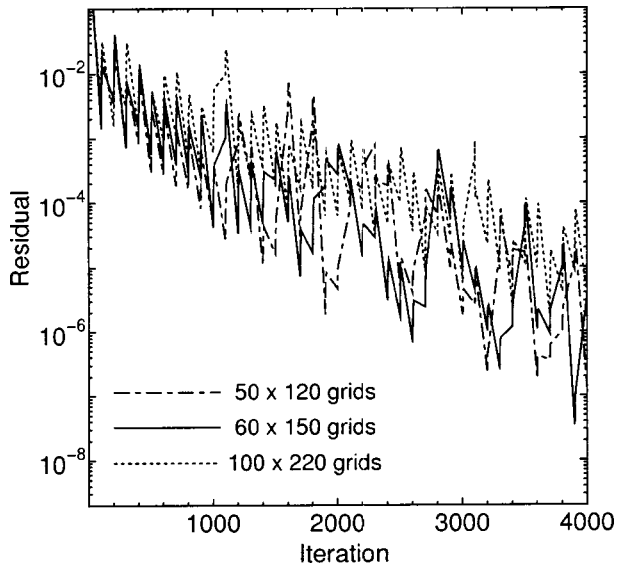

Fig. 2 Convergence history for three sets of grids

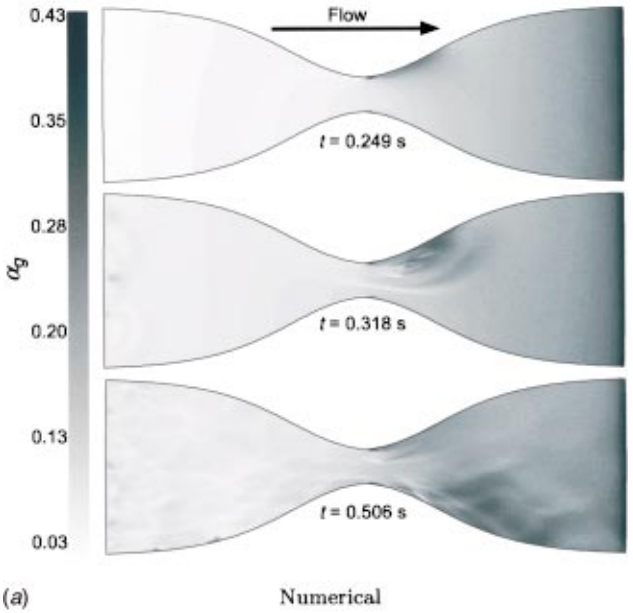

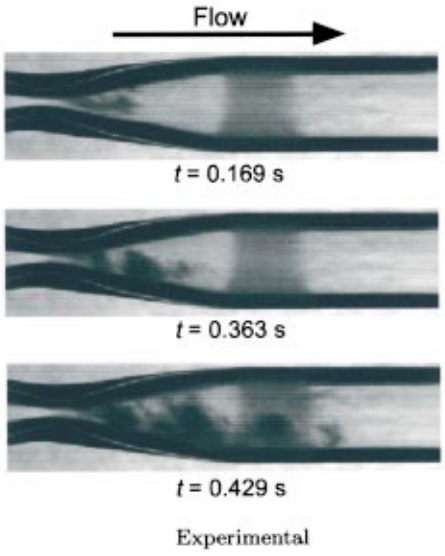

Fig. 3 Time evolution of void fraction distributions (direction of flow is left to right). (*a*) Present numerical results, (*b*) visualization measurement results (Initial measurement conditions: $p_{l(\mathrm{in})}=0.289$ MPa, $T_{l(\mathrm{in})}=4.50$ K, $p_{l(\mathrm{ex})}=0.130$ MPa).

lated solutions on three different grid densities: 50×120, 60×150, and 110×220 nodes. Figure 2 shows the convergence histories for three sets of computational grids. For all cases, the magnitude of the residuals decrease by at least two orders of magnitude within 4000 iterations. For a finer grid, convergences slow down, as expected. For all three grids, the iteration errors and uncertainties are assumed to be negligible in comparison with the grid errors. Since iterative errors are negligible, correction of solutions for iterative error is not required. As a result, we found that numerical results for all three grids show the same profiles, and the grid independence of the numerical results was confirmed. Thus, as a compromise between computer memory and accuracy, we chose to use the 60×150 grid in the ξ and η-directions for the calculations. The calculation is executed until an almost steady state of the cavitating flow is attained.

2.4 Results and Discussion. Figure 3 shows the numerical results of the transient evolution of the void fraction (α_g) contour, Fig. 4 shows the instantaneous liquid phase pressure (p_l) contour, and Fig. 5 shows the transient evolution of the liquid phase temperature (T_l) contour. The direction of flow is left to right. As shown by Fig. 3, when the exit section is opened instantaneously, pressurized liquid He I flows into the conversing section of the duct at high speed and is further accelerated by the decrease of the cross-sectional area, and p_l locally decreases in the nozzle throat section. It is clear that the phase change effectively occurs in the downstream of nozzle throat section and that a cloud cavity which consists of concentrated small bubbles is formed in the wall surface vicinity of the throat section. In addition, it is found that the cloud cavity is especially formed and grows on the upper wall surface of the diverging throat section due to the influence of the buoyancy which acts on the bubbles and the shear force which simultaneously acts on the bubbles in contact with the wall. Because the buoyancy acts on the bubbles, there is a tendency for the bubbles to migrate and aggregate on the upper wall surface. Thus, the void fraction profiles become asymmetric. As time t elapses, cavitation inception effectively occurs and the cloud cavity grows alongside the passage wall surface. When the magnitude of the cavity is above a certain size, the cavity is detached from the cloud, and it remains in the high volume fraction region as the gas phase moves downstream. Furthermore, with the elapse of time, the cloud cavity accompanying evaporation and condensation exhibits convective and dissipative behavior downstream of the diverging nozzle throat, and the gas phase spreads throughout the inner flow duct because of the decrease in the slip ratio and the gas phase velocity resulting from the sudden change of both longitudinal and transverse pressure gradients. As a result, it is found that a homogeneous profile of α_g is formed over the downstream duct.

As shown by Figs. 3 and 4, the void fraction α_g has a large value in the region where it is close to the cavity center, because the pressure gradient in the cloud cavity has a distribution which becomes negative from the contour of the cavity toward the center, and because the ratio where the bubbles accumulate increases as the position approaches the cavity center. Additionally, the expansion effect of bubbles becomes larger. Furthermore, in the region of the high volume fraction of the gas phase, the pressure distribution changes markedly because of the normal fluid-superfluid transition due to the momentum terms in Eqs. (6) and (7) that include the thermomechanical effect term, the momentum energy gradient term based on relative superfluid-normal fluid velocity, and the superfluid-normal fluid mutual friction interaction

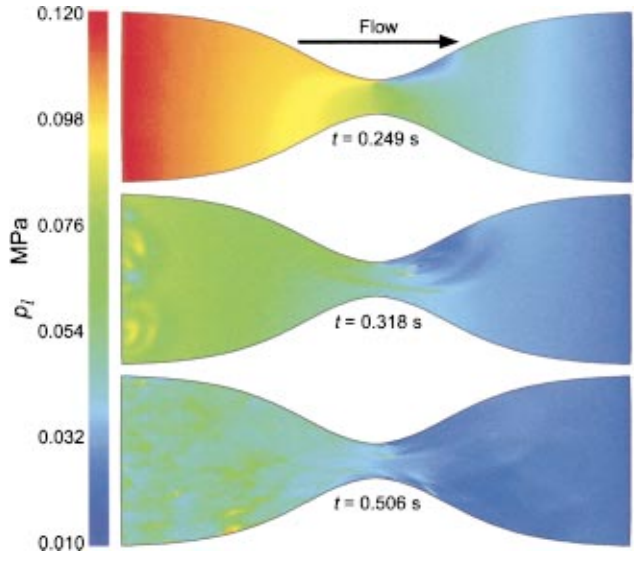

Fig. 4 Instantaneous liquid phase pressure contours (direction of flow is left to right)

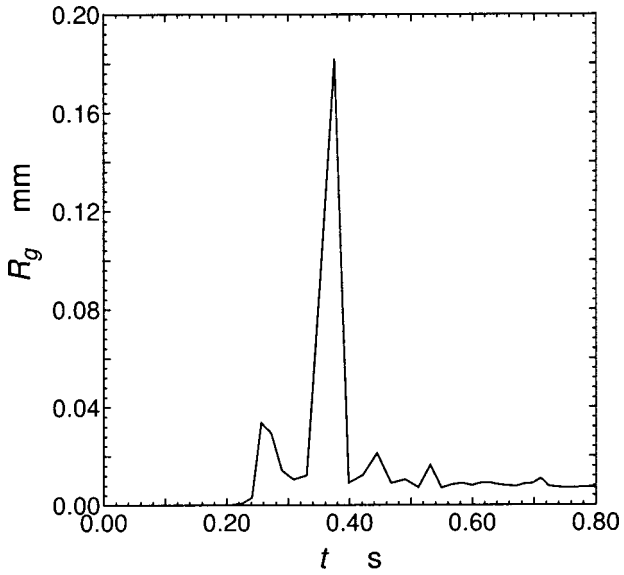

Fig. 6 Fluctuations of bubble radius as a function of time

term. In this numerical calculation, it is assumed that the existence of the large gas-phase volume fraction region indicates that the small size bubbles shown in Fig. 6 constitute a closely aggregated region and that the downstream flow state maintains a very closed bubbly flow in the large void fraction region. The bubbles are concentrated toward the center of the vortex due to the negative pressure gradient in the vortex.

Next, to confirm the validity of the numerical results, the present results on the void fraction profile are compared with the previous visualization measurement of cavitating flow of liquid He in a converging-diverging pipe which has the same geometry as that of the present computational nozzle shape, [8]. The initial conditions for this experiment are generally similar to the present numerical condition. However, because the experiment is conducted making use of only vacuum insulation, initial temperature of the working fluid is considered to be higher than the λ point, and quantitative comparison with the present result is difficult. According to these results, it is both numerically and experimentally found that cavitation inception occurs on the upper wall surface of throat. It is also found that the numerical results of the detachment and development of the cloud cavity, diffusion of the gas phase, and the time-dependent profiles of void fraction show qualitative agreement with the results of the visualization measurement.

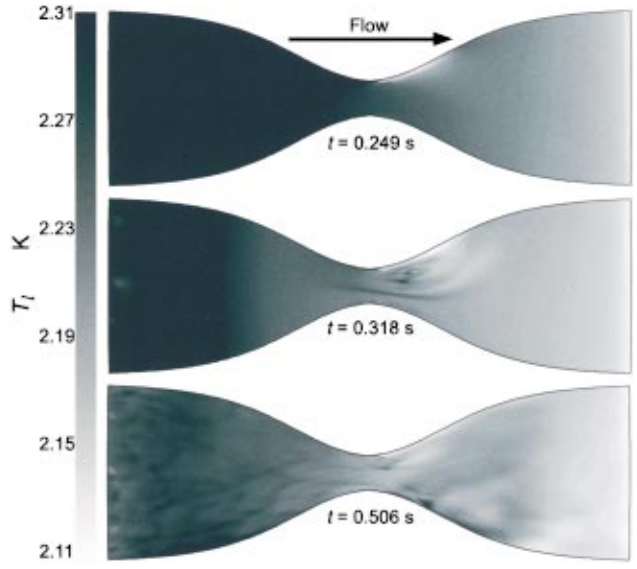

Fig. 5 Time evolution of liquid phase temperature profiles (direction of flow is left to right)

Focusing on Figs. 3 and 5, in the large α_g region in the vicinity of the wall surface from the position of the cloud cavity contour downstream of the throat where the vapor phase change actively occurs, it is found that the phase transition from He I to He II is generated (λ transition) and that it conspicuously exhibits the characteristics of superfluidity. The effect of superfluidity with He I to He II phase transition is mainly caused by the decrease in liquid phase temperature or internal energy due to the deprivation of latent heat for vaporization from the liquid phase and to the change of the specific heat of the liquid phase with the change of pressure gradient. From Fig. 5, it is especially found that the temperature around the interface between the large gas-phase volume fraction region and the liquid-phase region decreases with the increase in the phase change. The liquid-phase temperature decrease due to the latent heat or the energy exchange between liquid and vapor phase in the vaporization process is characterized by the interfacial energy transfer terms with the phase change in Eqs. (19) and (20). With time, the profile of the liquid phase temperature T_l gradually becomes homogeneous due to the effect of temperature diffusion and gas phase condensation. The tendencies of those numerical results for temperature decrease with the He I to He II phase transition show qualitative agreement with the experimental datum on the He I cavitation in the saturated condition by Ishii and Murakami [9].

Figure 6 shows the fluctuation of bubble radius, R_g, as a function of the time at position E (as depicted in Fig. 1) just downstream of the nozzle throat, where the cavitation actively occurs. From Figs. 3–6, it is clarified that the decrease of p_l induces an increase of α_g and that the expansion or contraction of bubble radius R_g corresponds to the change of p_l. However, the displacement magnitude of R_g has a small value. Thus, it is also clarified that the generated cavitation bubbles maintain a small size in the vaporization process and in the initial cavitating flow state.

Figures 7 and 8 show profiles of the liquid-phase normal fluid velocity component $u^i_{l(n)}$ and the superfluid velocity component $u^i_{l(s)}$ around the nozzle throat, respectively. The flow separation and backward flow of $u^i_{l(n)}$ locally occur in the vicinity of the wall of the throat section upstream of the cavitation inception point.

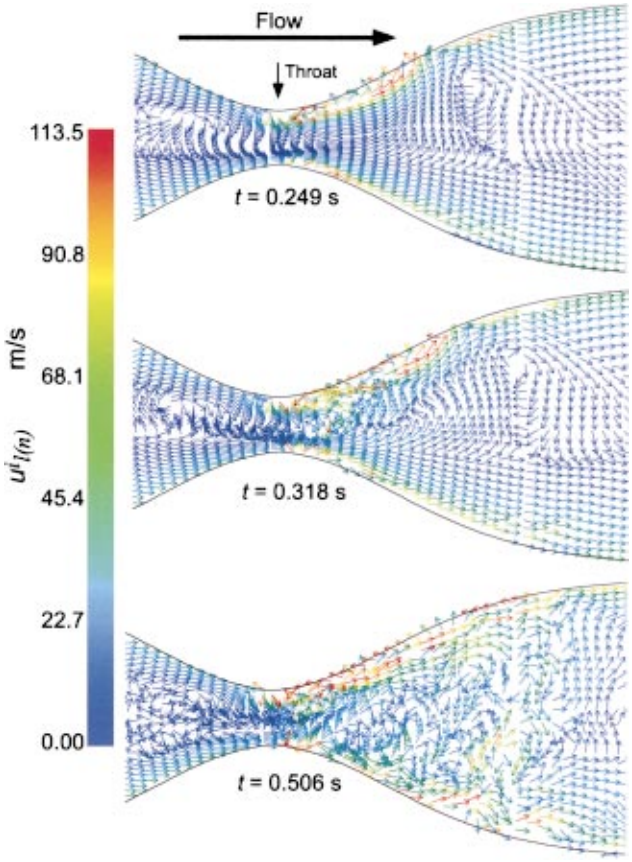

Fig. 7 Instantaneous normal fluid velocity vector (direction of flow is left to right)

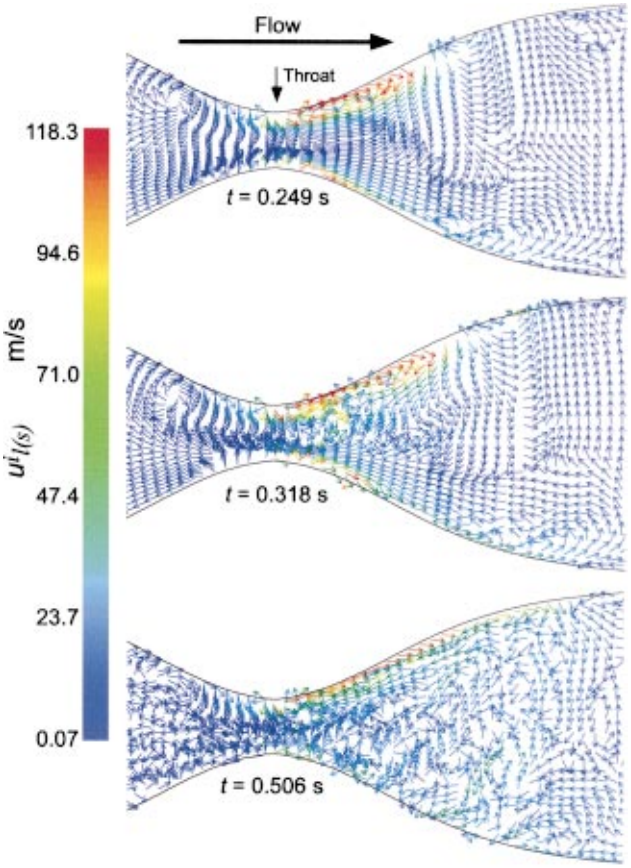

Fig. 8 Instantaneous superfluid velocity vector (direction of flow is left to right)

From comparison of Figs. 7 and 8 with Figs. 3 and 5, superfluid counterflow against the normal fluid flow is conspicuously found in the large void fraction region where the vaporization with He II phase transition actively occurs, especially in the region close to the center of the cloud cavity. The magnitude of $u^i_{l(n)}$ and $u^i_{l(s)}$ locally increases in the region where the cavitation is actively generated because of the increase in momentum exchange between the gas and liquid phases. With elapse of time t, vortices of normal fluid and superfluid are formed and advected downstream of the throat. Due to slight viscosity of normal fluid, the vortices are slightly different in shape. The superfluid counterflow against normal fluid is mainly caused by the momentum terms in Eqs. (6) and (7), i.e., the temperature gradient term (thermomechanical effect), and the momentum energy gradient term for superfluid-normal fluid relative velocity.

Figure 9 shows the local velocity fluctuations of normal fluid and superfluid as a function of the time at position E. Although the superfluid component is not generated in the initial flow condition, with the elapse of time, the superfluid counterflow whose direction of flow is opposite that of normal fluid is generated at the time of λ transition. When the flow state approaches the steady state, the magnitude of the superfluid velocity component decreases due to the suppression of the unsteady generation of cavity.

Figure 10 shows the instantaneous gas phase velocity u^i_g around the nozzle throat. In the initial flow state, it is found that the backward flow of u^i_g is generated upstream of the throat due to the effect of the separation wake of normal fluid in the vicinity of the throat wall. In addition to the formation of the cavity vortex and its growth, advection of the cavity cloud is found in the downstream region of the throat. With time, the gas-phase motion exhibits diffusing behavior, and the u^i_g profile takes on a different aspect from the liquid phase velocity profiles. The characteristic gas phase behavior in superfluid is not only due to the several additional forces based on Eq. (9), but also to the thermomechanical effect and other forces that act on the bubbles due to the superfluid generation based on the momentum terms in Eqs. (6) and (7). According to the numerical results on gas-phase behavior, it is clarified that the precise control of bubble motion and the superfluid multiphase flow state is possible by effective use of the characteristic effect of superfluidity such as the thermomechanical effect.

3 Conclusion

The two-dimensional characteristics of the cavitating flow of liquid helium in a converging-diverging nozzle near the λ point were numerically investigated to realize the further development and high performance of a superfluid cooling system or new cryogenic engineering applications. First, the governing equations of the cavitating flow of liquid helium based on the unsteady multifluid model were presented and several flow characteristics were numerically calculated, taking into account the effect of superfluidity. The main results obtained can be summarized as follows.

1. When the cavitation of He I is generated, the characteristics of superfluidity with λ transition are conspicuously found surrounding the cloud cavity and in the large gas-phase volume fraction region where the unsteady cavitation actively occurs. Also, the effect of superfluidity with He I to He II phase transition is mainly due to the decrease in liquid-phase temperature or internal energy due to the deprivation of latent heat for vaporization from the liquid phase.
2. The generation of the superfluid counterflow against normal fluid caused by the momentum terms based on superfluidity was

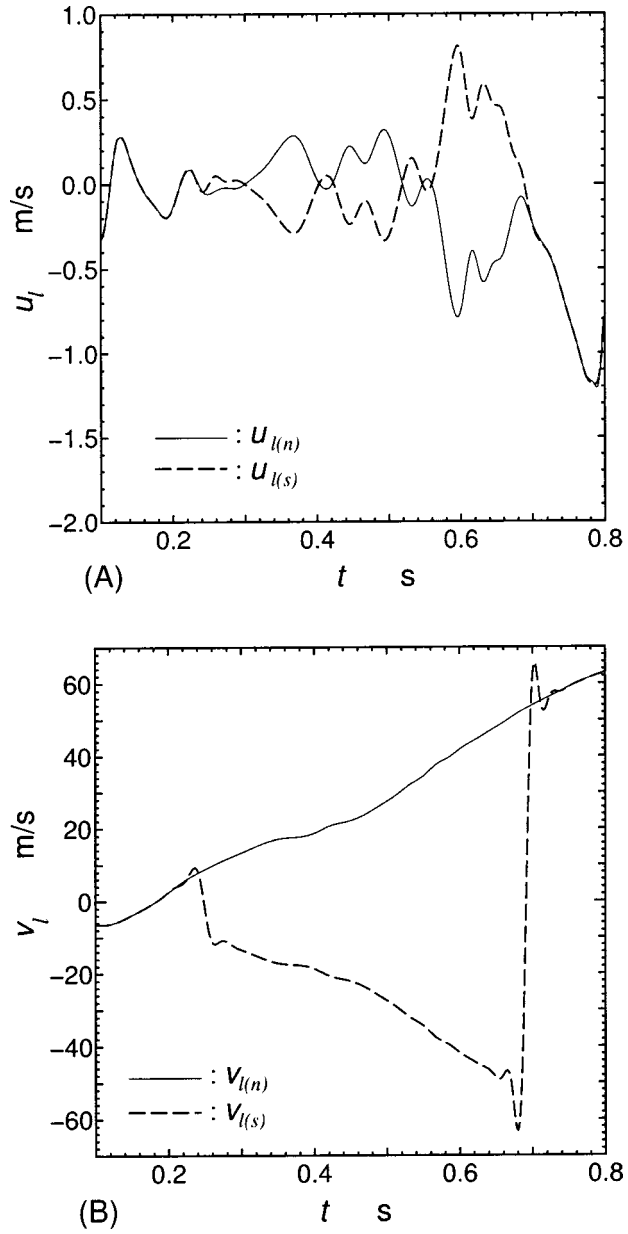

Fig. 9 Normal fluid and superfluid velocity fluctuations as a function of time; (*a*) ξ-direction component, (*b*) η-direction component

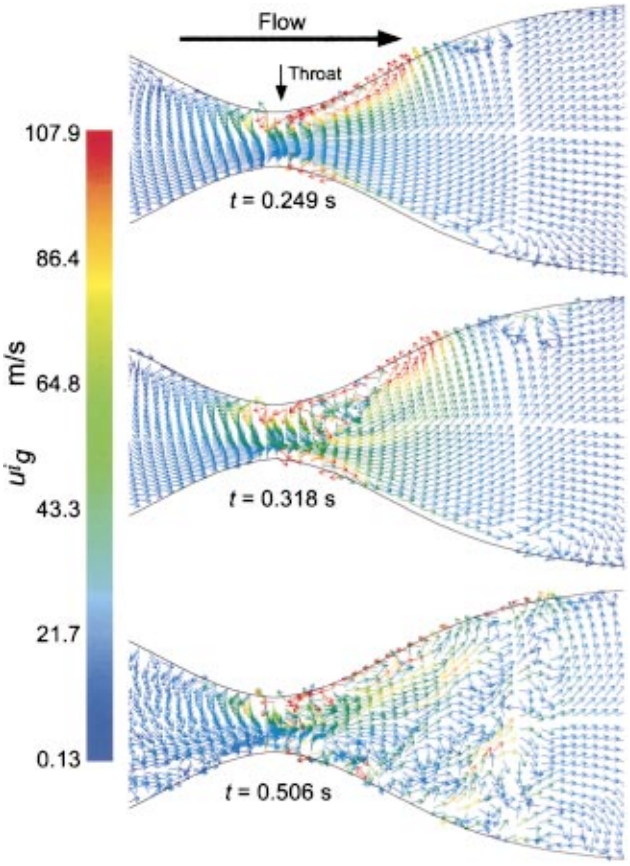

Fig. 10 Instantaneous gas phase velocity vector (direction of flow is left to right)

conspicuously found when the vaporization with He I to He II phase transition occurs. Furthermore, it was found that the gas-phase diffusion behavior with time was dominated not only by several additional forces in the gas-phase momentum equation, but also by the thermomechanical effect and the other forces that act on the bubbles due to the generation of superfluid.

Acknowledgments

The authors would like to thank Prof. Masahide Murakami (University of Tsukuba, Japan) for his helpful discussions. This work was supported by a Grant-in-Aid for Scientific Research (C. No. 13750131) from the Ministry of Education, Science and Culture, Japan.

Nomenclature

D = inlet width of duct
e = specific internal energy
e^{ijk} = permutation symbol
g_r^i = contravariant vector of gravitational acceleration
g^{ij} = fundamental metric tensor
h = specific enthalpy
J = momentum flux density
N = number density
p = absolute pressure
R = radius
S = specific entropy
T = absolute temperature
t = time
u = velocity component in the ξ-direction
u^i, u^j = contravariant velocity
v = velocity component in the η-direction
α = volume fraction
Γ = phase generation density
η = longitudinal coordinate
κ = ratio of specific heat
λ = thermal conductivity
μ = dynamic viscosity
ν = kinematic viscosity
ξ = transverse coordinate
ρ = density
Ω^i = contravariant angular velocity vector
∇_j = covariant differential

Subscripts

$( )_{(ex)}$ = exit section of the duct
$( )_g$ = gas phase
$( )^i$, $( )^j$, $( )^k$ = contravariant component
$( )_i$, $( )_j$, $( )_k$ = covariant component
$( )^{(i)}$ = interface
$( )_{(in)}$ = inlet section of the duct
$( )_l$ = liquid phase
$( )_{(n)}$ = normal fluid
$( )_{(s)}$ = superfluid
$( )_\lambda$ = lambda point

References

[1] Filina, N. N., and Weisend, J. G., 1996, *Cryogenic Two-Phase Flow*, Cambridge University Press, New York, pp. 20–76.
[2] Barron, R. F., 1999, *Cryogenic Heat Transfer*, Taylor & Francis, Philadelphia, PA, pp. 143–213.
[3] Van Sciver, S. W., 1996, *Helium Cryogenics*, Plenum Press, New York, pp. 77–130.
[4] Kamijo, K., Yoshida, M., and Tsujimoto, Y., 1993, ''Hydraulic and Mechanical Performance of LE-7 LOX Pump Inducer,'' AIAA J. Propul. Power, **9**(6), pp. 819–826.
[5] Daney, D. E., 1988, ''Cavitation in Flowing Superfluid Helium,'' Cryogenics, **28**, pp. 132–136.
[6] Van Sciver, S. W., 1999, ''Heat and Mass Transfer Process in Two Phase He II/Vapor,'' Cryogenics, **39**, pp. 1039–1046.
[7] Ishimoto, J., Oike, M., and Kamijo, K., 2001, ''Numerical Analysis of Two-Phase Pipe Flow of Liquid Helium Using Multi-Fluid Model,'' ASME J. Fluids Eng., **123**, pp. 811–818.
[8] Oike, M., Tokumasu, T., and Kamijo, K., 2001, ''Observation of Helium Two-Phase Flow in a Pipe,'' *Proceedings of the Fourth International Symposium on Cavitation*, C. E. Brennen, ed., Pasadena, CA (in CD-ROM).
[9] Ishii, T., and Murakami, M., 2002, ''Temperature Measurement and Visualization Study of Liquid Helium Cavitation Flow Through Venturi Channel,'' Adv. Cryog. Eng., **47B**, pp. 1421–1428.
[10] Tien, C. L., Majumdar, A., and Gerner, F. M., 1998, *Microscale Energy Transport*, Taylor & Francis, Washington, DC, pp. 187–226.
[11] Kataoka, I., and Serizawa, A., 1989, ''Basic Equations of Turbulence in Gas-Liquid Two-Phase Flow,'' Int. J. Multiphase Flow, **15**(5), pp. 843–855.
[12] Harlow, F. H., and Amsden, A. A., 1975, ''Numerical Calculation of Multiphase Fluid Flow,'' J. Comput. Phys., **17**, pp. 19–52.
[13] Yamamoto, S., Hagari, H., and Murayama, M., 2000, ''Numerical Simulation of Condensation Around the 3-D Wing,'' Trans. Japan Soc. Aero. Space Sci., **42**(138), pp. 182–189.
[14] Young, J. B., 1992, ''Two-Dimensional, Nonequilibrium, Wet-Stream Calculations for Nozzles and Turbine Cascades,'' ASME J. Turbomach., **114**, pp. 569–579.
[15] Barenghi, C. F., Donnelly, R. J., and Vinen, W. F., 1983, ''Friction on Quantized Vortices in Helium II: A Review,'' J. Low Temp. Phys., **52**, pp. 189–247.
[16] Bekarevich, I. L., and Khalatnikov, I. M., 1961, ''Phenomenological Derivation of the Equations of Vortex Motion in Helium II,'' Sov. Phys. JETP, **13**(3), pp. 643–646.
[17] Kashani, A., Van Sciver, S. W., and Strikwerda, J. C., 1989, ''Numerical Solution of Forced Convection Heat Transfer in He II,'' Numer. Heat Transfer, Part A, **16**, pp. 213–228.
[18] Cross, M. M., 1975, ''Viscosity-Concentration-Shear Rate Relations for Suspensions,'' Rheol. Acta, **14**, pp. 402–403.
[19] Tomiyama, A., Zun, I., Higaki, H., Makino, Y., and Sakaguchi, T., 1997, ''A Three-Dimensional Particle Tracking Method for Bubbly Flow Simulation,'' Nucl. Eng. Des., **175**, pp. 77–86.
[20] Fan, L. S., and Zhu, C., 1998, *Principles of Gas-Solid Flows*, Cambridge University Press, New York, pp. 87–129.
[21] Murai, Y., and Matsumoto, Y., 2000, ''Numerical Study of the Three-Dimensional Structure of a Bubble Plume,'' ASME J. Fluids Eng., **122**, pp. 754–760.
[22] Auton, T. R., Hunt, J. C. R., and Prud'homme, M., 1988, ''The Force Exerted on a Body in Invisid Unsteady Non-Uniform Rotational Flow,'' J. Fluid Mech., **197**, pp. 241–257.
[23] Clift, R., Grace, J. R., and Weber, M. E., 1978, *Bubbles, Drops, and Particles*, Academic Press, San Diego, CA, pp. 97–141.
[24] Dobran, F., 1988, ''Liquid and Gas-Phase Distributions in A Jet With Phase Change,'' ASME J. Heat Transfer, **110**, pp. 955–960.
[25] Hirt, C. W., and Romero, N. C., 1975, ''Application of a Drift Flux Model to Flashing in Straight Pipes,'' Los Alamos Scientific Laboratory Report, LA-6005-MS, pp. 1–16.
[26] Maynard, J., 1976, ''Determination of the Thermodynamics of He II from Sound-Velocity Data,'' Phys. Rev. B, **14**(9), pp. 3868–3891.
[27] Brooks, J. S., and Donnelly, R. J., 1977, ''The Calculated Thermodynamic Properties of Superfluid Helium-4,'' J. Phys. Chem. Ref. Data, **6**(1), pp. 51–104.
[28] McCarty, R. D., 1980, ''Thermodynamic Properties of Helium II from 0 K to the Lambda Transitions,'' NBS Technical Note, TN-1029.
[29] Lambaré, H., Roche, P., Balibar, S., Maris, H. J., Andreeva, O. A., Guthmann, C., Keshishev, K. O., and Rolley, E., 1998, ''Cavitation in Superfluid Helium in the Low Temperature Limit,'' Eur. Phys. J. B, **2**, pp. 381–391.
[30] Caupin, F., and Balibar, S., 2001, ''Cavitation Pressure in Helium,'' Phys. Rev. B, **B64**, 064507.
[31] Tomiyama, A., Hirano, M., 1994, ''An Improvement of the Computational Efficiency of the SOLA Method,'' JSME Inter. J. Series B, **37**(4), pp. 821–826.
[32] Amsden, A. A., and Harlow, F. H., 1970, ''The SMAC Method: A Numerical Technique for Calculating Incompressible Fluid Flows,'' Los Alamos Scientific Laboratory Report, LA-4370.

A Cavity Wake Model Based on the Viscous/Inviscid Interaction Approach and Its Application to Nonsymmetric Cavity Flows in Inducers

Yury Semenov[1]
e-mail: relcom@semenov.dp.ua

Yoshinobu Tsujimoto
e-mail: tujimoto@me.es.osaka-u.ac.jp

Osaka University,
Engineering Science,
1-3 Machikaneyama,
Toyonaka 560-8581, Osaka, Japan

A cavity wake model based on the flow interaction between the viscous wake behind the cavity and external inviscid cavity flow is proposed. The conditions of interaction between viscous and inviscid flows make it possible to obtain a unique solution of the problem. The viscous wake model is formulated within the theory of boundary layers. The problem for the external inviscid flow is considered in both nonlinear and linear formulation. The developed cavity wake model provides reasonable agreement with experimental data for cavitation performance and cavitation compliance over a wide range of cavitation numbers from cavitation inception to the super cavity flow. The cavity model is applied to predict nonsymmetric flows in inducers with two and more blades. The regions of nonsymmetric cavity flow are compared with those in experiments. It is found that the local head decrease of an inducer might be caused by the nonsymmetric cavity patterns. The predicted regions of a steady nonsymmetric cavity flow correlate with the region of cavitation instability observed in experiments. [DOI: 10.1115/1.1598990]

1 Introduction

It is well known that alternate blade cavitation in which the cavity length differs alternately can occur for inducers with even number of blades, [1]. Recently, this type of cavitation was observed by Bernardi et al. [2] and Yoshida et al. [3] for four-bladed inducers. With further decrease of the inlet pressure the alternate blade cavitation becomes unstable, [3–5], and rotating cavitation appears. For three-bladed inducers, rotating cavitation first appears followed by nonsymmetric steady cavitation pattern called ''uneven attached cavitation,'' [4]. Almost all analytical studies of cavity flows in inducers are aiming at the prediction of the symmetric cavity patterns and based on the theory of the potential flow. Recently, Horiguchi et al. [6] succeeded in predicting alternate blade cavitation using a closed cavity model but the uneven attached cavitation cannot be predicted by the closed cavity model.

The theory of free streamline flows has a cavity closure problem which requires various assumptions in the cavity closure region, [7–13]. Some of the cavity closure schemes, such as opened cavity models, can simulate approximately a wake behind the cavity. Stripling and Acosta [14] have applied the Joukowsky-Roshko scheme in which the cavity is closed on the flat plate which is parallel to the blade. Devis et al. [15] have assumed that the cavity is closed on the flat plate inclined with the angle 2.8 deg to the blade. For developed cavity flows Wu [13] proposed a scheme in which the cavity contours are connected to a wake with two parallel curves. In these wake models, the viscous properties of the fluid and the influences on the flow characteristics have not been taken into consideration.

The flow viscosity manifests itself in the two-phase turbulent cavity wake behind the cavity, [16], and influences the energy loss and inducer head. It is clear that the pressure balance between the inducer inlet and outlet should be satisfied for a nonsymmetric cavity flow. In order to predict the flow parameters at the outlet of the cascade, it is important to take the real properties of the fluid into consideration. In this connection, the present work focuses on both developing a cavity-wake model and studying nonsymmetrical cavity flows in inducers.

The concept of viscous/inviscid interaction proposed by Crocco and Lees [17] for separated turbulent flows is extended for cavitating flows. According to this concept, the flow region is divided into two subregions: the viscous two-phase wake region and the external inviscid flow region. These subregions are connected to each other by interaction conditions which provide a unique solution of the problem. Such idealization for high Reynolds number flows allows one to distinguish each specific region and use appropriate methods for solving the problems of inviscid and viscous flows, instead of solving the complete Navier-Stokes equations. In the wake subregion the problem is formulated within the theory of boundary layers. To solve the problem of the external inviscid flow we can use well-developed methods of the free streamline theory.

In order to identify the features of the flow behind the cavity, a nonlinear formulation of the external problem is employed for symmetric inducer flows. The external problem of the nonsymmetric cavity flow is solved within the linear theory using the method of singular integral equations, [18].

Owing to the complexity of the two-phase flow behind the cavity, it is necessary to make a series of substantial assumptions and introduce several empirical coefficients characterizing the turbulence and density of the two-phase flow. The model developed is applied to analyze various experimental data on cavitating inducers using a unique set of values for the empirical factors, to show the validity of the present model.

In real inducers the flow is three-dimensional with tip leakage cavitation and backflow cavitation. These effects cannot be taken into account in the two dimensional approach and we cannot expect quantitative agreement with experiments. So, the ultimate goal of the present study is to analyze the asymmetric cavitation

[1]On leave from the Institute of Technical Mechanics of the NAS and NSA of Ukraine, 15 Leshko-Popel' St., Dniepropetrovsk, 49005, Ukraine.

Contributed by the Fluids Engineering Division for publication in the JOURNAL OF FLUIDS ENGINEERING. Manuscript received by the Fluids Engineering Division May 21, 2002; revised manuscript received March 15, 2003. Associate Editor: S. L. Ceccio.

such as alternate blade cavitation and attached uneven cavitation within the framework of two-dimensional flow analysis.

The blade cavitation in inducers is accompanied by tip clearance cavitation and radial flows, [7]. The two-dimensional approach used in the present study fails to predict three-dimensional phenomena but provides prediction of such phenomena as alternate blade cavitation, attached uneven cavitation, and various types of cavitation instabilities.

2 Cavity Wake Model and Outer Inviscid Flow

The flow region shown in Fig. 1(*a*) is divided into the subregion **OKFF′TGH** of the internal turbulent flow and the subregion of the external inviscid flow outside the free boundaries **OD** and **TD′**. The tangential velocity of the inviscid flow on the boundaries **OD** and **TD′** should be equal to the velocity on the outer boundaries of the viscous flow **OKF** and **TF′**, respectively. The shape of boundaries **OKF** and **TF′** is determined from the calculation of the external inviscid flow.

Although the cavity wake is unsteady in its nature, we use a time-averaged flow to predict the steady performance of an inducer. The wake is treated by using integral relations for boundary layers, [17,19].

As shown in Fig. 1, the shape of the pressure side of the profile, $y_b(x)$, the blade thickness $\theta(x)$, the cascade spacing h and the stagger $\pi/2-\beta^*$, the inflow velocity v_1 and the angle of attack α are specified. The shape of the boundaries of interaction **OD**, $y_\delta^{up}(x)$, **TD′**, $y_\delta^{lw}(x)$ and the tangential velocity on them, $v_\delta(x)$, are determined by using the iteration process of coupling the viscous and inviscid flows as sketched in Fig. 2. For $0<x<C$ the lower boundary $y_\delta^{lw}(x)$ is given by $y_\delta^{lw}(x)=y_b(x)+\theta(x)$.

Based on the boundary layer assumptions the pressure gradient across the wake is assumed to be zero. From Bernoulli's equation, it follows that the tangential velocity on the boundary **TD′** is equal to the tangential velocity on the boundary **OD** at the same coordinate x in the wake region.

The inviscid flow is solved with the given tangential velocity $v_\delta(x)$ determined from the viscous flow analysis along the boundaries of interaction **OD** and **TD′**. The viscous flow in the wake is solved with the given boundary **OD**, $y_\delta^{up}(x)$, and **TF′**, $y_\delta^{lw}(x)$, determined from the inviscid flow analysis.

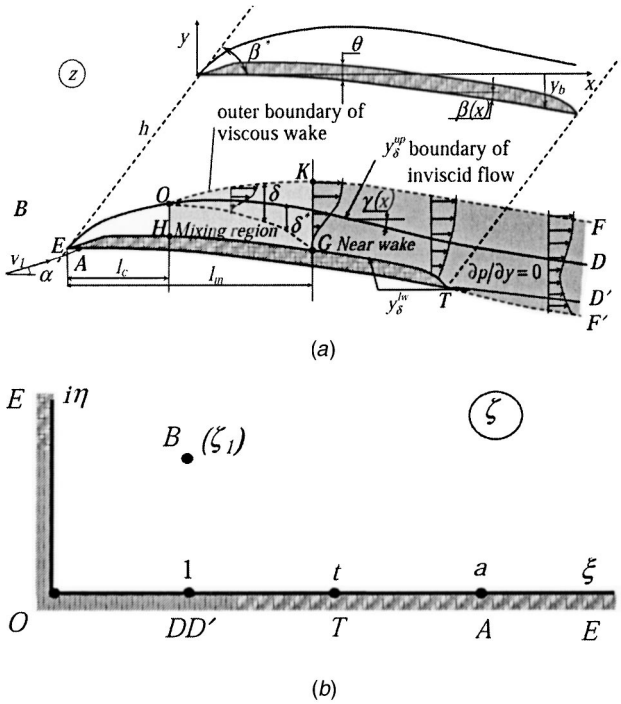

Fig. 1 (*a*) **Model of the cavity flow with viscous wake;** (*b*) **parameter domain**

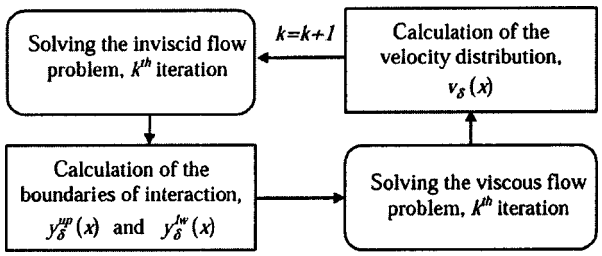

Fig. 2 Procedure of coupling the viscous and inviscid flow

2.1 External Inviscid Flow. The expressions of the complex conjugate velocity and the derivative of complex potential can be found by using Chaplygin's singular points method described by Gurevich [20] and its extension for curvelinear bodies, [21]. The correspondence between specific points in the physical plane z and those in the parameter domain ζ is shown in Fig. 1(*b*) with the same symbols. The final expressions for the complex conjugate velocity, dW/dz, and the derivative of the complex potential, $dW/d\varsigma$ have the following form:

$$\frac{dW}{dz}=-v_0\left(\frac{\varsigma-a}{\varsigma+a}\right)\exp\left[\frac{1}{\pi}\int_0^t\frac{d\gamma}{d\xi}\ln\left(\frac{\xi-\varsigma}{\xi+\varsigma}\right)d\xi+\frac{1}{\pi}\int_t^\infty\frac{d\beta}{d\xi}\ln\left(\frac{\xi-\varsigma}{\xi+\varsigma}\right)d\xi+i\gamma_0\right], \tag{1}$$

$$\frac{dW}{d\varsigma}=N\frac{\varsigma(\varsigma^2-a^2)}{(\varsigma^2-\varsigma_1^2)(\varsigma^2-\bar{\varsigma}_1^2)(\varsigma^2-1)}. \tag{2}$$

Here, v_0 is the velocity on the cavity surface, N is a scale factor, $\beta(\xi)$ is the slope of the blade $\beta(x)=dy_b/dx$ represented as a function of the coordinate ξ in the parameter domain, $\gamma(\xi)$ is the slope of the upper and lower free boundaries of the inviscid flow **OD** and **TD′**, $\gamma(\xi)=\gamma_{up}[x(\xi)]$, for $0\leqslant\xi\leqslant1$ and $\gamma(\xi)=\gamma_{lw}[x(\xi)]$, for $1\leqslant\xi\leqslant t$; $\gamma_0=\gamma(0)$, $\gamma_{up}(x)=dy_\delta^{up}/dx$, $\gamma_{lw}(x)=dy_\delta^{lw}/dx$.

The condition for the velocity at the upstream infinity, $v_1e^{-i\alpha}$, and the cascade periodicity, $he^{i\beta^*}$ are used to determine the values of parameters ζ_1, a, and N. These conditions are represented by

$$v_1e^{-i\alpha}=-v_0\left(\frac{\varsigma_1-a}{\varsigma_1+a}\right)\exp\left[\frac{1}{\pi}\int_0^t\frac{d\gamma}{d\xi}\ln\left(\frac{\xi-\varsigma_1}{\xi+\varsigma_1}\right)d\xi+\frac{1}{\pi}\int_t^\infty\frac{d\beta}{d\xi}\ln\left(\frac{\xi-\varsigma_1}{\xi+\varsigma_1}\right)d\xi+i\gamma_0\right], \tag{3}$$

$$he^{i\beta^*}=\oint_{\varsigma=\varsigma_1}\frac{dz}{d\varsigma}d\varsigma=\pi i\frac{N}{v_1}\frac{(\varsigma_1^2-a^2)\exp(i\alpha)}{(\varsigma_1^2-\bar{\varsigma}_1^2)(\varsigma_1^2-1)}. \tag{4}$$

The slope of the blade $\beta(x)$ is given in the physical plane. The function $\beta(\xi)$ in the parameter plane should be determined from

$$\frac{d\beta}{d\xi}=\frac{d\beta}{dx}\frac{dx}{d\xi}. \tag{5}$$

Since $dx/d\xi=\mathrm{Re}(dz/d\varsigma|_{\varsigma=\xi})$, $dz/d\varsigma=dW/d\varsigma 1/dW/dz$, dW/dz and $dW/d\varsigma$ are given by Eqs. (1) and (2) that include $(d\beta/d\xi)$, Eq. (5) gives an integro-differential equation in terms of $(d\beta/d\xi)$.

The boundaries of the external inviscid flow $y_\delta^{up}(x)$ and $y_\delta^{lw}(x)$ are calculated by integrating the expression $dz/d\varsigma$ along the real axis of the parameter domain.

Equation (1) leads to the following integral equation in terms of the function $\gamma(\xi)$, if the velocity on the boundaries **OD** and **TD′**, $v_\delta[x(\xi)]=|dW/dz|_{\varsigma=\xi}$, is specified.

$$\int_0^t \frac{d\gamma}{d\xi'}\ln\left|\frac{\xi'-\xi}{\xi'+\xi}\right|d\xi' = \pi\ln\left[\frac{v_\delta[x(\xi)]}{v_0}\left(\frac{\xi+a}{\xi-a}\right)\right] - \int_t^\infty \frac{d\beta}{d\xi'}\ln\left|\frac{\xi'-\xi}{\xi'+\xi}\right|d\xi', \quad 0\leqslant\xi\leqslant t. \tag{6}$$

We should note that the expression $dz/d\varsigma$ has a logarithmic singularity at the downstream infinity **D** ($\varsigma=1$). The change of the variable ξ with the spatial variable in the physical plane $s=-K'\ln|\xi-1|$, where K' is a coefficient, makes it possible to calculate the integrals in Eq. (1) near the point **D**. The boundaries **OD** and **TD′** are assumed to be parallel far downstream of the cascade. Thus, in the interval $1-\exp(-s_{\max}/K')<\xi<1+\exp(-s_{\max}/K')$ the function $\gamma(\xi)$ has a constant value, where $s_{\max}$ is the length of the streamline measured from the leading edge.

2.2 Time-Averaged Wake Flow. Formation of a re-entrant jet in the region of cavity closure has been observed in many experimental studies and described, in particular, by Furness and Hutton [22]. The numerical analysis of a re-entrant jet flow past a hydrofoil including two-dimensional and three-dimensional calculation is given by Dang and Kuiper [23]. The intensity of the re-entrant jet depends primarily on the shape of the hydrofoil and the angle of attack. For slender bodies with a small angle of attack, the re-entrant jet begins to interact with the free boundary of the main flow immediately after its formation and it cannot reach the point of cavity detachment, [16]. This process causes large vortices in the rear portion of the cavity, resulting in the flow recirculation and cloud cavitation. In the experimental study conducted by Wade and Acosta [24], no intensive re-entrant jets were observed in the cavity flow past a cascade.

Based on the these experimental observations, the beginning of the wake region is modeled by a time-averaged boundary **OH** upon which the density changes in a stepwise fashion from the vapor density ρ_v to a certain value ρ_0. Following the works [17] and [19] we use the terms ''mixing region'' and ''near wake'' for the regions **OHGK** and **KFF′G**, respectively. Due to the flow recirculation in the mixing region, the density changes slowly. For simplicity, it is assumed that the density ρ_0 in the mixing region is constant and $\rho_v\leqslant\rho_0\leqslant\rho$. A self-similar velocity profile is assumed between lower and upper boundaries of the mixing layer **OGK**. The flow attaches to the blade surface at the point **G** (Fig. 1). Downstream of the cross section **GK** the density increases rapidly due to higher pressure ($p>p_v$) and the absence of reversed flows. For simplicity, the density in the near wake is assumed to be equal to the liquid density.

Following the theory of separated flows, [19,25], a one-parameter family of velocity profile is assumed in the ''mixing region'' and ''near wake,''

$$\frac{u}{v_\delta}=1-mf(\bar{y}), \tag{7}$$

where $m=(v_\delta-u_0)/v_\delta$ is a form parameter of the velocity profile, $\bar{y}=y/\delta$ is the nondimensional coordinate across the wake, u_0, v_δ are the velocities on the lower and upper boundaries of the viscous wake, respectively, and $f(\bar{y})=2\bar{y}^3-3\bar{y}^2+1$ is the universal velocity defect function for the turbulent free mixing layers, [19]. Various dependences $f(\bar{y})$ were investigated but it was found that the choice of the function $f(\bar{y})$ has only a small effect on the results. A small change of the empirical coefficient of turbulent mixing K compensates for the effect of the function completely. For the velocity profile of Eq. (7), the displacement thickness δ^* and momentum thickness δ^{**} are given by

$$\delta^*=\int_0^\delta\left(1-\frac{\rho_0 u}{\rho v_\delta}\right)dy=H^*(m,r_0)\,\delta=\left(1-r_0+\frac{rm}{2}\right)\delta,$$
$$\delta^{**}=\int_0^\delta\frac{\rho_0 u}{\rho v_\delta}\left(1-\frac{u}{v_\delta}\right)dy=H^{**}(m,r_0)\,\delta=\frac{r_0 m}{2}\left(1-\frac{26}{35}m\right)\delta \tag{8}$$

where $r_0=\rho_0/\rho$ is nondimensional density.

2.2.1 Mixing Region. The convective terms in the X-component of momentum equation are ignored due to the low velocity in the recirculation region compared to the main flow velocity. It gives

$$\frac{dp}{dx}=\frac{\partial\tau}{\partial y},\quad \tau=\rho_0\chi v_\delta^2 \tag{9}$$

where the stress τ is calculated from the first Prandtl's model and χ is an empirical coefficient that characterizes the turbulence in the mixing region. Due to the two-phase flow in the mixing region, the tangential stress reaches its maximum value $\tau=\tau_{\max}$ at some thickness Δ which is proportional to the spacing of the cascade:

$$\frac{\partial\tau}{\partial y}=\frac{\tau_{\max}}{\Delta}=\frac{\chi\rho_0 v_\delta^2}{h}. \tag{10}$$

Integrating Eq. (9) with Eq. (10) along the mixing region and using Bernoulli's equation applied on the outer boundary of the region, we obtain the following expression for the velocity at the outer boundary of the mixing region:

$$v_\delta(x)=v_0\exp\left[-\frac{\chi r_0}{h}(x-l_c)\right],\quad l_c<x<l_m, \tag{11}$$

where v_0 is the velocity on the cavity surface.

The length of the mixing region l_m is determined from the condition of the flow attachment

$$\delta^*(l_m)=y_\delta^{up}(l_m)-y_\delta^{lw}(l_m). \tag{12}$$

The thickness of the mixing layer δ is determined from the relationship for free jet boundary layers

$$\delta=b(x-l_c), \tag{13}$$

where $b=b_0 r_0$ and b_0 is a coefficient determining the increase of the width of the free mixing layer for cavitation-free flows, [26].

The density in the mixing region is determined from the interpolation between the following two limiting cases. When the cavity length approaches zero ($l_c\to 0$), the nondimensional density should approach one ($r\to 1$). When the cavity length reaches some value corresponding to the throat of the blade channel ($l_{c\,\max}\approx h$), the choke effect causes transition from partial cavitation to supercavitation and consequently the density should approach zero ($r\to 0$), [14,24]. From the linear interpolation between the above two limiting cases, it is assumed

$$r_0=\rho_0/\rho=1-l_c/l_{c\,\max}. \tag{14}$$

2.2.2 Near Wake. Two functions, $v_\delta(x)$, and $m(x)$, describe the velocity field in the near wake region. In this region von Karman's momentum integral equation is applied and it is assumed that the coefficient of turbulent mixing, K, is constant.

$$\frac{d\delta^{**}}{dx}+(2\delta^{**}+\delta^*)\frac{d\ln v_\delta}{dx}=0, \tag{15}$$

$$K=\frac{1}{\rho v_\delta}\frac{d}{dx}\int_0^\delta\rho u\,dy=\frac{b_0}{2}. \tag{16}$$

Integrating the continuity equation across the wake we have the condition of interaction between viscous and inviscid flows in the form proposed by Crocco and Lees [17]

$$\frac{d\delta^*}{dx}=(\delta-\delta^*)\frac{d\ln v_\delta}{dx}+\frac{dy_\delta^{up}}{dx}-\frac{dy_\delta^{lw}}{dx}. \tag{17}$$

The value of $K=b_0/2$ corresponds to the self-similar boundary layer developing far from the wall and this value has been used throughout the present study. By using Eq. (8), we can reduce Eqs. (15)–(17) to the following system of ordinary differential equations:

$$A\frac{dP}{dx}=B, \tag{18}$$

where $P=\{p_i\}=\{m,v_\delta,\delta^*\}$, $A=\|a_{ij}\|$, $B=\{b_i\}$, $ij=1,3$. The elements of the matrix A and the vector B are presented in Appendix A. The system of Eqs. (18) is nonlinear due to the dependence of the coefficient a_{ij} on the variable p_i. The initial values of the variables in the wake are assumed to be the same as those at the end of mixing region, $x=l_m$.

2.3 Computational Adaptation. The solution algorithm of the integro-differential Eq. (5) and the integral Eq. (6) is based on the linear interpolation of the functions $\beta(\xi)$ and $\gamma(\xi)$ on the segment $\lfloor\xi_{j-1},\xi_j\rfloor$ of the real axis in the parameter domain, where $0\leqslant\xi_j\leqslant t$, $j=1$, M_1 and $t\leqslant\xi_j\leqslant\xi^*$, $j=1$, M_2 are fixed points. ξ^* is a large value, corresponding to the leading edge in the physical plane. The values $M_1=80$, $M_2=40$ provide sufficient accuracy. For each segment $\lfloor\xi_{j-1},\xi_j\rfloor$ it is assumed that

$$\frac{d\beta}{d\xi}=\beta_j'=\text{const},\quad j=1,\ M_2;\quad \frac{d\gamma}{d\xi}=\gamma_j'=\text{const},\quad j=1,\ M_1. \tag{19}$$

In view of Eq. (19) the functions $\beta(\xi)$ and $\gamma(\xi)$ have the form

$$\beta(\xi)=\sum_1^{i-1}\beta_j'\Delta\xi_j+\beta_i'(\xi-\xi_{i-1})+\beta_t,$$

$$\gamma(\xi)=\sum_1^{i-1}\gamma_j'\Delta\xi_j+\gamma_i'(\xi-\xi_{i-1})+\gamma_0, \tag{20}$$

where i is the index of the segment in which ξ is located, and $\xi_{i-1}<\xi<\xi_i$, $\beta_t=\beta(C)$ is the slope of the pressure side of the profile at the trailing edge **T**. The angle γ_0 is determined from the condition $\gamma(t)=\beta(t)=\Sigma_1^{M_1}\gamma_j'\Delta\xi_j+\gamma_0$, where t is the value of ξ corresponding to the trailing edge **T**. In view of Eq. (19), the integrals appearing in Eqs. (3) and (6) can be represented as

$$\frac{1}{\pi}\int_t^\infty\frac{d\beta}{d\xi}\ln\left(\frac{\xi-\varsigma}{\xi+\varsigma}\right)d\xi=\beta_j'q_j(\varsigma),$$

$$j=1,M_2;\quad\int_0^t\frac{d\gamma}{d\xi}\ln\left(\frac{\xi-\varsigma}{\xi+\varsigma}\right)d\xi=\gamma_j'q_j(\varsigma),\quad j=1,M_1 \tag{21}$$

where the coefficients $q_j(\varsigma)=1/\pi\int_{\xi_{j-1}}^{\xi_j}\ln(\xi-\varsigma/\xi+\varsigma)d\xi$ can be integrated analytically.

The integro-differential equation of Eq. (5) is solved by using a method of consecutive approximation using the relation

$$\beta_j'=\frac{\beta\lfloor x(\xi_j)\rfloor-\beta\lfloor x(\xi_{j-1})\rfloor}{\xi_j-\xi_{j-1}},\ \text{where}$$

$$x(\xi)=\text{Re}\left(\int_0^\xi\frac{dz}{d\varsigma}\bigg|_{\varsigma=\xi}d\xi\right),\quad j=1,M_2. \tag{22}$$

The integral Eq. (6) in view of Eq. (21) is reduced to a system of linear equations

$$q_{ij}\gamma_j'=g_i,\ \ i,j=1,M_1. \tag{23}$$

The term $q_{ij}=q_j(\bar{\xi}_i)$. $g_i(\bar{\xi}_i)$ is determined from the right-hand side of the Eq. (6) at the point $\bar{\xi}_i=0.5(\xi_{i-1}+\xi_i)$.

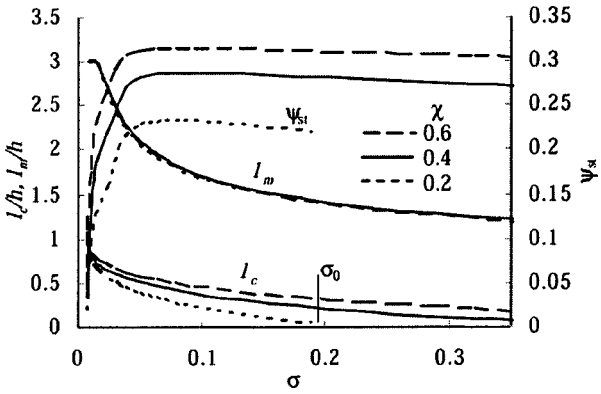

Fig. 3 Effect of choice of the coefficient χ on the cavity length, length of separated region, and static head coefficient for the flow parameters: blade angle $\beta=10$ deg, angle of attack $\alpha=5$ deg, solidity of the cascade $\tau=3$

The nonlinear system of ordinary differential equations, Eq. (18), is integrated using standard fourth-order Runge-Kutta's method. The iteration was repeated until the velocity distribution, $v_\delta(x)$, and the shape of the boundary of interaction, $y_\delta^{up}(x)$, satisfied $|v_\delta^{k+1}(x_j)/v_0-v_\delta^k(x_j)/v_0|<\varepsilon$, $|y_\delta^{upk+1}(x_j)/h-y_\delta^{upk}(x_j)/h|<\varepsilon$, where k is the number of iteration, $j=1$, M_1, and $\varepsilon=10^{-4}$ for the present study.

2.4 Examination of the Cavity Wake Model for Symmetric Flow. In this section we discuss the choice of the values of empirical factors and the validity of the model is examined by applying it to symmetrical cavitation. The wake model includes empirical coefficients b_0, χ, $l_{c\,\max}$. The coefficient b_0 represents the rate of increase of the free mixing layer width. Görtler's theory described by Schlichting [26] predicts $b_0=0.098$ at the boundaries of mixing layer with $(u/v_\delta)^2=0.1$ and $(u/v_\delta)^2=0.9$, and this value was used by Devis et al. [15] for modeling the cavity flows in inducers. We use this value for the present calculations. The coefficient of turbulent viscosity χ in the mixing region is chosen to provide good agreement between calculated and experimental cavitation performances of the inducers. It will be shown later that the values $\chi=0.4$ and $l_{c\,\max}=h$ provide good results for inducers. The effect of the predicted cavity length and the head coefficient on the value of χ is shown in Fig. 3. The cavity length and the head coefficient decrease with the decrease of the coefficient χ, but the total length of the cavity and mixing region, l_m, is not sensitive to the value of χ. Within the framework of the model of an ideal fluid the cavity length approaches zero ($l_c\to0$) with $\sigma\to\infty$ for the case with a sharp leading edge. The present model predicts a finite value σ_0 at which cavity length becomes zero ($\sigma_0\approx0.18$ at $\chi=0.2$ is shown in Fig. 3). The value of σ_0 depends on the values of parameters b_0, χ, $l_{c\,\max}$. It increases almost linearly with the increase of the empirical coefficient χ. For the chosen value $\chi=0.4$, $\sigma_0\approx0.4$ was obtained. It is expected that σ_0 corresponds to the inception cavitation number. Although the value $\sigma_0=0.4$ is quite reasonable for inducers, further experimental and theoretical study is needed to correlate σ_0 with inception.

The static head coefficient ψ_{st} is calculated as a part of the total head coefficient, [7],

$$\psi_{st}=\frac{gH_{st}}{\rho U_t^2}=\frac{1}{Q}\int_{r_h}^{r_t}\frac{p_2(r)-p_1(r)}{\rho U_t^2}2\pi rc_m(r)dr, \tag{24}$$

where $c_m(r)$ is the meridional velocity, Q is the volumetric flow rate, and p_1 and p_2 are the static pressure at the inlet and outlet, respectively. The following approximate relation can be obtained from Eq. (24) if we apply Bernoulli's equation to the inviscid flow and assume that $c_m(r)$ and $v_{\delta2}(r)/v_1(r)$ are constants

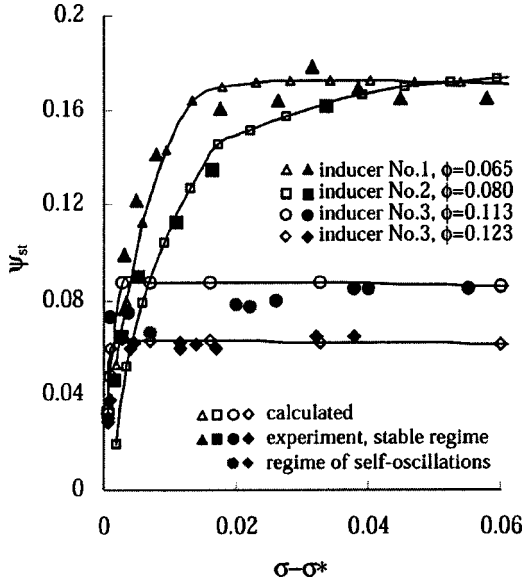

Fig. 4 Suction performance of the inducers compared with experiment

$$\psi_{st} \approx \frac{r^{*2}}{2r_t^2}(1+\phi^{*2})\left(1-\frac{v_{\delta 2}^2(r^*)}{v_1^2(r^*)}\right), \tag{25}$$

where $v_{\delta 2}$ is the velocity of the inviscid flow at the outlet of the cascade, ϕ^* is the flow coefficient at mean square radius $r^* = \sqrt{(r_h^2+r_t^2)/2}$.

In Fig. 4 the cavitation performances predicted by the model are compared with experimental data for inducer No. 1 and No. 2 described in Table 1. The comparison is made in terms of the relative cavitation number $\sigma-\sigma^*$ where the choke cavitation number σ^* is set $\sigma^*=\sigma^*_{\text{calc}}$ for predicted data and $\sigma^*=\sigma^*_{\text{exp}}$ for experimental data. The difference between σ^*_{calc} and σ^*_{exp} is caused by the leading edge thickness of the blades, [7]. For all predicted data shown in Fig. 4 the value $\chi=0.4$ has been used. It can be seen that this value provides good agreement between predicted and experimental head coefficients for various inducers over a wide range of cavitation number and flow coefficient including the region of the head breakdown.

Figure 5 shows the predicted cavity and wake shapes for the cascade at the tip, mid radius, and hub for inducer No. 1 under the conditions of uniform inlet pressure and axial velocity. The gray level corresponds to the level of density in the mixing region determined by Eq. (13). As can be seen, the cavity length decreases quite rapidly as we move from tip to hub although the angle of attack increases. Thus, the cavitation starts at the tip and then extends to the hub with decreasing inlet pressure. This is in agreement with various experimental observations.

Figure 6 compares the predicted nondimensional cavitation compliance $\tilde{C}_{\text{cav}} = -\partial \tilde{V}_c / \partial \sigma_{\text{tip}}$ with experimental data. The cavity volume is calculated as the radial integration of the area of the vapor fraction.

$$\tilde{V}_c = \frac{N}{V_{\text{ref}}} \int_{r_h}^{r_t} \left(\int_0^{l_c} y_\delta(x,r)dx + (1-r_0) \int_{l_c}^{l_m} y_\delta(x,r)dx \right) dr, \tag{26}$$

where $V_{\text{ref}} = 2\pi^2 r_t (r_t^2 - r_h^2)$ is the reference volume.

The experimental values for inducer No. 1 by Pilipenko et al. [27] were determined from a test under cavitation surge. The data of Saturn boosters engines J2 and F1, [28], are also shown. The presented model provides reasonable agreement with experimental data.

Table 1 Geometry of the inducers tested

Inducer	No. 1	No. 2	No. 3	No. 4	No. 5
Tip diameter, mm	120	156	127	149.8	149.8
Inlet hub diameter, mm	63	76	37	37.5	37.5
Outlet hub diameter, mm	63	76	65	79.4	76.4
Number of blades	2	3	3	3	4
Solidity at tip	3	2.5	2.5	1.9	2.97
Inlet blade angle, deg.	8.25	11	10	7.5	7.5
Outlet blade angle, deg.	8.25	11	12	9.0	9.0
Blade thickness at tip, mm	2	3	2.5	2	2
Blade thickness at hub, mm	4	5	3.5	5	5
Ref. to the experiment data	[27]	[27]	[30]	[4]	[3]

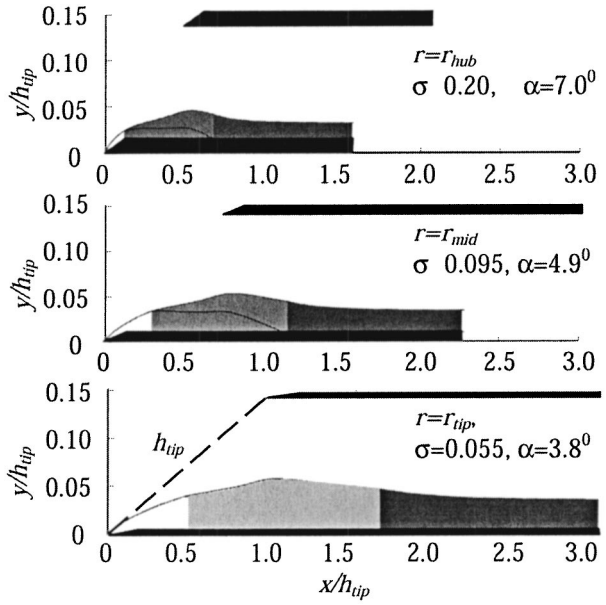

Fig. 5 Boundaries of the inviscid flow at the tip, middle and hub radius for the inducer No. 1

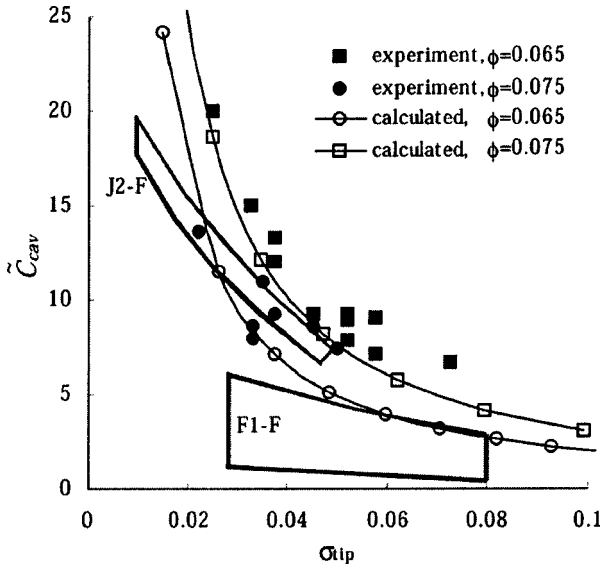

Fig. 6 Cavitation compliance prediction compared with experimental data for Inducer No. 1, [27], and experimental range of cavitation compliance for Saturn boosters engines J2 and F1, [28]

Real inducer flow is three-dimensional with tip clearance leakage and inlet backflow, [7]. These effects are not taken into account explicitly in the present model. However, $\chi=0.4$ is determined so that the predicted suction performance agrees with experiments, suggesting that the three-dimensional effects are implicitly taken into account in the choice of the value of χ. Although it is interesting to note that a unique set of values of empirical factors can nicely predict the suction performance of several inducers, there should be a certain limit for the quantitative prediction of inducer performance by the present two-dimensional model.

3 Nonsymmetric Cavity Flows in Cascades

Most of the studies on the steady cavitation in inducers consider equal cavitation for all of the blades. For attached uneven cavitation, [4], and alternate blade cavitation, [1], cavity length differs from blade to blade. For such cases each blade should be considered independently. Horiguchi et al. [6] have shown that alternate blade cavitation can be predicted by a closed cavity model by using a singularity method. In this section the effects of cavity wake on asymmetric cavitation are examined. The nonlinear mapping method becomes too complicated if we consider each blade independently. Here, the singularity method is used for the analysis of asymmetric cavitation combined with the cavity wake model.

3.1 Some Features of Using the Singularity Method With the Wake Model. The complex potential of the flow can be represented as the superposition of the complex potentials of the main flow $Ue^{-i\alpha}z$ and the complex potentialities of disturbance, w_n,

$$W(z)=Ue^{-i\alpha}z+\sum_{1}^{N} w_n(z), \tag{27}$$

where N is number of the cascade blades, w_n shows the disturbance of nth blade-cavity-wake and is represented by sources and vortices distributed along the blades. Details of the method are described in [6,18]. Here, we describe only the differences caused by the application of the cavity wake model.

The sources are distributed along the whole length of the blade to represent cavity and wake. On the boundary of interaction the tangential velocity is given from linearized Bernoulli's equation and the cavity wake analysis,

$$v_n(x)=\begin{cases} U+\dfrac{\sigma U}{2}, & 0\leqslant x\leqslant l_{cn} \\ u_n(x), & l_{cn}\leqslant x\leqslant C \end{cases}, \tag{28}$$

where l_{cn} is the cavity length, the functions $u_n(x)$ is the tangential velocity at the outer boundary of the viscous flow for the nth blade.

Since there are no sources for $x>C$ the source strength should approach zero at $x=C$:

$$q_n(C)=0, \quad n=1,N. \tag{29}$$

This condition is used instead of the cavity closure condition in the closed cavity model, [6].

The coupling procedure of the viscous and inviscid flows is the same as shown in Fig. 2. Although the solution of the external inviscid flow is linear, the solution of the total problem is nonlinear due to the nonlinearity of the model of the viscous wake, (18). The values $\chi=0.4$ and $l_{c\,\max}=0.7h$ were used in the calculations. A small change of the coefficient $l_{c\,\max}$ is needed ($l_{c\,\max}=0.7h$ instead of $l_{c\,\max}=h$) due to the difference in linear and nonlinear external inviscid flow solutions. Although an infinite number of blades of the cascade is considered, the periodicity of the flow over two or three blades is assumed for alternate blade cavitation and attached uneven cavitation.

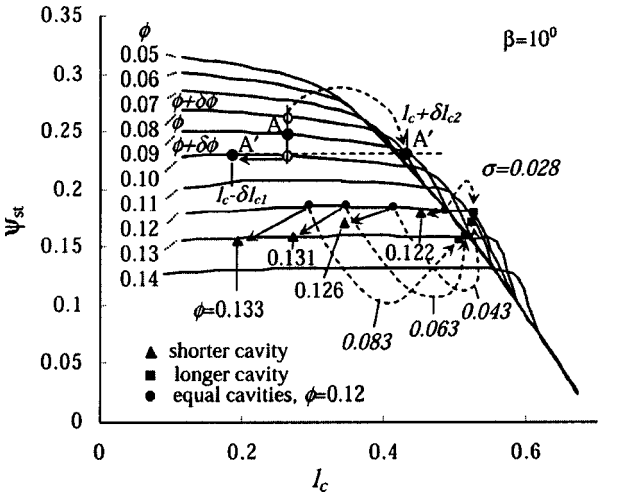

Fig. 7 Head dependences of the cascade versus cavity length for various flow rates in the case of symmetric cavity flow (solid lines) and alternate blade cavitation (closed squares for longer cavities and closed triangles for shorter cavities): blade angle 10 deg, solidity 2.5

3.2 Pressure Balance for Alternate Blade Cavitation. For alternate blade cavitation, the pressure increase in blade channels with a larger cavity should agree with that in the blade channels with a shorter cavity. This pressure balance is discussed here. The head in a particular blade channel depends on the flow rate and the degree of cavitation development in that channel. Usually, the inducer head and cavity length are considered to be functions of the cavitation number and flow rate, i.e., $\psi_{st}=\psi_{st}(\sigma,\phi)$, $l_c=l_c(\sigma,\phi)$. It is also possible to represent the head as a function of the cavity length and flow coefficient $\psi_{st}=\psi_{st}(l_c,\phi)$. This representation makes it possible to consider the head in different blade channels independently. The decrease of the head in one blade channel might be caused by the increase of the flow rate or by the choke of the flow due to cavitation. A combination of these phenomena can provide the equality of the pressure at the outlet of the blade channels.

Figure 7 shows the head versus cavity length for various flow coefficients for the equal cavity flow predicted by the present model. The static head coefficient is evaluated by Eq. (25) with $r^*=r_t$. We consider an arbitrary operational point $A(l_c,\phi)$ for the equal cavity flow. Under alternate blade cavitation this point moves to A' for one blade and to A'' for the next blade as shown in Fig. 7. If the alternate blade cavitation occurs, the flow rate in one channel will increase and that in the next will decrease. For the channel with increased/decreased flow rate, the cavity will be shorter/longer, and the developed head should be balanced. If the flow coefficient in one channel is increased, the cavity length and the head in the channel will be decreased: the point A moves to the point $A'(l_c-\delta l_{c1},\phi+\delta\phi)$. Since the total flow rate is kept constant, the flow coefficient in the second blade channel will be $\phi-\delta\phi$. Although the head coefficient near the point A increases with the decrease of the flow coefficient, it can decrease due to the cavitation development, at position A'' for example. Thus, the pressure can be balanced between blades channels:

$$\psi^r_{st}(l_c-\delta l_{c1},\phi+\delta\phi)=\psi^r_{st}(l_c+\delta l_{c2},\phi-\delta\phi). \tag{30}$$

Several results of alternate blade cavitation predicted by the present model are shown in Fig. 7 for the value $\phi=0.12$ with closed squares for the longer cavities and with closed triangles for the shorter one. We observe that the head is balanced in the each case. The operating points for each blade channel are approximately on the curves of equal cavity flow corresponding to the

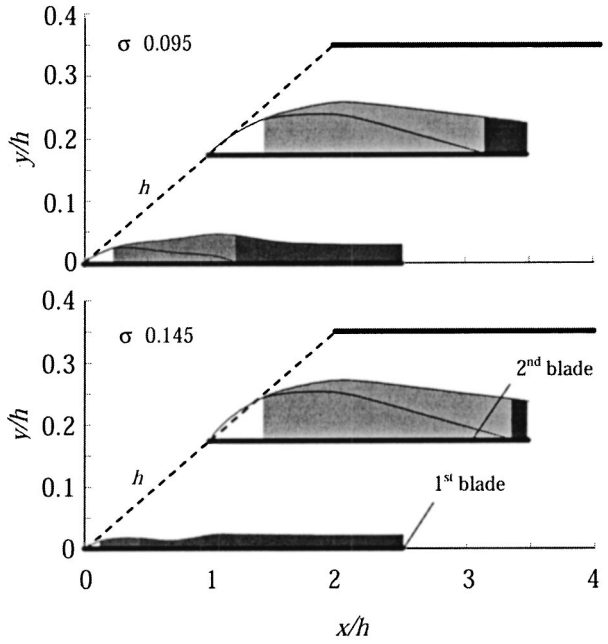

Fig. 8 Asymmetric cavity flow in the two-blade cascade: blade angle 10 deg, angle of attack 5 deg, solidity 2.5 for cavitation numbers 0.095 and 0.145

actual flow rate in the blade channel. The pressure balance cannot be examined with a closed cavity model, [6], since the pressure is always balanced for the closed cavity model.

3.2.1 Alternate Blade Cavitation. Figure 8 shows the predicted cavity and wake shapes of alternate blade cavitation for $\sigma=0.095$ and $\sigma=0.145$. The gray level corresponds to the level of density in the mixing region. As can be seen, the cavity shape differs alternately. With an increasing cavitation number the difference of the flow parameters on different blades increases.

Figure 9 compares the predicted cavitation performance with experimental results for inducer No. 5 (see Appendix B). The calculations are made at the mean square radius to compare the head. The region of alternate blade cavitation predicted at the tip is also shown. The comparison is made in relative cavitation number $\sigma-\sigma^*$. In the experiment, the alternate blade cavitation was observed in the region shown in the figure. A small effect on the head coefficient can be seen for $\phi=0.06$ but not for $\phi=0.08$. The present model fails to predict the head quantitatively in the case of the nonsymmetric flow. However, Fig. 9 shows that the predicted region of the alternate blade cavitation at the tip is in reasonable agreement with the experiment. The closed cavity model predicts much larger value of σ for alternate blade cavitation, [6]. In Fig. 9 the region of rotating cavitation is also shown. Rotating cavitation starts at a smaller cavitation number than does alternate blade cavitation.

3.2.2 Attached Uneven Cavitation. In three-bladed inducers the steady nonsymmetrical flow was observed in [4] and is named attached uneven cavitation (Fig. 11(*a*), the region marked ③). This cavitation pattern occurs at a smaller cavitation number than rotating cavitation. No steady flow pattern corresponding to attached uneven cavitation can be predicted by a closed cavity model, [6].

In Fig. 10 are shown the predicted lengths of cavities, l_c, total lengths of the cavity and mixing region l_m and the flow rate in the blade channels versus cavitation number for a three-bladed inducer. We set the blade numbering as shown in Fig. 10. In the direction of blade numbering, the cavity size changes smallest, largest, and then middle. This agrees with the experimental observation by Azuma et al. [29]. We have smaller flow rate for the blade channel with larger cavity. Thus, only one blade channel is choked with the largest cavity and smallest flow rate. With the decrease of the cavitation number the difference of the flow between channels also decreases and disappears at some small cavitation number near the head breakdown at which the mixing region extends to the trailing edge of the blade.

In Fig. 11(*a*) are shown the experimental suction performances and the map showing the occurrence regions of various types cavitation for inducer No. 4. The region 3 corresponds to attached uneven cavitation. In this region the flow is stable and a small head decrease can be observed. The region 4 corresponds to rotating cavitation. There is no head decrease in this region. The attached uneven cavitation occurs at slightly smaller cavitation numbers than for rotating cavitation.

In Fig. 11(*b*) are shown the suction performances predicted at the mean square radius, for inducer No. 4. The region of attached uneven cavitation predicted at the tip is also shown. The comparison of Figs. 11(*a*) and 11(*b*) shows that the region of attached uneven cavitation agrees with that predicted at the mean square radius and the region of rotating cavitation agrees with the region

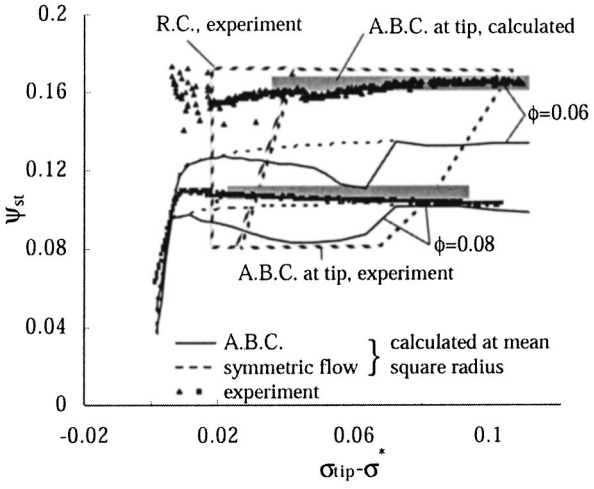

Fig. 9 Predicted head coefficient compared with experiment, plotted versus the relative to the choked cavitation number σ^*, for inducer No. 5; A.B.C. alternate blade cavitation; R.C. rotating cavitation

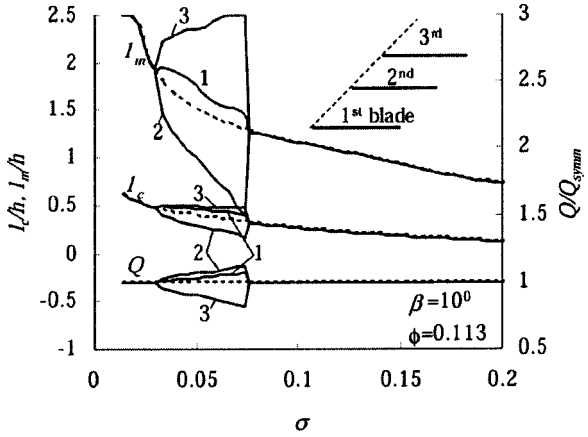

Fig. 10 Predicted cavity length, length of the mixing region and flow rate in the blade channels versus cavitation number for the three-blade cascade: blade angle 10 deg, flow coefficient 0.113, solidity 2.5

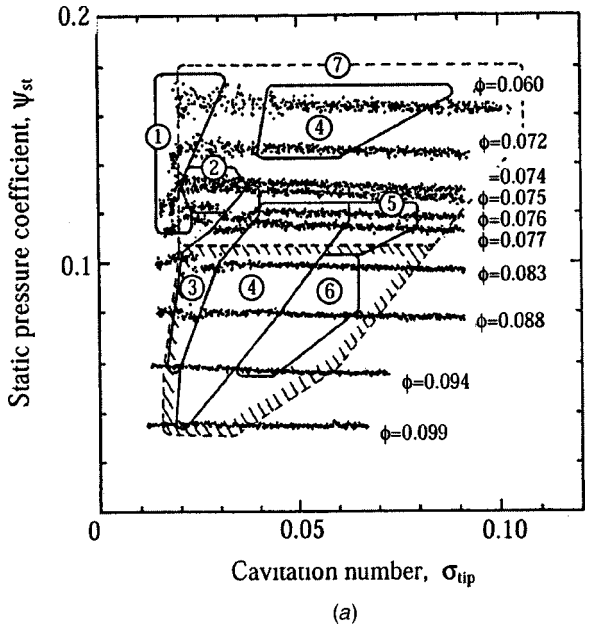

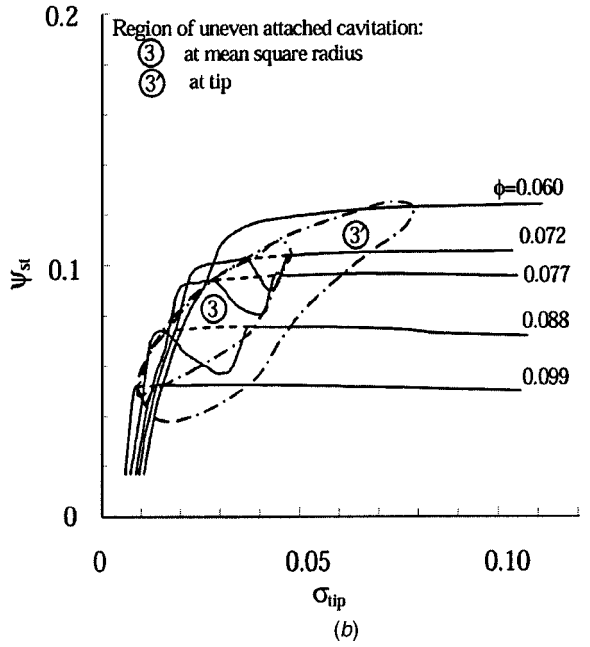

Fig. 11 (*a*) Experimental suction performances and map showing the occurrence regions of various oscillating cavitation types for inducer No. 4 (see Appendix B); (*b*) predicted suction performances and map of regions of the nonsymmetric flow for inducer No. 4 (see Appendix B)

predicted at the tip. Calculations at various radii show that the attached cavitation first appears at the tip and then extends to the hub with further decrease of inlet pressure. The significant influence of the backflows at the inlet for $\phi=0.06$, which is not taken into account, may cause the disagreement between the predicted and experimental cavitation performance.

Figure 12 compares the predicted region of alternate blade cavitation for two(four)-bladed inducers with the region of attached uneven cavitation for three-bladed inducers in the plane of the cascade solidity τ and the parameter $\sigma_{tip}/(2\alpha)$. The experimental points for inducer No. 4 and No. 5 as well as the results predicted by the closed cavity model are shown. It can be seen that the region of nonsymmetric cavitation for the two(four)-bladed inducers is larger than that for three-bladed inducers. The cavity wake model provides much better agreement with experiment than the closed cavity model [6], for the region of alternate blade cavitation in terms of $\sigma/(2\alpha)$.

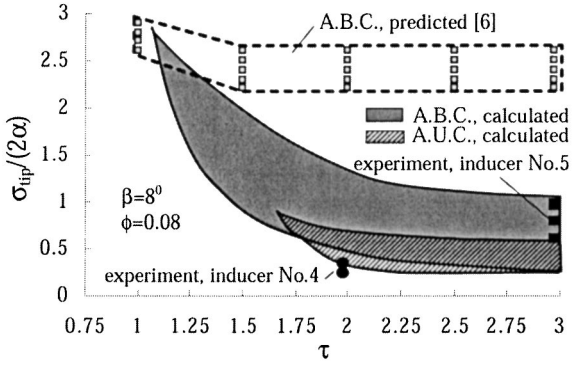

Fig. 12 Comparison of the regions of nonsymmetric flow past two and three-blades cascade in the plane of the cascade solidity and the parameter $\sigma_{tip}/(2\alpha)$: the blade angle $\beta=8$ deg, flow coefficient $\phi=0.084$; A.B.C. alternate blade cavitation, two(four)-bladed inducers; A.U.C. attached uneven cavitation, three-bladed inducers

Conclusions

A cavity wake model was presented for the prediction of steady cavitation performance of inducers. The model is based on the physics of the viscous flow in the wake and the interaction with outer inviscid cavity flow is taken into account. The wake model contains several empirical factors and it was applied to several inducers using a set of values for the empirical factors. It was shown that the model can predict the suction performance and cavitation compliance reasonably for a wide range of flow coefficients and cavitation numbers.

The model was applied to alternate blade cavitation for inducers with an even number of blades, to examine the pressure balance between the blade channels with larger and smaller cavities. It was clarified that the blade channel with a larger cavity has a smaller flow rate and the increase of Euler's head is balanced by head decrease due to cavitation. The model was further applied to an attached uneven cavitation for inducers with three blades which cannot be predicted by a closed cavity model. The wake model can predict the attached uneven cavitation and the relations cavity size and the flow rate in each channel was examined. It was shown that the onset range of $\sigma/(2\alpha)$ for alternate blade cavitation and attached uneven cavitation can be predicted more reasonably than the closed cavity model. The model can predict the ''dips'' in the suction performance curves associated with the alternate blade cavitation and attached uneven cavitation. However, the agreement of the predicted head with experimental results was not as good as in the cases of the first several inducers No. 1–No. 3, especially at lower flow rates. This shows the limitation of the present model for the quantitative prediction of the cavitation performance of real three-dimensional inducers.

Acknowledgments

This study was supported by the JSPS. The authors would like to thank the reviewers for their valuable comments.

Nomenclature

C_{cav} = quasi-steady cavitation compliance
b_0 = coefficient of free mixing layer increase
C = chord length
h = cascade spacing
i = imaginary unit in space, $i^2=-1$
K = coefficient of turbulent mixing
l_c = cavity length
l_m = total length of the cavity and mixing region
N = number of inducer blades
m = velocity profile form parameter
p, p_v = pressure and vapor pressure
r_0 = nondimensional density $=\rho_0/\rho$
S = inducer pitch
u = x-component velocity in the wake
v = tangential velocity
V_c = cavity volume
W = complex potential
y_δ = inviscid flow boundary
α = angle of attack
β^* = blade angle
$\beta(x)=dy_b/dx$ = slope of the blade
χ = coefficient of turbulent viscosity
δ = viscous layer thickness
δ^* = displacement thickness
δ^{**} = momentum thickness of the viscous layer
ϕ = flow coefficient
γ_0 = angle of cavity closure
θ = blade thickness
ρ = liquid density
ρ_0 = density in the mixing region
σ = cavitation number
σ^* = cavitation number for choked cavity flow
τ = tangential stress
ψ_{st} = static head coefficient
ζ = parameter region $=\xi+i\eta$

Subscripts

1 = parameters at inlet
2 = parameters at outlet
n = blade index
h = parameters at hub
t = parameters at tip
δ = parameters at outer boundary of viscous layer

Appendix A

Coefficients of the matrix A and vector B of Eq. (18):

$$a_{11}=\frac{\partial H^{**}}{\partial m}-H^{**}\frac{\partial \ln H^*}{\partial m},$$

$$a_{12}=\frac{2H^{**}+H^*}{v_\delta},\quad a_{13}=\frac{H^{**}}{\delta^*},\quad b_1=0,$$

$$a_{21}=-\delta^*\frac{\partial \ln H^*}{\partial m},\quad a_{22}=\frac{\delta^*(1-H^*)}{v_\delta},$$

$$a_{23}=1-H^*,\quad b_2=\frac{b_0H^*}{2},$$

$$a_{31}=0,\quad a_{32}=-\frac{\delta^*(1-H^*)}{H^*v_\delta},$$

$$a_{33}=1,\quad b_3=\frac{dy_\delta^{up}}{dx}-\frac{dy_\delta^{lw}}{dx}.$$

Appendix B

For inducers of varied pitch, in order to take into account increasing of the axial velocity due to the increasing hub diameter, the equivalent cascade of the profiles with blade angle β_{eq} is used:

$$\beta_{eq}(x)=\beta(x)-\Delta\beta(x),$$

where $\Delta\beta(x)=\mathrm{Arc}\tan(S_1/2\pi r^* r_t^2-r_h^2(o)/r_t^2-r_h^2[z(x)])-\beta_1$.

z is coordinate in axial direction and S_1, β_1 are the inducer pitch and blade angle at the inlet. Usually, inducers are designed such matter that $\beta_{eq}(x)\approx\beta_1$.

References

[1] Acosta, A. J., 1958, "An Experimental Study of Cavitating Inducer," *Proceedings of the 2nd Symposium on Naval Hydrodynamic*, ONR/ACR-38, pp. 533–557.
[2] de Bernardi, J., Joussellin, F., and Von Kaenel, A., 1993, "Experimental Analysis of Instabilities Related to Cavitation in a Turbopump Inducer," *1st International Symposium on Pump Noise and Vibrations*.
[3] Yoshida, Y., Tsujimoto, Y., Kataoka, D., Horiguchi, H., and Wahl, F., 2001, "Effects of Alternate Leading Edge Cutback on Unsteady Cavitation in 4-Bladed Inducers," ASME J. Fluids Eng., **123**, pp. 762–770.
[4] Tsujimoto, Y., Yoshida, Y., Maekawa, Y., Watanabe, S., and Hashimoto, T., 1997, "Observations of Oscillating Cavitation of an inducer," ASME J. Fluids Eng., **119**, pp. 775–781.
[5] Joussellin, F., Maitre, T., and Morel, P., 1998, "3D Cavity Shape in Inducer: Experimental Investigation and Numerical Predictions," *3rd Int. Symp. on Cavitation*, Grenoble, France.
[6] Horiguchi, H., Watanabe, S., Tsujimoto, Y., and Aoki, M., 2000, "A Theoretical Analysis of Alternate Blade Cavitation in Inducers," ASME J. Fluids Eng., **122**, pp. 156–163.
[7] Brennen C. E., 1994, *Hydrodynamics of Pumps*, Concepts ETI and Oxford University Press.
[8] Acosta, A. J., 1974, "Cavitation in Fluid Machinery," *Proc. of Cavitation Conference*, Heroit-Watt Univ. of Edinburg, Scotland, pp. 383–396.
[9] Arndt, R. E. A., 1981, "Cavitation in Fluid Machinery and Hydraulic Structures," Annu. Rev. Fluid Mech., **13**, pp. 273–328.
[10] Brennen, C. E., 1995, *Cavitation and Bubble Dynamics*, Oxford University Press, Oxford, UK.
[11] Furuya, O., 1975, "Exact Supercavitating Cascade Theory," ASME J. Basic Eng., **97**(4), pp. 129–141.
[12] Tulin, M. P., 1964, "Supercavitating Flows—Small Perturbation Theory," J. Ship Res., **7**(3), pp. 16–37.
[13] Wu, T. Y., 1972, "Cavity and Wake Flows," Annu. Rev. Fluid Mech., **4**, pp. 243–284.
[14] Stripling, L. B., and Acosta, A. J., 1962, "Cavitation in Turbopump—Part 1," ASME J. Fluids Eng., **84**, pp. 326–338.
[15] Devis, R. E., Coons, L. L., and Scheer, D. D., 1972, "Internal Streamline Flow Analysis for Turbopump Inducers Under Cavitating and Non-cavitating Conditions," J. Spacecr. Rockets, **9**(2), pp. 116–122.
[16] Knapp R. T., Daily, J. W., and Hammit, F. G., 1970, *Cavitation*, McGraw-Hill, New York.
[17] Crocco, L., and Lees, L., 1952, "A Mixing Theory for the Interaction Between Dissipative Flows and Nearly Isentropic Streams," J. Aerosp. Sci., **19**(10), pp. 649–676.
[18] Watanabe, S., Sato, K., Tsujimoto, Y., and Kamijo, K., 1999, "Analysis of Rotating Cavitation in Finite Pitch Cascade Using a Closed Cavity Model and a Singularity Method," ASME J. Fluids Eng., **121**, pp. 834–840.
[19] Gogish, L. V., and Stepanov, G. Yu., 1979, *Turbulent Separated Flows*, Nauka, Moscow (in Russian).
[20] Gurevich, M. I., 1965, *Theory of Jets in Ideal Fluids*, Academic Press, San Diego, CA.
[21] Woods, L. C., 1961, *The Theory of Subsonic Plane Flow*, Cambridge Univ. Press, London.
[22] Furness, R. A., and Hutton, S. P., 1975, "Experimental and Theoretical Studies on Two-Dimensional Fixed-Type Cavities," ASME J. Fluids Eng., **97**, pp. 515–522.
[23] Dang, J., and Kuiper, G., 1999, "Re-entrant Jet Modeling of Partial Cavity Flow on Three-Dimensional Hydrofoils," ASME J. Fluids Eng., **121**, pp. 781–787.
[24] Wade, R., and Acosta, A. J., 1967, "Investigation of Cavitating Cascades," ASME J. Basic Eng., **89**(4), pp. 1–14.
[25] Chang, P., 1966, *Separation of Flow*, Pergamon Press, New York.
[26] Schlichting, H., 1960, *Boundary Layer Theory*, McGraw-Hill, New York.
[27] Pilipenko V. V., Zadontsev V. A., and Natanzon M. S., 1977, "Cavitation Oscillations and Dynamics of Hydrosystems," Mashinostroenie, Moscow (in Russian).
[28] Brennen, C. E., and Acosta, A. J., 1973, "Theoretical, Quasi-Static Analyses of Cavitation Compliance in Turbopumps," J. Spacecr. Rockets, **10**(3), pp. 175–180.
[29] Azuma, S., Yoshida, Y., and Tsujimoto, Y., 2001, "Unsteady Blade Stress Caused by Rotating Cavitation," Turbomachinery, **29**(3), pp. 147–154 (in Japanese).
[30] Kamijo, K., Yoshida, M., and Tsujimoto, Y., 1993, "Hydraulic and Mechanical Performance of LE-7 LOX Pump Inducer," J. Propul. Power, **9**, pp. 819–826.

Experimental and Numerical Study of Unsteady Flow in a Diffuser Pump at Off-Design Conditions

Hong Wang
Post-Doctoral Research Fellow

Hiroshi Tsukamoto
Professor

Department of Biological Functions and Engineering,
Graduate School of Life Science and Systems Engineering,
Kyushu Institute of Technology,
1-1 Sensui-cho, Tobata,
Kitakyushu 804-8550, Japan

An experimental and numerical study was developed for the unsteady phenomena at off-design conditions of a diffuser pump. Unsteady pressure measurements were made downstream of the impeller, and the pressure fluctuations were analyzed using the ensemble averaging technique as well as the statistical and chaotic time series analysis. The unsteady flow was classified into five ranges as a result of the statistical and chaotic time series analysis. And a two-dimensional vortex method was employed to investigate the unsteady flow structure due to the interaction between impeller and diffuser vanes in a diffuser pump at various off-design conditions. The numerical results of unsteady flow at a partial discharge range (approximately 83% of the rated flow rate) show an asymmetrical separation bubble near the pressure surface of the impeller vane. The intermittence of the separation bubble may be the main factor to cause the unstable characteristics of the test diffuser pump. The calculated unsteady flow at the lower partial discharge range (50% of the rated flow rate) presents a rotating stall in the impeller passage as well as in the diffuser passage, which can be main cause of unstable characteristics there.
[DOI: 10.1115/1.1603305]

Introduction

In diffuser pumps, the centrifugal impeller interferes with the diffuser vanes and produces pressure fluctuations downstream of the impeller. These pressure fluctuations may become as large as the total pressure rise across the pump in the case of a small radial gap between the impeller and diffuser vanes. These fluctuations not only generate noise and vibration that cause unacceptable levels of stress and reduce component life due to fatigue, but also introduce unfavorable characteristics of pump performance even at or near the design point. Considerable experiments have been conducted in studying the interactions between the flow within the impeller and the diffuser vanes of centrifugal turbomachine at the rated flow rate since the 1960s, [1–8]. As discussed on axial turbines by Dring et al. [9], the interactions can be divided into potential and wake effects. The former affects both the impeller and the diffuser, and decreases with the increasing distance between blade rows. The latter impacts the flow downstream and should persist over larger distances. Recently Shi and Tsukamoto [10], and Wang and Tsukamoto [11] analyzed the potential and wake effects in a diffuser pump by comparing the calculated unsteady pressures with the measured ones.

Unsteady phenomena in diffuser pumps become more complicated at off-design operating conditions. At reduced flow rates, the flow rate and pressure of a pump become increasingly unstable. When substantial flow fluctuations are propagating at a low frequency along the circumference, but are limited to a part of the components (e.g., rotor, diffuser, or volute), the phenomenon is typically referred to as rotating stall. Yoshida et al. [12] investigated the rotating stall instability in a seven-bladed centrifugal impeller with a variety of diffusers. The stall propagation speed in the diffuser was less than 10% of the impeller speed, and it was most evident when the clearance between impeller and diffuser vanes was large. Using PIV and pressure fluctuation measurements, Sinha et al. [13] studied the occurrence of stall in a centrifugal pump with a vaned diffuser that has a gap of 20% of the impeller radius and 15.4% of the diffuser chord length. They demonstrated that the separation of the high-speed leakage flow in the gap from the exit side to the beginning of volute causes the onset of the rotating stall with 6.2% of the impeller speed.

However, it seems difficult to understand the unsteady phenomena only from experimental studies because of the complicated flow structures in pumps, especially at off-design conditions. Sun and Tsukamoto [14] calculated the off-design performance in a diffuser pump using a three-dimensional, unsteady RANS code with standard $k-\varepsilon$ turbulence models. Sano et al. [15] reported the numerical study of rotating stall in a pump vaned diffuser, in which the flow instabilities were observed in a range with negative slope of the pressure performance curve of the diffuser.

In spite of considerable efforts devoted to the study of rotating stall in pumps, the mechanism of the phenomenon has not yet been well understood. There exist some difficulties in employing the unsteady RANS solver: (1) mesh generation problem in the gap between the impeller and diffuser, (2) turbulence model problem in the complicated unsteady flow, and (3) convergence problem in grid and iteration number per time step. On the other hand, the vortex method can be applied easily to flows around complex geometry because it is grid-free. And the physical variables like vorticity, velocity, and pressure can be obtained directly without iteration process at every time step in the vortex methods, and thus there is no convergence problem for the vortex method. Moreover, Lagrangian representation of the evolving vorticity field in vortex methods is well suited to a moving boundary. In the present study, therefore, the vortex method, [11], was extended to the case of changing operating points at the off-design condition of pump. The pressure fluctuations due to the rotor-stator interaction and the rotating stall in a diffuser pump were calculated using the vortex method, and the calculated pressures were compared with the experimental data.

Contributed by the Fluids Engineering Division for publication in the JOURNAL OF FLUIDS ENGINEERING. Manuscript received by the Fluids Engineering Division November 20, 2002, revised manuscript received April 22, 2003. Associate Editor: Y. Tsujimoto.

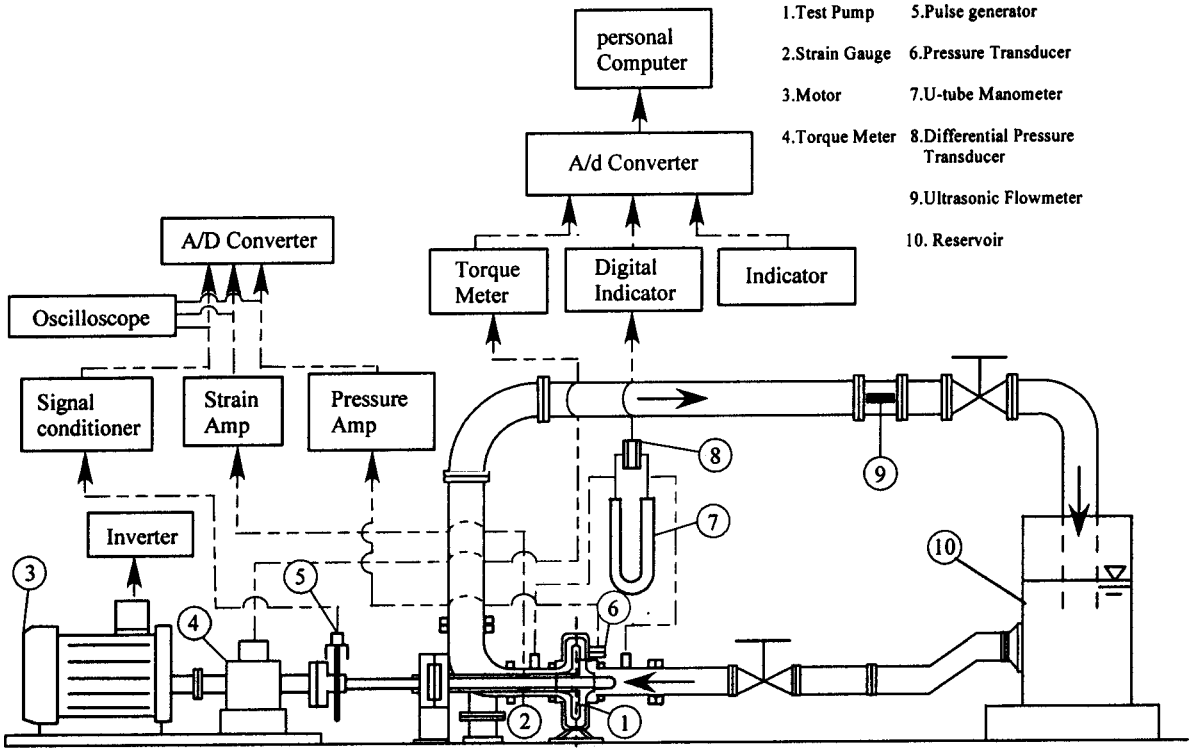

Fig. 1 Test rig and instrumentation system

Experimental Setup and Procedures

Figure 1 shows the test rig and the instrumentation system of the experiment. The experiment is conducted in a closed loop, which consists of a reservoir open to air, a suction valve, a test pump, a discharge pipe, and a discharge valve. The flow rate adjusted by the discharge valve is measured by the ultrasonic flowmeter installed in the discharge pipe. The rotational speed of the pump is detected by the pulse signals (60 pulses a revolution). In order to avoid cavitation, water is supplied into the suction port from a large reservoir with a water level of 1.6 m higher than the pump center through a short inlet pipe. The large reservoir is open to air, and thus there will not appear a marked low frequency oscillation in the present system, which usually happens in an airtight system due to the compressible air if existing.

The test pump is a centrifugal pump with a closed impeller illustrated in Fig. 2(*a*), and corresponds to one stage of a multistage centrifugal pump. Its principal specifications are summarized in Table 1. Figure 2(*b*) illustrates the unsteady pressure measurement stations on the shroud casing of the diffuser in the test pump. The measurement stations were arranged on the intersection of six radial and five streamwise grid lines in a blade-to-blade diffuser passage. Measurement stations were also arranged in other passages in order to measure the propagation of the pressure fluctuations toward the peripheral direction. The instantaneous suction and discharge pressure, as well as the unsteady pressure in the diffuser passage are measured by semiconductor-type pressure transducers, which are installed directly on the pressure taps in order to prevent the decrease of natural frequency in the pressure measurement systems. The instantaneous rotational speed and unsteady pressure are transmitted to an A/D convector and recorded on the data file in the computer.

Numerical Analysis

The two-dimensional unsteady viscous flow was calculated for the flow field around the impeller and vaned diffuser shown in Fig. 3 using the vortex method developed by the authors, [11]. The outline of the procedure will be described in this paper.

Flow Model. The continuous vorticity field is represented by the bound vortex elements γ_b adjoining the solid boundary, and the vortices γ_w emanating from the trailing edge and boundary layer. To satisfy the no-flux and no-slip boundary conditions simultaneously, in the present calculation, source panels σ are distributed just under the boundary surface as shown in Fig. 4, [16]. The wake and separated flow, which carry concentrations of vorticity, are traced by a Lagrangian scheme.

Unsteady Velocity. As an extension of the Biot-Savart law, [17], to two-dimensional unsteady viscous flow, the velocity $\mathbf{V}(\mathbf{r})$ in a domain S bounded by boundary L can be written as the sum of the velocity induced by all vortex elements in the domain S, and that induced by the absolute motion of the boundary L, that is

$$\beta\mathbf{V}(\mathbf{r}) = -\frac{1}{2\pi}\left[\int_S \frac{\boldsymbol{\omega}(\mathbf{r}_0)\times(\mathbf{r}_0-\mathbf{r})}{|\mathbf{r}_0-\mathbf{r}|^2}dS + \int_L \frac{\{\mathbf{V}(\mathbf{r}_0)\cdot\mathbf{n}_0\}(\mathbf{r}_0-\mathbf{r})}{|\mathbf{r}_0-\mathbf{r}|^2}dL - \int_L \frac{\{\mathbf{V}(\mathbf{r}_0)\times\mathbf{n}_0\}\times(\mathbf{r}_0-\mathbf{r})}{|\mathbf{r}_0-\mathbf{r}|^2}dL\right] \quad (1)$$

Here, $\mathbf{r}_0$ equals the position of the vortex elements or boundary elements, $\mathbf{r}$ equals the one where the velocity is being evaluated, and $\beta=1$ and 0.5 for $\mathbf{r}$ are in domain S and on boundary L, respectively.

Unknown Vorticity. The main problems in the present vortex method are how to represent the vorticity field and how to determine its position and strength to satisfy the boundary conditions. A Petrov-Galerkin boundary method, [18], was applied to determine the vorticity in the thin layer adjoining the solid boundary to satisfy the boundary conditions. As derived directly from the Navier-Stokes equations by the present authors, [11,19], the vorticity shedding from a stationary solid surface and a solid boundary rotating with angular velocity Ω can be determined by

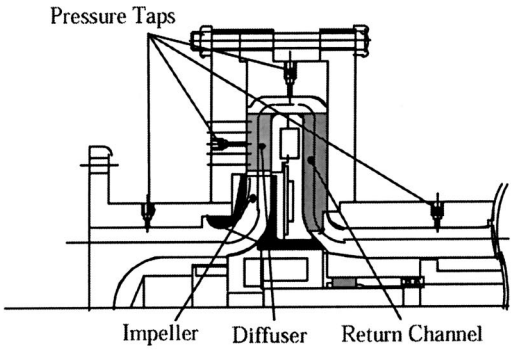

(*a*)

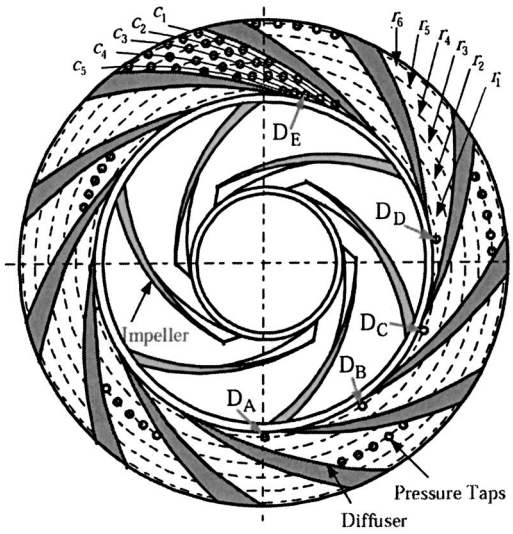

(*b*)

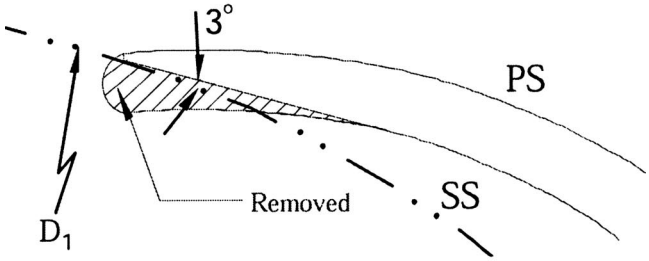

(*c*)

Fig. 2 Schematic configurations of test diffuser pump; (*a*) cross-sectional view of test pump, (*b*) impeller and diffuser, (*c*) leading edge of impeller vane

$$\Delta\Gamma_i = \int_{t_{j-1}}^{t_j}\int_{L_i}^{L_{i+1}} [\partial V_l/\partial t + \partial B/\partial L]dLdt \tag{2a}$$

and

$$\Delta\Gamma_i = \int_{t_{j-1}}^{t_j}\int_{L_i}^{L_{i+1}} [\partial W_l/\partial t + \partial B'/\partial L + (\partial\mathbf{\Omega}/\partial t\times\mathbf{r})\cdot\mathbf{l}]dLdt \tag{2b}$$

respectively, where $B' = B - \mathbf{U}\cdot\mathbf{V}$.

Table 1 Specifications of test pump

Rating:		**Impeller:**	
Q_0	4.4 m^3/min	R_2	165 mm
H_0	33.7 m	b_2	28 mm
N_0	1500 min^{-1}	β_2	24.3 deg
N_s	232 (m^3/min,m,min^{-1})	Z_i	6
Diffuser:		**Return Channel:**	
R_3	170 mm	R_5	240 mm
b_3, b_4	30 mm	b_5, b_6	34 mm
R_4	240 mm	R_6	120.5 mm
Z_d	11	Z_r	11
R_3/R_2	1.03	R_6/R_5	0.5

Unsteady Pressure. After the vorticity and velocity field are determined, the unsteady pressure can be calculated directly in the present two-dimensional flow calculation. The boundary element method was used to obtain the Bernoulli function B, [20]. In this study, an inner boundary surface L_2 was set between the rotor and stator as shown in Fig. 3, and by employing the Gaussian divergence theorem and the flow continuum equation, the following equation can be derived, [11]:

$$\begin{aligned}\beta_1 B'(\mathbf{r}) + \beta_2 B(\mathbf{r}) - \int_{L_i} B'(\mathbf{r}_0)\nabla G\cdot\mathbf{n}dL - \int_{L_d} B(\mathbf{r}_0)\nabla G\cdot\mathbf{n}dL \\ = \int_{L_i}\left(\frac{\partial\mathbf{\Omega}}{\partial t}\times\mathbf{r}_0\right)\cdot\mathbf{n}GdL - \Omega\int_{L_2}\frac{\partial V_r}{\partial\theta}GdL - \int_{L_2}(\mathbf{V}\cdot\mathbf{U})\nabla G \\ \cdot\mathbf{n}dL - \nu\int_{L_i+L_d}(\nabla G\times\boldsymbol{\omega})\cdot\mathbf{n}dL + \int_{S_1}\nabla G\cdot(\mathbf{W}\times\boldsymbol{\omega})dS \\ + \int_{S_2}\nabla G\cdot(\mathbf{V}\times\boldsymbol{\omega})dS\end{aligned} \tag{3}$$

where the values of β_1 and β_2 at $P(x_P, y_P)$ are shown in Table 2.

Instantaneous Flow Rate. The instantaneous pump operation is calculated by considering the change in the pump operating point. In the present calculation, the effects of pipe system was simplified by a equivalent pipe length, [21], and it was assumed that the pump delivers no elevation head, so the instantaneous flow rate $Q_i(t)$ can be calculated by

$$H(t) = (l_{eq}/gA_0)dQ/dt + \kappa H_0 Q^2/Q_0^2 \tag{4}$$

where H_0 and Q_0 are the rated total head and flow rates; $A_0 = \pi D_0^2/4$ is the nominal flow area; l_{eq} is equivalent pipe length referred to area A_0; and κ is the resistance coefficient. At every

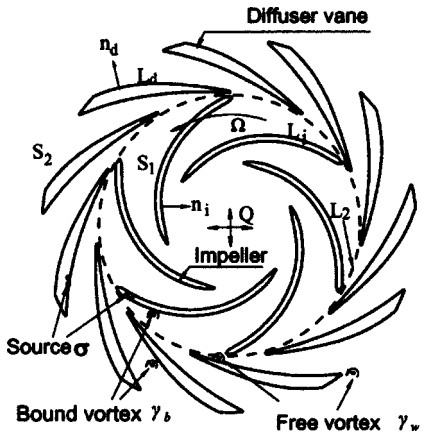

Fig. 3 Mathematical model for calculation

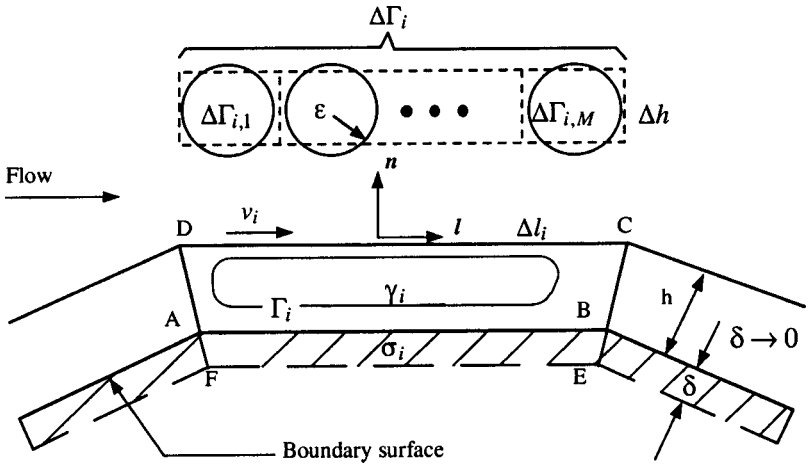

Fig. 4 Panel around solid boundary and nascent vortex elements

calculation step, the pump operating point is determined in the process of resolving iteratively the instantaneous flow rate and total head rise in Eqs. (3) and (4).

Calculation Condition and Numerical Uncertainty. In the present calculation, the thickness of the vortex panels adjoining the solid boundary is assumed to be $h/D_2=2.0/\sqrt{\mathrm{Re}}$. The instantaneous rotational speed of pump, $N(t)$, is assumed to be

$$N(t)=N_f(1-e^{-t/T_{na}}) \tag{5}$$

where $T_{na}=T_0$ was assumed in the present study.

Although the present vortex method is grid-free and deterministic, the numerical results may be affected by the number of panels on the boundary surface as well as the free vortices in the flow field. Thus the uncertainty analysis was conducted in detail in our previous study, [11], in which it was proven that accurate computations could be obtained from 240 time steps per revolution, 45 panels per blade, approximately 25,000 vortex elements for the rated operating condition, and whereas there are 30,000 vortex elements for the off-design operational condition. The present calculations were done for 198 time steps per revolution, 60 panels per blade, and approximately 30,000 vortex elements for the entire flow field. The time increment Δt is 2.02×10^{-4} seconds for 198 time steps per revolution under the rotational speed $N_0=1500$ min^{-1}. The computation was done during 30 revolutions, that is, 5920 time steps in 1.2 seconds. Therefore, the unsteady components can be captured in the frequency ranges from 1.67 Hz to 2475 Hz. The CPU time is about 330 hours (two weeks) on a Workstation VT-Alpha 666 (666 MHz Alpha processor, 1GB RAM).

Results and Discussion

Performances and Steady Pressure. The performance test of the diffuser pump has been conducted before going into the detailed unsteady pressure measurements. Figure 5(*a*) shows the measured and calculated performance curves of the test pump. The calculated flow rate and total pressure rise shown in this figure are time-averaged during the period of Nt from 6 to 16. The performance curve calculated by vortex method agrees qualita-

Table 2 Values of β_1 and β_2 in Eq. (6)

Locations of P	β_1	β_2
in S_1	1	0
on L_i	0.5	0
on L_2	0.5	0.5
in S_2	0	1
on L_d	0	0.5

*$\int_s B\cdot\nabla^2 G dS=-(\beta_1 B'+\beta_2 B)$

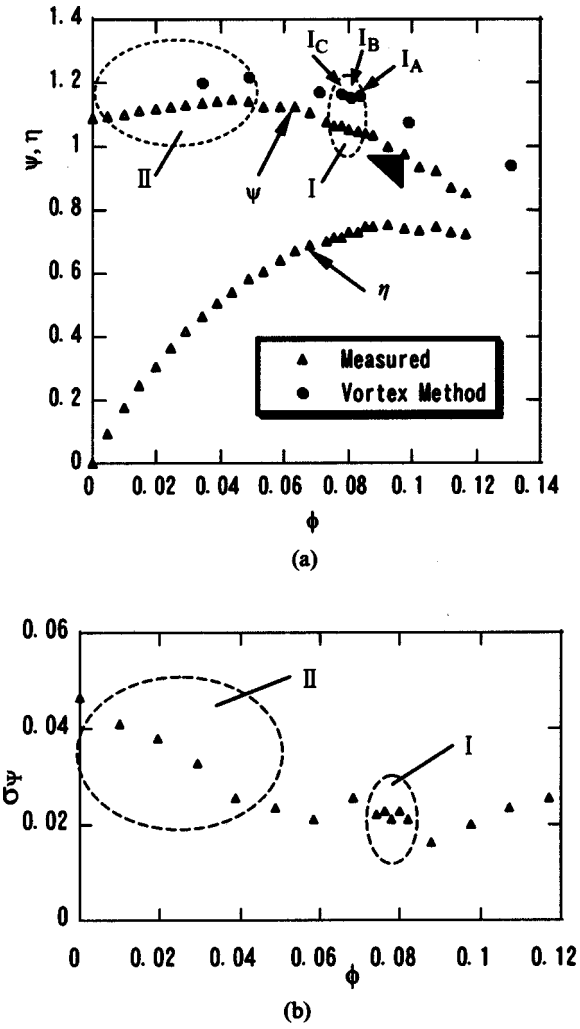

Fig. 5 Pump characteristics curve; (*a*) total pressure rise coefficient and pump efficiency and (*b*) standard deviation of total pressure rise, the experimental uncertainties $\psi=\pm1.0\%$, $\phi=\pm1.6\%$, and $\eta=\pm2.5\%$

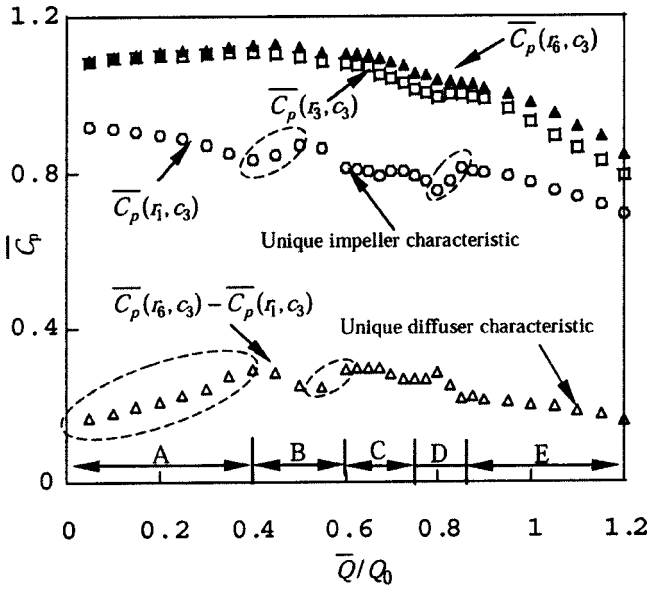

Fig. 6 Variation in steady pressure versus flow rate at the inlet, mid, and exit of diffuser passage; the experimental uncertainties $Q=\pm1.5\%$, and $C_p=\pm0.9\%$

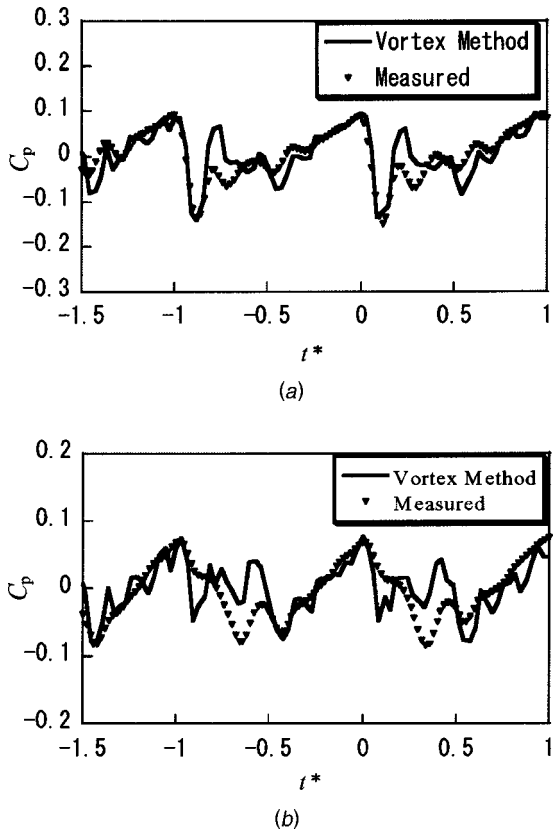

Fig. 7 Comparison of unsteady pressure in the time domain, (*a*) (r_1,c_1); (*b*) (r_1,c_3), the experimental uncertainties $C_p=\pm0.9\%$

tively with the measured one. However, the calculated absolute value is 10% bigger than the measured one because the hydraulic losses in the bend and return channel (see Fig. 2) are ignored in the present two-dimensional calculation. The performance curve

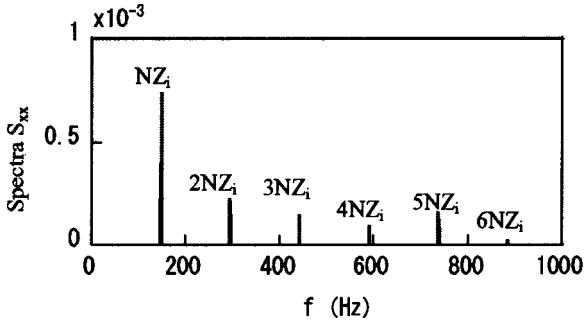

Fig. 8 Measured pressure fluctuations at station (r_1,c_1) in the frequency domain for the rated condition, the experimental uncertainties $S_{xx}=\pm1.8\%$

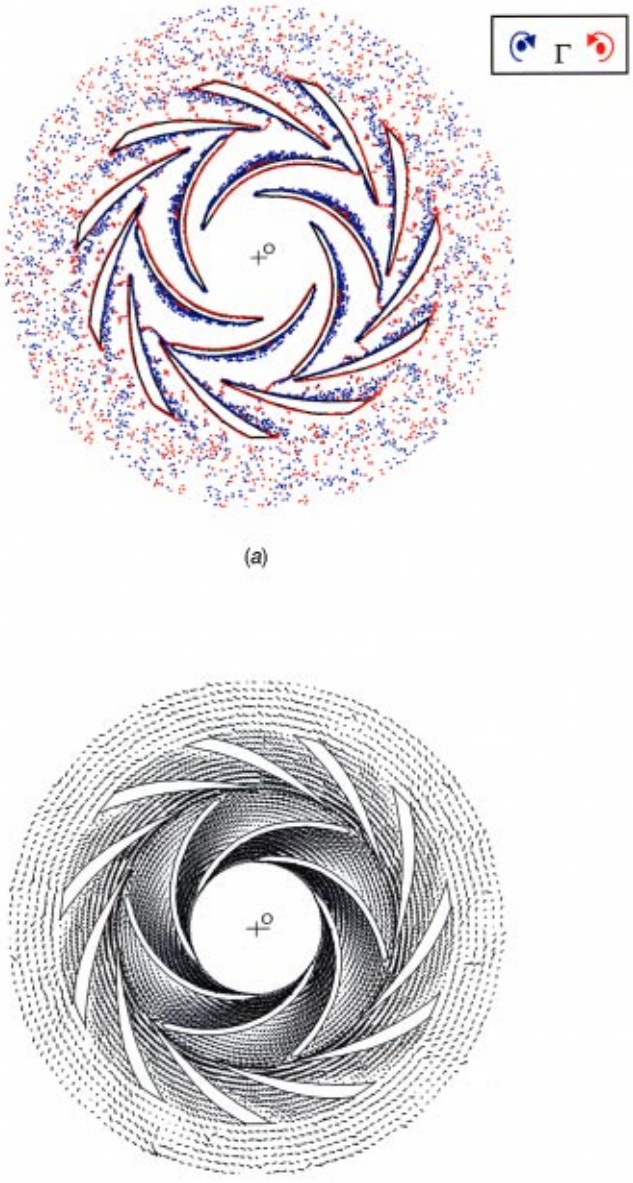

Fig. 9 Calculated flow pattern at $Nt=131/9$ for $\bar{Q}/Q_0\approx0.86$; (*a*) vortex pattern (*b*) velocity contour

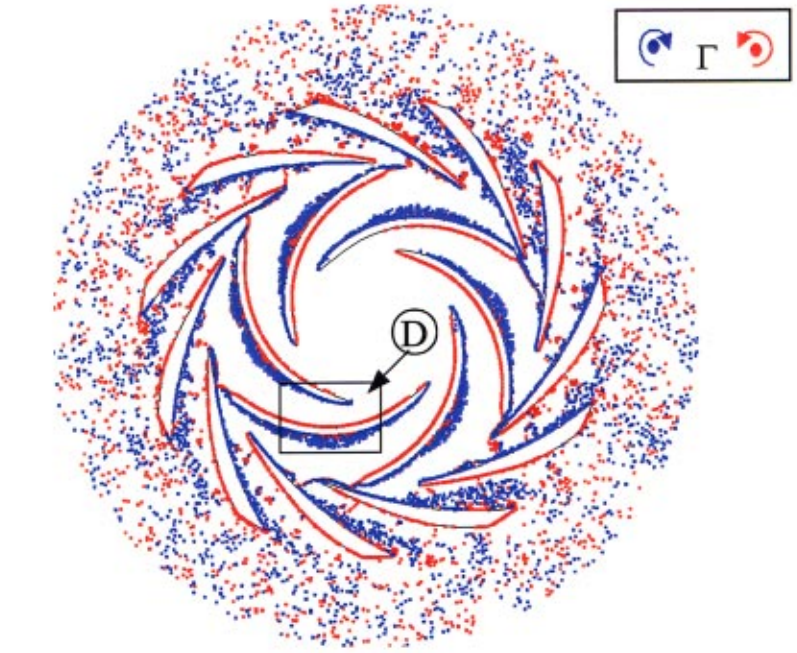

(a)

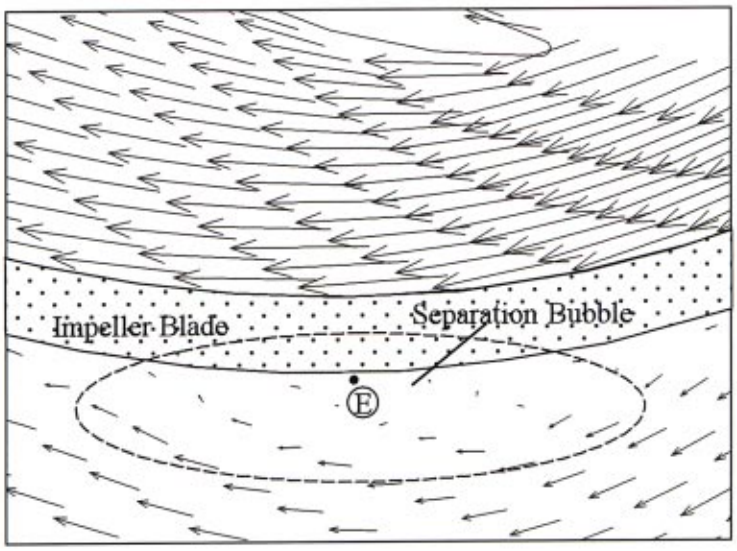

(b)

Fig. 10 Calculated flow pattern at $Nt=93/9$ for $\bar{Q}/Q_0\approx 0.83$; (*a*) vortex pattern, (*b*) velocity contour in area (D)

shows that there exists an evident positive slope below the 50% of the rated flow rate designated by II, and a slightly positive slope in a very small range at approximately 80 percent of the rated flow rate designated by I. As is well known, the diffuser pump becomes unstable when operating in these ranges with positive slope of characteristic curve. Figure 5(*b*) shows the standard deviation of the measured total pressure rise, σ_ψ. There exists marked increase in σ_ψ in these two ranges designated by I ($Q/Q_0\approx 0.8$) and II ($Q/Q_0<0.5$).

Figure 6 presents the time-averaged pressure coefficient $\overline{C_p}$ on the representative pressure taps (r_1,c_3) at the inlet, (r_3,c_3) at the mid, and (r_6,c_3) at the outlet of the diffuser passage. This figure also shows the $\{\overline{C_p}(r_6,c_3)-\overline{C_p}(r_1,c_3)\}$ which reflects the diffuser performances. At $Q/Q_0\approx 0.8$ and $0.4<Q/Q_0<0.6$ the slope of $\overline{C_p}(r_1,c_3)$ is positive, which shows the unique impeller performance. On the other hand, there exists positive slope of the unique diffuser performance at $Q/Q_0<0.4$ and $0.5<Q/Q_0<0.7$. Based on the positive slope of these characteristic curves, the entire operating range can be classified into five ranges from A to E as shown in Fig. 6.

Pressure Fluctuations at Rated Flow Rate. The spectrum

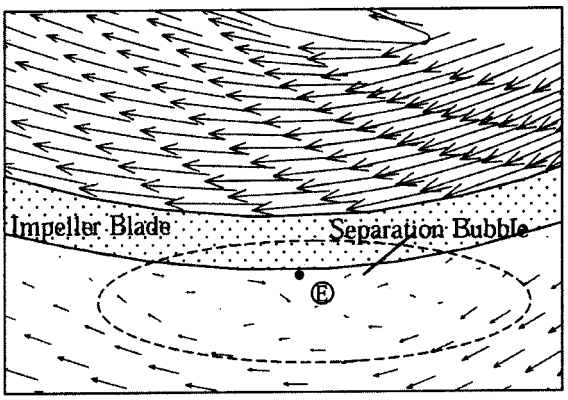

Fig. 11 Velocity contour at $Nt=93/9$ in area Ⓓ for $\bar{Q}/Q_0 \approx 0.80$

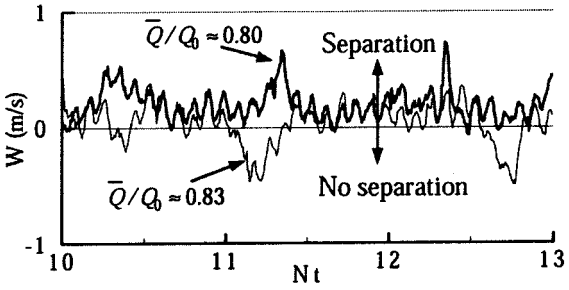

Fig. 12 Time histories of relative velocity at station Ⓔ

analysis was done for unsteady pressure data recorded with the sampling frequency of 2000 Hz in 50 seconds to capture the lower frequency components of the pressure fluctuations. Figures 7(*a*) and (*b*) show the comparisons of the time histories of the unsteady pressure calculated by vortex methods with the measured data at measurement stations (r_1,c_1) and (r_1,c_3) (see Fig. 2(*b*)). The measured unsteady pressures shown in these figures are phase-averaged in 100 revolutions of the impeller. Numerical and experimental pressures show the peak and valley due to the potential and wake effects in the rotor-stator interaction, as can be seen in Fig. 7(*a*). And the amplitude of the calculated unsteady pressure show good agreements with the measured one. Thus the present numerical results are acceptable, although they do not always coincide with the experimental data as shown in Fig. 7(*b*).

Figure 8 presents the power spectral density function of pressure measured at the pressure tap (r_1,c_1) for the rated condition. The unsteady pressure in the diffuser passage fluctuates with the impeller blade passing frequency NZ_i and its higher harmonics as shown in this figure. This characteristic agrees well with the previous analysis, [11], and therefore the present measured data are available to analyze the lower frequency components in the lower flow rates. There seems to exist no abnormal flow in the diffuser pump at the rated condition, in which lower frequency components are not dominant.

Unsteady Flow at Unstable Range. The unstable characteristics of the pump will be discussed by considering unsteady flows at the operating points I_A, I_B and I_C in unstable range I shown in Fig. 5.

Figure 9 shows the calculated vortex pattern and velocity contour at the normalized instant of $Nt=131/9$, for $Q/Q_0 \approx 0.86$ (the operating point I_A in Fig. 5). In Fig. 9(*b*), the vector in the impeller passage stands for the relative velocity, whereas the one in other passage represents the absolute velocity.

Figure 10 shows the calculated vortex pattern and velocity contour at the normalized time of $Nt=93/9$, for $Q/Q_0 \approx 0.83$ (the operating point I_B in Fig. 5). The comparison of the vortex patterns in Figs. 9 and 10 show that vortex layer on the pressure surface of the impeller vane is thicker in the latter case than in the former case. Figure 10(*b*) shows the velocity contour in the local area Ⓓ shown in Fig. 10(*a*). In Fig. 10(*b*), there exists a separating bubble near the pressure surface of the impeller vane.

Figure 11 shows the velocity contour at $Q/Q_0 \approx 0.80$ (the operating point I_C in Fig. 5) in the same local area Ⓓ and at the same instant $Nt=93/9$ as Fig. 10(*b*). There exists a separating bubble near the pressure side of the impeller vane.

Figure 12 shows the time histories of relative velocity at the location Ⓔ (see Figs. 10 and 11), which is near the midst of the pressure surface of the impeller vane and distant *h* from the pressure surface. The relative velocity with an anti-clockwise around the vane is defined to be positive. Therefore there exists a separating flow when the relative velocity shown in the figure is positive. Otherwise no separating flow appears near the pressure surface of the impeller vane. The separating bubble is found to be intermittent for $Q/Q_0 \approx 0.83$ as can be seen in Fig. 12. The intermittence of the separating bubble is thought to be one of the main factors to cause the unstable characteristic of the test diffuser pump around the rated flow rate.

Figure 13 presents the calculated results at $Q/Q_0=0.50$. Figure 13(*a*) shows the time histories of the circulation around diffuser vanes D1 to D11. Figures 13(*b*), (*c*), and (*d*) present the velocity contour in the diffuser pump at the instant $Nt=6$, 11 and 16 after the pump start, respectively. As can be seen in these figures, the diffuser vane D7, D3, and D9 are stalled completely at the instant $Nt=6$, 11, and 16, respectively. From Fig. 13(*b*) to (*d*), the circulation shown in Fig. 13(*a*) is found to be greater than 1 m^2/s on the stalled diffuser. Thus, the time histories of the circulation around diffuser vane show the propagation of stall among the diffuser passages.

The separating flow on the pressure surface of the impeller vane will be explained by considering the difference of the separating flow around a stationary blade from the one around a rotating blade in a rotating coordinates. In the relative velocity field expressed by

$$\nabla \times \mathbf{W} = \boldsymbol{\omega} - 2\boldsymbol{\Omega} \tag{6}$$

the flow relative to the rotating blade has a ''relative eddy,'' that is a distributed vorticity of magnitude 2Ω throughout the flow domain. Recently, Lewis [22] reported that the influence of the distributed vorticity 2Ω could be so dominant, notably for reduced flow rates, that a standing eddy was found on the driving surface of the blades in a centrifugal compressor. This standing eddy causes the separating flow on the pressure side of the impeller vane. In addition to that, the impeller vane inlet is removed at the suction side and the inlet blade angle is only 3 deg relative to the circumference to avoid the cavitation as shown in Fig. 2(*c*). This small inlet angle is thought to be one of the reasons why the separating flow appears first not on the suction side of the impeller vane but on the pressure side, even at the very reduced flow rates in the present test diffuser pump.

Unsteady Pressures at Unstable Range. Figure 14 presents the power spectrum of pressure fluctuations at the lower frequency domain on the pressure tap (r_1,c_3). In order to make the comparisons of the contributions of the lower frequency pressure fluctuations in the various flow rates, the power spectrum are normalized by the maximum value of S_{xx}, $RS_{xx}=S_{xx}/\max(S_{xx})$. In the range A ($\bar{Q}/Q_0<0.4$), there appear no dominant low frequencies less than the impeller rotating frequency as presented in Fig. 14(*a*). A dominant frequency of unsteady pressure appears at 0.3 Hz in the range B ($0.4 \leqslant \bar{Q}/Q_0<0.6$) as can be seen in Fig. 14(*b*). There exists a dominant frequency of unsteady pressure at 0.24 Hz in the range D ($0.75 \leqslant \bar{Q}/Q_0<0.85$) as shown in Fig. 14(*c*). No dominant low frequencies are found in the ranges C (0.6

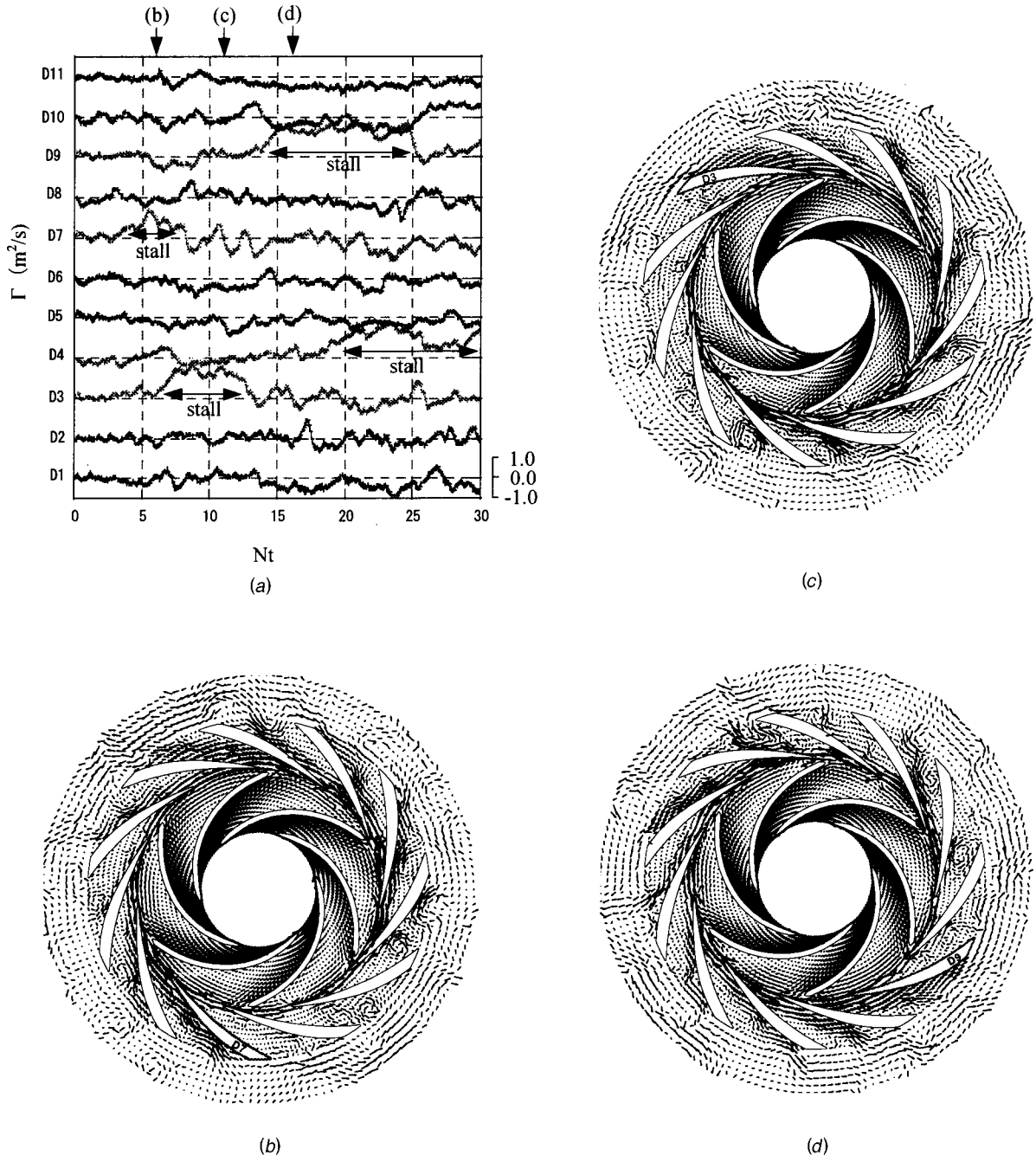

Fig. 13 Calculated flow pattern at low discharge range ($\bar{Q}/Q_0=0.50$); (*a*) circulation change around each diffuser vane, (*b*) velocity contour at $Nt=6$, (*c*) velocity contour at $Nt=11$, (*d*) velocity contour at $Nt=16$

$\leqslant \bar{Q}/Q_0 < 0.75$) and E ($0.85 \leqslant \bar{Q}/Q_0 < 1.20$) as shown in Fig. 14(*d*). These spectra of unsteady pressure showed that the dominant frequencies are the impeller blade passing frequency and its higher harmonics, and thus the pump is assumed to be stable in these two ranges.

Figures 15(*a*) and (*b*) show the normalized power spectra $RS_{xx}=S_{xx}/\max(S_{xx})$ of the unsteady pressures at the measurement station (r_3,c_3) for $Q/Q_0\approx 0.8$ and $Q/Q_0\approx 0.45$, respectively. The power spectra at the diffuser inlet measurement station (r_1,c_3) are shown in these figures for the comparisons. The magnitudes of the dominant lower frequency pressure components decrease from the diffuser inlet to the midst. The waveform of the power spectra at the midst is similar to the one at the inlet for $Q/Q_0\approx 0.8$, whereas the power spectra are different each other for $Q/Q_0\approx 0.45$. There exists no abnormal flow in the diffuser passage for $Q/Q_0\approx 0.8$, and thus the waveform of the power spectra at lower frequency has no evident change; whereas there exists complex separating flow or stall in the diffuser passage for $Q/Q_0\approx 0.45$, and thus the waveform of the power spectra at lower frequency shows evident change. These phenomena are verified in our numerical analysis as described later.

Figures 16(*a*) and (*b*) present the cross spectra of the unsteady pressure at the measurement station (r_1,c_3) between the diffuser passage D_E and D_D shown in Fig. 2(*b*) for $Q/Q_0\approx 0.8$ and $Q/Q_0\approx 0.45$, respectively. The cross spectra are normalized by the maximum value S_{xy}, $RS_{xy}=|S_{xy}|/\max(|S_{xy}|)$. The lower frequency pressure component is dominant at 0.24 Hz for $Q/Q_0\approx 0.8$, whereas the pressure component is dominant at 0.3 Hz and

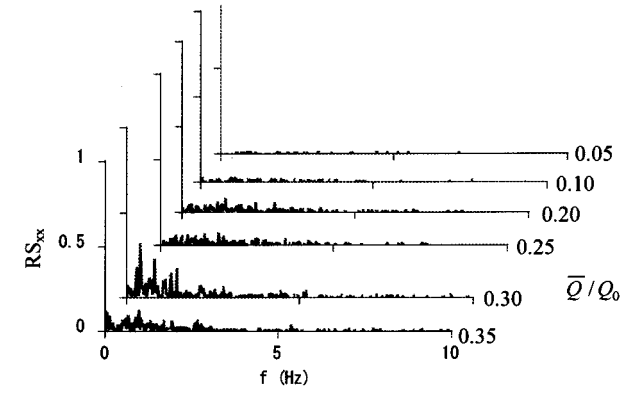

(*a*)

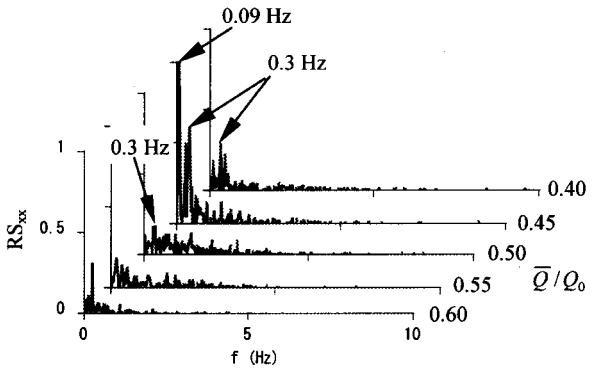

(*b*)

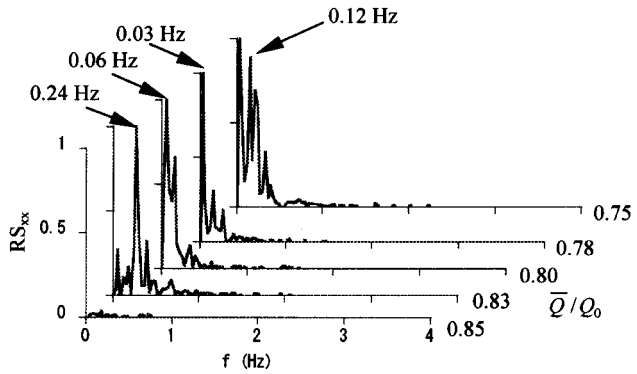

(*c*)

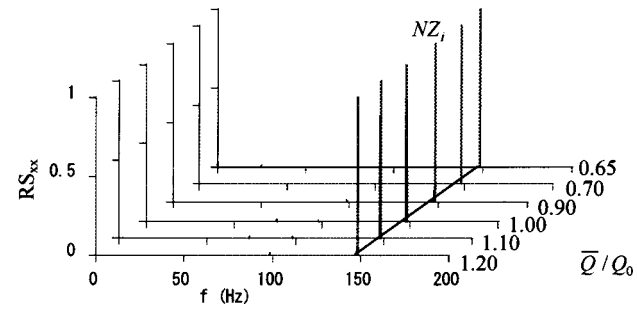

(*d*)

Fig. 14 Unsteady pressure at station (r_1, c_3) in the frequency domain; (*a*) $\bar{Q}/Q_0 = 0.35, 0.30, 0.25, 0.20, 0.10, 0.05$, (*b*) $\bar{Q}/Q_0 = 0.60, 0.55, 0.50, 0.45, 0.40$, (*c*) $\bar{Q}/Q_0 = 0.85, 0.83, 0.80, 0.78, 0.75$, and (*d*) $\bar{Q}/Q_0 = 1.20, 1.10, 1.00, 0.90, 0.70, 0.65$; the experimental uncertainties $Q = \pm 1.5\%$, $C_p = \pm 0.9\%$

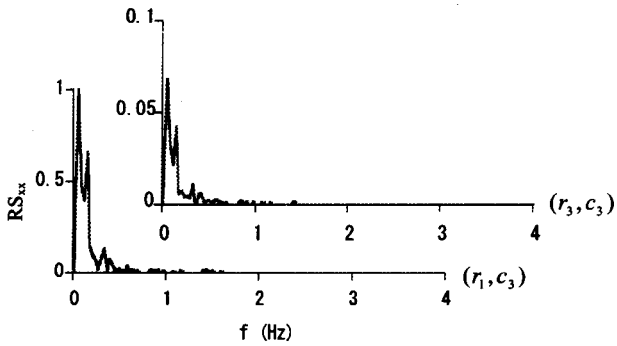

(*a*)

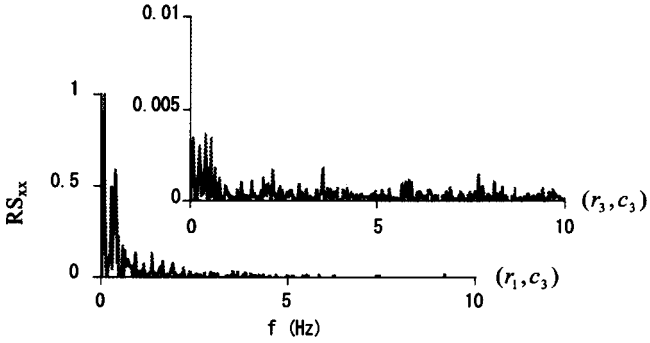

(*b*)

Fig. 15 Comparison of unsteady pressure in the frequency domain at stations (r_1, c_3) and (r_3, c_3); (*a*) $\bar{Q}/Q_0 = 0.80$ and (*b*) $\bar{Q}/Q_0 = 0.45$; the experimental uncertainties $Q = \pm 1.5\%$ $C_p = \pm 0.9\%$

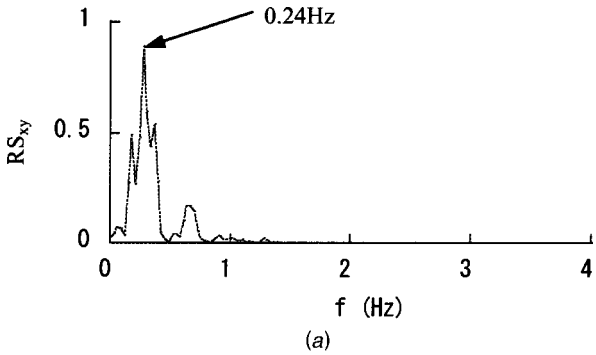

(*a*)

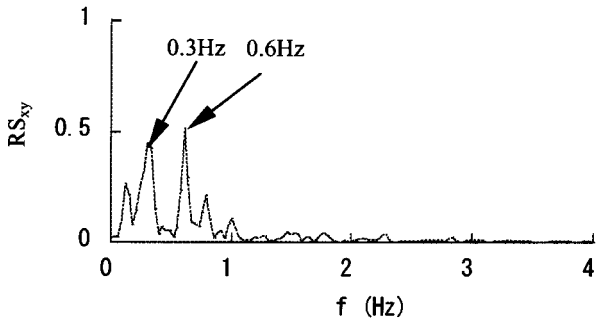

(*b*)

Fig. 16 Cross spectra at station (r_1, c_3) in D_E and D_D passage (see Fig. 2(*b*)); (*a*) $\bar{Q}/Q_0 = 0.80$ and (*b*) $\bar{Q}/Q_0 = 0.45$; the experimental uncertainties $Q = \pm 1.5\%$ $C_p = \pm 0.9\%$

Table 3 Cross spectra information at the dominant frequency of the unsteady pressure between passage D_E and D_D

$\overline{Q}/Q_0$	0.80		0.45		
f (Hz)	0.24	150 $=NZ_i$	0.30	0.60	150 $=NZ_i$
RS_{xy}	0.89	1.0	0.45	0.51	1.0
Coherence	0.98	0.99	0.99	0.99	0.99
Phase	57 deg	64 deg	50 deg	86 deg	50 deg
$\omega_c(f)/\Omega$	0.0018	1.09	0.0025	0.0029	0.85

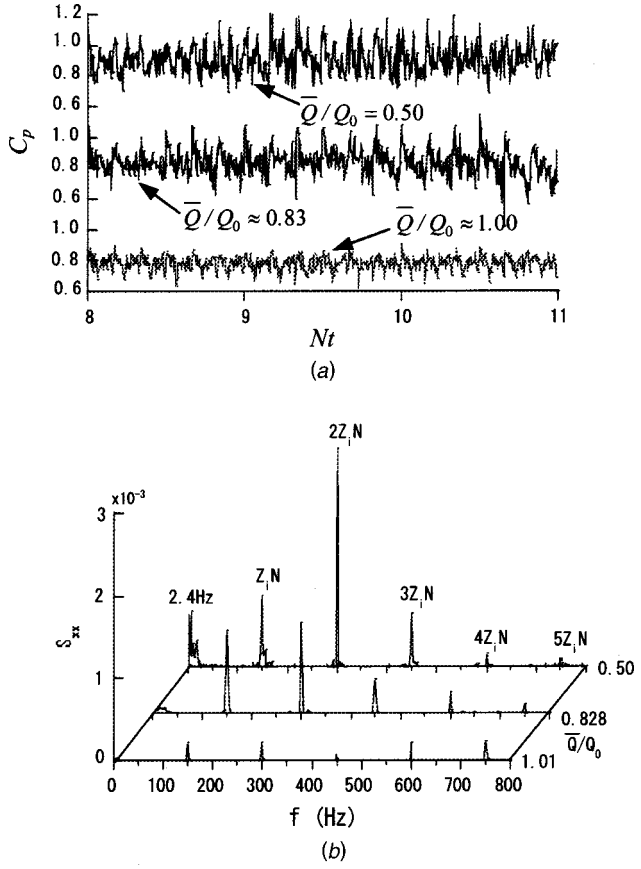

Fig. 17 Calculated unsteady pressure at station (r_1, c_3); (*a*) in time domain and (*b*) in frequency domain

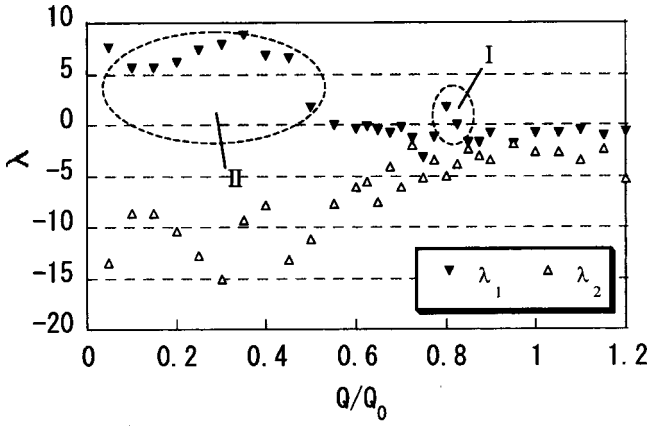

Fig. 18 The Liapunov exponents of unsteady pressure at station (r_1, c_3)

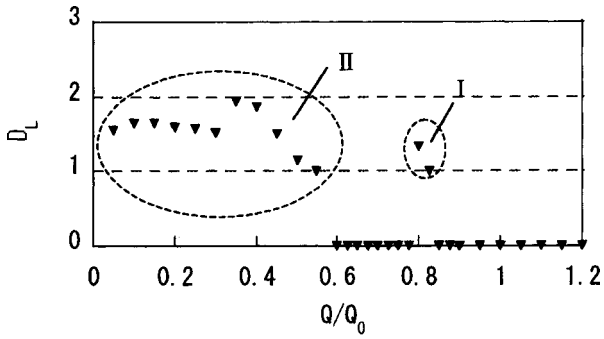

Fig. 19 The Liapunov dimension of unsteady pressure at station (r_1, c_3)

0.6 Hz for $Q/Q_0 \approx 0.45$. Table 3 presents the coherence, phase, and the propagation speed of the dominant lower frequency between the passage D_E and D_D. The dominant lower frequency pressure component is found to propagate with 0.2% of the revolution speed, and maybe attributed by a rotating stall.

Figures 17(*a*) and (*b*) depict the calculated pressure fluctuations on the representative pressure tap (r_1, c_3) (see Fig. 2(*b*)) at 50, 81, and 100% of the rated flow rate at the time and frequency domains, respectively. The present simulations demonstrate that, at the rated condition, the unsteady pressure in the diffuser passage fluctuates with the impeller blade passing frequency NZ_i and its higher harmonics. On the other hand, a dominant frequency of unsteady pressure appears at 2.4 Hz for $Q/Q_0 = 0.50$, which is thought to be the effect of the rotating stall in the diffuser passage, but that does not coincide with the measured frequency. The lowest frequency to be captured is 1.67 Hz in calculations, since the present result was obtained for 1.2 s (30 revolutions of the impeller) as described previously. In the experiment a dominant frequency appears at 0.3 Hz as presented in Fig. 14(*b*), while the frequency component of 0.3 Hz could not be captured in the calculation because of the limit of the computational time. The four diffuser blades have experienced stall for 1.2 s as shown in Fig. 13, and then it takes about 3.3 s for all 11 diffuser blades to experience the stall. The frequency of the stall propagation may, therefore, be supposed to be 0.3 Hz, which coincides to the measured value. It is also necessary to develop more comprehensive tools to analyze the rotating stall in the future research work, since the rotating stall is affected by many factors so that it appears in various ways at various flow rates and instants, [1,15]

Chaotic Time-Series Analysis. The time histories of the unsteady pressure fluctuations become irregularly random in the lower capacity ranges due to the effects of the complicated flows such as separating flow, rotating stall, and reverse flow in pumps as can be see in Fig. 17(*a*). In additions to the traditional signal processing technique like fast Fourier transformation, the chaotic time-series analysis is adopted to explore and extract the information hidden in the pressure fluctuations, [23–25]. If the pressure signal has resulted from a low-dimensional chaotic system, a technique of the chaotic time series can be employed to obtain some valuable information hidden in this apparently random signal, [23].

Figure 18 shows the first two Liapunov exponents of unsteady pressure at station (r_1, c_3). The first Liapunov exponents λ_1 are found to be positive in the two flow ranges; $Q/Q_0 \leqslant 0.5$ (range A and B) and $Q/Q_0 \approx 0.8$ (range D), and therefore the unsteady pressures are chaotic and unstable in these two ranges. Figure 19 shows the Liapunov dimension calculated from the same data as Fig. 18. The Liapunov dimension, one of the chaotic dimensions, is calculated by

$$D_L = m + \left(\sum_{i=1}^{m} \lambda_i \Big/ |\lambda_{K+1}| \right)$$

where $\Sigma_{i=1}^{m}\lambda_i > 0$, $\Sigma_{i=1}^{m+1}\lambda_i < 0$, λ_i are arranged in a descending order and K is the number that the first K Liapunov exponents are all positive. The Liapunov dimension is in the interval (1, 2), and thus, the unsteady pressures in these two ranges are resulted from a low-dimensional chaotic system.

Conclusion

An experimental and numerical study was conducted on the unsteady phenomena at the off-design conditions of a diffuser pump. As the result of the statistical and chaotic time series analysis of the measured and calculated unsteady pressures, the following conclusions are derived:

1. The impeller blade passing frequency and its higher harmonics are always dominant in the pressures downstream of the impeller for the whole flow range because of the rotor-stator interaction.
2. There exist some lower dominant frequencies in the pressures downstream of the impeller for unstable range because of the effects of the complicated flows such as separating flow, rotating stall and reverse flow in pumps. These lower dominant frequencies are dependent on the flow rate and the unsteady pressures are chaotic in these unstable ranges. The unsteady flow was classified into five ranges based on the flow structures:

a. range A at $Q/Q_0 \leqslant 0.40$, where the pump is unstable because of the separating flow and stall mainly in the diffuser.
b. range B at $0.4 < Q/Q_0 \leqslant 0.60$, where the pump is unstable due to the separating flow and stall in both impeller and diffuser, which are verified in the numerical calculations.
c. range C at $0.60 < Q/Q_0 \leqslant 0.75$, where the pump is stable.
d. range D at $0.75 < Q/Q_0 \leqslant 0.85$, where the pump is unstable because of the separating flow and stall in impeller, and where the numerical results of unsteady flow show the intermittent asymmetrical separation bubble near the pressure surface of the impeller vane, which may be one of the main factors to cause the unstable characteristics of the test diffuser pump.
e. range E at $0.85 < Q/Q_0 < 1.2$, where the pump is stable.

Acknowledgment

The study was supported by the Japanese Ministry of Education, Science and Culture under a grant-in-aid for Scientific Research, No. 09450081. This support is gratefully acknowledged.

Nomenclature

B = Bernoulli function $= p/\rho + V^2/2$
B' = relative Bernoulli function $= B - \mathbf{U}\cdot\mathbf{V}$
b = passage width
C_p = pressure coefficient $= (p - p_s)/(\rho U_2^2/2)$
ΔC_p = nondimensional unsteady pressure $= C_p - \overline{C_p}$
c = symbol of pressure traverse line
D = impeller diameter
D_L = Liapunov dimension
f = frequency
G = Green function
H = total head rise across pump
H_0 = rated total head
$\mathbf{k}$ = unit vector for z-direction in Cartesian system (x,y,z)
L = boundary of concerned domain
l_{eq} = equivalent pipe length
$\mathbf{l},\mathbf{n}$ = unit vector for longitudinal and normal directions on boundary L
N = rotational speed
Nt = number of impeller revolutions after its start $= \int_0^t N(t)dt$
PS = pressure surface
p = static pressure
p_s = static pressure at suction port
Q = flow rate
Q_0 = rated flow rate
R = radius
Re = Reynolds number $= D_2 V_0/\nu$
r, θ = cylindrical coordinates
S = entire region of concerned domain
SS = suction surface
S_{XX} = power spectra
T_0 = time required for one revolution of impeller
T_i = time required for one pitch of impeller blade
T_{na} = nominal acceleration time
t = time
t^* = nondimensional time $= t/T_i$
$\mathbf{U}$ = peripheral velocity
U_2 = peripheral speed of impeller
V_0 = meridian velocity at suction port
$\mathbf{V}$ = absolute velocity
$\mathbf{W}$ = relative velocity
Z = number of vanes
ϕ = flow rate coefficient $= Q/(2\pi R_2 b_2 U_2)$
Γ = circulation (counter clockwise is positive)
γ = vorticity in thin layer of fluid adjoining solid boundary L
η = pump efficiency
κ = resistance coefficient of pumping system
λ = Liapunov exponent
ν = kinematic viscosity
ρ = density
σ = source
Ω = angular velocity
$\boldsymbol{\omega}$ = vorticity
ψ = total pressure rise coefficient $= 2gH/U_2^2$

Subscripts

d = diffuser
i = impeller
r = return channel
1, 2 = impeller inlet and outlet
3, 4 = diffuser inlet and outlet
5,6 = return channel inlet and outlet
∞ = infinite

Superscript

$\bar{}$ = time-averaged value

References

[1] Brennen, C. E., 1994, *Hydrodynamics of Pumps*, Concept ETI, Inc. and Oxford University Press, pp. 173–218; 261–311.
[2] Tsukamoto, H., Uno, M., Hamafuku, H., and Okamura, T., 1995, "Pressure Fluctuation Downstream of a Diffuser Pump Impeller," The Second Joint ASME/JSME Fluids Engineering Conference, Forum of Unsteady Flow, ASME, New York, FED–Vol. 216, pp. 133–138.
[3] Arndt, N., Acosta, A. J., Brennen, C. E., and Caughey, T. K., 1989, "Rotor/Stator Interaction in a Diffuser Pump," ASME J. Turbomach., **111**, pp. 213–221.
[4] Arndt, N., Acosta, A. J., Brennen, C. E., and Caughey, T. K., 1990, "Experimental Investigation of Rotor/Stator Interaction in a Diffuser Pump With Several Vaned Diffusers," ASME J. Turbomach., **112**, pp. 98–107.
[5] Akin, O., and Rockwell, D., 1994, "Actively Controlled Radial Flow Pumping System: Manipulation of Spectral Content of Wakes and Wake-Blade Interactions," ASME J. Fluids Eng., **116**, pp. 528–537.
[6] Akin, O., and Rockwell, D., 1994, "Flow Structure in a Radial Flow Pumping System Using High-Image-Density Particle Image Velocimetry," ASME J. Fluids Eng., **116**, pp. 538–544.
[7] Eisele, K., Zhang, Z., and Casey, M. V., 1997, "Flow Analysis in a Pump Diffuser—Part 1: LDA and PTV Measurements of the Unsteady Flow," ASME J. Fluids Eng., **119**, pp. 968–977.
[8] Muggli, F. A., Eisele, K., Casey, M. V., Gulich, J., and Schachenmann, A.,

1997, ''Flow Analysis in a Pump Diffuser—Part 2: Validation and Limitations of CFD for Diffuser Flows,'' ASME J. Fluids Eng., **119**, pp. 978–984.
[9] Dring, R. P., Joslyn, H. D., Hardin, L. W., and Wagner, J. H., 1982, ''Turbine Rotor-Stator Interaction,'' ASME J. Eng. Gas Turbines Power, **104**, pp. 729–742.
[10] Shi, F., and Tsukamoto, H., 2001, ''Numerical Study of Pressure Fluctuations Caused by Impeller-Diffuser Interaction in a Diffuser Pump Stage,'' ASME J. Fluids Eng., **123**, pp. 466–474.
[11] Wang, H., and Tsukamoto, H., 2001, ''Fundamental Analysis on Rotor-Stator Interaction in a Diffuser Pump by Vortex Method,'' ASME J. Fluids Eng., **123**, pp. 737–747.
[12] Yoshida, Y., Murakami, Y., Tsurusaki, T., and Tsujimoto, Y., 1991, ''Rotating Stalls in Centrifugal Impeller/Vaned Diffuser Systems,'' Proceedings of the First ASME/JSME Joint Fluids Engineering Conference, ASME, New York, FED-107, pp. 125–130.
[13] Sinha, M., Pinarbashi, A., and Katz, J., 2001, ''The Flow Structure During Onset and Developed States of Rotating Stall Within a Vaned Diffuser of a Centrifugal Pump,'' ASME J. Fluids Eng., **123**, pp. 490–499.
[14] Sun, J., and Tsukamoto, H., 2001, ''Off-Design Performance Prediction for Diffuser Pumps,'' Proc. Instn. Mech. Engrs., Journal of Power and Energy—Part A, **215**, pp. 191–201.
[15] Sano, T., Yoshida, Y., Tsujimoto, Y., , T.Tsujimoto, T., Nakamura, Y., and Matsushima, T., 2002, ''Numerical Study of Rotating Stall in a Pump Vaned Diffuser,'' ASME J. Fluids Eng., **124**, pp. 363–370.
[16] Uhlman, J. S., and Grant, J. R., 1993, ''A New Method for the Implementation of Boundary Conditions in the Discrete Vortex Method,'' ASME 1993 Fluids Engineering Spring Meeting, Washington, DC, June.
[17] Wu, J. C., and Thompson, J. F., 1973, ''Numerical Solutions of Time-Dependent Incompressible Navier-Stokes Equations Using an Integro-Differential Formation,'' Comput. Fluids, **1**, pp. 197–215.
[18] Kempka, S. N., Glass, M. W., Strickland, J. H., and Ingber, M. S., 1999, ''A Galerkin Boundary Element Method for Solving the Generalized Helmholtz Decomposition,'' *Third International Workshop on Vortex Flows and Related Numerical Methods. ESAIM: Proceedings*, **7**, pp. 205–214.
[19] Wang, H., and Tsukamoto, H., 2001, ''A New Approach to the Vortex Method for Determination of Vorticity Shedding from Solid Boundary,'' *Proceedings of the Second International Conference on Vortex Methods*, Istanbul Technical University, Istanbul, Turkey, pp. 25–32.
[20] Uhlman, J. S., 1992, ''An Integral Equation Formation of the Equation of Motion of an Incompressible Fluid,'' Naval Undersea Warfare Center Technical Report 10-086, 15 July.
[21] Tsukamoto, H., Matsunaga, S., Yoneda, H., and Hata, S., 1986, ''Transient Characteristics of a Centrifugal Pump During Stopping Period,'' ASME J. Fluids Eng., **108**, pp. 392–399.
[22] Lewis, R. I., 2001, ''Extension of Vortex Methods to Flow Simulation of Mixed-Flow Turbomachines,'' *Proceedings of the Second International Conference on Vortex Methods*, Istanbul Technical University, Istanbul, Turkey, pp. 181–187.
[23] Takens, F., 1981, ''Detecting Strange Attractors in Turbulence,'' *Dynamical Systems and Turbulence* D. A. Rand and L. S. Young, eds., Springer, Berlin, pp. 366–381.
[24] Eckmann, J. P., Kamphorst, S. O., Ruelle, D., and Ciliberto, S., 1986, ''Liapunov Exponents From Time Series,'' Phys. Rev. A, **34**(6), pp. 4971–4979.
[25] Lin, T. J., Juang, R. C., Chen, Y. C., and Chen, C. C., 2001, ''Predictions of Flow Transitions in a Bubble Column by Chaotic Time Series Analysis of Pressure Fluctuation Signals,'' Chem. Eng. Sci., **56**, pp. 1057–1065.

The Inlet Flow Structure of a Centrifugal Compressor Stage and Its Influence on the Compressor Performance

Abraham Engeda

Yunbae Kim

Turbomachinery Laboratory,
Mechanical Engineering Department,
Michigan State University,
East Lansing, MI 48824

Ronald Aungier

Gregory Direnzi

Product Development,
Elliott Company,
Jeannette, PA

The performance of centrifugal compressors can be seriously degraded by inlet flow distortions that result from an unsatisfactory inlet configuration. In this present work, the flow is numerically simulated and the flow details are analyzed and discussed in order to understand the performance behavior of the compressor exposed to different inlet configurations. In a previous work, complementary to this present work, experimental tests were carried out for the comparison of a centrifugal compressor stage performance with two different inlet configurations: one of which was a straight pipe with constant cross-sectional area and the other a 90-deg curved pipe with nozzle shape. The comparative test results indicated significant compressor stage performance difference between the two different inlet configurations. Steady-state compressor stage simulation including the impeller and diffuser with three different inlets has been carried out to investigate the influence of each inlet type on the compressor performance. The three different inlet systems included a proposed and improved inlet model. The flow from the bend inlet is not axisymmetric in the circumferential and radial distortion, thus the diffuser and the impeller are modeled with fully 360-deg passages. [DOI: 10.1115/1.1601255]

Introduction

Some of the most under-analyzed components in a centrifugal compressor are the stationary inlet duct, volutes, and collectors. This has been primarily due to complex geometry, the high total cost of analysis, and uncertain gains in performance. The total analysis cost includes

- geometry setup time
- analysis time, and
- time iterating on geometry and analysis until an acceptable design is achieved.

As a result, the most widely practiced method of designing inlet ducts and volutes has been to use very simple, one-dimensional inviscid flow techniques. While this is a convenient and straightforward design methodology, the flow within these ducts is by no means one-dimensional.

It is currently believed that inlet ducts and volute loss account for four to six points of efficiency decrement in a typical centrifugal compressor stage. There is therefore strong interest to couple CFD analysis and experimental data and to use it in the design process for providing insights on minimizing losses in these components by isolating the mechanisms that contributes to entropy generation. The result will hopefully be more efficient centrifugal product for customers at higher profitability levels for the manufacturer.

Centrifugal compressors are reliable, compact, and robust; they have favorable resistance to foreign object damage; and are less affected by performance degradation due to fouling. They are found in small gas turbine engines, turbochargers, and refrigerators and are used extensively in the petrochemical and process industry. Since the centrifugal compressor finds a wide variety of applications, each application places its own demands on the design of the compressor. This wide range of demands on centrifugal compressors requires consideration of many design parameters. Most of the design requirements lie in one of two areas: stress considerations and aerodynamic performance. The allowable stress is limited by material properties and the capability to accurately predict blade and rotor steady-state and vibratory stress for complex impeller shapes at high rotational speeds. The aerodynamic requirement is to efficiently accomplish large air deflections and diffusion at high flow so as to achieve high pressure ratios. Minimizing passage flow areas is often an imposed constraint. Component matching is an essential aspect of design even with optimized individual components since it is the efficiency of the whole stage that ultimately matters. Thus, it is often required to redesign one or more components of the compressor due to improper matching and sometimes the efficiency of a component is sacrificed in order to achieve good matching.

Gas turbine compressors are especially demanding because of performance goals and mechanical demands. The requirements for these machines include medium to high pressure ratio, high efficiency at diverse speeds, restricted overall diameters, low impeller inertia, extended life, and the need to match the coupled gas turbine. However, range demands are usually not as great as for the other applications.

Process compressors cover an exceedingly wide range of applications and also must operate with different gases. The molecular weight and distribution of component gases may vary significantly during the lifetime of a given compressor. It is not uncommon to find applications that require 30 or 40% stable operating range to meet changes in operating conditions.

The refrigeration compressors are quite similar to the process compressors except that their stage pressure ratio and flow conditions are defined by a unique thermodynamic cycle. Due to the thermodynamic properties of refrigerants, these compressors frequently operate close to the top of the vapor dome and thus design calculations must be done using real gas properties. Perhaps the most distinguishing feature of the refrigeration compressor is the requirement for operation during very wide climatic conditions through summer and winter, thus requiring loads anywhere from 10 to 110% of the design load.

Contributed by the Fluids Engineering Division for publication in the JOURNAL OF FLUIDS ENGINEERING. Manuscript received by the Fluids Engineering Division July 30, 2001; revised manuscript received Apr. 26, 2003. Associate Editor: E. W. Graf.

Turbochargers by contrast require an extremely robust design and frequently employ cast materials. They are exposed to very harsh operating environments and require moderately thick leading edges in order to resist foreign object damage and in order to have high first bending mode natural frequencies to tolerate vibratory stresses better. In many cases, a very high flow coefficient or high specific speed design is required both from fundamental thermodynamics and to reduce the overall size and inertia. An exceedingly wide range is required for automotive turbocharger applications and for four-stroke diesel engine trucks, while large locomotive engines generally have a more restricted operating range.

Inlet Flow Structure and Its Effect on the Compressor Performance

A full summary of inlet distortion and its effect on a turbo compressor performance, with an extensive reference list, is given by Williams [1]. The distortion can be in static pressure or stagnation temperature, but the most common distortion is stagnation pressure. Such distortions often occur naturally because of the unsatisfactory nature of the inlet or because of operational effects. Very often the distortion is transient and it is generally recognized that the distortion will have little or no effect unless it persists for at least one revolution of the rotor. If it persists for longer than this it is normally treated as quasi-steady, i.e., the process is long in relation to the time between passage of rotor blades. The distortion pattern is normally nonuniform in the circumferential and the radial sense. Circumferential distortion seems to be the most serious.

Reid [2], showed the effect of circumferential distortion on the performance of a nine-stage compressor. The most significant change is the loss in surge margin, with surge occurring at very much lower pressure ratios for all speeds. Distortions with a large circumferential extent have a more pronounced effect on compressor performance.

Ariga [3] investigated experimentally the influence of inlet distortion on the performance of a low-speed centrifugal compressor with vaneless diffuser, mainly in the impeller with artificially created radial (hub and tip) and circumferential distortion generators by locating multiple layers of honeycomb at upstream of impeller and compared the result with the case of no distortion. According to his results, the distorted inlet profile degrades the impeller efficiency significantly by changing the incidence angle, especially in case of tip distortion. He observed the tendency that the performance degenerating effect due to the distortion grows as the rotational speed and the flow rate increases. The highest pressure and the lowest stable flow are achieved with inlets that have no distortion. Circumferential distortions create the largest loss of pressure ratio and flow range; radial distortions produce somewhat less deleterious effects, with tip distortions creating more degradation than hub distortions. His experimental results support the cause of the stage efficiency degradation for the present study that can be described as the combination of circumferential and tip distortion as well as the nonuniformity of the flow properties.

Using numerical simulation, Roberge et al. [4], Cain et al. [5], and Cheng et al. [6] among others have reported the importance of the flow structure and flow mechanism upstream of an impeller and its influence on the performance of the impeller and the stage as a whole.

As stated above, centrifugal compressors are increasingly utilized for various purposes, and the spatial restrictions become inherent with growing width of applications. As a consequence, a nonuniform flow is frequently generated at the impeller inlet. Inlet distortion is divided mainly into radial distortion and circumferential distortion. The former is further subdivided into tip distortion and hub distortion corresponding to the regions where the total pressure defect exists near a hub or a shroud side. These may actually occur in the following cases:

- Hub distortion: axisymmetric obstacles at a center portion of an inlet, such as a tachometer pick up, a hub cover, etc., or axisymmetric boundary layers of a return channel of multistage compressor.
- Tip distortion: axisymmetric boundary layers of an inlet duct or a return channel or axisymmetric obstacles such as an orifice plate.
- Circumferential distortion: nonaxisymmetric obstacles such as struts or a bending duct.

Necessity of 360 Model With Whole Passages

As has been shown and discussed in previous works, such as Kim et al. [7], an inlet that includes a bend as an inlet generates secondary flows consisting of twin vortices, which can result in severely distorted flow. These secondary flow effects only mix slowly in both the radial and circumferential directions (see Fig. 1). When an inlet system is used before a compressor stage, the efficiency and head are degraded, [7].

Since the distorted flow caused by the bend inlet system is not circumferentially uniform, it is necessary to model the complete compressor impeller. This does greatly increase complexity and run time.

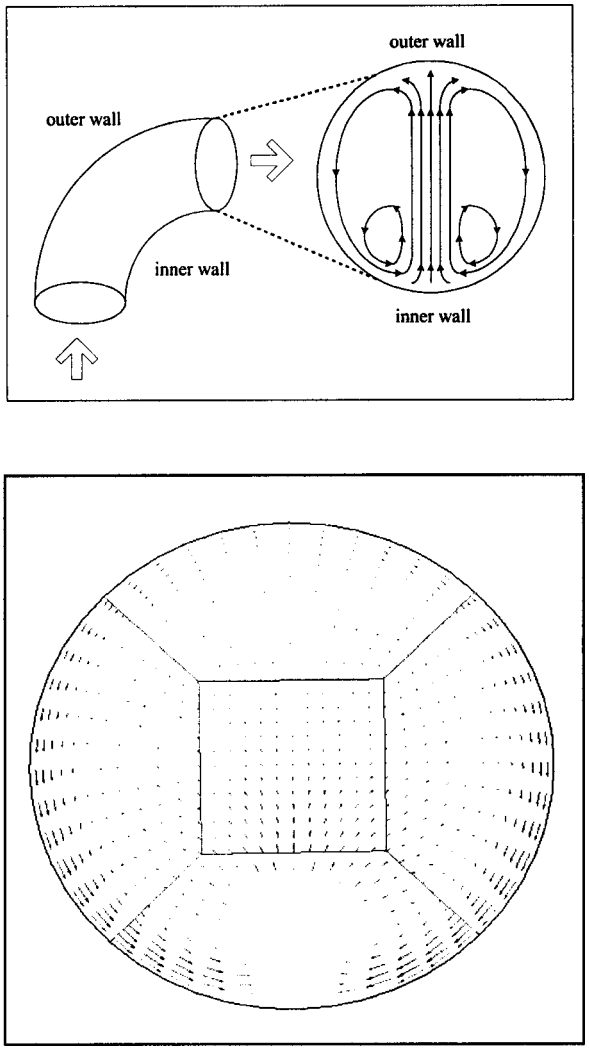

Fig. 1 Secondary flow structure in a bend inlet

CFD Model Description

The Code. TASCflow is a general purpose, commercially available CFD code, widely used in the turbomachinery industry. For the present study, TASCflow is used for the steady-state compressor stage numerical simulation. TASCflow solves the three-dimensional Reynolds stress-averaged Navier-Stokes equations for the mass-averaged velocity and the time-averaged density and pressure and energy. The mean form of the governing equations, expressed in a finite volume formulation that is fully conservative, is given below as follows:

1. Conservation of mass

$$\frac{\partial \rho}{\partial t} + \frac{\partial}{\partial x_j}(\rho u_j) = 0. \tag{1}$$

Conservation of momentum

$$\frac{\partial}{\partial t}(\rho u_i) + \frac{\partial}{\partial x_j}(\rho u_j u_i) = -\frac{\partial p}{\partial x_i} + \frac{\partial}{\partial x_j}\left\{\mu_{\text{eff}}\left(\frac{\partial u_i}{\partial x_j} + \frac{\partial u_j}{\partial x_i}\right)\right\} + S_{ui} \tag{2}$$

where $\mu_{\text{eff}} = \mu + \mu_t$. S_{ui} is the momentum source term for the impeller in the rotating frame of reference. The effect of coriolis and centripetal forces are modeled in the code by including

$$\mathbf{S}_{ui} = -2\boldsymbol{\Omega}\times\mathbf{U} - \boldsymbol{\Omega}\times(\boldsymbol{\Omega}\times\mathbf{r}). \tag{3}$$

Energy equation

$$\frac{\partial}{\partial t}(\rho H) - \frac{\partial P}{\partial t} + \frac{\partial}{\partial x_j}(\rho u_j H) = \frac{\partial}{\partial x_j}\left(\lambda \frac{\partial T}{\partial x_j} + \frac{\mu_t}{\text{Pr}_t}\frac{\partial h}{\partial x_j}\right) + S_E + \frac{\partial}{\partial x_j}\left\{u_i\left[\mu_t\left(\frac{\partial u_i}{\partial x_j} + \frac{\partial u_j}{\partial x_i}\right) - \frac{2}{3}\mu_t \frac{\partial u_l}{\partial x_l}\delta_{ij}\right]\right\} \tag{4}$$

where the total enthalpy is defined by $H = h + 1/2 u_i u_i + k$. In the rotating frame of reference, the rothalpy $I = H - \omega^2 R^2/2$ is advected in the energy equation in place of the total enthalpy.

A sliding interface is used between a stationary (i.e., inlet and downstream diffuser) and a rotating (i.e., impeller) component. Two models are available: one is the ''frozen rotor model'' and the other is the ''stage model.'' The stage model circumferentially averages the fluxes at the interface before the interpolation of the flow variables across the different frame of reference although the pressure distortion caused by any perturbation, for example the impeller and the diffuser leading edge, is still allowed. For axisymmetric inlet flow condition, the stage model can be used with only one passage utilizing a periodic boundary condition for the neighboring blade passages. This is an economic method of computing average stage performance.

The frozen rotor model achieves a frame change across the interface without a relative position change as well as without any interface averaging of flow variables. Flathers and Bache [8] used this model to predict the radial force of an impeller. The frozen rotor model is an exact representation of the case when the Strouhal number is zero, in which case either the sound speed is infinite or the impeller rotating speed is zero. When the Strouhal number is small enough, such as in the compressor stage simulations presented here (St is approximately 0.14 for all of the inlet models), the predicted result is a good approximation of the real situation. In the case of the frozen rotor model, all of the passages have to be modeled and this model is adequate to investigate the influence of the distorted flow caused by the bend inlet along the compressor stage flow passages since local flow features are allowed to transport across the interface. Thus, the nonuniformities of flow variables among the passages can be predicted, which results in different flow conditions at the compressor stage exit.

Verification of the Calculation. Griding used in this study was based on our extensive experience with similar geometry and the same flow solver. Special attention was paid to the grid clustering. Based on our previous experience with CFX TASCflow, [7], for each grid block, the adjacent cell volume ratio is less than 1.2. For the grid interface, the cells on each side are of similar size; the volume ratio is less than 1:1. To reduce the interpolation error, one-to-one grid interface (the cell surfaces on each side of the grid interface are of the same shape and same size, and are of same coordinates) is employed to the maximum possibility. Upon the simulations converge, the y^+ values are checked. On about 70% of the solid surface, y^+ value are in the range of 35~150, which is valid for logarithmic wall functions. Since the purpose of this paper is also to focus on the overall compressor performance, such grid size is acceptable as shown by Gu [9], who ran simulations on both fine meshes and coarse meshes to remove the dependence of the solution on the grid density. He used a fine grid size $121\times27\times25=81{,}675$ for one passage of the impeller and 231,710 for the volute. He also used a coarse grid size is $87\times16\times13=18{,}096$ points for one passage of the impeller and 145,535 for the volute. Also the validation of the code used in this paper for similar grid size to assess the overall performance of centrifugal compressors can be found in the work of Flathers et al. [8,10]. The dependence of the solution on turbulence models has not been conducted in this study, but a comprehensive assessment has been made by Lakshminarayana [11] on the computation of turbomachinery flows using κ–ε turbulence model. This is also supported by the results of Flathers et al. [8], whose result satisfactorily agreed with the experiment using this turbulence model for a similar compressor as used in this paper.

Grid Generation and Boundary Condition

The present compressor stage simulations used the ''flow generator'' concept. Thus all include 17 impeller blade passages and 16 diffuser vane passages were modeled. Attached was one of three different inlet models: sp_equi_bp, bp0, and bp2, which are developed and used for the numerical simulation in Kim et al. [7]. The model, sp_equi_bp, is used for the baseline of the compressor aerodynamic performance comparison without the secondary flow and the distortion effect, and bp0 is the original bend inlet. Since the actual compressor system includes an inlet casing as a part of the volute casing between the inlet and the impeller, the grid of each inlet is generated with the inlet casing as a whole block. An inlet casing is essentially a nozzle, and the purpose of having the inlet casing is to make the boundary layer blockage thinner for the flow before the impeller and to improve the velocity profile at the impeller shroud. However, in the case of the compressor with the bend inlet system, the further acceleration of the flow in the inlet casing after the distortion of the bend aggravates the flow distortion and causes higher incidence at the impeller leading edge.

In order to properly model the proposed new inlet, bp2 developed in Kim et al. [7], the compressor stage simulation with bp0 is carried out first and the static pressures at the bottom and the top wall of bp0 inlet model are evaluated to find the radial location of the vanes to be inserted in the bend passage using the generalized formula (Eq. (5)), [7].

$$p_{n-k+2} = p_{n+2} - \frac{k}{n+1}(p_{n+2} - p_1) = \frac{p_{n+2}}{1-\Delta^2}\left[(1-\Delta^2\Pi) - \left(\frac{r_1}{r_{n-k+2}}\right)^2(1-\Pi)\right] \tag{5}$$

where, $k=1$ (the first vane) and 2 (the second vane) for bp2 inlet model $\Delta = r_1/r_{n+2}$, $\Pi = p_1/p_{n+2}$ (r_4 and r_1 are the radial locations of the top and the bottom wall, $p4$ and $p1$ are the static pressures at the top and the bottom wall). (See Fig. 2.)

The grid of the three inlet models is shown in Fig. 3. For the inlet model, bp2, two vanes are modeled with zero thickness, a

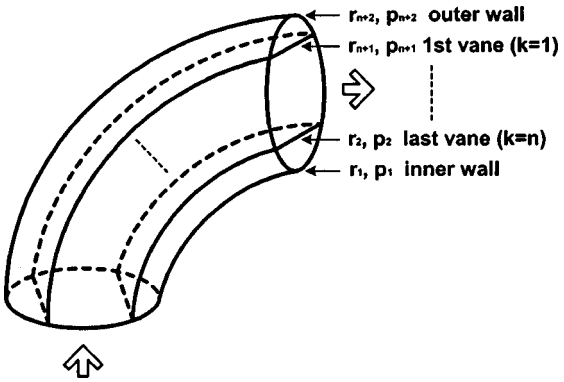

Fig. 2 Vane spacing for the location of each vane to be inserted in bp2 model; (*a*) bp0 (original bend inlet), (*b*) bp2 (two vane inserted model), (*c*) sp_equi_bp

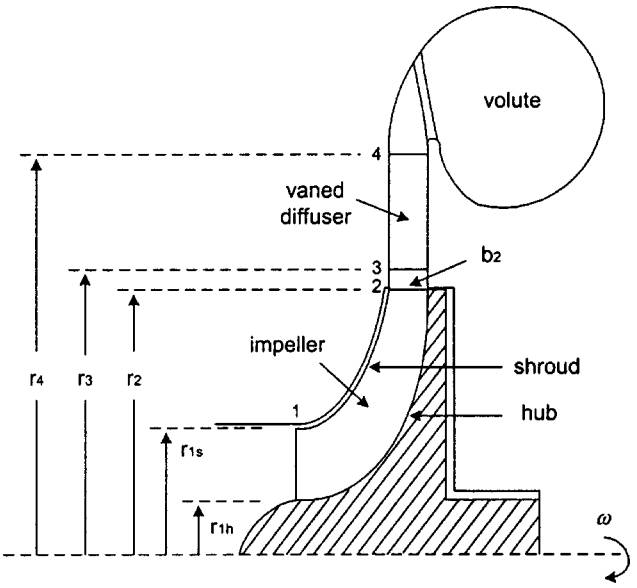

Fig. 4 Convention of the stations on compressor cross section

no-slip condition is applied to where the center of a zero thickness splitter would be to avoid disturbance on the flow regime. For each of the three inlet models, an inlet casing is attached at the end as a whole block. The convention of the stations used for the compressor stage performance calculation is indicated in Fig. 4. Station 1 and 2 are the impeller leading and trailing edge, and station 3 and 4 are the diffuser leading and trailing edge, respectively. Station 0 is the upstream of each inlet model as a compressor stage inlet.

Table 1 summarizes the grid sizes for each component and entire stage. The node indices, *I*, *J*, and *K* for the impeller and the diffuser are along the meridianal, circumferential (pitchwise), and radial (spanwise) direction. The grid of the full impeller and diffuser passages at mid span is shown in Fig. 5.

The second-order discretization scheme is used for the simulation and standard $k-\varepsilon$ model is adopted as a turbulence model combined with wall function approach that eliminates the necessity of discretely resolving the large gradients in the thin, near-wall region. The convergence criterion was set to the maximum residual of 10^{-4} for u, v, w, and p. The inflow boundary condition includes uniformly distributed total temperature and total pressure, which are adopted from the average values of experimental study, [7]. The inflow is assumed to be normal to the inlet surface, and the mass flow boundary condition is imposed at the diffuser exit surface. The wall is modeled as hydraulically smooth with an adiabatic condition. Frozen rotor models are adopted at the interfaces between the stationary and the rotating frame of reference: one at the interface between each of inlet model and the impeller, the other between the impeller and the diffuser. This allows the inlet distortion influence to be propagated across the different frames of reference as well as any pressure distortion caused by the impeller blade or the diffuser vane leading edge as described in the next section.

Table 1 Grid size of each component and entire stage for numerical simulation

Inlet Model With Inlet Casing	I×J×K	One Passage Model	I×J×K	Z	Entire Stage
sp_equi_bp	26×34×60	impeller	47×17×15	17	670245
bp0	28×18×80	diffuser	47×18×15	16	688665
bp2	25×18×96				658681

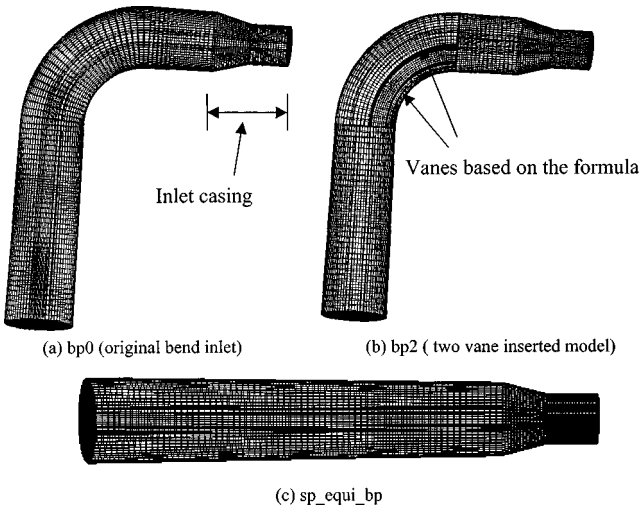

Fig. 3 Grid of inlet models used for compressor stage simulation

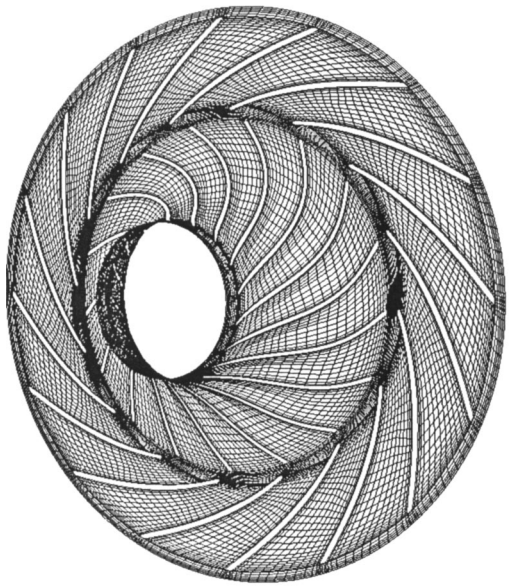

Fig. 5 Grid of 360-deg impeller and diffuser

Impeller-Diffuser Interaction

The interaction between an impeller and a vaned diffuser is essentially an unsteady phenomenon.

Fisher and Inoue [12] investigated the impeller-diffuser interaction experimentally with a low speed centrifugal compressor for four different diffusers. They observed large pitchwise variation among the passages at the impeller exit and concluded that the interaction between the impeller and the vaned diffuser is dependent on the leading edge of the diffuser vanes.

Dawes [13] carried out a numerical study to capture the unsteady interaction between a splittered centrifugal impeller and a vaned diffuser and observed very large periodic variations of velocity and flow angle in the entry zone to the diffuser. From the comparison between the unsteady time-averaged flow and the steady-state flow, the principal cause of the rather high loss levels observed in the diffuser is due to the strong spanwise distortion in swirl angle at the inlet, which initiates a strong hub corner stall rather than the unsteady effects.

Shum et al. [14] conducted a study of unsteady effects on impeller-diffuser interaction using numerical simulation for three different radial locations of the diffuser vane leading edge. They identified the consequent changes at the impeller exit with increasing interaction for smaller radial gap between the impeller exit and the diffuser vane leading edge. They concluded that the interaction can be mainly characterized as reduced slip, reduced blockage, and increased loss with the smaller radial gap. When the diffuser vane leading edge is closer to the impeller than the optimum gap, the increased loss overcame the benefits of the reduced slip and blockage. Although the changes in loss, blockage, and slip are due largely to unsteadiness, the consequent impacts on performance are mainly one-dimensional and the influence of flow unsteadiness on diffuser performance is found to be less important than the upstream effect.

Fatsis et al. [15] suggested the use of the acoustic Strouhal number in the case of compressible flow to quantify the relative effects of the rotation and pressure wave propagation. The acoustic Strouhal number is defined as

$$\mathrm{St}=\frac{fL}{c}. \tag{6}$$

Here, L is defined as the average length of an impeller blade passage and f is the number of rotations per second times the number of perturbation waves around the circumference.

After the compressor stage simulations, the Strouhal number is evaluated with the sound speed based on the average static temperature in the impeller passage and is shown to be approximately 0.14 for all depending on the inlet models at the design flow rate (with f replaced by rotation frequency). This indicates that the pressure wave propagation is much faster than the rotation of the impeller. Therefore, the frozen rotor model can be used for the compressor stage simulation presented here to include the pressure distortion and the impeller-diffuser interaction influence on the calculation of flow variables.

Simulation Results and Discussions

The compressor stage simulation results are presented based on circumferentially mass flow rate weighted averaging of flow variables at four stations for three different flow rates. The influences of each inlet model on the stage efficiency, the head coefficient as well as on the axial distortion between the impeller exit and the diffuser inlet are quantitatively compared. In addition, total pressure loss coefficient and pressure recovery coefficient for the diffuser are evaluated from the simulation results for each of inlet models.

Stage performance is compared for each inlet model based on three different flow coefficients that are defined as

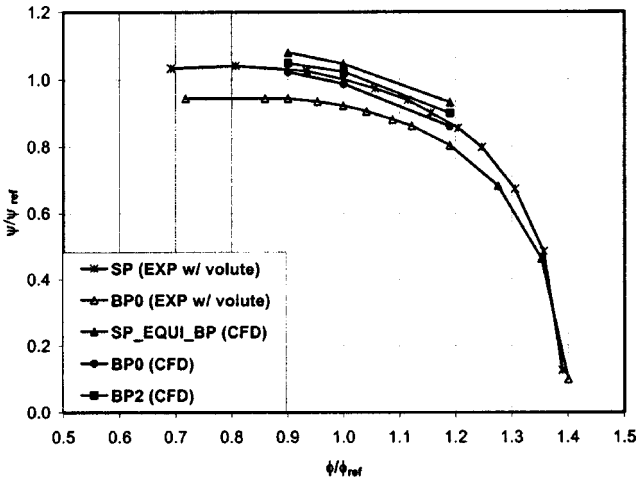

Fig. 6 Head coefficient comparison

$$\phi=\frac{Q}{\frac{\pi}{4}D_2^2U_2} \tag{7}$$

and the isentropic head coefficient between stage inlet and diffuser exit is given by

$$\psi_{is\ 0-4}=\frac{C_pT_{t0}\left[\left(\frac{P_{t4}}{P_{t0}}\right)^{\gamma-1/\gamma}-1\right]}{\frac{1}{2}U_2^2}. \tag{8}$$

The stage efficiency calculation is based on

$$\eta_{is\ 0-4}=\frac{\left(\frac{P_{t4}}{P_{t0}}\right)^{(\gamma-1/\gamma)}-1}{\frac{T_{t4}}{T_{t0}}-1}. \tag{9}$$

Figures 6 and 7 compare the head coefficient and the stage efficiency from the numerical simulation for three inlet models with the experimental test results reported, [7]. As it indicates, the bp2 model with two vanes inserted, based on the generalized formula, improved the efficiency by 3.11% at the higher flow rate, 2.88% at the design flow rate, and 2.17% at lower flow rate.

The reason for more efficiency improvement at higher flow rate is due to the fact that the flow distortion caused by the secondary flow in the case of the original bend inlet becomes more severe for

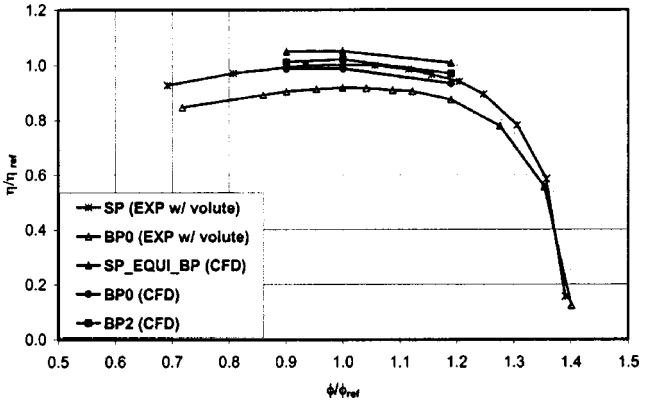

Fig. 7 Stage efficiency comparison

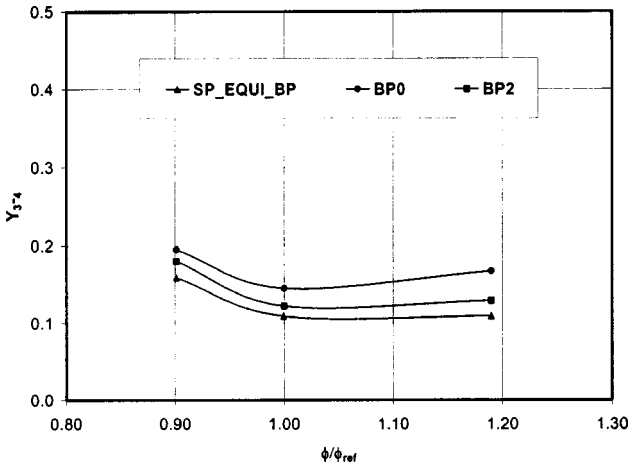

Fig. 8 Total pressure loss coefficient comparison

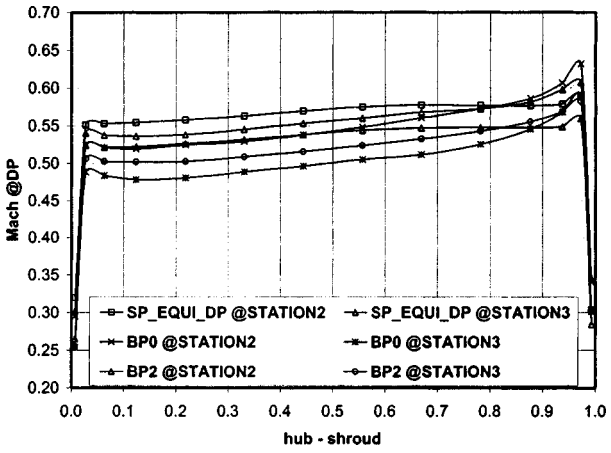

Fig. 11 Mach number comparison

higher mass flow rate and by inserting two vanes in the bend curvature, the secondary flow effect has been significantly reduced, [7], which results in relatively more efficiency improvement. The volute of the compressor stage is not modeled for the numerical simulation presented here. The discrepancies of the stage efficiency and the head coefficient between the experimental and the numerical simulation results are due to the volute effect, where more total pressure loss occurs, especially at the off-design point, since the volute was not modeled in the numerical simulation of this work.

In order to investigate the diffuser performance influenced by the inlet distortion, total pressure loss coefficient and diffuser pressure recovery coefficient between stations 3 and 4 are calculated and presented in Figs. 8 and 9. Total pressure loss coefficient based on the diffuser inlet dynamic pressure is given by

$$Y_{3-4}=\frac{P_{t3}-P_{t4}}{P_{t3}-P_3} \tag{10}$$

and the diffuser pressure recovery coefficient is defined as

$$Cp_{3-4}=\frac{P_4-P_3}{P_{t3}-P_3}. \tag{11}$$

The total pressure loss comparison of figures shows improvement for the bp2 inlet model as compared to the bp0. The improvements are made relatively more at higher flow rate, due to the reduced secondary flow effect and thus, smaller incidence at the diffuser leading edges. This tendency also appears in the comparison of diffuser pressure recovery coefficient as shown in Fig. 9.

As shown in Fig. 10, the diffuser inlet is much lower in the case of bp0 inlet. This implies severe incidence especially at the hub region of the impeller. Clearly, the bp2 model improved this effect considerably and improved the flow angle in terms of the magnitude as well as the uniformity at both hub and shroud region.

Mach number comparison at design flow is shown in Fig. 11. The discrepancy of Mach number between bp0 and bp2 model implies that total pressure loss is smaller in the impeller in the case of bp2 model. The higher Mach number near the shroud region is caused by locally low static temperature upon relatively high radial velocity.

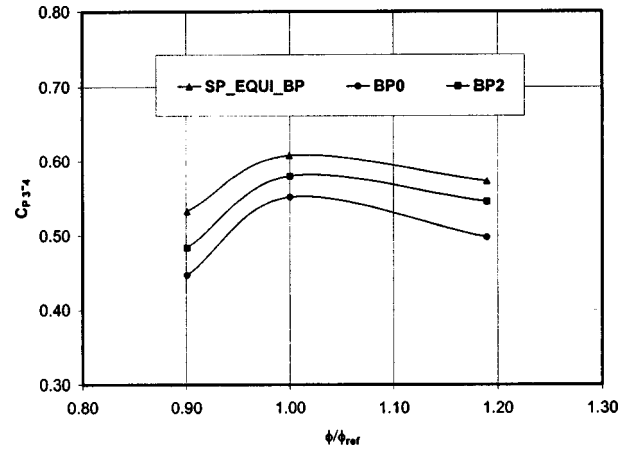

Fig. 9 Diffuser pressure recovery coefficient comparison

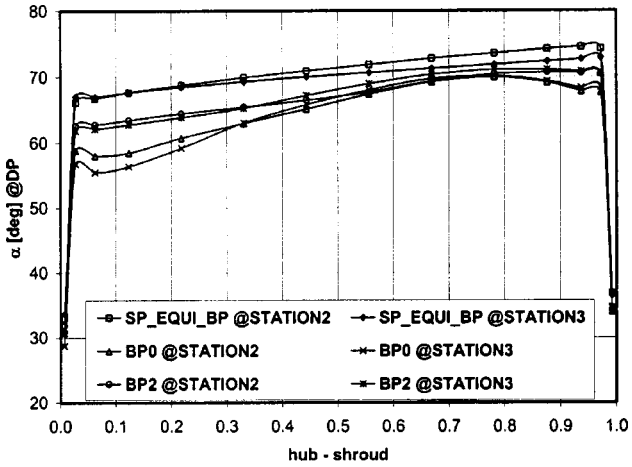

Fig. 10 Flow angle comparison at design point (*DP*)

Conclusions

The goal of the present work reported here was to evaluate the proposed inlet model, bp2 developed in Kim et al. [7] with the stage simulation including 360-deg models of the impeller and the diffuser as well as the three inlet models. The nonperiodic passage alignment due to the different number of blades and vanes for the impeller and the diffuser as well as the impeller-diffuser interaction resulted in the nonuniform flow distribution among the passages. The efficiencies and the head coefficients are calculated based on circumferentially mass flow weighted averaging of flow variables for the case of each inlet model and are compared with the experimental result carried out in Kim et al. [7]. The performance comparison clearly showed that the proposed inlet model, bp2 improved the stage efficiency about 3% compared with the

original inlet model, bp0. The discrepancies between the numerical and the experimental results are caused by the volute component that is not modeled for the numerical simulation presented here.

The diffuser performance influenced by inlet distortion was calculated and compared in terms of the pressure recovery coefficient and the total pressure loss coefficient. Both of the comparisons showed the improvement to be relatively greater at the higher flow rate for the bp2 model compared with the bp0 model. This is due to improved secondary flow effect especially at higher flow rate resulting from the two inserted vanes which result in smaller incidence at the diffuser leading edge.

Flow angle and Mach number between the impeller exit and the diffuser leading edge at design point are compared for the three inlet models and bp2 model indicated the improvement in terms of the magnitude and the uniformity at both the hub and shroud.

Although the present work did not include the volute of the compressor stage, the bp2 model showed the advantages over the original bend inlet, bp0 and it can be expected that the total benefit of bp2 model for the entire stage will be even better provided that the inlet distortion and the secondary flow effect in the case of the original bend inlet influenced the performance of the volute.

Nomenclature

b = passage width from hub to shroud
c = speed of sound
Cp = pressure recovery coefficient
C_p = specific heat at constant pressure
DP = design point
f = impeller rotating frequency
h = static enthalpy
H = total enthalpy
k = turbulent kinetic energy
k = vane position
L = mean flow passage length
Mach = Mach number
P = pressure
Q = volume flow rate
R = radial location of fluid particles in rotating frame
r = radial location of vanes or stations
St = Strouhal number
T = temperature
U_2 = blade peripheral speed at impeller tip
Y = total pressure loss coefficient

Greek

ϕ = flow coefficient
γ = specific heat ratio
η = efficiency
μ = dynamic viscosity
ω = impeller rotating speed (rad/s)
ψ = head coefficient

Subscripts

0 = station at pipe inlet
1 = station at pipe exit or impeller inlet
2 = station at impeller exit
3 = station at diffuser leading edge
4 = station at diffuser trailing edge
5 = station at volute inlet
6 = station at compressor discharge
h = hub
is = isentropic
n = number of vanes
ref = reference
s = shroud
t = total

References

[1] Williams, D. D., 1986, ''Review of Current Knowledge on Engine Response to Distorted Inlet Flow Conditions,'' AGARD Conference, Munich, *AGARD CP-400*.
[2] Reid, C., 1969, ''The Response of Axial Flow Compressors to Intake Flow Distortions,'' *ASME Paper No. 69-GT-29*.
[3] Ariga, I., Kasai, N., Masuda, S., Watanabe, Y., and Watanabe, I., 1982, ''The Effect of Inlet Distortion on the Performance Characteristics of a Centrifugal Compressor,'' *ASME Paper No. 82-GT-92*.
[4] Roberge, J. A., and Mathisen, P. P., 1999, ''Sensitivity Analyses to Assess the Use of CFD to Predict the Occurrence of Vortices Near Pump Intakes,'' ASME/JSME Joint Fluids Engineering Conference, *Paper No. FEDSM99-7224*.
[5] Cain, S. A., and Padmanabhan, M., 1999, ''Numerical Simulation of Flow Distribution and Swirl Due to a Combined Pipe Bend,'' ASME/JSME Joint Fluids Engineering Conference, *Paper No. FEDSM99-7217*.
[6] Cheng, K. C., Lin, R. C., and Ou, J. W., 1975, ''Fully Developed Laminar Flow in Curved Rectangular Channels,'' *ASME Paper No. 75-FE-4*.
[7] Kim, Y., Engeda, A., Aungier, R., and Direnzi, G., 2001, ''The Influence of Inlet Flow Distortion on the Performance of a Centrifugal Compressor and the Development of Improved Inlet Using Numerical Simulations,'' IMechE Part A, Journal of Power and Energy, **215**, pp. 1–16.
[8] Flathers, M., and Bache, G. E., 1999, ''Aerodynamically Induced Radial Forces in a Centrifugal Gas Compressor: Part 2—Computational Investigation,'' ASME J. Eng. Gas Turbines Power, **121**, pp. 725–734.
[9] Gu, F., Engeda, A., Cave, M., and Di Liberti, J.-L., 2001, ''A Numerical Investigation on the Volute/Diffuser Interaction Due to the Axial Distortion at the Impeller Exit,'' ASME J. Fluids Eng., **123**, pp. 475–483.
[10] Flathers, M., Bache, G. E., and Rainsberger, R., 1994, ''An Experimental and Computational Investigation of Flow in a Radial Inlet of an Industrial Pipeline Centrifugal Compressor,'' *ASME Paper No. 94-GT-134*.
[11] Lakshminarayana, B., 1991, ''An Assessment of Computational Fluid Dynamics Techniques in the Analysis and Design of Turbomachinery,'' ASME J. Fluids Eng., **113**, pp. 315–325.
[12] Fisher, E., and Inoue, M., 1981, ''A Study of Diffuser/Rotor Interaction in a Centrifugal Compressor,'' J. Mech. Eng. Sci., **23**, pp. 149–156.
[13] Dawes, W., 1995, ''A Simulation of the Unsteady Interaction of a Centrifugal Impeller With Its Vaned Diffuser: Flow Analysis,'' ASME J. Turbomach., **117**, pp. 213–222.
[14] Shum, Y., Tan, C., and Cumpsty, N., 2000, ''Impeller-Diffuser Interaction in a Centrifugal Compressor,'' ASME J. Turbomach., **122**, pp. 777–786.
[15] Fatsis, A., Pierret, S., and Van den Braembussche, R., 1995, ''3-D Unsteady Flow and Forces in Centrifugal Impellers With Circumferential Distortion of the Outlet Static Pressure,'' *ASME Paper No. 95-GT-33*.

Yoshiki Yoshida[1]
Associate Professor

Yoshinobu Tsujimoto
Professor

Goh Morimoto
Graduate Student

Hiroki Nishida
Undergraduate Student

Graduate School of Engineering Science,
Osaka University,
1-3 Machikaneyama, Toyonaka,
Osaka 560-8531, Japan

Shigeki Morii
Deputy Manager
Mitsubishi Heavy Industries, Ltd.,
Yokohama R&D Center,
12 Nishikimachi, Nakaku,
Yokohama, Kanagawa 231-8715, Japan

Effects of Seal Geometry on Dynamic Impeller Fluid Forces and Moments

This paper reports an experimental investigation of the rotordynamic fluid force and moment on a centrifugal impeller with three types of wear-ring seals; i.e., a face seal and two types of toothed seals. The impeller is equipped with a vaneless diffuser. Rotordynamic fluid forces and moments on the impeller in whirling motion were measured directly by using four-axis force sensor. Unsteady pressures were measured at several locations in the diffuser. It was found that, (1) at low flow rate, the fluid force and fluid force moment become maximum at a certain whirling speed caused by a coupling between the whirl motion and vaneless diffuser rotating stall and (2) the seal geometry with axial seal affects the direction of the coupled fluid force relative to the direction of eccentricity through the change in the unsteady leakage flow due to the whirl.
[DOI: 10.1115/1.1598988]

Introduction

For whirling motion, many experimental and analytical data have been obtained on the rotordynamic fluid forces on impellers. It is now widely recognized that the fluid forces on the impeller become destabilizing for the forward whirl at whirl speed ratio (ω/Ω) less than 0.5 (Jery et al. [1], Bolleter et al. [2], and Ohashi et al. [3]).

The reasons of the destabilizing forces are as follows. First, the destabilizing forces are caused by the unsteady interaction between an impeller and a volute casing (Adkins et al. [4] and Tsujimoto et al. [5]), or a vaned diffuser (Tsujimoto et al. [6]). In addition, it was pointed out that the unsteady flow in the impeller shroud leakage path, i.e., the side clearance between the impeller shroud and casing, plays an important role to generate the destabilizing forces on the shroud (Childs [7], Guinzburg et al. [8], and Uy et al. [9]). These are classified into the destabilizing fluid forces caused by the interaction between the impeller and the stationary part.

Secondly, the interaction of hydrodynamic instability, i.e., rotating stall with whirling motion may cause rotordynamic instabilities. Ohashi et al. [10] reported that the tangential fluid force on a whirling impeller with a vaned diffuser increased suddenly at low flow rate for the whirl speed ratio of $\omega/\Omega=0.05$. They attributed this destabilizing force to the rotating stall in the vaned diffuser. Recent experiment by Bently et al. [11] has shown that the fluid-induced direct stiffness drops dramatically under the rotating stall condition from the perturbation test of a centrifugal compressor. Yoshida et al. [12] also reported about a peak of destabilizing fluid force near the whirling speed ratio $\omega/\Omega=0.8$ at low flow rate. This peak is caused by the strong interaction between the whirl and rotating flow instability at impeller inlet, similar to the impeller rotating stall. However, to date the effect of the rotordynamic-hydrodynamic coupling has not been recognized clearly.

This paper presents the results of an investigation of the rotordynamic fluid forces and moments on an impeller with three types of wear-ring seals; i.e., a face seal, and two types of toothed seals. For the whirling motion, the variation of the seal clearance contributes to the rotordynamic fluid force through the unsteady flow in the impeller leakage path (Bolleter et al. [13]). Discussions on the interaction between the whirl and the flow instability in the vaneless diffuser are also made from the measurement results of unsteady pressure in the diffuser.

Experiment Facility

Description of Test Facility. Figure 1 shows the sketch of the mechanism used to generate the whirling motion. The inner sleeve supports the main shaft through two inner bearings eccentrically set to produce a whirling motion. The radius of the whirl orbit (eccentricity) was set $\varepsilon=1.05$ mm in the present test. The main shaft is driven by an AC motor with the rotational speed (Ω) through a universal joint, and the outer sleeve is driven by a DC motor controlled to run at a prescribed speed (ω). The whirling angular velocity, ω, is defined as positive when it is in the same direction as the impeller rotation, Ω. The main shaft speed was maintained at 400 ± 1 rpm, and the whirling speed ratio (ω/Ω) was varied in the range from -1.2 to $+1.2$. Uncertainty in the whirling speed ratio, ω/Ω, is ±0.002. Water was used as the working fluid to facilitate the measurement of the fluid forces.

Figure 2 shows the details around the impeller. Test impeller is a simple two-dimensional centrifugal impeller with logarithmic spiral blades, blade angle 60 deg from tangential. The number of blades is ten, inner (r_1) and outer radii (r_2) are 75 and 148 mm, and width (b_2) is constant 24 mm. The thickness of both front and back shrouds is 6 mm. The front and back shrouds of the impeller are perpendicular to the rotor. In the present experiments, therefore, unsteady pressure on the shroud generates no radial fluid force. It generates, however, the fluid force bending moment around the impeller center. We used the mechanical seal for the back seal, therefore there is no leakage flow through the clearance between the back shroud and housing. The leakage flow is limited

[1]Currently Senior Staff Researcher at the National Aerospace Laboratory, Kaduka Space Propulsion Laboratory, 1 Koganezawa, Kimigaya, Kakuda, Miyagi 981-1525, Japan. e-mail: kryoshi@kakuda-splab.go.jp

Contributed by the Fluids Engineering Division for publication in the JOURNAL OF FLUIDS ENGINEERING. Manuscript received by the Fluids Engineering Division December 18, 2001; revised manuscript received April 9, 2003. Associate Editor: B. Schiavello.

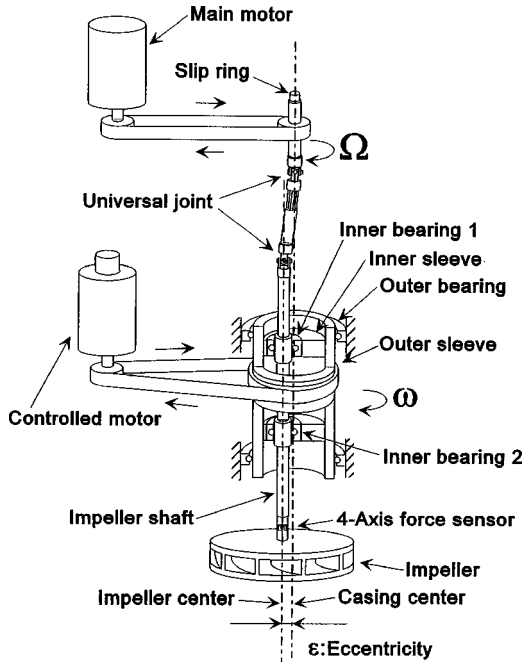

Fig. 1 Mechanism to produce the impeller whirling motion

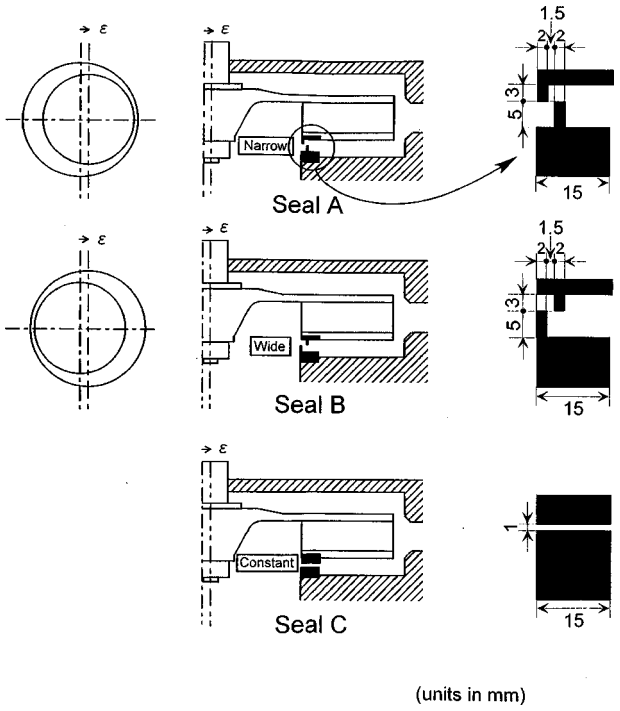

Fig. 3 Configuration of test seals, Seal A, B, and C

in the clearance between the front shroud and housing. The axial gap in the front cavity is 14 mm, radially constant. The impeller is equipped with a vaneless diffuser with inlet/outlet radius ratio $r_4/r_3=1.5$, and width $b_3=24.5$ mm. A symmetrical collector surrounds the vaneless diffuser. The test impeller has a wide radial Gap-A (= 12 mm) intentionally to minimize the fluid force on the impeller side plate.

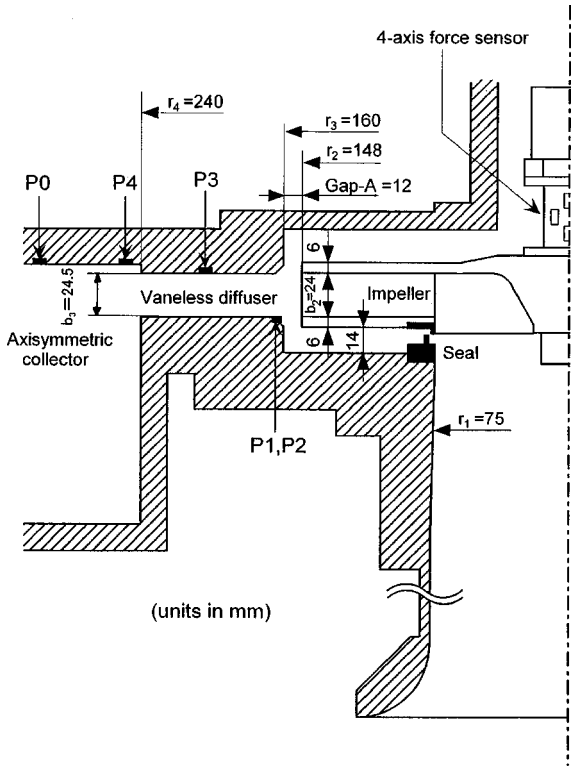

Fig. 2 Cross section of the test facility (impeller, vaneless diffuser, and collector)

In the present experiments, the measurements of the fluid forces on the impeller were conducted with three types of wear-ring seals. The configurations of the test seals are shown in Fig. 3. Seal A has a rotor tooth inside a stator tooth. The seal clearance in the angular direction becomes nonuniform due to the impeller whirl. For Seal A, the clearance becomes narrower in the direction of eccentricity, ε. To the contrary, Seal B has the rotor tooth outside the stator tooth. The clearance of Seal B becomes wider in the direction of eccentricity, ε. On the other hand, Seal C is a plain face seal, so that the clearance in the axial direction keeps constant (1 mm) independently of the eccentricity. For both Seal A and Seal B, there is no overlap between the rotor and stator tooth to minimize the fluid force on the seal itself. Under the condition without a shaft eccentricity ($\varepsilon=0$ mm), the nominal radial clearance of the seal is constant $S^*=1.5$ mm. In the present tests, the eccentricity $\varepsilon=1.05$ mm was used for the whirling motion. In this condition, the seal radial clearance (Seal A and B) varies in the range of $S=0.45$ mm$\sim$2.55 mm due to the impeller whirl. It could be inferred that the amount of leakage flow with Seal A is the same as that with Seal B. The amount of leakage flow with Seal C is less than that with Seal A and B. The variation of leakage flow with Seal A and B caused by the whirl motion is unsteady, however, that with Seal C is almost steady. A series of experiments was carried out to determine the effect of the seal geometry on the rotordynamic fluid forces. The configurations of test facility were kept the same except the wear-ring seal, which were only changed from Seal A to C.

Instrumentation and Data Acquisition System. The impeller is supported by the main shaft through a rotating force balance with a four-axis force sensor, as shown in Fig. 4. The force sensor is composed of two couples of parallel plates and four strain gauges per plate to measure the four-axis forces (two forces and two force moments). The output signals of the strain gauges are transferred to a data acquisition system through a slip ring, in which the four signal vector $\{V\}$ are converted to four component vector of two force and two moment $\{FM\}$ using a four-by-four transfer matrix $[A]$ (i.e., $\{FM\}=[A]\{V\}$). A preliminary set of dynamic calibration tests were conducted to obtain the transfer

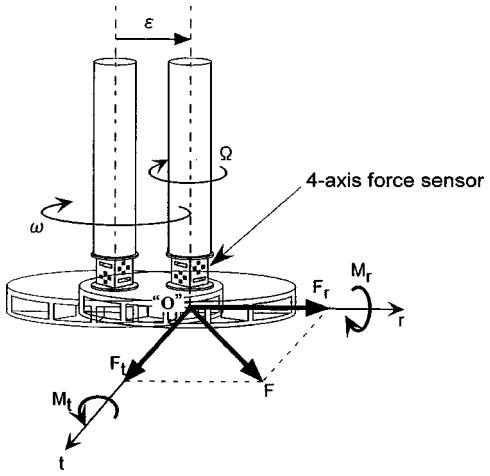

Fig. 4 Scheme showing the fluid-induced forces F_r and F_t, and force moments. M_r and M_t (ε: eccentricity, Ω: shaft rotational speed, ω: whirling speed, "O": impeller center on the whirl orbit, (r,t): radial and tangential to the whirl orbit)

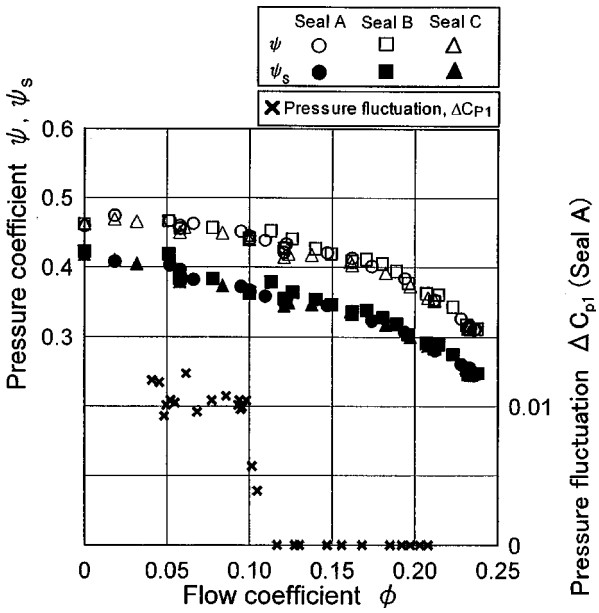

Fig. 5 Pressure performance of the test impeller ($\varepsilon=0$, $\omega/\Omega=0$). Pressure coefficient ψ at the collector, ψ_s at the diffuser inlet, and pressure fluctuation ΔC_{p1} at the diffuser inlet, versus flow coefficient ϕ (uncertainty in ψ, $\psi_s \pm 0.01$, in $\phi \pm 0.01$).

matrix $[A]$. The pure forces and/or moments on the impeller center "O" were applied to the four-axis sensor under rotating and whirling by using a rig of bearings, pulleys, cables, and weights. From the results of dynamic calibration test, the transfer matrix $[A]$ was determined.

Output signals are ensemble-averaged over 64 whirl orbits based on a triggering signal that indicates the instant when both the directions of the eccentricity and the impeller rotation come to a prescribed orientation. The fluid force and force moment are measured twice, that is, in air and in water at the same rotation and whirling speed. The former measurement provides the inertia force of the impeller itself due to the whirling motion. The fluid-induced force and force moment can be obtained by subtracting the former from the latter.

Figure 4 shows the coordinate system. The r-axis is set in the direction of eccentricity ε, and the t-axis is directed 90 deg from the r-axis in the direction of the impeller rotation. The fluid force F is applied to the center of the impeller "O" on the whirl orbit. The fluid force F is represented in radial (F_r) and tangential (F_t) components to the whirl orbit, which are useful for the rotor vibration analysis. Measured fluid forces are normalized as $(f_r, f_t) = (F_r, F_t)/(M_o \varepsilon \Omega^2)$, where $M_o = \rho \pi r_2^2 b_2$ is the mass of the fluid in the impeller. Uncertainty in the dimensionless fluid forces f_r and f_t is ± 0.3 (dimensionless value). The fluid force moment M applied on the impeller center "O" is represented with radial (M_r) and tangential (M_t) components as shown in Fig. 4. Measured fluid force moments are normalized as $(m_r, m_t) = (M_r, M_t)/(M_o\, r_2 \varepsilon \Omega^2)$. Uncertainty in the dimensionless fluid force moments m_r and m_t is ± 0.3 (dimensionless value). It should be noted here that the tangential fluid force, f_t, is destabilizing for the whirl when $f_t \times (\omega/\Omega) > 0$; i.e., f_t and ω/Ω are both positive or both negative.

P0, and P1~P4 in Fig. 2 show the locations of pressure taps to measure the steady and unsteady pressure. P0 at the collector wall, and P1 at the diffuser inlet were used to measure the steady pressure performance for ψ, and ψ_s with a manometer. In addition to this, taps P1~P4 were used to measure the unsteady pressure using flush mounted pressure transducers (Kyowa Electronic Instruments Corp. PS-2KB, strain-gauge type, resonance frequency is 24 kHz) to observe a rotating stall in the vaneless diffuser. P1 and P2 at the diffuser inlet are located at different circumferencial positions (separation angle 45 deg) to determine the number of cells and the propagation speed of diffuser rotating stall.

Results and Discussions

Pressure Performance and Rotating Flow Instability. Figure 5 shows the static pressure coefficient ψ at the collector, and ψ_s at the diffuser inlet plotted against the flow coefficient ϕ, with Seal A, B, and C and without the shaft eccentricity ($\varepsilon=0$). The design flow coefficient is $\phi_d = 0.210$, and nondimensional specific speed is 0.98. These performance curves have no positive slope all over the flow range. The differences between Seal A, B, and C are considerably small. From these results, it could be conclude that the seal geometries in the present test have almost no effect on the pressure performance. For the measurements of fluid force, the flow rate was varied widely from $\phi = 0.058$ to $\phi = 0.236$.

Figure 6 shows the spectral analyses of the pressure fluctuations at the diffuser inlet P1 for Seal A measured with decreasing flow rate. The amplitudes (zero-to-peak) of pressure fluctuations with dimensionless frequency $f^* = 0.22 \sim 0.30$ in Fig. 6 are also plotted in Fig. 5. The amplitude increases suddenly as the flow rate decreases less than $\phi = 0.10$. Phase difference of this frequency between P1 and P2 (located with the separation angle 45 deg) was $-40 \sim -50$ degrees. The same phenomena of these pressure fluctuations were observed for all seals (Seal A, B, and C). From these

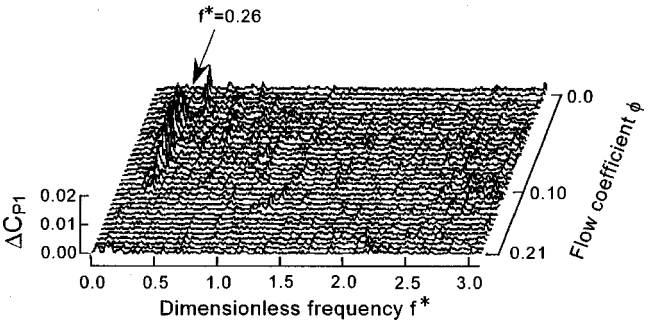

Fig. 6 Spectral analyses of pressure fluctuations at the diffuser inlet P1 in case of Seal A, for $\varepsilon=0$ and $\omega/\Omega=0$ (uncertainty in $\phi \pm 0.01$)

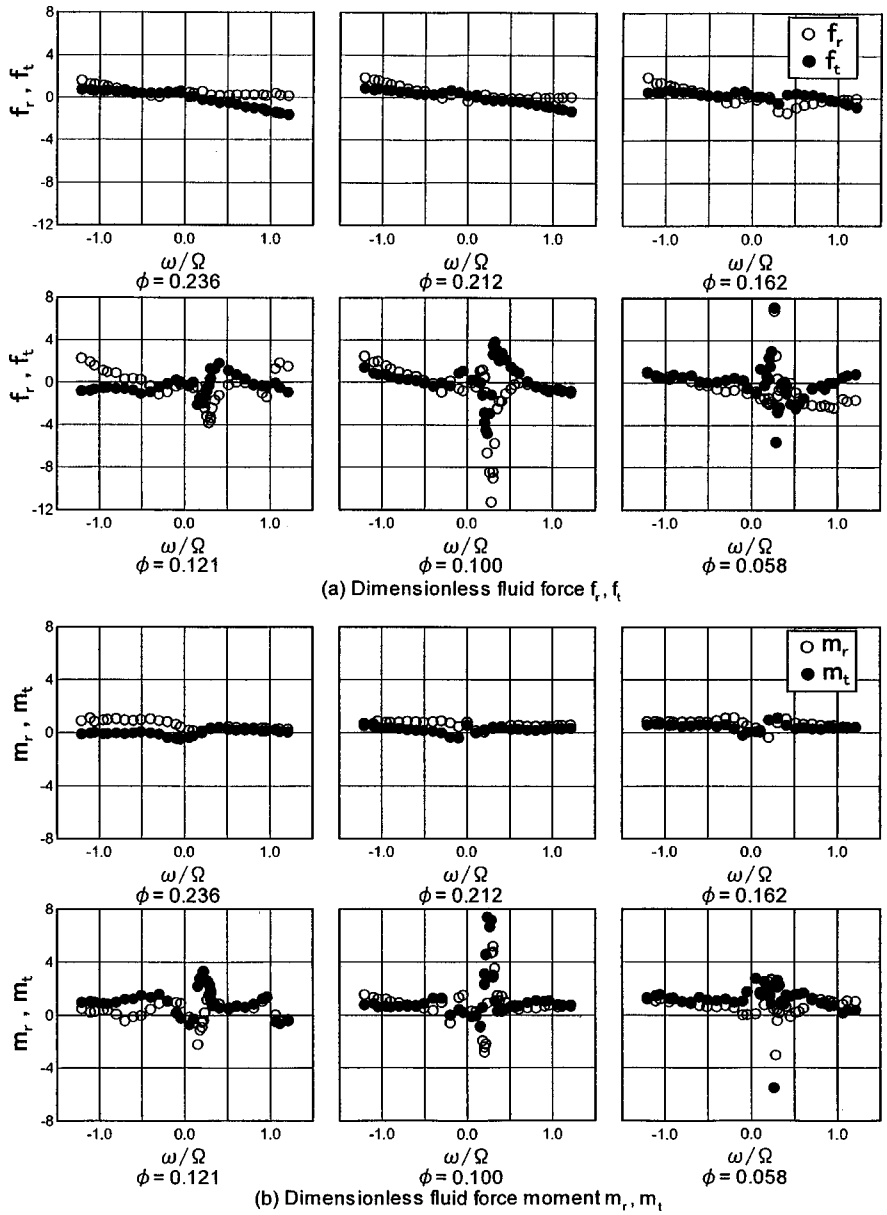

Fig. 7 Dimensionless fluid force f_r (○) and f_t, (●) and fluid force moment m_r (○) and m_t (●) on the impeller with Seal A versus whirling speed ratio ω/Ω for various flow coefficients ϕ ($\varepsilon = 1.05$ mm) (uncertainty in f_r, $f_t \pm 0.3$, m_r, $m_t \pm 0.3$, in $\omega/\Omega \pm 0.002$, in $\phi \pm 0.01$)

results, it was found that a rotating flow instability with one cell propagates in the same direction as impeller rotation. The detailed description of this flow instability will be presented later.

Fluid Forces and Fluid Force Moments on Impeller Measured With Force Balance. Figures 7, 8, and 9 show the dimensionless radial, f_r, tangential, f_t, fluid forces, and radial, m_r, tangential, m_t, fluid force moments on the impeller measured directly by the force sensor, plotted against the whirling speed ratio, ω/Ω, for various flow rates with Seal A, B, and C, respectively. At higher flow rate than $\phi = 0.162$, the fluid forces and fluid force moments are considerably small, and vary smoothly with the whirling speed. Moreover, seal geometry has almost no effect on the amount and the tendency of the fluid forces. However, in case of Seal A and B the forces and force moments change dramatically at flow rate smaller than $\phi = 0.121$, and ''peak'' appears near $\omega/\Omega = 0.2 \sim 0.3$. With Seal A and B, the tangential fluid forces are positive in a wide range of positive ω/Ω. In this region, the fluid force promotes the whirl instability. On the contrary, with Seal C, the peak force and moment are considerably small, and the range of ω/Ω where the tangential fluid force is positive, is small. So that, Seal C has beneficial effects on the shaft vibration for part flow operation as compared with Seal A and B.

In Fig. 9(*a*), calculation results of radial, f_r, and tangential, f_t, fluid forces by Shoji's two-dimensional vortex method, [14], are also shown for comparison. This calculation was assumed inviscid flow, applied only to the impeller without vaneless diffuser, and not included the effect of the seal leakage flow. All over the flow range, the calculated tangential force f_t is almost negative in positive whirl, and positive in negative whirl. Thus the fluid force has a damping effect on the whirling motion. The experimental results with Seal C agree well with the calculations qualitatively and quantitatively except for the region $\omega/\Omega = 0.2 \sim 0.3$ at low flow rate. From these results, it could be concluded that the fluid forces on the whirling impeller have a stabilizing effect on the whirl, as

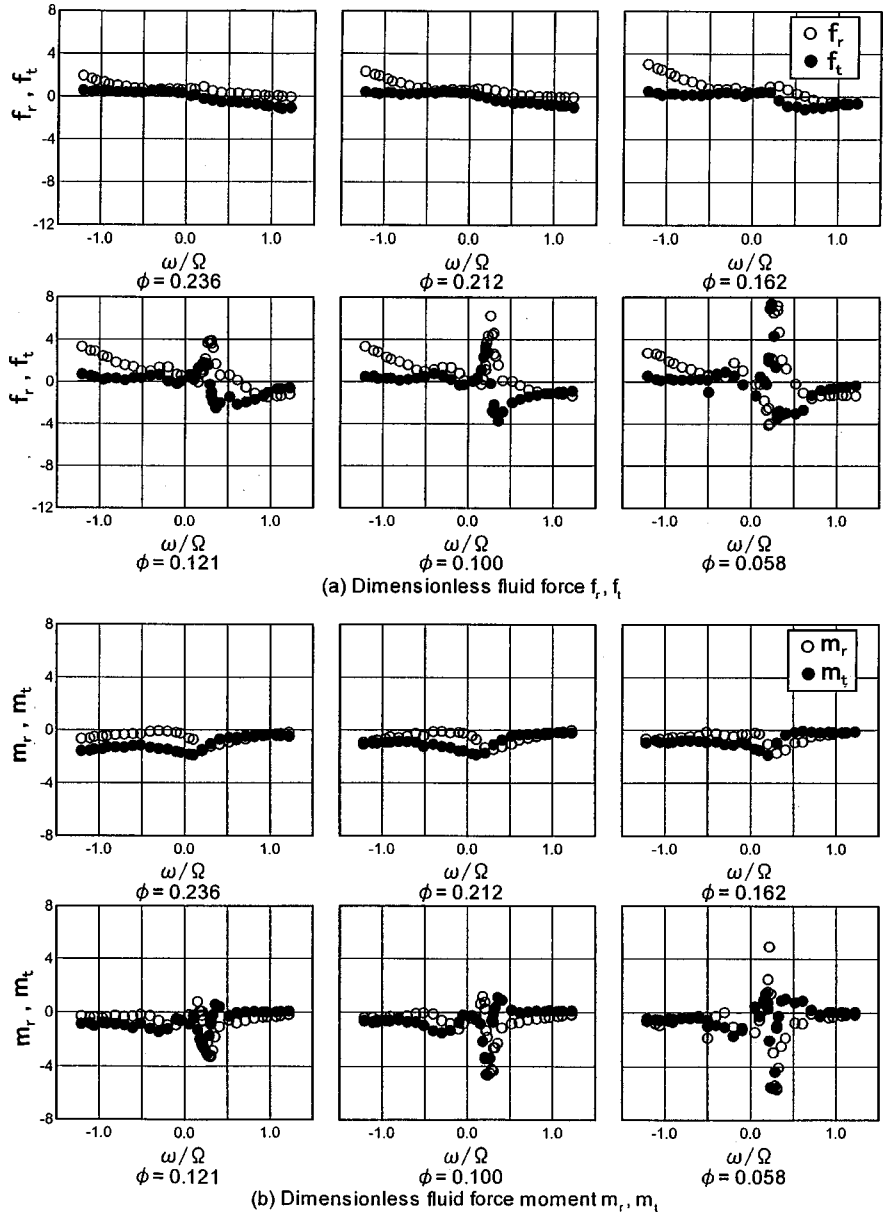

Fig. 8 Dimensionless fluid force f_r (○) and f_t, (●) and fluid force moment m_r (○) and m_t (●) on the impeller with Seal B versus whirling speed ratio ω/Ω for various flow coefficients ϕ ($\varepsilon = 1.05$ mm) (uncertainty in f_r, $f_t \pm 0.3$, m_r, $m_t \pm 0.3$, in $\omega/\Omega \pm 0.002$, in $\phi \pm 0.01$)

reported by Shoji and Ohashi [15], if there is no variation of seal leakage flow associated with the whirling motion, like Seal A and B.

However, it should be noted here that the change of fluid force and moment at $\omega/\Omega = 0.2 \sim 0.3$ is different for Seal A and B. The peak of f_r is negative in Seal A, although that is positive in Seal B. The same tendency can be observed in the fluid force moment. From these results, it was found that the seal geometry affected the direction of the peak fluid force and force moment through the variation of the leakage flow due to the impeller whirl, and also to the actual radial clearance in the direction of the eccentricity (Seal A: reduced clearance, Seal B: enlarged clearance).

Combined Effect of Whirling Motion and Rotating Stall. Tsujimoto et al. [16] calculated the fluid forces on a whirling impeller in a vaneless diffuser using two-dimensional vortical flow analysis. They reported that, the tangential fluid force becomes destabilizing at the whirling speed close to the propagation speed of a rotating stall in an impeller, or a diffuser. In addition, Tsujimoto et al. [17] calculated the critical flow angle and propagation speed of the rotating stall in vaneless diffusers with simple boundary conditions at the diffuser inlet and outlet. From this calculation, a rotating stall onset at flow rate $\phi = 0.062$, and propagation speed $\omega'/\Omega = 0.2$ can be obtained in the condition of the present experimental diffuser $r_4/r_3 = 1.5$. This propagation speed is near to $\omega/\Omega = 0.2 \sim 0.3$ where the fluid forces have a peak at low flow rate in the present experiment.

The combined effect of the whirl and rotating stall is investigated based on this prediction. Figure 10 presents the spectral analyses of pressure fluctuations at the diffuser inlet P1 and the output signal of the force sensor at various flow rates. The whirling speed with eccentricity $\varepsilon = 1.05$ mm is decreased continuously from $\omega/\Omega = +1.2$ to -1.2, while the flow rate is maintained constant.

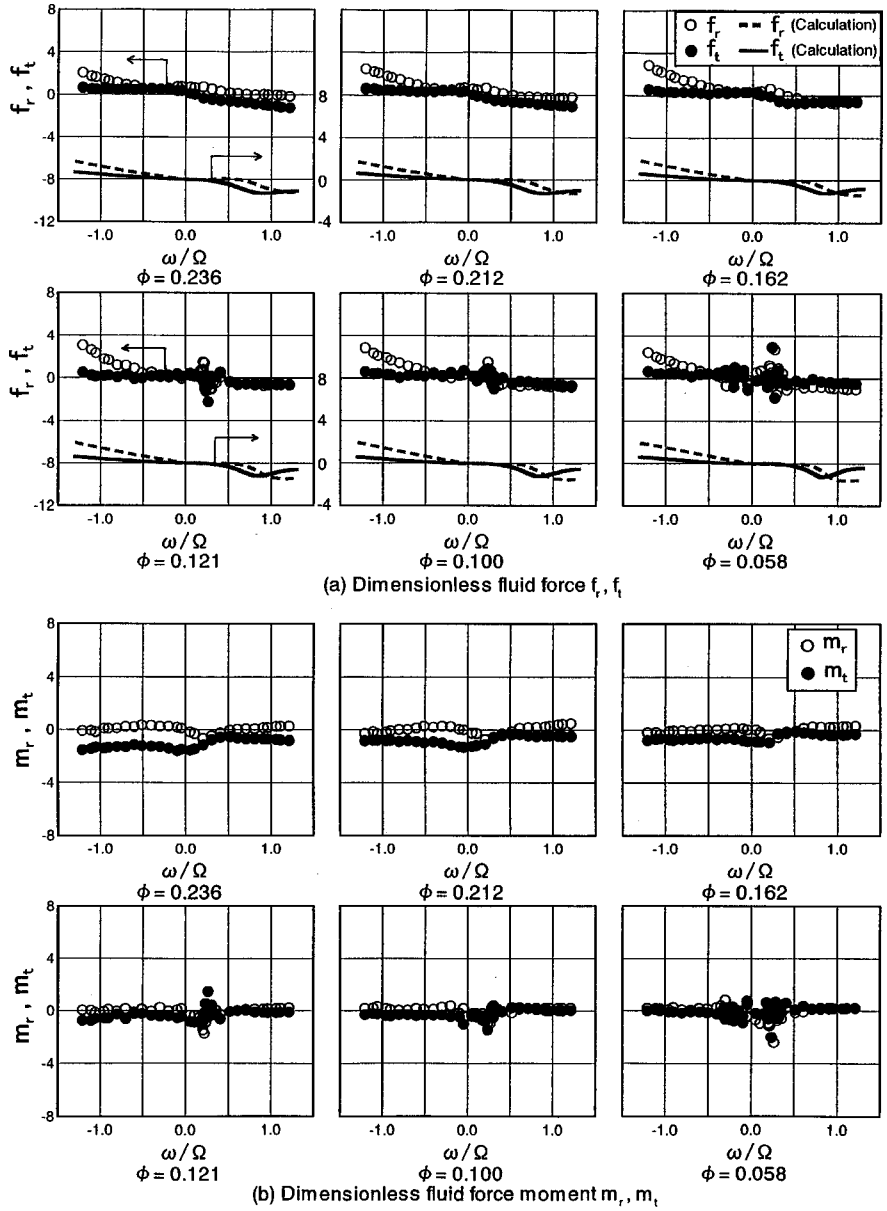

Fig. 9 Dimensionless fluid force f_r (○) and f_t, (●) and fluid force moment m_r (○) and m_t (●) on the impeller with Seal C versus whirling speed ratio ω/Ω for various flow coefficients ϕ (ε=1.05 mm) (uncertainty in f_r, f_t±0.3, m_r, m_t±0.3, in ω/Ω±0.002, in ϕ±0.01)

1. At high flow rate $\phi=0.236$, the dominant frequency of the pressure fluctuations is $f^*=|\omega/\Omega|$ due to the whirl. On the other hand, in the force sensor signal measured on the rotating shaft, there are the two components: (a) $f^*=|1.0-\omega/\Omega|$ caused by the fluid force due to the whirl (The reason of $|1.0-\omega/\Omega|$ for the force sensor signal is that the force sensor is installed in the relative rotating frame and the pressure sensor exists in the absolute frame; i.e., stationary casing), and (b) $f^*=1.0$ due to the electrical noise of the slip ring.

2. At flow rate $\phi=0.121$, the pressure fluctuations with $f^*=0.2\sim0.3$ due to the weak rotating stall appears at $\omega/\Omega=0.2\sim0.3$. This pressure fluctuation does not appear at the same flow rate under the condition of $\varepsilon=0$ and $\omega/\Omega=0$ as shown in Fig. 6. At $\omega/\Omega=0.2\sim0.3$, the amplitude of force sensor signal with $f^*=|1.0-\omega/\Omega|=0.7\sim0.8$ increases too. From these results, it is plausible that the rotating stall is induced and excited by the whirling motion which causes unsteady asymmetric pressure distribution at the diffuser inlet. The induced rotating stall is coupled with the whirling motion when the whirling speed is close to the propagation speed of the rotating stall.

3. At lower flow rate $\phi=0.100$, the strong rotating stall with $f^*\approx0.26$ (i.e., the propagation speed ratio $\omega'/\Omega\approx0.26$) occurs all over the range of $\omega/\Omega=+1.2\sim-1.2$. As a result, the component with $f^*=|1.0-\omega'/\Omega|\approx0.74$ of the force sensor signal appears clearly caused by the rotating stall. In addition, the component with $f^*=|1.0-\omega/\Omega|$ due to the whirl can be observed. The amplitude of the component with $f^*=|1.0-\omega/\Omega|$ increases at $\omega/\Omega\approx0.26$.

In order to examine the combined effects of the whirl and the rotating stall, two fluid forces were compared as follows. One is the fluid force, f_{RS}, caused by the rotating stall. The other is the rotordynamic fluid force, $f=(f_r^2+f_t^2)^{1/2}$. The fluid force f_{RS} was separated from the fluid force f based on the frequency using the

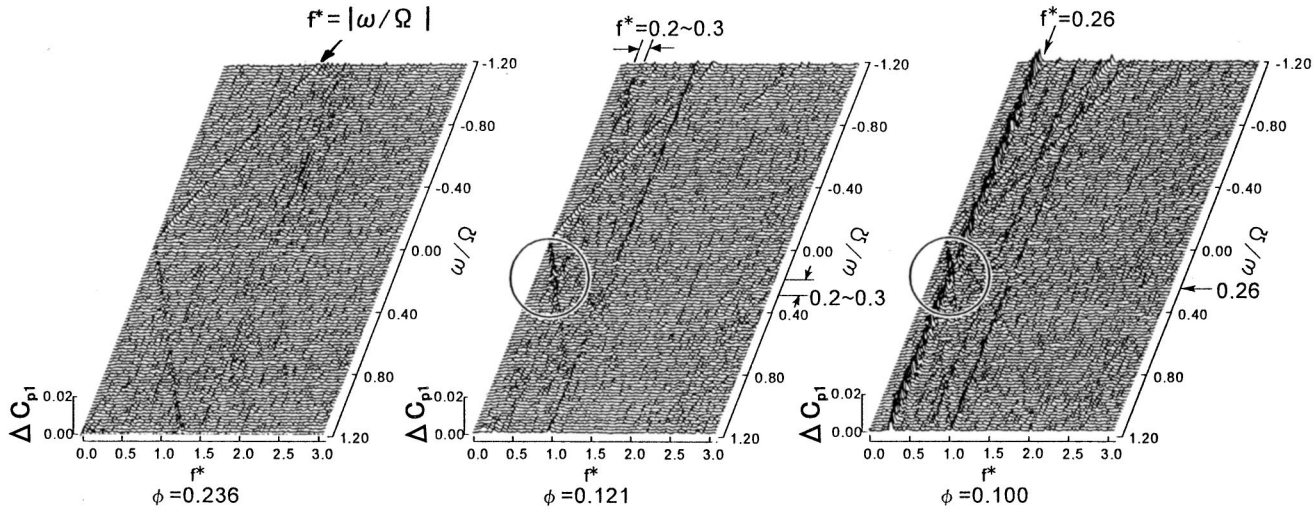

(a) Pressure fluctuations at the diffuser inlet, P1

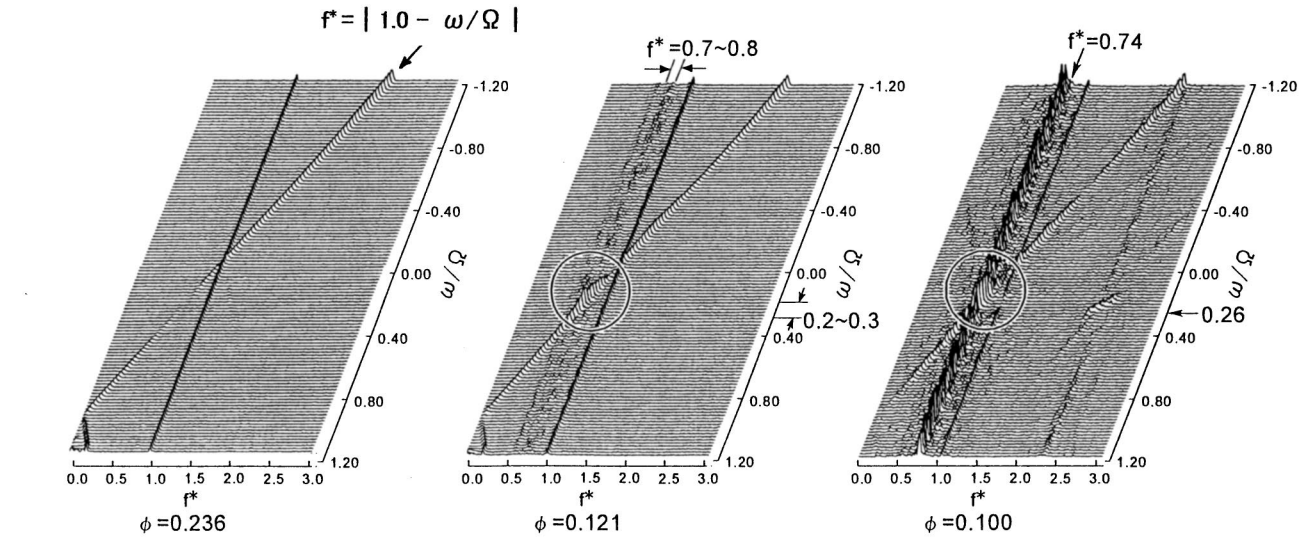

(b) Signal of force sensor

Fig. 10 Spectral analyses of the pressure fluctuations at the diffuser inlet P1 and the signal of force sensor for various flow rates in Seal A (ε=1.05 mm) (uncertainty in $\omega/\Omega \pm 0.002$, in $\phi \pm 0.01$)

phase-averaged conditioning; i.e., f_{RS} has the frequency $f^* = |1.0-\omega'/\Omega| \approx 0.74$ on the force sensor signal. Figure 11 shows the comparison of two forces, f_{RS} and f. At $\phi=0.236$ above design flow, there is no presence of f_{RS} caused by the rotating stall for any whirling speed. At $\phi=0.121$, f_{RS} does not appear except for the region $\omega/\Omega=0.2\sim0.3$. However, the rotordynamic fluid force f develops at $\omega/\Omega \approx 0.26$ caused by the induced rotating stall. At $\phi=0.100$, f_{RS} is almost constant $f_{RS} \approx 3.0$ except for $\omega/\Omega \approx 0.26$. Clearly, f increases dramatically larger than $f_{RS} \approx 3.0$ at $\omega/\Omega \approx 0.26$. Moreover, at lower flow rate $\phi=0.058$, f_{RS} increases $f_{RS} > 5.0$ at any whirling speed caused by the strong rotating stall, and also f increases remarkably at $\omega/\Omega \approx 0.26$.

From these results, it could be concluded that: (a) a rotating stall is induced at higher flow rate (still below design flow) by the whirling motion and coupled with the whirl, when the whirling speed becomes close to the propagation speed of the rotating stall, (b) a rotating stall occurs for any whirling speed at lower flow rate and is strongly enhanced when the whirling speed and the stall propagation speed become close each other.

Effect of the Seal Geometry. Figure 12 presents typical unsteady pressure patterns of the rotating stall in the vaneless diffuser for Seal A and B at $\omega/\Omega=0.26$, for $\phi=0.100$. This pressure pattern was obtained from the measurements of the pressure sensor, P1, P3, and P4 located at one angular position. Pressure fluctuations were phase conditional ensemble-averaged based on the trigger signal that indicates the instant when both the directions of the impeller whirl and the rotation of the rotating stall come to a prescribed orientation. The pressure pattern propagates in the direction of the impeller rotation coupled with the whirling motion. The patterns are similar to the experimental and theoretical results previously published (Tsujimoto et al. [17]). In this figure, *r* and *t*

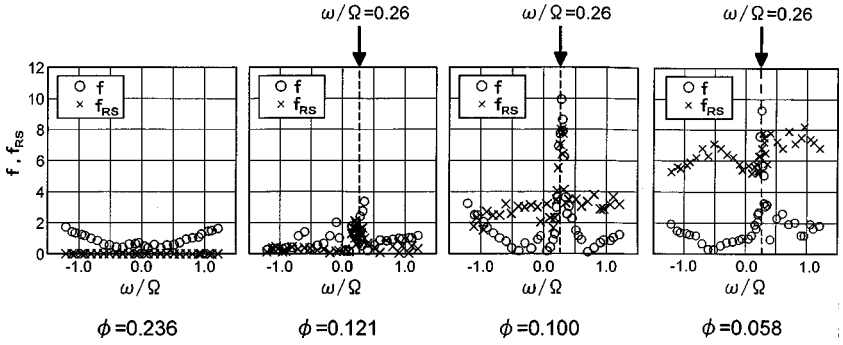

Fig. 11 Comparison of the dimensionless fluid force f (○) due to the whirl with the dimensionless fluid force f_{RS} (×) due to the rotating stall for various flow rates, in Seal A ($\varepsilon=1.05$ mm) (uncertainty in $f\pm0.3$, $f_{RS}\pm0.3$, in $\omega/\Omega\pm0.002$, in $\phi\pm0.01$)

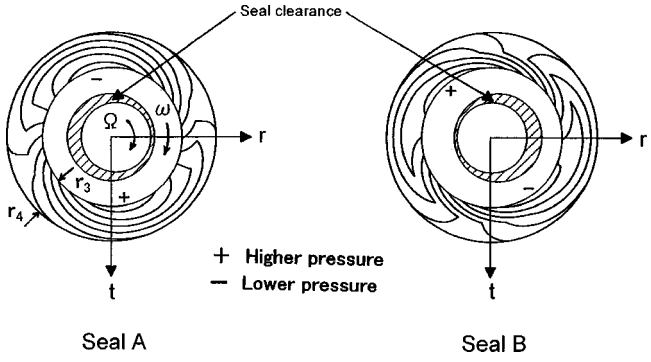

Fig. 12 Unsteady pressure pattern in the vaneless diffuser due to the rotating stall coupled with the whirl at $\omega/\Omega=0.26$ for $\phi=0.100$ in Seal A and B ($\varepsilon=1.05$ mm) (uncertainty in $\omega/\Omega\pm0.002$, in $\phi\pm0.01$)

axes are shown on the whirling coordinate of the impeller. It might be of interest to note that the pressure pattern of Seal A is almost contrary to that of Seal B with respect to the direction of shaft eccentricity, although both patterns are similar with respect to the seal clearance nonuniformity. From these observations, it was found that the variation of seal clearance in relation to the eccentricity is more important than the seal geometry for the coupling of rotating stall with the whirling motion.

The unsteady fluid forces on the impeller are calculated using the unsteady pressure measurements at the diffuser inlet, P1, to obtain a better understanding of the peak fluid force. The pressure fluid forces, f_{rp} and f_{tp}, are estimated by integrating the unsteady pressure on the impeller outlet including the impeller side plate. In this estimation, the unsteady forces resulted from the momentum transfer at the impeller inlet and outlet, and the rate of change of fluid momentum in the impeller are neglected. Figure 13 shows the comparison of directly measured fluid forces, f_r and f_t with estimated ones, f_{rp} and f_{tp} at $\phi=0.100$, for Seal A, B, and C. They agree well concerning the whirling speed ratio where the peak fluid force appears, and the difference of the direction of the

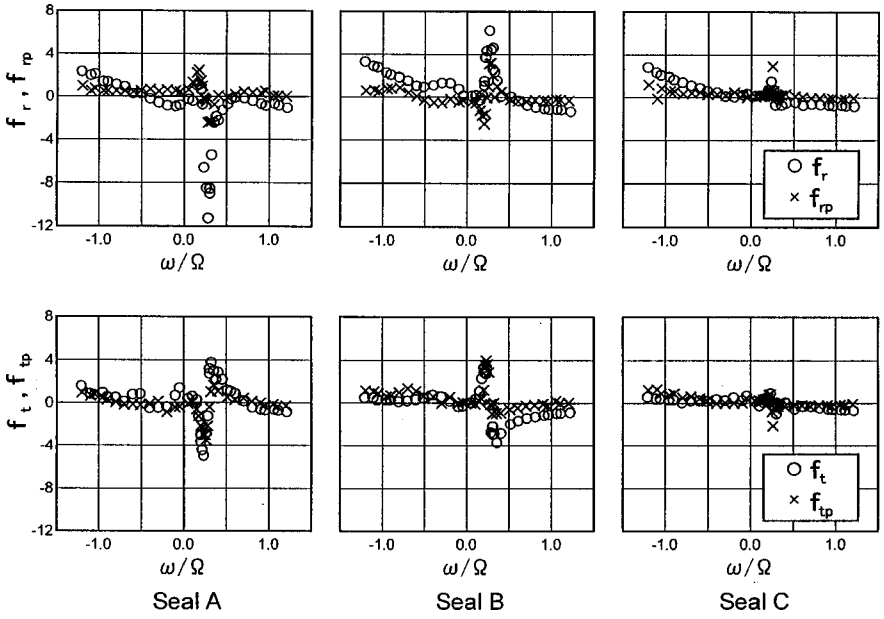

Fig. 13 Comparison of the dimensionless fluid force f_r and f_t (○) directly measured by the force sensor with the dimensionless pressure force f_{rp} and f_{tp} (×) estimated by the unsteady pressure at the impeller outlet, versus whirling speed ratio ω/Ω for $\phi=0.100$, in Seal A, B, and C ($\varepsilon=1.05$ mm) (uncertainty in f_r, $f_t\pm0.3$, f_{rp}, $f_{tp}\pm0.5$, in $\omega/\Omega\pm0.002$, in $\phi\pm0.01$).

fluid force for Seal A and B, although the amount of estimated pressure force is smaller than that of directly measured force. From these results, it was inferred that some fraction of the peak fluid force at $\omega/\Omega=0.2\sim0.3$ is generated by the pressure nonuniformity around the impeller due to the rotating stall.

On the other hand, Childs [7] calculated the unsteady flow in the leakage path between the impeller shroud and housing in whirling motion by using a bulk-flow model. In this calculation, he reported that the unsteady flow in the leakage flow path has a "resonance" at a certain whirling speed. From this prediction, it might be estimated that the leakage flow instability also plays an important role to couple the rotating stall with the whirling motion by means of the unsteady leakage flow through the Gap-A at the diffuser inlet.

Unfortunately, full confirmation of the unsteady leakage flow in the shroud leakage path has not been obtained in the present experiments. In order to explain all the effects of seal geometry, an extension of the experiment is underway with focus on the leakage flow, which will add to our understanding of the rotordynamic (whirl)-hydrodynamic (rotating stall, leakage flow) coupling.

Conclusions

From the experimental results and discussions, the following conclusions can be drawn:

1. the fluid forces on the whirling impeller have a stabilizing effect on the whirl basically at high flow rate.
2. at the whirling speed ratio $\omega/\Omega\approx0.26$, the fluid force has a destabilizing peak at low flow rate in the present experiment.
3. the peak of fluid force is caused by the coupling between the whirl and the rotating stall in the vaneless diffuser.
4. the change of seal geometry with axial seal (Seal A and B) affects the direction of the peak fluid force, and force moment through the unsteady leakage flow caused by the variation of the seal clearance due to the whirl.
5. the face seal (Seal C) that is characterized by no variation of seal clearance with whirling and so less contributive to unsteady leakage flow, shows less sensitivity to the whirling-rotating stall coupling effect.
6. it could be estimated that the unsteady leakage flow in the shroud leakage path plays an essential role for the occurrence of a coupling mechanism between the whirling motion and the vaneless diffuser rotating stall.

Acknowledgments

The authors wish to thank Mr. Tomoatu Inoue of Kyowa Electronic Instruments Corp. for the experimental support. They are also deeply grateful to Dr. Bruno Schiavello of Flowserve Pump Division for his helpful and useful comments. Also, express their gratitude for the effort of Mr. Kenta Yamamoto in support of this program as an undergraduate project at Osaka University.

Nomenclature

$[A]$ = four-by-four transfer matrix
b_2 = impeller axial width (see Fig. 2)
b_3 = diffuser axial width (see Fig. 2)
ΔC_p = coefficient of unsteady pressure Δp (zero-to-peak), normalized by $\rho(r_2\Omega)^2$
F = fluid force on impeller (see Fig. 4)
$\{FM\}$ = four-component vector of two force and two moment
F_r, F_t = fluid force, radial (r) and tangential (t) to the whirl orbit (see Fig. 4)
f = dimensionless fluid force on impeller normalized by $M_o\varepsilon\Omega^2=(f_r^2+f_t^2)^{1/2}$
f_r, f_t = dimensionless fluid force on impeller, radial (r) and tangential (t) to the whirl orbit, normalized by $M_o\varepsilon\Omega^2$
f_{rp}, f_{tp} = dimensionless fluid force due to unsteady pressure around the impeller, radial (r), and tangential (t) to the whirl orbit, normalized by $M_o\varepsilon\Omega^2$
f_{RS} = dimensionless fluid force caused by the rotating stall in vaneless diffuser, normalized by $M_o\varepsilon\Omega^2$
f^* = dimensionless frequency=frequency/$(\Omega/2\pi)$
Gap-A = radial clearance between impeller shroud edge and casing (see Fig. 2)
M = fluid force moment around the impeller center
M_r, M_t = fluid force moment, radial (r), and tangential (t) component (see Fig. 4)
M_o = reference value (mass of fluid in impeller) $=\rho\pi r_2^2 b_2$,
m_r, m_t = dimensionless fluid force moment on impeller, radial (r) and tangential (t) components, normalized by $M_o r_2\varepsilon\Omega^2$
"O" = center of impeller on the whirl orbit (see Fig. 4)
p = pressure
p_{t1} = total pressure at impeller inlet
Δp = unsteady pressure (zero-to-peak)
r = radius
(r,t) = radial and tangential axis (see Fig. 4)
r_1 = impeller inlet radius (see Fig. 2)
r_2 = impeller outlet radius (see Fig. 2)
r_3 = diffuser inlet radius (see Fig. 2)
r_4 = diffuser outlet radius (see Fig. 2)
S = seal radial clearance (S^*=nominal radial clearance with $\varepsilon=0$)
$\{V\}$ = four-component force sensor vector
ε = radius of circular whirl orbit (eccentricity)
ρ = fluid density
ϕ = flow coefficient=flow rate/$(2\pi r_2^2 b_2\Omega)$
ϕ_d = design flow coefficient
ψ = pressure coefficient (at collector PO)=$(p\text{-}p_{t1})/\rho(r_2\Omega)^2$
ψ_s = static pressure coefficient (at diffuser inlet P1)=$(p\text{-}p_{t1})/\rho(r_2\Omega)^2$
ω = whirling angular velocity
ω' = angular velocity of rotating stall
Ω = angular velocity of impeller
ω/Ω = whirl speed ratio
ω'/Ω = propagation speed ratio of rotating stall

References

[1] Jery, B., Acosta, A. J., Brennen, C. E., and Caughy, T. K., 1985, "Forces on Centrifugal Pump Impellers," *Proceedings of the 2nd International Pump Symposium*, Houston, TX, pp. 21–32.
[2] Bolleter, U., Wyss, A., Whelte, I., and Sturchler, R., 1987, "Measurement of Hydraulic Interaction Matrices of Boiler Feed Pump Impeller," ASME J. Vib., Acoust., Stress, Reliab. Des., **109**, pp. 144–151.
[3] Ohashi, H., Sakurai, A., and Nishihama, J., 1988, "Influence of Impeller and Diffuser Geometries on the Lateral Fluid Forces of Whirling Centrifugal Impeller," NASA CP. 3026, pp. 285–306.
[4] Adkins, D. R., and Brennen, C. E., 1988, "Analyses of Hydraulic Radial Forces on Centrifugal Pump Impeller," ASME J. Fluids Eng., **110**, pp. 20–28.
[5] Tsujimoto, Y., Acosta, A. J., and Brennen, C. E., 1988, "Theoretical Study of Fluid Forces on Centrifugal Pump Impeller Rotating and Whirling in a Volute," ASME J. Vib., Acoust., Stress, Reliab. Des., **110**, pp. 263–269.
[6] Tsujimoto, Y., Acosta, A. J., and Yoshida, Y., 1988B, "A Theoretical Study of Fluid Forces on Centrifugal Pump Impeller Rotating and Whirling in a Vaned Diffuser," NASA CP. 3026, pp. 307–322.
[7] Childs, D. W., 1989, "Fluid Structure Interaction Forces at Pump-Impeller-Shroud Surfaces for Rotordynamic Calculation," ASME J. Vib., Acoust., Stress, Reliab. Des., **109**, pp. 144–151.
[8] Guinzburg, A., Brennen, C. E., Acosta, A. J., and Caughy, T. K., 1994, "Experimental Results for the Rotordynamic Characteristics of Leakage Flow in Centrifugal Pump," ASME J. Fluids Eng., **116**, pp. 110–115.
[9] Uy, R. V., and Brennen, C. E., 1999, "Experimental Measurements of Rotordynamic Forces Caused by Front Shroud Pump Leakage," ASME J. Fluids Eng., **121**, pp. 633–637.
[10] Ohashi, H., Imai, H., Sakurai, A., and Nishihama, J., 1990, "Lateral Fluid Forces of Whirling Centrifugal Impellers With Various Geometries," *The 3rd Japan-China Joint Conference of Fluid Machinery*, **11**, pp. 147–153.
[11] Bently, D. E., and Goldman, P., 1998, "Destabilizing Effect of Aerodynamic

Forces in Centrifugal Compressors,'' *Proceedings of the 7th International Symposium on Transport Phenomena and Dynamics of Rotating Machinery*, Honolulu HI, **A**, pp. 306–315.
[12] Yoshida, Y., Tsujimoto, Y., Ishi, N., Ohashi, H., and Kano, F., 1999, ''The Rotordynamic Forces on an Open-Type Centrifugal Compressor Impeller in Whirling Motion,'' ASME J. Fluids Eng., **121**, pp. 259–265.
[13] Bolleter, U., Leibundgut, E., Sturchler, R., and McCloskey, L., 1989, ''Hydraulic Interaction and Excitation Forces of High Head Pump Impellers,'' *Proc. of the 3rd Joint ASCE/ASME Mechanical Conference*, pp. 187–193.
[14] Shoji, H., and Ohashi, H., 1987, ''Lateral Fluid Forces on Whirling Centrifugal Impeller (1st Report: Theory),'' ASME J. Fluids Eng., **109**, pp. 94–99.
[15] Shoji, H., and Ohashi, H., 1987, ''Lateral Fluid Forces on Whirling Centrifugal Impeller (2nd Report: Experiment in Vaneless Diffuser),'' ASME J. Fluids Eng., **109**, pp. 100–106.
[16] Tsujimoto, Y., and Acosta, A. J., 1987, ''Theoretical Study of Impeller and/or Vaneless Diffuser Attributed Rotating Stall and Their Effects on Whirling Instability of Centrifugal Impeller,'' Work Group on the Behavior of Hydraulic Machinery under Steady Oscillatory Conditions, Lille, France.
[17] Tsujimoto, Y., Yoshida, Y., and Mori, Y., 1994, ''Study of Vaneless Diffuser Rotating Stall Based on Two-Dimensional Inviscid Flow Analysis,'' ASME J. Fluids Eng., **118**(1), pp. 123–127.

Supersonic Through-Flow Fan Blade Cascade Studies

Christopher J. Chesnakas

Wing F. Ng

Mechanical Engineering Department,
Virginia Tech,
MC 0238,
Blacksburg, VA 24061

An investigation has been performed of the flow in a supersonic through-flow fan blade cascade. The blade shapes are those of the baseline supersonic through-flow fan (STF). Measurements were made at an inlet Mach number of 2.36 over a 15 deg range of incidence. Flowfield wave patterns were recorded using spark shadowgraph photography and steady-state instrumentation was used to measure blade surface pressure distributions and downstream flowfield. From these measurements, the integrated loss coefficients are presented as a function of incidence angle along with analysis indicating the source of losses in the STF cascade. The results are compared with calculations made using a two-dimensional, cell-centered, finite-volume, Navier-Stokes code with upwind options. Good general agreement is found at design conditions, with lesser agreement at off-design conditions. Analysis of the leading edge shock shows that the leading edge radius is a major source of losses in STF blades. Losses from the leading edge bluntness are convected downstream into the blade wake, and are difficult to distinguish from viscous losses. Shock losses are estimated to account for 70% to 80% of the losses in the STF cascade. © *2003 American Institute of Physics.* [DOI: 10.1115/1.1601257]

Introduction

The rapid growth in air traffic across the Pacific has sparked renewed interest in supersonic passenger transports. The current generation of aircraft engines, however, do not perform well at supersonic cruise. In order to make such supersonic transports economically viable, supersonic cruise engines must be improved in both weight and efficiency.

One component of the supersonic cruise engine which could be improved substantially in both of these areas is the inlet. A supersonic inlet for a typical gas turbine engine must be capable of decelerating the supersonic inflow to subsonic speeds at the engine face. This deceleration of the flow is not easily managed, and shock and boundary layer losses are inevitable. In order to minimize these losses, a long and heavy inlet employing variable geometry is necessary. Thus, an inlet for a typical supersonic cruise engine is both heavy and inefficient.

As far back as 1958, Ferri [1] pointed out that a fan capable of accepting supersonic axial flow would allow for the use of a light, simple inlet with high pressure recovery at supersonic cruise. As envisioned by Ferri [1], the fan would operate with a normal shock in the rotor passage, and the outlet flow would be subsonic. The efficiency of such rotors, however, is not high, due to the large losses from the passage normal shock. A more promising way of increasing the compression system (inlet plus compressor) efficiency is to employ a fan in which the flow is axially supersonic throughout. First proposed by Advanced Technology Laboratory, Inc. and studied under NASA contract (Trucco), [2], flow in this engine would still need to be diffused to subsonic velocity, but the losses in such a diffusion process would be confined to only the fraction of air which goes through the core, and thus overall losses would be reduced. The weight of the supersonic through-flow fan (STF) equipped engine would be reduced relative to a conventional turbofan engine since, not only would a lighter inlet be needed, but fewer stages would be required—the STF being capable of much higher pressure ratios than lower speed fans.

Several studies have been conducted to estimate the performance potential of the STF equipped engine. Tavares [3] suggested that a STF efficiency of 68% is required to provide a performance advantage over a turbojet engine for a Mach 2.7 transport. Champagne [4] suggested that a STF engine equipped Mach 2.3 transport would have a 14% increase in range compared to a conventional turbofan due to the 9% reduction in specific fuel consumption and 31% reduction in installed engine weight. Franciscus and Maldonado [5] found that for a Mach 3.2 transport with a 5000 mile range, a STF engined aircraft would have a takeoff gross weight 13% less than an aircraft equipped with an advanced turbine bypass engine.

Unfortunately, all these studies suffer from a lack of experimental data confirming the assumed fan performance. Only two experimental studies to date have examined the performance of supersonic axial blading. Savage et al. [6] examined the performance of a transonic rotor operating above design speed in a Mach 1.5 flow and obtained limited performance data. Breugelmans [7] tested a rotor designed for Mach 1.5 inlet flow, but was unable to obtain substantial data due to early rotor blade failure. In both cases, the rotor operated with a normal shock in the rotor, and therefore, the exit velocity was axially subsonic.

In order to better quantify the performance potential of the STF, the NASA Lewis Research Center undertook a program to design, build, and test a proof-of-concept supersonic through-flow fan stage. The fan stage was designed for a total pressure ratio of 2.45 at a fan face Mach number of 2.0. The design of the fan stage and the details of the blading are described by Schmidt et al. [8].

As a part of this program, two-dimensional cascade studies of mean blade sections were undertaken in the Virginia Tech supersonic cascade wind tunnel. These cascade studies were undertaken in order to obtain an understanding of the flow physics and loss mechanisms in the supersonic through-flow fan, and to establish a database on supersonic through-flow fan performance.

This paper will detail the results of the experimental cascade studies and analyze the results in light of the above stated objectives. The results will be compared to CFD calculations of the cascade flow in order that the capabilities and limitations of these codes can be assessed for the problem of STF design. The results of the testing and the computational predictions of the flow will be analyzed in light of a shock loss model in order to better understand the loss mechanisms in the STF cascade.

Experimental Apparatus

All measurements were conducted in the Virginia Tech supersonic cascade wind tunnel. This blow-down facility was equipped

Contributed by the Fluids Engineering Division for publication in the JOURNAL OF FLUIDS ENGINEERING. Manuscript received by the Fluids Engineering Division March 12, 2002; revised manuscript received March 27, 2003. Associate Editor: W. W. Copenhaver.

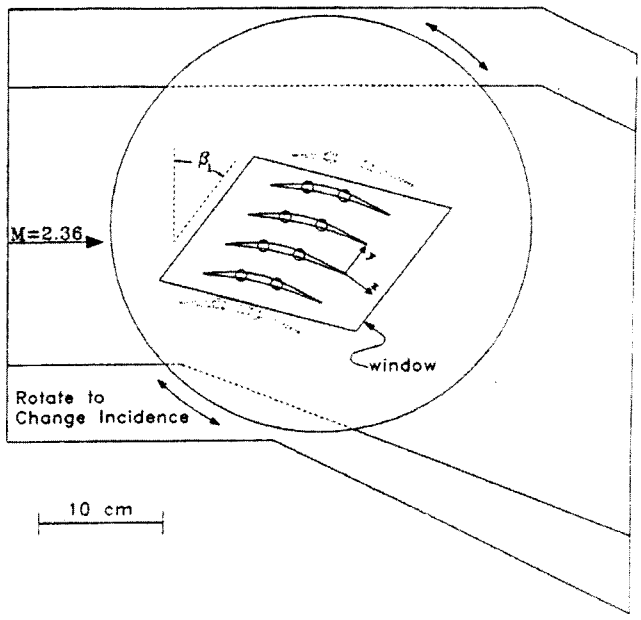

Fig. 1 Cascade test section

with a two-dimensional Mach 2.36 nozzle and a 15.2×22.9 cm (6×9 inch) test section. The cascade wind tunnel was typically operated at a total pressure of 400 kPa and a total temperature of 285 K, for a Reynolds number of approximately 4.4×10^5 per cm. The air was dried and filtered to reduce the level of particulates in the flow. Upstream of the nozzle, the settling chamber was equipped with flow straighteners and screens to reduce large scale turbulence. The freestream turbulence intensity is approximately 1%, and the flow Mach number is uniform to ±0.05. Characteristics of the tunnel flow are more fully documented in Chesnakas [9,10].

Placed into the test section of this tunnel was the cascade illustrated in Fig. 1. The cascade consisted of six blades mounted on a circular back-plate that could be rotated to obtain any desired inflow angle. "Design incidence," $i=0°$, is defined as the condition at which the flow is parallel to the blade suction surface at the leading edge. Measurements were made at inflow angles $i=-10°$, $-5°$, $0°$, and $+5°$. All measurements downstream of the cascade are referred to an $x-y-z$ coordinate system in which the z-direction is along the blade span, the y-direction is parallel to a line connecting the blade trailing edges, and the x-coordinate is in the axial direction. The origin of the coordinate system is at midspan of the trailing edge of the third blade from the bottom of the cascade as shown in Fig. 1. In order to obtain the shadowgraphs of the blade passage, the blades were mounted in a plexiglas window. For LDV measurements, a second set of doors was used with a 90-mm-diameter Schlieren quality glass window mounted to provide access to the blade trailing edge region.

The cascade blade shapes were derived from the NASA Lewis baseline STF rotor at midspan. The cascade consisted of six full-scale blades with chord length, c, of 100.3 mm, spacing, s, of 30.2 mm, and span of 152 mm. The solidity, σ, of the blades was 3.32 and the maximum blade thickness was 5.8 mm. Details of the blade shape can be found in Chesnakas [9,10].

No endwall suction is applied in the test section. Due to the high supersonic axial Mach number in the cascade, the flow is hyperbolic, and the characteristics are fairly shallow. Any disturbance caused by thickening of the endwall boundary layer can only propagate a limited distance toward the center of the blade passage. As a consequence, the axial-velocity density ratio (AVDR), $(\rho u)_2/(\rho u)_1$, is 1, and the flow at the center of the passage is two-dimensional. This is in contrast to lower speed cascades which are elliptical in nature. In subsonic-axial cascades, the thickening endwall boundary layer can influence flow even in the center of the passage, and the AVDR is typically greater than 1. Oil streaks on the blade surfaces and downstream Pitot measurements verified the two-dimensionality of the STF cascade flow at midspan. Blade-to-blade periodicity and measurement repeatability, as documented in Chesnakas [9,10], were both quite good.

It should be noted that there are some features of supersonic-axial blading that makes the operation of this cascade quite different from that of cascades in which the blading is supersonic relative to the blades but subsonic in the axial direction. The first of these is that, since the flow is supersonic in the axial direction at the inlet of the cascade, shocks coming off of the leading edge will be contained within the blade passage. Since no waves propagate in front of the blades, no "unique incidence" condition exists for supersonic axial blading. Also, since the flow is supersonic axial at the exit of the cascade, the static pressure at the exit of the cascade is prescribed by the inlet conditions, and back pressure is not an independent parameter.

The supersonic through-flow fan blade cascade was examined using four different sets of instrumentation. The first of these was a spark shadowgraph system. Since the blades were mounted in a plexiglas window, the shadowgraphs revealed the flow structure throughout the entire blade passage.

Blade surface pressures were obtained with a set of instrumented blades. Sixteen pressure taps were placed on each surface in one blade passage, from $x/c=0.038$ to $x/c=0.962$. These pressures are reported here normalized by the settling chamber total pressure. The total uncertainty in the pressure measurements is $\pm1.2\%$—approximately the size of the symbols on the plots that follow.

Pitot and static pressures in the region downstream of the blades were measured with a unique Pitot/static probe fully described in Chesnakas [9,10]. The probe, in brief, is a horizontal rake consisting of a center-mounted Pitot tube, with a static pressure tap on a vertical, sharp-edged plate on either side of the Pitot tube. Since the static and Pitot taps are horizontally separated, the probe is only suitable for flows which are invariant in the horizontal direction (two-dimensional). The probe was traversed downstream of the cascade in the y-direction (along a line parallel to the cascade). From these Pitot and static measurements, the Mach number, total pressure, and mass flux could be calculated.

Finally, velocities in the cascade were measured with a two-component laser Doppler velocimeter (LDV). When combined with a simultaneous measurement of the flow total temperature, these measurements could also be used to find the Mach number of the flow. The system, in brief, was a two-color, two-component, dual-beam system utilizing the blue (488 nm) and green (514.5 nm) lines of an etalon equipped argon-ion laser. The fringe spacing for each component was approximately 7 μm. The system was set to measure velocity components at plus and minus 45 deg to the mean flow. One of each of the blue and green beams was frequency shifted by 40 MHz, so that the fringes would move in the direction of the flow, and angular bias would be minimized. Light was collected in direct forward scatter, and counters with 1 ns resolution clocks were used to measure the time for eight fringe crossings. At each measurement position, 1024 data points were taken, and the mean velocity of the flow was taken as the arithmetic mean of the 1024 measurements. The LDV system could be positioned to an accuracy of 0.05 mm. Turbulence information was also acquired with the LDV, but the results of that were presented in a separate paper, (Andrew [11]).

Seeding particles for the LDV system consisted of 0.6 μm polystyrene latex spheres (PSL), which were suspended in ethanol and injected directly into the tunnel approximately 3 m upstream of the nozzle throat. The 0.6-μm PSL was chosen to maximize scattered light while minimizing particle lag. The 0.6-μm particles follow the flow closely through most of the blade passage, and only lag the flow significantly in very small regions behind the

Table 1 Uncertainty analysis, summary

	Freestream		Wake		
	Probe	LDV	Probe	LDV	Mass Averaged
M	±3.7%	±2.6%	±2.0%	±1.7%	-
p_t	±7.4%	±5.4%	±2.3%	±2.4%	±7.1%
V	-	±1.2%	-	±1.3%	
i	-	±0.9°	-	±0.9°	
ω					±0.068

cascade shocks (Chesnakas [9,10]). Comparison of the data rate when injecting pure ethanol into the flow relative to the case of no ethanol injection confirmed complete evaporation of the ethanol carrier. Electron microscopy revealed excellent particle size uniformity and very little agglomeration of the seeder output Chesnakas [9,10]. Pitot/static probe measurements upstream of the cascade showed the seeder to have no measurable effect on the cascade inflow.

The measurement uncertainty for the Pitot/static probe and the LDV system is detailed in Chesnakas [9,10], and is summarized in Table 1. Uncertainties listed include both bias and precision errors. Bias errors, in general, predominate.

Computational Analysis

A computational simulation of the flow through the supersonic through-flow fan blade cascade was performed in order to aid in the interpretation of the experimental data and to gain an understanding of the capabilities and limitations of computational fluid dynamics (CFD) to predict the flow in a STF. The CFD code used in this research (algorithm for the Navier-Stokes equations using a Riemann solver, ANSERS) was based on the algorithm of Taylor [12]. This code is the two-dimensional version of the three-dimensional code (CFL-3D) by Thomas and Walters [13]. This time-marching method solves the compressible, complete N-S equations in generalized coordinates. The governing equations are solved in integral conservation law form using a cell-centered, finite-volume formulation. The inviscid flux terms were evaluated using van Leer's flux vector splitting method. In this paper, spatial discretization for the inviscid flux terms is third-order accurate upwind-biased. Viscous fluxes are differenced using second-order-accurate central differences. Only limited study on grid resolution was performed in this research. Results presented in the paper was based on a 65×210 grid. Additional calculations were performed on a grid twice as dense. Solutions were grid independence in most part of the flowfield, except at location of shock/boundary layer interaction. A unique grid was used for each inflow angle. Turbulence was modeled using the Baldwin-Lomax eddy viscosity model, assuming turbulent flow from the leading edge of the blade. This model was chosen for its computational simplicity.

In general, separated regions within the STF flowfield caused the solutions to be oscillating in nature, which necessitated an excessively large number of iterations for convergence. The number of required iterations was typically 12,000, and were carried out at a CFL number of 6. The applied convergence iteration was the consistency of the skin friction over an interval of 1500 iterations; the completed pressure distributions converged more quickly.

Supersonic flow at the upstream, inflow boundary dictate that four boundary conditions be specified there in an explicit manner. These are density, two components of velocity, and pressure. At the outflow boundary, supersonic exit flow requires that four boundary conditions are extrapolated from the computational domain. Density, two components of velocity, and pressure were extrapolated to the outflow boundary for this purpose. The remaining two outer boundary segments are specified as periodic over the cascade pitch. Two types of boundary conditions are appropriate at the inner boundary: a no-slip, adiabatic condition at the wall, and periodicity along the wake centerline.

All calculations were performed with an inflow Mach number of 2.36. Four incidence angles were analyzed in order that the effect of entrance flow angle could be evaluated. All calculations were within 1 deg of the nominal measured incidence angles of $i=-10$ deg -5 deg, 0 deg, and 5 deg, and will be referred to in this paper by these nominal values.

Grid independence of the results was confirmed. Adequate clustering was verified to resolve the viscous layers and the shock layer sufficiently. Cluster of the grid was based on experimental results. Further details on the CFD simulation can be found in Chesnakas [9,10].

Results

Design Incidence. A shadowgraph of the cascade operating at design incidence is shown in Fig. 2. In this shadowgraph, the flow is coming in from the left in the direction of the blade suction surface (upper) leading edge. The shocks coming off the leading edge can be seen to be contained within the blade passage. This indicates that the component of velocity in the axial direction (perpendicular to the cascade) is supersonic. The leading edge shock from the suction side of the leading edge intersects the pressure surface (lower) at approximately 12% chord, and generates a reflected shock. There is no indication of boundary-layer separation at this shock/boundary-layer interface either in the shadowgraph or in the surface oil flow visualizations of Andrew [14]. The leading edge shock from the pressure side intersects the suction surface at approximately 55% chord and reflects weakly. Although not evident in the shadowgraph, the surface oil flow visualizations of Andrew [14] indicate that there is a mild separation at this point, with the flow quickly reattaching. Originating from the trailing edge are a pair of ''fishtail'' shocks. These shocks exist to equilibrate the flows from the suction and pressure surfaces, which arrive at the trailing edge at slightly different pressures and slightly different flow angles. The blade wake is only

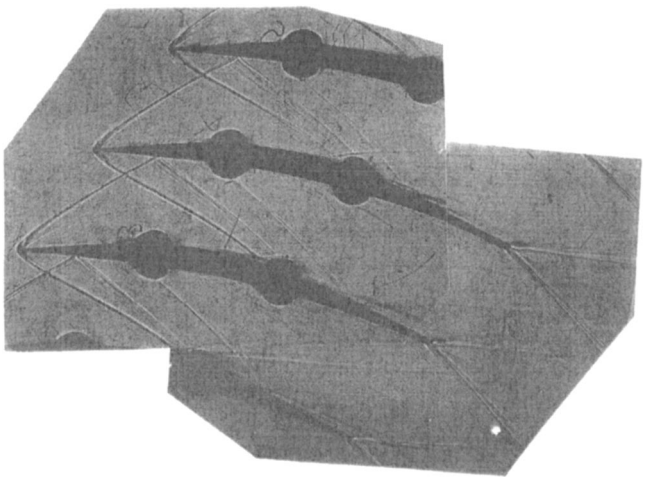

Fig. 2 Cascade shadowgraph, design incidence, $\beta_1=37$ deg. The pressure probe is visible on the lower right hand corner.

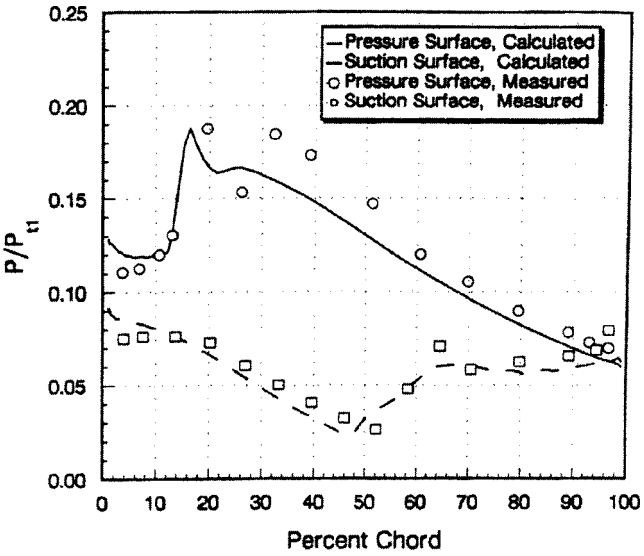

Fig. 3 Blade surface pressure, design incidence

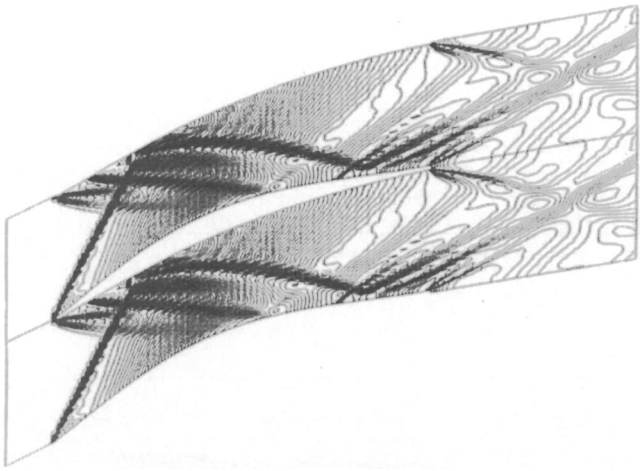

Fig. 4 Contour plot of static pressure at design incidence, calculated

weakly visible in the shadowgraph, and little about its extent or structure can be inferred. Visible in the bottom right of the shadowgraph is one of the pressure probes used downstream of the cascade.

The fact that this cascade operates with almost no boundary-layer separation would be considered unusual if this were a conventional, subsonic-axial cascade, but should not be too surprising for supersonic-axial flow. If the cascade blade shapes are examined, it can be seen that, with these blades the flow is turned toward the axial direction as it passes through the cascade, and so the passage area increases. Since there is supersonic inflow, the increase in passage area dictates that the Mach number increase and the static pressure drop through the blade passage. This favorable pressure gradient is a unique feature of supersonic throughflow blading that limits boundary-layer growth and helps to prevent massive boundary-layer separation.

The existence of this overall favorable pressure gradient in the cascade is confirmed with the blade surface pressure measurements. The blade static pressure distribution for the case of design incidence are shown in Fig. 3. It can be seen that the pressure on the suction surface initially rises slightly as the flow is compressed through the slight concavity of the suction surface at the leading edge. After this initial rise, the static pressure decreases monotonically until approximately 55% chord, where the pressure side leading edge shock intersects the suction surface. After the pressure rise from this shock—and two other mild shocks, visible in Fig. 2, which closely follows—the pressure over the last 30% of the suction surface is nearly constant, rising slightly toward the trailing edge.

Measurements of the pressure surface static pressure at design incidence can be similarly matched to flow features revealed in the shadowgraph. These measurements show the pressure increasing slowly over the first 10% of the blade, and then increasing sharply around 15% chord where a shock from the leading edge intersects the pressure surface. After the sharp rise in pressure from this shock, the surface pressure drops and then rises again from the convergence of compression waves originating from the concave portion of the leading edge suction surface into a ''recompression'' type shock. Past this second wave, the pressure drops steadily from 35% chord to the trailing edge. At the trailing edge, the pressure side and suction side pressures are nearly equal.

Comparison of the measured cascade flowfield to the calculated flowfield yields generally good agreement. Figure 4 shows a contour plot of the calculated static pressure at design incidence. Comparison of this plot with Fig. 2 illustrates that the positions of the leading edge shocks agree quite well in both of these figures, as do the positions of the reflected shocks in the blade passage. Comparison of Fig. 4 with Fig. 2 also shows that the positions of the fishtail shocks are predicted accurately. The measured and calculated blade static pressures are shown in Fig. 3. It can be seen that the agreement between the calculated and measured blade static pressure is generally good, with the following caveats. The calculated static pressure over the last part of the blade is low. Also, the calculated static pressure does not show the pressure peak measured at about 32% chord on the pressure surface of the blade. It is surmised that the grid is not sufficiently refined in the region where the compression waves from the suction surface coalesce to adequately resolve this pressure rise.

The conditions downstream of the cascade at design incidence can be seen in Figs. 5 and 6. In these plots, the Mach number and total pressure at $x/c=0.37$ from both the Pitot/static probe and the LDV measurements, and from the CFD calculations are presented. (LDV total pressure results are obtained by combining the LDV velocity measurements, a total temperature measurement, and the Pitot pressure as explained in Chesnakas [9,10]). In these figures,

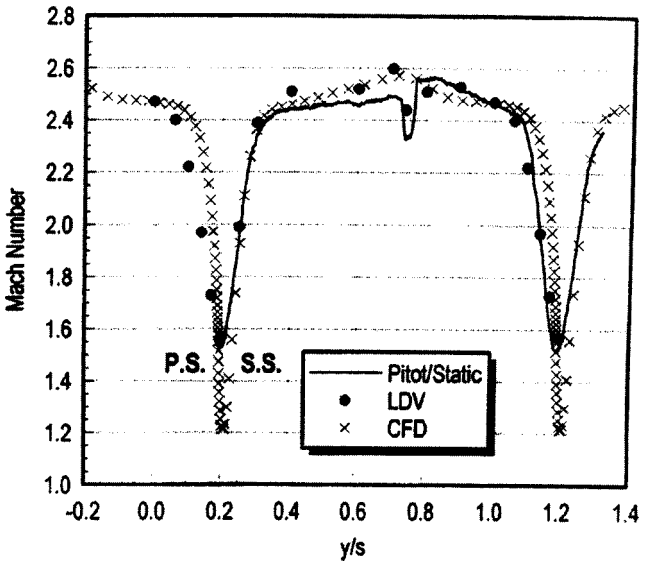

Fig. 5 Downstream Mach number, /=0 deg, $x/c=0.37$, measured and calculated. (Note the presence of the fishtail shock at $y/s=0.75$.)

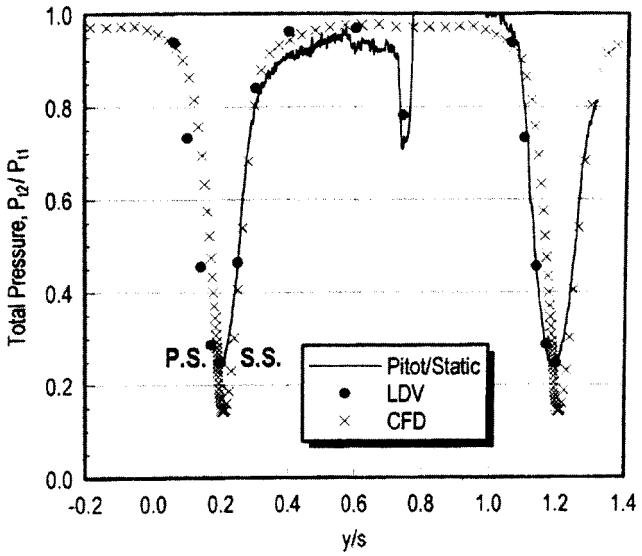

Fig. 6 Downstream total pressure, $i=0°$, $x/c=0.37$, measured and calculated. (Note the presence of fishtail shock at $y/s=0.75$.)

the wakes are quite distinct from the passage flow. The Pitot/static probe measurements also clearly show the location of the fishtail shocks—which at this axial location are coincident—with a spike in the profiles at mid passage. This spike in the profiles occurs when the shock disrupts the flow about the probe and alters its response (and thus the ''LDV'' total pressure as well). Notable in these figures is the good agreement between the LDV and Pitot/static probe measurements, particularly in the wake. All measurements agree within the experimental uncertainty. In the center of the passage, total pressure losses are small, and the region of measured total pressure greater than 1 is within the uncertainty band.

It should also be noted that there is generally good agreement between the calculated profiles and the experimental data. The calculated Mach number and total pressure agree quite well in the blade passage and the locations of the wakes are accurately predicted. The shortcoming of the calculated profiles is in the wake region, where the minimum Mach number and total pressure is overestimated—perhaps due to the difficulty of applying the Baldwin-Lomax model in a free shear layer.

−10 Degree Incidence. Figure 7 shows the flow through the cascade at −10 deg incidence. At this incidence, the shock coming off the suction side of the leading edge is much stronger than in the design case. The shock structure revealed in the shadowgraph clearly indicates a strong shock/boundary-layer interaction where this shock impinges on the pressure surface, approximately 17% chord. In the photograph, compression waves can be seen to originate from the pressure surface just upstream of the impinging shock as the flow is deflected by the separation zone. These compression waves then coalesce to form a ''separation shock.'' Just downstream of the shock impingement point, the shadowgraph shows another shock emanating from the pressure surface. This shock exists due to the flow reattaching after turning around a separation bubble. This is in agreement with Andrew's, [14], surface oil flow visualizations. Further evidence of flow reattachment is visible on the pressure surface at approximately 73% chord, where a wave approaching the pressure surface can be seen to impinge. If the flow at this point had been separated, the flow near the blade would have been subsonic. All waves impinging on the suction surface can be seen to reflect weakly, without causing large separations of the suction surface boundary layer. The surface oil flow visualization of Andrew [14] indicate that there are,

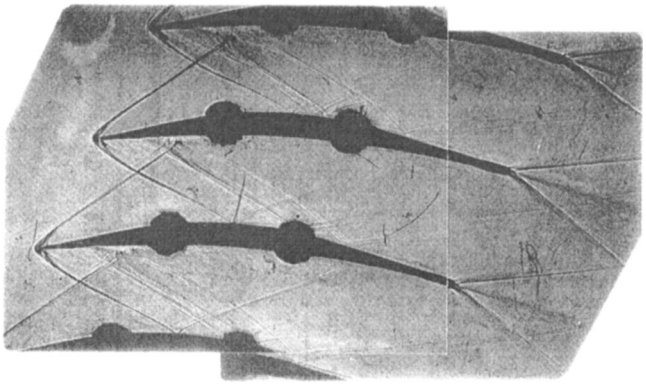

Fig. 7 Cascade shadowgraph, −10° incidence, $\beta_1=27°$

however, small separations on the suction surface at 43%, 55% and 74% chord due to shock impingement. Again, the fishtail shocks are clearly visible downstream of the blades, but the wake is only faintly visible.

Figure 8 shows a contour plot of the calculated static pressure at −10 deg incidence. Comparison of this plot of the calculated flowfield with the shadowgraph in Fig. 7 shows lesser agreement than for the design case. The source of the poorer performance of the calculation is the strong shock/boundary-layer interaction. The CFD calculation shows a separation bubble at the shock impingement point, but the measured upstream influence of the separation zone, as revealed by the blade surface pressure, and the downstream reattachment point of the boundary layer, as revealed in the shadowgraph, are not correctly predicted. Further, the imprecise modeling of the separation zone on the pressure side of the blade has a marked influence on the downstream conditions. As can be seen in Fig. 9—a plot of the measured and calculated downstream Mach number profiles at −10 deg incidence, the Pitot/static measurements show the wake to be thicker on the pressure side than on the suction side. This behavior is not predicted by the code, which shows the wake to be roughly symmetric. Thus, the code not only fails to describe the extent of the separation region, it also fails to describe the separation region's influence on the rest of the flowfield. The narrow wake region in the calculated profile suggests that the code does not correctly predict the magnitude of losses generated by the boundary-layer separation.

Integrated Loss Coefficients. The measurements presented above show a great deal about the detailed structure of the cascade

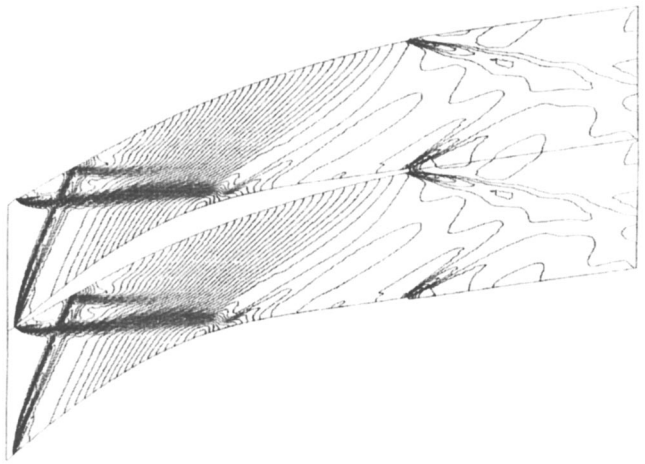

Fig. 8 Contour plot of static pressure at −10° incidence, calculated

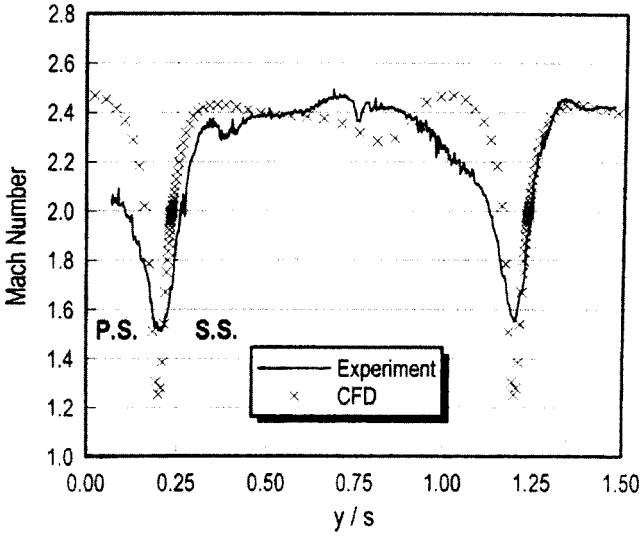

Fig. 9 Mach Number Profiles, $I=0°$, $x/c=0.37$, measured and calculated

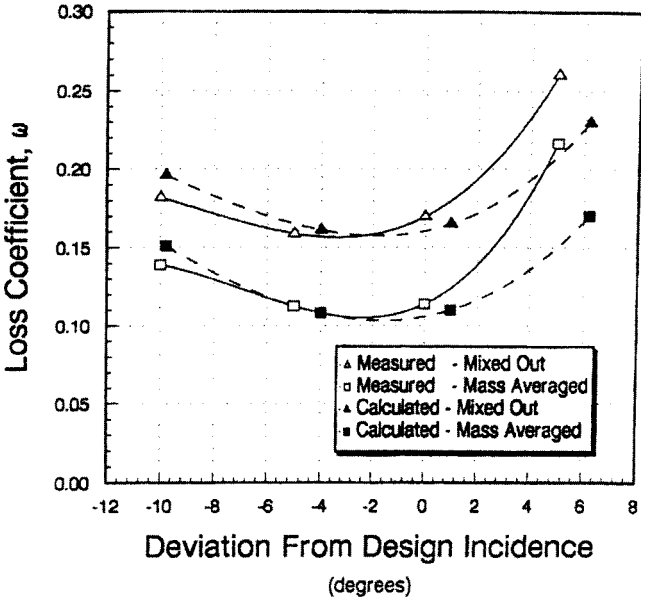

Fig. 10 Integrated loss coefficients, measured and calculated

flowfield, but, in the form presented, say little about the performance of the cascade. In order to obtain a global assessment of the cascade performance, the detailed measurements of the downstream flowfield described above must be integrated. This is done in two ways. In the first of these, the average downstream total pressure, $\overline{p_{t2}}$, is found by integrating the mass flux weighted value of p_{t2} along a line parallel to the cascade across one blade passage. That is

$$\overline{p_{t2}}=\frac{\int_o^s (\rho u)_2 p_{t2} dy}{\int_o^s (\rho u)_2 dy} \tag{1}$$

and then the mass-averaged loss coefficient, ϖ_2, is calculated from

$$\varpi_2=\frac{1-\overline{p_{t2}}/p_{t1}}{1-p_1/p_{t1}}. \tag{2}$$

The second way of calculating an average downstream value is to postulate a station far downstream of the cascade, Station 3, at which all quantities are mixed out and uniform across the blade passage. The mixed-out loss coefficient will always be larger than the mass-averaged loss coefficient since the mixing out process generates entropy.

The loss coefficients calculated from the Pitot/static probe data and the CFD calculations are plotted in Fig. 10. In analyzing these results, it must be understood that the high Mach numbers in the cascade make an accurate total pressure measurement difficult. Keeping this in mind, some trends in the loss plots can be seen.

There is generally good agreement between the calculated and measured loss coefficients, with the exception of $+5$ deg incidence—where the calculated losses seem to be low. This discrepancy is presumably from the difficulty in modeling the strong shock/boundary-layer interaction at this incidence. The comparison of the measured and calculated integrated loss profiles is perhaps more favorable than the comparison of the measured and calculated downstream profiles, since the integration process tends to hide the discrepancies which exist between the two profiles.

The loss bucket for the STF cascade is shown in Fig. 10. The measurements suggest that the minimum loss angle is somewhere between design incidence and $i=-5$ deg, and the minimum loss coefficient is 0.11 mass averaged or 0.16 mixed-out. In general, the mixed-out loss coefficients are 30% higher than the mass-averaged loss coefficients. The losses rise sharply at positive incidence, but only slightly at negative incidence.

The analysis of the downstream profiles can also be used not only to determine the average losses for the blades, but to determine the source of the losses as well. Schreiber [15] reasoned that for supersonic blading, viscous losses are generated only in the boundary layers, and appear downstream only in the wake region. Shocks, however, extend all the way across the blade passage, and so the shock losses account for all the losses in the core flow, and some of the losses in the wake. By assuming that at the edge of the wake all losses are due to shocks, and that the shock losses vary linearly across the wake, the viscous and shock losses can be approximated. This is illustrated in Fig. 11. In Table 2, the losses are split in this fashion. The losses listed in Table 2, however, are

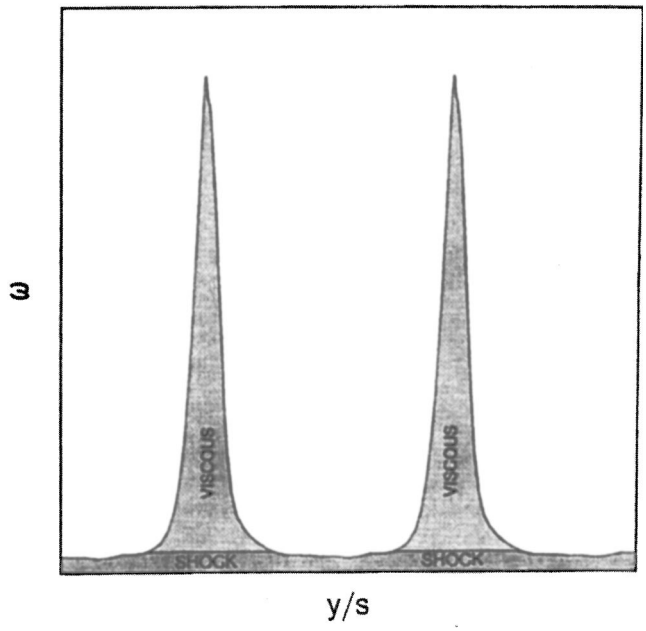

Fig. 11 Approximation of viscous and shock losses

Table 2 Measured passage and wake losses

	Measured				Calculated			
i	ϖ_2	ϖ_3	ϖ_w	ϖ_{pg}	ϖ_2	ϖ_3	ϖ_w	ϖ_{pg}
−10deg	0.139	0.182	0.077	0.062	0.151	0.196	0.058	0.093
−5deg	0.112	0.159	0.072	0.040	0.108	0.161	0.070	0.038
0deg	0.114	0.170	0.076	0.038	0.110	0.165	0.072	0.038
5deg	0.216	0.260	0.064	0.152	0.170	0.230	0.076	0.094

referred to as passage losses, ϖ_{pg}, and wake losses, ϖ_w, rather than shock and viscous losses, since this method for determining the source of the cascade losses was developed for use in subsonic-axial, supersonic-relative blading, and not for supersonic through-flow blading. (Note that the flow reacts in a uniform way to obstructions it encounters. The notion of shock and viscous losses was beneficial only to allow easier estimation of the blade losses with lower-order models.) The analysis in the next section will show that adjustments to this method are required in order to properly differentiate the shock and viscous losses in a supersonic through-flow cascade. If one were to use this method without modifications, one would come to mistaken conclusions about the sources of the losses in supersonic through-flow blading.

Shock Loss Model

The losses arising from shocks at the leading edge of the compressor blades were modeled with an empirical shock loss model to examine the effects of the shock losses in isolation from viscous effects. The basis for the modeling of the leading edge shocks is the detached shock wave model of Moeckel [16]. This model is designed to predict the location and form of shocks standing off of an isolated body in a supersonic flow. The STF blades are, of course, not isolated bodies, but the model is easily extended to model the leading edge shocks from these blades.

Moeckel [16] used as the starting point for his model the assumption that the shape of any shock wave standing off a planar body would be a hyperbola. He further made the assumption that the upper and lower asymptotes of the hyperbola would be left and right running Mach waves. In this way, the shock strength would go to zero far from the body. The sonic point on the shock, that is the point on the shock behind which the flow is at Mach 1, is known if the incoming Mach number and the form of the shock wave is known. Moeckel [16] assumed that the sonic line, that is the locus of points in the flow at which the flow is sonic, is a straight line as shown in Fig. 12. Moeckel [16] then used these assumptions on the shock wave and sonic line shapes to solve for the location of the shock sonic point, S, and thus the form and location of the detached shock wave, by solving the conservation of mass in the region bounded by the detached shock, the sonic line, the body, and the stagnation streamline. With this analysis, he was able to calculate the location of point S as a function of the incoming Mach number, M, and the height of the body at the sonic point, y_{sb}.

To model the leading edge shocks of the STF cascade, Moeckel's, [16], model was applied with the following modifications. The stagnation streamline was assumed to intersect the blade at the furthest point forward on the leading edge. If a blade surface was at a positive incidence, δ, to the flow, the solution found using Moeckel's, [16], method was patched to an oblique shock with turning δ at the point on Moeckel's, [16], shock profile where the flow would be turned by δ. The shock wave off the suction surface and the shock wave off the pressure surface were then computed independently. With the shape of the waves known, the total pressure loss across each shock could be found. To obtain the total pressure ratio across both shocks, the total pressure ratios across each shock were multiplied. The interaction between the two shocks and the reflections of the shocks were considered of secondary importance, and so ignored.

The pitchwise distribution of shock losses calculated with this model at design incidence are plotted in Fig. 13. As a reference, the distribution of loss from all sources, as calculated using ANSERS just past the trailing edge, are also plotted in Fig. 13. (Note that the local minimum in the calculated profile in the wake is due to the low mass flux just behind the blade.) The interesting thing to note from these profiles is that the shock loss model has generated loss profiles with wakes. The peaks in the total loss profiles calculated from the shock model are, of course, not wakes

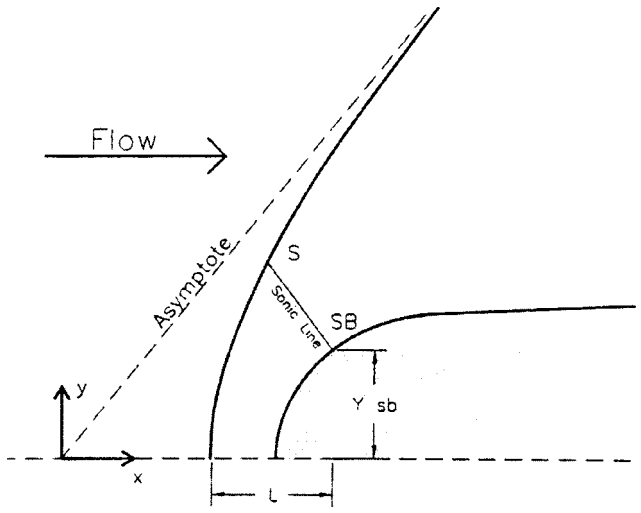

Fig. 12 Graphical representation of Moeckel's shock model

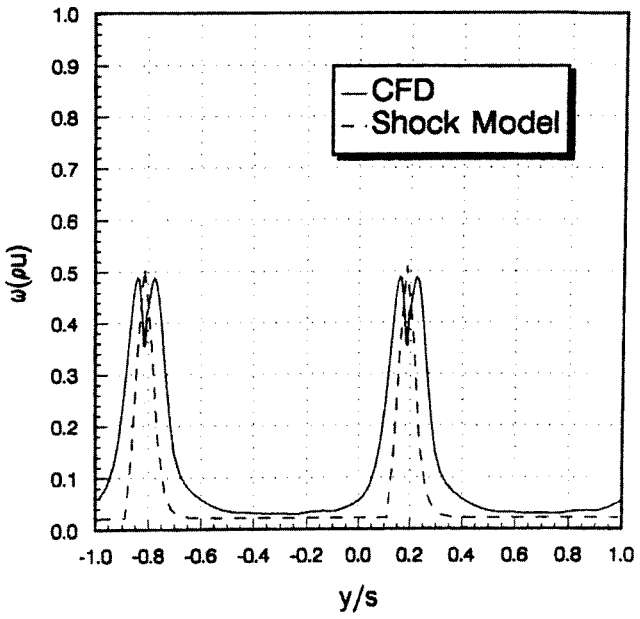

Fig. 13 Mass flux weighted loss profiles at design incidence

Table 3 Losses from leading edge bluntness and calculated total losses

i	ϖ_b	ϖ_2
−10deg	0.032	0.151
−5deg	0.036	0.108
0deg	0.036	0.110
+5deg	0.035	0.170

in the conventional sense, since the model is an inviscid one. What these results show is that the leading edge shocks generate an ''inviscid wake'' due to the fact that the shock waves are strongly curved near the leading edge. The shocks are strongest just in front of the leading edge, where they are normal to the flow. Due to the high freestream Mach number, these losses diffuse very little from the near blade region as the flow moves downstream. The maximum shock losses then appear in the same region downstream of the blades as the viscous losses and are impossible to distinguish.

The losses from the leading edge shocks can be determined from the inviscid profiles in Fig. 13 by first integrating the quantity $p_{t2}(\rho u)_2$ across the blade passage to obtain the mass-averaged total pressure, and then using Eq. (2) to find the mass-averaged loss coefficient. The loss coefficient for sharp blades (with no standoff shocks) can be similarly determined, using the value of p_{t2}/p_{t1} at the center of the passage to calculate the mass-averaged loss coefficient. The loss contribution from the leading edge bluntness, ϖ_b, is then determined by subtracting losses for sharp blades from the losses generated by the blunt blades. The losses calculated using this method are listed in Table 3, with the total calculated losses also listed for comparison. The losses from the leading edge bluntness vary little with incidence angle and range from 0.032 to 0.036. As can be seen in Table 3, this is a significant fraction of the total losses. The bluntness losses range from 21% to 33% of the total losses; this from a leading edge radius of only 0.18 mm. Perhaps just as important as the magnitude of the leading edge bluntness loss is the fact that the loss shows up in the wake region—a region normally associated with viscous losses. About 50% of the losses in the wake, losses that appeared to be viscous losses, are actually shock losses. The source of these losses was not apparent in either the experimental or CFD data.

It is evident that the loss accounting methods used for lower speed supersonic cascades—described in the last section—are not valid in the supersonic through-flow fan cascade. Using those methods, it is calculated that the shock losses are 40% to 50% of the total losses. If the accounting is adjusted to reflect the substantial inviscid loss in the wake region, the loss distribution changes considerably.

As shown in Table 4 and Fig. 14, it is now apparent that shock losses are the major source of losses in the STF cascade. Shock losses account for 70% to 80% of the total losses in the cascade. The modeling of the leading edge shocks has shown that the leading edge radius has a major effect on the losses in the STF, and that ignoring the leading edge bluntness will cause any understanding of the loss generation mechanisms to be grossly in error.

When compared to conventional supersonic blading, the magnitude of the shock losses in the STF is, at first, surprising. In

Table 4 Loss sources in the STF cascade

	Measured			Calculated		
i	ϖ_2	ϖ_v	ϖ_s	ϖ_2	ϖ_v	ϖ_s
−10deg	0.139	0.045	0.094	0.151	0.026	0.125
−5deg	0.112	0.036	0.076	0.108	0.034	0.074
0deg	0.114	0.040	0.074	0.110	0.036	0.074
5deg	0.216	0.029	0.187	0.170	0.041	0.129

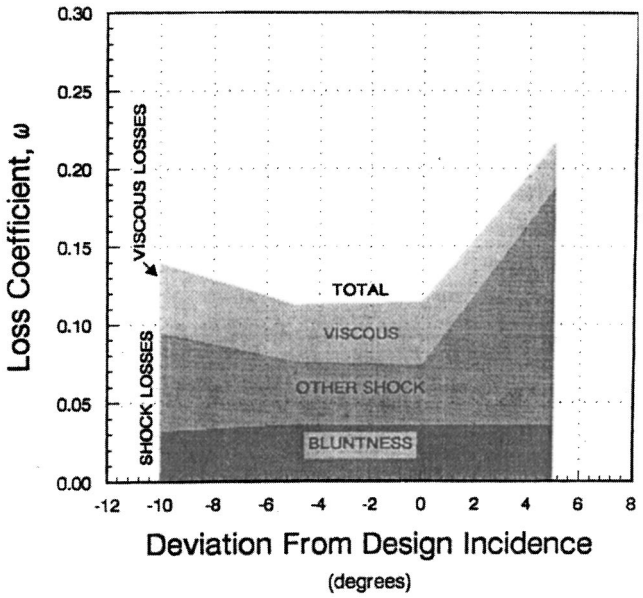

Fig. 14 Loss generation in the STF cascade, from Pitot/static data

subsonic axial supersonic cascades, a *normal* shock exists in the blade passage, and the shock losses range between 20% and 40% of the total. In the STF cascade, all shocks are *oblique*, and yet the shock losses are about 70% to 80% of the total. This seemingly contradictory result is the consequence of three effects. The first two relate to the behavior of shocks in the STF and the last one relates to the behavior of the boundary layer. First, at the high Mach numbers in the STF blade passages, significant losses can be generated even by oblique shocks. Thus, the expectation that the normal shock in conventional supersonic blading will generate higher losses than the oblique shock in these blades is not valid. Second, at the Mach numbers in the STF, small departures from a sharp leading edge can cause large shock losses. The losses due to the leading edge bluntness in subsonic axial blading are small by comparison. Finally, with the generally favorable pressure gradient in the blade passage, viscous losses are kept under control. When weak shocks intersect the boundary layer, the boundary layer does not separate. When stronger shocks do cause separation, the boundary layer quickly reattaches. In subsonic axial blading, the pressure gradient is adverse, and the boundary layer fully separates in the vicinity of the passage shock. Thus, the comparison of STF blading to low Mach number supersonic blading can be misleading.

Discussion

Comparisons of the measured cascade data to numerical predictions made with a two-dimensional, finite-volume CFD code show that the flow is predicted well at the design condition, but that off-design predictions are less satisfying. The downfall of the numerical predictions of the STF cascade flow is the inability to adequately model the flow in regions of strong shock/boundary-layer interaction. At the design condition, shocks within the blade passage are relatively weak, and large regions of separated flow do not occur. When the blades are at large angles of attack, the shocks generated at the leading edge of the blades are much stronger, and separation bubbles occur where these shocks impinge upon the boundary layer. The code does predict the presence of separated regions, but comparison of the computed flow to the cascade data shows that neither the extent of the upstream influence nor the location of the downstream reattachment point of the separated regions are correctly calculated. The errors in the modeling of the strong shock/boundary-layer interaction cause discrepancies with the cascade data not just in the immediate vicinity of the separation bubble, but also far downstream in the wake.

The heart of the problem in calculating the strong shock/boundary-layer interactions at off design lies in the modeling of the turbulence in separated flows. The modeling of the turbulence in high speed separated flows is difficult, and is the subject of much ongoing research.

This discussion of the shortfalls of modeling the flow in a STF with computational fluid dynamics should not be interpreted as indicating that the codes are not useful tools. On the contrary, this code actually does a very good job of predicting the flow at design and -5 deg incidence, and the -10 deg and $+5$ deg calculations are not badly inaccurate. The losses predicted by the code generally agree well with the measured losses. The above discussion is merely intended to point out the limitations of these numerical tools when used to predict the flow through supersonic through-flow blading so that the analyst can better interpret the results. In this context, it is just as important to understand what the numerical model cannot do as to understand what it can.

Conclusions

The supersonic through-flow fan is a new and unproven technology. In an attempt to gain an understanding of the operation of this new type of compressor, a study has been conducted to thoroughly document the mean flow in a cascade of baseline STF blades. Through a combination of flow visualization techniques, pressure probe measurements, and two-dimensional LDV measurements, a detailed picture of the flow physics and the loss mechanisms in a STF has emerged.

Comparisons of the measured cascade data to numerical predictions made with a two-dimensional, finite volume CFD code show that the flow is predicted well at the design condition, but that at off design, some discrepancies exist between the measured and calculated flow. The numerical solutions of the STF cascade flow deviate from the measured flow due to the inability to adequately model the flow in regions of strong shock/boundary-layer interaction. The discrepancies, however, are not large enough to greatly affect the integrated loss coefficients for the cascade.

A simple model was developed to predict the losses from the lead edge shocks based on the detached shock model of Moeckel [16]. When the results of this model were combined with the experimental and computational data, it became clear that shock losses were the major source of losses in the STF cascade. The model shows that a small but finite leading edge radius can generate substantial losses in supersonic through-flow blading. In this cascade, the blades have a leading edge radius of only 0.18 mm and this leading edge bluntness accounts for up to 34% of the total losses. Because these losses are generated very close to the blade surface, they appear downstream in the wake region. In both the experimental and CFD data, the source of these losses is not apparent. Downstream of the blades, the leading edge bluntness losses are hidden by the viscous losses.

Using the loss accounting techniques developed for lower speed supersonic blading, nearly all the losses in the wake region are attributed to viscous effects. Using those methods, one would come to the conclusion that shocks account for 35% to 55% of the total losses, depending on the incidence angle. The model developed here for the leading edge shock losses demonstrates that about 50% of the wake losses are actually due to inviscid effects. Using this information, it then becomes apparent that the shocks account for 70% to 80% of the total losses. The loss accounting techniques for subsonic axial, supersonic blading are clearly not applicable to supersonic through-flow blading.

The magnitude of the shock losses found in this cascade has important implications for the designers of future supersonic through-flow blading. It is clear that control of the shocks in a STF has to be a top priority. The shape of the leading edge is particularly important in this respect. A sharp, thin leading edge will be needed to keep the shock losses to a minimum.

It should be remembered that, although the losses in this cascade are relatively high, these blade sections are from a *proof-of-concept* supersonic through-flow fan. These blades were not designed with high performance as a goal, but rather were designed somewhat conservatively. The primary objectives were to design a moderate performance fan that would demonstrate the possibilities of supersonic through-flow blading, and would lead to a better understanding of the flow physics of supersonic through-flow fans. The cascade studies of these blades have shown that through better control of the shock losses, substantial improvements in the fan performance should be possible. These cascade studies have also shown that computational fluid dynamic codes are capable of accurately modeling the flow through well behaved blades. Thus, the direction is clear and the tools are available to proceed with higher performance supersonic through-flow fan designs.

Acknowledgments

This work was supported by the Turbomachinery Technology Branch at the NASA Lewis Research Center, Dr. L. J. Bober, Branch Chief. The authors are indebted to Dr. D. L. Tweedt, the technical monitor for the grant, for his many helpful discussions. The authors would also like to thank Mr. C. L. Ball and Mr. R. Moore for their continued support of this program. The authors also wish to acknowledge the contributions of Mr. R. D W. Bowersox, who assisted with the shadowgraphs, and Mr. P. L. Andrew, who assisted with the LDV measurements and provided the surface oil flow visualizations.

Nomenclature

c = chord
i = incidence angle relative to design
M = Mach number
p = pressure
s = blade spacing
u = velocity component in the x-direction
V = total velocity
x = distance in the axial direction
y = distance in the direction of the cascade line
z = distance in the spanwise direction
ρ = density
σ = solidity, c/s
ω = loss coefficient
δ = shock turning angle

Subscripts

1 = upstream of the cascade
2 = downstream of the cascade
3 = far downstream of the cascade (mixed out)
b = bluntness
pg = passage
s = shock
t = total
v = viscous
w = wake

References

[1] Ferri, A., 1956, "Problems Related to Matching Turbojet Engine Requirements to Inlet Performance as Function of Flight Mach Number and Angle of Attack," *Air Intake Problems in Supersonic Propulsion*, J. Fabri, ed., AGARDograph No. 27, AGARD, France.
[2] Trucco, H., 1975, "Study of Variable Cycle Engines Equipped with Supersonic Fans, Final Report," NASA CR-134777.
[3] Tavares, T. S., 1985, "A Supersonic Fan Equipped Variable Cycle Engine for a Mach 2.7 Supersonic Transport," NASA CR-177141.
[4] Champagne, G. A., 1988, "Payoffs for Supersonic Through Flow Fan Engines in High Mach Transports and Fighters," AIAA Paper 88-2945.
[5] Franciscus, L. C., and Maldonado, J. J., 1989, "Supersonic Through-Flow Fan Engine and Aircraft Mission Performance," AIAA Paper 89-2139.
[6] Savage, M., Boxer, E., and Erwin, J. R., 1961, "Resume of Compressor Research at the NACA Langley Laboratory," J. Eng. Power **83**, pp. 269–285.
[7] Breugelmans, F. A. E., 1975, "The Supersonic Axial Inlet Component in a Compressor," ASME Paper 75-GT-26.
[8] Schmidt, J. F., Moore, R. D., Wood, J. R., and Steinke, R. J., 1987, "Supersonic Through-Flow Fan Design," AIAA Paper 87-1746.

[9] Chesnakas, C. J., 1991, ''Experimental Studies in a Supersonic Through-Flow Fan Blade Cascade,'' Ph.D. dissertation, Virginia Tech, Blacksburg VA.
[10] Chesnakas, C. J., Andrew, P. L., and Ng, W. F., 1991, ''An LDV Evaluation of Particle Lag Prediction Techniques in Supersonic Flows,'' 1991 Yokohama International Gas Turbine Congress, Yokohama, Japan.
[11] Andrew, P. L., and Ng, W. F., 1994, ''Turbulence Characteristics in a Supersonic Cascade Wake Flow,'' ASME J. Turbomach., **116**, pp. 586–596.
[12] Taylor, A. C, III, 1989, ''Convergence Acceleration of Upwind Relaxation Methods for the Navier-Stokes Equations,'' Ph.D. dissertation, Virginia Tech, Blacksburg, VA.
[13] Thomas, J. L., and Walters, R. W., 1987, ''Upwind Relaxation Algorithms for the Navier-Stokes Equations,'' AIAA J., **25**(4), pp. 527–534.
[14] Andrew, P. L., 1992, ''Experimental and Numerical Investigations of the Off-Design Flow Physics in a Supersonic Through-Flow Fan Cascade,'' Ph.D. dissertation, Virginia Tech, Blacksburg, VA.
[15] Schreiber, H. A., 1986, ''Experimental Investigations on Shock Losses of Transonic and Supersonic Compressor Cascade,'' *Transonic and Supersonic Phenomena in Turbomachines*, AGARD CP-401.
[16] Moeckel, W. E., 1949, ''Approximate Method for Predicting the Form and Location of Detached Shock Waves Ahead of Plane or Axially Symmetric Bodies,'' NACA TN 1920.

Unsteady Gust Response of Road Vehicles

Antonio Filippone
Department of Mechanical, Aerospace and Manufacturing Engineering,
UMIST,
Manchester M60 1QD, UK

A theoretical model based on an indicial method is proposed to simulate the unsteady response of a series of road vehicles, including high-speed trains, sports utility vehicles, sports cars, caravans, and pick-up trucks. The response is described in the frequency domain by the aerodynamic admittance for both side force and yawing moment. The properties of the admittance function are discussed for basic two-dimensional geometries, and the existence of critical damping is shown for a number of cases. The vehicles are undergoing aerodynamic forcing in the form of a gust. Systems with one degree-of-freedom were considered. The results show that the main parameters affecting the vehicle's aerodynamic response are the mean vehicle length compared to the wave length of the gust, and the inclination of the nose. [DOI: 10.1115/1.1603304]

1 Introduction

The aerodynamics of road vehicles is generally unsteady because of the proximity of other vehicles, wind shear, and natural gusts, e.g., cross wind effects, particularly around exposed areas. Simulations of transients and gust conditions are difficult to perform, and reliable experimental data are scarce.

Unsteadiness in the form of lateral gusts is known to affect the handling of some vehicles. Cross winds on high-speed trains have become increasingly important, because the speeds have increased, just as the inertial masses have decreased. Strong gusts decrease the loading of the wheels on the windward side, which compromises the train's stability at high speeds. A train that encounters a gust at the exit of a tunnel is another critical scenario (Schetz [1]).

Performing laboratory experiments to simulate impulsive side winds requires placing the vehicle in a wind tunnel with a system capable of producing aerodynamic forcing of known characteristics in the transverse direction (frequency, wave length, shape, spectra). A discussion of methods for carrying out these experiments, and their limitations, was published by Bearman and Mullarkey [2].

Problems characterized by reduced frequencies (as defined later) $k>0.2$ must be considered highly unsteady. The study of the unsteady flow occurring at relatively large frequencies can be pursued through the use of the indicial functions. This approach was devised to describe the system's response in the time domain by using an appropriate sequence of step changes in the aerodynamic forcing, and by deriving the corresponding transfer functions. Some of these methods are now quite well established, and applications range from airfoil theory to the fixed and rotary wing (Leishman [3]). Their usefulness is particularly exciting when the indicial functions can be expressed in analytical form. In fact, using the Duhamel superposition, solutions can be obtained by straightforward methods, either directly or by numerical integration. More complex forcing functions can be studied using Fourier transforms.

The study of these flows is best performed in the frequency domain, because the power spectra density (PSD) are easily found from the admittance values.

The first mathematical formulations of indicial methods go back to the 1930s: Theodorsen [4] derived expressions for the aerodynamic forces on an oscillating airfoil or airfoil-flap combination with three independent degrees-of-freedom; Wagner [5] derived indicial functions for the time-dependent lift of an airfoil subject to impulsive change in the angle of attack. Küssner [6] modeled the response of an airfoil to a sharp-edged fixed gust. From these basic formulations, extensions were made possible by a number of authors. One case that is necessary to mention is the theory of Drischler and Diederich [7] which is the starting point of the theoretical formulation of the present study. Drischler and Diederich proved that the speed of the travelling sharp-edged gust has a strong effect on the lift and moment response. The system undergoing lateral gusts is obviously forced to accelerate in that direction, at a rate depending on the inertial masses involved (some of these cases were calculated by Drischler and Diederich for a number of wings). This lateral acceleration was not part of the present study.

The paper focusses on two aspects: (1) on the formulation of suitable transfer functions for the lift/side force and pitching/yawing moment in the frequency domain and (2) on the application of the theory to road vehicles of arbitrary configuration (in the $\{x,z\}$-plane) undergoing gusts of any frequency. No yawed conditions will be considered (for reasons explained in the theoretical derivation). Two quantities are of interest: the maximum side force and yawing moment response, and the time lag of the response with respect to the forcing function.

The model presented in this paper was published in a detailed form in an earlier study, Filippone-Siquier [8]. Here only the governing equations are given, along with the reference systems and the basic definitions of the main quantities.

2 Theoretical Model

The admittance H is the ratio between aerodynamic loads (side force and yawing moment) in unsteady state and the loads created by a forcing of the same amplitude and infinitely large wave length (e.g., quasi-steady loads). The relationship between the admittance and the power spectra density,

$$\mathrm{PSD}(k)\sim 2H^2(k), \tag{1}$$

is relatively simple, since it does not require the Fourier transform of the system's response in the time domain. A suitable form of the transfer function $H(k)$ is the subject of this theory.

The flow model is a two-dimensional incompressible potential flow subject to sufficiently small perturbations. The direction of the normal to the plane flow is affected by no separation in the case of lifting surfaces. For the vehicles that were considered for this study, there is a bluff body separation problem. There is a strong limitation only for cases of large yaw angles, as shown later.

Consider the reference system of Fig. 1 in the plane $\{x,z\}$ of the flow, and a downstream travelling gust normal to this plane characterized by a *gust speed parameter*

Contributed by the Fluids Engineering Division for publication in the JOURNAL OF FLUIDS ENGINEERING. Manuscript received by the Fluids Engineering Division November 11, 2002; revised manuscript received April 21, 2003. Associate Editor: J. Katz.

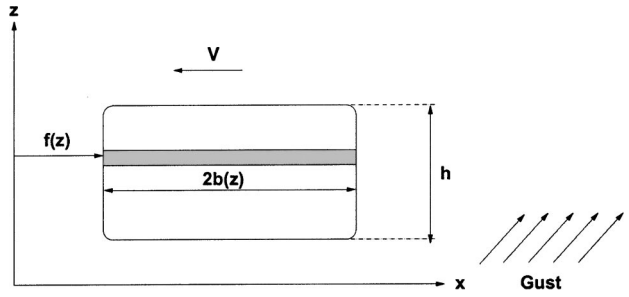

Fig. 1 Reference system

$$\lambda = \frac{V}{V+V_g} = \frac{1}{1+V_g/V}. \tag{2}$$

In Eq. (2) V is the speed of the system and V_g is the speed of the gust. The gust speed parameter is singular at $V_g/V=-1$. If the gust is convected by the free stream, then $V_g=0$, and the gust is said to be ''stationary.''

In this reference system the aerodynamic admittance of an arbitrary two-dimensional body is found from

$$H(k) = \frac{1}{h}\int_{D_z} r(z) H_\lambda[r(z)k] e^{-i\varphi(z)k} dz \tag{3}$$

where

$$H_\lambda = e^{-i\lambda k}\left\{[J_0(\lambda k) - iJ_1(\lambda k)]C(k) + \frac{1}{\lambda} iJ_1(\lambda k)\right\} \tag{4}$$

is the admittance for the infinite swept lifting surface (e.g., a body of constant length and infinite width). The factor $C(k)$ in Eq. (4) is the Theodorsen function, [4],

$$C(k) = F(k) + iG(k) \tag{5}$$

with

$$F(k) = \frac{J_1(J_1+Y_1)+Y_1(Y_1-J_0)}{(J_1+Y_0)^2+(Y_1-J_0)^2}$$

$$G(k) = \frac{Y_1Y_0+J_1J_0}{(J_1+Y_0)^2+(Y_1-J_0)^2}. \tag{6}$$

The quantities J_0, J_1, Y_0, Y_1 are Bessel functions of the first and second kind in the argument k. The expression of these functions is found in many handbooks of mathematics (for example, Press et al. [9]). The Theodorsen function can be plotted in several ways; a particularly useful one is the plot of the phase lag $G(k)$ of the airfoil lift against the reduced frequency (Leishman [10]).

Equation (4) is the basic transfer function for the infinite lifting surface. Equation (3) is an integral form of $H_\lambda(k)$ obtained from the concept of ''strip theory'' applied to a finite body; $H_\lambda(k)$ must be calculated only once, and can be used for an arbitrary body. The strip theory is based on the assumption (now widely accepted) that the downwash velocity at one spanwise location does not affect the downwash at a nearby position. Note that $H_\lambda(k)$ is a complex function, fully defined by the magnitude of the response and its time lag with respect to the forcing, just as the Theodorsen's function.

The frequency ω of the forcing function (in a oscillatory flow) is related to the reduced frequency by

$$\omega t = \left[\frac{\omega b(z)}{V}\right]s + \left[\frac{\omega f(z)}{V}\right] = \frac{b(z)}{b}ks + \frac{f(z)}{b}k \tag{7}$$

where s is the reduced time, $s=Vt/b$; $b(z)$ is the local length of the body; $f(z)$ is the local position of the leading edge line, Fig. 1. Two functions, appearing in Eq. (3) and Eq. (7), are

$$r(z) = \frac{b(z)}{b} \tag{8}$$

$$\varphi(z) = \frac{f(z)}{b}. \tag{9}$$

These definitions can be replaced in Eq. (7). For the reduced frequency one uses the average body length, $\bar{b}$, or the streamwise reference length, L_{ref}.

Equation (3) shows that *at a given frequency the admittance (e.g., the side force and side force coefficient) is inversely proportional to the profile width (or height).*

Some general properties of the admittance function are easily found. From Eq. (4) one finds that the limit

$$\lim_{k\to 0} H_\lambda(k) = 1 \tag{10}$$

for all the values of the gust speed ratio λ. This result is coherent with the definition of admittance as a limit of quasi-steady forcing response.

For $\lambda=1$, $\log|H|$ has an asymptote in $-(1/2)\log k$ for k tending to infinity. For $\lambda\neq 1$, $\log|H_k|$ is an oscillating function bounded by two asymptotes whose slope is $\pm 1/2$. For $\lambda<1$, H_λ has a maximum at the frequency $k\sim 1/\lambda$. Its magnitude and bandwidth vary approximately with $1/\lambda$. For $\lambda<1$ there is no maximum.

2.1 Reduced Frequency. Some definitions are needed to establish the relationship between the reduced frequency k and the frequency f (in Hz), and the relationship between a characteristic length and the wave length of the aerodynamic forcing.

The gust wave length λ_g is related to its frequency f and the absolute propagation speed by

$$\lambda_g = \frac{V+V_g}{f} = \lambda\frac{V}{f}. \tag{11}$$

If L_{ref} is the reference length of the vehicle, then

$$\frac{L_{\text{ref}}}{\lambda_g} = \frac{L_{\text{ref}}}{V+V_g}f = \frac{L_{\text{ref}}}{V+V_g}\frac{\omega}{2\pi} = \frac{k}{2\pi}. \tag{12}$$

Therefore the ratio between gust wave length and vehicle's reference length is inversely proportional to the reduced frequency; the reduced frequency is proportional to the number of gust wave lengths contained in the reference length:

$$\frac{\lambda_g}{L_{\text{ref}}} = \frac{2\pi}{k}, \quad k = \frac{L_{\text{ref}}}{\lambda_g} \tag{13}$$

For an airfoil, the characteristic length is the chord. In this case there are at least three ways to define the reduced frequency: one is to use the mean body length, one is to use the maximum length, and finally the body height, d. As to the reference speed, it seems appropriate to use the absolute velocity $V+V_g$, although V alone could be used. The use of $L_{\text{ref}}=b_{\max}$ does not account for the actual shape of the vehicle, and in this case one could choose the height d instead. When comparing with reference data, the reduced frequency must be defined coherently. Similar incongruence is sometimes found in the definition of the admittance function (some examples are given below).

2.2 Admittance for the Moment. The admittance for the yawing moment around the axis a of a two-dimensional body of length $L_{\text{ref}}=2b$ and infinite width is found from

$$H_\lambda^M(k) = \left(a+\frac{1}{2}\right)[J_0(\lambda k) - iJ_1(\lambda k)]C(k) - \frac{i}{2\lambda}(\lambda+2a)J_1(\lambda k) - \frac{1-\lambda}{2\lambda}J_2(\lambda k) \tag{14}$$

where J_2 is an integer Bessel function of order 2. Equation (14) can be simplified in at least two cases: If $a=-1/2$, then

$$H_\lambda^M(k)=\frac{\lambda-1}{2\lambda}[J_2(\lambda k)-iJ_1(\lambda k)]. \tag{15}$$

If $\lambda=1$, then

$$H_{\lambda=1}^M(k)=\left(a+\frac{1}{2}\right)H_{\lambda=1}(k), \tag{16}$$

e.g., the admittance for the yawing moment is proportional to the admittance for the side force, and the two functions are in phase at all frequencies. Normalization of Eq. (16) is done with $a+1/2$, so as to have a unit response in the limit of quasi-steady flow. This, again, is coherent with the assumption that a very long wave length gust does not affect the steady-state loads.

2.3 Effect of Vehicle Length. The effect of the vehicle length on the aerodynamic admittance can be found in closed form if one considers a rectangle of height d and length $L=ARd$, where AR is the aspect ratio (a factor greater than zero). From Eq. (3) $r(z)=1$, $f(z)=$constant, $\varphi(z)=$constant. Therefore

$$H(k)=\frac{1}{h}e^{-i\varphi k}\int_{D_z}H_\lambda(rk)dz=\frac{r}{h}H_\lambda(k) \tag{17}$$

that can be further simplified by taking appropriate coordinate systems. The function H_λ given by Eq. (4) is not dependent on the geometrical parameter r, therefore *for given height the admittance of a rectangle is independent of the aspect ratio* d/L.

The leading edge line is invariant to yawing or stretching, therefore it is not possible to simulate yawed conditions. The same conclusion can be reached by looking at the transfer function: This is not dependent on the length of the vehicle. Therefore, the transfer function is invariant to the yaw. This is clearly a drawback, though an obvious one: yawed flaws of bluff bodies feature large areas of flow separation and unsteadiness.

2.4 Critical Damping. The critical damping is the opposite of the resonant (or proper) frequency, at which the system's response would be infinite. In a critical damping situation the unsteady forcing creates virtually no loads. The existence of critical damping in this theory arises from the presence of the Bessel functions. The way these operate depends on the integral of Eq. (3).

The admittance for a generic rectangular shape is shown in Fig. 2 for different gust speed ratios. Critical damping occurs at a number of frequencies (generally higher than most practical applications) for positive values of the gust speed ratio, $\lambda>0$. For $\lambda=0$, the unsteady forces may be amplified at some frequencies. Figure 3 shows the magnitude and the phase lag of $H_M(k)$ for the same body. A more interesting analysis would be the phase diagram Real$[H_\lambda(k)]$, Imag$[H_\lambda(k)]$ (not shown here for brevity).

Similar critical damping can be found from other simple geometries, such as a triangular shape or a parallelogram of arbitrary inclination. A parallelogram is defined by the geometric parameter $p=b/L\tan\alpha$, where α is the angle with the vertical.

In this case $b(z)=L/2$, $r(z)=1$, $f(z)=z\tan\alpha$. Since $b(z)$ is a constant, a closed-form expression for the admittance is found:

$$H(k)=H_\lambda(k)e^{-ipk\lambda}\frac{\sin(pk\lambda)}{pk\lambda}. \tag{18}$$

Critical damping is found at $k_c=n\pi/p\lambda$, with $n=1,2,3\ldots$. The inclination α of the system is the main geometrical parameter with respect to the aerodynamic response to transverse gusts. The larger the parameter α, the lower the frequency from where the unsteady response is weak.

For a circle of radius R centered in $\{R,0\}$ the relevant quantities in Eq. (3) are

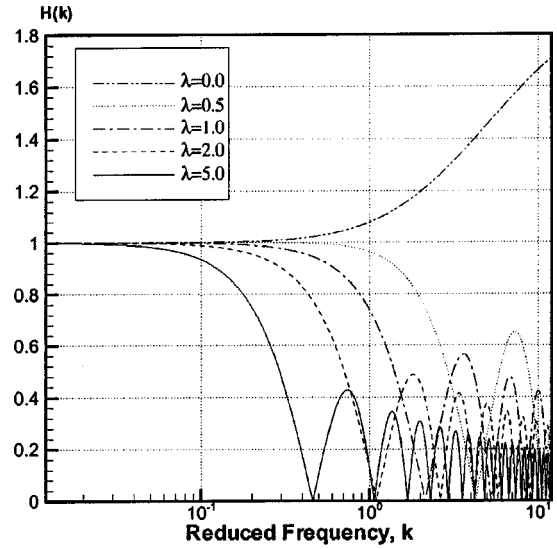

Fig. 2 Computed aerodynamic admittance (side force) for a rectangular body for different gust speed ratios (as indicated)

$$\bar{b}=\frac{\pi R}{2},\quad f(z)=R(1-\cos\beta),\quad \varphi(z)=\frac{2(1-\cos\beta)}{\pi},$$

$$r(z)=\frac{4\cos|\beta|}{\pi}$$

with $\beta=\sin^{-1}(y/R)$. These parameters introduced in the admittance equations (Eq. (3) and Eq. (4)) yield an expression that cannot be solved in closed form, because it involves trigonometric functions in implicit form.

The numerical results, Fig. 4, show that the circle has a number of frequencies with critical damping, the smallest one being $k_c\sim5.13$ at $\lambda=1$. Different critical damping frequencies are found for different gust speed ratios: with $\lambda=0.5$ the smallest critical frequency is $k_c\sim10.38$; no critical frequencies are found with a stationary gust.

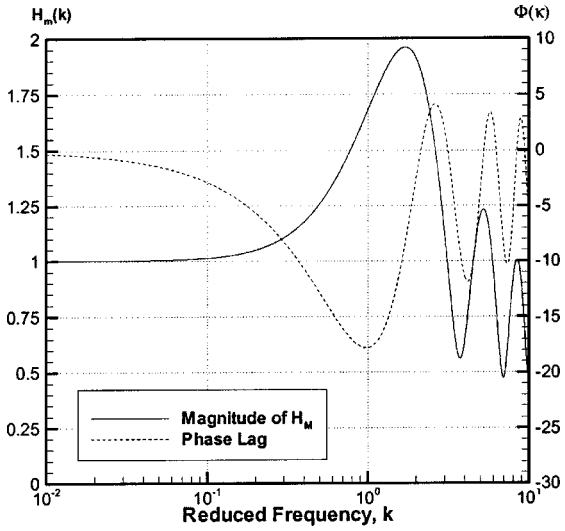

Fig. 3 Magnitude and phase lag of the yawing moment admittance for a rectangular body, $\lambda=1$, $\alpha=1/4$

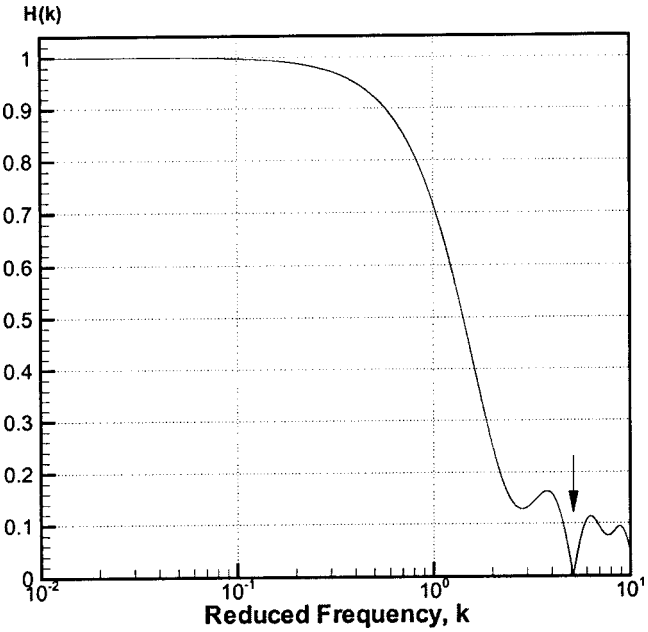

Fig. 4 Admittance for a circle, λ=1, critical frequency $k=5.13$

3 Simulation Method

The basic step for the simulation of generic shape from the governing equations of the present theory to the actual integration, requires the knowledge of the body length $b(z)$ at a given height and the function φ, as defined by Eq. (9).

The area A of the arbitrary body is found by a Montecarlo method, which is also straightforward with complex geometries. The body's mean length is $b=A/h$. The body is divided numerically into a number n of horizontal strips. The strip length is $b_i=A_i/dz_i$. The function $f(z)$ is found from the position of the leading edge. An example of integration for the SUV is shown in Fig. 5. Figure 6 shows the admittance for the side force at five gust speed ratios. The result is that the aerodynamic forcing drops at frequencies decreasing with the increasing gust speed ratio.

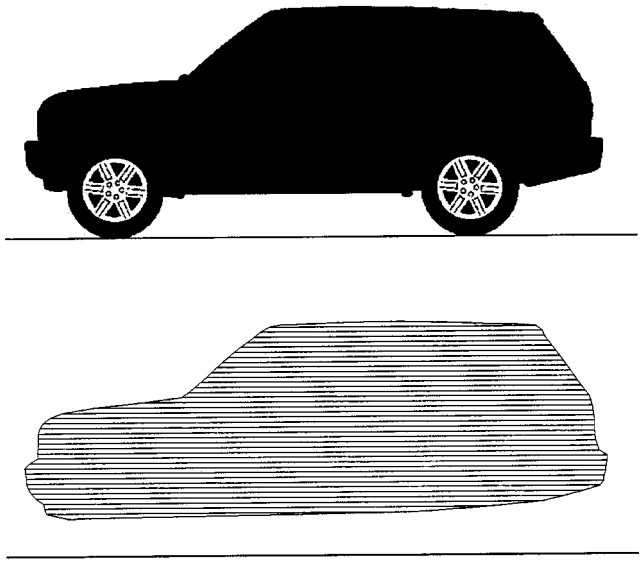

Fig. 5 Side view of SUV and computational model without wheels

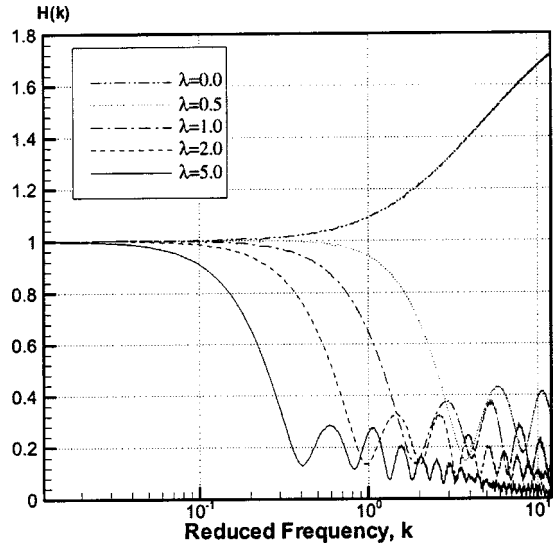

Fig. 6 Computed aerodynamic admittance for the model of Fig. 5 for different gust speed ratios (as indicated)

3.1 Calculation of Side Force and Yawing Moment. In Ref. [8] Filippone and Siquier proved that the mean square side force $\overline{C_S^2}$ is related to the mean square gust angle $\sqrt{\alpha^2}=\overline{(w/V)^2}$ at a reference frequency k_o by

$$\overline{C_S^2}=\left[4\pi^2 p_g\int_0^\infty \frac{|H(k)|^2 f(k,k_0)}{\phi(0)}dk\right]\overline{\left(\frac{w}{V}\right)^2} \tag{19}$$

where $|H(k)|$ is the magnitude of the complex number $H(k)$; $p_g=L_{\text{ref}}/2b$ is the gust parameter; $f(k,k_o)$ is the function defined by

$$f(k,k_0)=\{\text{sinc}^2[p_g(k_0-k)]+\text{sinc}^2[p_g(k_0+k)] -\cos(2p_g k_0)\text{sinc}[p_g(k_0+k)]\text{sinc}[p_g(k_0-k)]\}. \tag{20}$$

In the latter equation $\text{sinc}(x)=\sin(x)/x$ denotes the sine circular function; $f(k,k_o)$ assumes maximum value at $k=k_o$, and its oscillations are damped on either side of this frequency, at a rate depending on the gust parameter p_g. Finally,

$$\phi(\tau)=\frac{1}{2T}(T-\tau)\cos(\omega_0\tau)-\frac{1}{2T}\left(\frac{\sin(\omega_0(2T-\tau))-\sin(\omega_0\tau)}{2\omega_0}\right) \tag{21}$$

is the gust auto-correlation function evaluated at $\tau=0$. In Eq. (21) T is the time needed by the gust to travel the reference length with the speed V, e.g., $T=L_{\text{ref}}/V$; ω_o is the frequency associated to k_o.

The integral term in Eq. (19) depends on the admittance over the whole spectrum of frequencies and on the reference frequency k_o. Hence $\sqrt{\overline{C_S^2}}$ varies linearly with the root mean square gust angle $\sqrt{\alpha^2}$. This linear dependence is also valid for the yawing moment coefficient, C_Y. This coefficient is called c_1 for the side force and c_2 for the yawing moment.

Integration of Eq. (19) is carried out as follows:

$$I=\int_0^\infty \frac{|H(k)|^2 f(k,k_0)}{\phi(0)}dk\sim\frac{1}{\phi(0)}\sum_{i=1}^{n}|H(k_i)|^2 f(k_i,k_o)\Delta k_i \tag{22}$$

with

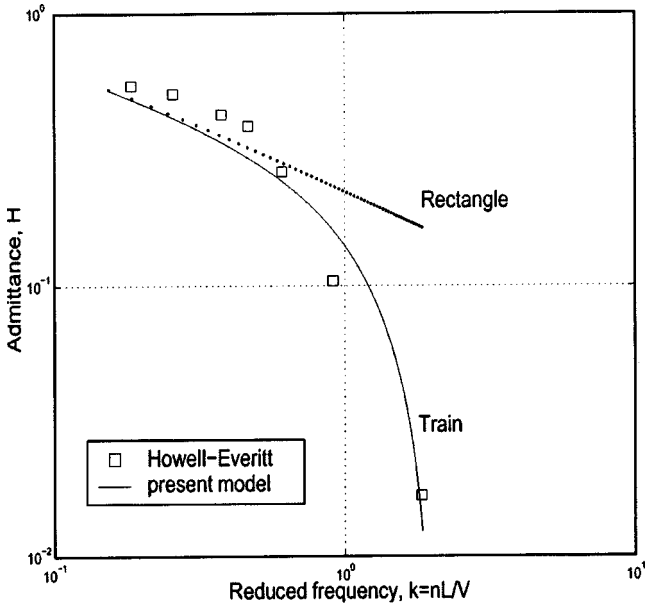

Fig. 7 Comparison with Howell and Everitt's data [11] in double logarithmic scale

$$\phi(0) \sim \frac{1}{2} - \frac{1}{2}\frac{\sin(2\omega_o T)}{2\omega_0 T} \tag{23}$$

that is a simplification of Eq. (21), and is easily calculated using the sine circular function. In practice, the integral of Eq. (22) converges rapidly.

3.2 Comparison With Howell-Everitt's Results. Howell and Everitt [11] performed experiments on a 1:25 scale train model mounted on a track in a wind tunnel. This model experienced lateral squared gusts created by centrifugal blowers mounted side by side. The model had two degrees-of-freedom (in pitch and yaw). Lift and side force admittance were measured.

Using the same two-dimensional shape from a side view, the admittance function for the side force was computed and compared to the wind tunnel data.

The admittance against the reduced frequency used by these authors $k=nd/V=n/2g$ was plotted in Fig. 7; n is the gust frequency (cycles/second), $2g$ is the gust wavelength, and d the model width. Also the admittance of a rectangular body whose length is b is drawn in Fig. 7, to show that the vehicle nose has an important role in the determination of its lateral response (a double log scale was used, as in the reference data). It was concluded that the side force has a strong attenuation for a gust wave length about twice the vehicle length (see Eq. (13)).

The correlation between wind tunnel and predicted data is satisfactory, although the reference data are not matched exactly. However, the wind tunnel experiments were conducted on models with two degrees-of-freedom, were affected by the ground proximity (that can be corrected empirically), and were run at a Reynolds number $\mathrm{Re}=1.7\cdot 10^5$ (based on the vehicle's width), which is probably around the critical range where the viscous cross-flow effects become substantial.

3.3 Comparison With Bearman-Mullarkey's Results. Three of the shapes considered by Bearman and Mullarkey are shown in Fig. 8. These are a family of simplified road vehicles characterized by a back angle "BA" variable between 0 and 40°.

These authors published side force and yawing moment admittance measurements for their BA40 vehicle at yaw angles β up to 10° and reduced frequencies $k=0.54$ and $k=0.99$ for root mean square gust angle of $\sqrt{\alpha^2}=2.5°$. The data for the side force show

Fig. 8 Vehicles BA0, BA20, BA40 considered by Bearman and Mullarkey [2]

little or no variation over the 0 to 5° yaw conditions at both frequencies, while the admittance for the yawing moment is slightly decreasing over the same range of yaw angles. The present calculations at $\beta=0$, as compared to the experimental data are as follows: $H=0.89$ at $k=0.54$ (wind tunnel: $H=0.87$); $H=0.66$ at $k=0.99$ (wind tunnel: $H=0.67$). The yawing moment was largely underestimated at both frequencies. No explanation could be found, except perhaps that the reference point for the yawing moment (1/4 of the mean length b) was not the same as in the experimental case.

The fact that values of the forces and yawing moments are constant over a narrow range of yaw angles ($-5<\beta<+5°$) suggests that the three-dimensional effects and the effects of bluff body separation can be safely neglected under these conditions.

These authors also show the aerodynamic admittance of side force and yawing moment for the geometry BA0 up to frequencies $k=1.8$ in zero mean yaw angle, $\beta=0$. The wind tunnel values are well below unity for $k<1$, suggesting that the normalization was not done as it was assumed in the present theory (by definition, for $k\rightarrow 1$ the loads tend to the quasi-steady case, and therefore the admittance must have a unit value). Unless we assume that there is an inversion of the data at values $k<0.2$, the results of the present theory must be scaled down to compare with the general trend of the admittance (such an inversion would not be predicted by the theory). The results are shown in Fig. 9, as obtained for a stationary gust, $\lambda=0$ (because the gusts are convected downstream with the free stream velocity). The dip at $k\sim 1$ could not be explained. (No log scale was used in this case, as in the reference data.)

The calculated coefficients in the mean square side force $\overline{C_S^2}$ versus mean square gust angle (Eq. (19)) and mean square yawing moment vs mean square gust angle are summarized in Table 1.

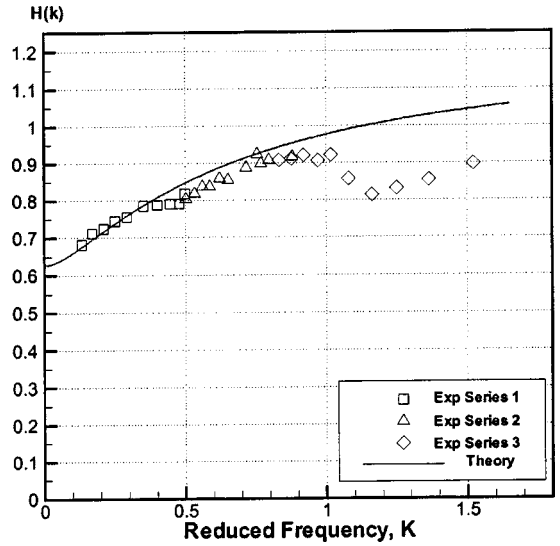

Fig. 9 Admittance for the side force of vehicle BA0, set at $\beta=0$, with a stationary gust, $\lambda=0$, compared with the experimental data of [2]

Table 1 Calculated side force and yawing moment coefficients

	BA0	BA20	BA40
c_1	0.0392	0.0321	0.0308
c_2	0.0067	0.0059	0.0053

Using the coefficients in Table 1 for the vehicle BA20, the predicted values of C_S and C_Y have been compared in Fig. 10 with the data of Bearman and Mullarkey.

4 Results for Road Vehicles

Different road vehicles were calculated. Figure 11 shows a comparison of the function $H(k)$ for four different vehicles in the range of reduced frequencies most likely to occur in practice. At a frequency $k=1$ it was found $H\sim0.698$ for the caravan, $H\sim0.643$ for the sports utility vehicle, $H\sim0.549$ for the sports car, and $H\sim0.396$ for the light pick-up truck. Therefore it appears that at this frequency (as well as lower frequencies), the caravan is the road vehicle subject to the largest unsteady forcing; the light pick-up truck is relatively unaffected by the same aerodynamic forcing, and therefore more stable.

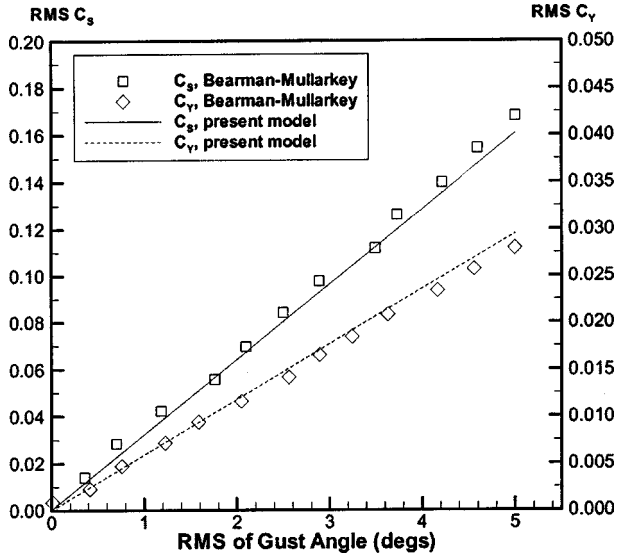

Fig. 10 RMS of side force and yawing moment for $\sqrt{\alpha^2}$ compared with the experimental data [2]

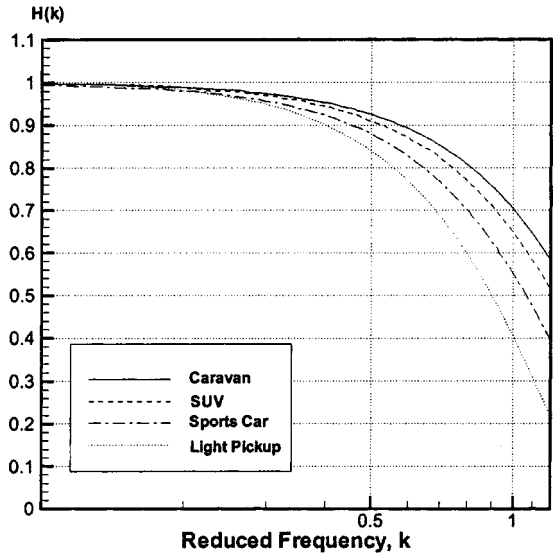

Fig. 11 Admittance for four different vehicles, for the gust speed ratio λ=1

Table 2 Calculated admittance values different road vehicles

Vehicle	$\overline{b}/L_{\text{ref}}$	$H(k=\pi)$	$k(H=0.5)$
Caravan	0.844	0.466	1.321
SUV	0.758	0.356	1.213
Sports car	0.690	0.332	1.057
Light pickup	0.619	0.145	0.900

If one defines the cutoff frequency as the reduced frequency at which the system's response decays to a fraction of the quasi steady response (for example, 0.5) then Table 2 shows that (1) cutoff frequencies increase with increasing ratio $\overline{b}/L_{\text{ref}}$ (e.g., the ratio of the mean length over the reference length) and (2) for a given gust whose wave length is twice the reference length (e.g., $k=\pi$, from Eq. (12)) the system's response increases with the increasing $\overline{b}/L_{\text{ref}}$.

No experimental data are available to validate the results shown in Fig. 11. One must rely on the comparison with Howell and Everitt's results for the high speed train, to conclude that the results are physically reasonable, and that the most important point is the cutoff length of the vehicle for a given gust wavelength.

5 Conclusions

The theoretical model for the aerodynamic admittance of side force and yawing moment has been developed from an extension of the theory of Drischler and Diederich, based on the assumption of two dimensional and small perturbation flow. The theory can be applied to the study in the frequency domain of the unsteady response of a three dimensional body at small yaw angles.

The analysis has shown that for simple two-dimensional shapes there is a large number of frequencies yielding critical damping. This is associated to the oscillatory behavior of the Bessel functions in the transfer function.

The response to sinusoidal forcing of arbitrary frequency by gusts in a wide range of speeds has been calculated for a number of road vehicles. It is shown that the forcing generally decreases with the increasing frequency, with a rate depending essentially on the mean vehicle's length. Similar results have been obtained for a high-speed train, in the simplifying assumption of one degree-of-freedom. Comparison with the experimental results available were good, even with all the approximations of the case. The model can be further extended as to include two degrees-of-freedom, arbitrary gusts, and load and stability effects on the vehicle.

However, reliable experimental data in the frequency domain would be needed for a complete validation of the model.

Nomenclature

a = position of the rotation axis
$\underline{b}$ = half-length of the body
$\overline{b}$ = mean value of $b(z)$ over D_z
c_1, c_2 = coefficients for the mean side force/mean yawing moment
$C(k)$ = Theodorsen's function, Eq. (5)
C_S = side force coefficient
C_Y = yawing moment coefficient
d = model width
D_z = profile's extent in z-direction $|D_z|=h$
f = gust frequency
$F(k)$ = indicial lift force in Theodorsen's function
$f(k,k_o)$ = function defined by Eq. (20)
$G(k)$ = indicial phase lag in lift response (Theodorsen)
i = imaginary unit

$H_\lambda(k)$ = aerodynamic admittance of airfoil with sharp-edged traveling gust
$H_\lambda^M(k)$ = yawing moment admittance of airfoil with sharp-edged traveling gust
$H(k)$ = aerodynamic admittance of a two-dimensional body
$J_n(k)$ = Bessel function of order n, first kind
k = reduced frequency, Eq. (7)
L_{ref} = reference length
n = number of strips, or gust frequency
p_g = gust parameter $p_g = L_{\text{ref}}/2\overline{b}$
$r(z)$ = defined by Eq. (8)
s = reduced time; dimensionless distance in average body lengths
t = time
T = reference time in Eq. (21)
V = vehicle's velocity
V_g = gust convecting velocity in the coordinate system of the atmosphere

Greek Symbols

α = angle with the vertical direction of the vehicle's nose; gust angle
β = yaw angle
λ = gust speed parameter, Eq. (2)
λ_g = gust wavelength
$\phi(s)$ = gust autocorrelation function
$\varphi(z)$ = defined by Eq. (9)
ω = pulsation in a harmonic movement

Subscripts/Superscripts

$(\,)_g$ = gust
$\underline{(\,)}_\lambda$ = gust speed ratio λ as a parameter
$\overline{(\,)^2}$ = mean square value over full oscillation
$(\,)_c$ = critical value

References

[1] Schetz, J. A., 2001, "Aerodynamics of High-Speed Trains," Annu. Rev. Fluid Mech., **33**, pp. 371–414.
[2] Bearman, P. W., and Mullarkey, S. P., 1994, "Aerodynamic Forces on Road Vehicles due to Steady Side Winds and Gusts," *Road Vehicle Aerodynamics*, Royal Aeronautical Society Conference, Loughborough University, UK, pp. 4.1–4.12.
[3] Leishman, J. G., 1997, "Unsteady Aerodynamics of Airfoils Encountering Traveling Gusts and Vortices," J. Aircr., **34**(6), pp. 719–729.
[4] Theodorsen, T., 1935, "General Theory of Aerodynamic Instability and the Mechanism of Flutter," NACA Report 496.
[5] Wagner, H., 1925, "Über die Entstahung des dynamischen Auftriebes von Tragflügeln," Z. Angew. Math. Mech., **5**(1), pp. 17–35.
[6] Küssner, H. G., 1936, "Zusammenfassender bericht über den instationären auftreib von flügeln," Luftfahrtforschung, **13**(12), pp. 410–424.
[7] Drischler, J. A., and Diederich, F. W., 1957, "Lift and Moment Responses to Penetration of Sharp-Edged Travelling Vertical Gusts, With Application to Penetration of Weak Blast Waves," NACA TN 3956, May.
[8] Filippone, A., and Siquier, J., 2003, "Aerodynamic Admittance of Two-Dimensional Bodies," J. Aero. Royal Soc., **107**(1073), pp. 405–418.
[9] Press, W. H. et al., 1992, *Numerical Recipes*, Cambridge Univ Press, New York, Chap. 6.
[10] Leishman, J. G., 2000, *Principles of Helicopter Aerodynamics*, Cambridge Aerospace Series, Cambridge University Press, New York.
[11] Howell, J. P., and Everitt, K. W., 1983, "Gust Response of a High Speed Train Model," *Aerodynamics of Transportation*, T. Morel and J. Miller, eds., ASME, New York, **7**, pp. 81–89.

Integral Solution for the Mean Flow Profiles of Turbulent Jets, Plumes, and Wakes

Amit Agrawal
e-mail: agrawaa@me.udel.edu

Ajay K. Prasad
e-mail: prasad@me.udel.edu

Department of Mechanical Engineering,
University of Delaware,
Newark, DE 19716

Integral methods are used to derive similarity solutions for several quantities of interest including the cross-stream velocity, Reynolds stress, the dominant turbulent kinetic energy production term, and eddy diffusivities of momentum and heat for axisymmetric and planar turbulent jets, plumes, and wakes. A universal constant is evaluated for axisymmetric and planar plumes. The cross-stream velocity profiles show that jets and axisymmetric plumes experience an outflow near the axis and an inflow far away from it. The outflow is attributed to the decay of the centerline velocity with downstream distance, and the extent and magnitude of outflow correlates with the streamwise decay of the centerline velocity. It is also shown that the entrainment velocity should not in general be equated to the product of the entrainment coefficient and the centerline velocity. It is found that, due to similar governing equations, profiles for jets and plumes are qualitatively similar. Our results show that the derived quantities are strong functions of streamwise and cross-stream positions, in contrast to previous approaches that assumed constant (in the cross-stream direction) eddy viscosity and thermal diffusivity. The turbulent Prandtl number is approximately equal to unity which matches the value quoted in the literature.
[DOI: 10.1115/1.1603303]

Introduction

Jets, plumes, and wakes are examples of free shear flows. A jet is produced when fluid exits a nozzle with some initial momentum. On the other hand, plumes are driven purely by buoyancy addition at the source. Jets and plumes spread laterally by engulfing (entraining) ambient fluid. The momentum contained within the jet remains constant at any streamwise cross section, whereas the momentum contained within the plume increases monotonically with the streamwise coordinate while maintaining a constant buoyancy. The width of jets and plumes increases at the cost of velocity. Wakes are produced behind an object placed in a freestream, and manifest themselves in the form of a velocity deficit profile.

Jets, plumes, and wakes exhibit self-similarity beyond a certain downstream distance such that a characteristic length and velocity can be used to scale all distances and velocities in the flow. Analyses and measurements have traditionally focused on the self-similar region because fewer independent variables are involved making it is easier to interpret the results. For jets, plumes and wakes, the time-averaged centerline velocity is generally chosen as the characteristic velocity, the time-averaged centerline temperature differential (with respect to the ambient) is used as the characteristic temperature scale, whereas the cross-stream distances are scaled with the local width. Although more analysis is available for planar cases, it is somewhat easier to setup experimentally an axisymmetric jet, plume, or wake, compared to their planar counterparts. Consequently, more experimental data is available for the axisymmetric case, [1–5].

In the self-similar region of the flows under consideration, the traditional approach is to first perform an order of magnitude analysis of the Navier-Stokes equations. A boundary layer approximation is usually applied, allowing a substantial reduction in the number of terms. The resulting terms are then scaled using the appropriate length, velocity, and temperature scales. Further, by invoking conservation of momentum and buoyancy for jets and plumes, respectively, one can obtain the streamwise variation of width, centerline velocity and temperature, [6]. Because the number of unknowns exceeds the number of equations by one, the analysis fails to provide the cross-stream variation of these quantities. Of key interest is the functional form of the streamwise velocity in the cross-stream direction.

One approach to close the system of equations is to assume that the eddy viscosity (ν_T) is constant in the cross-stream direction, [6–10]. The equations are then solved to obtain the required functional form. With this approach, one obtains $U/U_c = \mathrm{sech}^2(A\xi)$ for a plane jet where $A = 0.706$, and $(1+B\xi^2)^{-2}$ for a round jet where $B = 0.661$, [7]. The intent of this paper is to follow the *opposite* approach, i.e., we select a functional form for the streamwise velocity profile based on experimental data to close the system of equations, and subsequently derive expressions for several useful quantities (including ν_T, which can show a cross-stream variation depending on the choice of the functional form).

Numerous experimental and numerical studies on free-shear flows have been undertaken by various groups in the past. Most of these studies measure (or compute) the streamwise velocity profile, and fit a simple mathematical expression to the data. The literature reveals that many researchers, [1–3,11–16] prefer the Gaussian function to approximate the streamwise velocity and temperature profiles. Our own measurements of axisymmetric jets also reveal that overall the Gaussian profile is a superior fit to the data. As an example, we plot in Fig. 1 the normalized streamwise velocity data for an axisymmetric jet of water issuing from a 2-mm orifice into a large tank; data were acquired using two-dimensional PIV at $110 \leqslant z/d \leqslant 175$ (see [17] for experimental details). The computed profile for Reynolds stress is compared with experimental measurements made by the authors later in the paper to provide additional validation for the choice of the Gaussian streamwise velocity profile. For these reasons, we preferred the Gaussian profile to the other choices as the input functional form for our analysis. Some previous researchers have employed an approach similar to ours to verify certain difficult measurements—for example, Wygnanski and Fiedler [5] and Gutmark and Wygnanski [18] verified their measurements of Reynolds stress against values computed from their streamwise velocity profile using an intergal approach.

Contributed by the Fluids Engineering Division for publication in the JOURNAL OF FLUIDS ENGINEERING. Manuscript received by the Fluids Engineering Division July 22, 2002; revised manuscript received May 6, 2003. Associate Editor: J. S. Marshall.

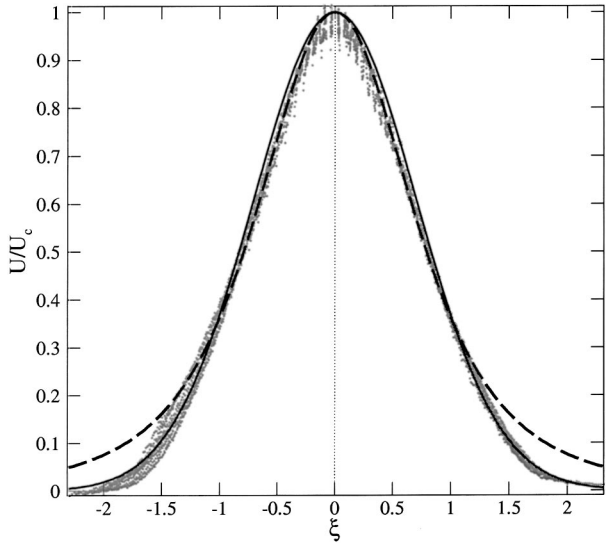

Fig. 1 Streamwise velocity profiles for jets (—— axisymmetric jet from Gaussian profile, -- axisymmetric jet from polynomial profile, [7], dots from experiment, [7]

Perhaps because the primary aim of these researchers was to verify measurements, they did not exploit integral theories to its full extent, nor did they discuss the properties of the expressions that they derived. In fact, explicit expressions for even basic quantities are not readily available in the literature. The aim of this paper is to extract a complete set of results from the integral method. We derive a host of useful expressions and explore their properties in physical terms. As we show, several interesting features of the flow can be obtained, and some probable misconceptions can be corrected in this manner. Further, upon contrasting appropriate solutions (for example jets versus plumes, axisymmetric versus planar), our approach yields some new insights.

The basic approach adopted here comprises the following three steps. First, we assume an analytical expression for the mean streamwise velocity U (and temperature). Second, the expression for U is substituted into the continuity equation along with the assumption of the centerline velocity variation, and integrated to determine the mean cross-stream velocity profile. Third, the expressions for U and V are substituted into the simplified momentum (and energy) equations, and integrated to determine the Reynolds stress (and velocity-temperature correlations). These expressions can then be employed to derive a number of useful quantities. Integral methods are shown here to be successful in reproducing experimental results for standard jets, plumes and wakes (axisymmetric and planar) which are commonly used as model flows in a variety of situations. Our results should serve as a useful reference for such studies. However, it should be remembered that integral methods may have restricted application to more complex turbulent flows, [13], where it is difficult to assign profile shapes, and relate entrainment rates to local influences in complex environments.

The relevant governing equations for jets and wakes are the continuity and the streamwise momentum equation. The two additional momentum equations, cross stream and azimuthal, relate pressure with the fluctuating components of velocity, and the fluctuating components of velocity with themselves, respectively; in this paper, we are not interested in exploring these relationships. For plumes, an additional equation for temperature is required. By symmetry considerations, both the cross-stream velocity and the Reynolds stress are zero at the centerline. We have used this condition throughout this paper to evaluate the constant of integration.

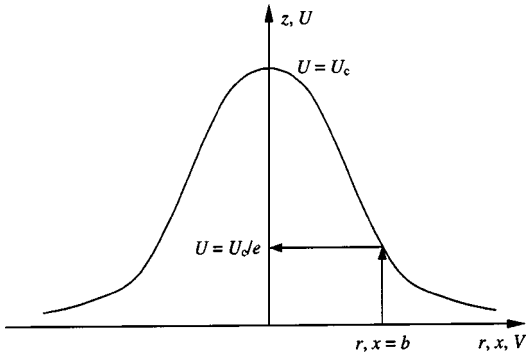

Fig. 2 Coordinate system for planar (x,z) and axisymmetric (r,z) jets, plumes, and wake. For wakes, U represents the velocity defect.

Turbulent Jets

Axisymmetric Jets. The continuity equation for the time-averaged velocities in cylindrical coordinates (see Fig. 2 for the coordinate system used in this paper) is

$$\frac{1}{r}\frac{\partial rV}{\partial r}+\frac{\partial U}{\partial z}=0. \tag{1}$$

In the self-similar region, the simplified streamwise momentum equation can be obtained using an order of magnitude analysis as, [6],

$$V\frac{\partial U}{\partial r}+U\frac{\partial U}{\partial z}+\frac{1}{r}\frac{\partial r\overline{uv}}{\partial r}=0 \tag{2}$$

where the overbar denotes time-averaged quantities.

For the self-similar axisymmetric jet, U_c varies as z^{-1}, while b increases linearly with z, [6]. By approximating the streamwise velocity at any downstream location by a Gaussian, [3,11–13,17], (see also Fig. 1)

$$\begin{aligned}U(r,z)&=U_c(z)\exp(-r^2/b^2(z))\\&=U_c(z)\exp(-r^2/c^2z^2)\\&=U_c(z)\exp(-\xi^2),\end{aligned} \tag{3}$$

one can solve for V by substituting Eqs. (3) into (1):

$$\frac{V}{U_c}=\frac{c}{2\xi}(-1+\exp(-\xi^2)+2\xi^2\exp(-\xi^2)). \tag{4}$$

$V(\xi)/U_c$ is plotted in Fig. 3 and reveals that, contrary to the connotation of an inflow implied by the term "entrainment," the cross-stream flow in the vicinity of the centerline is actually outward, i.e., $V(\xi)/U_c\geqslant 0$ for $0\leqslant\xi\leqslant 1.12$. ($V(\xi)/U_c=0$ at the centerline, reaches a maximum of 0.018 at $\xi=0.54$ and declines back to zero at $\xi=1.12$.) The reason for such an outflow is that the centerline velocity decreases as z^{-1}, and *not* because of the Gaussian streamwise velocity profile assumption. $V(\xi)/U_c<0$ (i.e., inward) for $\xi>1.12$, reaches a minimum of -0.022 at $\xi=2.08$ and asymptotes to 0 as $\xi\to\infty$. It should be pointed out that $V\to 0$ much more slowly than U, i.e., although the central region is dominated by the axial component of velocity, the cross-stream flow predominates far away from it.

According to [11], the entrainment coefficient α can be defined using the incremental volume flux as

$$\frac{d\mu}{dz}=2\pi bU_c\alpha, \tag{5}$$

where μ for axisymmetric jets is given by

$$\mu=\int_0^\infty 2\pi rU(r)dr.$$

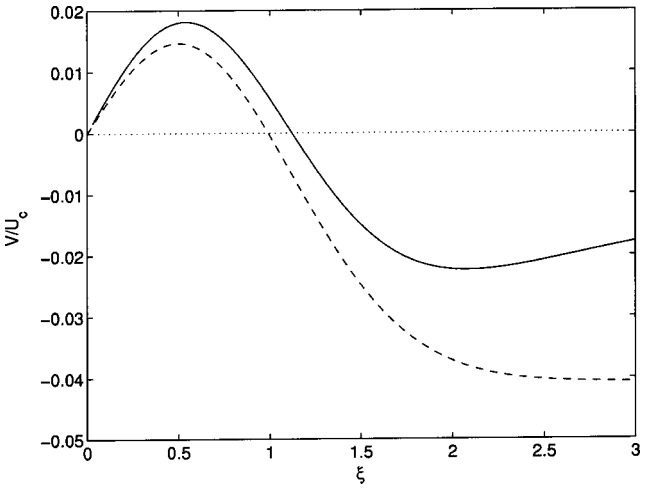

Fig. 3 Cross-stream velocity profiles for jets (—— axisymmetric jet, -- planar jet)

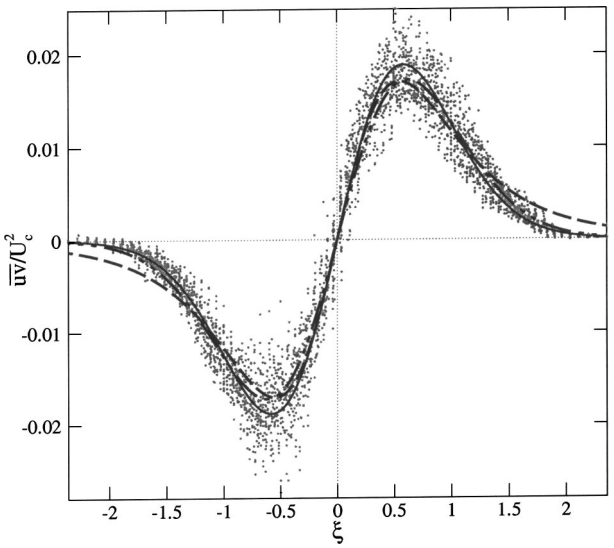

Fig. 4 Reynolds stress profiles for jets (—— axisymmetric jet from Gaussian profile, -- axisymmetric jet from polynomial profile, [7], -.. planar jet, dots from experiment)

It is readily seen that $d\mu/dz$ is the incremental volume flux entering the jet through a circular control surface at large r, i.e.,

$$\frac{d\mu}{dz} = \lim_{r\to\infty} -2\pi r V.$$

From Eq. (4), V/U_c for large ξ can be approximated as $-c/2\xi$. Our result gives

$$\frac{d\mu}{dz} = 2\pi r \frac{c}{2\xi} U_c = 2\pi b U_c \frac{c}{2}. \tag{6}$$

By equating Eqs. (5) and (6), we get $\alpha = c/2 = 0.0535$, which is the same value as obtained by [11]. From Fig. 3, it is seen that Turner's [11] statement: ''the inflow velocity at the 'edge' of the flow is some fraction α of the maximum mean upward velocity,'' is not strictly correct, because V/U_c never reaches 0.0535 for any value of ξ. However, it is easily shown, [19], that the *inward extension* of the curve $c/2\xi$ (the asymptotic curve for V/U_c at large ξ) intersects the jet edge ($\xi=1$) with a value of $c/2$.

Equation (4) can also be derived using a control volume approach—by equating the difference of volume flux at two successive downstream stations to the incoming fluid volume. As seen in Fig. 3 the maximum value of V is just 2% of U_c, making it rather difficult to measure precisely, and therefore it is less frequently presented in the literature, [4,5].

The V profile can be used to directly determine the spread rate, c. Researchers in the past have determined c by curve fitting experimental data for U. However, determining c from the experimental profile for V may be advantageous since the location and height of the extrema can be unambiguously determined. However, as stated above, the experimental uncertainty in V can be substantial. (A comparison of the derived cross-stream velocity profile with the experimental data is provided in [20].)

One can insert the time-averaged profiles for U and V into Eq. (2), to obtain the time-averaged profile for Reynolds stress $\overline{uv}$ as

$$\frac{\overline{uv}}{U_c^2} = \frac{c}{2\xi}(\exp(-\xi^2) - \exp(-2\xi^2)). \tag{7}$$

The maximum for Reynolds stress lies at $\xi=0.58$ (Fig. 4). Wygnanski and Fiedler [5] provide a plot for Reynolds stress by integrating their streamwise velocity profile. However, they do not provide an explicit expression for it.

Figure 4 also shows our experimentally measured Reynolds stress for a (water) jet at Re=3000 using PIV. The experimental data can be compared with the analytical result based on the Gaussian profile and the one derived using the $(1+B\xi^2)^{-2}$ profile, [7], where $B=0.661$. We see that the latter result does not match as well, justifying the selection of the Gaussian profile for our analysis. Additionally, our analytical result matches very well with the Reynolds stress data of [5,18].

Planar Jets. It is worthwhile to compare the results for an axisymmetric jet against a planar jet. For planar jets the continuity and momentum equations are, respectively, [6]:

$$\frac{\partial V}{\partial x} + \frac{\partial U}{\partial z} = 0, \tag{8}$$

$$V\frac{\partial U}{\partial x} + U\frac{\partial U}{\partial z} + \frac{\partial \overline{uv}}{\partial x} = 0. \tag{9}$$

Like axisymmetric jets, plane jets have a linear spread rate and are well approximated by a Gaussian velocity profile, [13,15], (given again by Eq. (3) where ξ is now $x/b(z)$), but now the centerline velocity decays as $z^{-1/2}$, [6]. Integrating Eq. (8) using (3) we obtain

$$\frac{V}{U_c} = \frac{c}{4}(4\xi\exp(-\xi^2) - \sqrt{\pi}\,\mathrm{erf}(\xi)). \tag{10}$$

This expression has also been obtained by [15]. Similar to the axisymmetric case, we find an outflow near the jet axis, and an inflow far away from it. The maximum outflow occurs around $\xi=0.5$ (which is very close to the axisymmetric case) and the flow turns inward for $\xi \geqslant 0.99$- this value is slightly smaller than for axisymmetric jets (Fig. 3).

Similar to the axisymmetric case we can define the coefficient of entrainment following Turner [11]:

$$\frac{d\mu}{dz} = 2\alpha U_c, \tag{11}$$

where μ is now given by

$$\mu = \int_{-\infty}^{\infty} U dx.$$

Inserting Eq. (3) and differentiating with respect to z, we obtain

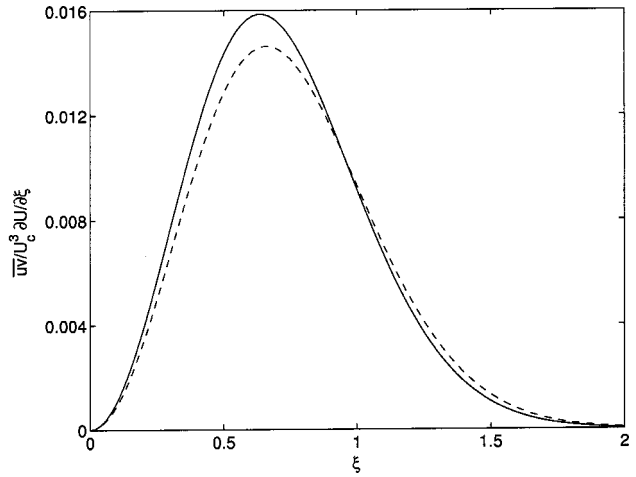

Fig. 5 Dominant kinetic energy production term profiles for jets (—— axisymmetric jet, -- planar jet)

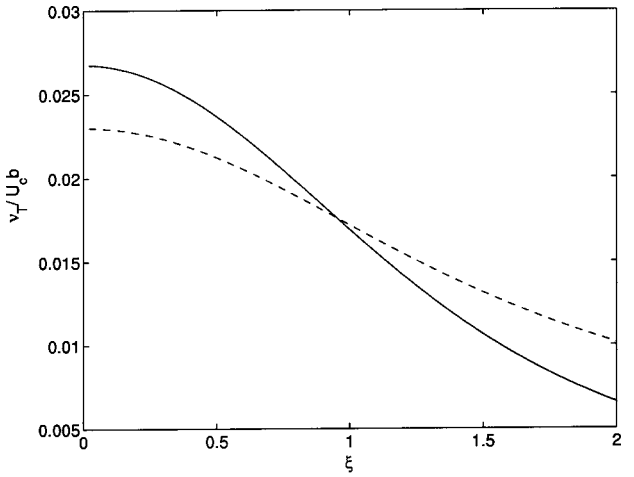

Fig. 6 Cross-stream variation of eddy viscosity for jets (—— axisymmetric jet, -- planar jet)

$$\frac{d\mu}{dz} = \frac{\sqrt{\pi}}{2} U_c c. \tag{12}$$

Equating Eqs. (11) and (12), we get $\alpha = \sqrt{\pi} c/4 = 0.041$ (from Fig. 5 of Gutmark and Wygnanski [18], we estimate $c = 0.092$). It should be pointed out that the cross-stream velocity does become equal to αU_c for large ξ. Turner's [11] statement that the inflow velocity at the edge of the jet equals αU_c is thus seen to apply strictly in the case of planar free-shear flows.

Ramaprian and Chandrasekhara [15] measured α for planar jets as $\alpha = V_e/U_c = 0.045$. The slight discrepancy might be due to the fact that their measurements, [15], were made rather close to the nozzle ($5 \leqslant z/d \leqslant 60$) and therefore, the jet might not have achieved complete self-similarity.

As before, the momentum Eq. (9) along with the expressions for U and V can be used to solve for the Reynolds stress as

$$\frac{\overline{uv}}{U_c^2} = \frac{\sqrt{\pi} c}{4} \exp(-\xi^2) \mathrm{erf}(\xi). \tag{13}$$

The plot looks similar to that of axisymmetric jets with a maximum at $\xi = 0.62$ and 0 for $\xi = 0$ and large ξ (Fig. 4). In fact, the maxima lie at almost the same ξ and are of nearly the same magnitude. Although U profiles for the two cases considered above are similar, their V and the governing Eqs. (2) and (9) are very different. Thus it is not expected that $\overline{uv}$ would look so similar. This similarity is due to the fact that $U \partial U/\partial z$ is the dominating term, and behaves similarly for the two cases.

The dilution rates can be computed from

$$\frac{1}{\mu} \frac{d\mu}{dz} = \frac{c}{b} \quad \text{(axisymmetric jets)} \tag{14}$$

$$\frac{1}{\mu} \frac{d\mu}{dz} = \frac{c}{2b} \quad \text{(planar jets)}. \tag{15}$$

Because the spread rates for the two cases are virtually identical, it is obvious that axisymmetric jets dilute twice as rapidly as their planar counterparts (axisymmetric jets entrain circumferentially, while planar jets entrain from the two sides only). Greater mixing in the axisymmetric jets is consistent with the faster decay of their centerline velocity with down-stream distance. It should be pointed out that, since $b \sim z$, $1/\mu(d\mu/dz) \sim z^{-1}$, i.e., the dilution rate keeps decreasing with downstream distance.

The complete turbulent kinetic energy equation can be found in the literature (e.g., for axisymmetric jets see [5]). The dominant kinetic energy production term is $\overline{uv} \partial U/\partial \xi$. Using Eqs. (3), (7), and (13) we can write

$$\left| \frac{\overline{uv}}{U_c^3} \frac{\partial U}{\partial \xi} \right| = c(\exp(-2\xi^2) - \exp(-3\xi^2)) \quad \text{(axisymmetric jets)}$$

$$\left| \frac{\overline{uv}}{U_c^3} \frac{\partial U}{\partial \xi} \right| = \frac{\sqrt{\pi} c}{2} \xi \exp(-2\xi^2) \mathrm{erf}(\xi) \quad \text{(planar jets)}.$$

The production term has a maximum around $\xi = 0.6$ (close to the maximum of the $\overline{uv}$ term) and reduces to zero for large ξ (Fig. 5).

Again, the maxima of the production terms for axisymmetric and planar jets lie at almost the same ξ. The magnitude of the turbulent kinetic energy term for axisymmetric jets is slightly larger than planar jets. The similarity of these terms is due to the fact that both $\overline{uv}$ and $\partial U/\partial \xi$ resemble each other closely for the two cases considered here.

One can derive corresponding expressions for ν_T for the axisymmetric and planar jets using

$$\overline{uv} = -\nu_T \frac{\partial U}{\partial r}, \tag{16}$$

as

$$\frac{\nu_{T_{\text{axisym.}}}}{U_c b} = \frac{c}{4} \frac{1 - \exp(-\xi^2)}{\xi^2},$$

and

$$\frac{\nu_{T_{\text{planar}}}}{U_c b} = \frac{\sqrt{\pi} c}{8} \frac{\mathrm{erf}(\xi)}{\xi}.$$

Because $\nu_T \sim U_c b$ (product of the integral velocity and length scales), we can expect $\nu_{T_{\text{axisym.}}} \sim z^0$ ($b \sim z$, and $U_c \sim z^{-1}$ for axisymmetric jets) and, $\nu_{T_{\text{planar}}} \sim z^{1/2}$ ($b \sim z$, and $U_c \sim z^{-1/2}$ for planar jets), i.e., not only is ν_T a function of radius, it can also be a function of z. Lessen [21] predicted identical z-dependences for ν_T based on the principle of marginal instability. While the streamwise variation of ν_T is well known, ν_T is generally assumed to be independent of ξ, [6–10]. The results presented next indicate that this need not be true.

The eddy viscosity ν_T for the axisymmetric and planar cases are plotted in Fig. 6. ν_T is a maximum at the center of the jet and decays to 0 for large ξ. For the axisymmetric case we find that

$\nu_T(\xi=0)$ is 2.3 times greater than $\nu_T(\xi=\sqrt{2})$. ($\xi=\sqrt{2}$ represents the e^{-2} point of the Gaussian.) For the planar case, this ratio is about 1.7. Townsend [8] also observes that ν_T should diminish as the jet edge is approached because the measured velocity profiles approach zero more rapidly than the profiles calculated on the basis of constant ν_T. Pope [9] states that ν_T is within 15% of the value 0.028 over bulk of the (axisymmetric) jet, and therefore ν_T can be assumed constant, independent of ξ.

Turbulent Plumes

Axisymmetric Plumes. The continuity equation remains the same as Eq. (1) for axisymmetric plumes, whereas a buoyancy term appears in the simplified momentum Eq. (2), [13,14]:

$$V\frac{\partial U}{\partial r}+U\frac{\partial U}{\partial z}+\frac{1}{r}\frac{\partial r\overline{uv}}{\partial r}=g\beta\theta. \tag{17}$$

The $g\beta\theta$ term in Eq. (17) differentiates the plume from the jet. The temperature equation can be obtained starting from

$$V\frac{\partial \theta}{\partial r}+U\frac{\partial \theta}{\partial z}+\frac{\partial \overline{v\,\theta'}}{\partial r}+\frac{\partial \overline{u\,\theta'}}{\partial z}+\frac{\overline{v\,\theta'}}{r}=\gamma\left(\frac{\partial^2\theta}{\partial r^2}+\frac{1}{r}\frac{\partial\theta}{\partial r}+\frac{\partial^2\theta}{\partial z^2}\right),$$

using scaling arguments (similar to jets), to finally arrive at ([13,14])

$$V\frac{\partial \theta}{\partial r}+U\frac{\partial \theta}{\partial z}+\frac{1}{r}\frac{\partial r\overline{v\,\theta'}}{\partial r}=0. \tag{18}$$

A Gaussian profile is commonly used in the literature to approximate the distributions for velocity and temperature in plumes, [1,2,11,13,14,16]. From similarity considerations, the centerline velocity and temperature for axisymmetric plumes vary, respectively, as $z^{-1/3}$ and $z^{-5/3}$ while the width increases linearly, [6]. Therefore, the streamwise velocity is given by Eq. (3), while the temperature in the plume can be written as

$$\theta(r,z)=\theta_c(z)\exp(-r^2/c_T^2z^2)=\theta_c(z)\exp(-H^2\xi^2), \tag{19}$$

where $c_T\neq c$, i.e., temperature and velocity need not spread at identical rates. In fact $c/c_T=H$ is 1.2 for axisymmetric plumes, [11].

Again, from the continuity Eq. (1) and using the decay rate of the centerline velocity, one can derive

$$\frac{V}{U_c}=\frac{c}{\xi}\left(-\frac{5}{6}+\frac{5}{6}\exp(-\xi^2)+\xi^2\exp(-\xi^2)\right). \tag{20}$$

The plot of V/U_c closely resembles axisymmetric jets—plumes experience outflow near the centerline, and an inflow far away from it. However, the maximum positive V is now just 0.4% of U_c (for $\xi=0.33$), while the maximum negative value of 3.8% lies at $\xi=1.87$ (Fig. 7). The cross-stream velocity changes sign at $\xi=0.595-$ much earlier than for jets. This is due to the presence of buoyancy. In fact, the presence of buoyancy in the plume creates contrasting effects near the center and far away from it when compared to the axisymmetric jet. Buoyancy causes the centerline velocity to decay less slowly than the jet. Consequently, the magnitude of the outflow near the centerline is smaller for the plume resulting in a smaller positive V. Secondly, because buoyancy is continuously increasing the momentum of the plume, there is a larger volume influx from its lateral surface. Hence, larger inflow velocities are seen far away from the centerline. This larger inflow is responsible for greater mixing in plumes. Sreenivas and Prasad [22] have proposed a model based on vortex dynamics to explain the greater entrainment in the plumes. It is again found that the inflow velocity *never* equals αU_c for axisymmetric plumes. The expression for V/U_c for axisymmetric plumes can also be found in [1] and the plot in [1,23].

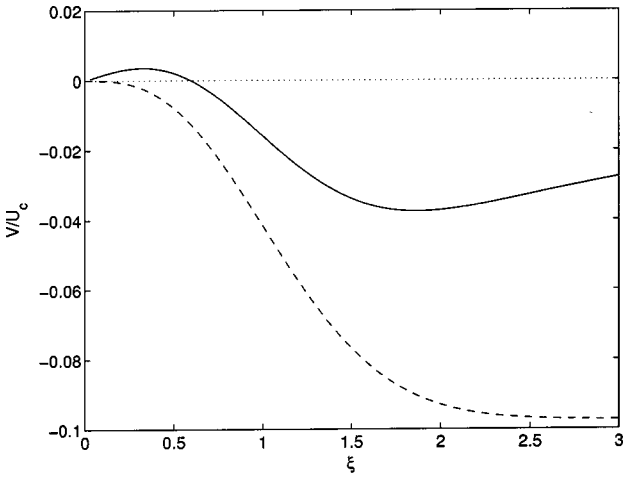

Fig. 7 Cross-stream velocity profiles for plumes (—— axisymmetric plume, -- planar plume)

Similar to axisymmetric jets, for large ξ we can approximate V/U_c as $-5c/6\xi$. The incremental volume flux entrained by the plume is again given by Eq. (5), while our result gives

$$\frac{d\mu}{dz}=\lim_{r\to\infty}-2\pi rV=2\pi r\frac{5c}{6\xi}U_c=2\pi bU_c\frac{5c}{6}.$$

From this, we get $\alpha=5c/6=0.0833$ (using $c=0.100$, [11]). The same value of α was obtained by [11].

Integrating the momentum Eq. (17) using Eqs. (3) and (20) yields

$$\frac{\overline{uv}}{U_c^2}=\frac{c}{\xi}\left(\frac{5}{6}\exp(-\xi^2)-\frac{1}{2}\exp(-2\xi^2)\right)$$
$$-\frac{g\beta b\,\theta_c}{2H^2U_c^2\xi}\exp(-H^2\xi^2)+\frac{K}{\xi}$$

where K is a constant of integration. Using the condition that $\overline{uv}$ is bounded at $\xi=0$, we obtain $K=-c/3+g\beta b\,\theta_c/2H^2U_c^2$, which leads to

$$\frac{\overline{uv}}{U_c^2}=\frac{c}{\xi}\left(\frac{5}{6}\exp(-\xi^2)-\frac{1}{2}\exp(-2\xi^2)-\frac{1}{3}\right)$$
$$+\frac{g\beta b\,\theta_c}{2H^2U_c^2\xi}(1-\exp(-H^2\xi^2)). \tag{21}$$

The condition of self-similarity forces $g\beta b\,\theta_c/U_c^2$ to be a constant, [6], but its value is not directly reported in the literature. However, it can be determined by fitting experimental data. For example, using Beuther et al.'s [24] data we estimate $g\beta b\,\theta_c/2H^2U_c^2=0.034$. Dai et al.'s [1] data similarly indicates a value of 0.027. Using the latter value, $\overline{uv}<0$ for $\xi\geqslant 1.5$, whereas the former value gives $\overline{uv}>0$ for all ξ. A negative Reynolds stress for plumes is unphysical (this is also supported by the data of [1]). Therefore, we use the former value of 0.034 hereafter. Thus,

$$\frac{g\beta b\,\theta_c}{2H^2U_c^2}=0.034=0.34c\approx\frac{c}{3},$$

implying that $K\approx 0$, and $g\beta b\,\theta_c/U_c^2=0.096$. Setting $K=0$ reduces Eq. (21) to

$$\frac{\overline{uv}}{U_c^2}=\frac{c}{6\xi}(5\exp(-\xi^2)-3\exp(-2\xi^2)-2\exp(-H^2\xi^2)).$$

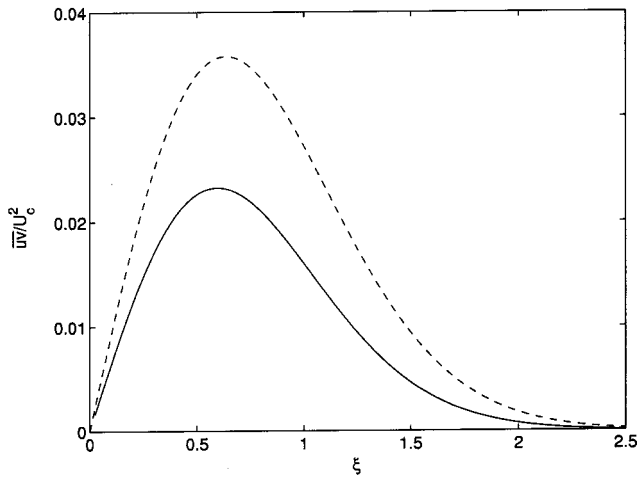

Fig. 8 Reynolds stress profiles for plumes (—— axisymmetric plume, -- planar plume)

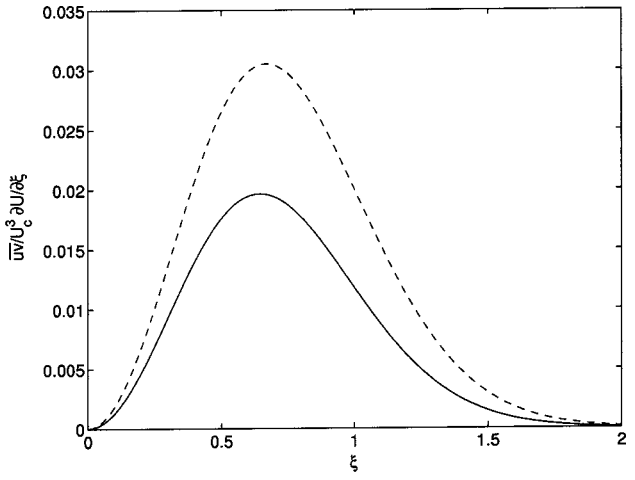

Fig. 10 Dominant kinetic energy production term profiles for plumes (—— axisymmetric plume, -- planar plume)

The behavior of $\overline{uv}$ shown in Fig. 8 looks similar to $\overline{uv}$ of axisymmetric jets. In fact the maxima lie at almost the same ξ ($=0.6$). As can be intuitively expected, Reynolds stress for plumes is larger than jets. Interestingly, this similarity in $\overline{uv}$ for axisymmetric jets and plumes can be inferred by noting that the above expression reduces to Eq. (7) for $H=1$ (although $H=1.2$ for axisymmetric plumes).

From the temperature Eq. (18) and using Eqs. (3), (19), and (20) one can obtain

$$\frac{\overline{v\theta'}}{U_c\theta_c}=\frac{5c}{6\xi}(1-\exp(-\xi^2))\exp(-H^2\xi^2). \tag{22}$$

From the plot in Fig. 9 the cross-stream velocity-temperature correlation remains positive for all ξ with a maximum value of 0.026 at $\xi=0.51$.

The production term is obtained as

$$\left|\frac{\overline{uv}}{U_c^3}\frac{\partial U}{\partial \xi}\right|=\frac{c}{3}(5\exp(-2\xi^2)-3\exp(-3\xi^2) -2\exp(-(H^2+1)\xi^2)).$$

This has a maximum of 0.020 around $\xi=0.6$ (Fig. 10). This plot matches that of axisymmetric jets quite closely with maxima at almost the same ξ. As expected the production term for the plumes is larger than jets for all ξ.

The dilution rate can be calculated from

$$\frac{1}{\mu}\frac{d\mu}{dz}=\frac{5c}{3b}. \tag{23}$$

Comparing Eqs. (14) and (23), we find that entrainment, and hence dilution rate for axisymmetric plumes is about 1.6 times greater than for axisymmetric jets.

The normalized eddy viscosity can be obtained using Eq. (16) as

$$\frac{\nu_T}{U_c b}=\frac{c}{12\xi^2}(5-3\exp(-\xi^2)-2\exp(-(H^2-1)\xi^2)).$$

Here again the variation with ξ is large. In fact, the ratio of $\nu_T(\xi=0)$ to $\nu_T(\xi=\sqrt{2})>2$ (Fig. 11). In addition, $\nu_T\sim z^{2/3}$.

For plumes, a further assumption of constant (in cross-stream direction) eddy thermal diffusivity, γ_T has been made by the researchers in the past to obtain the functional forms of the similarity functions where

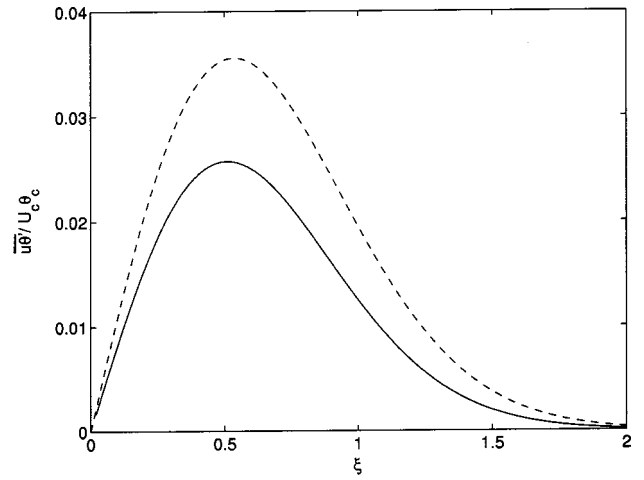

Fig. 9 Velocity-temperature correlation for plumes (—— axisymmetric plume, -- planar plume)

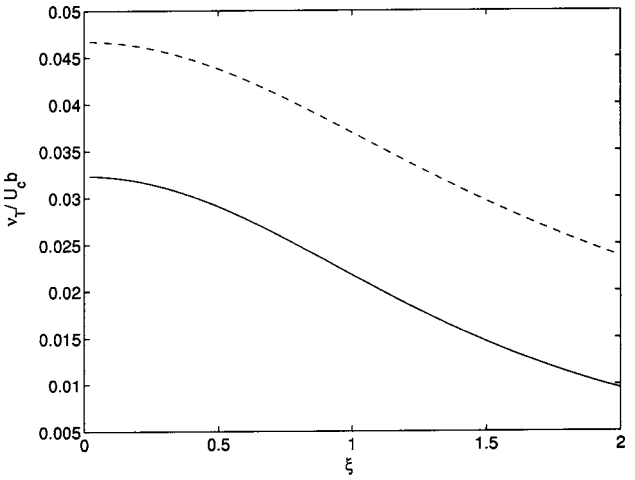

Fig. 11 Cross-stream variation of eddy viscosity for plumes (—— axisymmetric plume, -- planar plume)

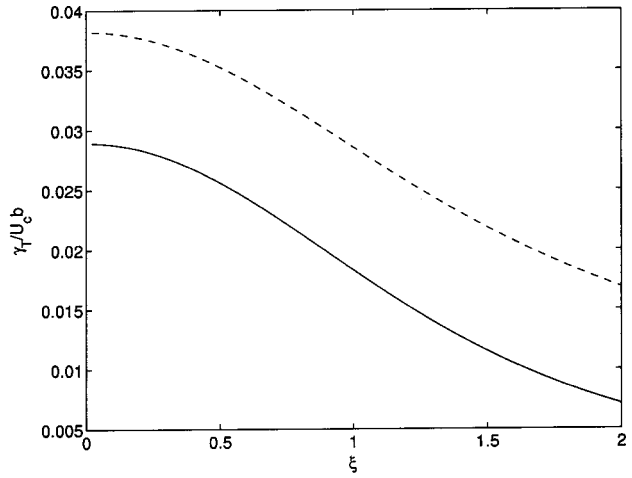

Fig. 12 Cross-stream variation of eddy thermal diffusivity for plumes (—— axisymmetric plume, -- planar plume)

$$\overline{v\,\theta'} = -\gamma_T \frac{\partial \theta}{\partial r}. \tag{24}$$

Our approach provides the radial variation in γ_T (using Eqs. (19) and (22)) as

$$\frac{\gamma_T}{U_c b} = \frac{5c}{12H^2\xi^2}(1-\exp(-\xi^2)).$$

Figure 12 reveals that $\gamma_T/(U_c b)$ has a value of 0.029 at the centerline while it drops to 0.012 for $\xi=\sqrt{2}$, i.e., the radial variation in γ_T is substantial. Moreover, γ_T is a function of downstream distance, i.e., $\gamma_T \sim z^{2/3}$. Knowing the distribution of both ν_T and γ_T we can obtain the turbulent Prandtl number, Pr_T as a function of ξ as

$$\mathrm{Pr}_T = \frac{\gamma_T}{\nu_T} = \frac{5}{H^2}\,\frac{1-\exp(-\xi^2)}{5-3\exp(-\xi^2)-2\exp(-(H^2-1)\xi^2)}.$$

It is interesting to note that unlike ν_T and γ_T, Pr_T is independent of the spread rate and z. Moreover, Pr_T is not such a strong function of radial position as ν_T and γ_T. Pr_T varies from 0.9 at the centerline to 0.8 at $\xi=\sqrt{2}$ (Fig. 13). Physical arguments can be used to show that $\mathrm{Pr}_T \approx 1$, [25], and our result is in good agreement.

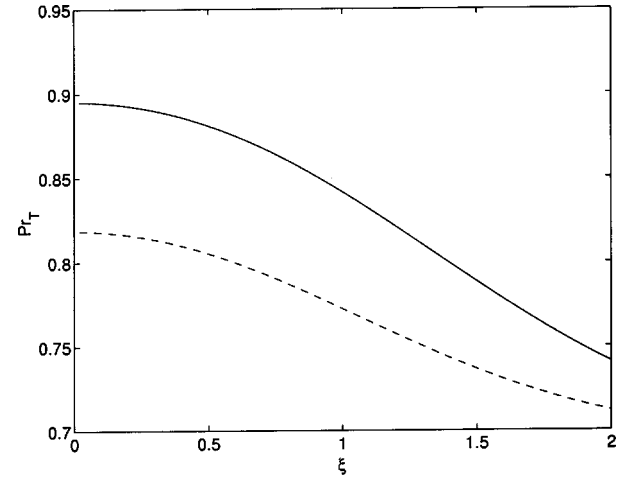

Fig. 13 Cross-stream variation of turbulent Prandtl number for plumes (—— axisymmetric plume, -- planar plume)

Planar Plumes. The continuity equation for planar plumes is the same as for planar jets (Eq. (8)), while the momentum equation can be derived by adding the buoyancy term to the planar jet momentum equation, [6],

$$V\frac{\partial U}{\partial x} + U\frac{\partial U}{\partial z} + \frac{\partial \overline{uv}}{\partial x} = g\beta\theta. \tag{25}$$

The temperature equation in the self-similar regime is given by ([6])

$$V\frac{\partial \theta}{\partial x} + U\frac{\partial \theta}{\partial z} + \frac{\partial \overline{v\,\theta'}}{\partial x} = 0. \tag{26}$$

Here the centerline temperature varies as z^{-1}, while it is interesting to note that the centerline velocity does not change downstream, [6], i.e., presence of buoyancy prevents the decay of the centerline velocity. This has an interesting consequence for the cross-stream velocity, expressed mathematically as

$$\frac{V}{U_c} = \frac{c}{2}(2\xi\exp(-\xi^2) - \sqrt{\pi}\,\mathrm{erf}(\xi)).$$

Unlike axisymmetric plumes, we find that planar plumes do not experience an outflow near the centerline; V/U_c is small for $\xi<0.54$ (less than 10% of its asymptotic value of 0.098) and remains negative throughout, i.e., the flow is always towards the axis (Fig. 7). Qualitatively the plot is similar to planar jets. Buoyancy causes planar plumes to entrain more than planar jets like their axisymmetric counterparts.

Similar to planar jets, we can obtain the coefficient of entrainment as

$$\alpha = \frac{\sqrt{\pi}c}{2}.$$

Using $c=0.11$, [16], we obtain $\alpha=0.0975$.

The Reynolds stress is given by

$$\frac{\overline{uv}}{U_c^2} = \frac{\sqrt{\pi}c}{2}\left(\mathrm{erf}(\xi)\exp(-\xi^2) - \frac{\mathrm{erf}(\sqrt{2}\xi)}{\sqrt{2}}\right) + \frac{\sqrt{\pi}g\beta b\,\theta_c}{2HU_c^2}\mathrm{erf}(H\xi). \tag{27}$$

Note that the constant of integration is zero in Eq. (27), and for similarity to exist $g\beta b\,\theta_c/U_c^2$ should be a universal constant, [6]. The experimental data of Ramaprian and Chandrasekhara [16] indicates $H=1.2$ (identical to axisymmetric plumes). We estimate the value of $\sqrt{\pi}g\beta b\,\theta_c/2HU_c^2$ (denoting this by C) as 0.069 which gives $\overline{uv}_{\max}/U_c^2=0.036$ at $\xi=0.63$. (The maximum value is very close to the value of 0.035 predicted by Malin and Spalding [26]). For Ramaprian and Chandrasekhara's [16] data we obtain $C=0.062$, but we find that $\overline{uv}$ becomes negative for $\xi>1.6$. As in the case of axisymmetric plumes, $\overline{uv}$ should remain positive for all ξ (this is also supported by the data of [16]). Hence, we will use $C=0.069$ to obtain

$$\frac{\sqrt{\pi}g\beta b\,\theta_c}{2HU_c^2} = 0.069 = 0.71\,\frac{\sqrt{\pi}c}{2} \approx \frac{\sqrt{\pi}c}{2}\,\frac{1}{\sqrt{2}},$$

and $g\beta b\,\theta_c/U_c^2=0.093$ which is very close to the value for axisymmetric plumes. Equation (27) can then be simplified to (see Fig. 8)

$$\frac{\overline{uv}}{U_c^2} = \frac{\sqrt{\pi}c}{2}\left(\mathrm{erf}(\xi)\exp(-\xi^2) - \frac{\mathrm{erf}(\sqrt{2}\xi)}{\sqrt{2}} + \frac{\mathrm{erf}(H\xi)}{\sqrt{2}}\right).$$

While it is known that $H=1.2$, an interesting result is obtained by substituting $H=\sqrt{2}$ in the above expression. Then, it is seen that $\overline{uv}$ for planar plumes is twice that of planar jets (Eq. 13).

The velocity-temperature correlation for planar plumes is given by

$$\frac{\overline{v\theta'}}{U_c\theta_c}=\frac{\sqrt{\pi}c}{2}\,\mathrm{erf}(\xi)\exp(-H^2\xi^2).$$

As for axisymmetric plumes, the velocity-temperature correlation is also positive with a maximum of 0.035 at $\xi=0.53$ (Fig. 9). Note that for both axisymmetric and planar plumes, the maximum value of $\overline{v\theta'}$ is to the left of the maximum for $\overline{uv}$.

We can obtain the production term as

$$\left|\frac{\overline{uv}}{U_c^3}\frac{\partial U}{\partial\xi}\right|=\sqrt{\pi}c\left(\xi\,\mathrm{erf}(\xi)\exp(-2\xi^2)-\frac{\xi\,\mathrm{erf}(\sqrt{2}\xi)\exp(-\xi^2)}{\sqrt{2}}+\frac{\xi\,\mathrm{erf}(H\xi)\exp(-\xi^2)}{\sqrt{2}}\right).$$

As for jets and axisymmetric plumes, this term has a maximum value around $\xi=0.6$ (Fig. 10). In fact, the maximum lies at almost the same location as the maximum of Reynolds stresses. It should be pointed out that unlike for jets, the production term for planar plumes is larger than their axisymmetric counterparts.

The dilution rate for planar plumes can be obtained as

$$\frac{1}{\mu}\frac{d\mu}{dz}=\frac{c}{b}. \tag{28}$$

As expected, the dilution rate of planar plumes is higher than planar jets (compare Eqs. (15) with (28)). Interestingly, it is equal to the dilution rate of axisymmetric jets (Eqs. (14) and (28)).

Once again, we can derive expressions for ν_T, γ_T, and Pr_T and question the validity of assigning constant cross-stream values to them.

$$\frac{\nu_T}{U_cb}=\frac{\sqrt{\pi}c}{4\xi\exp(-\xi^2)}\left(\mathrm{erf}(\xi)\exp(-\xi^2)-\frac{\mathrm{erf}(\sqrt{2}\xi)}{\sqrt{2}}+\frac{\mathrm{erf}(H\xi)}{\sqrt{2}}\right),$$

$$\frac{\gamma_T}{U_cb}=\frac{\sqrt{\pi}c}{4H^2\xi}\,\mathrm{erf}(\xi),$$

$$\mathrm{Pr}_T=\frac{1}{H^2}\,\frac{\sqrt{2}\,\mathrm{erf}(\xi)\exp(-\xi^2)}{\sqrt{2}\,\mathrm{erf}(\xi)\exp(-\xi^2)-\mathrm{erf}(\sqrt{2}\xi)+\mathrm{erf}(H\xi)}.$$

Turbulent eddy viscosity and thermal diffusivity are plotted in Figs. 11 and 12, respectively. Both ν_T and $\gamma_T\sim z$. Pr_T has a maximum value of 0.82 (at the centerline) while it drops to 0.74 for $\xi=\sqrt{2}$ (Fig. 13). It is again reassuring to note that $\mathrm{Pr}_T\approx1$ as predicted by physical arguments, [25].

Turbulent Wakes

Axisymmetric Wakes. Unlike jets and plumes, wakes have a nonlinear spread rate. The continuity equation for axisymmetric wakes remains the same as Eq. (1), while the momentum equation can be derived as for axisymmetric jets. However, here u'/U_c is of order unity, i.e., the velocity fluctuations are of the order of the velocity defect, [6]. This simplifies the momentum equation further:

$$U\frac{\partial U}{\partial z}+\frac{1}{r}\frac{\partial r\overline{uv}}{\partial r}=0. \tag{29}$$

It is interesting to note that V does not appear in the streamwise momentum equation. This is because in the momentum equation $V\partial U/\partial r=\mathcal{O}(U_c^2/L)$, while $U\partial U/\partial z=\mathcal{O}(U_0U_c/L)$; since $U_c/U_0=\mathcal{O}(b/L)$, the former can be discarded.

Using a Gaussian profile for the velocity defect, the streamwise velocity is given by

$$U(r,z)=U_0-U_c(z)\exp(-r^2/b^2)=U_0-U_c(z)\exp(-\xi^2). \tag{30}$$

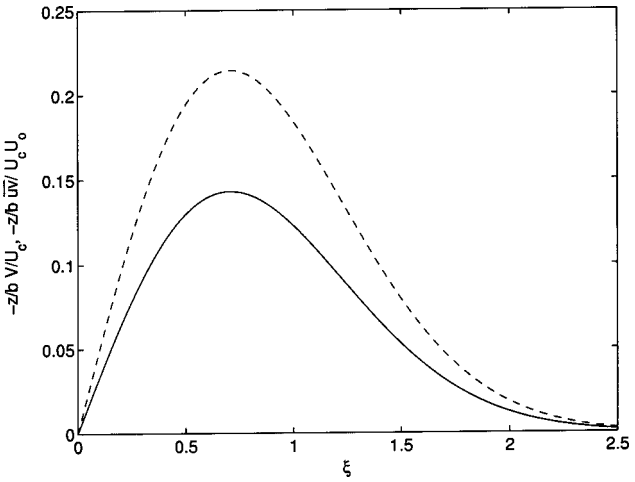

Fig. 14 Cross-stream velocity and Reynolds stress profiles for wakes (—— axisymmetric wake, -- planar wake)

In the self-similar region U_c decreases as $z^{-2/3}$, while b increases as $z^{1/3}$, [6]. Keeping these in mind, we can obtain V from the continuity Eq. (1) as

$$\frac{V}{U_c}=-\frac{b\xi}{3z}\exp(-\xi^2). \tag{31}$$

As for planar plumes, inflow occurs for all ξ with a maximum at $\xi=0.71$.

Reynolds stress can be obtained using Eqs. (29) and (30) as

$$\frac{\overline{uv}}{U_c^2}=\frac{b}{12z\xi}\left(1-\exp(-2\xi^2)+2\xi^2\exp(-2\xi^2)-\frac{4U_0}{U_c}\xi^2\exp(-\xi^2)\right). \tag{32}$$

It should be mentioned that in this case the integration constant is nonzero (actually $K=b/12z\xi$). It is not possible to plot Eq. (32) without knowing U_0/U_c. However, since $U/U_0=\mathcal{O}(1)$, one can simplify the momentum equation by replacing $U\partial U/\partial z$ by $U_0\partial U/\partial z$, [6], to obtain:

$$U_0\frac{\partial U}{\partial z}+\frac{1}{r}\frac{\partial r\overline{uv}}{\partial r}=0. \tag{33}$$

On comparing Eqs. (1) and (33), we can see that they are identical ($\overline{uv}/U_0$ replaces V). Hence it is not surprising to see

$$\frac{\overline{uv}}{U_0U_c}=-\frac{b\xi}{3z}\exp(-\xi^2), \tag{34}$$

which is exactly the same expression as for V/U_c. It should, however, be noted that $\overline{uv}$ has been normalized with U_0U_c and not U_c^2. $\overline{uv}/U_0U_c$ and V/U_c are plotted in Fig. 14.

We will use the expression for $\overline{uv}$ given by Eq. (32) to obtain the production term and the radial variation in turbulent eddy viscosity as

$$\left|\frac{\overline{uv}}{U_c^3}\frac{\partial U}{\partial\xi}\right|=\frac{b}{6z}\left(1-\exp(-2\xi^2)+2\xi^2\exp(-2\xi^2)-\frac{4U_0}{U_c}\xi^2\exp(-\xi^2)\right)\exp(-\xi^2),$$

$$\frac{\nu_T}{U_c b} = \frac{b}{24 z \xi^2 \exp(-\xi^2)} \left(1 - \exp(-2\xi^2) + 2\xi^2 \exp(-2\xi^2) - \frac{4U_0}{U_c} \xi^2 \exp(-\xi^2) \right).$$

Planar Wakes. The continuity equation for planar wakes is given by Eq. (8) while the momentum equation is, [6],

$$U \frac{\partial U}{\partial z} + \frac{\partial \overline{uv}}{\partial x} = 0. \tag{35}$$

U_c varies as $z^{-1/2}$, while b increases as $z^{1/2}$ for planar wakes, [6,21]. Integrating the continuity Eq. (8) gives

$$\frac{V}{U_c} = -\frac{b\xi}{2z} \exp(-\xi^2). \tag{36}$$

Comparing Eqs. (31) and (36), we see that the inward velocity is very similar. However, the decay with z is slightly different for the two cases.

Reynolds stress can be obtained from the momentum Eq. (35) using Eq. (30):

$$\frac{\overline{uv}}{U_c^2} = \frac{b}{16z} \left(-4\xi \exp(-2\xi^2) + \sqrt{2\pi}\, \mathrm{erf}(\sqrt{\pi}\xi) - \frac{8U_0}{U_c} \xi \exp(-\xi^2) \right).$$

The production term is

$$\left| \frac{\overline{uv}}{U_c^3} \frac{\partial U}{\partial \xi} \right| = \frac{b\xi}{8z} \left(-4\xi \exp(-2\xi^2) + \sqrt{2\pi}\, \mathrm{erf}(\sqrt{\pi}\xi) - \frac{8U_0}{U_c} \xi \exp(-\xi^2) \right) \exp(-\xi^2).$$

ν_T can be obtained as

$$\frac{\nu_T}{U_c b} = \frac{b}{32 z \xi \exp(-\xi^2)} \left(-4\xi \exp(-2\xi^2) + \sqrt{2\pi}\, \mathrm{erf}(\sqrt{\pi}\xi) - \frac{8U_0}{U_c} \xi \exp(-\xi^2) \right).$$

Simplifying the momentum equation as was done with axisymmetric wakes, and using it to obtain the simplified Reynolds stress

$$\frac{\overline{uv}}{U_0 U_c} = -\frac{b\xi}{2z} \exp(-\xi^2), \tag{37}$$

which, as expected, is the same expression as for V/U_c for planar wakes (Fig. 14).

It is not possible to compare the production terms for the axisymmetric and planar wakes because U_0 is unknown. However, if we use the simplified expressions for the Reynolds stress (Eqs. (34) and (37)), we can write the productions terms as

$$\frac{\overline{uv}}{U_0 U_c^2} \frac{\partial U}{\partial \xi} = \frac{2b}{3} \frac{\xi^2 \exp(-2\xi^2)}{z} \quad \text{(axisymmetric wakes)}$$

$$\frac{\overline{uv}}{U_0 U_c^2} \frac{\partial U}{\partial \xi} = \frac{b\xi^2 \exp(-2\xi^2)}{z} \quad \text{(planar wakes)}.$$

These two terms differ just by a constant.

The simplified expressions for ν_T (using Eqs. (16), (30), (34), and (37)) are

$$\nu_{T_{\text{axisym.}}} = -\frac{U_0 b^2}{6z},$$

$$\nu_{T_{\text{planar}}} = -\frac{U_0 b^2}{4z}.$$

Since U_0 is invariant with z, we obtain $\nu_{T_{\text{axisym. wake}}} \sim z^{-1/3}$ while $\nu_{T_{\text{planar wake}}} \sim z^0$, in agreement with Lessen's predictions, [21]. Remarkably, the dependence of ν_T on ξ disappears for wakes.

Conclusions

A comprehensive analysis has been conducted for six standard cases (axisymmetric and planar jets, plumes, and wakes). Expressions for cross-stream velocity, Reynolds stress, and turbulent kinetic energy production terms are derived for these cases assuming a Gaussian streamwise velocity distribution. The plots are compared amongst themselves and provide several insights.

1 Expressions for cross-stream velocity indicate outflow for jets and axisymmetric plumes near the axis, while inflow occurs in the far field. Planar plumes do not experience any such outflow. Outflow of fluid near the axis is a natural consequence of the decay of the centerline velocity with downstream distance (and not because of the assumed Gaussian velocity profile). The decay rates of axisymmetric jets, planar jets, and axisymmetric plumes are, respectively, z^{-1}, $z^{-1/2}$, $z^{-1/3}$, while the radial extents of outflow are $r/b \leqslant 1.12$, 0.99, 0.59. Moreover, the decay rate for planar plumes varies as z^0 and these do not experience any outflow. Thus, a higher decay rate correlates with a larger radial extent of outflow. See Agrawal et al. [20] for more discussion on the coupling between the decay of the centerline velocity and the radial extent of the outflow.

2 Expressions for the entrainment coefficients of planar jets and plumes are developed along the lines of their axisymmetric counterparts. It is found that for planar jets and plumes $V_e = \alpha U_c$; this is, however, not true for axisymmetric cases. Hence, contrary to conventional belief, the entrainment velocity *should not* be equated to αU_c for axisymmetric jets and plumes.

3 The value of the universal constant $g\beta b\theta_c / U_c^2$ is estimated as 0.096 and 0.093 for axisymmetric and planar plumes, respectively.

4 Reynolds stress and the dominant turbulent kinetic energy production term for jets and plumes are qualitatively the same with a maximum around $\xi = 0.6$. Magnitudes for jets and axisymmetric plumes are nearly the same. These are much smaller than for planar plumes.

5 Unlike plumes and jets, the normalized cross-stream velocity and Reynolds stresses for wakes are functions of downstream distance. In addition, the turbulent kinetic energy production term for axisymmetric and planar wakes has the same cross-stream distribution.

6 Cross-stream variations for ν_T, γ_T, and Pr_T are shown to be significant, therefore, the use of constant values of ν_T and γ_T in the cross-stream direction is unjustified. Pr_T is found to lie between 0.9 and 0.7 for axisymmetric and planar plumes.

7 Our analysis reveals that the eddy viscosity is independent of the cross-stream coordinate for axisymmetric and planar wakes.

Acknowledgments

This work was supported by National Science Foundation, under grant NSF-ATM-9714810. We thank Prof. Pablo Huq of the College of Marine Studies, University of Delaware, for encouraging us to undertake this study and helpful discussions.

Nomenclature

- b = width (defined as $U(b)/U_c = e^{-1}$ for jets and plumes, and $(U_0 - U(b))/U_c = e^{-1}$ for wakes)
- c = spread rate $= db/dz$
- c_T = spread rate for temperature
- d = diameter of the nozzle
- g = acceleration due to gravity

H = c/c_T
K = constant of integration
L = downstream distance scale
p = time-averaged pressure
Pr_T = turbulent Prandtl number
r = cross-stream coordinate used for axisymmetric case
T = temperature
T' = fluctuating temperature
T_0 = ambient fluid temperature (assumed constant)
T_c = time-averaged centerline temperature
u, v = fluctuating components of velocity
u' = fluctuating velocity scale
U = time-averaged streamwise velocity
U_0 = free stream velocity
U_c = time-averaged centerline velocity (for wakes—velocity defect at the centerline)
V = time-averaged cross-stream velocity
V_e = time-averaged entrainment velocity
x = cross-stream coordinate used for planar case
z = coordinate along the axis
α = coefficient of entrainment
β = coefficient of thermal expansion
γ = thermal diffusivity
γ_T = turbulent thermal diffusivity
θ = $T-T_0$
θ' = $T'-T_0$
θ_c = T_c-T_0
μ = volume flux
ν_T = eddy viscosity
ξ = nondimensional cross-stream coordinate ($=r/b$ for axisymmetric case, $=x/b$ for planar case. See Fig. 2)
ρ = density

References

[1] Dai, Z., Tseng, L. K., and Faeth, G. M., 1995, "Velocity Statistics of Round, Fully Developed, Buoyant Turbulent Plumes," ASME J. Heat Transfer, **117**, pp. 138–145.

[2] George, W. K., Alpert, R. L., and Tamanini, F., 1977, "Turbulence Measurements in an Axisymmetric Buoyant Plume," Int. J. Heat Mass Transfer, **20**, pp. 1145–1153.

[3] Bhat, G. S., and Narasimha, R., 1996, "A Volumetrically Heated Jet: Large Eddy Structure and Entrainment Characteristics," J. Fluid Mech., **325**, pp. 303–330.

[4] Hussein, H. J., Capp, S. P., and George, W. K., 1994, "Velocity Measurements in a High Reynolds Number, Momentum-Conserving Axisymmetric Turbulent Jet," J. Fluid Mech., **258**, pp. 31–75.

[5] Wygnanski, I., and Fiedler, H., 1969, "Some Measurements in a Self-Preserving Jet," J. Fluid Mech., **38**, pp. 577–612.

[6] Tennekes, H., and Lumley, J. L., 1972, *A First Course in Turbulence*, MIT Press, Cambridge, MA, pp. 127–142.

[7] White, F. M., 1974, *Viscous Fluid Flow*, McGraw-Hill, New York, pp. 508–510.

[8] Townsend, A. A., 1976, *The Structure of Turbulent Shear Flow*, Cambridge Univ. Press, Cambridge, UK, pp. 188–219.

[9] Pope, S. B., 2000, *Turbulent Flows*, Cambridge Univ. Press, Cambridge, UK, pp. 102–120.

[10] Lesieur, M., 1990, *Turbulence in Fluids*, Kluwer, Dordrecht, The Netherlands, pp. 120–126.

[11] Turner, J. S., 1986, "Turbulent Entrainment: The Development of the Entrainment Assumption, and Its Application to Geophysical Flows," J. Fluid Mech., **173**, pp. 431–471.

[12] List, E. J., 1982, "Turbulent Jets and Plumes," Annu. Rev. Fluid Mech., **14**, pp. 189–212.

[13] Chen, C. J., and Rodi, W., 1980, *Vertical Turbulent Buoyant Jets—A Review of Experimental Data*, Pergamon Press, Oxford, UK, pp. 11–12.

[14] Gebhart, B., Jaluria, Y., Mahajan, R. L., and Sammakia, B., 1988, *Buoyancy-Induced Flows and Transport*, Hemisphere, Washington, DC, pp. 661–663.

[15] Ramaprian, B. R., and Chandrasekhara, M. S., 1985, "LDA Measurements in Plane Turbulent Jets," ASME J. Fluids Eng., **107**, pp. 264–271.

[16] Ramaprian, B. R., and Chandrasekhara, M. S., 1989, "Measurements in Vertical Plane Turbulent Plumes," ASME J. Fluids Eng., **111**, pp. 69–77.

[17] Agrawal, A., and Prasad, A. K., 2002, "Properties of Vortices in the Self-Similar Turbulent Jet," Exp. Fluids, **33**, pp. 565–577.

[18] Gutmark, E., and Wygnanski, I., 1976, "The Planar Turbulent Jet," J. Fluid Mech., **73**, pp. 465–495.

[19] Narasimha, R., 2001, private communication.

[20] Agrawal, A., Sreenivas, K. R., and Prasad, A. K., 2003, "Velocity and Temperature Measurements in an Axisymmetric Jet With Cloud-Like Off-Source Heating," Int. J. Heat Mass Transfer, to appear.

[21] Lessen, M., 1978, "On the Power Laws for Turbulent Jets, Wakes and Shearing Layers and Their Relationship to the Principal of Marginal Instability," J. Fluid Mech., **88**, pp. 535–540.

[22] Sreenivas, K. R., and Prasad, A. K., 2000, "Vortex-Dynamics Model for Entrainment in Jets and Plumes," Phys. Fluids, **12**, pp. 2101–2107.

[23] Lumley, J. L., 1971, "Explanation of Thermal Plume Growth Rates," Phys. Fluids, **14**, pp. 2537–2538.

[24] Beuther, P. D., Capp, S. P., and George, W. K., Jr., 1979, "Momentum and Temperature Balance Measurements in an Axisymmetric Turbulent Plumes," ASME Paper No. 79-HT-42.

[25] Kays, W. M., and Crawford, M. E., 1980, *Convective Heat and Mass Transfer*, McGraw-Hill, New York, pp. 267–268.

[26] Malin, M. R., and Spalding, D. B., 1984, "The Prediction of Turbulent Jets and Plumes by Use of the k-ω Model of Turbulence," PhysicoChemical Hydrodynamics, **5**, pp. 153–198.

Resolving Turbulent Wakes

Stephen A. Jordan
Naval Undersea Warfare Center,
Code 74,
Newport, RI 02841
e-mail: jordansa@npt.nuwc.navy.mil

Resolving the turbulent statistics of bluff-body wakes is a challenging task. Frequently, the streamwise grid point spacing approaching the vortex exit boundary is sacrificed to gain near full resolution of the turbulent scales neighboring the body surface. This choice favors the solution strategies of direct numerical and large-eddy simulations (DNS and LES) that house spectral-like resolving characteristics with inherent dissipation. Herein, two differencing stencils are tested for approximating four forms of the convective derivative in the DNS and LES formulations for incompressible flows. The wake spectral characteristics and conventional parameters are computed for Reynolds numbers Re=200 (laminar wake) and Re=3900. These tests demonstrated reliable stability and spectral-like accuracy of compact fifth-order upwinding for the advective derivative and fourth-order cell-centered Padé (with fourth-order upwinding interpolation) for the Arakawa form of the convective derivative. Specifically, observations of the DNS computations suggest that best results of the wake properties are acquired when the inertial subrange of the spectral energy is fully resolved at the grid-scale level. The LES solutions degraded dramatically only when the fifth-order upwind stencil resolved the spanwise periodic turbulence. Although the dynamic subgrid-scale model showed strong participation on the instantaneous level, its spectral contributions were negligible regardless of the chosen grid-scale scheme. [DOI: 10.1115/1.1603302]

Introduction

Before the past decade, constructive gains in our physical understanding of turbulent wakes came essentially from over a century of laboratory measurements. Collectively, flow past a circular cylinder has become the canonical test problem. The experimental evidence at subcritical Reynolds numbers (laminar separation) reveals a wake that is enriched with turbulent physics quite different than say the streaks and bursts observed for wall bounded flows. For example, the notable work of Cantwell and Coles [1] presented detailed measurements of the vortex formation kinematics that lead to the discovery of the evolution of saddle points between successive vortices in the immediate near wake. They concluded that a substantial part of the turbulence produced coincides with these fine-scale regions. Further upstream, Wei and Smith [2] observed the creation of high-frequency small-scale turbulent vortices as the final stage of the transition process held within the separated shear layers. Spanwise, these Kelvin-Helmholz (K-H) vortices distort to periodic cellular structures that align themselves in the streamwise direction. These two works clearly illustrate that the underlying mechanics of the turbulent wake are small-scale events.

Until the advent of supercomputers, computational efforts accomplished little beyond the experimental measurements towards improving our key knowledge about the cylinder turbulent wake. Some attempted to resolve the small-scale physics using only two-dimensional simulations. But as concluded by Cantwell and Coles [1], the production of turbulence is a three-dimensional vortex stretching phenomena at the intermediate scales of the global spectrum. Useful computations that addressed the underlying physics surfaced less than a decade ago by employing the relatively new advances in the computational methodologies of direct numerical and large-eddy simulations (DNS and LES). These techniques are slowly expanding our insight into the turbulent wake physics; particularly its three-dimensional nature at low subcritical Reynolds numbers (Re). But the resolving power of the respective solution schemes is typically designed below the local small-scale events of turbulence production and the shear-layer K-H vortices at Re in the moderate category.

Contributed by the Fluids Engineering Division for publication in the JOURNAL OF FLUIDS ENGINEERING. Manuscript received by the Fluids Engineering Division July 11, 2002, revised manuscript received April 21, 2003. Associate Editor: F. F. Grinstein.

When resolving the smallest scales of turbulence one must be concerned about controlling the aliasing error. This error can originate from the discrete approximations of the nonlinear term as first recognized by Platzman [3] where kinetic energy aliases back to the respective lower scales of the spectrum. DNS computations without an intrinsic mechanism for minimizing this error will become unstable as these spurious grid-scale waves grow. High accuracy schemes of even order (fourth, sixth, etc.) fall within this category because the leading term in the truncation error is dispersive. These schemes commonly require a separate form of artificial dissipation added to the DNS computation. Assessing the resultant impact ''a priori'' on the resolved turbulence is difficult and generally gives turbulent energy spectra that are unnaturally damped at the high wave number range. Alternatively, one can require the scheme to be energy conserving to control the aliasing error. However, we have yet to see a stable spectral-like energy-conserving scheme for the general class of turbulent wakes that is applicable to complex discretized domains.

In most LES computations, the prime criticism of the numerical approximations is the assurance that the truncation errors of the nonlinear terms do not mask the essential contributions from the subgrid model. This concern is raised not only for upwind schemes, but includes low-order central stencils as well. Under coarse gridding we know that explicit upwind differencing for the nonlinear terms assures stability, but certain restrictions arise because the dissipation error interferes with the model stress contributions and damps (or even dumps) the finest resolved turbulent energy. Developers circumvent these drawbacks by devising routines with low-order central differencing or high-order compact schemes coupled with explicit spatial filtering to attenuate the dispersed unresolved energy. However, this latter approach can be effectively no better than the former in terms of its net resolving efficiency. In this case, their difference rests essentially on the added CPU cost.

The present work draws attention to the needed resolving power within a DNS or LES approach for capturing small-scale turbulent wake events. We seek useful discretization schemes that posses a high level of resolving efficiency by appearing spectral-like while maintaining a long-term stable computation. We will specifically examine the resolving power of compact differencing as applied to turbulent bluff-body wakes. Lele [4] already gave us a comprehensive understanding about their benefits over explicit differencing, but herein we will reach somewhat beyond that view

when dealing with the present application. Incompressible flow past the circular cylinder at subcritical Re will serve as a suitable canonical test case. Choosing the cylinder topology for computing wake turbulence by the DNS and LES methodologies is appealing for several reasons. From the resolution perspective, one can easily redistribute the upstream grid spacing for fulfilling the finer requirement downstream. With this improved spacing one can potentially resolve higher Re wakes simply by simulating a broader wavenumber spectrum. Outside of pure spectral methods, this single perception ignores an important ingredient intrinsic in the DNS and LES solutions. Low-order-accurate schemes can locate turbulent fluctuations up to the π wave, but their resolving power is far less than optimum for capturing the respective smaller-scale events. Detecting these physics requires an even finer resolution to compensate for their low resolving efficiency. Realistically, the higher Re computations (near critical for example) demand both fine grid spacing as well as spectral-like characteristics of the grid-scale numerics.

For the present wake computations, the governing formulations are cast into a curvilinear coordinate framework so that they are not stalled by irregular or nonorthogonal grid topologies. Under a typical fixed-grid computation, the flow predictions proceed over a decaying downstream spatial resolution. Thus, preserving an accurate and stable DNS or LES computation at the respective Re demands a compact scheme that houses both a strong resolving and dissipating nature near the finest resolved scales. We expect to sufficiently resolve the small-scale events of the turbulent wake when given adequate spatial resolution while concurrently dissipating the under-resolved energy over poor grid spacing further downstream. One can fulfill these requirements by carefully selecting the appropriate upwind and central compact differencing schemes. Before discussing the specifics regarding this solution strategy, we will briefly present the derivations of the governing DNS and LES equations in conservative form for complex domains.

Resolved and Dynamic Modeled Field Equations

The impetus of the present work is the spatial resolution of the turbulent circular cylinder wake at subcritical Re using stable spectral-like compact differencing schemes. These schemes will be applied to both the DNS and LES system of equations. The LES governing equations are derived by spatially filtering the corresponding DNS system where all turbulent scales removed by the filter process are classified as the subgrid-scales (SGS). As noted earlier, both the DNS and LES equations will be transformed to a curvilinear coordinate system (ξ, η, ζ in the streamwise, transverse, and spanwise directions, respectively). Although this transformation is straightforward for the DNS system, the LES derivation formally involves two spatial operations.

Resolved Field. The order of spatial operations is important to ensure that the filter is not ill-defined, [5]. By performing the transformation operation first, one guarantees that the filter kernel is directed along the curvilinear lines. Starting with the conservative Cartesian form of the Navier-Stokes equations along with continuity, the governing LES system appears as

$$\text{Continuity:} \quad \frac{\partial \overline{U^k}}{\partial \xi^k} = 0 \tag{1a}$$

$$\text{Momentum:} \quad \frac{\partial \sqrt{\tilde{g}}\,\overline{u_i}}{\partial t} + \frac{\partial \overline{U^k}\,\overline{u_i}}{\partial \xi^k} = \frac{\partial \sqrt{\tilde{g}}\,\tilde{\xi}^k_{x_j}\overline{p}}{\partial \xi^k} + \frac{\partial \sigma_i^k}{\partial \xi^k} + \frac{1}{\mathrm{Re}}\frac{\partial}{\partial \xi^k}\left[\sqrt{\tilde{g}}\tilde{g}^{kl}\frac{\partial \overline{u_i}}{\partial \xi^l}\right]. \tag{1b}$$

The transformation operation redefines the real SGS stress (σ_i^k) in terms of the resolved Cartesian ($\overline{u},\overline{v},\overline{w}$) and contravariant ($\overline{U},\overline{V},\overline{W}$) velocity components; specifically, $\sigma_i^k = \overline{U^k u_i} - \overline{U^k}\,\overline{u_i}$). The contravariant velocity components are evaluated in terms of their resolved counterparts by $\overline{U^k} = \sqrt{\tilde{g}}\tilde{\xi}^k_{x_j}\overline{u_j}$. In these definitions, the overbar denotes the filter operation, and the tilde symbolizes implicit filtering of the metric coefficients ($\tilde{\xi}^k_{x_j}$) and Jacobian ($\sqrt{\tilde{g}}$) through their numerical approximation, [5]. In the present applications, the above LES equation system (as well as its DNS complement) was solved in the computational space by the procedure described in Jordan and Ragab [6].

Modeled Field. A vital aspect of the LES computation seeks to show reasonable participation by the SGS model in the total predicted statistics of the turbulent wake. Although one would expect this prospect to be a sufficient condition for the LES computation, previous authors claim little success using the popular turbulent eddy-viscosity scaling law, [7,8], regardless of the formal order of the resolved field solution. Apparently, this SGS model suitably stabilizes the computation by dissipating the forward scatter of kinetic energy across the cutoff wave number, but yields only minor contributions in the overall turbulent statistics. To focus our attention strictly on this model, we will assume that the filter width of the resolved field equations (Eq. (1)) is synonymous with the grid spacing. Under this premise, we will not consider mixed-model formulations that include the Leonard and cross terms. Furthermore, complex domains generally lead to cutoff of the resolved wavenumbers that vary locally due to the nonuniformity of the physical domain spatial discretization. Herein, we carefully generate the grid spacing (given ''a priori'' knowledge of the wake's spectral content) to ensure that the cutoff wave number lies within the equilibrium range of the local energy spectra. This requirement is an essential prerequisite for the eddy-viscosity relationship before anticipating realistic contributions to the overall stress fields.

The following version of the dynamic eddy-viscosity relationship for the SGS stress field is derived for the transformed space according to the spatial order-of-operations described by Jordan [9]. This model is equally capable of capturing backscatter of turbulent energy as transferred from the modeled scales to the finest resolved ones across the cutoff wave number. In its contravariant form

$$\sigma_i^k - \tfrac{1}{3}\,\tilde{\varsigma}^k_{x_j}\tau_{ll} = 2C\overline{\Delta^2}\,\overline{|S|}\,\overline{S_i^k} \tag{2}$$

where the variable C is considered as the dynamic coefficient. The filtered metric term $\tilde{\varsigma}^k_{x_j}$ transforms the trace of the Cartesian stress tensor (τ_{ll}), which is coupled with the transformed pressure variable in the computation. The turbulent eddy-viscosity (ν_T) is expressed as $\nu_T = C\overline{\Delta^2}\,\overline{|S|}$ where $\overline{|S|} = \sqrt{2\overline{S_{ij}S_{ij}}}$ is the magnitude of the resolvable strain-rate tensor (S_{ij}) and Δ is the local filter width. Like the velocity components, the contravariant of the strain-rate tensor ($\overline{S_i^k}$) is defined as $\overline{S_i^k} = \sqrt{\tilde{g}}\tilde{\xi}^k_{x_j}\overline{S_{ij}}$ where $\overline{S_{ij}}$ is computed along the curvilinear lines in the physical domain.

Dynamic Coefficient. Derivation of a unique expression for dynamic computation of the model coefficient starts with explicitly filtering the grid-scale LES equations a second time by a test filter (caret symbol). Its width ($\hat{\Delta}_t$) is set at twice the local grid spacing; $\hat{\Delta}_t = 2\overline{\Delta}_s$. Test filtering along the curvilinear lines is easily achieved in either the physical domain or computational space because all required explicit filtering occur after the coordinate transformation operation. When filtering in the nonuniform physical domain, one can avoid the associated second-order error by numerically evaluating each contributing first-order term prior to the explicit filter operation. We must also be careful to insure rotational invariance of C in both the physical domain and transformed space. The proper procedure requires writing the error function in the physical domain, then minimizing its square to give

$$C = \frac{L_i^k \cdot M_i^k}{2\overline{\Delta}^2 M_m^k \cdot M_m^k} \tag{3}$$

for the model coefficient. Notice that this expression operates on the inner product of the Cartesian tensor components of L_i^k and M_i^k in the computational space. Those tensors are defined

$$L_i^k = T_i^k - \hat{\sigma}_i^k \tag{4a}$$

$$T_i^k - \tfrac{1}{3}\tilde{s}_{x_j}^k T_{ll} = 2C\hat{\bar{\Delta}}^2 |\hat{\bar{S}}| \hat{\bar{S}}_i^k \tag{4b}$$

$$M_i^k = \alpha^2 |\bar{\bar{S}}| \bar{\bar{S}}_i^k - \overline{|\bar{S}| S_i^k} \tag{4c}$$

with filter width ratio $\alpha = 2$. Specific information about the dynamic eddy-viscosity model that discusses its proper implementation and ''a priori'' response within the turbulent wake was recently described in detail by Jordan [9].

Compact Differencing

In the following DNS and LES wake computations, we will treat several forms of the convective derivative with spectral-like resolution. Inasmuch as the truncation error will be several orders higher than the second-order-accurate SGS model, we should expect dominant pockets of contributing eddy viscosity throughout the entire turbulent wake. An attempt to implement high-order compact schemes for all the remaining terms is a difficult and expensive task, especially when dealing with complex topologies. Besides the diffusive and pressure terms, we must approximate the SGS model and the metric coefficients with high-order differencing to guarantee accuracy beyond second-order throughout the domain. Moreover, all explicit filtering must be performed in the computational space when the LES system of equations is placed in a curvilinear coordinate framework. Thus, in view of the advanced techniques for adaptive gridding the simpler choice may be to locally adjust the grid spacing in response to the respective demands placed on the spatial resolution.

Forms of the Convective Derivative. We will resolve the transformed convective derivative by compact differences in one of four forms.

$$\text{Divergent } (D) \quad \frac{\partial \overline{U}^k \overline{u_i}}{\partial \xi^k} \tag{5a}$$

$$\text{Advective } (A) \quad \frac{\partial \overline{U}^k \overline{u_i}}{\partial \xi^k} = \overline{U}^k \frac{\partial \overline{u_i}}{\partial \xi^k} + \overline{u_i} \frac{\partial \overline{U}^k}{\partial \xi^k} = \overline{U}^k \frac{\partial \overline{u_i}}{\partial \xi^k} \tag{5b}$$

$$\text{Rotational } (R) \quad \frac{\partial \overline{U}^k \overline{u_i}}{\partial \xi^k} = \overline{U}^k \frac{\partial \overline{u_i}}{\partial \xi^k} = \overline{U}^k \frac{\partial \overline{u_i}}{\partial \xi^k} - \sqrt{\tilde{g}} \tilde{\xi}_{x_i}^k \overline{u_j} \frac{\partial \overline{u_j}}{\partial \xi^k} + \frac{\partial \tfrac{1}{2}\sqrt{\tilde{g}} \tilde{\xi}_{x_i}^k \overline{u_j u_j}}{\partial \xi^k} \tag{5c}$$

$$\text{Arakawa } (K) \quad \frac{\partial \overline{U}^k \overline{u_i}}{\partial \xi^k} = \frac{1}{2}\left[\frac{\partial \overline{U}^k \overline{u_i}}{\partial \xi^k} + \overline{U}^k \frac{\partial \overline{u_i}}{\partial \xi^k} + \overline{u_i} \frac{\partial \overline{U}^k}{\partial \xi^k} \right] \tag{5d}$$

The first form is the divergent form, which easily conserves turbulent momentum and energy (with continuity satisfied) using the proper symmetric differencing stencils, [10]. Conversely, the advective form of the transformed Navier-Stokes equations is nonconservative in both turbulent energy and momentum unless the solutions fully satisfy continuity, [10,11]. This particular form is well suited for high-order upwinding when designing DNS strategies for solving incompressible wake flows because of the expected absence of any discontinuities. As illustrated by Tennekes and Lumley [12], decomposing the divergent form can derive a rotational form of the convective derivative. Herein, we group the kinetic energy term (third term) of this form as an ingredient in the resolved pressure gradient. Mansour et al. [13] proved that the rotational form conserves both momentum and energy in the theoretical sense. However, standard discretization schemes that employ staggered or semi-staggered grid molecules, to offset the pressure and velocity nodes for preserving strong coupling, violate the energy-conservation principle. Moreover, the leading error of the rotational form close to wall boundaries is on the order of Re_τ^2 (based on the shear velocity, u_τ), which is 10^2 to 10^3 times larger than alternate forms of the convective derivative, [14].

Finally, the fourth form derives its roots from the numerical stability improvements accomplished by Arakawa [15]. Arakawa focused on correcting the ''noodling'' problem near wave number cutoff (observed erroneous flow structures due to aliasing and poorly resolved waves) that leads to uncontrolled growth of turbulent energy distributed over the upper 1/3 of computed wave numbers. The Arakawa form conserves momentum and energy in the discrete sense (under symmetric stencils) and gives superior grid-scale solutions over the rotational form near solid wall boundaries, [15,16]. Kravchenko and Moin [17] advocate the Arakawa form for minimizing aliasing errors and promoting numerical stability in LES computations.

Treatment of the Convective Derivative. The ''noodling'' problem coined by Arakawa is a prime threat of numerical instability. Without a natural dissipative element in the compact scheme (to augment the SGS model), the flow solutions may ultimately diverge. Alternatively, one can control these waves through intermittent explicit high-order adaptive filtering. But for complex irregular domains this choice introduces a third spatial operation when deriving the final form of the LES equations and its coupling with the convective derivative differencing does not commute, lowers the resolving efficiency and is difficult to implement simultaneously in three dimensions. These latter facts were demonstrated by Ladeinde et al. [18] who computed the kinetic energy spectra of decaying isotropic turbulence using both fourth-order and sixth-order compact schemes that were coupled with various orders of filtering. Over a relatively broadband range of finest resolves scales ($\sim$1/2 decade), Ladeinde et al. were able to reproduce the damped-energy effect of a low-order explicit upwind scheme or the excess-energy tailing of unresolved scales simply by varying the coefficients associated with the specific compact filter kernel. More recently, Visbal and Rizzetta [19] were able to duplicate the correct energy spectral distribution for the same test case as Ladeinde et al. using high-order compact filter kernels throughout the solution domain.

Inasmuch as the turbulent wake houses strong convective pockets of concentrated energy production near the exit boundary, [1], intermittent dissipation is necessary to insure sufficient damping of the under-resolved energy. We cannot expect enough help from the SGS model if one resorts to a dynamic eddy-viscosity formulation. This conclusion become apparent ''a priori'' in view of the model performance studies by Jordan [9] and the experimental evidence of Cantwell and Coles [1] for the circular cylinder wake. While the latter measurements unveiled strong correlation between the regions of peak turbulent energy production and peak Reynolds shear stress, the former evaluations noted the complete inability of the dynamic eddy-viscosity model to capture the real shear stress. Thus in the vain of a ''true'' LES computation, one can argue that a user can rely on the inherent dissipative element of a high-resolution upwind approximation for the resolved scales to inhibit spurious oscillations near cutoff. To address this issue, we will start with treatment of the convective derivative by using two possibilities that hold reasonably high resolving efficiency and natural stability characteristics.

Compact Upwind Differencing. Compact upwind differencing offers strong stability where specific stencils can be derived that house good resolving qualities while suppressing spurious

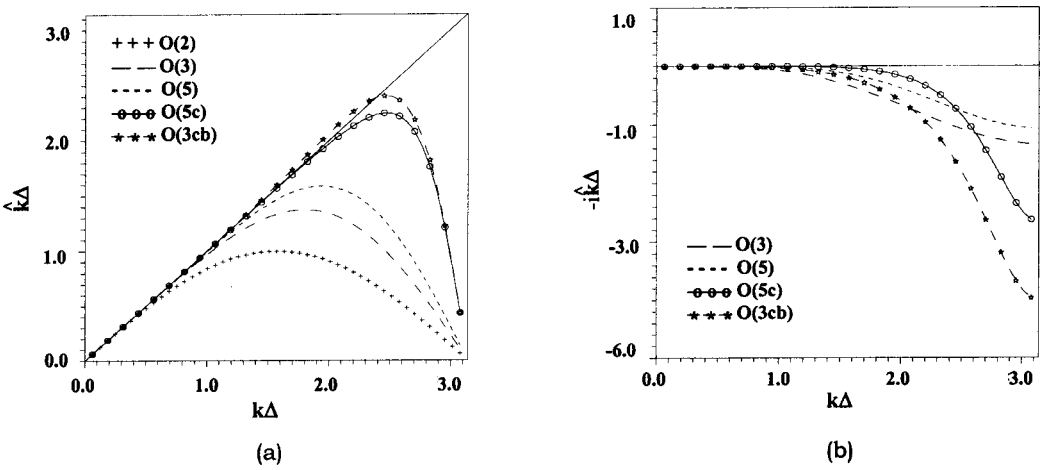

Fig. 1 Dispersive (*a*) and dissipative (*b*) errors of the present compact upwind differences compared to three explicit schemes; O(2) explicit second-order central differences, O(3) explicit third-order upwind, O(5) explicit fifth-order upwind, O(5c) compact fifth-order upwind, and O(3cb) one-sided compact third-order upwind

instabilities. Adams and Shariff [20] demonstrated these characteristics by testing both low and high dissipative hybrid schemes for shock-turbulence interaction problems over uniform grids. They noted that their compact upwind biased scheme preserved a good dispersive nature while adequately extinguishing poorly resolved turbulence. Herein, a compact upwind scheme that holds strong resolving power for the non-conservative forms of the convective derivative is tested for resolving the turbulent wake. In particular, the stencil is three-point implicit and four-point explicit whose spatial accuracy is fifth-order. For the general velocity variable q, its derivative (q') in the curvilinear coordinate framework (unit spacing) is evaluated at grid point (i) by

$$\alpha q'_{i+1}+\beta q'_i+\gamma q'_{i-1}=aq_{i+1}+bq_i+cq_{i-1}+dq_{i-2} \quad (6a)$$

where $\langle \alpha,\beta,\gamma,a,b,c,d\rangle=\langle 3{,}18{,}9{,}10{,}9{,}-18{,}-1\rangle$ for $U^k>1$. Normal to no-slip boundaries, this compact scheme can approximate the convective derivative no closer than the second internal point.

Adjacent to walls, most developers commonly treat the convective derivative with low-order one-sided differences or explicit filtering. These approaches always lead to poor resolution qualities near the wall that degrades the adjacent field accuracy. One can compensate this loss with finer grid spacing, but we know that this simple fix dramatically raises the computational requirement and taxes stability. Herein, we choose to apply one-sided compact third-order upwind differences to the first field point that closely matches the resolution efficiency (or slightly better) of the field solution. This stencil appears as

$$q'_i+\lambda q'_{i+1}=rq_{i+1}+sq_i+tq_{i-1} \quad (6b)$$

where $\langle \lambda,r,s,t\rangle=\langle 2{,}2.5{,}-2{,}-0.5\rangle$ when $U^k>0$. An important consequence of combining Eqs. (6*a*) and (6*b*) is that the implicit tridiagonal entries are automatic for the field points with only a simple Dirichlet contribution from the boundary.

Upwind Interpolation and Cell-Centered Differencing. An alternate choice to a compact upwind stencil is cell-centered Padé-type differencing for evaluating the conservative convective derivative. However, we found that coupled high-order Padé-type differencing for the interpolation and differencing phases generally lead to divergent solutions starting in the wake regions of coarse gridding. Specifically, ''wiggles'' appeared early in the pressure contours that were largely attributed to the redistribution of poorly resolved small-scale energy. Numerical stability was strongly enhanced by switching to compact upwinding for computing the cell velocity fluxes. This idea tackles regions of expected poor resolution especially near vortex exit. We found that upwind interpolation ($\tilde{q}$) of the node velocity variables to compute the cell fluxes dampened the spurious oscillations that were seen when using the respective Padé stencil. The contravariant velocity components served to orient the stencil direction. For fourth-order accuracy, the backward scheme ($U^k>0$) appears as

$$\alpha\tilde{q}_{i+1}+\beta\tilde{q}_i+\gamma\tilde{q}_{i-1}=aq_{i+1/2}+bq_{i-1/2}+cq_{i-3/2} \quad (7)$$

where $\langle \alpha,\beta,\gamma,a,b,c\rangle=\langle 1{,}10{,}5{,}5{,}10{,}-1\rangle$. Regardless of the flow direction, this stencil cannot be applied any closer to nonperiodic boundaries than the second internal cell face. Tests showed that a one-sided third-order interpolation for the first cell face is inconsistent with the adjacent field stencil (singularities arise). To avoid this complication we evaluated the flux vector on first cell face off all nonperiodic boundaries explicitly to the second-order.

Staying with fourth-order field accuracy, the conservative convective flux (f') is now evaluated at each node point given the interpolated flux (f) according to

$$\alpha f'_{i+1}+f'_i+\alpha f'_{i-1}=a(f_{i+1/2}+f_{i-1/2}) \quad (8a)$$

with $\langle \alpha,a\rangle=\langle 22{,}24\rangle$. Like the fifth-order scheme, we can use compact third-order accuracy near the boundaries

$$f'_i+\alpha f'_{i+1}=rf_{i-1/2}+sf_{i+1/2}+tf_{i+3/2} \quad (8b)$$

with the coefficients $\langle \alpha,r,s,t\rangle=\langle -1{,}1{,}2{,}-1\rangle$.

Resolving Power. Differencing the DNS and LES convective derivatives introduces a low-pass filter that lowers the accuracy of resolved wave numbers $k<k_{\max}$; $k_{\max}$ is the cutoff wave number defined by the respective grid spacing ($k_{\max}=\pi/\Delta_g$). This reduction varies according to the resolving power of the numerical approximation that is selected for the convective terms. We can quantity this power by performing a Fourier analysis of the above stencils and then examine the resultant modified wave numbers ($\hat{k}$). Each upwind scheme will produce both real and imaginary expressions for $\hat{k}$ that reveal its dispersive ($\hat{k}_r$) and dissipative ($\hat{k}_i$) nature, respectively. Conversely, the Padé-type stencils are strictly dispersive.

The resolving power of the compact upwind stencils (Eqs. (6)) is compared in Fig. 1 to an explicit second, third, and fifth-order approximation. One can see that both upwind schemes share similar resolution properties that excel well beyond the explicit evaluations. This simple fact is a distinct advantage over many similar approximations by guaranteeing consistent resolution efficiency

Table 1 Modified cutoff wave numbers k_r and k_i (scaled by $k_{max}=\pi/\Delta$) where all resolved waves are at least 90% resolved (see Fig. 1 for notation)

Stencil	O(2)	O(3)	O(5)	O(5c)	O(3cb)
$\tilde{k}_r\Delta/\pi$	0.25	0.59	0.45	0.53	0.72
$\tilde{k}_i\Delta/\pi$	···	0.37	0.53	0.66	0.47

throughout the entire field; especially near the boundaries. Their spectral-like character is further given in Table 1, which lists the scaled cutoff wave number ($\lambda=\hat{k}/k_{max}$) where the resolving efficiency (ε) drops to about 90%; i.e., $\varepsilon_r=\hat{k}_r(\lambda\pi)/\lambda\pi$, [4]. By accepting this cutoff as a reasonable benchmark, the table shows a 50% gain in resolving power of the fifth-order compact upwind differences over its explicit counterpart and at least a 200% better efficiency than explicit second-order central differences.

The dissipative error of the proposed compact upwinding is compared to explicit third-order and fifth-order upwind differences in Fig. 1(*b*). Both compact approximations soften attenuation of the oscillations until much higher wave numbers. For instance, the fifth-order scheme lowers the dissipation error for $k\Delta<0.80\pi$ and $k\Delta<0.85\pi$ compared to the explicit fifth and third-order upwinding, respectively. This benefit is emphasized in Table 1 where the dissipation error of this compact scheme is reduced by 25% compare to its explicit counterpart for waves that are 90% resolved. An unfortunate consequence of using compact third-order upwinding is that its dissipative error will severely damp most of the fine-scale fluctuations near the walls given the same spacing as the field. Moreover, contributions from the SGS model will most likely be negligible near the walls. To minimize these adverse effects, we must cluster the grid lines near the wall. This practice is not uncommon because the flow gradients are highest there. But according to Fig. 1(*b*), the first point spacing should be at least 20% finer than the immediate adjacent field spacing to circumvent overdamping of the fluctuating flow components near the wall.

When interpolation (or explicit filtering) is executed prior to the differencing approximation, the respective wave numbers are modified twice. We can quantify the resultant values by including the transfer function that is associated with the interpolation (or pre-filtering) phase. In terms of the present grid molecule involving interpolation, this function measures the fraction of the wave's amplitude that is transmitted from the node points to the cell interfaces. In our analysis, it does not matter whether we pre or post-interpolate if the boundary conditions are assumed to be periodic. Pre-interpolating evaluates the convective fluxes as

$$G\tilde{q}=Aq \tag{9}$$

where the transfer function (T_r) of any wave is synonymous with the matrix $G^{-1}A$. The Padé differencing stencil operates on the interpolated quantities as

$$H\tilde{q}'=B\tilde{q} \tag{10a}$$

or

$$\tilde{q}'=(G^{-1}A)(H^{-1}B)q. \tag{10b}$$

Fourier analysis of a single $\tilde{q}'$ wave leads to the modified wave numbers shown in Fig. 2 for the various stencils studied herein. This figure also shows the resultant wave numbers of explicit sixth-order and compact eighth-order filtering acting before compact fourth-order differencing. Clearly, the net resolving efficiency of the compact fourth-order approximation could drop below simple explicit second-order differencing at the higher wave numbers ($k\Delta>3\pi/4$) if the stencil operates on sixth-order explicitly filtered quantities. This fact easily explains why one would gain an enhanced stability in the corresponding DNS and LES computations. As an alternative, we can control the high wave number energy with only a 10% loss of resolving power (Table 2) if standard compact interpolation ($4ci$) is introduced rather than explicit filtering.

But the coupling of fourth-order Padé schemes for the interpolation and differencing phases of the convective derivative approximation is still well below reasonable resolving efficiency. Our resolving efficiency is strong for only about one-half ($\lambda\sim0.53\pi$) of the resolved wave numbers. Alternatively, we can gain substantial resolution power and control stability if the interpolation phase incorporates the fourth-order upwind stencil in Eq. (7). We will not lose the option of evaluating the conservative form of the convective derivative by Padé differencing the cell fluxes. The resultant modified wave numbers are much like that of the compact fifth-order upwind stencil. Moreover, nearly 3/4s ($\lambda\sim0.72\pi$) of the waves are well resolved. This gain is attributed to the substantial improvement in the transfer function of compact upwind interpolation. Only a 3% loss of wave amplitude is realized at $\lambda\sim0.72\pi$ (90% resolving efficiency) for the upwind interpolation phase versus a 32% reduction using a fourth-order Padé scheme. Controlling the high wave number aliasing and underresolved energy is handled by the dissipative error introduced during the upwind interpolation phase. As shown in Fig. 2(*c*), this error is scattered over the upper 1/3 of the resolved waves.

Wake Simulations

The turbulent wake of the circular cylinder holds a wealth of complex flow behavior. The historical evidence unveils three well-known regimes that constitute distinct physics. In the immediate wake, the formation region is relatively quiescent in view of its streamwise coherency. In addition to the streamwise and transverse grid resolution, accurate prediction of the turbulent statistics in this regime is equally dependent on the flow domain spanwise length and respective point spacing. Adjoining the vortex formation regime is an upper and lower free-shear layer that house the defining physics of transition to turbulence. Properly resolving transition in these layers requires concentrated streamwise and transverse gridding much finer than the adjacent outside inviscid and inside formation regions. Beyond these two domains lies the Karman vortex street.

Resolving the structural content of these three regimes at all scales is well beyond the scope of our intent. The impetus herein is achieving accurate and stable solutions of the wake statistics by implementing spectral-like differencing stencils in the conservative and non-conservative forms of the convective derivative. Changing either the derivative form or the differencing stencil can control stability of the computation, but the resolution character of the latter largely governs the solution accuracy. Through previous experimental measurements and computational results, Kolmorgorov scaling is provided at specific points within the three regimes of the near wake. Herein, this information permits careful comparisons of the spectral content of the computed wake statistics relative to wave number cutoff.

Spatial Resolution. To resolve the turbulent statistics of this canonical flow by DNS computation at Re=3900 ($Re=UD/\nu$), a fixed symmetric O-type grid was generated with $321\times241\times64$ points in the streamwise (ξ lines), transverse (η lines) and spanwise directions (z or ζ lines), respectively. Jordan [5,9] discussed the specific spatial resolution characteristics of this structured grid that justify its use for a DNS computation at Re=3900. For the present O-type grid, the circular boundaries emanate 12 diameters from the cylinder center and a transformed set of Euler equations were found satisfactory to exit the shed vortices with no pressure reflections directed upstream. A branch cut was inserted upstream of the cylinder to circumvent additional numerical complexities needed to resolve the wake turbulence across the cut.

Spacing along the circumferential η-lines is uniform, but these lines were clustered toward the cylinder surface to avert biasing resolution of the dissipation rate, [5,9]. The 64 points in the spanwise direction are uniformly distributed over πD length with pe-

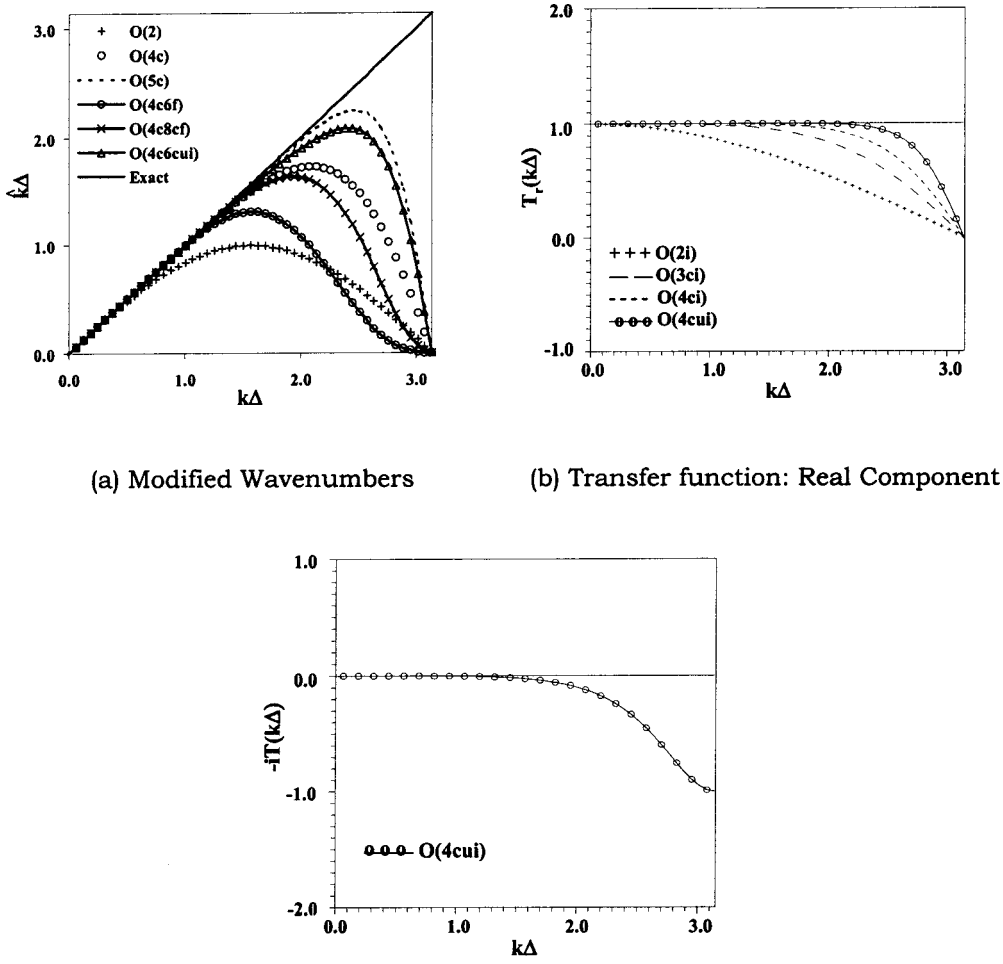

Fig. 2 Differencing, interpolation and filtering stencils; notation O–indicates order; 2, 3, 4, 5 and 6–order number; c–compact differencing; cf–compact filtering; i–explicit point interpolation; f–explicit filtering; ci–compact interpolation; cui–compact upwind interpolation. Example, O(4c4cui) denotes fourth-order compact differencing of fourth-order compact upwind interpolated quantities.

riodic end conditions. According to the empirical expression $\lambda_z/D \sim 20\,\mathrm{Re}^{-1/2}$ by Mansy et al. [21] and Williamson [22], this spacing resolves each spanwise wavelength (λ_z) of the large-scale streamwise eddies by a minimum of seven points of fourth-order accuracy. We note that the scaled inertial subrange of the wake turbulence is fully resolved up to nearly five diameters downstream.

The LES grid houses twice the grid spacing in all directions ($161\times121\times32$ points). Comparatively, this grid yields less than 1/2 the number of computational points generated for case 2 by Kravchenko and Moin [23] who solved this flow by a B-spline technique. The resolved scales of the present LES grid include a portion of the inertial subrange up to seven diameters downstream. Spanwise, cutoff lies near the lower end of the inertial subrange. Thus, the combined dissipative mechanism of the grid-scale numerics and the SGS model are expected to stabilize the computations by sufficiently dissolving the energy scales over the latter 40% of the near wake grid.

Table 2 Modified cutoff wave numbers k_r (scaled by $k_{max}=\pi/\Delta$) where all resolved waves are at least 90% resolved (see Fig. 2 for notation)

Stencil	O(2)	O(4c)	O(4c6f)	O(4c4ci)	O(4c4cui)	O(5c)
$k_r\Delta/\pi$	0.25	0.59	0.45	0.53	0.72	0.79

Inasmuch as the instantaneous flow constitutes three elements (global mean, periodic mean, and random), the random field statistics are acquired by phase averaging. Below, the computed turbulent energy spectra depict averaging of three datasets. Each dataset is in-phase according to the measured Strouhal number St=0.21, [24]; St=fU/D where f is the shedding frequency of the shed Karman vortices. Averaging three datasets (with a 50% overlap) reduced the predicted dissipation rate error in the DNS computations to within 2% of the experimental measurements. This procedure produced over 300 spanwise realizations for determining the energy spectra from the DNS results where each computational point is treated as a separate event.

Low-Re Simulations: Re=200. Before attempting to resolve the turbulent wake physics, we desire to perform several preliminary tests to essentially assess the solution accuracy of the proposed stencils as applied to the various forms of the convective derivative. Three-dimensional simulations at Re=200 will serve our intention where the near wake is laminar, but unsteady. The streamwise and transverse grid resolutions (121×99) are identical

Table 3 Parameters from simulations of the cylinder wake at Re=200 (see Fig. 2 for notation); C_L: lift coefficient, C_D: drag coefficient, St: Strouhal number, l_c: formation length, C_{pB}: base pressure coefficient, and θ_s: separation angle

Parameters	Experiments	Computations					
		81×85×3 [25]	$D(4c4ci)$	$D(4c4cui)$	$A(5c)$	$R(4c4cui)$	$K(4c4cui)$
C_L	···	±0.65	±0.51	±0.18	±0.38	±0.52	±0.34
C_D	1.3 Wille [31]	1.31±0.04	1.39±0.025	1.29±0.005	1.35±0.05	1.44±0.08	1.31±0.03
St	0.182±0.03 Norberg [32]	0.20	0.201	0.195	0.195	0.195	0.195
l_c	1.4 Gerrard [33]	···	1.44	1.35	1.35	1.47	1.45
$-C_{pB}$	0.86 Norberg [32]	···	1.09	1.05	1.13	1.36	1.09
θ_s	115°±1° D&H [34]	···	112	113	113	113	113

References cited in Table are [31–34].

to the grid spacing tested by Jordan and Ragab [6]. To capture the spanwise fluctuations, we added 32 points equally distributed over πD length in the z-direction.

Table 3 lists several mean characteristics (time-averaged over seven shedding cycles) that are commonly compared when testing the accuracy of proposed solution methodologies for the cylinder low-Re wake. Experimental measurements from various sources are included in the table as well as the computations by Rosenfeld et al. [25] who used a second-order-accurate technique over a slightly coarser grid (81×85×3). Apart from the rotational form, the predicted mean properties of each simulation closely agree with the experimental evidence. The inaccuracies given by the rotational form are directly attributed to the large truncation error emanating normal from the cylinder surface. The largest error is evident in the predicted mean base pressure coefficient (C_{pB}), which is also depended on the neighboring streamwise and spanwise resolutions. However, at this Re this parameter is only weakly depended on the spanwise fluctuations since they were typically less than 10% of the mean streamwise velocity inside the formation region.

DNS and LES Results. In the DNS computations, the fifth-order compact stencil was combined with standard fourth-order Padé differencing in the spanwise direction; notation A(5c4ci). Knowing that wavenumber cutoff is beyond the inertial subrange throughout the formation region of the DNS grid at Re=3900, we would not expect notable improvements in the energy spectra predictions by increasing the spatial accuracy of the advective derivative (ξ,η-directions) from the explicit third-order to the compact fifth-order scheme. This deduction is clearly evident in the comparisons to the experimental data along the circumferential line $r/D=3.0$ as illustrated in Fig. 3(a). Cutoff at this radius is $k\eta_d=0.125$, which extends into the dissipation range of the energy spectra. Although a minor improvement is indicated, sufficient spatial resolution is provided to alleviate overdamping of the finest resolved scales by either scheme.

Further downstream at $r/D=7.0$ (Fig. 3(b)), where cutoff $k\eta_d=0.07$ lies near the upper bound of the inertial subrange, the superior resolving power of the compact fifth-order upwind stencil becomes apparent over the explicit third-order scheme. The dissipative error of the third-order stencil shows distinct signs of excessive damping over nearly 1/2 of the grid-scales. At cutoff, the dissipation rate in Kolmorgorov units of the third-order scheme is only 1/3 of that resolved by the compact stencil (Fig. 4(a)). The truncation error of the former stencil clearly governs dissipation of the energy forward scatter when cutoff lies within the inertial subrange. The effects on turbulence production are equally dam-

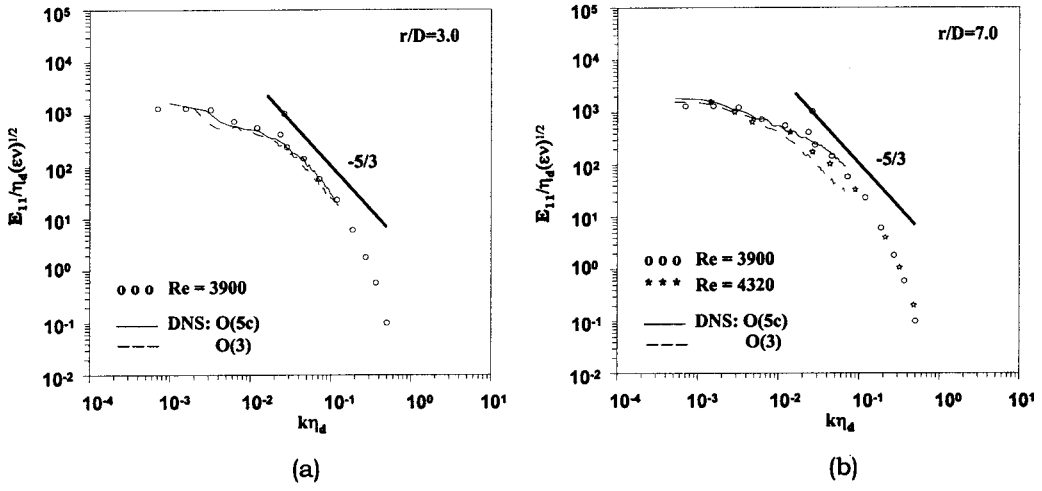

Fig. 3 DNS results of the explicit third-order and compact fifth-order differencing (advective derivative) of the streamwise energy spectra (in Kolmorgorov units) compared to the experimental measurements, [24,26]

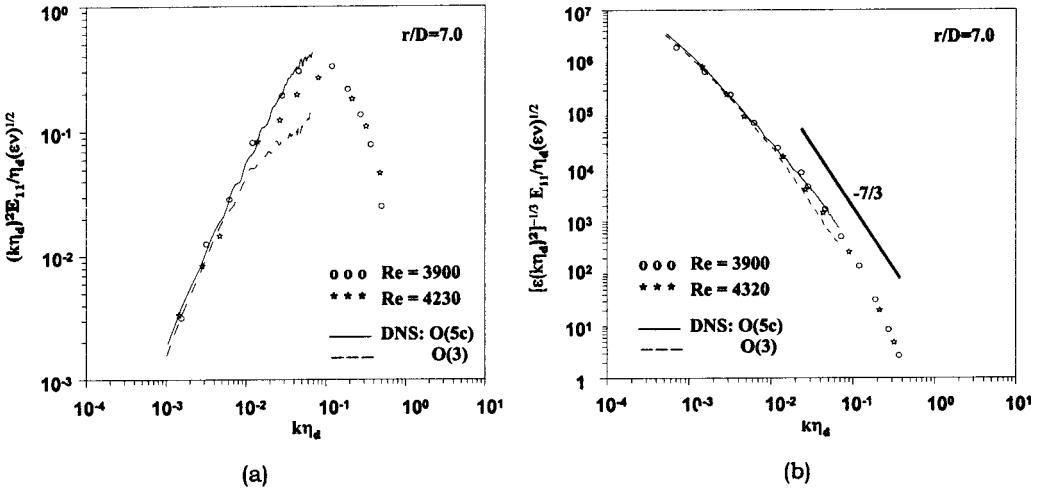

Fig. 4 DNS results of the explicit third-order and compact fifth-order differencing (advective derivative) of the streamwise dissipation rate and turbulence production (both in Kolmorgorov units) compared to the experimental measurements, [24,26]

aging. As shown in Fig. 4(*b*), the energy produced in the near wake at this downstream location is only 1/2 of the experimental data. Conversely, the truncation error of the compact fifth-order stencil shows no marked degradation on the resolved production and dissipation of turbulence even when the cutoff wave number extends into the inertial subrange of the corresponding energy spectra.

In the following LES results, upwind interpolation was necessary in the spanwise direction to maintain converging solutions; notation A(5c4cui). Phased-averages of the streamwise total energy spectra (resolved plus model) are compared to the experimental measurements, [24,26], in Fig. 5(*a*) at downstream radii $r/D=1.0$ (formation region) and $r/D=5.0$ (vortex street). This figure includes the energy profile of explicit fifth-order upwind differencing for the convective derivative at location $x/D=5.0$ as reported by Beaudan and Moin [27]. Their computations as well as the experimental measurements were converted from the frequency spectrum to the wave number spectrum using Taylor's hypothesis, [24]. Interestingly, their explicit upwinding still severely damped the finest resolved wavenumbers compared to the present compact fifth-order stencil even though they implemented a finer spatial resolution ($144\times136\times48$ grid). The present LES profile at $r/D=5.0$ shows a slight degradation of the predicted spectral energy that is largely attributed to the cutoff wave number lying inside the lower bound of the inertial subrange ($k\eta_d=0.041$). Specifically, the spectral energy is under-predicted at cutoff by about 50%. The figure also shows the phased-averaged energy spectra of the corresponding SGS field. Encouraging signs are indicated at the lower wave numbers where the model contributions improve with decreasing spatial resolution. Unfortunately, opposite contributing characteristics are evident at the resolved moderate to high wave numbers. Overall, the model contributions to the total energy field are essentially negligible.

A striking degradation of resolved energy only became apparent when the advective derivative in the spanwise direction was switched from the A(4cui) scheme to the compact fifth-order stencil A(5c). The harmful effects that were originally discovered by Beaudan and Moin [27] are clearly reproduced in the energy spectra, which are shown in Fig. 5(*b*). We can observe discernible damping of the transverse spectra (E_{22}) even when the inertial subrange is fully resolved at the grid-scale level ($k\eta_d=0.142$ at $r/D=1.0$). Notably, the SGS model spectra are equally affected

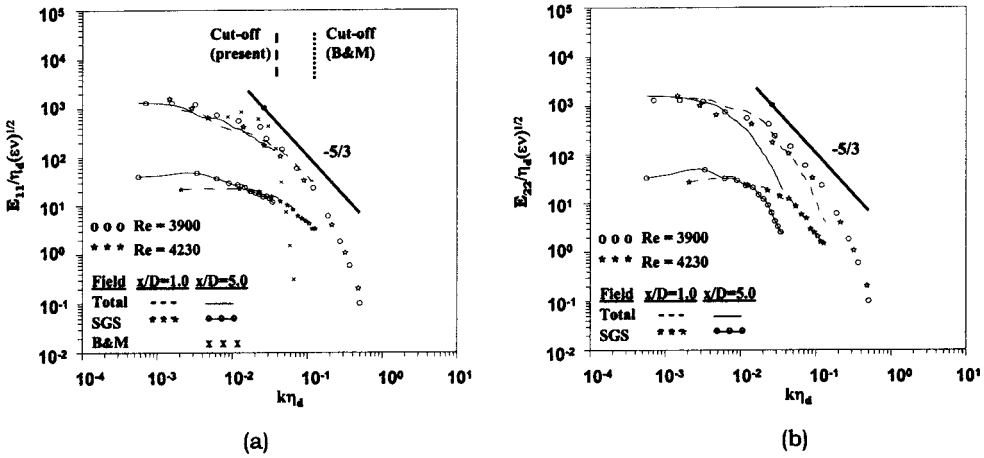

Fig. 5 Phase-averaged LES computations using the compact stencil A(5c4cui); (*a*) comparisons of the streamwise energy spectra to the experimental measurements, [24,26] and LES results of Beaudan and Moin [27], (*b*) switch from fourth-order Padé to compact fifth-order stencil in spanwise direction A(5c5c)

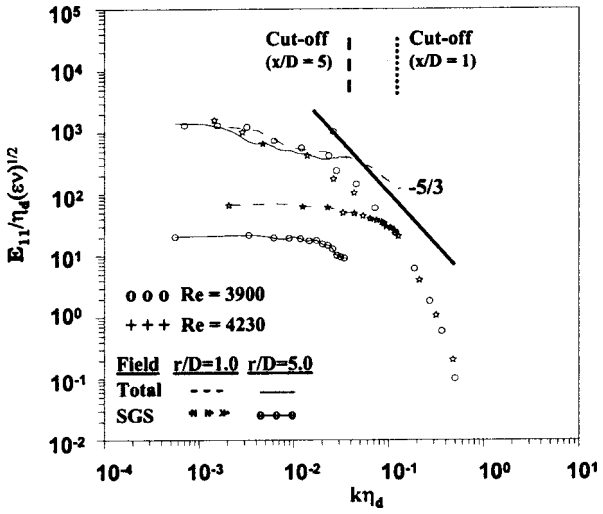

Fig. 6 Comparisons of the streamwise energy spectra to the experimental measurements [24,26] along radii $r/D=1.0$ and $r/D=5.0$; scheme K(4cui)

by the stencil change. This result is expected because the SGS model contributions are determined through explicit filtering the finest scales of the resolved field.

The streamwise energy spectra as predicted by the K(4cui) scheme is compared to the experimental measurements, [24,26], in Fig. 6. The notation K(4cui) denotes cell-centered fourth-order Padé differences with fourth-order upwind interpolation as applied to the Arakawa form of the convective derivative in all directions. Similar to the previous fifth-order stencil for the advective derivative (Fig. 5(*a*)), the K(4cui) scheme gives the correct spectral magnitudes and distribution of the resolved energy-bearing scales of both the fine-grid formation region and coarse-grid wake. However, this conservative scheme also generated an excessive energy buildup over the upper 25% of resolved wave numbers at $r/D=1.0$ that comprise the inertial subrange ($k\eta_d=0.142$). While the stencil is apparently stable enough to insure convergent solutions over coarse grid-spacing, the SGS model coupled with the inherent dissipative element of upwind interpolation does not sufficiently control aliasing of the finest grid scales. Moreover, the eddy-viscosity model responds to aliasing by over-contributing broadband SGS energy for this same range of resolved wave numbers. We can further observe that the SGS model performance is counter-productive, meaning that contributions degrade with downstream distance over all resolved scales.

The instantaneous spanwise structure of the turbulent wake is an excellent indicator of the expected energy spectra. Evidence of this fact is displayed in Fig. 7 for the three stencils just discussed where the pressure contours resemble $2D$ spanwise-streamwise cuts taken along the downstream symmetry plane ($x/D \geqslant 0.5$). We first note that each stencil resolves the largest scales equally as indicated by their similar maxima and minima. However, the left figure, which denotes compact fifth-order differences in all directions, clearly lacks the intermediate and fine turbulent scales that constitute the resolved inertial subrange within the formation region. Conversely, the K(4cui) scheme results as shown in the center figure are plagued by aliasing in the vortex street due in an insufficient grid resolution and under-achieving SGS model. The turbulent physics of the wake are best resolved by the present grid-spacing using the compact fifth-order stencil in the wake directions coupled with the fourth-order cell-centered Padé scheme (with upwind interpolation) for differencing the spanwise convective derivative; notation A(5c4cui). These results suggest that given permanent restrictions on generating sufficient spatial resolution throughout the turbulent wake, a suitable differencing strategy is a spectral-like upwind scheme for the convective derivative in the direction of degrading spatial resolution with momentum and energy conservation satisfied in the spanwise periodic direction.

We can further explore the resolution efficiency of the A(5c4cui) scheme by comparing the total Reynolds stresses and mean streamwise velocity (Fig. 8) transverse to the wake centerline to the hot wire measurements, [28], and previous LES results, [27,29,30]. Apart from the peak values, the present normal stress distributions within the formation region closely agree with the fine-grid second-order LES results. However, the peak experimental values are replicated to within 5% by the A(5c4cui) scheme. The mean velocity profiles indicate a U-shape that differs from the experimentally measured V-shape. Recently, this difference has received much attention and is argued to be attributed to the spanwise resolution. Kravchenko and Moin [23] achieved the U-shaped profile by using 48 points equally distributed over πD length. Their LES computations were second-order accurate and divergence-free with fine O-type gridding. But as illustrated in the

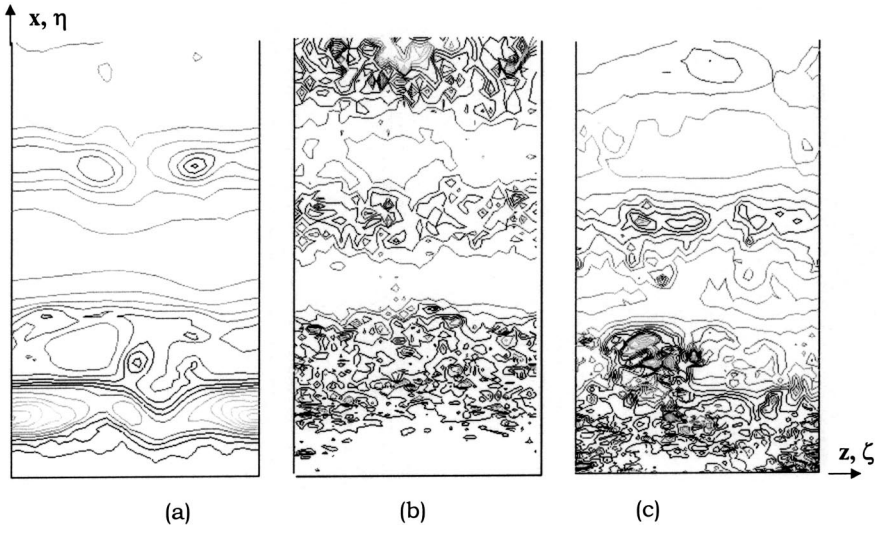

Fig. 7 Spanwise-streamwise instantaneous pressure contours; stencil A(5c5c), max. 0.41, min. −1.5, incr. 0.065; (*b*) stencil K(4cui), max. 0.15, min. −1.5, incr. 0.055; (*c*) stencil A(5c4cui), max. 0.30, min. −1.5, incr. 0.06

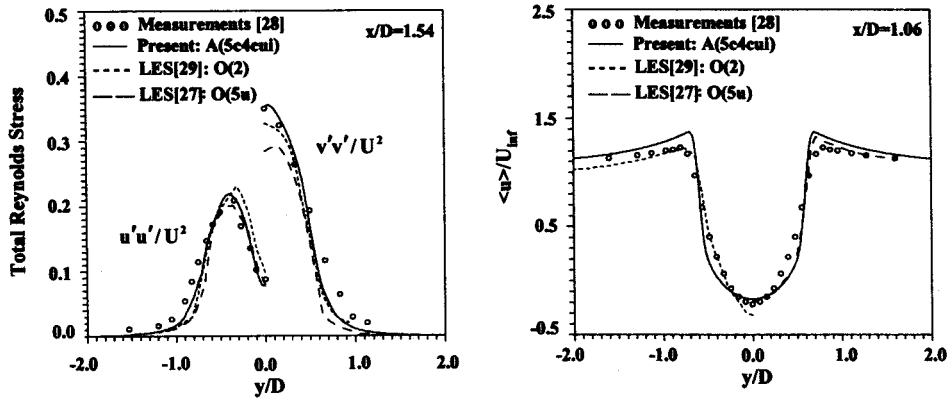

Fig. 8 Comparisons of the time-averaged streamwise ($u'u'$) and transverse ($v'v'$) total Reynolds stress using the A(5c4cui) scheme to the experimental measurements, [37], and previous LES results, [32,33]

figure, these same profiles can be predicted with 32 points (33% reduction) if one substitutes the fifth-order compact stencil for discretizing the advective form of the convective derivative. We note that the LES computations shown in the figure over-predict the mean streamwise velocity within the free-shear layers. This result is a direct consequence of the O-type grid where concentrating sufficient resolution locally within the shear layers is a difficult task.

Apart from the observed disparity in the energy spectra and turbulent structure, we can still pose a final argument favoring the two upwind strategies of differencing and interpolation. The parameters list in Table 4 best gauge the accuracy of the numerics and the adequacy of the wake's grid resolution. Each LES computation listed in the table implemented a spanwise length (L_z) of π diameters. Both upwinding strategies generated comparable mean values for these cylinder wake parameters within the experimental uncertainties. In view of the three analogous computations, this evidence indicates that one can attain equivalent accuracy with less spatial resolution by substituting as the convective element either compact fifth-order upwinding for approximating the nonconservative advective derivative or the cell-center fourth-order stencil for differencing the conservative Arakawa term. However, either choice must be coupled with a conservative stencil in the spanwise periodic direction.

Final Remarks

Today, fluid dynamists who are attempting to resolve the turbulent wake structure and statistics of bluff-bodies have essentially two core options of control when implementing a DNS or LES methodology. Over the past decade, we have learned much about the requirements of one option for improving our predictive accuracy; namely, the grid resolution. Most notably, accurate prediction of the near wake's streamwise pressure field when using discretization techniques demands sufficient length and spacing width in the spanwise direction to resolve the turbulent content of the local contributing structures. Moreover, the far-field vortex exit boundary should be placed sufficiently downstream (at least ten diameters beyond the formation region) to permit use of coarse grid spacing and approximating flow boundary conditions outside the field of interest.

Table 4 Mean parameters from simulations of the cylinder wake at Re=3900 (see Table 3 for parameter notation); 1: Ref. [27], 2: Ref. [29], 3: Ref. [30], 4: advective form (Stencil 5*c4cui*), 5: Arakawa form (Stencil 4*c4cui*), 6: advective form (Stencil 5c5c)

Parameter	Experiment	LES Computations ($L_z=\pi D$)					
		$144\times136\times48^1$	$165\times165\times32^2$	9×10^5 cells^3	$161\times121\times32^4$	$161\times121\times32^5$	$161\times121\times32^6$
C_D	0.98±0.05 Norberg [35]	1.00	1.07	1.31	1.04	1.01	1.18
St	0.215±0.005 Cardell [36]	0.203	···	0.216	0.214	0.195	0.195
C_{pB}	−0.90±0.05 Norberg [35]	−0.95	−1.01	···	−0.97	−0.94	−1.23
l_c	1.33±0.2 Cardell [36]	1.36	1.20	1.00	1.28	1.32	1.41
$C'_{p_{\max}}$	0.08 (Re=5,000) Norberg [32]	···	···	···	0.067	0.061	0.179
u'_p	0.21 Lourenco&Shih [28]	0.18	···	···	0.23	0.25	0.40
θ_s	85±2 Son et al. [37]	86	88	···	85.4	85.4	85.4

References cited in Table are [28], [32], [35–37].

The second option of choice that strongly influences the solution accuracy certainly deserves more attention than the preceding one. This option was the focus of the present development. Previously, we learned that explicit upwinding for discretizing the convective derivative is suitable only under fine gridding of DNS quality. This fact is confirmed under the present DNS predictions of the turbulent wake where explicit third-order upwinding and compact fifth-order upwinding attained equal results of turbulent spectral energy only when the respective inertial subrange was fully resolved at the grid-scale level. These stencils approximated the advective form of the convective derivative for solving the incompressible wake flow of the circular cylinder at the subcritical Reynolds number of Re=3900.

• But the present compact fifth-order upwind stencil (with compact third-order upwinding for the first field point off the wall boundary) holds spectral-like resolution power far superior than its companion explicit schemes. This characteristic proved exceptional when wave number cutoff of the grid-scales approached the upper bound of the inertial subrange. The inherent dissipative element associated with this upwind stencil as given by the truncation error provided enough damping in the poorly resolved turbulent regions near vortex exit to sustain convergence without discernible ''wiggles'' in the local instantaneous pressure contours. Overall, the stencil relaxes the CPU requirement of the DNS computation by properly resolving the wake spectral physics at wave number cutoff that approaches the upper limit of the inertial subrange.

The present LES simulations, as well as numerous previous works, provide us with some useful insight toward resolving turbulent wakes. But high-order symmetric stencils breed instabilities when they are applied to the divergent form of the convective derivative over coarse spatial resolution.

• The present compact fourth-order upwind interpolation of the nodal quantities that provides the convective flux for symmetric cell-centered stencils supplies sufficient dissipation of the numerical instabilities to maintain converging solutions. However, we note that its inherent dissipative element coupled with the dynamic form of the SGS model lacked full control over aliasing when the wave number cutoff fell within the lower limit of the inertial subrange in the energy spectra; such as the near wake exit boundary.

Ensuring that wavenumber cutoff lies within the inertial subrange in the spanwise direction quickly taxes the CPU requirement. Consequently, most gridding of bluff-body wakes (including the present grid) under-resolve the inertial subrange in the spanwise direction. The grid cells near the body typically own aspect ratios much higher than those further downstream. When attempting to invoke the spectral-like fifth-order upwind stencil in all directions, the spectral distributions showed excessive damping that extended well into the energy range. Loss of this energy was due to the coarse spanwise grid-scales and lead to under-predicted mean pressures in the formation region and consequently an over-predicted mean drag coefficient.

• The correct energy spectral distributions and mean parameters of the wake came when the fifth-order upwind stencil in the spanwise direction was replaced by the fourth-order cell-centered Padé approximation with fourth-order upwind interpolation. This final strategy for approximating the nonlinear convective derivative supplies the proper dispersive and dissipative properties of each stencil given a simple structured grid-scaling of the turbulent wake.

We close these remarks with the following thought. Attempts to improve the statistical contributions of the dynamic SGS model proved futile by simply raising the resolving efficiency of the grid scales. Outside of the critical damping just discussed, the spectral distribution and low magnitudes of the model energy were essentially independent of the tested convective derivative or stencil. Conversely, a close look at the instantaneous turbulent eddy viscosity revealed levels increasing with degrading spatial resolution and exceeding the molecular viscosity by a order-of-magnitude when the inertial subrange was largely unresolved. This observation suggests that the dynamic eddy-viscosity form of the SGS model can respond to stabilize the LES computation in the coarse grid regions of the turbulent wake when one improves the resolving power of the differencing approximations for the convective derivative at the grid-scale level.

Acknowledgments

The author gratefully acknowledges the support of the Office of Naval Research (Dr. L. Patrick Purtell and Ronald D. Joslin, Program Officers), Contract No. N0001402WX20965, and the In-House Independent Research Program (Mr. R. Philips, Coordinator) at the Naval Undersea Warfare Center Division Newport. Also, this author thanks the NAVOCEANO DoD MSRC facility for use of their SV1 computer systems.

References

[1] Cantwell, B., and Coles, D., 1983, ''An Experimental Study of Entrainment and Transport in the Turbulent Near Wake of a Circular Cylinder,'' J. Fluid Mech., **136**, pp. 321–374.
[2] Wei, T., and Smith, C. R., 1986, ''Secondary Vortices in the Wake of Circular Cylinders,'' J. Fluid Mech., **169**, pp. 513–533.
[3] Platzman, G. W., 1961, ''An Approximation to the Product of Discrete Functions,'' J. Meteorol., **18**, pp. 31–37.
[4] Lele, S. K., 1992, ''Compact Finite Difference Schemes With Spectral-Like Resolution,'' J. Comput. Phys., **103**, pp. 16–42.
[5] Jordan, S. A., 1999, ''A Large-Eddy Simulation Methodology in Generalized Curvilinear Coordinates,'' J. Comput. Phys., **148**, pp. 322–340.
[6] Jordan, S. A., and Ragab, S. A., 1996, ''An Efficient Fractional-Step Technique for Unsteady Three-Dimensional Flows,'' J. Comput. Phys., **127**(0170), pp. 218–225.
[7] Smagorinsky, J., 1963, ''General Circulation Experiments With the Primitive Equations, I. The Basic Experiment,'' Mon. Weather Rev., **91**, pp. 99–164.
[8] Germano, M., Piomelli, U., Moin, P., and Cabot, W. H., 1991, ''A Dynamic Subgrid-Scale Eddy Viscosity Model,'' Phys. Fluids, **3**, pp. 1760–1765.
[9] Jordan, S. A., 2001, ''Dynamic Subgrid-Scale Modeling for Large-Eddy Simulations in Complex Topologies,'' ASME J. Fluids Eng., **123**, pp. 1–10.
[10] Morinishi, T. S., Lund, T. S., Vasilyev, O. V., and Moin, P., 1998, ''Fully Conservative Higher Order Finite Difference Schemes for Incompressible Flow,'' J. Comput. Phys., **143**, pp. 90–124.
[11] Vasilyev, O. V., 1998, ''On the Construction of High Order Finite Difference Schemes on Non-Uniform Meshes With Good Conservation Properties,'' Center for Turbulence Research, Annual Research Briefs.
[12] Tennekes, H., and Lumley, J. L., 1972, *A First Course in Turbulence*, The MIT Press, Cambridge, MA.
[13] Mansour, N. N., Moin, P., Reynolds, W. C., and Ferziger, J. H., 1979, ''Improved Methods for Large-Eddy Simulation of Turbulence,'' *Turbulent Shear Flows I*, Springer-Verlag, New York, pp. 386–400.
[14] Horiuti, K., 1987, ''Comparison of Conservative and Rotational Forms in Large-Eddy Simulations of Turbulent Channel Flow,'' J. Comput. Phys., **71**(2), pp. 343–370.
[15] Arakawa, J., 1966, ''Computational Design for Long-Term Numerical Integration of the Equations of Fluid Motion: Two-Dimensional Incompressible Flow, Part I,'' J. Comput. Phys., **1**(1), pp. 119–143.
[16] Piomelli, U., Ferizer, J. H., and Moin, P., 1988, ''Model for Large-Eddy Simulation of Turbulent Channel Flow Including Transpiration,'' Department of Mechanical Engineering Report, TF-32, Stanford University, Stanford, CA.
[17] Kravchenko, A. G., and Moin, P., 1997, ''On the Effect of Numerical Errors in Large Eddy Simulations of Turbulent Flows,'' J. Comput. Phys., **131**, pp. 310–322.
[18] Ladeinde, F., Cai, X., Visbal, M. R., and Giatonde, D. V., 2001, ''Turbulence Spectra Characteristics of High Order Schemes for Direct and Large Eddy Simulation,'' Appl. Numer. Math. **36**, pp. 447–474.
[19] Visbal, M. R., and Rizzetta, D. P., 2002, ''Large-Eddy Simulations on Curvilinear Grids Using Compact Differencing and Filtering Schemes,'' ASME J. Fluids Eng., **124**, pp. 836–847.
[20] Adams, N. A., and Shariff, K., 1996, ''A High-Resolution Hybrid Compact-ENO Scheme for Shock-Turbulence Interaction Problems,'' J. Comput. Phys., **127**(0170), pp. 218–225.
[21] Mansy, H., Yang, P., and Williams, D. R., 1990, ''Quantitative Measurements of Three-Dimensional Structures in the Wake of a Circular Cylinder,'' J. Fluid Mech., **270**, pp. 277–296.
[22] Williamson, C. H., 1995, ''Vortex Dynamics in the Wake of a Cylinder,'' *Fluid Vortices: Fluid Mechanics and Its Application*, **30**, S. L. Green, ed., Kluwer, Dordrecht, The Netherlands, pp. 155–134.
[23] Kravchenko, A. G., and Moin, P., 2000, ''Numerical Studies of Flow Over a Circular Cylinder at Re_D=3900,'' Phys. Fluids, **12**(2), pp. 403–417.

[24] Ong, L., and Wallace, J., 1996, ''The Velocity Field of the Turbulent Very Near Wake of a Circular Cylinder,'' Exp. Fluids, **333**, pp. 375–402.
[25] Rosenfeld, M., Kwak, D., and Vinokur, M., 1993, ''A Fractional-Step Solution Method for the Unsteady Incompressible Navier-Stokes Equations in Generalized Coordinate Systems,'' NASA Tech Briefs ARC-12621, Ames Research Cneter, Moffett Field, CA.
[26] Uberoi, M. S., and Freymuth, P., 1969, ''Spectra of Turbulence in Wakes Behind Circular Cylinders,'' Phys. Fluids, **12**(7), pp. 1359–1363.
[27] Beaudan, P., and Moin, P., 1994, ''Numerical Experiments on the Flow Past a Circular Cylinder at Sub-Critical Reynolds Number,'' Report No. TF-62, Stanford, University, Stanford, CA.
[28] Lourenco, L. M., and Shih, C., 1993, ''Characteristics of the Plane Turbulent Near Wake of a Circular Cylinder, a Particle Image Velocimetry Study,'' private communication, (taken from Ref. [27]).
[29] Breuer, M., 1998, ''Numerical and Modeling Influences on Large-Eddy Simulations for the Flow Past a Circular Cylinder,'' Int. J. Heat Fluid Flow, **19**, pp. 512–521.
[30] Lubcke, H., Schmidt, S., Rung, T., and Thiele, F., 2001, ''Comparison of LES and RANS in Bluff-Body Flows,'' J. Wind. Eng. Ind. Aerodyn., **89**, pp. 1471–1485.
[31] Wille, R., 1960, ''Karman Vortex Streets,'' Adv. Appl. Mech., **6**, p. 273.
[32] Norberg, C., 1994, ''An Experimental Investigtion of the Flow Around a Circular Cylinder: Influence of Aspect Ratio,'' J. Fluid Mech., **258**, pp. 287–316.
[33] Gerrard, J. H., 1978, ''An Experimental Investigation of the Oscillating Lift and Drag of a Circular Cylinder Shedding Turbulent Vortices,'' Philos. Trans. R. Soc. London, Ser. A, **288**, p. 358.
[34] Dimopoulos, H. G., and Hanratty, T. J., 1968, ''Velocity Gradients at the Wall for Flow Around a Cylinder for Reynolds Numbers Between 60 and 360,'' J. Fluid Mech., **33**, Part 2, pp. 303–319.
[35] Norberg, C., 1987, ''Effects of Reynolds Number and a Low-Intensity Free-Stream Turbulence on the Flow Around a Circular Cylinder,'' No. 87/2, Chalmer University of Technology, Gothenburg, Sweden.
[36] Cardell, G. S., 1993, ''Flow Past a Circular Cylinder With a Permeable Splitter Plate,'' *Ph.D. thesis*, Graduate Aeronautical Laboratories, California Institute of Technology, Pasadena, CA.
[37] Son, J. S., and Hanratty, T. J., 1969, ''Velocity Gradients at the Wall for Flow Around a Cylinder at Reynolds Numbers From 5×10^3 to 10^5,'' J. Fluid Mech., **35**, Part 2, pp. 353–368.

Mixing and Entrainment Characteristics of Circular and Noncircular Confined Jets

Ghanshyam Singh
Research Scholar

T. Sundararajan[1]
Professor
e-mail: tsundar@pallava.iitm.ernet.in

K. A. Bhaskaran
Professor

Department of Mechanical Engineering,
Indian Institute of Technonogy Madras,
Chennai 36, India

The present work deals with the experimental investigation of entrainment characteristics of confined/semiconfined circular and noncircular jets. The jet fluid, after issuing out of a nozzle of circular or noncircular cross section, enters a circular mixing tube of larger area, and during this process it entrains some ambient fluid into the mixing tube. The flow is incompressible and isothermal at a jet Reynolds number of 7200. The experimental results obtained in the study are first validated with the approximate theoretical analysis of Pritchard et al. (1997) and also with the similarity solution proposed by Becker et al. (1963) for circular nozzles. It is observed that the similarity solution is applicable for circular as well as noncircular jets in the region close to the jet axis and away from the nozzle exit plane. The entrainment ratio increases to a maximum value as the jet location is shifted away from the tube inlet; for the configurations studied, enhancement up to 30% has been observed in the entrainment ratio with shift in jet location. For a smaller mixing tube diameter and jet located at the inlet of the mixing tube, the circular jet entrains more than noncircular jets. For a larger mixing tube or shifted jet locations, the noncircular jets entrain more of ambient fluid, in general. Among the different noncircular geometries considered, the jet having the cross section of an isosceles triangle causes maximum entrainment. [DOI: 10.1115/1.1595676]

Introduction

Confined turbulent jets are encountered in several applications such as jet pumps, ejectors, combustors, thrust augmentors in VTOL/STOL aircraft, and noise suppression devices. In the case of combustion appliances such as atmospheric aerated burners, efficient combustion depends on the amount of primary air entrained by the jet issuing from a nozzle or orifice. The shape of the nozzle cross section can play an important role in enhancing the level of air entrainment and the extent of mixing between the fuel jet and primary air within the mixing tube. The present study deals with the experimental investigations of primary atmospheric air entrainment and the spread for circular and noncircular jets issuing into a circular tube. For the sake of simplicity, the jet fluid has also been taken as air.

Flow structure of a confined jet differs fundamentally from that of a free jet because of the facts that the flow momentum is not conserved and adverse pressure gradient caused by confinement considerably alters the entrainment ratio and mixing. But it has been observed that the initial region still bears some of the essential features of a free jet. As pointed out by Rajaratnam [1], the assumption of self-preservation of velocity profile for circular confined jets is also valid in the region downstream of the potential core. In the pioneering work by Craya and Curtet [2], the flow field for confined co-flow jets has been described and predicted with the help of a nondimensional parameter called the Craya-Curtet number (C_t). The experimental studies of Becker et al. [3] have shown that the flow and mixing characteristics of an isothermal confined jet are unique functions of C_t. For confined jets, where the velocity of the co-flowing stream is unknown, Pritchard et al. [4] have proposed an analytical expression for the entrainment ratio based on simple momentum and energy balance.

In recent years, efforts have been made to characterize the jet flow field, using both numerical simulation and detailed experiments (Singh et al. [5], Miller et al. [6], and Dahm and Dimotakis [7]). In order to enhance entrainment and mixing, various techniques have been developed which include active and passive flow control. In active flow control, mixing can be enhanced either by forcing the jet at a frequency close to one of its natural frequencies with the help of acoustic or electromagnetic devices (Zaman and Hussain [8,9] and Husain et al. [10]) or by adding secondary flow with or without swirl upstream of the nozzle (Martin and Meiburg [11]). However, passive flow control is much simpler and economical, and can be achieved in several ways: placement of an obstruction-like body in the near field of the jet, introduction of tabs or notches at the nozzle exit (Tong and Warhaft [12], Rajagopalan and Antonia [13], and Olsen et al. [14]) and changes in the nozzle cross section from circular to noncircular shape (Krothapalli et al. [15], Vandersburger and Ding [16], and Tam [17]).

In the past 15 years, considerable understanding has been gained on flow control using noncircular jets, (Gutmark and Grinstein [18]). In shear flow control methods, the basic idea is to destroy the symmetry present in circular jets, by manipulating the natural development of the small as well as large-scale structures. As a result, the flow becomes fully three-dimensional and gives rise to greater entrainment and mixing.

Most of the studies mentioned above deal with noncircular free jets. Only a few studies are available on the flow characteristics of jets which mix with atmospheric air entrained due to ejector action, in a mixing tube (Kolluri et al. [19]). Typically, this situation arises in a Bunsen burner with air vent open, or in an atmospheric aerated burner. At present, available comparative studies on the turbulent mixing characteristics of circular and noncircular jets of various shapes under similar experimental conditions are rather limited (Mi et al. [20]). Also, a complete understanding of the confined noncircular turbulent jet flow is yet to evolve. In particular, effects of parameters such as the diameter ratio between the jet and mixing tube, jet location with respect to the tube inlet, etc., need to be clarified. Therefore, the main objective of the present study is to experimentally investigate the entrainment behavior of various noncircular jets and compare the features with those of a circular jet of the same flow area.

[1]To whom correspondence should be addressed.

Contributed by the Fluids Engineering Division for publication in the JOURNAL OF FLUIDS ENGINEERING. Manuscript received by the Fluids Engineering Division Apr. 25, 2002; revised manuscript received Mar. 3, 2003. Associate Editor: M. Ötügen.

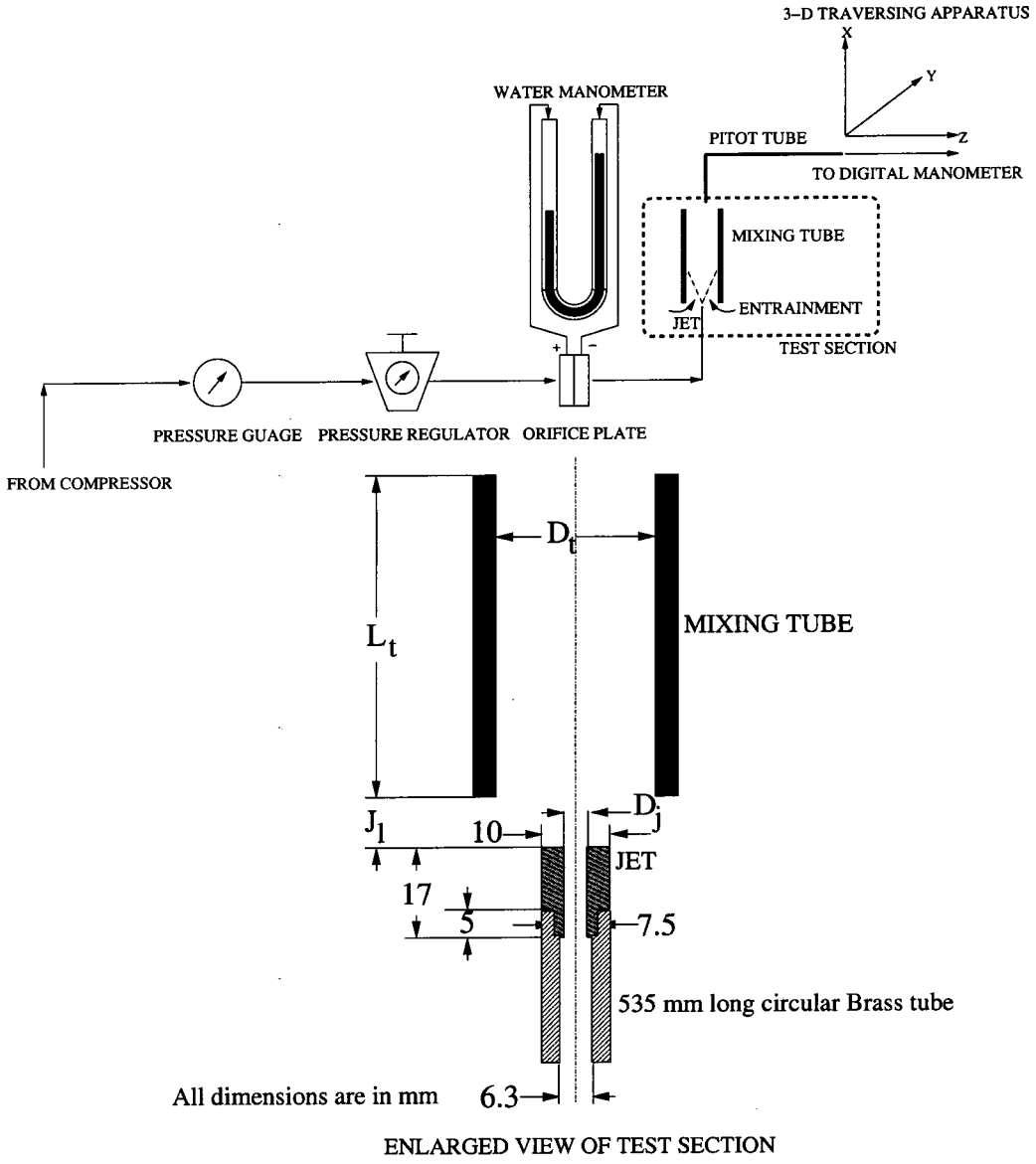

Fig. 1 Schematic diagram of the experimental setup

Experimental Procedure

Experimental Setup. Figure 1 shows the schematic of experimental setup used for the measurement of entrainment. A sharp-edged orifice of 2 mm diameter with standard taps connected to a water-filled manometer has been designed to measure the jet flow rate. It was calibrated using a positive displacement-type flow meter, which can measure flow rate with an accuracy of 1.667×10^{-5} m^3/s. Eight different nozzles were used in the present study, and the relevant dimensions of the noncircular jets, in terms of equivalent circular jet radius, are shown in Fig. 2. The dimensions are so chosen that the flow cross-sectional area (A_j) is equal for every jet considered. In order to fabricate noncircular jets, a through-hole was first made using a CNC wire-cutting machine in a copper plate of 17 mm thickness (see enlarged view in Fig. 1). This hole was later enlarged to the required noncircular orifice shape of 3 mm equivalent diameter, using a wire of 0.02 mm diameter in the CNC machine. As length-to-diameter ratio of the nozzle is 5.67, the boundary layer thickness at the nozzle exit is expected to be only a small fraction of the equivalent jet diameter ($D_j=\sqrt{4A_j/\pi}$). A traversing apparatus with a least count of 0.1 mm has been used to locate the Pitot tube, while measuring the flow velocity.

Total pressure and static pressure probes were used for measuring the mean axial velocity. Differential pressure was measured using a digital micro-manometer with a least count of 0.01 mm water column. In order to study the effect of mixing tube diameter on entrainment, three acrylic tubes of 39 mm, 65 mm, and 90 mm diameter were taken. During the initial experimental studies, the length of the mixing tube was kept same, while the diameter was varied. This resulted in the jet not expanding up to the full cross section of the tube in the case of larger diameter tube; consequently, flow visualization using smoke revealed reverse flow close to the exit of the mixing tube. Therefore, in order to keep the system of jet and mixing tube hydrodynamically consistent, the length-to-diameter ratio of all the tubes was kept the same (i.e., 4.2) and this length of the tube was just adequate for the jet to expand up to the full cross section of the tube. Care has been taken to ensure concentricity, by aligning the jet and mixing tube

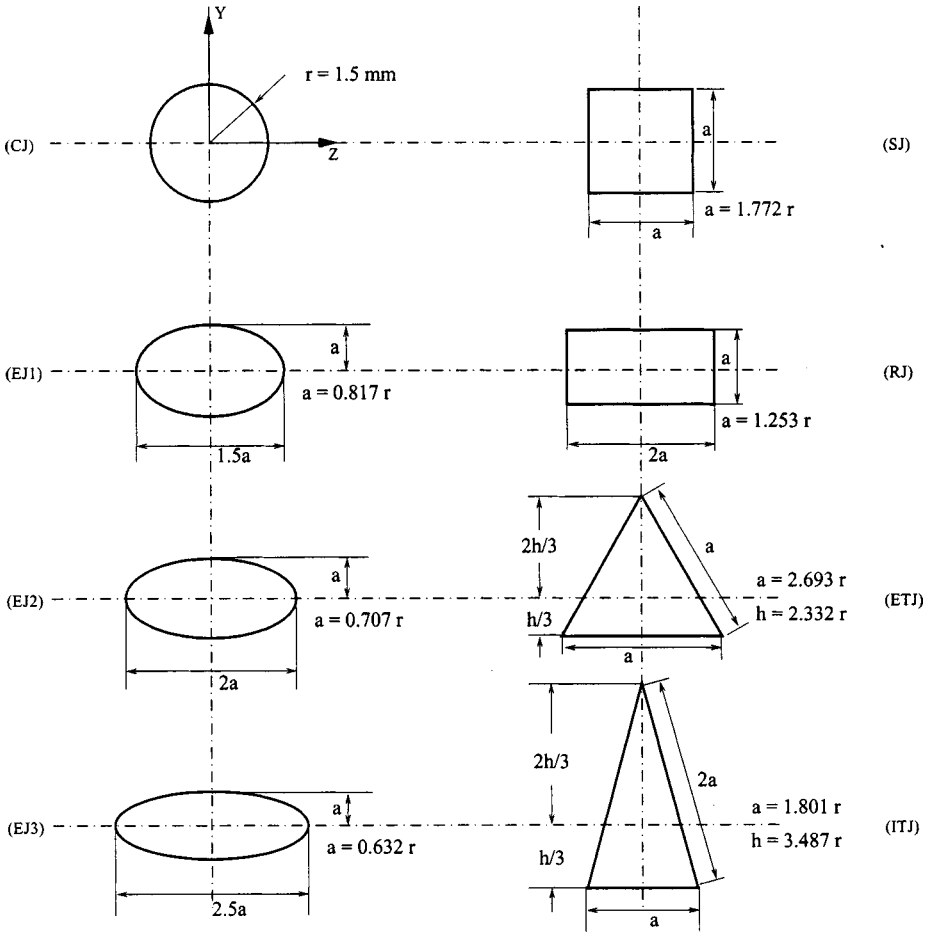

Fig. 2 Dimensions of various jets used in the study

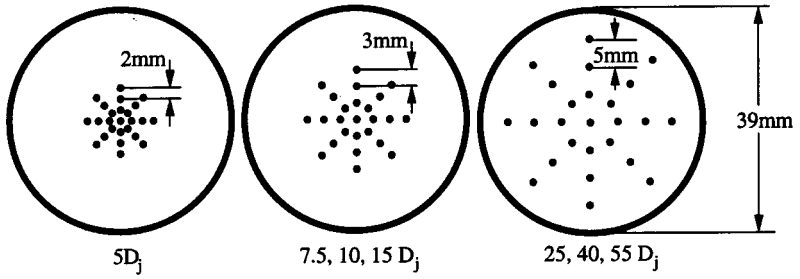

Fig. 3 Measurement stencil, showing radial interval for different planes. (The corresponding axial locations are indicated below each stencil.)

axes mechanically as well as hydrodynamically. Mechanical alignment between the mixing tube and jet nozzle was ensured with the help of suitable adapter-like devices and the alignment was subsequently verified by the hydrodynamic method using a Pitot tube traverse.

Experimental Conditions. Experiments were performed for constant density flow at atmospheric temperature. Compressed air was used for the nozzle stream, with a constant air flow rate of 2.92×10^{-4} kg/s ($Q=2.4\times10^{-4}$ m^3/s), maintained using a flow regulator. The corresponding Reynolds number (Re_j) based on equivalent jet diameter D_j and average inlet velocity U_j is 7200. The average jet inlet velocity here is defined as $U_j=Q/A_j$.

As indicated in earlier studies (Ghanshyam Singh et al. [5]), the entrainment ratio varies if the jet location is shifted away from the mixing tube inlet. In order to quantify the variation in the entrain-

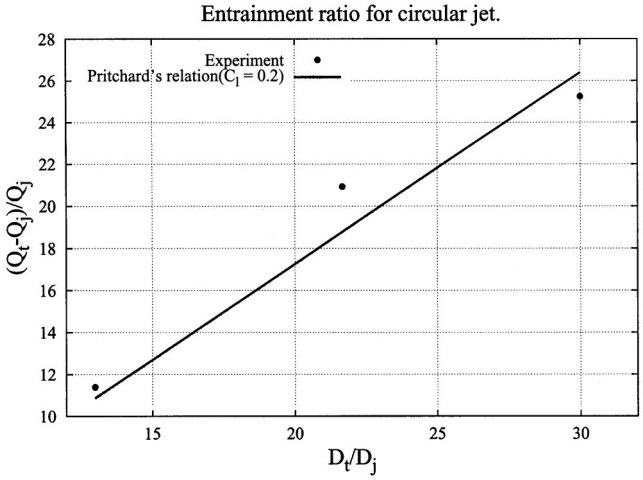

Fig. 4 Comparison between experiments and Pritchard's relation

Table 1 Scatter in maximum entrainment ratio

Tube Diameter	CJ	EJ1	EJ2	EJ3	SJ	RJ	ETJ	ITJ
39 mm	12.81±0.10	12.39±0.10	12.29±0.15	12.21±0.19	12.50±0.04	12.18±0.16	12.54±0.22	12.54±0.17
90 mm	30.77±0.49	29.36±0.50	32.69±0.50	29.01±0.17	28.91±0.50	31.28±0.30	30.16±0.47	31.71±0.56

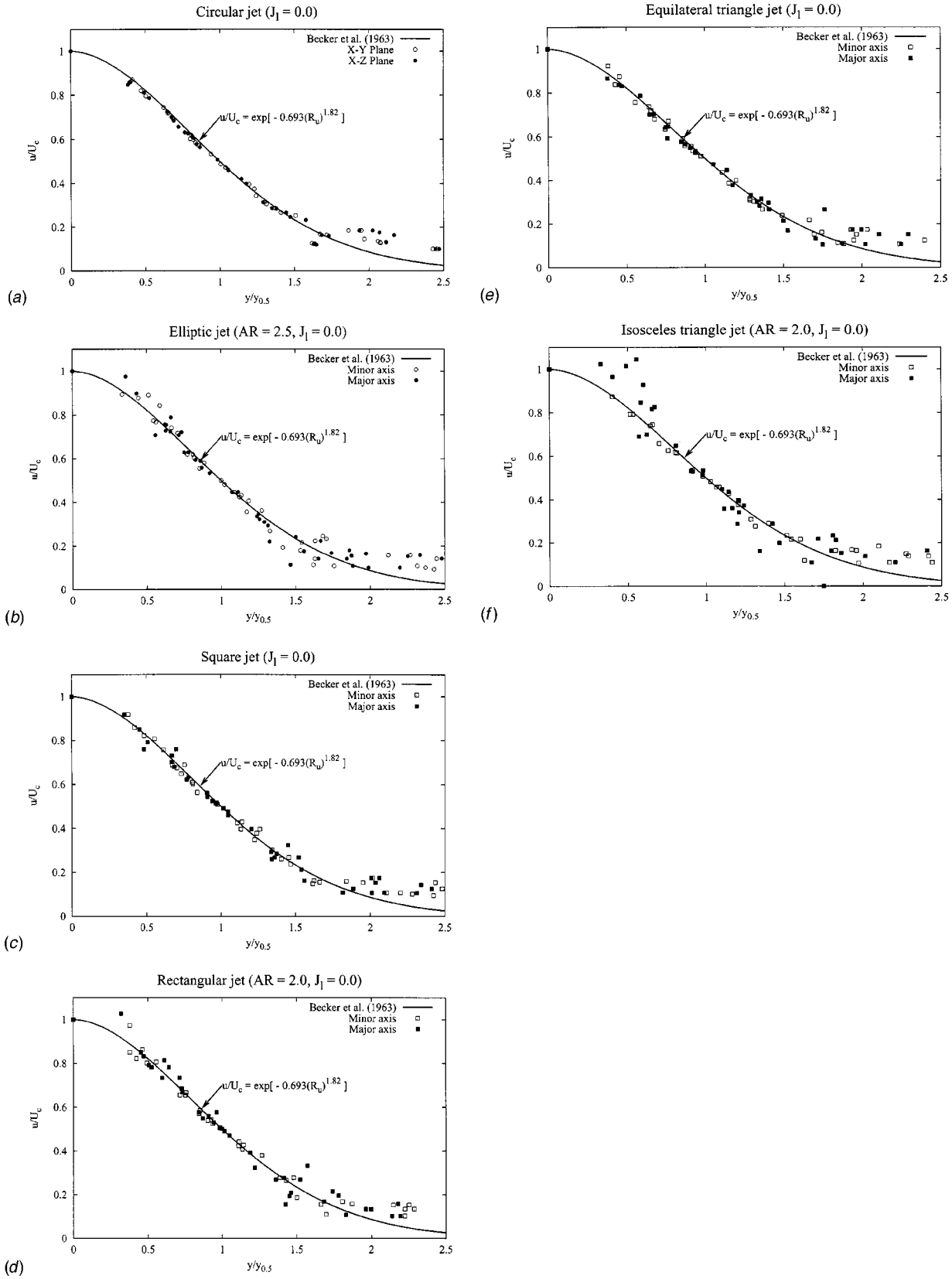

Fig. 5 Velocity profile on major and minor axis for various jets

ment ratio for different relative positions of the jet with respect to the mixing tube inlet, jet location (J_l) was varied in steps of five equivalent jet diameters (D_j) up to 25 D_j.

For the case with a 39 mm tube diameter and jet located at the base plane ($J_l=0$), detailed in-plane measurements were also carried out at the axial locations of 5, 7.5, 10, 15, 25, 40, and 55 jet diameters within the mixing tube. On each plane, 25 points with radial intervals as indicated in the measurement stencil (Fig. 3), were taken. For all other jet locations, measurements were carried out only at the top most plane. Here, the primary objective was to quantify the variation in entrainment ratio. The entrainment ratio has been estimated as

$$R=\frac{Q_t-Q_j}{Q_j} \tag{1}$$

where $Q_t=\int_0^{r_t}u2\pi r dr$.

Also, Q_j and Q_t are the volume flow rates within the jet and mixing tube, respectively, and u is the axial velocity. The selection of a suitable plane to evaluate Q_t is very important because of the presence of recirculation zone inside the mixing tube in many cases. In the present study, entrainment estimation based on the exit plane was found to give the most reliable and physically realistic results. Gaussian quadrature was used to integrate the velocity data over the flow cross section, to obtain the entrainment ratio. Measurements were repeated at least three times in each case. The repeatability of the measured data for entrainment ratio is illustrated in Table 1 using the scatter observed between different experimental runs for identical flow conditions. It is evident that the scatter is less than 1.8% for the entire range of conditions employed for the circular and noncircular jets.

Results and Discussion

In order to confirm the consistency of the experimental procedure, entrainment ratio for a circular jet was measured for three different mixing tube diameters having aspect ratio (D_t/D_j) 13.0, 21.67, and 30.0, at a fixed jet velocity. In this measurement, the nozzle exit was aligned exactly with the mixing tube inlet ($J_l=0$). Based on a simple mass and momentum balance, Pritchard et al. [4] proposed an expression for the entrainment ratio in the form

$$R_c=\frac{-(1+\sigma)}{2}+\sqrt{\frac{\sigma A_t}{A_j(1+C_l)}} \tag{2}$$

where σ is the density ratio (ρ_j/ρ_∞), C_l is the loss coefficient and A_t and A_j are the mixing tube and jet areas, respectively. The present results are compared in Fig. 4 with the predictions obtained from Eq. (2), for an assumed loss coefficient value C_l of 0.2. The entrainment ratio is expected to vary linearly with mixing tube diameter as per Eq. (2) and for the three aspect ratio values considered in the present study, the experimental data are reasonably close to the corresponding theoretical value.

Mean Velocity Field. Figures 5(*a–f*) show the radial profiles of mean axial velocity for circular and noncircular jets at different normalized axial positions. In these figures, the mean axial velocity $u(x,y)$ is normalized with the respective value at the centerline, i.e., $u(x,0)$ and the radial distance is scaled by the jet half-width ($y_{0.5}$). It should be possible to reduce many radial profiles into a single curve by such normalized representation, if the velocity profile exhibits self-similarity. The jet half-width is defined as the transverse distance from the jet axis to the location where the mean axial velocity $u(x,y)$ is half of the centerline value $u(x,0)$. Figure 5(*a*) shows that the velocity profiles for circular jet at different sections on the *X-Y* and *X-Z* planes (please refer to Figs. 2(*a*) and 2(*b*)) almost completely reduce to a single curve. Becker et al. [3] proposed a similarity solution of the form $u/U_c=\exp[-0.693(R_u)^{1.82}]$, where $R_u=y/y_{0.5}$ for constant density jets.

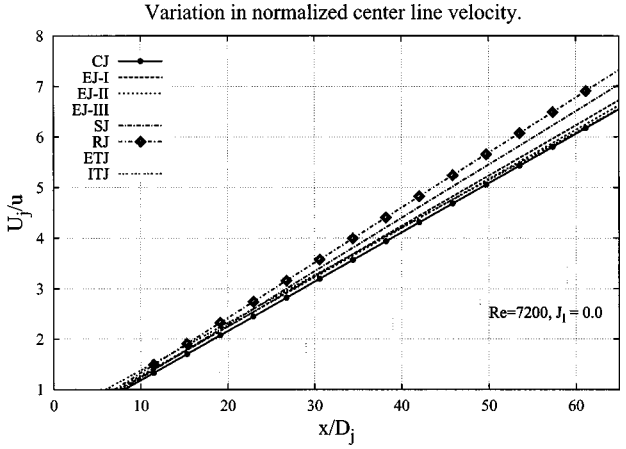

Fig. 6 Centerline velocity decay

The present experimental observations shown in Fig. 5(*a*) are in complete agreement with the equation proposed by Becker et al. [3] in the core region of circular jet. For the zone close to the wall ($y/y_{0.5}>1$), however, the similar profile does not apply due to the growth of boundary layer along the wall of the mixing tube and the recirculatory zone which may exist at the enterance of the mixing tube. For noncircular jets also, similar profile appears to be approximately valid in the jet core region; however, a considerable scatter is also observed in the data as compared to the equation proposed by Becker et al. [3]. For noncircular jets of unit aspect ratio (for the shapes of square and equilateral triangle), the scatter is observed to be relatively less. For jets with aspect ratio different from one (cross-sectional shapes of ellipse, rectangle, and isosceles triangle) scatter is more in the initial region ($y/y_{0.5}<1$) close to the nozzle exit where $u/U_c\simeq 1$ and the zone close to the wall of mixing tube ($y/y_{0.5}>1$). The large scatter in the initial region can be attributed to the occurrence of three-dimensional flow phenomena such as axis switching; the large scatter near the wall could be due to the growth of wall boundary layer, the presence of recirculatory zone, and the three-dimentionality of the flow.

Jet Decay. In Fig. 6, the reciprocal of the normalized centerline velocity (U_j/u) is plotted as a function of the normalized axial distance, (x/D_j) for different jets. Experimental data shows that the rectangular jet decays faster by about 10% than the circular jet. Also, the decays for all the other noncircular jets fall between these two. The decay of isosceles triangular jet also comes very close to that of the rectangular jet. A higher rate of decay is an indication of better mixing and earlier studies have found that the asymmetry present in the noncircular jets promotes mixing.

Jet Spread. Figures 7(*a–c*) show a comparison of the streamwise variations of jet half-widths (normalized by D_j) for different jet configurations. In order to avoid clutter, the jet-half widths on major and minor axis planes (S_y and S_z, respectively) have been plotted separately for the elliptic jets, rectangular jets, and triangular jets (Figs. 7(*a–b*)). Figure 7(*c*) shows the variation in equivalent jet half-width, defined as $S_{eq}=(S_yS_z)^{1/2}$ following Husain and Hussain [21]. Comparisons of the spread rates along the two planes have also been shown in Figs. 8(*a–c*), for some typical cases. In earlier studies (Husain and Hussain [21] and Ho and Gutmark [22]), it has been observed that before the first axis-switch, jets spread at a much higher rate in the minor plane than in the major plane; after this the slope of the half width in major plane is slightly higher than that in the minor plane. The crossover point between the spread rates along the two planes can be identified as the location of axis-switching. Similar features have been observed in the figures shown. It can be noticed from Fig. 7(*c*)

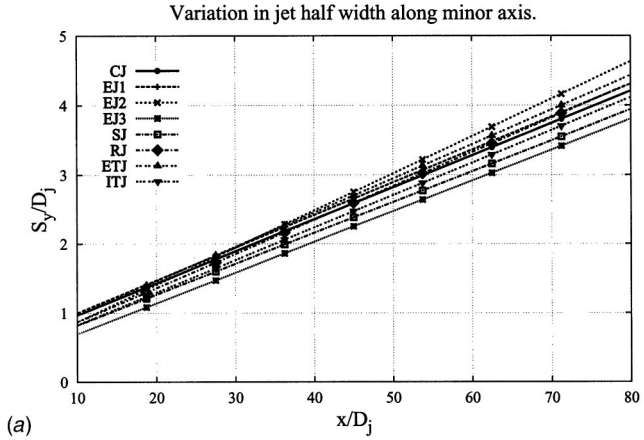

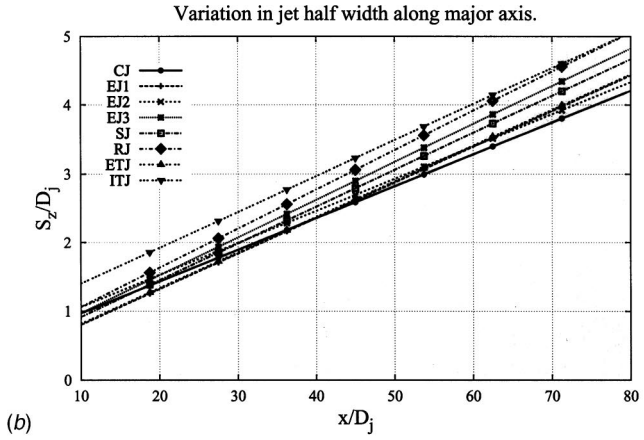

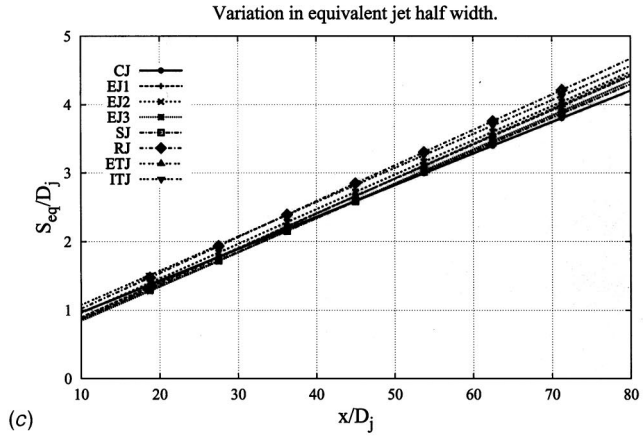

Fig. 7 Jet half-width variation for mixing tube diameter 39 mm ($D_t/D_j=13$)

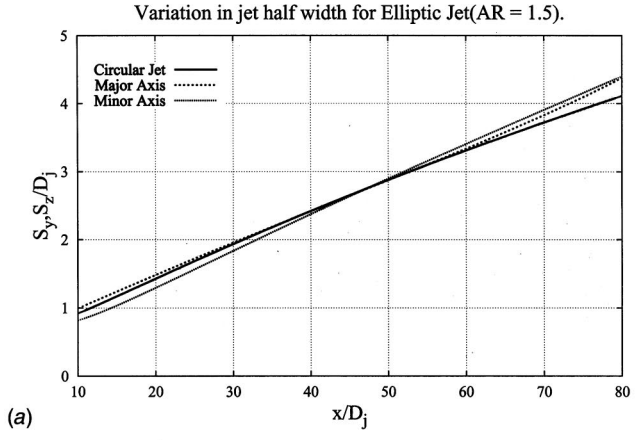

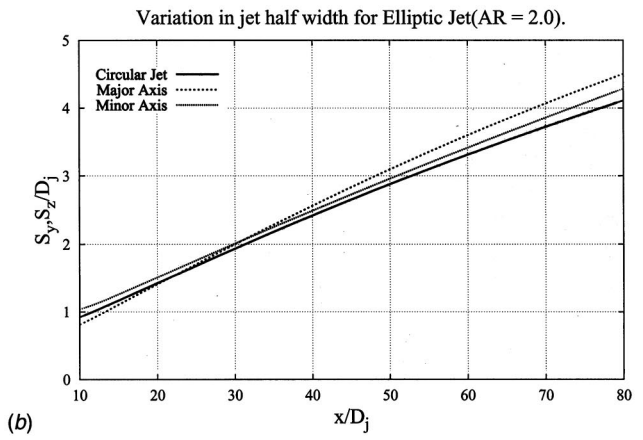

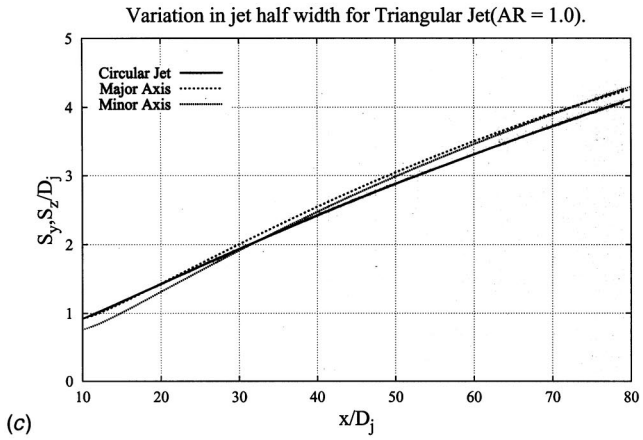

Fig. 8 Comparisons of spread rates along two planes. 39 mm.

that the noncircular jets spread faster than the circular jet with the maximum spread rate for rectangular and isosceles triangular jets. These observations are in agreement with the earlier findings of Miller et al. [6] that jets with elongation and corners spread faster due to the presence of large-scale structures and three-dimensionality of flow.

Entrainment. Figures 9(*a–d*) show the variation of experimentally measured entrainment ratio as a function of jet location for two different mixing tubes of diameter 39 mm (9(*a*), 9(*b*)) and 90 mm (9(*c*), 9(*d*)). It is seen from the figures that as the position of the jet shifts away from the mixing tube inlet, entrainment ratio increases because of exposure of the jet to the free atmosphere. However, as the jet location is shifted further away, the jet expands almost up to the size of the mixing tube and any further shift causes spillage; hence, the flow rate through the tube is reduced. Thus, for any jet configuration and mixing tube diameter, there is an optimal location of the nozzle exit, for which the entrainment attains a peak value.

The magnitude of the peak and the corresponding distance of shift (J_l) for different jets depend upon the location of the axis switching, the strength of the recirculation zone formed at the mixing tube inlet and the diameter of the mixing tube. For a smaller mixing tube, noncircularity of the jet does not seem to be very effective in promoting entrainment due to strong interaction between the jet and the boundary layer near the tube wall. Hence

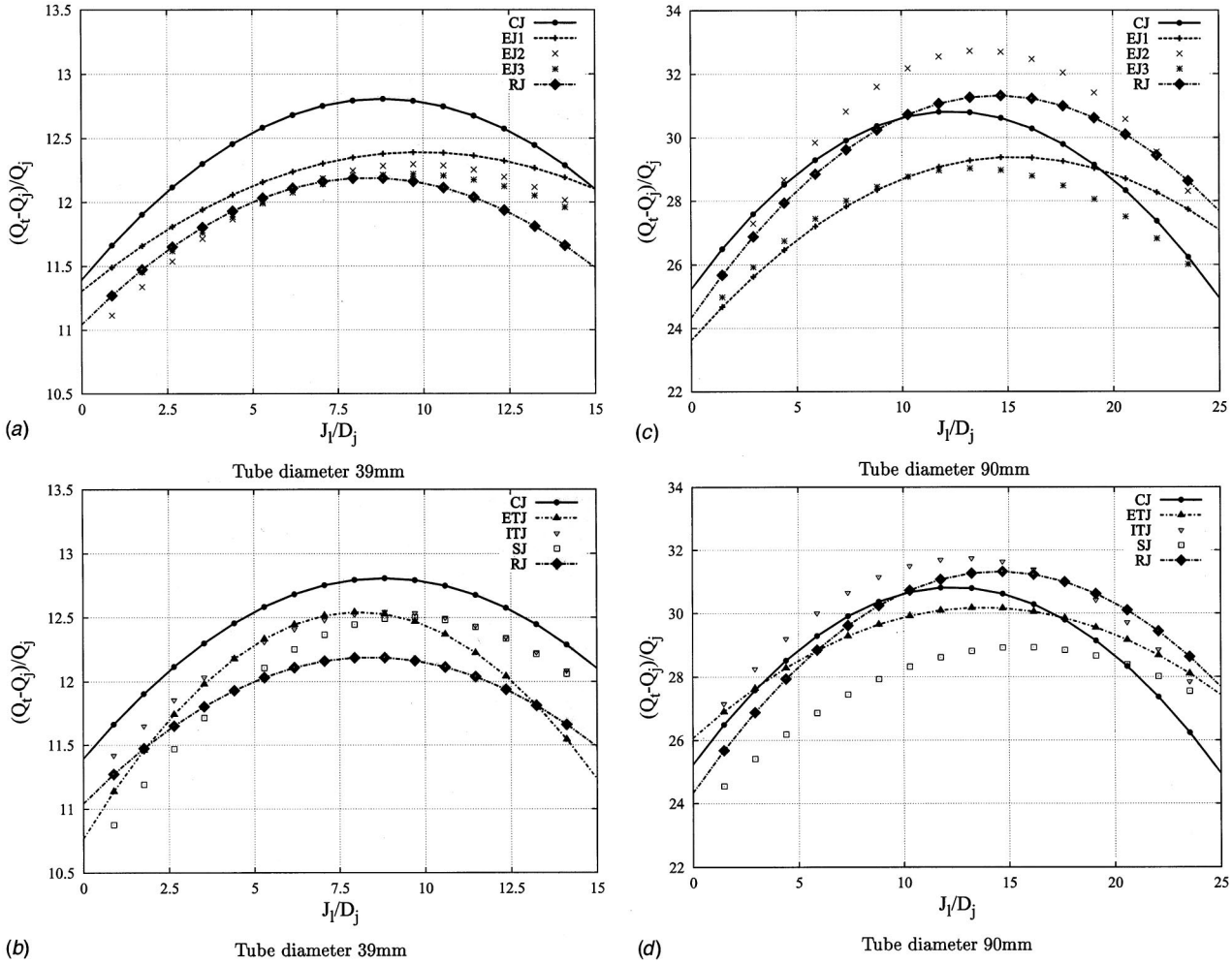

Fig. 9 Entrainment variation with jet location

the circular jet exhibits maximum level of entrainment for this case. For a larger mixing tube, however, noncircular jets achieve higher level of entrainment since axis-switching and other three-dimensional flow phenomena play a greater role. Enhancement up to 20% was seen in the entrainment ratio for the smaller mixing tube and it increased up to 30% for the larger mixing tube.

Correlation for Entrainment Ratio. In order to predict the variation in entrainment ratio for different noncircular jets, based on the experimental data obtained in the present study, a correlation has been developed. The existing Pritchard's relation for confined circular jet has been modified to incorporate the effect of jet location and distinct features of noncircular jets such as the number of corners and elongation. In order to incorporate the effect of jet location, a second-order polynomial has been fitted for each jet, as seen from the curves shown in Fig. 9(*a–d*). Also, the present investigations and earlier studies on three-dimensional jets show that elongation and corners help in promoting the level of entrainment. Entrainment is expected to increase with the inverse of the number of corners and with the jet aspect ratio. In order to highlight the effects of such geometrical parameters, the number of corners (N) and the jet aspect ratio (A) have been taken as exponents of the *perimeter ratio* between the noncircular and circular jets (P_{nc}/P_c), in the correlation expression. In the present study, it has been observed that as the location of the jets shifts away, the slope of the entrainment ratio curve for noncircular jets increases as compared to that of the circular jet. This has been incorporated in the correlation by including the location, i.e., X in the exponent to the *perimeter ratio*. The final form of the correlation along with the four empirically determined constants is shown in Eq. (3). The number of corners N varies from three for triangular jet to ∞ for circular and elliptic jets.

$$R_{nc}=R_c[\alpha X^2+\beta X+1]\left[\frac{P_{nc}}{P_c}\right]^{[(\beta X+1)(\gamma/N+\eta A)]} \tag{3}$$

where $\alpha=-0.0009$, $\beta=0.021$, $\gamma=0.15$, and $\eta=0.018$.

In Fig. 10, results using Eq. (3) are compared with the actual experimental data. It is noticed that the maximum deviation between the correlation and the data is within $\pm 5\%$.

Conclusions

- The experimental study shows that noncircular jets provide greater entrainment and mixing with ambient fluid than circular jets, in general. However, the entrainment ratio depends on the mixing tube diameter.
- It is noticed that for a smaller mixing tube, circular jet has more entrainment than noncircular jets (with the maximum difference of 20%) when the nozzle exit location coincides with that of the tube inlet. For a larger mixing tube, and jet locations coinciding with the tube inlet ($J_j=0.0$), isosceles triangular jets provide largest entrainment which is nearly 10% more than that of the circular jet. When the location of jet is shifted away from the mixing tube inlet, entrainment ratio for all the noncircular jets is found to be more as com-

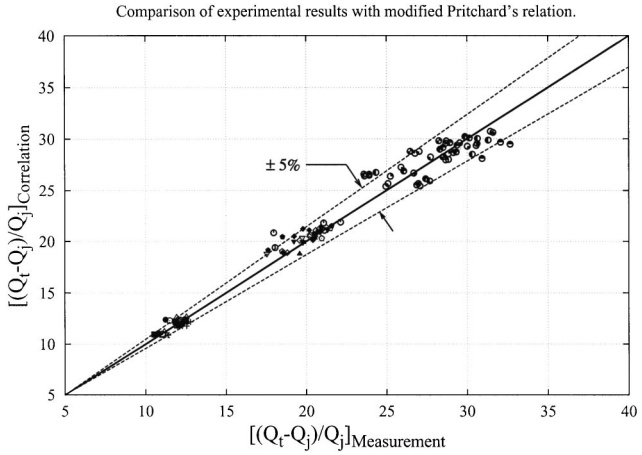

Fig. 10 Parity plot showing comparison between correlation and experimental data

pared to that of the circular jet. Enhancement of up to 30% has been obtained for the entrainment ratio, by shifting the jet location.

Nomenclature

A = ratio of major to minor jet axis
A_j = jet cross section area
AR = aspect ratio (D_t/D_j)
C_l = loss coefficient
D_j = equivalent jet diameter ($\sqrt{4A_j/\pi}$)
D_t = mixing tube diameter
J_l = jet standoff distance
N = number of corners
P = perimeter
Q = volume flow rate
R = entrainment ratio
r = radius
Re_j = Reynolds number (D_jU_j/ν)
S_y = jet half-width (major axis)
S_z = jet half-width (minor axis)
S_{eq} = equivalent jet half-width
T_l = mixing tube length
u = axial velocity
U_c = centerline velocity
U_j = average jet velocity (Q/A_j)
x = axial distance
X = normalized distance (x/D_j)
y, z = transverse distances
Y, Z = ($y/D_j, z/D_j$)
$y_{0.5}$ = jet half-width (circular jet)

Subscripts

c = circular
j = jet
l = length
nc = noncircular
t = tube
∞ = ambient

Greek Symbols

σ = density ratio
ρ = density
ν = viscosity

Abbreviations

CJ = circular jet
ETJ1 = elliptic jet (A=1.5)
ETJ2 = elliptic jet (A=2.0)
ETJ3 = elliptic jet (A=2.5)
SJ = square jet
RJ = rectangular jet
ETJ = equilateral triangular jet
ITJ = isosceles triangular jet

References

[1] Rajaratnam, N., 1976, *Developments in Water Science: Turbulent Jets*, Elsevier, Amsterdam.
[2] Craya, A., and Curtet, R., 1955, "On the Spreading of a Confined Jet," C.R. Acad. Sci. Paris, **241**(1), pp. 621–622.
[3] Becker, H. A., Hottel, H. C., and Williams, G. C., 1963, "Mixing and Flow in Ducted Turbulent Jets," *9th Int. Symp. Combustion*, The Combustion Institute, Pittsburgh, PA, pp. 7–20.
[4] Prichard, R., Guy, J. J., and Conner, N. E., 1977, *Industrial Gas Utilization*, Bowker, New Providence, NJ.
[5] Singh, G., Sundararajan, T., and Shet, U. S. P., 1999, "Entrainment and Mixing Studies for a Variable Density Confined Jet," Numer. Heat Transfer, Part A, **35**, pp. 205–223.
[6] Miller, R. S., Madina, C. K., and Givi, P., 1995, "Numerical Simulation of Non-circular Jets," Comput. Fluids, **24**(1), pp. 1–25.
[7] Dahm, W. J. A., and Dimotakis, P. E., 1987, "Measurements of Entrainment and Mixing in Turbulent Jets," AIAA J., **25**, pp. 1216–1223.
[8] Zaman, K. B. M., and Hussain, A. K. M. F., 1980, "Vortex Pairing in a Circular Jet Under Controlled Excitation," J. Fluid Mech., **101**, pp. 449–491.
[9] Zaman, K. B. M., and Hussain, A. K. M. F., 1981, "Turbulence Suppression in Free Shear Flows by Controlled Excitation," J. Fluid Mech., **103**, pp. 133–159.
[10] Husain, H. S., Bridges, J. E., and Hussain, A. K. M. F., 1988, "Turbulence Management in Free Shear Flows by Control of Coherent Structures," *Transport Phenomena in Turbulent Flows*, M. Hirata and N. Kasagi, eds., Hemisphere, Washington, DC, pp. 11–130.
[11] Martin, J. E., and Meiburg, E., 1988, "Numerical Investigation of Three-Dimensionally Evolving Jets Subjected to Axisymmetric and Azimuthal Perturbations," J. Fluid Mech., **230**, pp. 271–318.
[12] Tong, C., and Warhaft, Z., 1994, "Turbulence Suppression in a Jet by Means of Fine Ring," Phys. Fluids, **6**, pp. 328–334.
[13] Rajagopalan, S., and Antonia, R. A., 1998, "Turbulence Reduction in the Mixing Layer of a Plane Jet Using Small Cylinders," Exp. Fluids, **25**, pp. 96–103.
[14] Olsen, J. F., Rajagopalan, S., and Antonia, R. A., 1999, "Influence of Stationary and Rotating Cylinders on a Turbulent Plane Jet," *Engineering Turbulence Modeling and Experiments*, W. Rodi and M. Laurence, eds., Elsevier, New York, **4**, pp. 423–442.
[15] Krothapalli, A., Baganoff, D., and Karamcheti, K., 1981, "On the Mixing of Rectangular Jets," J. Fluid Mech., **107**, pp. 201–220.
[16] Vandersburger, U., and Ding, C., 1995, "Self-Excited Wire Method for the Control of Turbulent Mixing Layers," AIAA J., **33**, pp. 1032–1037.
[17] Tam, C. K. W., 1998, "Influence of Nozzle Geometry on the Noise of High Speed Jets," AIAA J., **8**, pp. 1396–1400.
[18] Gutmark, E. J., and Grinstein, F. F., 1999, "Flow Control With Non-Circular Jets," Annu. Rev. Fluid Mech., **31**, pp. 239–272.
[19] Kolluri, P., Kamal, A., and Gollahalli, S. R., 1996, "Application of Noncircular Primary-Air Inlet Geometries in the Inshot Burners of Residential Gas Furnaces," ASME J. Energy Resour. Technol., **118**, pp. 58–64.
[20] Mi, J., Nathan, G. J., and Luxton, R. E., 2000, "Centerline Mixing Characteristics of Jets From Nine Differently Shaped Nozzles," Exp. Fluids, **28**, pp. 93–94.
[21] Husain, H. S., and Hussain, A. K. M. F., 1989, "Elliptic Jets. Part 1. Characteristics of Unexcited and Excited Jets," J. Fluid Mech., **208**, pp. 257–320.
[22] Ho, C. M., and Gutmark, E., 1987, "Vortex Induction and Mass Entrainment in a Small-Aspect-Ratio Elliptic Jet," J. Fluid Mech., **179**, pp. 383–405.

Behavior of Radial Incompressible Flow in Pneumatic Dimensional Control Systems

G. Roy

D. Vo-Ngoc

Faculty of Engineering,
Université de Moncton,
Moncton, NB E1A 3E9, Canada

D. N. Nguyen
Department of Mechanical Engineering,
Université Laval,
Québec, G1K 7P4, Canada

P. Florent
Laboratory of Fluid Mechanics,
Université de Valenciennes,
Valenciennes, France

The application of pneumatic metrology to control dimensional accuracy on machined parts is based on the measurement of gas flow resistance through a restricted section formed by a jet orifice placed at a small distance away from a machined surface. The backpressure, which is sensed and indicated by a pressure gauge, is calibrated to measure dimensional variations. It has been found that in some typical industrial applications, the nozzles are subject to fouling, e.g., dirt and oil deposits accumulate on their frontal areas, thus requiring more frequent calibration of the apparatus for reliable service. In this paper, a numerical and experimental analysis of the flow behavior in the region between an injection nozzle and a flat surface is presented. The analysis is based on the steady-state axisymmetric flow of an incompressible fluid. The governing equations, coupled with the appropriate boundary conditions, are solved using the SIMPLER algorithm. Results have shown that for the standard nozzle geometry used in industrial applications, an annular low-pressure separated flow area was found to exist near the frontal surface of the nozzle. The existence of this area is believed to be the cause of the nozzle fouling problem. A study of various alternate nozzle geometries has shown that this low-pressure recirculation area can be eliminated quite readily. Well-designed chamfered, rounded, and reduced frontal area nozzles have all reduced or eliminated the separated recirculation flow area. It has been noted, however, that rounded nozzles may adversely cause a reduction in apparatus sensitivity. [DOI: 10.1115/1.1598991]

1 Introduction

When air exits a cylindrical nozzle and impinges a flat plate, the resulting flow is axisymmetric and is commonly referred to as a ''radial flow.'' When the nozzle is very close to the plane and its frontal surface is relatively significant in size with respect to the jet, then the flow becomes a radial flow between two coaxial disks with axial approach flow. The pressure upstream of the jet is very sensitive to changes in the distance between the nozzle and the plane. This characteristic is used to advantage in industrial metrology. The study of radial flow, either as flow between disks or between a nozzle and a flat plate, has been the subject of numerous research projects over the past half century, [1–3], etc. However, research work of such flows for applications in dimensional pneumatic control is limited. The radial flow between a nozzle and a flat plate for specific applications in pneumatic metrology has, to our knowledge, only been recently considered by a group of researchers at the Université de Valenciennes in France, [4,5]. These studies have been mainly experimental in nature. Pressure distributions on a flat plate were measured and seemed to indicate the presence of a low-pressure separation area for cases using the standard nozzle. Various nozzle geometries were studied and, in some cases, the low pressure area was eliminated. No experimental flow visualization techniques were used (or velocity fields measured—mainly due to the very limited space between the flat plate and the nozzle) and therefore no information on the entire flow field was found. Furthermore, cases studying impinging jets for very small distances separating the nozzle and the flat plate ($\delta/D<0.5$, where δ is the distance separating the nozzle and the flat plate and D is the nozzle diameter), are quite sparse and are also mainly experimental, [6]. This range is actually of interest in industrial metrology applications. However, the nozzles used in the work are thin walled and therefore do not consider the effects of confinement. Only recently, [7], have numerical studies been made in the case of an impinging jet at distances in this range ($\delta/D<0.5$) with an interest in the effects of confinement. In the particular case of pneumatic metrology applications, one can note that because of the small distance ''δ'' between the nozzle and the flat plate ($100\ \mu m \leqslant \delta \leqslant 200\ \mu m$ compared to a nozzle external diameter of 4 mm), the only practically measurable quantity is the wall pressure distribution on the surface of the flat plate. Information on the entire radial flow field between the nozzle and the plate can therefore be more easily obtained by numerical simulation, which is presented in this paper. This paper follows the work by Crnojevic et al. [5]. The results presented by these authors on the influence of the regulator orifice diameter and injection nozzle geometry on the flow structure in pneumatic dimensional control systems were mainly experimental, although some insight into numerical results were presented. The bulk of this numerical work is presented here.

2 Pneumatic Dimensional Control Basics

Pneumatic controllers are quite popular today in industrial applications. They can be used in high precision applications (order of a few microns), no physical contact is made between the nozzle and the surface of the machined part, part cleaning is done as the process is on-going, they can measure multiple dimensions simultaneously, they are robust, and internal dimensions can easily be measured (i.e. holes/bores). In industrial applications today, one can find a few different variations of the basic pneumatic dimensional control apparatus. Most of these are now based on the detection of a pressure differential inside the apparatus, [8,9]. This pressure differential is highly dependent on the distance ''δ'' between the nozzle and the surface of the machined part (controlled

Contributed by the Fluids Engineering Division for publication in the JOURNAL OF FLUIDS ENGINEERING. Manuscript received by the Fluids Engineering Division June 14, 2002; revised manuscript received Apr. 1, 2003. Associate Editor: E. W. Graf.

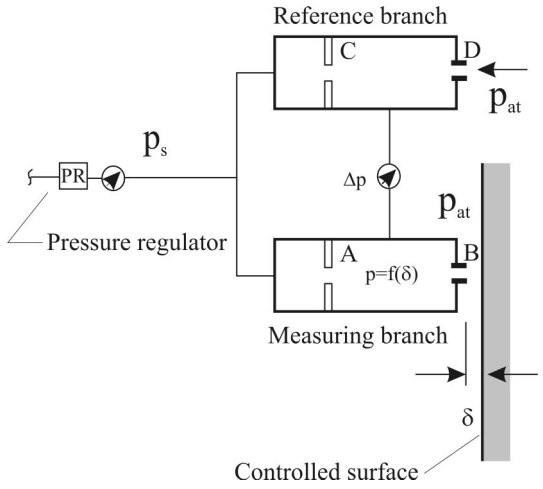

Fig. 1 Basic pneumatic controller

surface). Quite a large variety of operating pressures can be found with these various methods (as low as 1.5 kPa or as high as 400 kPa). A typical differential apparatus is illustrated in Fig. 1. In this type of apparatus, air under constant pressure flows through two orifices A and B placed in series. The static pressure "p" in the chamber between the two orifices is a function of the ratio of their two areas. For a desired setting, the area of orifice A is fixed and therefore the pressure in the chamber is a function of the distance "δ" separating the nozzle B from the machined part, [8]. For a given supply pressure, the distance δ can therefore be measured with proper calibration. In the differential apparatus, two branches are used, one is used as a reference and the other as the measuring branch. This arrangement is preferred as Δp readings in this case are practically insensitive to supply pressure "p_s" fluctuations. Although industrial pneumatic controllers are a well-established and credible way of performing dimensional control in industrial environments, as in any other type of controller some minor problems are found to exist. Nozzle fouling is one of them. Annular regions of dirt and oil deposits are often found on the frontal surfaces of the injection nozzles, Fig. 2. The resulting fouling requires that the controllers be cleaned and calibrated at shorter than desired intervals. In this present paper, we are specifically concerned with the behavior of the flow between a nozzle and a flat plate with particular considerations for the influence of the injection nozzle geometry on the resulting flow field. It is expected that a simple change in nozzle geometry may help alleviate nozzle fouling. The effects of any changes in nozzle geometry on apparatus sensitivity must also be verified, as this is of great importance in industrial applications.

3 Modeling and Simulation

3.1 Problem Configuration. The problem configuration is illustrated in Fig. 3. The nozzle and flat plate are stationary and a flow rate Q is axially injected into the domain of interest. The nozzle, which has an interior radius of "R_i" and an exterior radius of "R_e," is separated from the flat plate by a distance of "δ." Typical industrial configurations have a clearance space "h" with the main body of the nozzle (generally ≈ 2 to 3 R_i) which extends to a radius of R_d of approximately 5 R_i. Typical industrial dimensions are $R_i = 1$ mm, $R_e = 2$ mm, and $\delta = 0.15$ mm.

3.2 Governing Equations. For the purposes of this initial study, the laminar axisymmetric flow of a viscous incompressible and isothermal fluid between a nozzle and a flat plate is considered. The fluid properties are assumed constant and all external forces are considered negligible. Under these assumptions, the dimensionless governing equations for this type of flow can be written in cylindrical coordinates as follows [10]:

Conservation of momentum in the radial direction:

$$\overline{u}\frac{\partial \overline{u}}{\partial \overline{r}} + \overline{w}\frac{\partial \overline{u}}{\partial \overline{z}} = -\frac{\partial \overline{p}}{\partial \overline{r}} + \frac{1}{\overline{r}}\frac{\partial}{\partial \overline{r}}\left(\overline{r}\frac{\partial \overline{u}}{\partial \overline{r}}\right) + \frac{\partial^2 \overline{u}}{\partial \overline{z}^2} - \frac{\overline{u}}{\overline{r}^2}, \tag{1}$$

Conservation of momentum in the axial direction:

$$\overline{u}\frac{\partial \overline{w}}{\partial \overline{r}} + \overline{w}\frac{\partial \overline{w}}{\partial \overline{z}} = -\frac{\partial \overline{p}}{\partial \overline{z}} + \frac{1}{\overline{r}}\frac{\partial}{\partial \overline{r}}\left(\overline{r}\frac{\partial \overline{w}}{\partial \overline{r}}\right) + \frac{\partial^2 \overline{w}}{\partial \overline{z}^2}, \tag{2}$$

Continuity equation:

$$\frac{\partial(\overline{r}\overline{u})}{\partial \overline{r}} + \frac{\partial(\overline{r}\overline{w})}{\partial \overline{z}} = 0, \tag{3}$$

where, in these equations, "$\overline{r}$" and "$\overline{z}$" are the dimensionless radial and axial coordinates; "$\overline{u}$" and "$\overline{w}$" are the dimensionless radial and axial velocity components; and "$\overline{p}$" is the dimensionless pressure. For the derivation of the Eqs. (1)–(3), the quantities R_i, ν/R_i, and $\rho(\nu/R_i)^2$ were adopted as reference length, velocity, and pressure. R_i, ν, and ρ are, respectively, the internal radius of the nozzle, the kinematic viscosity, and density of the fluid. From this normalization, several characteristic variables defining the geometry of the problem, as well as the flow Reynolds number, are found: $\beta = R_e/R_i$, $\eta = \delta/R_i$, $\lambda = h/R_i$, $\beta_d = R_d/R_i$, and $\mathrm{Re} = 2Q/\pi\nu R_i$, where Q is the volumetric flow rate at the inlet of the nozzle.

3.3 Numerical Approach. The numerical method used in this study to solve the governing equations is the SIMPLER algorithm developed by S.V. Patankar [11]. The standard second-order central difference formulation was used throughout the computational domain. In the past, this method has been successfully used in similar cases involving fluid flow and heat transfer simulations. Although the region of interest is limited in the space between the nozzle and the plate, the calculation domain is extended over a large space adjacent to the nozzle, up to $\overline{r} = \beta_d$, in order to obtain good results in the area of interest, Fig. 4. The calculation domain is divided into several regions with different grid generations in accordance to geometry and flow conditions of each region. The

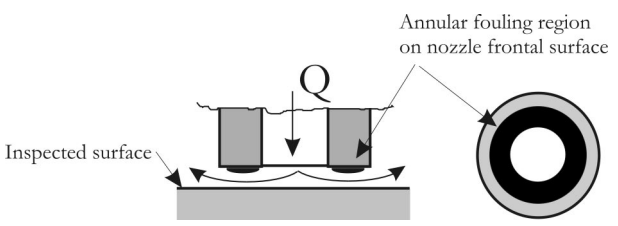

Fig. 2 Nozzle fouling (not to scale)

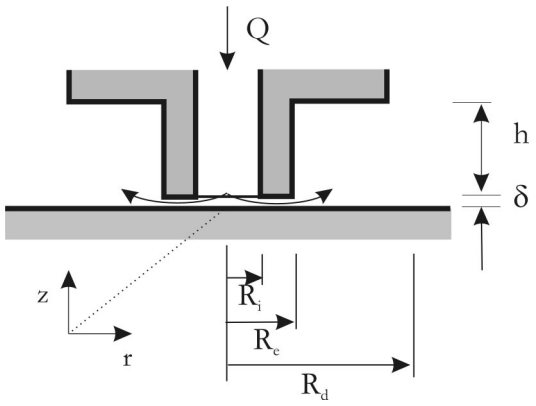

Fig. 3 Problem configuration

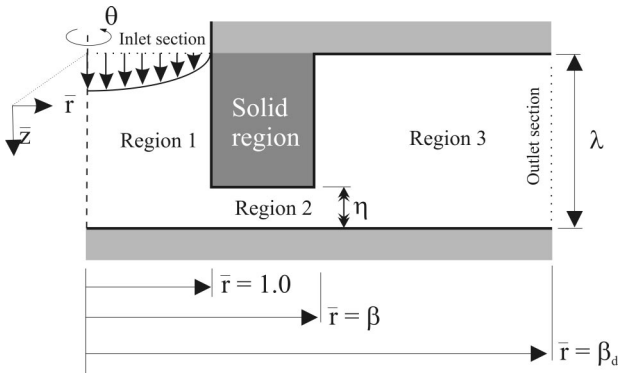

Fig. 4 Considered domain for calculations

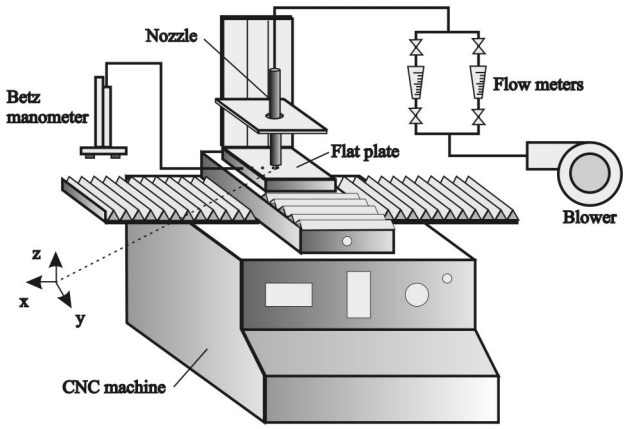

Fig. 6 Experimental setup

nonuniform exponential grid generation scheme used was proposed by Patankar [11] and also used, for example, by Prakash et al. [3]. This scheme allows for a highly packed grid generation near solid walls where important gradients are found and a more relaxed generation where conditions are less critical. Grid sensitivity testing was conducted. Figure 5 illustrates result comparisons for a few of the considered grids in region 2 (see Fig. 4). In Fig. 5(*a*), the radial velocity profils for two radial stations ($\bar{r}=1.0$ and 1.5) are presented while in Fig. 5(*b*), the wall pressure distributions are illustrated. As can be seen, results for the 40 (axial)×100 (radial) and 32 (axial)×100 (radial) grids are essentially the same in all presented plots and, therefore, a grid of 32×100 in the region of interest has been chosen for subsequent simulations. The chosen overall grid for the entire calculation domain was 92×202 in the axial and radial directions, respectively. For the selected grid in the region of interest (region 2, Fig. 4), the average aspect ratio of the control volumes is 2 to 1 (radial to axial directions, respectively). Near the walls, this ratio increases to a maximum value of approximately 4 to 1. Although Patankar [11] states that that no universal rule exists about what maximum (or minimum) ratio adjacent grid intervals should maintain, the grid used here certainly lies in what is, by others, considered to be very acceptable values. While the no-slip condition is used on solid walls, the effects of different chosen velocity profiles which verify only mass conservation at the inlet and outlet sections of the domain have been considered (i.e., imposed mass flow rate). Parabolic and constant velocity profiles have been tested at the inlet section and several other profiles including a combination of a wall jet and a boundary layer type profile at the exit section were tested and results compared at various sections in the calculation domain. Results have shown that the flow structure in the inner region of particular interest (the space between the nozzle and the flat plate) is not affected by the choice of these boundary conditions, as long as the extent of the calculation domain is large enough and that the inlet tube is sufficiently long (approximately $L/R_i=2.0$ and $R_d/R_i \geq 4$, respectively). For the particular case of the above-mentioned combination wall-jet boundary layer profile for the outlet section, results have shown that good numerical results can be obtained far beyond the exit section of the nozzle. The convergence criteria for all computations presented in this paper were based on the degree of mass conservation obtained over each control volume in the computational domain. These errors gradually decreased with the number of iterations and were generally in the order of 0.01% for all considered cases. This criterion generally corresponds to a precision of approximately 10^{-4} for all independent variables (velocity components and pressure).

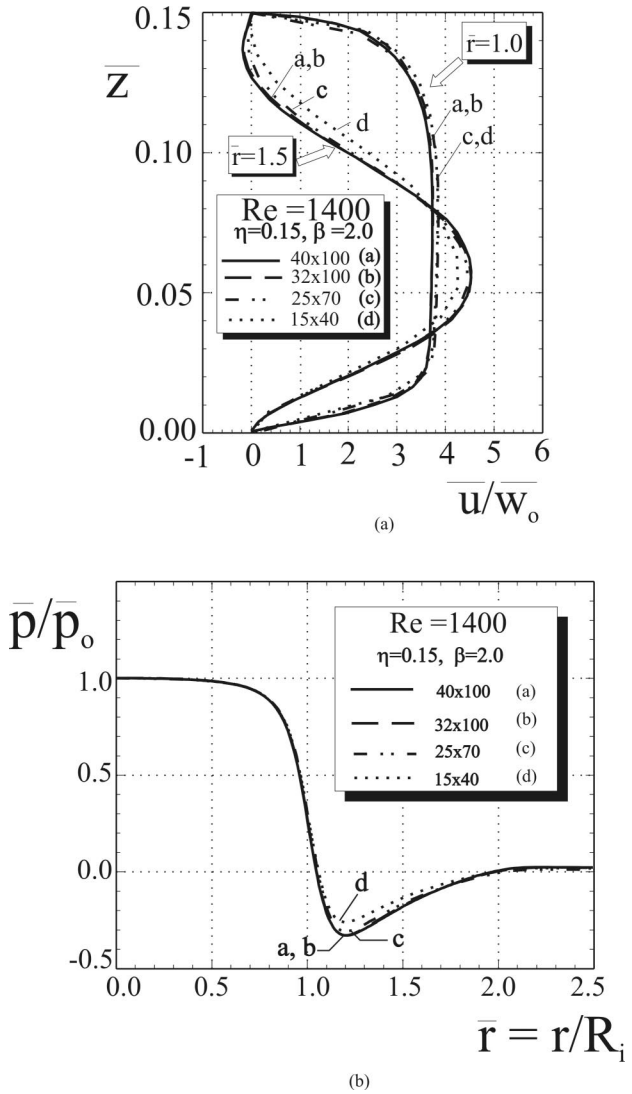

Fig. 5 Grid sensitivity analysis

4 Experimental Setup

A test rig was built in order to investigate experimentally the effects of the nozzle geometry on the flow field between the nozzle and the flat plate. The results obtained were used to be compared to/validate those obtained numerically. Also, the effects of the nozzle geometry on apparatus sensitivity are more practically verified with the test rig. The installation, shown schematically in Fig. 6, was basically built on an existing CNC machine

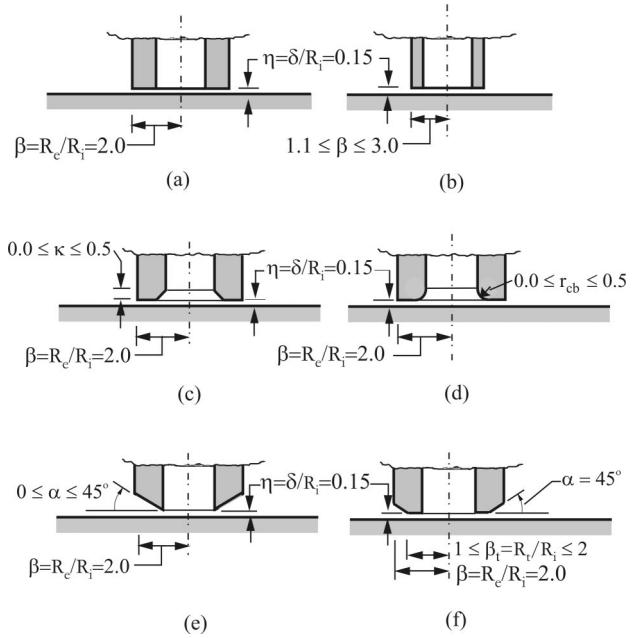

Fig. 7 Considered nozzle geometries

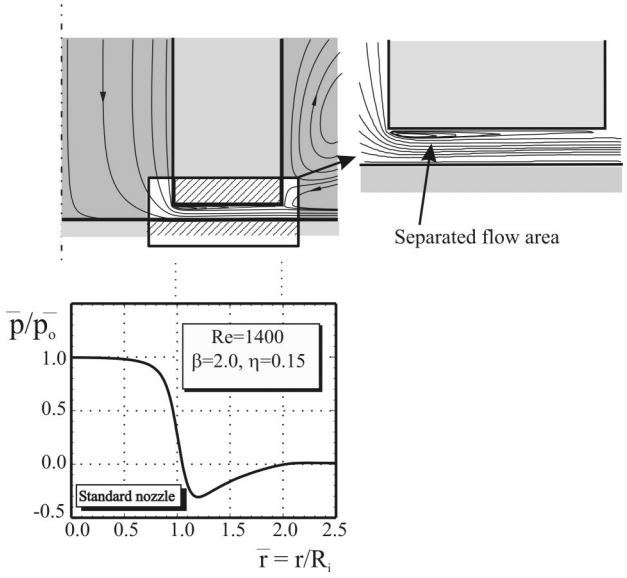

Fig. 8 Flow behavior for standard nozzle

tool positioning system (TORCAM), providing accurate displacements on three axes. Geometrically similar nozzles to those found in industrial applications were used (i.e., $R_i=10$ mm, $R_e=20$ mm with $\delta=1.5$ mm). Air flow was provided by the blower from an aerodynamic test rig (TecQuipment AF10). Pressure distributions on the flat plate were measured by moving the flat plate and measuring the static pressure via a pressure tap on the bottom of the plate. Repetitivity and the axisymmetric nature of the wall distributions were checked by moving the nozzle back and forth through the entire nozzle diameter with repect to the pressure tap. This is of course done while keeping the distance separating the nozzle and the flat plate constant. When considering the effects of the distance separating the nozzle and the flat plate, the nozzle is centered on the pressure tap and the pressure is recorded for multiple distance values. In both cases, sufficient time was allowed for the flow to settle thus giving good steady-state readings. Flowmeters, manometers, and thermocouples were carefully installed to record, respectively, the flow rate inside the system, the static pressure on the flat plate and the temperature in the system. Uncertainty of the experimental data presented in this paper is less than 2%. More information on the experimental setup can be obtained in the Ref. [12].

5 Numerical Results and Discussions

5.1 Influence of Nozzle Geometry on Flow Behavior. The injection nozzles considered in this present paper are illustrated in Fig. 7. There are six basic nozzle geometries considered: the standard nozzle (Fig. 7(*a*)), a reduced or expanded frontal area nozzle (i.e., narrow to large, Fig. 7(*b*)), an internally chamfered nozzle (Fig. 7(*c*)), an internally rounded nozzle (Fig. 7(*d*)), an externally chamfered nozzle (Fig. 7(*e*)), and an externally chamfered and truncated nozzle (Fig. 7(*f*)). The influences of various important parameters including η, β, α, β_t, κ, and r_{cb} are considered in this present paper. Results presented, unless otherwise stated, for: Re $=1400$, $\eta=0.15$, and $\beta=2.0$.

5.2 Standard Nozzle Flow Behavior. The general flow pattern for the standard nozzle is shown in Fig. 8. As clearly seen in these figures, a separated flow area is found on the frontal surface of the injection nozzle. For the considered parameters (Re $=1400$, $\beta=2.0$, $\eta=0.15$), the recirculation bubble covers the entire frontal area of the nozzle. Also of interest is the wall pressure distribution on the flat plate. The radial area at the entrance of the space between the nozzle and the flat plate is smaller than the area of the inlet tube ($A_{\text{space}}=2R_i\pi\delta<A_{\text{tube}}=\pi R_i^2$). This is true as long as $2\delta<R_i$, which is the case for all results presented here. As a result, the airflow is accelerated and a corresponding pressure drop is observed. A negative low-pressure area is also found to exist. This can be attributed to a *vena contracta* effect at the entrance of the space between the nozzle and the flat plate. This corresponds with the results found in the experimental work by Crnojevic et al. [5]. Clearly, this separated flow area is the probable cause of fouling in industrial applications.

5.3 Effects of Nozzle Frontal Section. The first considered external modification is to modify the injection nozzle wall thickness. Intuitively, a reduction in frontal surface would reduce confinement effects and generally reduce the formation of stagnation areas. The effects of the frontal surface are therefore studied, as well as an expanded surface nozzle. Figures 9(*a–c*) show general flow patterns for cases where $\beta=1.25$, 1.5, and 3.0 ($\beta=2.0$ is the

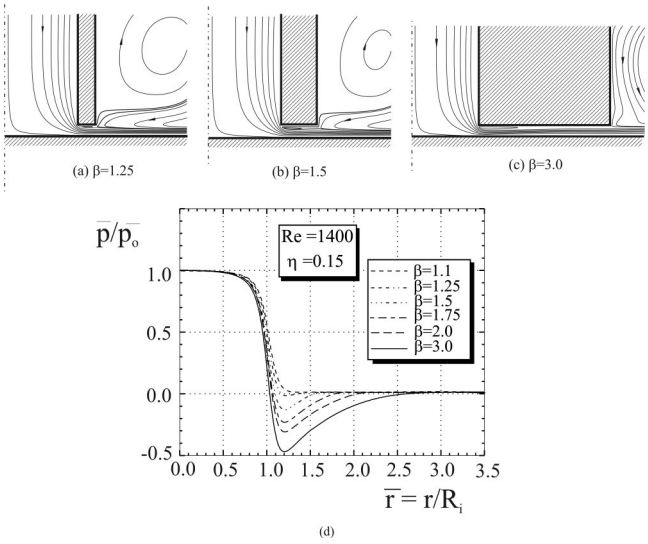

Fig. 9 Influence of nozzle frontal area on flow behavior

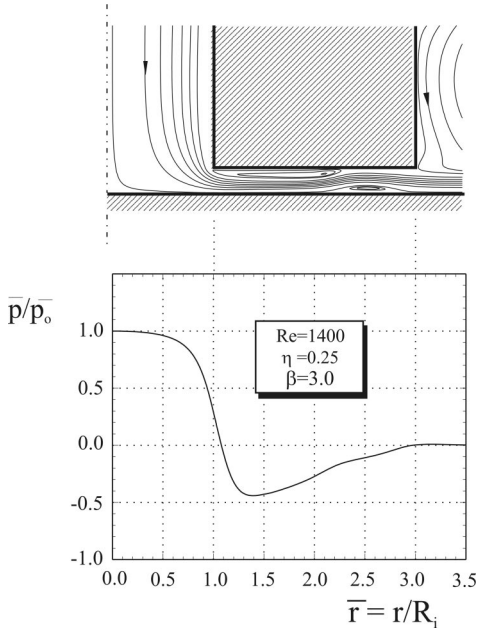

Fig. 10 Effects of confinement in large diameter nozzle ($\eta = 0.25$)

standard nozzle shown in Fig. 8). One can easily see that for the flow conditions studied (Re=1400, $\eta=0.15$) and for thicknesses of at least up to $\beta=2.0$, the recirculation areas cover the entire frontal surfaces of the nozzles. Also, as can be seen in Fig. 9(*d*), the effects of greater confinement are reflected in the increase in the reduction of pressure to the minimum values of the wall pressure distribution. One can thus easily conclude that a minimal wall thickness is preferable in order to keep low-pressure stagnation areas from forming. The influence of the frontal area of the nozzle and flow confinement can further be seen in Fig. 10. In the presented case, the external radius of the injection nozzle is as in Fig. 9(*c*) (i.e., $\beta=3.0$), however, in this particular case, the distance separating the nozzle and the flat plate is slightly increased to $\eta=0.25$. This distance could easily be found in practical situations, especially considering that the gap between the nozzle and the flat plate can vary somewhat during a typical operational cycle. For the injection Reynolds number used, a second recirculation bubble is found downstream on the surface of the flat plate. This type of flow behavior had been noticed previously by McGinn [13] in his experimental work on flow without swirl between two parallel discs with central injection. This type of flow behavior would also be undesirable in industrial applications, thus reinforcing the importance of having the smallest possible nozzle frontal area.

5.4 Internal Modifications to Standard Nozzle. With the intent of finding solutions to the fouling problem, various geometrical modifications to the standard nozzle are made. The first series of modified nozzles incorporate internal changes in the basic standard nozzle geometry. In this present section, we will consider the nozzles illustrated in Figs. 7(*c*) and 7(*d*). The nozzle shown in Fig. 7(*c*) incorporates an internal chamfer while the second considered geometry, Fig. 7(*d*), is an internally rounded nozzle. Results for internally chamfered nozzles are presented in Fig. 11 while results for the rounded nozzle are presented in Fig. 12. The interest here resides in the influence of the chamfer width "κ" and of the radius of internal rounding "r_{cb}." For all considered values of "κ," the angle of internal chamfer is set to 45°. One can see that for the three considered cases for each geometry ($\kappa=0.25$, 0.333, and 0.5 for the internally chamfered and $r_{cb}=0.25$, 0.333, and 0.5 for the rounded nozzle), the flow recirculation area on the frontal surface of the injection nozzle seems to have been eliminated. This can most certainly be attributed to the fact that the change in flow direction is less drastic for cases with an internal chamfer or rounding when compared to a standard nozzle. In the case of an internal chamfer, however, even though the obtained results do not show any separated flow/recirculation area on the inner inclined surface of the nozzle, it is quite conceivable that this type of behavior be present under certain circumstances, especially for larger "κ" values. Wall pressure distributions for internally chamfered nozzles and for the rounded nozzles are, respectively, shown in Figs. 10(*d*) and 11(*d*). When compared to the standard nozzle, one can see that the sharp decreases in pressure, as well as the minimum pressure point, are displaced towards the periphery of the nozzle with an increase in the width of the chamfer or rounding. This is to be expected as the change in flow section is more gradual and that the minimum flow section is also displaced towards the periphery. The reduction of pressure to the minimum pressure point also decreases with an increase in chamfer width. This can be attributed to the fact that the maximum velocity in the section between the nozzle and the flat plate is certainly of lesser importance with an increase in chamfer width. Although both internally modified nozzles have the same general effect on flow behavior in the region between the

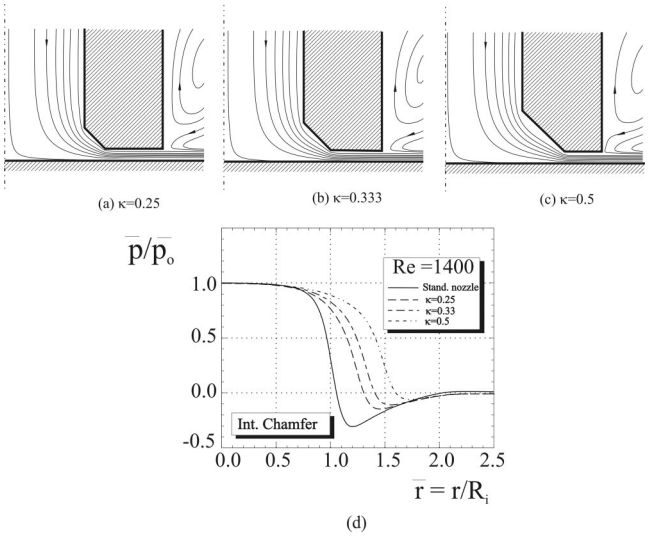

Fig. 11 Flow behavior for internally chamfered nozzle

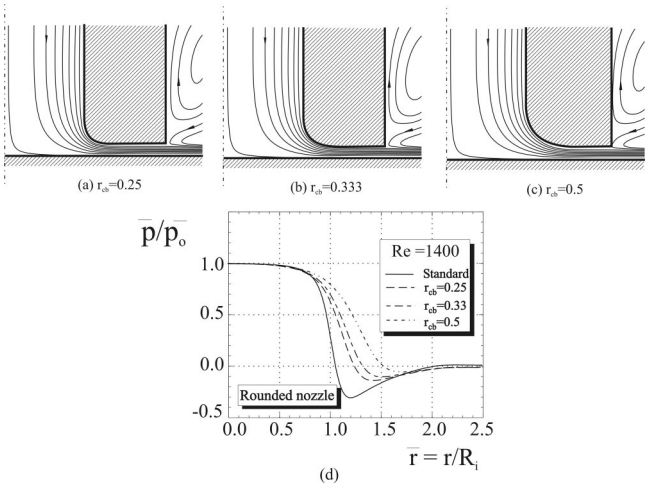

Fig. 12 Flow behavior for rounded nozzle (Re=1400, $\beta=2.0$, $\eta=0.15$)

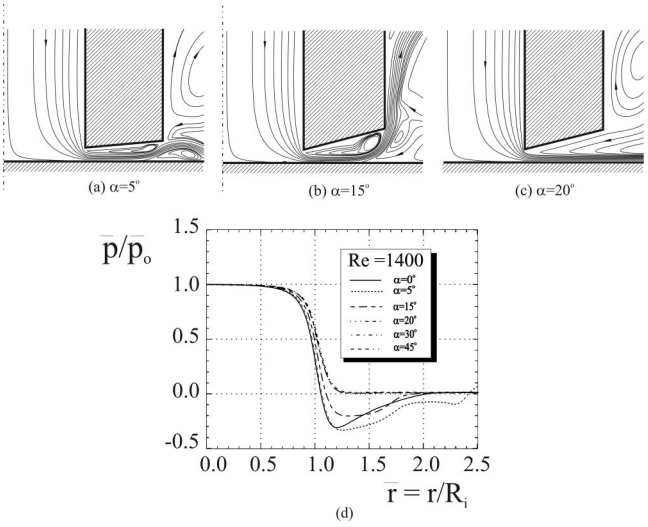

Fig. 13 Effects of chamfer angle (Re=1400, $\eta=0.15$)

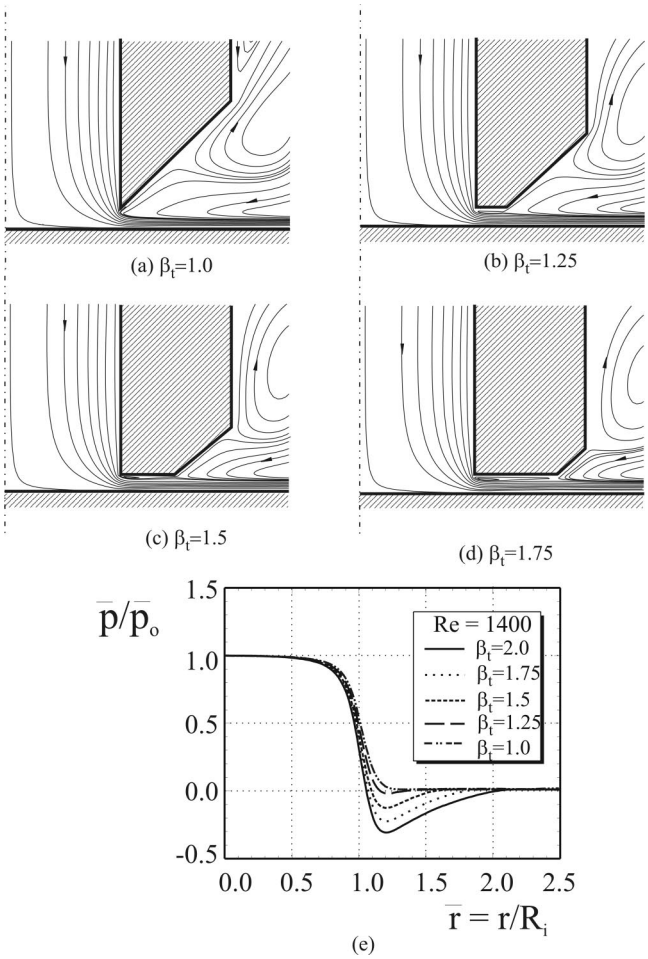

Fig. 14 Effects of truncated width (Re=1400, $\eta=0.15$, $\beta=2.0$, $\alpha=45°$)

frontal surface of the nozzle and the flat plate, the rounded nozzles seems to be a more appropriate solution to nozzle fouling problems compared to the internally chamfered nozzle. This is mainly due to the possible separated flow areas on the internal surfaces of the nozzle in the case of an internally chamfered nozzle. As we will later see, internal modifications to an injection nozzle can possibly lead to a reduction in apparatus sensitivity. We will therefore consider external modifications to the standard injection nozzle in the following section.

5.5 External Modifications to Standard Nozzle. The last two considered cases shown in Figs. 7(*e*) and 7(*f*) are for external modifications to the standard injection nozzle used in industrial metrology applications. The first of these is the externally chamfered nozzle (Fig. 7(*e*)) and the second is a chamfered and truncated nozzle (Fig. 7(*f*)). Results for the chamfered nozzle are shown in Fig. 13. Results show that in the case of a chamfered nozzle, the separated flow area can be eliminated as long as the angle of cut is greater than approximately 20°, Fig. 13(*c*). This can also be noticed on the wall pressure distributions shown in Fig. 13(*d*). For cut angles greater than 20°, one can notice that no negative pressure areas are found at the surface of the flat plate. Confinement effects have therefore practically disappeared for these cases. In cases where $0° \leqslant \alpha \leqslant 20°$, illustrated in Figs. 13(*b*) and 13(c), flow patterns are quite particular but very plausible. For values of up to at least 15°, the flow reattaches to the frontal surface of the nozzle, thus creating a recirulation bubble. For greater angles, the flow does not reattach and fluid is drawn from the area surrounding the nozzle. Results for the chamfered and truncated nozzle are presented in Figs. 14(a–e). A chamfer angle of 45° was used for all considered cases. One can see that as long as a nozzle frontal area parallel to the flat plate exists, a separated flow zone is found (Figs. 14(*b*), (*c*), and (*d*)). One can see that these results are comparable to the cases where the influence of nozzle thickness were considered. Thus, the relevance of the reduction of the frontal area of the nozzle. One general industrial consideration that should be accounted for is the fact that a reduction in frontal area of a nozzle (either chamfered or narrow) increases the risk of nozzle damage in industrial applications (i.e., if nozzle inadvertently touches the controlled surface). An alternate solution would be to reduce the frontal area of the injection nozzle as much as possible (either chamfered and truncated nozzle or a narrow nozzle) but giving it some rigidity by having a somewhat small frontal area. A general comparison of the wall pressure distributions of the various considered nozzles is shown in Fig. 15. One point of interest is that the narrow nozzle (reduced frontal area, $\beta=1.5$ in this case) and the chamfered and truncated nozzle ($\beta_t=1.5$) have practically the same wall-pressure distribution. This can be attributed to the fact that they both have the same frontal areas. As previously noticed, the negative low-pressure area corresponds to the width of the frontal areas of the nozzles (i.e., $\bar{r}=\beta=\beta_t=1.5$). In the cases of internally modified nozzles,

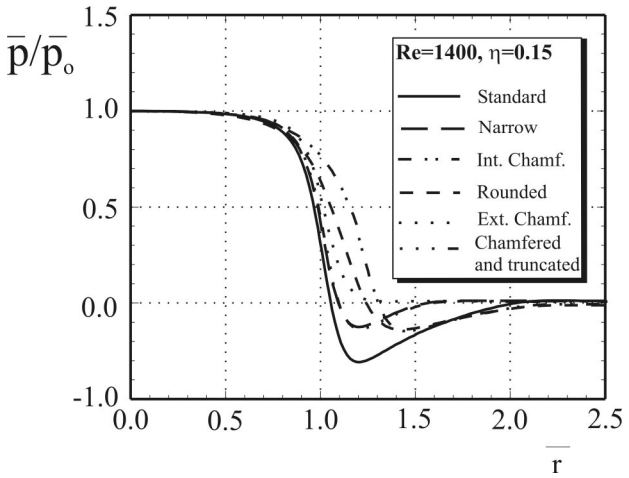

Fig. 15 Wall pressure distributions comparisons for different nozzle types (Re=1400, $\eta=0.15$)

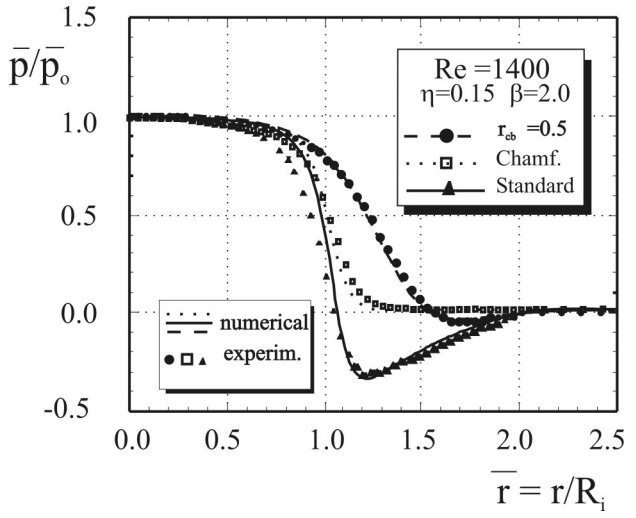

Fig. 16 Numerical and experimental result comparisons

for $\kappa=\overline{r}_{cb}=0.5$, one can see that the drop in wall pressure distribution for the internally chamfered nozzle is somewhat farther out towards the periphery of the nozzle when compared to the internally rounded nozzle. This can be attributed to the fact that the internally chamfered nozzle has a more pronounced change in flow section when compared to the rounded nozzle.

5.6 Numerical and Experimental Result Comparison. Numerical results presented thus far in this paper have been, for the most part, confirmed by experimental measurements, some of which are given in Fig. 16. Results are presented for the standard nozzle compared with a chamfered nozzle (45°) and with a rounded nozzle ($\overline{r}_{cb}=0.5$). One can see that good agreement exists between numerical and experimental results. This agreement indicates that the hypothesis on laminar incompressible flow used in the mathematical formulation of the problem was adequate. A more complete model considering compressibility and turbulence is currently under investigation. The obtained numerical results will be compared to experimental results pertaining to actual industrial operational conditions.

5.7 Influence of Nozzle Geometry on Sensitivity. As previously mentioned, the effects of nozzle geometry on the sensitivity of an apparatus must also be considered. Apparatus sensitivity is basically a measure of how the pressure changes in a measuring branch with a change in the distance separating the nozzle from the controlled surface. Figure 17(*a*), obtained from curve-fitting experimental data, illustrates how the pressure at the center of the flat plate varies as a function of the distance δ (or η). Results are presented for the three principal nozzle types considered (standard, rounded, and externally chamfered). The data were obtained by gradually increasing the distance separating the nozzle and the flat plate. Before every reading, time was given as to allow the manometer to settle (i.e., measurements were made in steady-state conditions). As we are more interested in how pressure varies with a variation in the distance δ, the second graph illustrates the gradient $dp/d\eta$. One can see that for the range of interest (i.e., $0.10<\eta<0.30$), the nozzle that offers the best sensitivity, represented by the greater nomal pressure gradient in absolute value $|dp/d\eta|$, is the chamfered nozzle. The negative aspect of the gradient comes from the fact that an increase in distance η brings on a reduction in pressure. We can also see from Fig. 17(*b*) that the nozzle that is least sensitive is the rounded nozzle. However, if we consider extreme cases where the nozzle is very close to the surface to be measured ($\eta<0.15$), the use of either modified nozzle would improve apparatus sensitivity. Fragility considerations aside, the completely chamfered nozzle will offer the best overall performance.

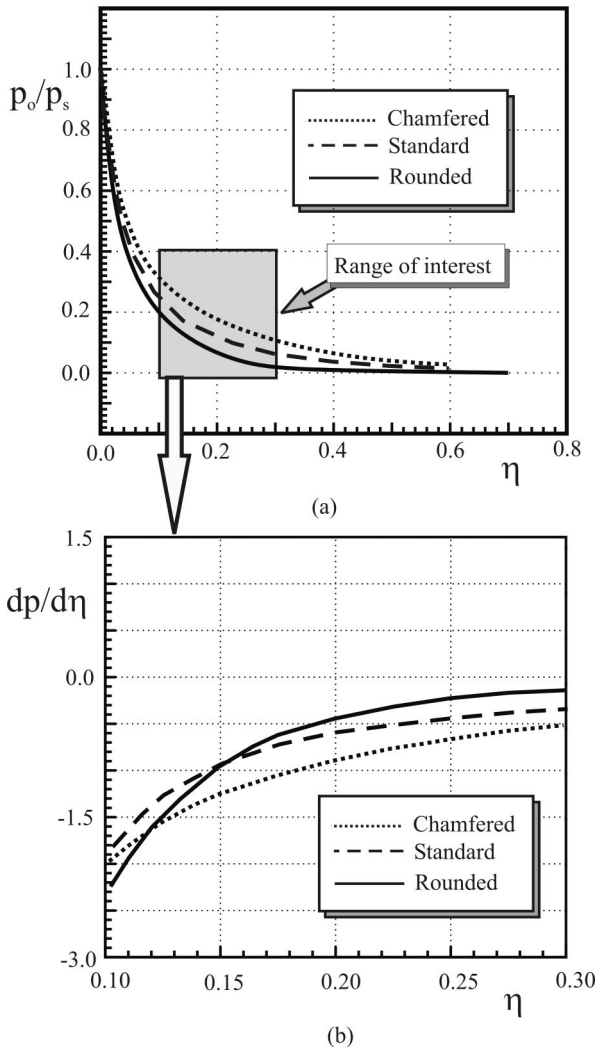

Fig. 17 Effects of nozzle geometry on sensitivity

6 Conclusion

An investigation of the radial flow between an injection nozzle and a flat plate has been presented in this paper. Results have shown that a judicious choice of the nozzle geometry can help eliminate the separated flow area found in the case of a standard nozzle. This recirculation zone is the probable cause of injection nozzle fouling found in industrial applications. Results have shown that an internally modified nozzle or an externally (completely) chamfered nozzle will eliminate the separated flow area. However, it was also shown that a rounded nozzle could hinder apparatus sensitivity at larger values of η. The use of an externally chamfered nozzle could therefore represent an interesting solution to the fouling problem.

Acknowledgments

The authors of this present paper wish to thank the Natural Science and Engineering Research Council of Canada as well as the Université de Moncton for their financial support.

Nomenclature

α = chamfer angle (deg)
δ = distance separating nozzle and plate
h = nozzle body clearance space
K = width of internal chamfer
L = inlet tube length
μ = fluid absolute viscosity
ν = fluid kinematic viscosity
p = pressure
p_o = pressure at center of plate
p_s = supply pressure
p_{at} = ambiant pressure
Δp = apparatus pressure differential
Q = volumetric flow rate
r = radial coordinate
ρ = fluid density
R_i = internal radius of injection nozzle
R_d = radius of calculation domain
R_e = external radius of injection nozzle
R_{cb} = radius of curvature, rounded nozzle
R_t = radius of truncated frontal area
θ = tangential coordinate
u = radial fluid velocity component
w = axial fluid velocity component
z = axial coordinate

Nondimensional quantities

$\beta = R_e/R_i$
$\beta_t = R_t/R_i$
$\beta_d = R_d/R_i$
$\eta = \delta/R_i$
$\kappa = K/R_i$
$\lambda = h/R_I$
$\overline{p} = p/\rho(\nu/R_i)^2$
$\overline{r} = r/R_I$
$r_{cb} = R_{cb}/R_I$
Re = Reynolds number, $\mathrm{Re}=2Q/R_i\pi\nu$
$\overline{u} = u/(\nu/R_i)$
$\overline{w} = w/(\nu/R_i)$
$\overline{z} = z/R_i$

References

[1] Moller, P. S., 1963, ''Radial Flow Without Swirl Between Parallel Discs,'' Aeronaut. Q. pp. 163–186.
[2] Ishizawa, S., Watanabe, T., and Takahashi, K., 1987, ''Unsteady Viscous Flow Between Parallel Disks With a Time-Varying Gap Width and a Central Fluid Source,'' ASME J. Fluids Eng., **109**, pp. 395–402.
[3] Prakash, C., Powle, U. S., and Suryanarayana, N. V., 1985, ''Analysis of Laminar Flow and Heat Transfer Between a Stationary and a Rotating Disk,'' AIAA J., **23**, pp. 1666–1667.
[4] Bettahar, A., 1993, ''Application des écoulements radiaux à la métrologie pneumatique dimensionnelle,'' Ph.D. thesis, Université de Valenciennes, France.
[5] Crnojevic, C., Roy, G., Florent, P., and Bettahar, A., 1997, ''Influence of Regulator Diameter and Injection Nozzle Geometry on Flow Structure in Pneumatic Dimensional Control Systems,'' ASME J. Fluids Eng., **119**, pp. 609–615.
[6] Lytle, D., and Webb, B. W., 1994, ''Air Jet Impingement Heat Transfer at Low Nozzle-Plate Spacings,'' Int. J. Heat Mass Transfer, **17**, pp. 1687–1697.
[7] Behnia, M., Parneix, S., Shabany, Y., and Durbin, P. A., 1999, ''Numerical Study of Turbulent Heat Transfer in Confined and Unconfined Impinging Jets,'' Int. J. Heat Fluid Flow, **20**, pp. 1–9.
[8] Wattebot, L., 1937, ''L'amplification pneumatique: Principe, Théorie,'' Journal de Mécanique, pp. 70–72.
[9] Fortier, M., 1950, ''Applications industrielles des écoulements gazeux à la vitesse critique,'' Revue chaleur et Industrie, **299**, p. 145.
[10] Schlichting, H., 1979, *Boundary Layer Theory*, McGraw-Hill, New York.
[11] Patankar, S. V., 1980, *Numerical Heat Transfer and Fluid Flow*, McGraw-Hill, New York.
[12] Roy, G., 1997, ''Contribution à l'étude de l'écoulement radial: Applications en métrologie industrielle,'' Ph.D. thesis, Université Laval, Québec, Canada.
[13] McGinn, J. H., 1956, ''Observations on the Radial Flow of Water Between Fixed Parallel Plates,'' Appl. Sci. Res., **5**, pp. 255–264.

Measurements of Resistance of Individual Square-Mesh Screens to Oscillating Flow at Low and Intermediate Reynolds Numbers

Ray Scott Wakeland
e-mail: wakeland@psu.edu

Robert M. Keolian

The Pennsylvania State University,
Graduate Program in Acoustics,
P.O. Box 30,
State College, PA 16804-0030

Measurements are reported of pressure losses across single screens subjected to low-frequency oscillating flow for $0.002 \lesssim Re_d \lesssim 400$, where Re_d is Reynolds number based on wire diameter and peak approach velocity. Several correlation methods are examined. Extensive comparisons are made between present oscillating-flow results and previous reports of the resistance of screens to steady flow. Defining oscillating results in terms of peak amplitudes, the oscillating and steady-flow resistances are found to be the same, including behavior in the intermediate Reynolds number region that departs from correlations of the form $ARe^{-1}+B$. The friction factor is also found to depend on Reynolds number, but not independently on oscillation amplitude, over the range of conditions measured. [DOI: 10.1115/1.1601254]

1 Introduction

This paper reports measurements of the resistance to oscillating flow of individual woven-wire screens. Previous investigators have measured the hydraulic resistance of individual screens in steady flow, and of packed beds of multiple screens (including regenerators) in steady and in oscillating flow.

Our interest in screens in oscillating flow stems from their use in thermoacoustic refrigerators and heat engines (see, for example, Ref. [1]). Many of the steady-flow studies of single screens were motivated by the use of screens in wind tunnels to reduce turbulence and variations in velocity across the tunnel. Screens are sometimes used in thermoacoustic devices for similar purposes, such as to stop jets from impinging on heat exchangers. We are investigating the use of single screens as fin components in very short, oscillating-flow heat exchangers for use in novel thermoacoustic devices.

Our test apparatus operates at low frequencies (0.125 to 9 Hz) and large strokes (up to 13.9 cm). At low frequencies, where the viscous penetration depth is larger than the openings in the screen, the pressure drop across a screen is expected to be largely independent of frequency, and this is what we observe. Some of our measurements, however, are made using screens of very course mesh, for which 9 Hz is a ''high'' frequency, so that the flow resistance increases with frequency for fixed Reynolds numbers. For those screens, this paper includes only the lowest frequency data, where the frequency effect is smallest.

The flow resistance of a porous medium is generally characterized by a region of low Reynolds number (Re), where the pressure drop Δp is proportional to Re^{-1}, a region of high Reynolds number, where Δp is independent of Re, and an intermediate region of transition between the other two. Our apparatus allows measurements in the low and intermediate Reynolds number regimes, with low Mach number (<0.024), for screens oriented normal to the flow.

Much of the paper is devoted to comparisons between our data and those reported by previous investigators for steady flow or for multiple screens. This turns out to be a difficult task because of the diversity of approaches that have been used in analyzing and reporting results. Overall, we conclude that steady-flow correlations of single screens may be applied to screens in low-frequency oscillating flow.

2 Description of Measurement System

The test section is placed in a measurement apparatus, shown in Fig. 1, that is vertically symmetrical about the test section except for the shaker at the bottom. The APS Dynamics shaker, [2], moves a metal end-plate that is connected to the stationary parts of the duct via a square polyurethane bellows. Just above the bellows is a heat exchanger, used for other applications, that acts as a flow straightener in the present experiment. Next is an 18.5-cm-long square-sided diffuser section that matches the inside dimensions of the bellows and flow straightener to those of the test duct. Between the diffuser and the test duct are two layers of window screen (of the same type as screen 16–10 in Table 1) to further reduce the possibility of turbulence from the bellows entering the test duct. The test duct, made of acrylic, has square 29.2 cm$\times$29.2 cm inner cross-sectional dimensions. The half of the test duct below the test section is 30.5 cm long, with a flange at the top for mounting test sections. Above the test section these parts are repeated in reverse order. The top and bottom end-plates are coupled by rigid connecting rods, so that the end-plates go up and down together, driven by the single shaker. The test section, ducts, and diffusers are held fixed relative to the base of the shaker (and the lab) by a large support frame (not shown). In Fig. 1, the end-plates are at their lowest point, so that the upper bellows is compressed and the lower bellows is expanded.

Also attached to the shaker (but not shown in the diagram) is a strut structure that supports suspension springs. The spring stiffness combines with the mass of the moving parts to give a resonance frequency around 4 Hz. This choice of spring stiffness allows the shaker to oscillate the end-plates to its full stroke at up to 5 Hz while still allowing the full stroke at 0.125 Hz. The amplitude diminishes as the frequency is increased above 5 Hz due to amplifier limitations. All experiments are conducted in air at ambient atmospheric pressure and temperature, which are measured at the beginning of each measurement run to determine the air density ρ and kinematic viscosity ν.

The position of the end-plates is measured with a Schaevitz linear variable differential transformer (LVDT), [3], biased and demodulated with a Schaevitz ATA 2001 processor. This unit contains a fourth-order low pass filter that causes a phase shift that

Contributed by the Fluids Engineering Division for publication in the JOURNAL OF FLUIDS ENGINEERING. Manuscript received by the Fluids Engineering Division Oct. 25, 2002; revised manuscript received Apr. 21, 2003. Associate Editor: M. V. Ötügen.

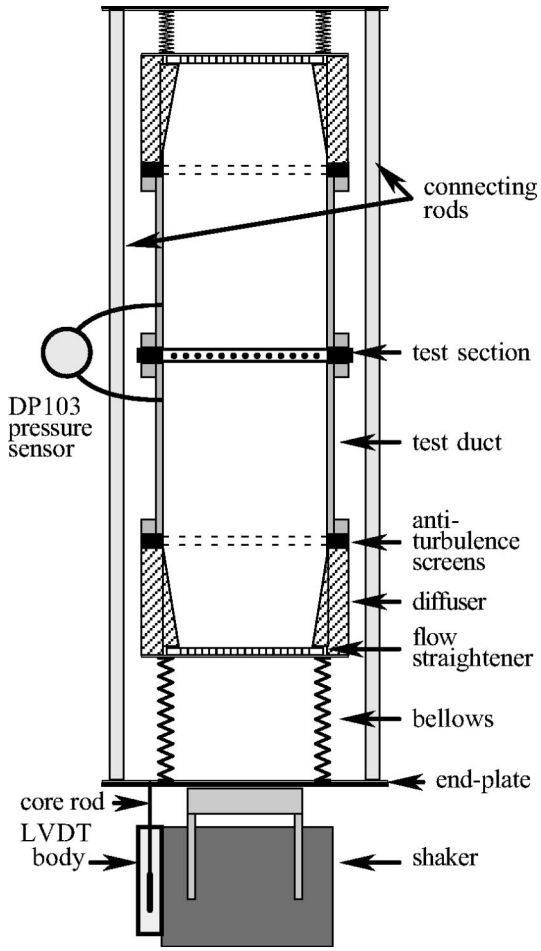

Fig. 1 Schematic of the measurement apparatus

grows in magnitude approximately linearly to −1.28 deg at 10 Hz. This phase shift (along with the less significant amplitude change) was measured directly by modulating the unit's bias signal so as to emulate an LVDT signal of known phase, and comparing the ATA 2001's output to the known modulation. This measurement is used to correct the LVDT signal before it is converted into an end-plate position amplitude.

The gas velocity is inferred from the end-plate position measurement. The bellows has inner dimensions of 25.4 cm and outer dimensions of 30.5 cm, for an effective inner side length of 27.9 cm. The stroke (peak-to-peak displacement amplitude) of the air is therefore $(27.9/29.2)^2$ times the 15.2 cm shaker stroke, for a maximum air stroke of 14.0 cm which, at 5 Hz, gives a maximum air speed of about 2.2 m/s.

The pressure drop across the test section is measured with a Validyne DP103 variable-reluctance differential pressure sensor, [4], biased at 5 kHz and demodulated with a lock-in amplifier with minimum filtering. The Validyne sensor was suggested by two regenerator pressure-drop papers, [5,6], and was selected because it has the appropriate sensitivity for this measurement and responds down to 0 Hz. It has a replaceable diaphragm, and we use the thinnest available diaphragm (#6) to give the greatest sensitivity (35 Pa maximum). In the course of the experiment it was discovered that, at least with this diaphragm, the DP103 is far from flat in either frequency or phase, even below 10 Hz. Therefore the DP103 is calibrated against an Endevco 8510–B–1 piezoresistive pressure sensor (6895 Pa maximum) which, while presumed to be flat from 0 to 10 Hz, is not sufficiently sensitive for direct use in the experiment. The Endevco is in turn calibrated at 0 Hz against an Omega PCL9001 pressure calibrator, [7], that was itself recently calibrated by the manufacturer.

The position and pressure sensor signals are digitized with a computer data acquisition board. Fourier transforms are performed on both signals to obtain their amplitudes at the driving frequency and their relative phase. All oscillating flow calculations are based on peak amplitudes of pressure drop and velocity, written Δp and u, of the driving frequency component.

The two sides of the pressure sensor are connected by tubes to ports on opposite sides of the test section. (The calibration is done using the same tubing.) The separation of the ports depends on the thickness of the frame that is used to mount the test section. For the bare duct, with no test section and the flanges from the top and bottom portions of the test duct in direct contact, the ports are separated by 16.36 cm. The longer of the two support frames is 0.95 cm long.

In this measurement, the inertial contribution to the pressure is quite significant. The part of the total pressure difference peak

Table 1 Test screen dimensions. The fourth column, "$\beta \rightarrow \phi$ error," is used to give an estimate of the uncertainty in β, ϕ, and D_h. The uncertainties on A_0 are 2%, except or the four highest porosity screens, which have an uncertainty up to 5%.

Screen	β	ϕ	$\beta \rightarrow \phi$ Error	D_h	d_1 (mm)	m_1 (1/m)	d_2 (mm)	m_2 (1/m)	A_0
8–63	0.265	0.589	14%	2.19	1.524	320	1.524	317	204
14–35	0.299	0.608	13%	1.26	0.775	551	0.851	563	160
50–9	0.303	0.665	3.4%	0.45	0.229	1969	0.229	1969	117
4–120	0.306	0.609	13%	4.60	2.972	152	2.921	152	138
40–10	0.360	0.714	0.2%	0.63	0.254	1575	0.254	1575	71.9
16–28	0.399	0.676	8.5%	1.23	0.584	630	0.597	618	69.8
6–63	0.400	0.679	8.2%	3.23	1.511	236	1.549	244	72.5
14–28	0.407	0.691	6.8%	1.52	0.660	551	0.699	516	63.0
24–14	0.478	0.731	5.6%	0.88	0.305	948	0.343	957	40.3
20–16	0.483	0.746	3.8%	1.14	0.381	787	0.394	787	36.1
10–32	0.487	0.742	4.6%	2.20	0.762	394	0.775	394	36.1
80–3.7	0.496	0.758	2.9%	0.29	0.094	3150	0.094	3150	34.1
12–28	0.552	0.779	3.6%	1.93	0.546	472	0.551	465	24.4
8–35	0.556	0.796	1.6%	3.07	0.762	317	0.813	329	23.1
4–63	0.578	0.807	1.4%	6.57	1.562	154	1.575	152	20.6
8–28	0.608	0.811	2.7%	3.05	0.686	317	0.737	303	17.4
6–35	0.649	0.844	0.9%	4.66	0.864	229	0.864	221	13.2
3–63	0.671	0.856	0.7%	9.37	1.562	119	1.600	109	12.2
16–10	0.719	0.863	2.0%	4.88	0.241	630	0.241	630	8.6
4–35	0.736	0.886	0.5%	6.88	0.889	163	0.876	158	7.7
16–9	0.753	0.881	2.3%	1.55	0.203	626	0.216	636	5.7

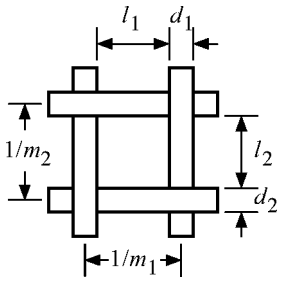

Fig. 2 Screen dimensions

amplitude Δp that is due to the resistance of the test section is the portion that is in phase with the velocity, i.e., in quadrature with the position. If θ is the phase angle between the pressure and the position (not velocity), then the inertial (reactive) and resistive components of the pressure are given, respectively, by

$$\Delta p_{\text{inertial}} = \Delta p \cos\theta \quad \text{and} \quad \Delta p_{\text{quad}} = -\Delta p \sin\theta. \tag{1}$$

For each data collection run, the maximum Reynolds number at 5 Hz is determined, and a set of test Reynolds numbers below the maximum is selected. For each frequency, all of the available Reynolds numbers within the stroke limit are tested. The computer attempts to adjust the shaker stroke to match each selected Reynolds number, which it does to within a percent in most cases.

3 Test Screens

All of the test screens are made of round steel wire, except for one piece of aluminum window screen. All are nominally square plane weave with a single wire size. However, many of these screens are "not of precision manufacture," to borrow a phrase from Ref. [8]. Several previous investigators, [9–11], have pointed out that small errors in the dimensions of a screen result in large errors in various calculated parameters that are used in data reduction. Therefore, the dimensions of each screen are measured. The screen dimensions are defined in Fig. 2. Average wire-to-wire distance $1/m$ (m for "mesh," also called "pitch") is measured by counting wires over a distance of at least 25 cm. Wire diameter d is measured with a digital vernier caliper by sampling many wires and judging a best typical diameter. In each direction, the variation in wire diameter is very small, but some screens have significantly different diameters in the two directions. In many of the screens, the measured diameter is less than the nominal size. Measured values are used in all calculations, except that the wire diameter of the screen with the smallest wire (screen 80–3.7) has wire too small to measure accurately by caliper, and the nominal value is used. We refer to each screen by its nominal size in English units, so that the screen called 16–28 has approximately 16 wires per inch with wire diameters of about 0.028 inches. Measured screen dimensions are found in Table 1.

Many of the correlations discussed in Section 6 make use of a screen "porosity" based on "free flow area," i.e., the ratio of the orthogonally projected open area of the screen to the total cross-sectional area, so this calculated value is included in the table. Referring to Fig. 2, this orthogonal porosity β is

$$\beta \equiv (1 - d_1 m_1)(1 - d_2 m_2), \tag{2}$$

or simply $\beta = (1 - md)^2$ for truly square screens where $d_1 = d_2 = d$ and $m_1 = m_2 = m$. In other calculations where wire diameter is called for, we use the mean value, $d_m = (d_1 + d_2)/2$.

Also appearing in the table is a volumetric porosity ϕ, defined simply as the ratio of connected void volume V_{void} to the total volume of the sample V_{total},

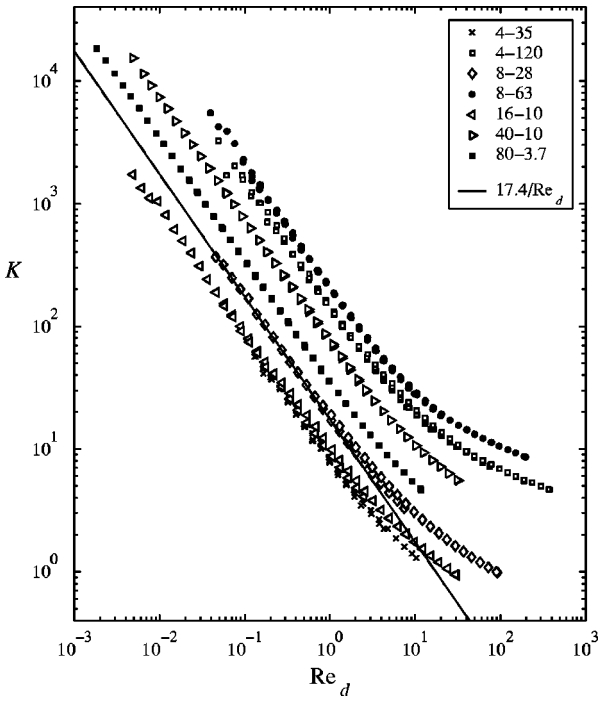

Fig. 3 Seven example data sets

$$\phi \equiv \frac{V_{\text{void}}}{V_{\text{total}}}. \tag{3}$$

This quantity is easy to measure accurately for materials such as screens (stacked or individual), where there are no isolated holes (such as can occur in a foam) and where the density ρ_{solid} of the solid material is known, simply by weighing the material and dividing by the screen volume to obtain its density $\rho_{\text{porous medium}}$,

$$\phi = \frac{\rho_{\text{porous medium}}}{\rho_{\text{solid}}}. \tag{4}$$

The values in Table 1 were determined in this way (by weight) rather than calculating from mesh and wire dimensions. The volume of each screen was determined by measuring its area (approximately 0.930 cm^2 in each case) and multiplying by $d_1 + d_2$. In this study, the screen thickness is always taken to be $d_1 + d_2$, the thickness of an ideal plane screen, even in the cases of the heaviest screens, which sometimes depart from ideality in that the wires in one direction appear to bend more than wires in the other direction.

Screens are selected to cover as large a range of porosity as possible in readily available sizes, covering $0.265 \leqslant \beta \leqslant 0.753$ and $0.589 \leqslant \phi \leqslant 0.886$. Some of the screens have the largest available wire size (up to 2.95 mm), to get the largest possible Reynolds number based on wire diameter. One screen has wire smaller than this by a factor of 30, and hydraulic diameters cover a range equally large. Some screens are chosen to have similar porosities but very different wire sizes. Toward the low porosity end, for example, the screen with 2.95 mm mean wire diameter (screen 4–120) has nearly the same β as screen 50–9, which has wire less than a tenth as large.

4 Results

Figure 3 shows seven representative data sets. In the figure the data are plotted in terms of Reynolds number based on wire diameter,

$$\text{Re}_d \equiv \frac{u d_m}{\nu}, \tag{5}$$

and the simple loss factor K,

$$K = \frac{\Delta p_{\text{quad}}}{\rho u^2/2}. \tag{6}$$

In Eqs. (5) and (6), u is the "superficial," "freestream," or "approach" velocity, i.e., the velocity of the gas when it is in the test duct, not the higher velocity when it is within the pores of the screen. Note that the Reynolds numbers and loss factors that we are examining for oscillating flow are *not* instantaneous values throughout the cycle. Rather, Reynolds numbers are based on the peak velocity amplitudes, and loss factors are based on the peak amplitude of the resistive component of the oscillating pressure.

The finest mesh screen, 80–3.7, has high flow resistance, and therefore gives very clean data to the lowest Reynolds number of any screen, but the wires are so small that the highest Reynolds numbers are below the "knee" seen in the curves of other screens. Screens 4–120 and 8–63 both have large enough pressure drops to give good measurements at low Reynolds number, but these two screens also have large enough wire diameters that the shape of the curve can be determined well above the knee.

Both 4–120 and 8–63 also have small enough openings (small $l = m^{-1} - d$ in Fig. 2) that the results are independent of frequency. The 8–63 data shown in Fig. 3 includes frequencies 0.125, 0.25, 0.5, 1, 3, 5, 7, and 9 Hz, but all the points fall so close to a single curve that the data for most Reynolds numbers merge into a single dot. In other plots in this paper, frequencies above 5 Hz are not included. Data are presented for most screens at 0.5 Hz and 5 Hz, giving the largest possible range of Reynolds number with this apparatus.

As the frequency increases, the viscous penetration depth decreases, and eventually the hydraulic resistance begins to increase with frequency. In this investigation we are interested in only the low frequency results. For screens where the hole size is larger than the viscous penetration depth of $\sqrt{2\nu/\omega} = 1.0$ mm at $\omega = 2\pi$ (5 Hz), the 5 Hz data do not fall on the same curve as the lower frequencies. Screen 8–28 has a large enough opening ($l_2 = 2.56$ mm) to see this effect in Fig. 3: The data points for 0.5 Hz and 5 Hz do not lie exactly on top of each other in the region of overlapping Reynolds number. The difference is small enough for this screen, however, that the 5 Hz points are retained, since they contain the information about the curve above the knee.

Screen 4–35, in contrast, has such large openings that only the lowest frequencies (0.125, 0.25, and 0.5 Hz) are presented. For this reason, the shape of the knee of the curve cannot be determined for this screen. Furthermore, this screen has so little resistance that the scatter in the data becomes large at low Reynolds number. Thus, data are presented over a somewhat limited range of Reynolds number. It is enough data, however, to make a fair estimate of the coefficient A_0 of a fit line A_0/Re_d, discussed later in this section.

Screen 16–10 has about the same porosity as 4–35, and the curves for these two screens lie close together. Since 16–10 has higher resistance, however, the data are good to lower Re_d, and since the openings are much smaller, the 5 Hz data can be used, so that the results go to higher Re_d as well.

At even higher Reynolds numbers, the pressure drop curves for porous media approach a constant value. Unfortunately, with our apparatus in its current configuration we are unable to measure this feature. Our data cover the range $0.0018 < \text{Re}_d < 380$.

For each screen, log-log plots of K versus Re_d are fit at low Re_d with a line A_0/Re_d. In Fig. 3, the line $17.4/\text{Re}_d$ is shown fitting the data for screen 8–28. The value of the fit parameter A_0 is tabulated for each screen in Table 1. In cases such as screen 8–28, where there is some discrepancy between the 5 Hz data and lower frequency data, we have favored the low frequency data in making the fit.

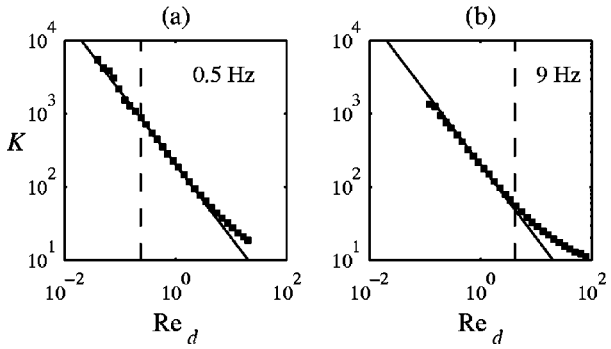

Fig. 4 Measurements do not show an expected change in loss factor near the amplitude where the gas stroke equals the wire diameter, shown by the vertical dashed line for data at 0.5 Hz (part (*a*)) and 9 Hz (part (*b*)). The solid diagonal line in each plot is $K = 204\ \text{Re}_d^{-1}$.

A surprising feature of these oscillating flow measurements is that, within the range of our experimental conditions, the functional form of the flow resistance with Reynolds number seems to be independent of oscillation amplitude. In particular, there is no detectible transition near where the oscillation peak-to-peak amplitude is equal to the screen thickness. Because velocity depends on both amplitude and frequency, this condition occurs at a different Reynolds number for each frequency, so amplitude effects should be easily distinguished from Reynolds number effects. However, for each screen, our data fall along a single curve of K versus Re_d. Consider the data from screen 8–63 shown in Fig. 4. For this screen, the data span the $2x_1 = d_m$ condition for each frequency. At 0.5 Hz the stroke-equals-thickness condition occurs when $\text{Re}_d = 0.23$, shown in the Fig. 4(*a*) by the vertical dashed line. The 0.5 Hz data cover a range from $0.17 < 2x_1/d_m < 87$. At 9 Hz (Fig. 4(*b*)), $2x_1 = d_m$ when $\text{Re}_d = 4.2$, with data covering $0.029 < 2x_1/d_m < 19$. We would have expected some sort of change (probably an increase in the product $\text{Re}_d K$), if not exactly at $2x_1 = d_m$, then at least *at some point* in the measured range, but we observe none.

5 Uncertainties

5.1 Uncertainties in Screen Parameters. The volumetric porosity ϕ can be determined from measurements of screen dimensions alone, or from screen thickness and the independent measurement of mass. The agreement between these two methods gives an indication of the uncertainty of ϕ, β, and D_h. The column labeled "$\beta \rightarrow \phi$ error" in Table 1 shows the discrepancy between ϕ calculated using mass and ϕ calculated using only the measurements of the *m*s and *d*s that are used to calculate β and D_h. The errors are less than 4% for most screens and less than 8.5% for all except the three screens that have a combination of large wires and tight mesh, where the error shoots up to 14%. These large errors are systematic in that the *m*s and *d*s always predict a ϕ that is larger than that determined from weighing. From visual inspection it is evident that in the low-porosity screens, the wires in one direction bend back and forth more than the wires that run in the other direction. That is, the discrepancy is more one of *geometry* than of measurement. Thus, we take the uncertainty in both β and ϕ, which are calculated from our distance measurements, to be less than 8% for all screens, whereas the uncertainty in D_h, which is a combination of both scale and geometry, grows to 14% for the low-porosity screens. The uncertainty in d_m would then be $8\%/2 = 4\%$.

5.2 Uncertainties in Velocity and Pressure. The measurement of pressure magnitude is the most accurate in the experiment, with an uncertainty less than 1.5%. The Endevco standard has been calibrated repeatedly using a variety of independent

means, and the comparison calibration of the Validyne sensor used in the experiment makes use many cycles of oscillation and is very repeatable, with only 0.6% variation over a period of three months.

The measurement of the shaker stroke by means of LVDT has, by itself, an uncertainty less than 1%. Unfortunately, the *gas velocity* at the test section depends on the effective area of the bellows, the uncertainty of which is difficult to determine directly. Therefore, we check the gas velocity by measuring the oscillation pressure in the empty duct, as described in the next section.

The most difficult part of the measurement is the phase of the pressure. We wish to measure the flow resistance of the screens. In an oscillating flow, however, the pressure has both a (reactive) inertial component and a resistive component. The inertial component is the pressure required simply to oscillate the mass of the gas back and forth in the duct in the absence of shear forces from the walls or screen. This component is in phase with the displacement. The resistive portion is in phase with the velocity, and thus in quadrature with the displacement. To extract the quadrature component of the pressure, we need to know the phase. In the comparison calibration, the phase of the Endevco is taken to be zero. While we believe this to be accurate, we do not have a direct method of calibrating the phase at these extremely low frequencies. To study the uncertainty in phase of our overall measurement system, measurements were made of two known cases, described next.

5.3 Validation With Known Cases. The measurement system is validated by measuring two cases for which there are good theoretical predictions, the empty test duct, and a set of parallel plates.

The behavior of gas oscillating in a duct depends on the ratio of duct size to viscous penetration depth. When our test duct is left empty, it is ''very large'' even at 0.5 Hz, where the viscous penetration depth is 3 mm. Except for the small boundary layer near the walls, the gas oscillates essentially as a uniform slug, [12],[1] and the peak pressure difference between the sensors is nearly $\Delta p = \rho L \omega u$, where L is the distance between the sensors and ω is the circular frequency of oscillation. Figure 5(*a*) shows the error between the measured Δp and the expected Δp for very small velocities (0.029 m/s, shown by ◦) and very large velocities (1.08 m/s, shown by +) at frequencies between 0.25 and 10 Hz. (It is not possible to obtain the highest velocities at low frequencies because of stroke limitations or at high frequencies because of amplifier limitations.) Most points lie within 2.5% of the expected value. Frequencies below 0.25 Hz have such a low pressure drop in the empty duct that the signal is lost in the noise.

Earlier measurements had pressure values that were systematically low. Repeated measurements of the empty duct with various pressure sensor spacings, as well as measurements on parallel plates, led us to conclude that the effective bellows area was too large by 3%, and a correction of this value has been incorporated into all subsequent measurements. In this sense, the more accurately known pressure magnitude measurements have been used to calibrate the volume displacement to achieve the 2.5% uncertainty shown in Fig. 5(*a*).

While the resistance of the empty duct is very small, it is not too small for us to detect in the form of the small phase shift between pressure and displacement, as shown in Fig. 5(*b*). The heavy solid curve is the theoretical value, [1]. The low-amplitude results are extremely good below 6 Hz but go bad quickly at higher frequencies. The high-amplitude results have an error of about 0.25°. Recall that most of the measurements reported in this paper are made at 5 Hz and 0.5 Hz.

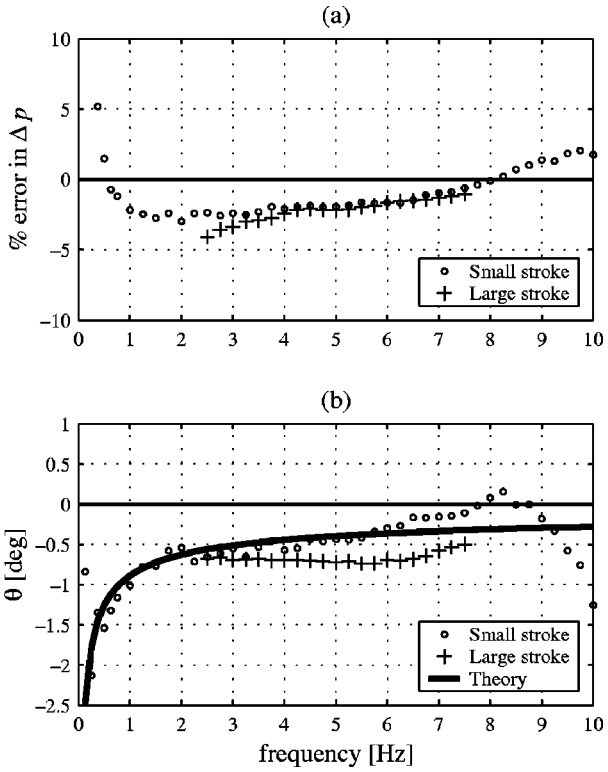

Fig. 5 Results from the empty duct, used to estimate uncertainties in the gas velocity and the phase of the pressure

The theoretical value of phase shown in Fig. 5(*b*) is calculated on the assumption of laminar oscillating flow. Turbulent flow would result in larger (but not well-known) phases. The agreement in Fig. 5(*b*) supports our belief that the flow in the duct is essentially laminar slug flow. The flow quality was also checked qualitatively by injecting smoke into the duct and watching it oscillate (or viewing it before and after oscillation in the case of large amplitude and frequency). With no oscillation, of course, there is a slow rate of change of shape of the smoke filaments. This rate was not noticeably increased by oscillation, even for smoke near the walls. We are, unfortunately, not equipped to make quantitative measurements of turbulence in the duct.

Another case for which there is a solid theoretical result is a set of parallel plates, [1], with the restriction that the stroke must be much smaller than the length of the plates. A test section was constructed of 45 thin (0.635 mm) brass plates, 5.08 cm in the flow direction, and spaced 0.635 cm apart. Figure 6 shows measurements for small stroke ($\leqslant$4 mm), with the theoretical result shown by the solid curve. As the frequency increases, the inertial component of the pressure increases as frequency squared, and the phase between pressure and displacement becomes small, so even the very small error in phase seen in Fig. 5(*b*) leads to significant error in the loss factor, as plotted in Fig. 6(*d*). At 5 Hz the error is about 2%, and at 0.5 Hz it is 5%.

The resistive pressure drop and phase shift due to these parallel plates is similar to that for our test screens. The phase shift for the parallel plates is 26° at 0.5 Hz and 3.4° at 5 Hz. For two-thirds of the screens, the phase shifts are greater than this even at the lowest amplitudes, so the uncertainty should be less than the 2 to 5% for the parallel plates. For the seven screens with the largest values of β, the phases do fall below the parallel plate value for the

[1]The transition from laminarity to turbulence in oscillating flow is more complicated than that for steady flow, depending both on peak Reynolds number and on the ratio of the duct cross-sectional size to the viscous penetration depth. Four flow regimes have been identified: laminar, weakly turbulent, conditionally turbulent, and fully turbulent. The present empty duct flows are all ''weakly turbulent,'' characterized by very small turbulent perturbations of the laminar flow n the core flow, and an unperturbed boundary layer. For our duct dimensions and frequencies, the velocity is essentially uniform across the duct except for the small boundary layer, regardless of the turbulence regime.

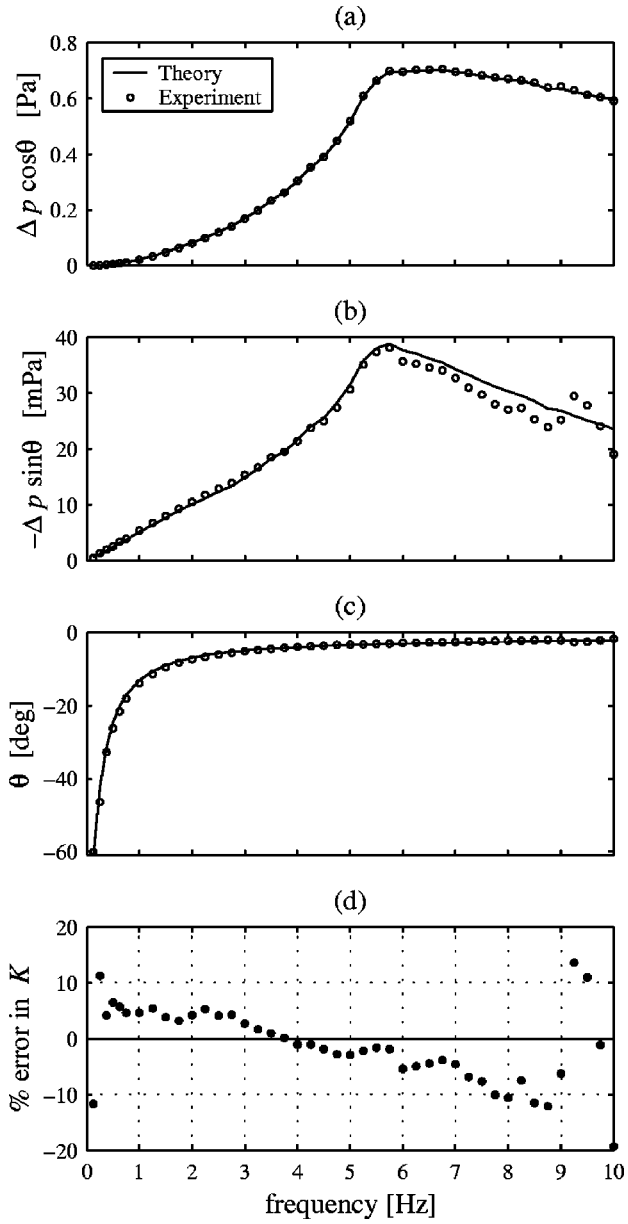

Fig. 6 Experimental and theoretical results from parallel plates at low amplitude, used to study the overall uncertainty in *K*

smallest amplitudes. We estimate that the error in some of the individual pressure measurements for the least resistive screen (3–63) might be as large as 30%.

5.4 Uncertainties in Reynolds Number. The uncertainty in Reynolds numbers is dominated by the uncertainty in characteristic dimension; 4% for d_m and 8 to 14% for D_h. Even though the temperature was only measured once at the start of each measurement run, the uncertainty in ν is less than 1%. Even for the most dissipative screen, the heating due to flow through the screens averages less than 10 mW over the course of a run. Even if this heating were confined to the heat capacity of the air in the test duct, the temperature rise would be only 1 K during the course of a run. Changes in ambient temperature in the room are a more likely source of variation, and these are never observed to be as much as 2 K over the course of a measurement run, and this would still change ν by only 1.2%.

5.5 Uncertainties in A_0. The values of A_0 in Table 1 are obtained by fitting K versus Re_d curves by eye. In most cases this is extremely easy, with an uncertainty of less than 2% for all but a couple of the highest porosity screens, where the scatter in the data leads to an uncertainty of possibly as much as 5%, as judged by repeating the fitting process after an interval of several weeks, and then again many weeks later.

6 Comparison to Measurements and Correlations of Previous Investigators

Definitions of Reynolds number and friction factor, and methods of reducing the data to simple correlations, have proliferated. Thirty-five years ago, Pinker and Herbert [13] observed ''a rather bewildering number of permutations available for attempting a correlation of incompressible data.''

Two general approaches have been most common. Researchers measuring the resistance of single screens in steady flow have tended to use the parameters β and Re_d (Eqs. (2) and (5)). That is, they have favored orthogonal porosity and wire diameter in making correlations. Researchers measuring packed beds of multiple screens have naturally tended away from ''free flow area,'' which is a fuzzy concept for a randomly oriented stack of screens, and meaningless for most porous media. They tend to use volumetric porosity to characterize the openness of the screen. Many of these same researchers base Reynolds number on hydraulic diameter D_h, usually defined as four times the ratio of the void volume V_{void} to the wetted surface area A_w,

$$D_h = \frac{4V_{\mathrm{void}}}{A_w}. \tag{7}$$

Models of packed screens have assumed that all of the surface area of all of the wire is wetted, in which case the hydraulic diameter is related to the wire diameter d_m by

$$D_h = d_m \frac{\phi}{1-\phi}. \tag{8}$$

Some correlations make use of a Reynolds number based on the ''pore diameter,'' the geometric mean of the sides of the screen opening,

$$l_m \equiv \sqrt{l_1 l_2}, \tag{9}$$

or some related parameter, and some even mix β, ϕ, D_h, and l.

Using any of these definitions, the friction factor is inversely proportional to Re in the low Reynolds number region and independent of Re in the high Reynolds number region, with some intermediate region between. Very few investigators (including the present authors) have managed to make measurements in all three regions. Often, however, measurements in one region have been used to draw conclusions about results over the entire range.

The reader is reminded at this point that when we compare oscillating flow data to steady flow data, we are always using peak velocity amplitude and peak resistive pressure amplitude to calculate the various loss factors and Reynolds numbers described in the following.

6.1 Correlations for Single Screens Based on Wire Diameter and Open Area. Steady flow correlations based on wire diameter and β have generally taken the form

$$K = G(\beta)\left(\frac{A}{\mathrm{Re}_d} + B\right), \tag{10}$$

where G is a function of β only, and A and B are constants. Pinker and Herbert identified several commonly used G functions such as

$$G_1 \equiv \frac{1-\beta}{\beta^2}, \tag{11}$$

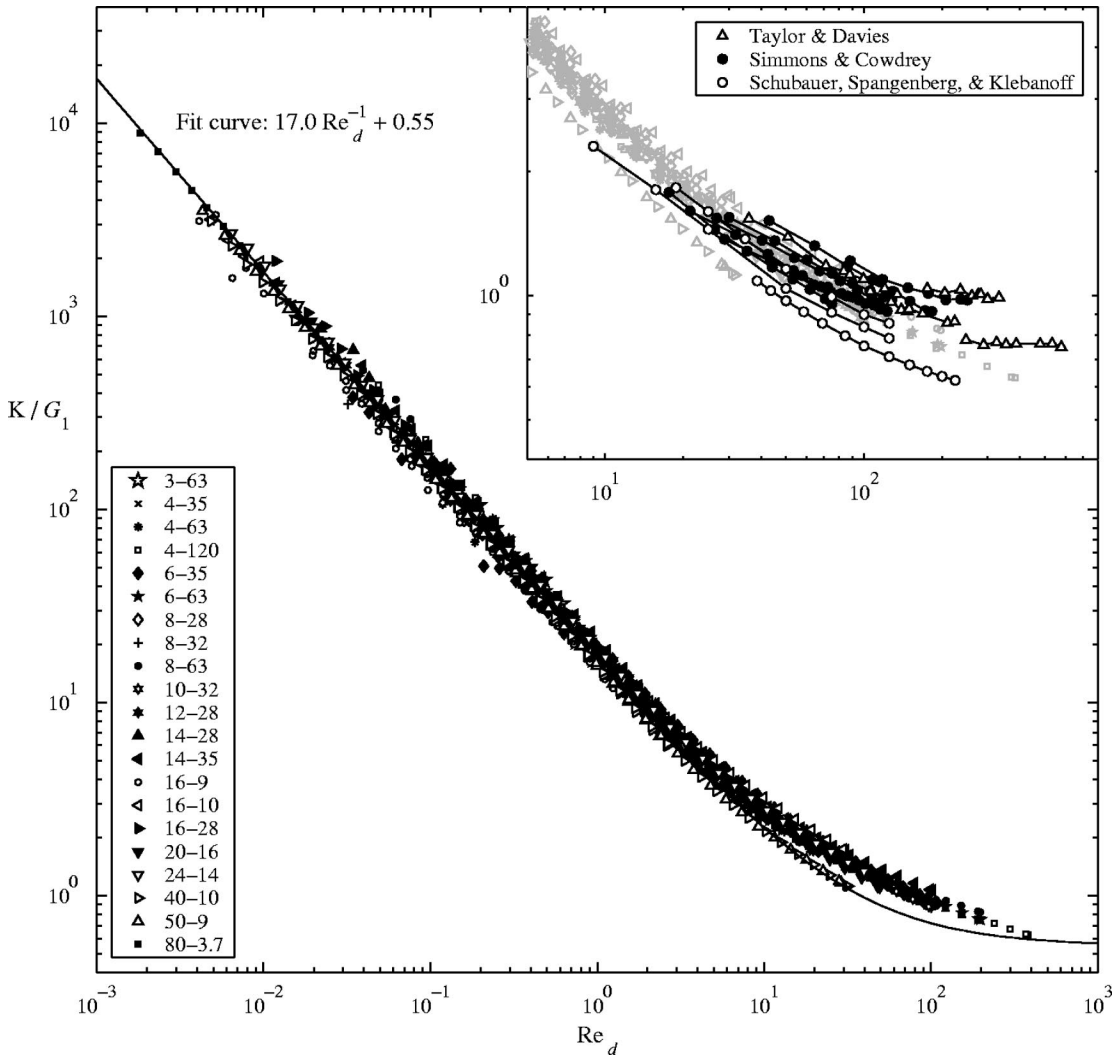

Fig. 7 Correlation of data from all 21 test screens using the function G_1

$$G_2 \equiv \frac{1-\beta^2}{\beta^2}, \tag{12}$$

$$G_3 \equiv \frac{(1-\beta)^2}{\beta^2}. \tag{13}$$

Though intuitively appealing, G_3 has not been found to yield simple correlations and has not appeared in recent papers. The constants A and B are different depending on which G is used. We use subscripts 1 and 2 so that

$$K = G_1\left(\frac{A_1}{\mathrm{Re}_d} + B_1\right) \quad \text{and} \quad K = G_2\left(\frac{A_2}{\mathrm{Re}_d} + B_2\right). \tag{14}$$

We use A_0 to refer to fits to uncorrelated data ($G_0 = 1$) from individual screens at low Reynolds number, $K = A_0/\mathrm{Re}_d$.

Our data are best correlated using G_1, as shown in Fig. 7. Figure 7 presents the data from all 21 of our test screens, a total of 1535 data points. This correlation method is particularly good at reducing the data spread in the low Reynolds number region ($\mathrm{Re}_d < 1.5$).

Another useful way to represent the low-Reynolds number data is to plot A_0 for each screen. In Fig. 8(*a*), $A_0\beta^2$ is plotted versus β. The various screens are well correlated using G_1 to the extent that the points in Fig. 8(*a*) fall along a straight line passing through the point ($\beta = 1, A_0\beta^2 = 0$). The magnitude of the slope of this line is the parameter A_1 in Eq. (14). A least-squares fit suggests $A_1 = 17.4$ (with a correlation coefficient of 0.955), but this seems to us to weight too heavily the points of low β, where the scatter is largest. Taking A_0/G_1 for each screen and averaging the results suggests $A_1 = 16.8$. We judge the best fit to be $A_1 = 17.0$, which gives the solid fit line plotted in Fig. 8(*a*). This result is the coefficient 17.0 in the fit curve $17.0\,\mathrm{Re}_d^{-1} + 0.55$ that is plotted in Fig. 7.

There are $N = 837$ points with $\mathrm{Re}_d < 1.5$. The relative standard deviation of these points from the line $K/G_1 = 17.0/\mathrm{Re}_d$ is 11%. Because the relative (percent) deviation is approximately constant, and because we wish to weight all of the points equally, we calculate this relative standard deviation σ according to

$$\sigma^2 = \frac{1}{N}\sum_{i=1}^{N}\left(\frac{K_i/G_{1,i} - K_i^{\mathrm{fit}}/G_{1,i}}{K_i^{\mathrm{fit}}/G_{1,i}}\right)^2, \tag{15}$$

where $K_i^{\mathrm{fit}}/G_{1,i} = A_1\,\mathrm{Re}_{d,i}^{-1}$, with $A_1 = 17.0$. The values of A_0/G_1

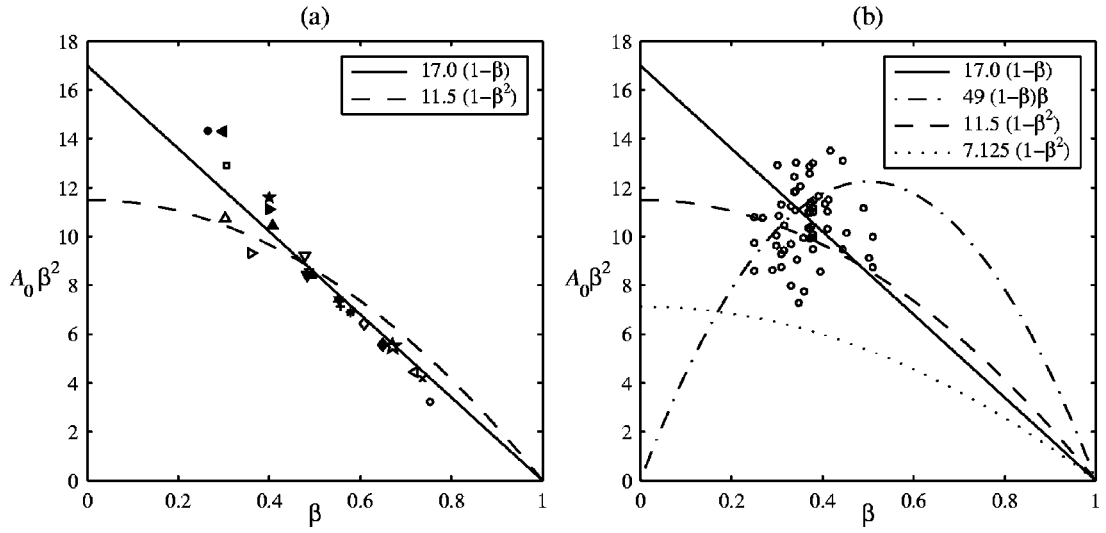

Fig. 8 Plots of A_0 for (*a*) our data, and (*b*) Ehrhart's data, [16]

range from a minimum of 13.1 to a maximum of 20.3, so the largest deviations in the data are about 21%, twice the standard (root-mean-square) deviation.

6.1.1 Intermediate Re_d. Some early investigators presented raw data of measurements at intermediate Reynolds numbers. The inset in Fig. 7 shows data points taken from tables in Taylor and Davies [9] and Simmons and Cowdrey [14], and from curves of the lowest velocity data from Schubauer, Spangenberg, and Klebanoff [8]. The steady-flow data from these three references overlie our oscillating-flow data, indicating that the oscillating and steady-flow resistance are the same in the intermediate Reynolds number region.

Further support for this conclusion comes from comparison to the data of Groth and Johansson [15], shown in Fig. 9(*a*). Groth and Johansson presented results for seven screens, covering a larger range of Reynolds number than the earlier investigators, penetrating slightly into both the high and low Re_d regions. We obtained their data by xerographically enlarging their plot and measuring the positions of the points with a vernier caliper, which method was used on other graphical sources as well. Groth and Johansson's results are shown in Fig. 9(*a*) correlated with G_1 and in Fig. 9(*b*) using G_2. They used the G_2 correlation, but G_1 works at least as well in reducing the spread of their data.

The four parts of Fig. 9 are all plots of our complete data set (in gray), but each with a different correlation. Figure 9(*a*) is a plot of K/G_1 versus Re_d; that is, it is the same as Fig. 7, but on the same scale as Figs. 9(*b*)–(*c*), to aid visual comparison of the different correlations, with each plot having six cycles on the abscissa and 4 1/2 cycles on the ordinate. Figure 9(*b*) is a plot of K/G_2 versus Re_d. The correlations in Figs. 9(*c*) and (*d*) are discussed in later sections.

Comparison of our oscillating-flow data to the steady-flow data from Refs. [8,9,14] (inset of Fig. 7) and from Ref. [15] (Figs. 9(*a*) and (*b*)) indicates that the steady flow and oscillating flow results are the same in the intermediate Reynolds number region. Not only do the results match in magnitude, they match in functional shape. The functional form $A\,\mathrm{Re}_d^{-1}+B$ is the simplest that might represent pressure drops through porous media, and it seems to work well for many ''packed columns,'' such as beds of granular materials, [16]. For single screens in steady flow, however, such a fit underpredicts the resistance in the intermediate Reynolds number regime. Log-log plots of measurements from individual screens (Fig. 3) show a straight line below $\mathrm{Re}_d \simeq 3$, a knee covering $3 \lesssim \mathrm{Re}_d \lesssim 30$, and an almost straight line for Re_d from 30 to at least 300. Ehrhardt [17] measured the flow resistance of individual screens over a range $0.3 \lesssim \mathrm{Re}_d \lesssim 300$, and his plots show this same pattern. Annand's fit to Refs. [8,9,14] is also clearly less curved (i.e., has a smaller second derivative) in the intermediate Reynolds number region than is a function $A\,\mathrm{Re}_d^{-1}+B$ that fits at high and low Reynolds numbers. (Annand's fit is presented only graphically in his paper, and is not reproduced here.) Brundrett [11] developed a correlation using data from these and other sources, and he concluded that it was necessary to add a ''blending'' term in order to match the data in this region. Finally, Wieghardt [18] correlated the data from these same sources with a straight line with slope $-1/3$.

Wieghardt believed that it should be possible to compare a screen to a collection of cylinders, with a velocity equal to the peak velocity u/β inside a screen pore, so he used G_1 in his correlation and a Reynolds number equal to Re_d/β. His final correlation was $K=6.5G_1[\mathrm{Re}_d/\beta]^{-1/3}$. This is equivalent to use of Re_d with a correlating function equal to $G_1\beta^{1/3}$. Annand decided that G_2 gave a better correlation for this data. In the intermediate Reynolds number range, our data correlate about equally well using G_1 or G_2. For our low Reynolds number data, however, G_2 does not provide as good a correlation as G_1, as discussed in the next section.

6.1.2 Low Re_d. Our low Re_d data correlate best using G_1, with a standard deviation of 11% from the line defined by $A_1=17.0$. Using G_2, shown in Fig. 9(*b*), the standard deviation (defined similarly to Eq. (15)) has a minimum value of 19% when $A_2=12.0$. The value of $A_2=11.5$ plotted in the figure is closer to being centered between the minimum and maximum data point values.

Published data for comparison at low Reynolds numbers are scarce. Ehrhardt [17] reported in tabular form results equivalent to our A_0 from careful measurements of the flow resistance of 60 screens at low and intermediate Reynolds numbers. Unfortunately, Ehrhardt did not report similarly careful measurements of the screens' dimensions. Instead, it seems that he reports only nominal, manufacturer values. The consequence is that the scatter in the data is too large to be of use in determining a correlation function using β. A plot of Ehrhardt's results is given in Fig. 8(*b*). Evidence that the large scatter in Fig. 8(*b*) is the product of inaccurate screen dimensions comes from Ehrhardt's measurements of the resistances of nine pairs of nominally identical screens from different manufacturers. Ehrhardt's A_0's for these supposedly identical pairs of screens differ from each other by as much as 34%, with an average discrepancy of 16%.

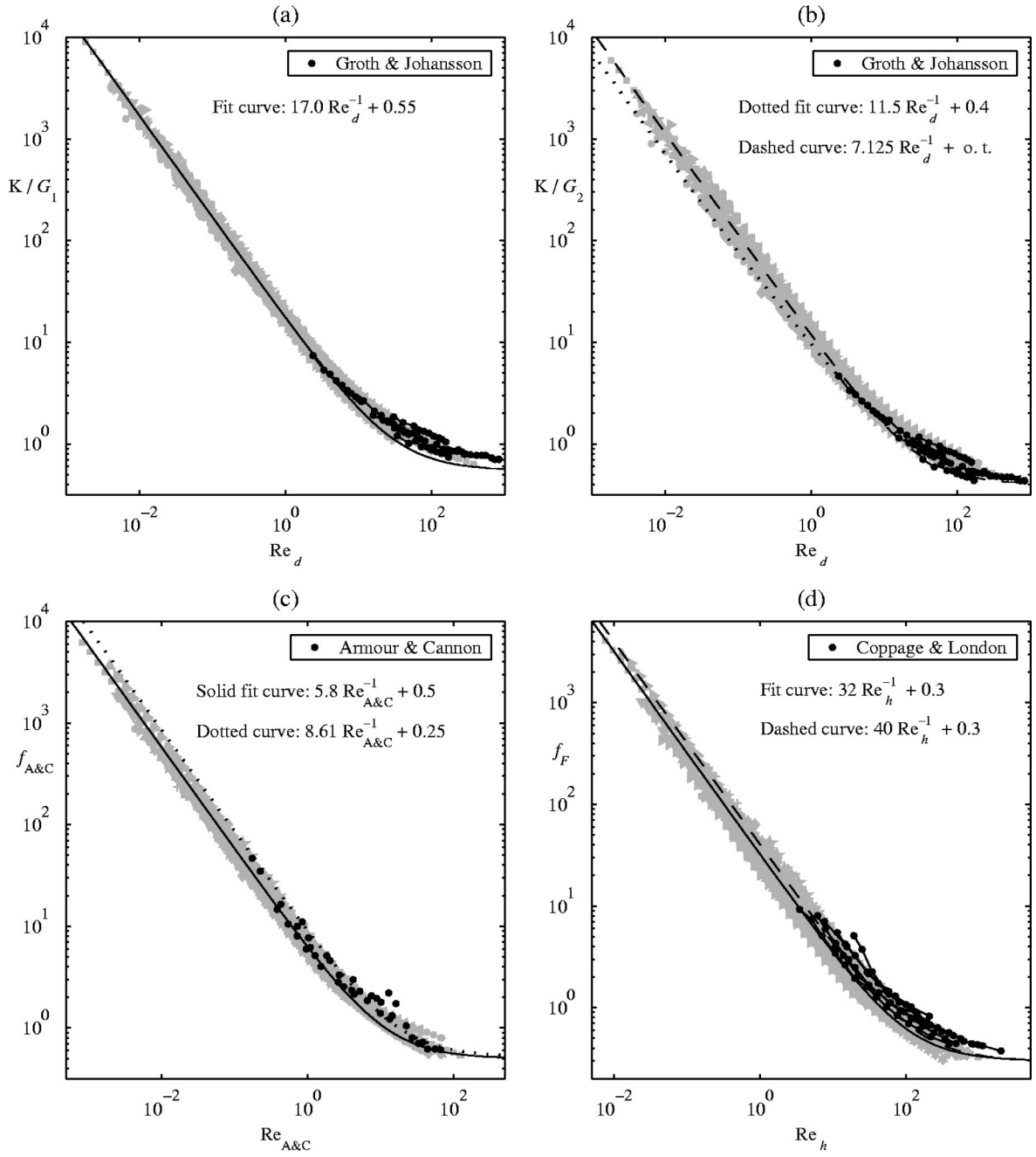

Fig. 9 Various correlation methods

Ehrhardt based his fit on the work of Wieghardt, using Re_d/β for Reynolds number and G_1 for the correlation. Ehrhardt's fit $[K/G_1=49(\mathrm{Re}_d/\beta)^{-1}+0.72]$ appears in Fig. 8(*b*) as $49(1-\beta)\beta$, the dash-dot curve. All that can really be concluded from Ehrhardt's A_0 data is that a fit curve should pass near the point ($\beta=0.35$, $A_0\beta^2=11$), which our G_1 fit ($17.0(1-\beta)$) does. The G_2 fit to our data ($11.5(1-\beta^2)$, dashed curve) also passes near the center of Ehrhardt's cluster of points.

Cornell [19] developed a correlation for data from pre-1958 sources (some of which we have been unable to obtain) that is presented as a family of curves on a log-log plot of K/G_1 versus Re_d/β, with separate straight lines for $\beta=0.2$, 0.3, 0.4, 0.5, 0.6, and 0.7 at low Re_d. The plot is small and difficult to measure accurately, but multiplying the appropriate β by our best estimate of the A for each line we get the equivalent A_0 values 17.1, 19.0, 17.5, 17.8, 17.2, and 16.9, for an average A_0 of 17.6. This is 3.5% larger than our value of 17.0.

Chhabra and Richardson [20] measured flow resistance at very low Reynolds numbers ($4\times10^{-6}<\mathrm{Re}_d<7\times10^{-4}$) using solutions of glucose and water for the single orthogonal porosity $\beta=0.34$. Their result is $A_1=17.0$, which is the same as our result, and right in the center of Ehrhardt's cluster.

Brundrett [11] collected data from various sources to develop a correlation using G_2 that is claimed to apply to Re_d from 10^{-4} to 10^4. Brundrett's only source of data below $\mathrm{Re}_d=2$ comes from Munson [21], who measured pressure drops across screens when the approaching flow was a fully developed laminar duct flow. That is, Munson's approaching flow was parabolic in profile.

Brundrett converted Munson's results into uniform flow results by "assuming that the pressure drop across each screen was not dependent upon radial position, and hence, was constant at each and every point of the screen." This conversion gave $A_2=7.125$, which is 38% lower than our fit of the G_2 correlation of our data.

We believe that the comparison of our data to the data of Chhabra and Richardson, the correlation of Cornell, and the collective result of Ehrhardt's data, supports the conclusion that the steady-flow and oscillating-flow resistances are the same for single screens at low Reynolds numbers, just as they are in the intermediate regime. That Brundrett's low-Reynolds-number fit, shown as the dotted line in Fig. 8(*b*), passes below all of our points, and below *all* of Ehrhardt's points, even with their considerable scatter, makes us doubt the validity of the assumptions that Brundrett used to convert Munson's data.

Both Chhabra and Richardson's and Munson's data suggest that the low Re relation $K \propto \mathrm{Re}^{-1}$ continues down to at least $\mathrm{Re}_d = 10^{-6}$.

6.1.3 High Re_d. Our data do not reach high enough Re_d to make an accurate determination of the coefficient B in a fit. To the extent that a given correlation does reduce the data to a single curve, an upper limit on B is set by the points with the highest Reynolds numbers. In our case, the data from screen 4–120 set upper limits of about $B_1=0.55$ and $B_2=0.45$. Curiously, this is consistent with data of Groth and Johansson and Pinker and Herbert when the data are correlated with G_2, but not with G_1.

Pinker and Herbert [13] did careful studies at high velocities to separate the effects of Reynolds number and Mach number. Their data (from four screens) led them to prefer a G_2 correlation, with $B_2 \simeq 0.5$. They also plotted their data using G_1, with $B_1 \simeq 0.8$, which is too large to be consistent with our oscillating-flow data. Cornell [19] plotted data of his own and of others at high Reynolds number using G_1, and it also clusters around $B_1 \simeq 0.8$. Comparing Figs. 9(*a*) and (*b*) we see that Groth and Johansson's highest Re_d points lie above ours in (*a*) but not in (*b*). Clearly, high Reynolds number single-screen oscillating flow data are needed.

Most researchers have used either G_1 or G_2 for the entire range of Re_d. We know of no reason, however, to believe that the low and high Reynolds number resistance depend on porosity in the same way. It could be, for example, that a better correlation would take the form $K=G_1A_1\,\mathrm{Re}_d^{-1}+G_2B_2$.

6.2 The Correlation of Armour and Cannon. Armour and Cannon [22] measured pressure drops through single layers of a variety of types of screen and correlated their data with a unique method using the volumetric porosity ϕ. They considered the avoidance of the use of fractional open area to be "a great advance" because certain types of weaves ("dutch" weaves) that are useful for filtration have *no* open area projected on a plane normal to the flow direction. We have had limited success with most correlation methods involving ϕ, but this method is an exception, giving the excellent results shown in Fig. 9(*c*).

Armour and Cannon defined a friction factor

$$f_{\mathrm{A\&C}} \equiv \frac{\Delta p}{0.5\rho(u/\phi)^2}\,\frac{D/2}{QL}, \tag{16}$$

and a Reynolds number that can be written as

$$\mathrm{Re}_{\mathrm{A\&C}} \equiv \frac{(u/\phi)}{\nu}\,\frac{{D_h}^2}{16\phi D}. \tag{17}$$

The length L is the screen thickness, which is just $2d_m$ for ideal plane screens. The parameter Q is a "shape factor" that is one for plane weaves. The parameter D is the "effective channel diameter." For plane screens, $D=l_m$, the geometric mean of the sides of the rectangular opening. Armour and Cannon's correlation is unique in using both D_h and l_m as parameters. It is interesting to note that, for dutch weaves, even Armour and Cannon do not have an expression for D; they used "the screen particle retention rating as specified by the screen manufacturer."

Using this correlation on our data gives a fit of $f_{\mathrm{A\&C}} = 5.8\,\mathrm{Re}_{\mathrm{A\&C}}^{-1}+0.5$, with a standard deviation of 15% at low Reynolds numbers (using a $\mathrm{Re}_{\mathrm{A\&C}}=0.7$ as approximately equivalent to the $\mathrm{Re}_d=1.5$ that is used for the G_1 and G_2 correlations to define "low" Re_d). This is almost as good as the G_1 correlation, but without the use of β, as desired. Also plotted in Fig. 9(*c*) are Armour and Cannon's data points for four screens with plane square weaves. These points are taken from their plot, which does not indicate which of the points are from which screen. The agreement between their data and ours is quite good. Their fit to their data is $f_{\mathrm{A\&C}}=8.6\,\mathrm{Re}_{\mathrm{A\&C}}^{-1}+0.5$, shown in Fig. 9(*c*) as the dotted curve. This curve falls above all of our data, but it also falls above most of their data for *plane square weave*. Their curve does pass though the middle of their complete data set, which includes points from screens with four other types of weave. This suggests to us that their "shape factor" Q does not fully account for the differences between screen types.

6.3 Comparison to Studies Using Stacks of Screen. Stacks of screens are important in the areas of thermoacoustics and Stirling-cycle devices because they are used as regenerators. The literature of stacked screens is fairly extensive, and includes oscillating flow data. We cannot examine all of it in this paper, but we feel that it is important to compare our single-screen oscillating flow data to at least some stacked screen measurements.

The relationship between the hydraulic resistance of a single screen and that of a packed stack of screens is unclear. Coppage and London [23] reported that the resistance of a stack of 40 screens is twice at big as that for a stack of 20 screens, but we know of no studies that compare, say, the resistance of 1, 2, 3, and 4 screens in contact. Coppage and London did compare stacks of close-packed screens to stacks with some space between the screens, using a friction factor in which the overall regenerator length L was replaced by the screen thickness times the number of screens. They found that "the effects of screen separation on flow friction are quite marked" at low Reynolds numbers, with a decrease in pressure drop of up to 25% when the space between the screens was twice the screen thickness. This indicates that single-screen friction factors should be lower than those for packed stacks of screen.

A packed stack of screens is clearly an example of a porous medium. Porous media are often characterized in terms of a Reynolds number Re_h and Fanning friction factor f_F based on hydraulic diameter and volumetric porosity ϕ,

$$\mathrm{Re}_h \equiv \frac{(u/\phi)D_h}{\nu} \tag{18}$$

and

$$f_F \equiv \frac{\Delta p}{0.5\rho(u/\phi)^2}\,\frac{D_h}{4L}. \tag{19}$$

The length of the regenerator in the flow direction is L. Many papers also use a friction factor that is four times as large as the Fanning friction factor. We convert all quoted results into f_F.

6.3.1 Steady-Flow Data for Stacked Screens. Our data are plotted in terms of f_F versus Re_h in Fig. 9(*d*), in gray, along with our fit curve, $f_F=32\,\mathrm{Re}_h^{-1}+0.3$. The $f_F-\mathrm{Re}_h$ system does not work particularly well for the purposes of reducing our data to a single curve; the standard deviation below $\mathrm{Re}_h=5.5$ (which is roughly equivalent to $\mathrm{Re}_d=1.5$) is 24%. Our motivation for plot-

ting the data in this way is that this system is used in many publications including *Compact Heat Exchangers* by Kays and London [24], which is cited often in the thermoacoustics and Stirling literature as a source of steady-flow stacked-screen data. The screen data presented by Kays and London comes from the work of Coppage and London [25].[2] Their data for six sizes of screen in steady flow are plotted in black in Fig. 9(*d*). Also appearing in the plot as a dashed line is Organ's fit, [26], to Kays and London's presentation of these and other, [25], measurements, $f_F = 40\,\mathrm{Re}_h^{-1} + 0.3$. The center of our data is about 20% lower than the center of Coppage and London's. This is similar to the reduction they saw by introducing space between their screens.

6.3.2 Oscillating-Flow Data for Stacked Screens. Tanaka, Yamashita, and Chisaka [27] used the $f_F - \mathrm{Re}_h$ system to report measurements of pressure drops through regenerators in oscillating flow. They fit their screen-regenerator data with $f_F = 43.8\,\mathrm{Re}_h^{-1} + 0.40$, 10% higher than Organ's fit to Kays and London's steady-flow graphs and 33% higher than our single-screen oscillating-flow results at low Re_h. Hsu, Fu, and Cheng [6] on the other hand, recently measured stacked-screen regenerators in oscillating flow over an exceptionally large range of Re_h and came up with $f_F = 27.3\,\mathrm{Re}_h^{-1} + 0.25$. Disturbingly, this is 38% lower than Tanaka's measurement of exactly the same physical situation. Their introduction implies that the discrepancy may be due to Tanaka's and others' inference of gas velocity from piston position, rather than direct measurement, or that previous investigators did not measure over a large enough range in Reynolds number to accurately determine the coefficients. When considering this question, it should be taken into account that Hsu et al. used a Validyne DP103 for pressure measurements, and they state that ''for the low-frequency application of this experiment, a static calibration is adequate.'' Our experience is different, using the same DP103 transducer housing but using a thinner diaphragm. Their measurements were carried out at 4 Hz. Our DP103 is 7.3% less sensitive at 4 Hz than at 0.125 Hz. On the other hand, our sensor also exhibits a large phase shift at 4 Hz, whereas their plots show pressure and velocity in phase, so their less sensitive version of the sensor may not have the same frequency response as ours. However, we must recommend caution to future investigators who might consider using this sensor for measurement of unsteady pressures.

Hsu et al. and Zhao and Cheng [5] quoted previous researchers who found that pressure drops though screen regenerators were higher in oscillating flow than what was predicted from steady-flow correlations. When Hsu et al. measured pressure drops through their regenerators with both steady and oscillating flow, however, they concluded that ''the correlation between pressure-drop and velocity for oscillating flows is the same as the steady flow correlation.'' They also concluded that an additional term was necessary in the correlation function to match the data in the intermediate Reynolds number region. That is, the intermediate Reynolds number pressure drop deviates from $A\,\mathrm{Re}^{-1} + B$ for packed screens as well as for single screens.

7 Conclusions

We report measurements of pressure drops across individual woven-wire screens subjected to low-frequency oscillating flow in the region $0.002 \lesssim \mathrm{Re}_d \lesssim 400$. The flow resistance depends on Reynolds number, but we do not observe any separate dependence upon the ratio of oscillation amplitude to wire diameter, as we would have expected. With the correlating function $G_1 = (1-\beta)/\beta^2$, the data collapse to a single curve to within a standard deviation of about 11%. A correlation of the form

$$\frac{\Delta p}{\rho u^2/2} = \frac{1-\beta}{\beta^2}\left(\frac{17.0}{\mathrm{Re}_d} + 0.55\right) \tag{20}$$

works very well below $\mathrm{Re}_d = 2$, but underestimates K for $2 \lesssim \mathrm{Re}_d \lesssim 200$. A log-log plot of the data in this intermediate Reynolds number region is fairly straight, so a Wieghardt-style correlation such as $K = 4.6 G_1\,\mathrm{Re}_d^{-1/3}$ works well for $2 \lesssim \mathrm{Re}_d \lesssim 400$. This behavior in the intermediate Reynolds number region has also been observed by previous investigators who studied steady-flow through single screens, and also by Hsu et al. for stacks of screens.

If a correlation using volumetric porosity is desired, we recommend the method developed by Armour and Cannon.

Keeping in mind our use of peak velocity and pressure amplitudes to calculate Reynolds numbers and loss factors for oscillating flow, comparison of the present low-frequency oscillating-flow data to previous studies of steady flow through single screens suggests that the flow resistances are the same for these two cases, provided that the size of the holes in the screen are smaller than a viscous penetration depth. Our results are about 20% lower than stacked-screen steady-flow friction factors reported by Coppage and London. Previous studies of pressure drops though stacked screens in oscillating flow fall both significantly above and significantly below the present results, making comparison difficult.

Acknowledgments

This work was supported by the Office of Naval Research, with supplementary support from the Pennsylvania Space Grant Consortium.

Nomenclature

A_w = wetted area (m^2)
A = coefficient in correlation
B = coefficient in correlation
D_h = hydraulic diameter (m)
G = correlating funcion
K = pressure loss factor*
Δp = pressure difference* (Pa)
Re = Reynolds number*
$\mathrm{Re}_{A\&C}$ = Reynolds number from Ref. [22]
Re_d = Re based on wire diameter
Re_h = Re based on hydraulic diameter
V = volume (m^3)
d = wire diameter (m)
f_F = Fanning friction factor
$f_{A\&C}$ = friction factor from Ref. [22]
l = screen gap (m)
m = screen mesh (m^{-1})
u = approach velocity* (m/s)

Greek Letters

β = orthogonal porosity
ν = kinematic viscosity (m^2/s)
ϕ = volumetric porosity
ρ = density (kg/m^3)
θ = phase angle
ω = angular frequency of oscillation (radians/s)

Subscripts

1, 2 = screen coordinate direction (on *d*, *l*, *m*)
m = mean of value in directions 1 and 2
0, 1, 2 = correlation number (on *A*, *B*, *G*)

[2]We transcribe the data of Ref. [23] from [25], which contains the same data in larger graphs than the original paper. We transcribe only the screen data, which covers the low Reynolds numbers. Kays and London's higher Reynolds number data come from measurements on matrices of crossed rods, together with converting these into results equivalent to those from woven screens.

*For oscillating flow cases, u, Δp, K, and all Reynolds numbers refer to *peak*, not instantaneous, quantities.

References

[1] Swift, G. W., 2002, *Thermoacoustics: A Unifying Perspective for Some Engines and Refrigerators*, Acoustical Society of America, asa.aip.org
[2] APS Dynamics, Inc., Carlsbad, CA. www.apsdynamics.com
[3] Lucas Control Systems, Schaevitz Sensors, Hampton, VA, www.schaevitz.com
[4] Validyne Engineering Corp., Northridge, CA. www.validyne.com
[5] Zhao, T. S., and Cheng, P., 1996, ''Oscillatory Pressure Drops Through a Woven-Screen Packed Column Subjected to a Cyclic Flow,'' Cryogenics, **36**(5), pp. 331–341.
[6] Hsu, C.-T., Fu, H., and Cheng, P., 1999, ''On Pressure-Velocity Correlation of Steady and Oscillating Flows in Regenerators Made of Wire Screens,'' Trans. ASME, **121**, pp. 52–56.
[7] Omega Engineering, Inc., Stamford, CT. www.omega.com
[8] Schubauer, G. B., Spangenberg, W. G., and Klebanoff, P. S., 1950, ''Aerodynamic Characteristics of Damping Screens,'' NACA T.N. 2001.
[9] Taylor, G. I., and Davies, R. M., 1944, ''The Aerodynamics of Porous Sheets,'' AES Rep. & Mem. 2237.
[10] Annand, W. J. D., 1953, ''The Resistance to Air Flow of Wire Gauzes,'' J. R. Aero. Soc., **57**, pp. 141–146.
[11] Brundrett, E., 1993, ''Prediction of Pressure Drop for Incompressible Flow Through Screens,'' ASME J. Fluids Eng., **115**, pp. 239–242.
[12] Hino, M., Sawamoto, M., and Takasu, S., 1976, ''Experiments on Transition to Turbulence in a Oscillatory Pipe Flow,'' J. Fluid Mech., **75**, pp. 193–207.
[13] Pinker, R. A., and Herbert, M. V., 1967, ''Pressure Loss Associated With Compressible Flow Through Square-Mesh Wire Gauzes,'' J. Mech. Eng. Sci., **9**(1), pp. 11–23.
[14] Simmonds, L. F. G., and Cowdrey, C. F., 1945, ''Measurements of the Aerodynamic Forces Acting on Porous Screens,'' AES Rep. & Mem. 2276.
[15] Groth, J., and Johansson, A. V., 1988, ''Turbulence Reduction by Screens,'' J. Fluid Mech., **197**, pp. 139–155.
[16] Ergun, S., 1952, ''Fluid Flow Through Packed Columns,'' Chem. Eng. Prog., **48**(2), pp. 89–94.
[17] Ehrhardt, G., 1983, ''Flow Measurements for Wire Gauzes,'' Int. Chem. Eng., **23**(3), pp. 455–465 (translated from Aufbereitungstechnik, 1981, **22**(7), pp. 374–382).
[18] Wieghardt, K. E. G., 1953, ''On the Resistance of Screens,'' Aeronaut. Q., **IV**, pp. 186–192.
[19] Cornell, W. G., 1958, ''Losses in Flow Normal of Plane Screens,'' Trans. ASME, **80**, pp. 791–799.
[20] Chhabra, R. P., and Richardson, J. F., 1985, ''Flow of Liquids Through Screens: Relationship Between Pressure Drop and Flow Rate,'' Chem. Eng. Sci., **40**(2), pp. 313–316.
[21] Munson, B. R., 1988, ''Very Low Reynolds Number Flow Through Screens,'' Trans. ASME, **110**, pp. 462–463.
[22] Armour, J. C., and Cannon, J. N., 1968, ''Fluid Flow Through Woven Screens,'' AIChE J., **14**(3), pp. 415–420.
[23] Coppage, J. E., and London, A. L., 1956, ''Heat Transfer and Flow Friction Characteristics of Porous Media,'' Chem. Eng. Prog., **52**, pp. 57F–63F.
[24] Kays, W. M., and London, A. L., 1998, *Compact Heat Exchangers*, 3rd Ed., Krieger, Malibar, FL.
[25] Tong, L. S., and London, A. L., 1957, ''Heat Transfer and Flow Friction Characteristics of Woven-Screen and Cross-Rod Matrixes,'' Trans. ASME, **79**, pp. 1558–1570.
[26] Organ, A. J., 1992, *Thermodynamics and Gas Dynamics of the Stirling Cycle Machine*, Cambridge University Press, New York, Fig. 7.4.
[27] Tanaka, M., Yamashita, I., and Chisaka, F., 1990, ''Flow and Heat Transfer Characteristics of the Stirling Engine Regenerator in an Oscillating Flow,'' JSME Int. J., **33**(3), pp. 283–289.

Turbulent Boundary Layers Over Surfaces Smoothed by Sanding

Michael P. Schultz
Naval Architecture & Ocean Engineering Department,
United States Naval Academy,
Annapolis, MD 21402

Karen A. Flack
Mechanical Engineering Department,
United States Naval Academy,
Annapolis, MD 21402

Flat-plate turbulent boundary layer measurements have been made on painted surfaces, smoothed by sanding. The measurements were conducted in a closed return water tunnel, over a momentum thickness Reynolds number (Re_θ) range of 3000 to 16,000, using a two-component laser Doppler velocimeter (LDV). The mean velocity and Reynolds stress profiles are compared with those for smooth and sandgrain rough walls. The results indicate an increase in the boundary layer thickness (δ) and the integral length scales for the unsanded, painted surface compared to a smooth wall. More significant increases in these parameters, as well as the skin-friction coefficient (C_f) were observed for the sandgrain surfaces. The sanded surfaces behave similarly to the smooth wall for these boundary layer parameters. The roughness functions (ΔU^+) for the sanded surfaces measured in this study agree within their uncertainty with previous results obtained using towing tank tests and similarity law analysis. The present results indicate that the mean profiles for all of the surfaces collapse well in velocity defect form. The Reynolds stresses also show good collapse in the overlap and outer regions of the boundary layer when normalized with the wall shear stress. [DOI: 10.1115/1.1598992]

Introduction

The importance of rough wall, turbulent boundary layers is well established. In a large number of engineering applications, from pipe flow to flow over a ship's hull, boundary layers develop over surfaces that are rough to an appreciable degree. For this reason, a significant body of research has focused on quantifying the effect of surface roughness on boundary layer structure. Numerous experimental investigations of rough wall, turbulent boundary layers have been conducted including the studies of Clauser [1], Hama [2], Ligrani and Moffat [3], Krogstad and Antonia [4–6], and others. Raupach et al. [7] provides an excellent review of much of this work. The majority of these investigations have centered on flows over simple, well-defined roughness patterns such as transverse bars, mesh screen, sandgrains, and circular rods. While use of simple roughness geometry is attractive since it is easily defined and can be parametrically altered, it is not representative of most roughness of engineering interest. A notable exception was the study of Acharya et al. [8] that documented the effect of surface roughness caused by machining, such as that observed on turbine blades.

In many cases, turbulent flows evolve over painted surfaces that have been smoothed by sanding (e.g., sailing hulls and wind and water tunnel models). In a previous study using a towing tank, Schultz [9] documented the effect of sanding on surface roughness and frictional resistance of flat plates; however, no measurements of the mean and turbulent velocity profiles were made. The purpose of the present investigation is to document the mean velocity and Reynolds stress profiles over these surfaces and compare them to smooth and sandgrain rough walls (i.e., sandpaper covered surfaces). This should provide a framework from which to address the similarities and differences observed in turbulent boundary layers on sanded, painted surfaces to those developing over smooth and sandgrain surfaces.

The mean velocity profile in the overlap and outer region for a smooth wall, turbulent boundary layer can be expressed as

$$U^+ = \frac{1}{\kappa}\ln(y^+) + B + 2\omega(y/\delta)\Pi/\kappa. \quad (1)$$

Clauser [1] argued that the primary effect of surface roughness was to cause a downward shift in the logarithmic region of the mean velocity profile for the boundary layer. For so-called "*k*-type" rough walls, the downward shift, ΔU^+, called the roughness function, correlates with k^+, the roughness Reynolds number, defined as the ratio of the roughness length scale, *k*, to the viscous length scale, ν/u_τ. The mean velocity profile in a rough wall boundary layer is, therefore, given as

$$U^+ = \frac{1}{\kappa}\ln((y+\varepsilon)^+) + B - \Delta U^+ + 2\omega((y+\varepsilon)/\delta)\Pi/\kappa. \quad (2)$$

Hama [2] showed that by evaluating Eqs. (1) and (2) at $y = y + \varepsilon = \delta$, the roughness function is found by subtracting the rough wall log-law intercept from the smooth wall intercept, *B*, at the same value of Re_{δ^*}. The roughness function can be expressed as

$$\Delta U^+ = \left(\sqrt{\frac{2}{C_f}}\right)_s - \left(\sqrt{\frac{2}{C_f}}\right)_R. \quad (3)$$

It should be noted that Eq. (3) is only valid provided the mean velocity profiles collapse in velocity defect form, given as, [1],

$$\frac{U_e - U}{u_\tau} = f\left(\frac{y}{\delta}\right). \quad (4)$$

Collapse of the mean defect profiles for rough and smooth walls is consistent with the turbulence similarity hypotheses of Townsend [10] and Perry and Li [11] that state that turbulence outside of the roughness sublayer (i.e., the layer of fluid immediately adjacent to the roughness) is independent of the surface condition at sufficiently high Reynolds number. A majority of the experimental evidence seems to support the universality of the defect law. Some recent research, however, indicates that surface roughness alters the velocity defect profile, [4,8], leads to a higher degree of isotropy of the Reynolds normal stresses, [4–6], and changes the Reynolds shear stress profiles in the outer region of the boundary layer, [4–6]. Another outstanding issue is the ability to characterize the roughness function (ΔU^+) for a generic surface by a physical measurement of the surface roughness (*k*) alone.

The goal of the present experimental investigation is to document the mean velocity and Reynolds stress profiles on painted surfaces smoothed by sanding. These are compared with profiles over smooth and sandgrain rough walls. An attempt to identify a suitable roughness scaling parameter for the roughness function

Contributed by the Fluids Engineering Division for publication in the JOURNAL OF FLUIDS ENGINEERING. Manuscript received by the Fluids Engineering Division August 19, 2002; revised manuscript received March 23, 2003. Associate Editor: M. V. Otügen.

Table 1 Description and roughness statistics of the test surfaces

Specimen	R_a (μm)	R_q (μm)	R_t (μm)	R_z (μm)	Description
Smooth	NA	NA	NA	NA	Cast acrylic surface
60-grit sandpaper	126±5	160±7	983±89	921±82	60-grit commercial wet/dry sandpaper
220-grit sandpaper	30±2	38±2	275±17	251±14	220-grit commercial wet/dry sandpaper
Unsanded	9±1	12±1	76±8	71±7	Unsanded, sprayed polyamide epoxy
60-grit sanded	5±1	4±1	36±4	32±3	Sprayed polyamide epoxy sanded with 60-grit wet/dry sandpaper
120-grit sanded	4±1	3±1	26±2	23±2	Sprayed polyamide epoxy sanded with 120-grit wet/dry sandpaper

Uncertainties represent the 95% confidence precision bounds

for this particular class of surfaces is made. These results are compared with the roughness function measured indirectly for these surfaces by Schultz [9] using frictional resistance measurements on towed flat plates.

Experimental Facilities and Method

The present experiments were carried out in the closed circuit water tunnel facility at the United States Naval Academy Hydromechanics Laboratory. The test section is 40 cm by 40 cm in cross section and is 1.8 m in length, with a tunnel velocity range of 0–6.0 m/s. In the present investigation, the freestream velocity was varied between $\sim$1.0 m/s–3.5 m/s ($\mathrm{Re}_x = 1.4\times10^6 - 4.9\times10^6$). Flow management devices include turning vanes placed in the tunnel corners and a honeycomb flow straightener in the settling chamber. The honeycomb has 19 mm cells that are 150 mm in length. The area ratio between the settling chamber and the test section is 20:1, and the resulting freestream turbulence intensity in the test section is $\sim$0.5%.

The test specimens were inserted into a flat-plate test fixture mounted horizontally in the tunnel. The test fixture is similar to that used by Schultz [12]. The fixture is 0.40 m in width, 1.68 m in length, and 25 mm thick. It is constructed of a high density foam core covered with carbon fiber reinforced plastic skins and was mounted horizontally in the tunnel's test section along its centerline. The leading edge of the test fixture is elliptically shaped with an 8:1 ratio of the major and minor axes. The forward most 200 mm of the plate is covered with 36-grit sandpaper to trip the developing boundary layer. The use of a strip of roughness was shown by Klebanoff and Diehl [13] to provide effective boundary layer thickening and a fairly rapid return to self-similarity. The test specimen mounts flush into the test fixture and its forward edge is located immediately downstream of the trip. The removable test specimens are fabricated from 12-mm thick cast acrylic sheet 350 mm in width and 1.32 m in length. The boundary layer profiles presented here were taken 1.35 m downstream of the leading edge of the test fixture. Profiles taken from 0.75 m to the measurement location confirmed that the flow had reached self-similarity. The trailing 150 mm of the flat plate fixture is a movable tail flap. This was set with the trailing edge up at $\sim$5 deg in the present experiments to prevent separation at the leading edge of the plate. The physical growth of the boundary layer and the inclined tail flap created a mildly favorable pressure gradient at the measurement location. The acceleration parameter (K) varied from 7.4×10^{-8} at the lowest freestream velocity to 2.0×10^{-8} at the highest freestream velocity. The pressure gradient did not vary significantly between the test specimens.

Six test surfaces were tested in the present study (Table 1). Three served as controls. One was a smooth cast acrylic surface. The other two were sandgrain rough surfaces; one covered with 60-grit wet/dry sandpaper and the other with 220-grit wet/dry sandpaper. The remaining three test surfaces consisted of acrylic plates initially painted with several coats of marine polyamide epoxy paint manufactured by International Paint. The paint was applied with a spray gun. One surface was tested in the unsanded condition. One was wet sanded with 60-grit sandpaper. The final test surface was wet sanded with 120-grit sandpaper. All the sanding in the present experiment was carried out by hand with the aid of a sanding block using small circular motions. The surfaces were carefully cleaned with water and a soft cloth to remove grit and detritus left behind by the sanding process. Further detail of the surface preparation is given in Schultz [9]. The surface roughness profiles of the test plates were measured using a Cyber Optics laser diode point range sensor (model #PRS 40) laser profilometer system mounted to a Parker Daedal two-axis traverse with a resolution of 5 μm. The resolution of the sensor is 1 μm with a laser spot diameter of 10 μm. Data were taken over a sampling length of 50 mm and were digitized at a sampling interval of 25 μm. Ten linear profiles were taken on each of the test surfaces. No filtering of the profiles was conducted except to remove any linear trend in the trace. A description of the test surfaces along with the surface roughness statistics is given in Table 1. It should be noted that an error in the calibration used in [9] led to a systematic underestimate of the roughness height parameters. This has been remedied and the roughness height parameters given here have been verified using a second profilometer.

Velocity measurements were made using a TSI IFA550 two-component fiber-optic LDV system. The LDV used a four beam arrangement and was operated in backscatter mode. The probe volume diameter was $\sim$90 μm, and its length was $\sim$1.3 mm. The viscous length (ν/u_τ) varied from a minimum of 5 μm for 60-grit sandpaper at the highest Reynolds number to 24 μm for the smooth wall at the lowest Reynolds number. The diameter of the probe volume, therefore, ranged from 3.8 to 18 viscous lengths in the present study. The LDV probe was mounted on a Velmex three-axis traverse unit. The traverse allowed the position of the probe to be maintained to $\pm$10 μm in all directions. In order to facilitate two-component near-wall measurements, the probe was tilted downwards at an angle of 4 deg to the horizontal and was rotated 45 deg about its axis. Velocity measurements were conducted in coincidence mode with 20,000 random samples per location. Doppler bursts for the two channels were required to fall within a 50 μs coincidence window or the sample was rejected.

In this study, the skin-friction coefficient, C_f, for the smooth surface was found using the Clauser chart method, [1], with log-law constants $\kappa = 0.41$ and $B = 5.0$. For the rough walls, C_f was obtained using a procedure based on the modified Clauser chart method given by Perry and Li [11]. To accomplish this, the wall datum offset was first determined using an iterative procedure. This involved plotting U/U_e versus $\ln[(y+\varepsilon)U_e/\nu]$ for points in the log-law region (points between $(y+\varepsilon)^+ = 60$ and $(y+\varepsilon)/\delta = 0.2$) based on an initial guess of u_τ obtained using the total stress method detailed below. The wall datum offset was initially taken to be zero and was increased until the goodness of fit of linear regression through the points was maximized. This was

Table 2 Boundary layer parameters for the test cases

Specimen	Test Case	U_{e_1} (ms^{-1})	Re_θ	$C_f\times10^3$ Clauser	$C_f\times10^3$ Total Stress	δ (mm)	δ^* (mm)	θ (mm)	H	ΔU^+
Smooth	1	0.94	2950	3.44	3.32	28	3.8	2.9	1.30	—
	2	2.60	7020	2.99	3.04	26	3.2	2.5	1.27	—
	3	2.99	8080	2.92	2.82	27	3.2	2.5	1.26	—
	4	3.58	9680	2.82	2.77	26	3.2	2.5	1.26	—
60-grit sandpaper	1	0.93	3720	4.82	4.55	33	5.1	3.7	1.38	4.5
	2	2.53	10600	5.04	5.29	33	5.5	3.9	1.42	7.4
	3	3.12	13800	4.87	5.09	33	5.9	4.1	1.44	8.0
	4	3.58	16400	4.84	5.13	34	6.1	4.3	1.43	8.3
220-grit sandpaper	1	0.95	3420	3.52	3.66	33	4.7	3.5	1.36	1.3
	2	2.60	8930	3.79	3.90	29	4.3	3.2	1.34	3.9
	3	3.07	11000	3.89	3.77	30	4.5	3.3	1.36	4.8
	4	3.63	12900	3.85	3.69	30	4.6	3.4	1.36	5.2
Unsanded	1	0.93	3170	3.40	3.31	31	4.1	3.2	1.30	0.3
	2	2.50	8080	3.05	3.14	31	3.8	2.9	1.29	0.9
	3	3.11	10500	2.94	2.98	31	4.0	3.1	1.29	1.3
	4	3.59	11900	2.95	2.87	31	4.0	3.1	1.29	1.6
60-grit sanded	1	0.95	2830	3.50	3.46	27	3.8	2.9	1.31	0.2
	2	2.53	6720	3.07	2.93	27	3.2	2.5	1.27	0.2
	3	3.09	8200	2.98	2.78	28	3.2	2.5	1.27	0.4
	4	3.52	9260	2.94	2.87	27	3.2	2.5	1.26	0.5
120-grit sanded	1	1.00	2920	3.46	3.43	28	3.9	3.0	1.32	0.0
	2	2.50	7070	3.06	2.93	26	3.2	2.5	1.26	0.2
	3	3.01	9700	2.81	2.65	28	3.8	3.0	1.27	0.2
	4	3.69	11400	2.83	2.68	28	3.6	2.9	1.25	0.3

considered the proper wall datum offset. The following formula was then used to determine C_f based on the slope of the regression line, [14]:

$$C_f = 2\kappa^2\left(\frac{d(U/U_e)}{d(\ln[(y+\varepsilon)U_e/\nu])}\right)^2. \tag{5}$$

For all the test surfaces, the total stress method was also used to verify C_f. It assumes a constant stress region equal to the wall shear stress exists in the inner layer of the boundary layer. If the viscous and turbulent stress contributions are added together, an expression for C_f may be calculated as the following evaluated at the total stress plateau in the inner layer:

$$C_f = \frac{2}{U_e^2}\left[\nu\frac{\partial U}{\partial y} - \overline{u'v'}\right]. \tag{6}$$

Uncertainty Estimates

Precision uncertainty estimates for the velocity measurements were made through repeatability tests using the procedure given by Moffat [15]. Ten replicate velocity profiles were taken on both a smooth and a rough plate. The standard error for each of the measurement quantities was then calculated for both samples. In order to estimate the 95% confidence limits for a statistic calculated from a single profile, the standard deviation was multiplied by the two-tailed t value ($t=2.262$) for nine degrees-of-freedom and $\alpha=0.05$, as given by Coleman and Steele [16]. LDV measurements are also susceptible to a variety of bias errors including angle bias, validation bias, velocity bias, and velocity gradient bias, as detailed by Edwards [17]. Angle or fringe bias is due to the fact that scattering particles passing through the measurement volume at large angles may not be measured since several fringe crossings are needed to validate a measurement. In this experiment, the fringe bias was considered insignificant, as the beams were shifted above a burst frequency representative of twice the freestream velocity, [17]. Validation bias results from filtering too close to the signal frequency and any processor biases. In general these are difficult to estimate and vary from system to system. No corrections were made to account for validation bias. Velocity bias results from the greater likelihood of high velocity particles moving through the measurement volume during a given sampling period. The present measurements were burst transit time weighted to correct for velocity bias, as given by Buchhave et al. [18]. Velocity gradient bias is due to variation in velocity across the measurement volume. The correction scheme of Durst et al. [19] was used to correct u'. The corrections to the mean velocity and the other turbulence quantities were quite small and therefore neglected. An additional bias error in the v' measurements of $\sim$2% was caused by introduction of the w' component due to inclination of the LDV probe.

These bias estimates were combined with the precision uncertainties to calculate the overall uncertainties for the measured quantities. The resulting overall uncertainty in the mean velocity is $\pm1\%$. For the turbulence quantities $\overline{u'^2}$, $\overline{v'^2}$, and $\overline{u'v'}$, the overall uncertainties are $\pm2\%$, $\pm4\%$, and $\pm7\%$, respectively. The precision uncertainties in C_f were calculated using a series of repeatability tests, in a manner similar to that carried out for velocities. These were combined with bias estimates to calculate the overall uncertainty in C_f. The uncertainty in C_f for the smooth walls using the Clauser chart method is $\pm4\%$, and the uncertainty in C_f for the rough walls using the modified Clauser chart method was $\pm7\%$. The increased uncertainty for the rough walls resulted mainly from the extra two degrees-of-freedom in fitting the log law (ε and ΔU^+). The uncertainty in C_f using the total stress method is $\pm8\%$ for both the smooth and rough walls. The uncertainties in δ, δ^*, and θ are $\pm7\%$, $\pm4\%$, and $\pm5\%$, respectively.

Results and Discussion

The experimental conditions for each of the test cases are presented in Table 2. Significant increases in the physical growth of the boundary layer were noted on the unsanded and sandgrain rough surfaces compared to the smooth wall. The average increases in δ, δ^*, and θ for the unsanded surface were 16%, 19%, and 17%, respectively. The 60-grit sandpaper showed increases of 24%, 70%, and 50%, while the 240-grit sandpaper had increases of 14%, 36%, and 27% in δ, δ^*, and θ, respectively. The increase measured in these quantities compared to the smooth wall for both of the sanded surfaces was within the experimental uncertainty. The skin-friction coefficient determined using the Clauser chart and the total stress methods showed good agreement in this investigation, as the two fell within the uncertainty for all of the test cases. The values of C_f and u_τ used in the results that follow were

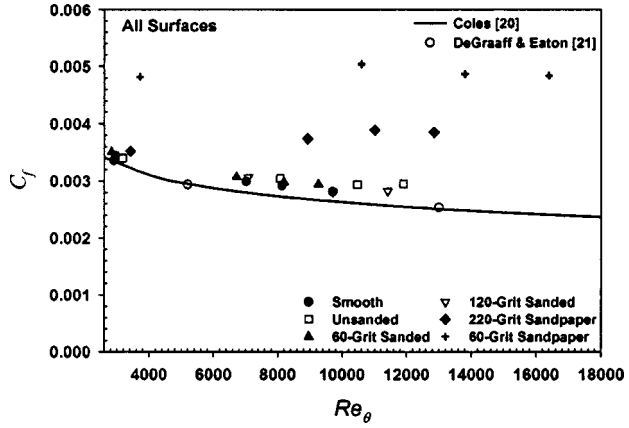

Fig. 1 Skin-friction coefficient versus momentum thickness Reynolds number. (Overall uncertainty in C_f: smooth wall, ±4%; rough wall, ±7%.)

determined using the Clauser chart method. This method was selected due to its lower overall uncertainty. Figure 1 presents C_f versus Re_θ for all the test surfaces. The smooth wall results of Coles [20] and DeGraaff and Eaton [21] are shown for comparison. The present smooth wall C_f values were systematically higher than the results of Coles and DeGraaff and Eaton by ~6% and ~4%, respectively. This may have been due to the elevated freestream turbulence intensity in the test facility and a slightly favorable pressure gradient, both of which would tend to increase C_f. It should be noted, however, that the present results agree with those of the previous investigations within the combined uncertainties of the measurements. The C_f values for the sanded and unsanded surfaces are observed to rise slightly above the smooth wall curve as Re_θ increases, however, the increases were still within the uncertainty of the measurements. The sandgrain rough surfaces both exhibited a significant increase in C_f over the entire range of Re_θ. At the highest Reynolds number, C_f was 87% higher than the smooth curve for the 60-grit sandpaper and was 43% higher for the 220-grit sandpaper.

Figure 2 shows the mean velocity profiles in wall variables for all of the test surfaces at the highest freestream velocity. The smooth profile follows the smooth wall log-law well in the overlap region. The rough surfaces also display a linear log region that is shifted by ΔU^+ below the smooth profile. As expected, a trend of increasing ΔU^+ with increasing roughness height is observed. Sanded surfaces smoother than 120-grit sanded were not tested,

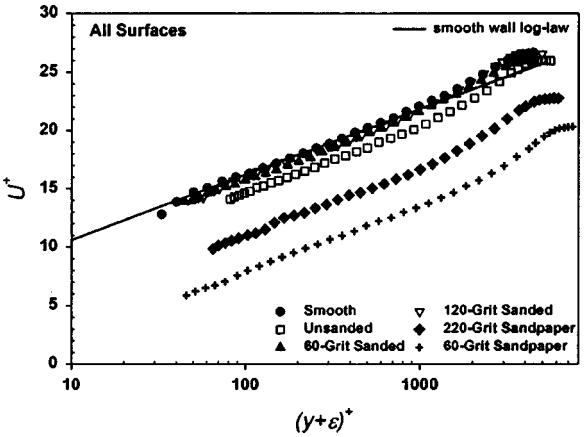

Fig. 2 Mean velocity profiles in wall coordinates for all surfaces at the highest freestream velocity. (Overall uncertainty in U^+: smooth wall, ±4%; rough wall, ±7%.)

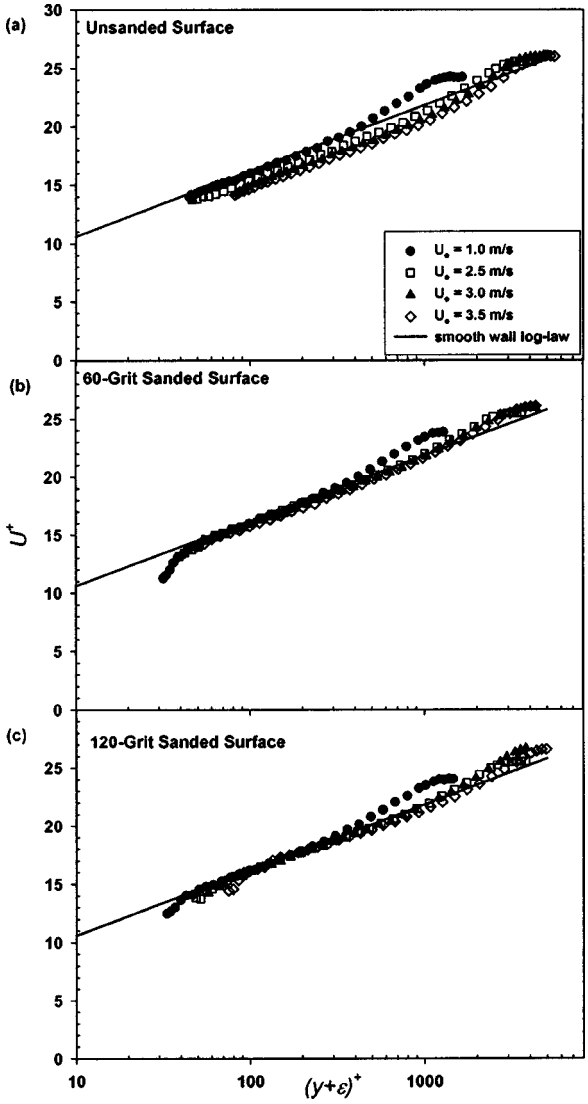

Fig. 3 Mean velocity profiles in wall coordinates for (*a*) the unsanded surface, (*b*) the 60-grit sanded surface, and (*c*) the 120-grit sanded surface. (Overall uncertainty in U^+, ±7%.)

because, as illustrated in Fig. 2, the velocity profiles were virtually collapsed with the smooth profile at this surface finish. However, in a previous study (Schultz [9]), small but significant differences in the overall frictional resistance of towed plates were observed on smoother surfaces. This implies that a roughness function may exist for surfaces sanded with finer grit sandpaper, however, they are difficult to measure using velocity profile methods. The mean velocity profiles for the sanded surfaces in wall coordinates are shown in Fig. 3. Figure 3(*a*) shows the profiles for the unsanded surface. An increase is seen in ΔU^+ with increasing unit Reynolds number, as expected. In Figs. 3(*b*) and 3(*c*), a similar trend is observed, but the changes in ΔU^+ with increasing unit Reynolds number are very small.

Figure 4 presents the roughness functions (ΔU^+ versus k^+) for all of the rough test surfaces. The Colebrook-type, [22], roughness function for naturally occurring roughness given by Grigson [23] and the Nikuradse-type, [24], roughness function for uniform sand given by Schlichting [25] are shown for comparison. The painted surfaces show good agreement ($R^2 = 0.9$) with a Colebrook-type roughness function using $k = 0.39\,R_a$. Using k based on the other roughness height parameters shown in Table 1 gave similar agreement with a Colebrook-type roughness function for these surfaces.

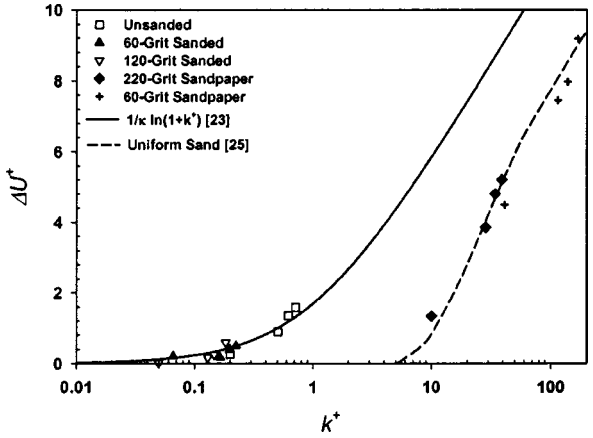

Fig. 4 Roughness functions (ΔU^+ versus k^+) for the rough specimens. (Overall uncertainty in ΔU^+, ±10% or ±0.2 whichever is greater.)

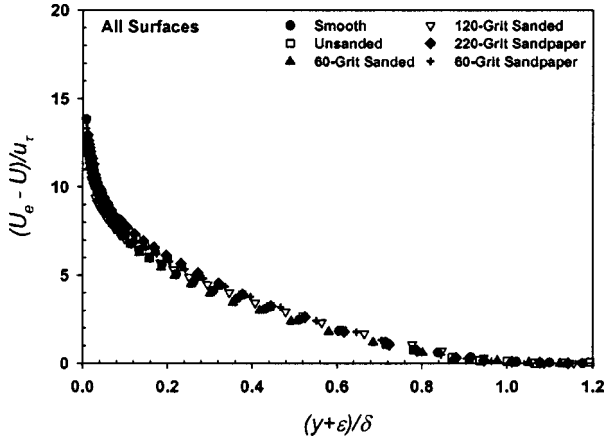

Fig. 6 Velocity defect profiles for all surfaces at the highest freestream velocity. (Overall uncertainty in $(U_e-U)/u_\tau$: smooth wall, ±5%; rough wall, ±7%.)

The sandgrain rough surfaces agree well with a Nikuradse-type roughness function with $k=0.75\,R_t$. This indicates that for these relatively simple roughness geometries a single roughness height parameter is a sufficient scaling parameter to characterize the physical nature of the surface. Acharya et al. [8] have shown that for surfaces representative of those on gas turbine blades, a texture parameter such as the root mean square deviation in the surface slope angle may be required to serve as an additional scaling parameter. It should be noted that the effect of changing the choice of k on the roughness function for a given surface is to simply shift the curve along the horizontal axis without changing its shape, since ν/u_τ and ΔU^+ are determined by the flow. Figure 5 shows the present roughness functions for the painted surfaces along with the results from similar surfaces determined by Schultz [9] using towing tank measurements and boundary layer similarity law analysis. Overall, there is good agreement between the data sets and the Colebrook-type roughness function using $k=0.39\,R_a$. These data indicate that the roughness functions determined indirectly using overall skin-friction resistance measurements and similarity law analysis can provide results that agree with those determined directly using the mean velocity profile as was argued by Granville [26].

The mean velocity profiles in defect form (Eq. (4)) for all test surfaces at the highest freestream velocity are presented in Fig. 6. The velocity defect profiles exhibit good collapse in the overlap and outer regions of the boundary layer. This supports a universal velocity defect profile for rough and smooth walls as first proposed by Clauser [1] and also lends support to the boundary layer similarity hypotheses of Townsend [10] and Perry and Li [11] that state that turbulence outside of the roughness sublayer is independent of the surface condition at sufficiently high Reynolds number. Acharya et al. [8] also noted good collapse to a universal defect profile for mesh and machined surface roughness but observed significant scatter for sand-cast surfaces.

The normalized, axial Reynolds normal stress ($\overline{u'^2}/u_\tau^2$ or equivalently $\rho\overline{u'^2}/\tau_w$) profiles for all test surfaces at the highest freestream velocity are presented in Fig. 7. Also shown for comparison are the results of the smooth wall direct numerical simulation (DNS) by Spalart [27] at $\mathrm{Re}_\theta=1410$ and the smooth and rough wall experimental results of Perry and Li [11] at $\mathrm{Re}_\theta=11{,}097$ and 7645, respectively. Good collapse of $\overline{u'^2}/u_\tau^2$ profiles is observed in both the overlap and outer regions of the boundary layer. This is in agreement with the findings of Perry and Li [11] and Krogstad and Antonia [4–6] who also observed no significant difference in the axial Reynolds normal stress profiles for smooth and rough walls outside of the inner region when they were normalized using u_τ^2. It should be noted that the present results also show good quantitative agreement with those of Perry and Li [11]. The mixed scaling ($\overline{u'^2}/u_\tau U_e$) recently proposed by DeGraaff and Eaton [21] based on a smooth wall study was also tried on the

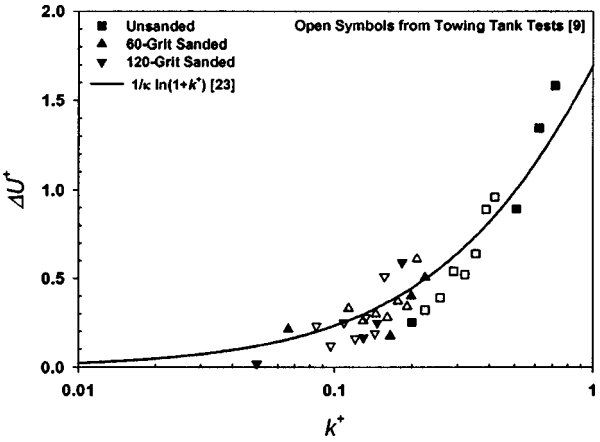

Fig. 5 Roughness functions (ΔU^+ versus k^+) for the painted surfaces. (Overall uncertainty in ΔU^+, ±0.2.)

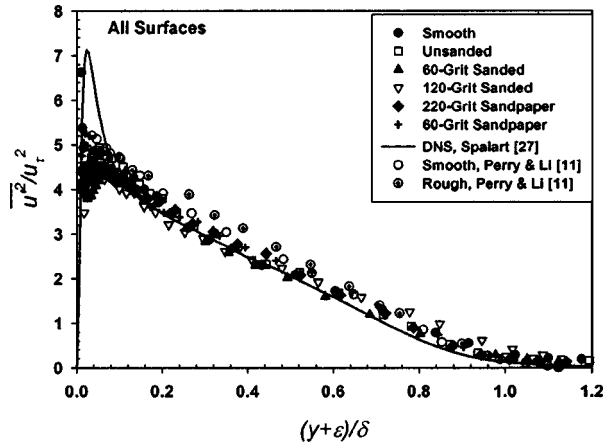

Fig. 7 Normalized axial Reynolds normal stress profiles for all surfaces at the highest freestream velocity. (Overall uncertainty in $\overline{u'^2}/u_\tau^2$: smooth wall, ±5%; rough wall, ±7%.)

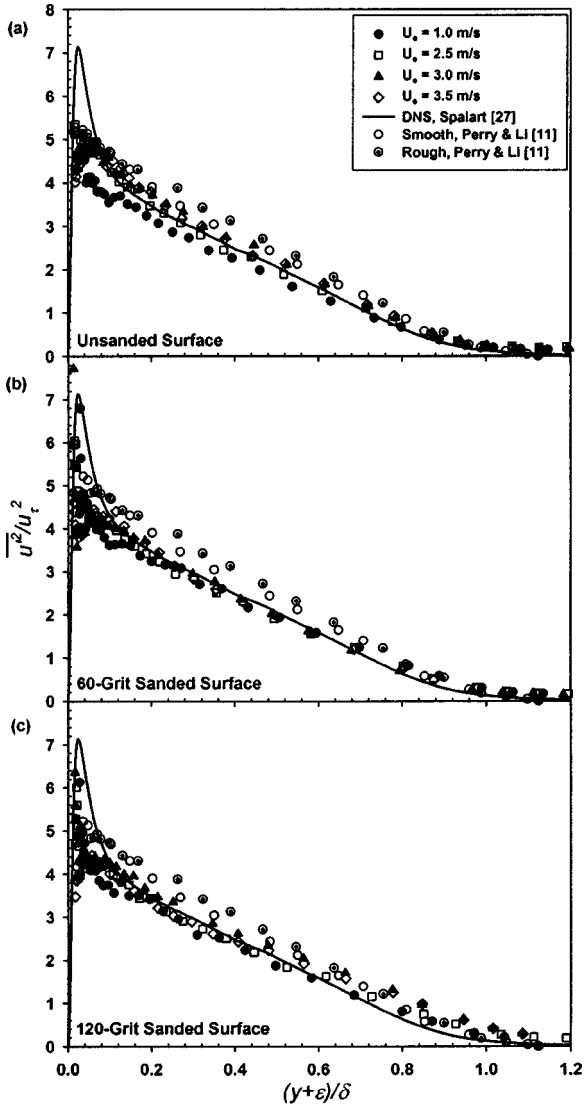

Fig. 8 Normalized axial Reynolds normal stress profiles for (*a*) the unsanded surface, (*b*) the 60-grit sanded surface, and (*c*) the 120-grit sanded surface. (Overall uncertainty in $\overline{u'^2}/u_\tau^2$, ±7%.)

present results. While it provided good collapse of the smooth wall results, it did not collapse the profiles from the different rough walls as effectively as u_τ^2. The normalized, axial Reynolds normal stress ($\overline{u'^2}/u_\tau^2$) profiles for the unsanded, 60-grit sanded, and 120-grit sanded surfaces are presented in Fig. 8. The profiles at the three highest Reynolds numbers for all of these surfaces numbers show good collapse. The lowest Reynolds number profiles are slightly below the other profiles in all cases. This is probably due to the fact that the momentum thickness Reynolds number was relatively low ($\mathrm{Re}_\theta<3200$). Coles [20] gives $\mathrm{Re}_\theta>6000$ to achieve a fully developed, equilibrium turbulent boundary layer. Again, the agreement of the present results with the smooth and rough wall results of Perry and Li [11] is within the experimental uncertainty.

The normalized, wall-normal Reynolds normal stress ($\overline{v'^2}/u_\tau^2$ or equivalently $\rho\overline{v'^2}/\tau_w$) profiles for all test surfaces at the highest freestream velocity are presented in Fig. 9. Again, the results of the smooth wall DNS by Spalart [27] and the smooth and rough wall experimental results of Perry and Li [11] are given for comparison. Good collapse of $\overline{v'^2}/u_\tau^2$ profiles is noted in both the

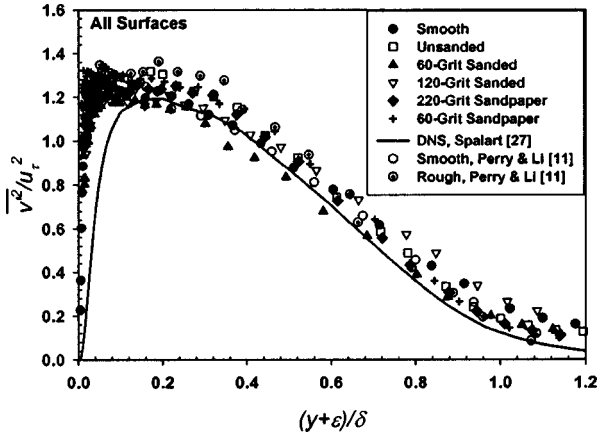

Fig. 9 Normalized wall-normal Reynolds normal stress profiles for all surfaces at the highest freestream velocity. (Overall uncertainty in $\overline{v'^2}/u_\tau^2$: smooth wall, ±6%; rough wall, ±8%.)

overlap and outer regions of the boundary layer. This is in agreement with the findings of Perry and Li [11] who also observed no significant difference in the wall-normal Reynolds normal stress profiles for smooth and rough walls outside of the near wall region when they were normalized using u_τ^2. Krogstad and Antonia [4–6] noted a large increase in $\overline{v'^2}/u_\tau^2$ well into the outer region of the boundary layer for mesh and circular rod roughness. They attributed this to an increase in the inclination angle of the large-scale structures, which tended to make the turbulence in the outer region more isotropic. Schultz [12] also observed this on flows over filamentous algae roughness but showed sandgrain roughness results collapsed well with smooth wall profiles. Further research is needed to show what surface properties are necessary to produce these changes in the boundary layer structure. It should be stated that the present results in Fig. 9 agree within their experimental uncertainty with those of Perry and Li [11]. The normalized, wall-normal Reynolds normal stress ($\overline{v'^2}/u_\tau^2$) profiles for the unsanded, 60-grit sanded, and 120-grit sanded surfaces are presented in Fig. 10. The profiles at the three highest Reynolds for all of these surface numbers show good collapse. The lowest Reynolds number profiles are slightly below the other profiles in all cases and show better agreement with the low Reynolds number DNS of Spalart [27].

The normalized, Reynolds shear stress ($-\overline{u'v'}/u_\tau^2$ or equivalently $-\rho\overline{u'v'}/\tau_w$) profiles for all surfaces at the highest freestream velocity are presented in Fig. 11. The results of the smooth wall DNS by Spalart [27], the smooth wall experimental results of DeGraaff and Eaton [21] at $\mathrm{Re}_\theta=13{,}000$, and the rough wall experimental results of Ligrani and Moffat [3] at $\mathrm{Re}_\theta=18700$ are shown for comparison. Reasonably good collapse of the $-\overline{u'v'}/u_\tau^2$ profiles is observed in both the overlap and outer regions of the boundary layer. This is in agreement with the measurements of Ligrani and Moffat [3] who also observed no significant difference between the Reynolds shear stress profiles for smooth and rough walls outside of the near wall region when they were normalized using u_τ^2. Krogstad and Antonia [4–6] noted a significant increase in $-\overline{u'v'}/u_\tau^2$ well into the outer region of the boundary layer for mesh and circular rod roughness. Schultz [12] also observed this on flows over filamentous algae roughness but showed sandgrain roughness collapsed well with smooth wall profiles. The present results in Fig. 11 agree within experimental uncertainty with those of DeGraaff and Eaton [21] and Ligrani and Moffat [3]. On the roughest surface, the 60-grit sandpaper, a local increase in $-\overline{u'v'}/u_\tau^2$ was observed in the inner region of the boundary layer. This increase persisted out to a distance of

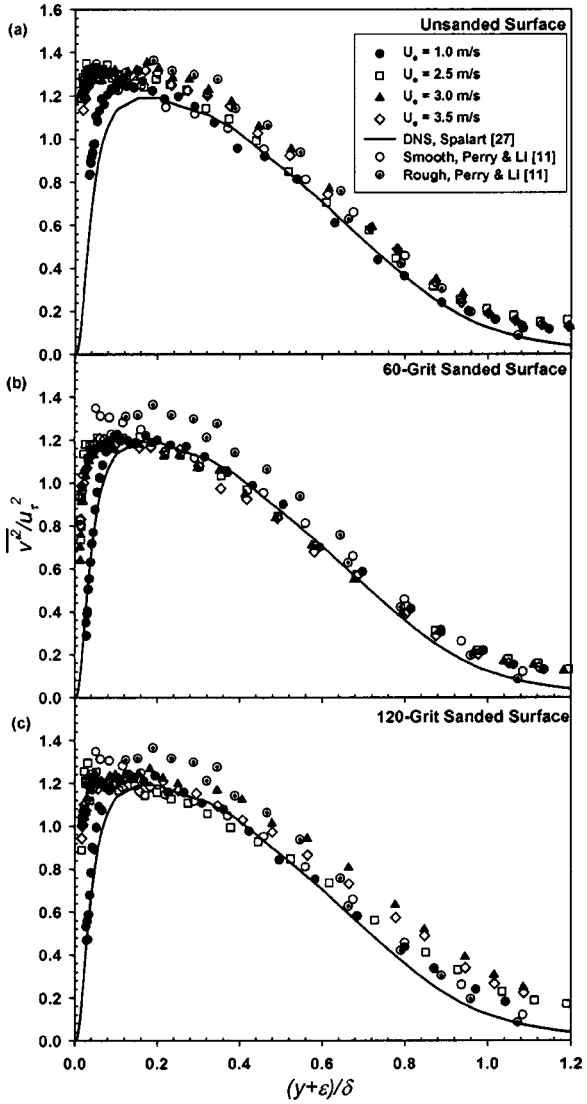

Fig. 10 Normalized wall-normal Reynolds normal stress for (*a*) the unsanded surface, (*b*) the 60-grit sanded surface, and (*c*) the 120-grit sanded surface. (Overall uncertainty in $\overline{v'^2}/u_\tau^2$, ±8%.)

$\sim 4k$ from the wall. Outside of this distance, the profile collapsed well with the others. The normalized, Reynolds shear stress ($-\overline{u'v'}/u_\tau^2$) profiles for the unsanded, 60-grit sanded, and 120-grit sanded surfaces for all freestream velocities are presented in Fig. 12. Again, agreement within the experimental uncertainty was observed between the present results and those of the previous experimental studies.

Conclusion

Comparisons of turbulent boundary layers developing over painted surfaces, smoothed by sanding with smooth and sandgrain walls have been made. An increase in the physical growth of the boundary layer was measured for the unsanded and the sandgrain roughness. A significant increase in C_f was also observed for the sandgrain surfaces. The change in these parameters for the sanded surfaces was within the experimental uncertainty. The roughness functions (ΔU^+) for the sanded surfaces measured in this study agree within their uncertainty with previous results obtained using towing tank tests and similarity law analysis. The present results show that the mean profiles for all of the surfaces collapse well in velocity defect form. Furthermore, the profiles of the normalized

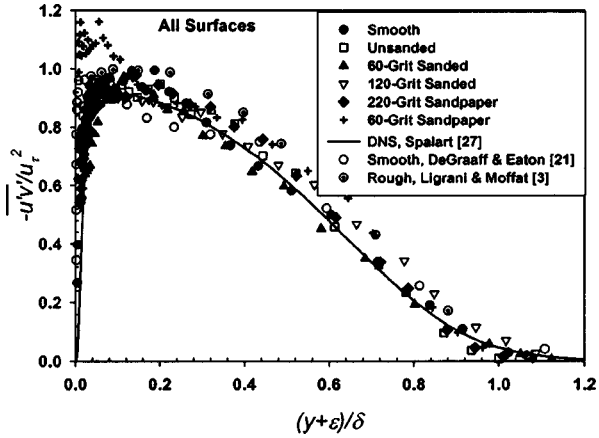

Fig. 11 Normalized Reynolds shear stress profiles for all surfaces at the highest freestream velocity. (Overall uncertainty in $-\overline{u'v'}/u_\tau^2$: smooth wall, ±8%; rough wall, ±10%.)

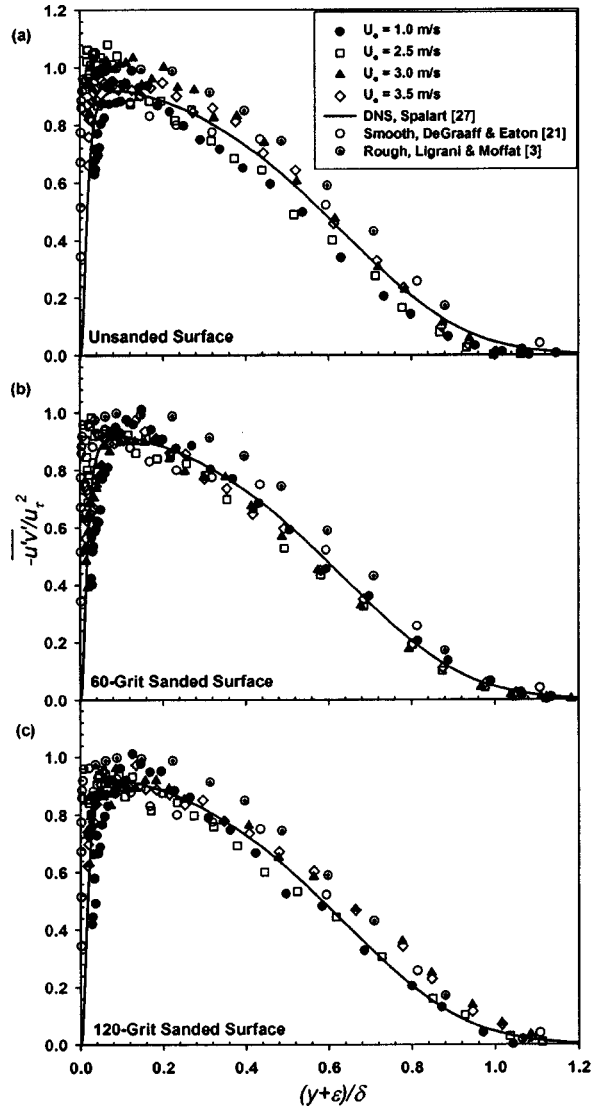

Fig. 12 Normalized Reynolds shear stress profiles for (*a*) the unsanded surface, (*b*) the 60-grit sanded surface, and (*c*) the 120-grit sanded surface. (Overall uncertainty in $-\overline{u'v'}/u_\tau^2$, ±10%.)

Reynolds stresses ($\overline{u'^2}/u_\tau^2$, $\overline{v'^2}/u_\tau^2$, and $-\overline{u'v'}/u_\tau^2$) for both the smooth and rough surfaces show agreement within experimental uncertainty in the overlap and outer regions of the boundary layer. These results lend support to the boundary layer similarity hypotheses of Townsend [10] and Perry and Li [11].

Acknowledgments

MPS would like to acknowledge the Office of Naval Research for the financial support of this research under grant #N00014-02-WR20325 administered by Dr. Steve McElvaney. Many thanks go to Mr. Don Bunker, Mr. Steve Enzinger, Mr. John Zseleczky, and the rest of the USNA Hydromechanics Lab staff for their valuable help in providing technical support for the project. We are indebted to Prof. Peter Bradshaw and Prof. Ralph Volino for many constructive comments about drafts on this manuscript. We would also like to thank Mr. Bill Beaver of the USNA Technical Support Division who constructed the flat plate test fixture and Prof. Michelle Koul for use of the laser profilometer.

Nomenclature

B = smooth wall log-law intercept, 5.0
C_f = skin-friction coefficient, $(\tau_w)/[(1/2)\rho U_e^2]$
k = arbitrary measure of roughness height
K = acceleration parameter, $(\nu/U_e^2)(dU_e/dx)$
N = number of samples in surface profile
R^2 = coefficient of determination
R_a = centerline average roughness height, $(1/N)\Sigma_{i=1}^{N}|y_i|$
R_q = root mean square roughness height, $\sqrt{(1/N)\Sigma_{i=1}^{N}y_i^2}$
R_t = maximum peak to trough height, $y_{\max}-y_{\min}$
R_z = ten point roughness height, $(1/5)\Sigma_{i=1}^{5}(y_{\max\,i}-y_{\min\,i})$
Re_x = Reynolds number based on distance from leading edge, $U_e x/\nu$
Re_{δ^*} = displacement thickness Reynolds number, $U_e\delta^*/\nu$
Re_θ = momentum thickness Reynolds number, $U_e\theta/\nu$
U = mean velocity in the x-direction
U_e = freestream velocity
ΔU^+ = roughness function
$\overline{u'^2}$ = streamwise mean square fluctuating velocity
$\overline{u'v'}$ = mean product of instantaneous streamwise and wall-normal fluctuating velocity
u_τ = friction velocity, $\sqrt{\tau_w/\rho}$
$\overline{v'^2}$ = wall-normal mean square fluctuating velocity
x = streamwise distance from plate leading edge
y = normal distance from the wall
δ = boundary layer thickness $(y@U=0.995U_e)$
δ^* = displacement thickness, $\int_0^\delta(1-U/U_e)dy$
ε = wall datum offset
κ = von Karman constant$=0.41$
ν = kinematic viscosity of the fluid
Π = wake parameter
θ = momentum thickness, $\int_0^\delta(U/U_e)(1-U/U_e)dy$
ρ = density of the fluid
τ_w = wall shear stress
ω = wake function

Superscripts

$+$ = inner variable (normalized with u_τ or u_τ/ν)

Subscripts

min = minimum value
max = maximum value
R = rough surface
S = smooth surface

References

[1] Clauser, F. H., 1954, "Turbulent Boundary Layers in Adverse Pressure Gradients," J. Aeronaut. Sci., **21**, pp. 91–108.
[2] Hama, F. R., 1954, "Boundary-Layer Characteristics for Rough and Smooth Surfaces," Transactions SNAME, **62**, pp. 333–351.
[3] Ligrani, P. M., and Moffat, R. J., 1986, "Structure of Transitionally Rough and Fully Rough Turbulent Boundary Layers," J. Fluid Mech., **162**, pp. 69–98.
[4] Krogstad, P.-Å., Antonia, R. A., and Browne, L. W. B., 1992, "Comparison Between Rough- and Smooth-Wall Turbulent Boundary Layers," J. Fluid Mech., **245**, pp. 599–617.
[5] Krogstad, P.-A., and Antonia, R. A., 1999, "Surface Roughness Effects in Turbulent Boundary Layers," Exp. Fluids, **27**, pp. 450–460.
[6] Antonia, R. A., and Krogstad, P.-Å., 2001, "Turbulence Structure in Boundary Layers Over Different Types of Surface Roughness," Fluid Dyn. Res., **28**, pp. 139–157.
[7] Raupach, M. R., Antonia, R. A., and Rajagopalan, S., 1991, "Rough-Wall Turbulent Boundary Layers," Appl. Mech. Rev., **44**(1), pp. 1–25.
[8] Acharya, M., Bornstein, J., and Escudier, M. P., 1986, "Turbulent Boundary Layers on Rough Surfaces," Exp. Fluids, **4**, pp. 33–47.
[9] Schultz, M. P., 2002, "The Relationship Between Frictional Resistance and Roughness for Surfaces Smoothed by Sanding," ASME J. Fluids Eng., **124**, pp. 492–499.
[10] Townsend, A. A., 1976, *The Structure of Turbulent Shear Flow*, Cambridge University Press, Cambridge, UK.
[11] Perry, A. E., and Li, J. D., 1990, "Experimental Support for the Attached-Eddy Hypothesis in Zero-Pressure Gradient Turbulent Boundary Layers," J. Fluid Mech., **218**, pp. 405–438.
[12] Schultz, M. P., 2000, "Turbulent Boundary Layers on Surfaces Covered with Filamentous Algae," ASME J. Fluids Eng., **122**, pp. 357–363.
[13] Klebanoff, P. S., and Diehl, F. W., 1951, "Some Features of Artifically Thickened Fully Developed Turbulent Boundary Layers With Zero Pressure Gradient," NACA TN 2475.
[14] Lewthwaite, J. C., Molland, A. F., and Thomas, K. W., 1985, "An Investigation into the Variation of Ship Skin Frictional Resistance with Fouling," Transactions Royal Institute of Naval Architects, **127**, pp. 269–284.
[15] Moffat, R. J., 1988, "Describing the Uncertainties in Experimental Results," Exp. Therm. Fluid Sci., **1**, pp. 3–17.
[16] Coleman, H. W., and Steele, W. G., 1995, "Engineering Application of Experimental Uncertainty Analysis," AIAA J., **33**(10), pp. 1888–1896.
[17] Edwards, R. V., 1987, "Report of the Special Panel on Statistical Particle Bias Problems in Laser Anemometry," ASME J. Fluids Eng., **109**, pp. 89–93.
[18] Buchhave, P., George, W. K., and Lumley, J. L., 1979, "The Measurement of Turbulence With the Laser-Doppler Anemometer," Annu. Rev. Fluid Mech., **11**, pp. 443–503.
[19] Durst, F., Fischer, M., Jovanovic, J., and Kikura, H., 1998, "Methods to Set Up and Investigate Low Reynolds Number, Fully Developed Turbulent Plane Channel Flows," ASME J. Fluids Eng., **120**, pp. 496–503.
[20] Coles, D., 1962, "The Turbulent Boundary Layer in a Compressible Fluid," The Rand Corp., Report R-403-PR.
[21] DeGraaff, D. B., and Eaton, J. K., 2000, "Reynolds-Number Scaling of the Flat-Plate Turbulent Boundary Layer," J. Fluid Mech., **422**, pp. 319–346.
[22] Colebrook, C. F., 1939, "Turbulent Flow in Pipes With Particular Reference to the Transition Between Smooth and Rough Pipe Laws," Journal of Civil Engineers, **11**, pp. 133–157.
[23] Grigson, C. W. B., 1992, "Drag Losses of New Ships Caused by Hull Finish," J. Ship Res., **36**, pp. 182–196.
[24] Nikuradse, J., 1933, "Laws of Flow in Rough Pipes," NACA Technical Memorandum 1292.
[25] Schlichting, H., 1979, *Boundary-Layer Theory*, 7th Ed., McGraw-Hill, New York.
[26] Granville, P. S., 1987, "Three Indirect Methods for the Drag Characterization of Arbitrarily Rough Surfaces on Flat Plates," J. Ship Res., **31**, pp. 70–77.
[27] Spalart, P. R., 1988, "Direct Simulation of a Turbulent Boundary Layer up to $\mathrm{Re}_\theta=1410$," J. Fluid Mech., **187**, pp. 61–98.

Yandong Hu
Department of Mechanical & Industrial Engineering,
University of Toronto,
5 King's College Road,
Toronto, Ontario M5S 3G8, Canada

Carsten Werner
Department of Mechanical & Industrial Engineering,
University of Toronto,
5 King's College Road,
Toronto, Ontario M5S 3G8, Canada and
Department of Biocompatible Materials,
Institute of Polymer Research,
Hohe Strasse 6,
01069 Dresden, Germany

Dongqing Li[1]
Department of Mechanical & Industrial Engineering,
University of Toronto,
5 King's College Road,
Toronto, Ontario M5S 3G8, Canada
e-mail: dli@mie.utoronto.ca

Influence of Three-Dimensional Roughness on Pressure-Driven Flow Through Microchannels

Surface roughness is present in most of the microfluidic devices due to the microfabrication techniques or particle adhesion. It is highly desirable to understand the roughness effect on microscale flow. In this study, we developed a three-dimensional finite-volume-based numerical model to simulate pressure-driven liquid flow in microchannels with rectangular prism rough elements on the surfaces. Both symmetrical and asymmetric roughness element arrangements were considered, and the influence of the roughness on pressure drop was examined. The three-dimensional numerical solution shows significant effects of surface roughness in terms of the rough elements' height, size, spacing, and the channel height on both the velocity distribution and the pressure drop. The compression-expansion flow around the three-dimensional roughness elements and the flow blockage caused by the roughness in the microchannel were discussed. An expression of the relative channel height reduction due to roughness effect was presented.
[DOI: 10.1115/1.1598993]

1 Introduction

A lab-on-a-chip device is a miniaturized laboratory on a chip consisting of a network of microchannels. Precise manipulation of biological liquids is key to the performance of the biochip devices. Fundamental understanding of liquid flow through the microchannels is therefore important to the design and operation of the biochip devices. In addition to the interfacial electrokinetic properties, the surface roughness of the microchannels plays an important role in determining the flow characteristics. Generally, the microchannel surface has certain degrees of roughness generated by the manufacturing techniques or by adhesion of biological particles from the liquids. Liquid flows through the microchannels are influenced by the presence of the rough elements on the microchannel surface.

In the literature there are a few studies of microchannel flow related to surface roughness. These are experimental investigations of flow and heat transfer in microtubes, [1], of diameters ranging from 50 to 254 μm and in trapezoidal microchannels, [2,3], of hydraulic diameters ranging from 51 to 169 μm. The observed increase in flow friction and the decrease in heat transfer were attributed to surface roughness effects, [1–3].

The purpose of this study is to examine the influence of micron-sized rough elements on pressure-driven flow in microchannels by three-dimensional numerical simulations. We consider the rough microchannel wall as a homogeneous surface with uniformly distributed rough elements. Furthermore, to simplify the modeling and numerical simulation, we consider the rough elements to be cylinders with a square cross section. Two types of the roughness element arrangement on the microchannel wall are considered as shown in Figs. 1(*a*) and (*b*). These roughness elements block the flow and increase the pressure drop over the microchannel. The pressure drop is a key parameter for controlling the liquid flow through the lab chips.

Generally, flows in most microfluidic systems, whether pressure or electrokinetically driven, are limited to the low Reynolds number regime, (i.e., $\mathrm{Re}<1$). For conventional external flows at high Reynolds numbers, for example, flow crossing banks of tubes, [4], the states of the flow within the bank are dominated by boundary layer separation effects and by wake interactions, both of which may cause complicated, asymmetrical flow patterns. However, this will not occur for the flow in low Reynolds number regime as considered here.

In this study we consider pressure-driven flow in a slit microchannel formed by two parallel surfaces with rough elements, as illustrated in Fig. 2. For the two arrangements of rough elements as shown in Fig. 1, the influence of the rough element size, height, density and the channel sizes on the flow in microchannels will be examined. In order to compare the results with that of smooth microchannels, we use the microchannels' height as the characteristic length in the model. To our knowledge, this is the first theoretical study to investigate micro roughness effect on liquid flow through microchannels.

2 Theoretical Model

In a number of recent studies, computational fluid dynamics modeling has proven to be an excellent tool for analyzing flow in microfluidic systems and devices, [5,6]. In this section, we will present the relevant equations, primary assumptions, simulation conditions, and the numerical method.

2.1 Modeling Assumptions and Basic Equations. Liquid flow through a slit microchannel with rough elements on the surfaces is illustrated in Fig. 2. Further analysis and simplification are required for developing a proper model and using computational fluid dynamics method to solve the problem. In this paper, the Reynolds number is given by $\mathrm{Re}=\rho U_0 H/\mu$, where H is a characteristic length taken as the channel height, U_0 is the characteristic velocity taken as the average velocity of the minimum cross sec-

[1]To whom correspondence should be addressed.

Contributed by the Fluids Engineering Division for publication in the JOURNAL OF FLUIDS ENGINEERING. Manuscript received by the Fluids Engineering Division Sept. 12, 2002; revised manuscript received Apr. 22, 2003. Associate Editor: T. B. Gatski.

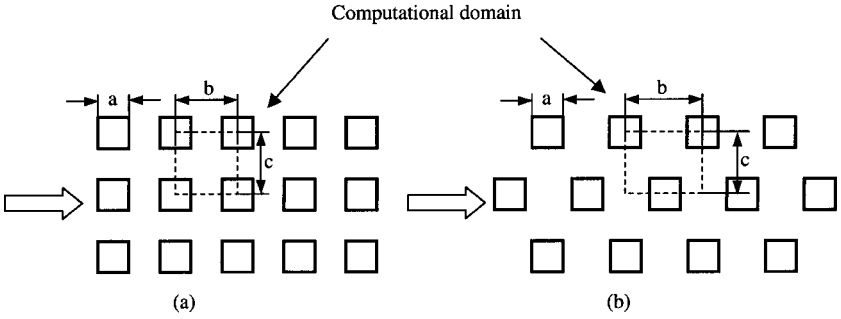

Fig. 1 The roughness arrangements on the homogeneous microchannel wall: (*a*) symmetrical arrangement and (*b*) asymmetrical arrangement, and the corresponding computational domains from the top view

tion of the channel, ρ is the fluid's density, and μ is the fluid's dynamic viscosity. In order to evaluate the influence of the roughness on the flow through such a microchannel, one must know the flow in a smooth microchannel. The steady-state flow in smooth channels is called the Poiseuille flow, [7]. The pressure gradient of the Poiseuille flow in a slit channel is related to the average velocity and the channel height by

$$\frac{\Delta p}{\Delta x} = \frac{12 \cdot \mathrm{Re} \cdot \mu^2}{\rho \cdot H^3} \tag{1a}$$

where Δp is the pressure drop between the inlet and the outlet. Nondimensionalizing the pressure gradient by $P = p/(\mu U_0/H)$ and $X = x/H$, the above equation can be rewritten as

$$\frac{\Delta P}{\Delta X} = 12. \tag{1b}$$

This equation will also be used to verify the numerical methods and the computer programs we have developed.

In this study, the flow is limited to a low Reynolds regime ($0.001 < \mathrm{Re} < 10$), turbulence and the wake region between two rough elements can be neglected. Therefore, at the tail region of each roughness element, the flow between the two elements is symmetrical with respect to the central line along *x*-direction. We consider the flow as a steady-state fully developed flow in the whole channel. Sparrow et al. [8] and Jubran et al. [9], in their forced convection channel flow experiments, both showed that the flow reached a fully developed state after five rows of three-dimensional roughness elements. This implies that the flow-developing region is very short. In the fully developed region, the flow pattern and the pressure drop for every roughness element is the same, while the absolute pressure will continuously decrease along the flow. Therefore, to reduce the amount of computation, we will consider a unit of the channel surface area as shown in Figs. 1(*a*) and (*b*) as the computational domain. The results from this domain will provide all details of the flow patterns and the pressure drop for each roughness element, and can be extended to the whole flow field in the microchannel.

Furthermore, the channel width is considered much larger than the channel height so that the channel sidewall effect can be neglected. Finally, water is chosen as the liquid and the flow is considered at a constant temperature of 20°C. The property of the liquid is constant, i.e., the density ρ is 1000 kg/m^3, and the kinematic viscosity ν is 1.006×10^{-6} m^2/s.

Introducing the following nondimensional parameters $U = u/U_0$, $V = v/U_0$, $W = w/U_0$, $X = x/H$, $Y = y/H$, $Z = z/H$, $P = p/(\mu U_0/H)$ and using the definition of the Reynolds number, the nondimensional form of the Navier-Stokes equations, and the continuity equation for the system concerned here can be written in the following form:

$$\begin{cases} \mathrm{Re} \cdot \left(U\dfrac{\partial U}{\partial X} + V\dfrac{\partial U}{\partial Y} + W\dfrac{\partial U}{\partial Z} \right) = -\dfrac{\partial P}{\partial X} + \dfrac{\partial^2 U}{\partial X^2} + \dfrac{\partial^2 U}{\partial Y^2} + \dfrac{\partial^2 U}{\partial Z^2} \\ \mathrm{Re} \cdot \left(U\dfrac{\partial V}{\partial X} + V\dfrac{\partial V}{\partial Y} + W\dfrac{\partial V}{\partial Z} \right) = -\dfrac{\partial P}{\partial Y} + \dfrac{\partial^2 V}{\partial X^2} + \dfrac{\partial^2 V}{\partial Y^2} + \dfrac{\partial^2 V}{\partial Z^2} \\ \mathrm{Re} \cdot \left(U\dfrac{\partial W}{\partial X} + V\dfrac{\partial W}{\partial Y} + W\dfrac{\partial W}{\partial Z} \right) = -\dfrac{\partial P}{\partial Z} + \dfrac{\partial^2 W}{\partial X^2} + \dfrac{\partial^2 W}{\partial Y^2} + \dfrac{\partial^2 W}{\partial Z^2} \end{cases} \tag{2}$$

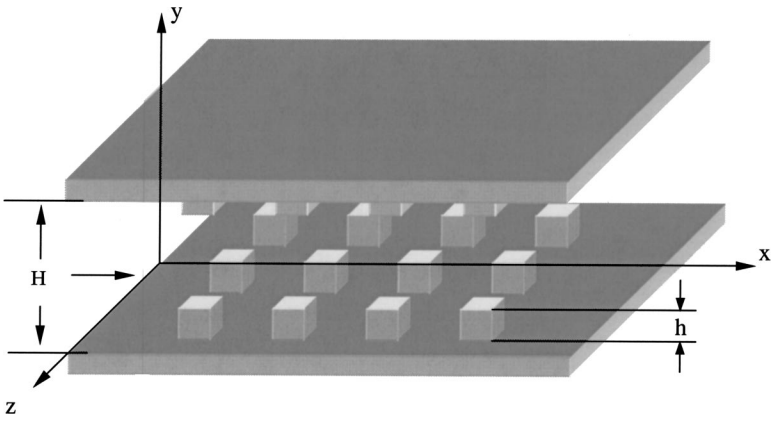

Fig. 2 Illustration of flow through a slit microchannel with rectangular prism rough elements on the surfaces

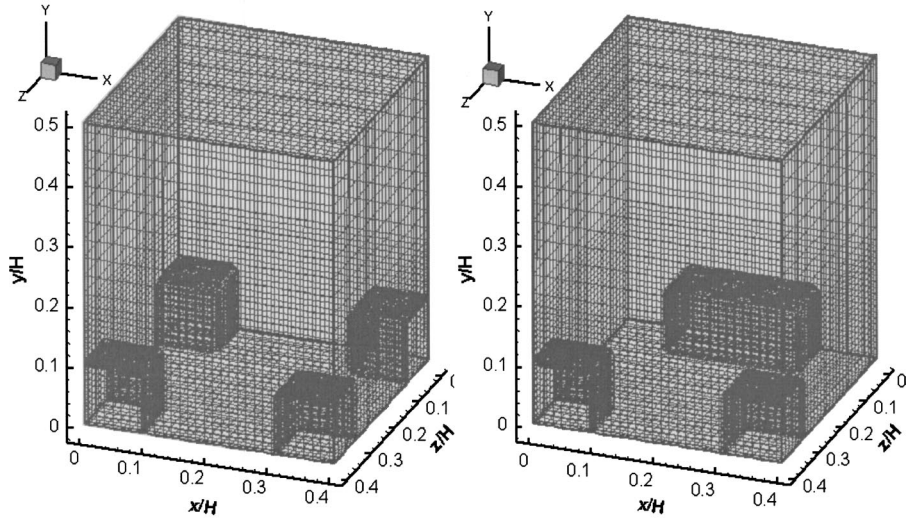

Fig. 3 Illustration of three-dimensional computational grids for the cases (*a*) symmetrical arrangement and (*b*) asymmetrical arrangement with $a=1.0\,\mu$m, $b=2.0\,\mu$m, $H=5\,\mu$m, and $h=0.5\,\mu$m

$$\frac{\partial U}{\partial X}+\frac{\partial V}{\partial Y}+\frac{\partial W}{\partial Z}=0. \tag{3}$$

The above-described liquid flow through a slit microchannel with rough surfaces is governed by Eqs. (2) and (3). It should be noted that the above equations are nonlinear and coupled with each other. They can only be solved numerically. However, finding a numerical solution to these equations is not a trivial task. Saving computational memory and time is very important in developing a practical numerical method to solve these equations.

2.2 Solution Domain, Boundary Conditions, and Numerical Method. The solution domain and the grid arrangement are shown in Figs. 3(*a*) and (*b*). In the *x*-*z*–plane, we take one period as the computational domain. The height of the computational domain is chosen as the half of the microchannel height because of the symmetry. Grid will be refined at the bottom region in order to obtain sufficiently accurate numerical solutions around the small roughness elements. The grid system is $32\times32\times32$ in the *x*, *y*, *z*-directions, respectively.

Three boundary planes, the top and two side planes of the computational domain are subject to the symmetric boundary conditions. That is, for velocity component parallel to the plane, the change of the velocity component normal to the plane is zero; for velocity component normal to the plane, the velocity component itself is zero. The symmetric boundary conditions are shown in Eqs. (4*a*), (4*b*), and (4*c*)

$$\text{at } Z=0 \quad \frac{\partial U}{\partial Z}=0, \quad \frac{\partial V}{\partial Z}=0, \quad W=0 \tag{4a}$$

$$\text{at } Z=c/H \quad \frac{\partial U}{\partial Z}=0, \quad \frac{\partial V}{\partial Z}=0, \quad W=0 \tag{4b}$$

$$\text{at } Y=0.5 \quad \frac{\partial U}{\partial Y}=0, \quad V=0, \quad \frac{\partial W}{\partial Y}=0. \tag{4c}$$

The bottom plane of the computational domain is subject to the no-slip boundary conditions:

$$\text{at } Y=0 \quad U=0, \quad V=0, \quad W=0. \tag{4d}$$

The inlet and outlet boundaries of the computational domain are treated to satisfy the following conditions: (a) flow profiles at the two planes are fully developed and (b) flow is periodical, i.e., all the flow characteristics are periodical according to the geometric period. This kind of flow is called periodic, fully developed flow, first introduced by Patankar and Sparrow in 1977, [10]. Assume that *s* is the length of one geometric period. For the case studied here, *s* is the length of the computational domain in *x*-direction. When the flow is in a fully developed state, we have the following periodic boundary conditions:

$$u(x,y,z)=u(x+s,y,z)$$

$$v(x,y,z)=v(x+s,y,z)$$

$$w(x,y,z)=w(x+s,y,z).$$

Due to the periodical characteristic, the investigation for one period can represent the solution of the whole flow field. In the present paper, the method for solving the fully developed fluid flow is as follows: using the periodical boundary condition to set the inlet flow velocity equal to the latest iteration result of the outlet flow velocity after each iteration. More specifically, first, the calculation is done based on an assumed initial velocity distribution and on the fully developed outlet boundary condition. Then, set the inlet boundary condition to be the calculated outlet boundary condition. The calculation repeats until the calculated inlet and outlet velocity satisfy the periodical condition. This method for solving fully developed periodical flow cases can also be found elsewhere, [11].

For the initial values:

$$\text{at } X=0 \quad U=1, \quad V=0, \quad W=0 \tag{4e}$$

$$\text{at } X=b/H \quad U=1, \quad V=0, \quad W=0. \tag{4f}$$

For later iterations:

$$\text{at } X=0 \quad U|_{X=0}=U|_{X=b/H}, \quad V|_{X=0}=V|_{X=b/H}, \quad W|_{X=0}=W|_{X=b/H} \tag{4g}$$

$$\text{at } X=b/H \quad \frac{\partial U}{\partial X}=0, \quad V|_{X=0}=V|_{X=b/H}, \quad W|_{X=0}=W|_{X=b/H}. \tag{4h}$$

Table 1 Comparison of the analytical and the numerical solutions for flow in a smooth microchannel

Re	$\Delta p/\Delta x$ (Pa/m)		
	Analytical	Numerical	Difference %
0.001	9.6E+04	9.590076E+04	0.1
0.01	9.6E+05	9.590240E+05	0.1
0.1	9.6E+06	9.590000E+06	0.1
1.0	9.6E+07	9.590040E+07	0.1
10.0	9.6E+08	9.589441E+08	0.1

Equations (2) and (3) were solved over the computational domain by using the finite volume approach, [12], and SIMPLEC algorithm. As part of the computational domain, the virtual flow in the roughness is also solved using the extension of computational region approach, [12], which considers the roughness element as a kind of fluid with extremely high viscosity.

3 Results and Discussion

By solving Eqs. (2) and (3) over the computational domain described above, the structure of the flow patterns and the influence of roughness on the pressure drop were obtained for the two types of roughness arrangements. A series of geometric parameters used in the calculations are listed below. For both symmetrical and asymmetrical arrangements,

1. the roughness height (h): 0.1 μm, 0.5 μm, 1.0 μm, 2.0 μm;
2. the roughness size (a): 0.1 μm, 0.5 μm, 1.0 μm, 1.5 μm;
3. the roughness spacing (b or c): 2.0 μm, 5 μm, 10 μm, 15 μm, 30 μm, 50 μm; where b is the distance between the center of the rough elements in x-direction, c is the distance between the center of the rough elements in z-direction. Here we consider only $b=c$ situations; and
4. the channel height (H): 5.0 μm, 7 μm, 10 μm, 15 μm, 30 μm, 50 μm.

The above parameters are chosen to reflect the conditions in practical microfluidic devices. The size of the microchannels for most lab-on-a-chip devices ranges from 10 to 100 μm. Some devices designed for the sizing and sorting of DNA have the channel depth only 3 μm, [13]. The surface roughness dimensions are largely dependent on the methods and the processes of the fabrication and the materials. The reported surface roughness ranges from 0.1 μm to 2 μm, [1–3].

To examine our computer programs we first calculated liquid flow in a smooth microchannel. The same computational domain, same boundary conditions and the same numerical methods were applied to the smooth microchannel. The comparison between the numerical results and the results from the analytical solution (Eq. (1)) are shown in Table 1. As clearly seen from Table 1, the excellent agreement indicates the reliability and the accuracy of the developed computer programs.

3.1 Flow Patterns and Pressure Field. The side views of the streamline profile of the symmetrical and the asymmetrical arrangements are shown in Figs. 4(a) and (b). Also in Fig. 4, the gray level (from dark to white) represents the nondimensional velocity value (from 0 to a maximum). Comparing the flow patterns of the two arrangements, we can see that in both cases, the flow velocity behind the roughness elements and close to the upper surface of the elements is very small. This indicates that the roughness exerts a significant effect on the flow field. Note that Fig. 4 shows the flow fields at the symmetrical plane ($z=0$), the closed streamlines in Fig. 4(a) represent a dead zone, the size of the dead zone depends on the roughness dimension and the spacing between the rough elements. The streamlines from the top view are shown in Figs. 5(a) and (b) for the two roughness element arrangements. It can be seen that, along the flow direction, the liquid expands in the wider space between two elements and then compresses in the narrower path periodically. During such a periodical expansion-compression flow, there is more surface friction effect than in the case of parallel flow through a smooth channel.

Three-dimensional streamlines are shown in Figs. 6(a) and (b) for the two types of roughness element arrangement. These figures give an overall view of the fluid flow over these elements. We can also see that the curvature of the streamline in the asymmetrical case is bigger than that of the symmetrical case. From this we expect that the roughness influence of the asymmetrical case is bigger than that of the symmetrical case.

Figures 7(a) and (b) show the top view of the pressure fields and Figs. 7(c) and (d) show the side view of the pressure fields for the two types of roughness element arrangement, respectively. The gray scale from light to dark represents the relative pressure

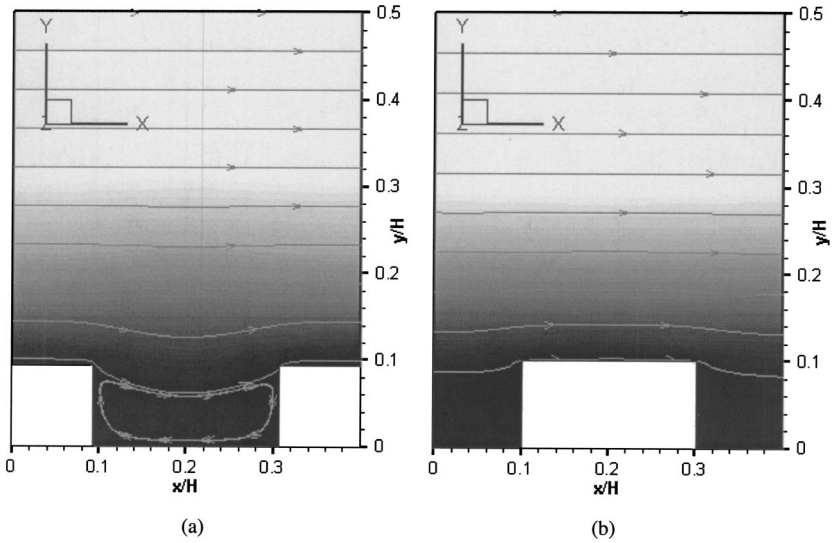

Fig. 4 The side view of the flow field: (a) streamlines of the symmetrical arrangement with $a=1.0$ μm, $b=2.0$ μm, $H=5$ μm, $h=0.5$ μm, Re=0.1, and (b) streamlines of the asymmetrical arrangement with $a=1.0$ μm, $b=2.0$ μm, $H=5$ μm, $h=0.5$ μm

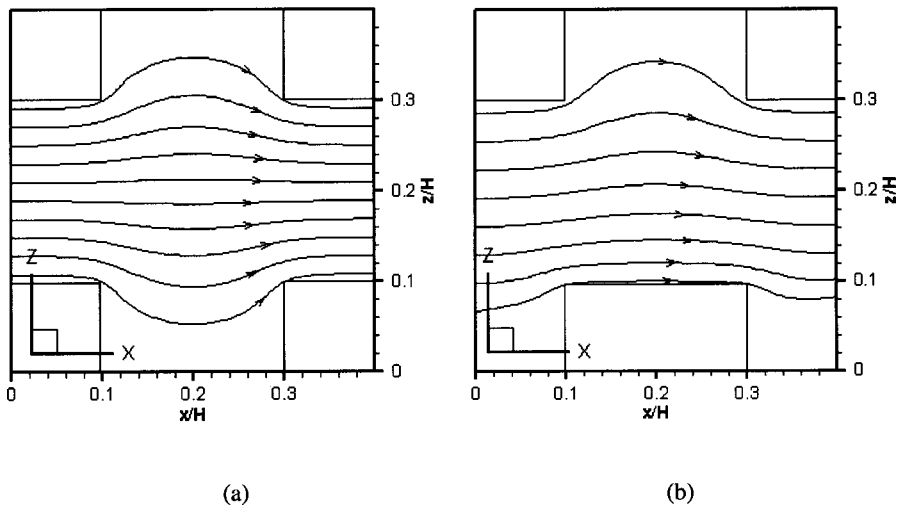

Fig. 5 The top view of the streamlines of (*a*) the symmetrical arrangement with $a=1.0\ \mu$m, $b=2.0\ \mu$m, $H=5\ \mu$m, $h=0.5\ \mu$m, and (*b*) the asymmetrical arrangement with $a=1.0\ \mu$m, $b=2.0\ \mu$m, $H=5\ \mu$m, $h=0.5\ \mu$m

from the maximum to the minimum. The top view shows the pressure fields on the horizontal plane at the middle of the roughness elements. For the channel with symmetrically arranged roughness, as shown in Fig. 7(*a*), the dark regions occur at the tail region of the rough elements and at the downstream subchannel (i.e., flow path between two rough elements). The contour patterns of the pressure field imply that the flow in the subchannels parallel to the main flow direction is similar to the flow in a smooth channel, and these subchannels are the main zones of acceleration ($dp/dx<0$) close to the roughness. However, in the subchannels perpendicular to the main flow direction the flow retardation occurs (i.e., $dp/dx>0$). In the center zones surrounded by four roughness elements the expansion and then the compression take place. For the channels with asymmetrically arranged roughness, as shown in Fig. 7(*b*), the retardation zones occur at the tail of rough element. The acceleration region for this type of arrangement is a leaned band between the two rough elements, and the acceleration direction is not parallel to the bulk flow direction. The pressure field also shows that the distance between compression and expansion or between two acceleration zones in the channel with asymmetrical roughness arrangement is much smaller than in the channel with symmetrical roughness arrangement.

The typical side view of the pressure field is taken at the vertically symmetrical plane. As shown in Figs. 7(*c*) and (*d*), expansions and compressions occur in both the horizontal and vertical directions. Above approximately one time of the rough element height from the top of the rough element, the pressure patterns are essentially the same as that in smooth channels. This indicates the vertical dimension of the flow region disturbed by the presence of the surface rough elements. These figures also show that the minimum pressure zones occur at the top tail region and the maximum pressure zones happen at the top front side of the rough elements, and the acceleration takes place at the top surface and around the top corners of the rough element, resulting in flow recirculation between the roughness elements.

In all the results, the calculated non-dimensional pressure gra-

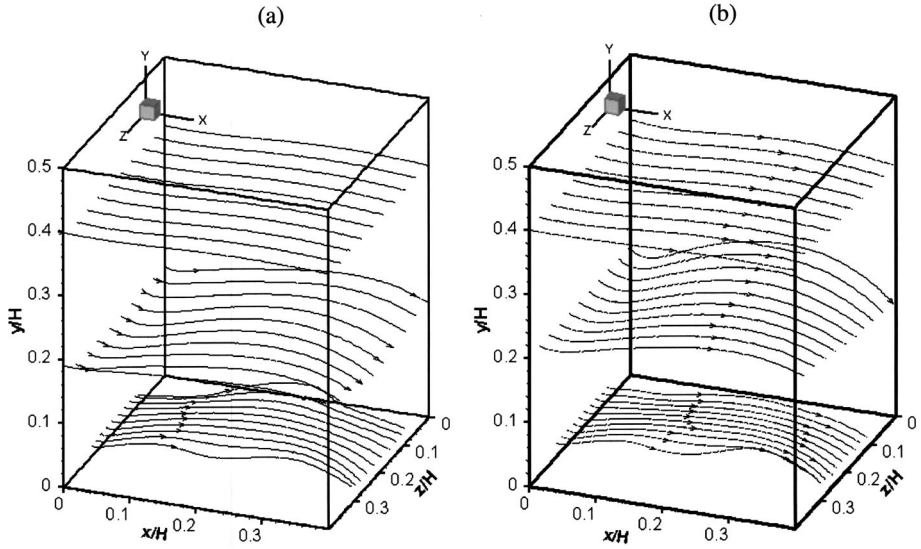

Fig. 6 The three-dimensional streamlines of (*a*) the symmetrical arrangement with $a=1.0\ \mu$m, $b=2.0\ \mu$m, $H=5\ \mu$m, $h=0.5\ \mu$m, and (*b*) the asymmetrical arrangement with $a=1.0\ \mu$m, $b=2.0\ \mu$m, $H=5\ \mu$m, $h=0.5\ \mu$m

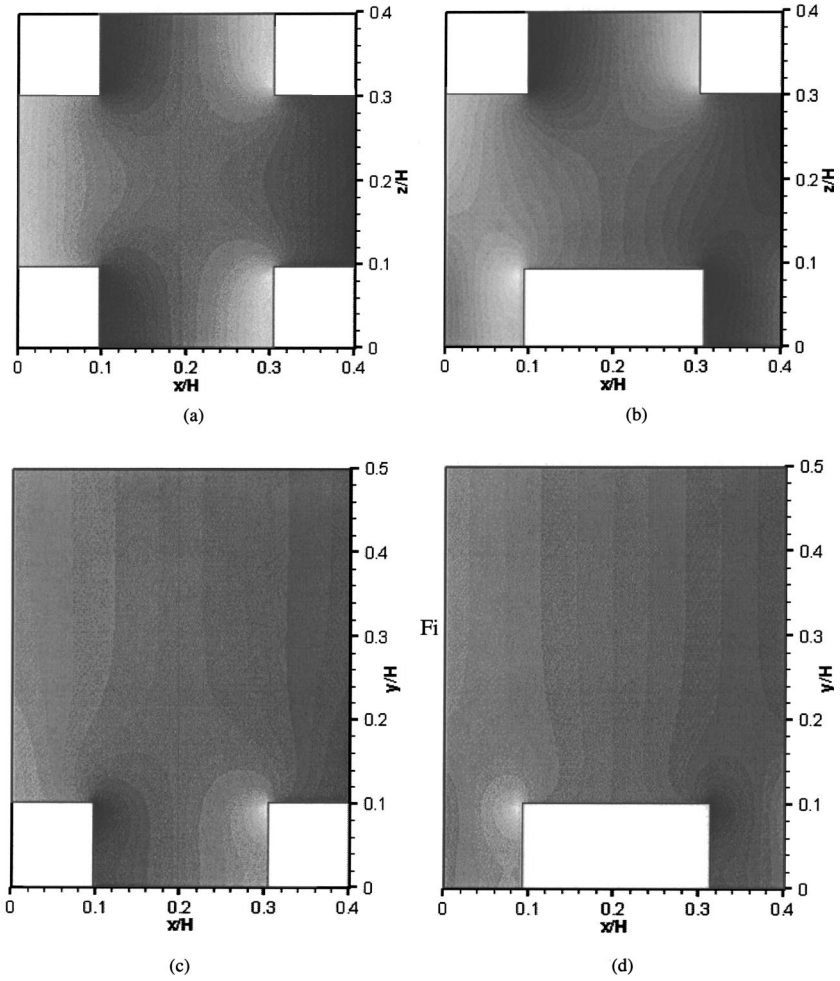

Fig. 7 The pressure fields: (*a*) the top view of the symmetrical arrangement, plane $Y=0.045$; (*b*) the top view of the asymmetrical arrangement, plane $Y=0.045$; (*c*) the side view of the symmetrical arrangement, plane $Z=0$; and (*d*) the side view of the asymmetrical arrangement, plane $Z=0$. All figures have the same parameters set as $a=1.0\ \mu$m, $b=2.0\ \mu$m, $H=5\ \mu$m, $h=0.5\ \mu$m.

dient $\Delta P/\Delta X$ is essentially a constant in the range of Re $=0.001\sim10$. This is because a fully developed laminar flow was considered, and the entrance effect was ignored. For these low Reynolds number flows, the diffusion terms in Eq. (2) are the dominant terms to determine the non-dimensional pressure field even under the roughness disturbances.

3.2 Influence of the Roughness Element Height. The influence of the rough element height for the two types of arrangements is shown in Fig. 8, where the other parameters were chosen as $H=5\ \mu$m, $a=1\ \mu$m, and $b=2\ \mu$m. From Fig. 8, one sees that the existence of the roughness greatly increases the pressure drop in comparison with that of the smooth channel. As the roughness height increases, the pressure gradient increases significantly. This may be understood as that the extent of the stagnant liquid increases proportionally to the increase of the roughness height. Comparing the results of the symmetric and asymmetric arrangements, we see that the flow resistance in the asymmetrical case is higher than that in the symmetrical case, and as the roughness height increases the difference between these two cases becomes larger.

3.3 Influence of the Roughness Element Size. The influence of the rough element size on the pressure drop per unit length is shown in Fig. 9, where the other parameters were chosen as $H=5\ \mu$m, $h=1.0\ \mu$m, and $b=2\ \mu$m. As seen from these two

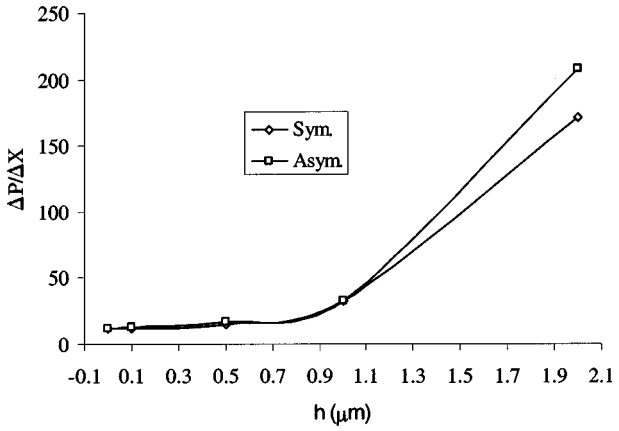

Fig. 8 Nondimensional pressure gradient versus the roughness height with $a=1.0\ \mu$m, $b=2.0\ \mu$m, and $H=5\ \mu$m

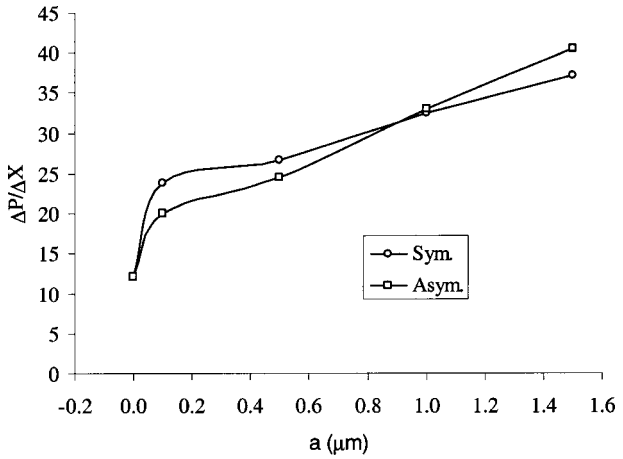

Fig. 9 Nondimensional pressure gradient versus the roughness size with $h=1.0\ \mu$m, $b=2\ \mu$m, and $H=5\ \mu$m

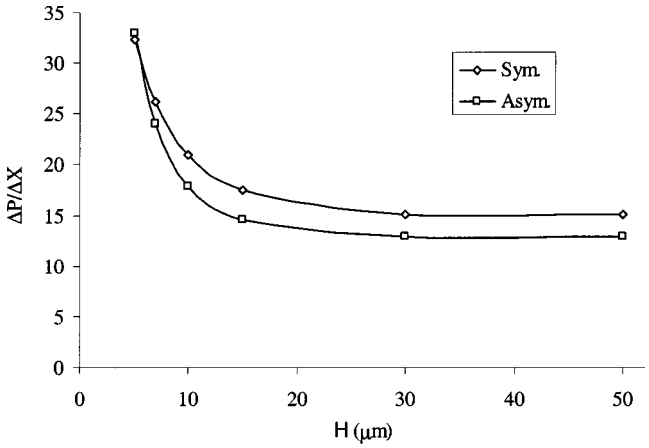

Fig. 11 Nondimensional pressure gradient versus the rough microchannel height with $h=1.0\ \mu$m, $a=1.0\ \mu$m, and $b=2.0\ \mu$m

figures, the pressure gradient increases as the rough element size increases, although the effect is not as strong as the effect of the roughness element height. These results can be easily understood: As the roughness size increases, the distortion of the streamlines induced by the roughness elements is larger, producing a greater surface friction.

It should be noted that, in Fig. 9, the nondimensional pressure gradient curve sharply increases when the roughness height increases from 0 to about 0.1 μm. This reflects a qualitative change from flow through smooth channel to flow experiencing an eminent roughness blockage effect. When the roughness size is in the range of about 0.1 μm$\sim$0.5 μm, the nondimensional pressure gradient increases slowly. In this range of the roughness size, compression, and expansion is the main factor influence the pressure gradient. When the roughness size is in the range of about 0.5 μm$\sim$1.5 μm, the recirculation or stagnation in the roughness tail region is the major cause of the pressure drop. Because the flow compression-expansion and the flow recirculation (or stagnation) have different degrees of influence to the pressure drop, the slope of the $\Delta P/\Delta X \sim a$ curve is lower in the range 0.1 μm$\sim$0.5 μm than in the range 0.5 μm$\sim$1.5 μm under the specified condition.

3.4 Influence of the Roughness Spacing. Figure 10 shows the influence of the separation distance between the roughness elements on the pressure drop for the two arrangements. The constant parameters used in Fig. 10 are $H=5\ \mu$m, $h=1\ \mu$m, $a=1\ \mu$m. The pressure drop per unit length is examined under six different separation distance values. Figure 10 shows that as the separation distance between the rough elements increases, the pressure drop per unit length is decreasing rapidly. When the separation distance is beyond about 30 μm, under the specified conditions, the pressure drops of both the two arrangement cases are close to that of a smooth microchannel. This can be understood that as the roughness spacing increases, the density of the roughness elements decreases; in most time the liquid flows between the roughness elements and the streamline distortion can be recovered. Therefore, for per unit length of the flow field the pressure drop decreases.

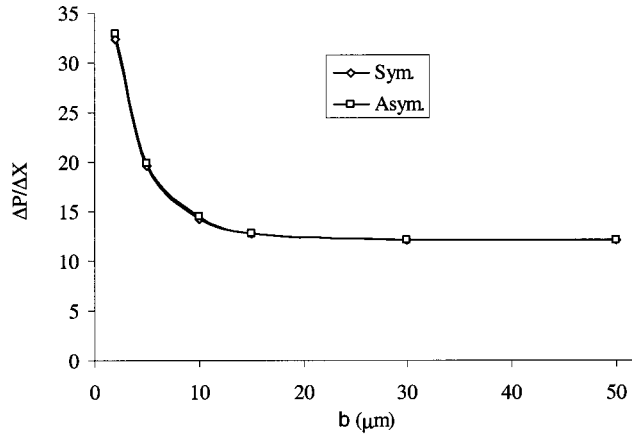

Fig. 10 Nondimensional pressure gradient versus the roughness spacing with $a=1\ \mu$m, $h=1\ \mu$m, and $H=5\ \mu$m

3.5 Influence of the Channel Height. Figure 11 shows the influence of the channel height on the pressure drop for the two roughness element arrangements, where the parameters of the roughness are: $h=1\ \mu$m, $a=1\ \mu$m, $b=2\ \mu$m. According to the definition of the nondimensional pressure gradient in this paper, the nondimensional pressure gradient in smooth channels is constant and independent of the channel height. However, for the microchannels with rough elements, the nondimensional pressure gradient depends on the channel height. Figure 11 clearly show that as the channel height increase the effect of roughness elements on the flow is reduced, and hence the pressure drop in a rough channel decreases, approaching to that of the smooth channel.

3.6 Difference Between the Symmetrical and Asymmetrical Arrangements. It is not surprising that in most figures we see the pressure drop for asymmetrical arrangement is greater than that of the symmetrical case. However, as show in Fig. 9, for the same roughness spacing $b=2\ \mu$m, when the roughness size is less than 1.0 μm, the pressure drop of the symmetrical case is greater than that of the asymmetrical case. When the roughness size is greater than 1.0 μm, the situation changes to its normal state. The reason is that when the roughness size is smaller than a certain value the effect of expansions and compressions does not act as the most important factor upon pressure drop under the same Reynolds number, and the pressure drop is mainly determined by the obstructions of the roughness elements. For one period of flow, there are only three roughness elements in the asymmetrical case, so that the obstruction to the flow is less than that in the symmetrical case, which has four roughness elements in one period. While for bigger roughness sizes, the effect of expansions and compressions acts as the most important factor under a certain Reynolds number. For the asymmetrical arrangement, the periodical expansion and compression is more sudden than that of the symmetrical case, and hence create more kinetic energy losses.

3.7 Relative Channel Height Reduction. In comparison with the flow in a smooth channel at given flow rate, a higher pressure drop occurs for the flow in a rough microchannel of the same channel height. Such a higher pressure drop would occur in an equivalent smooth channel of a smaller channel height. Therefore, it is more informative to express the roughness effect in terms of the relative channel height reduction. We define the relative channel height reduction as $\varepsilon = 1 - H_R/H$, where H_R is the apparent channel height calculated from Eq. (1). By using a Taylor series expansion of ε as function of the roughness size, the roughness spacing, the roughness height and rough channel height, at a point ($a_0 = 1.0\,\mu$m, $b_0 = 2\,\mu$m, $h_0 = 1.0\,\mu$m, $H_0 = 5\,\mu$m), and performing curve fitting to the simulation results, the following equations were obtained for the symmetrical and the asymmetrical arrangements of the roughness elements:

$$\varepsilon_{\text{Sym.}} = 0.1495 + 0.0772a - 0.0505b + 0.0018b^2 + 0.3088h - 0.041H + 0.0018H^2 \quad (5a)$$

$$\varepsilon_{\text{Asym.}} = 0.1992 + 0.1246a - 0.0505b + 0.0018b^2 + 0.3145h - 0.0618H + 0.002H^2. \quad (5b)$$

It should be noted that Eq. (5) is valid under the following conditions: the fluid is water, a, b, h, H are measured in microns, and $0.1\,\mu\text{m} < a < 1.5\,\mu\text{m}$, $0.1\,\mu\text{m} < h < 2.0\,\mu\text{m}$, $2\,\mu\text{m} < b < 20\,\mu\text{m}$, $5\,\mu\text{m} < H < 20\,\mu\text{m}$, $0.001 < \text{Re} < 10$. When $20\,\mu\text{m} < b < 50\,\mu\text{m}$ or $20\,\mu\text{m} < H < 50\,\mu\text{m}$, we can approximately use $b = 20\,\mu$m or $H = 20\,\mu$m to estimate the relative channel height reduction. With these expressions of the relative channel height reduction, we can use the roughness geometry parameters to estimate the relative channel height reduction, and hence the pressure drop for a given flow rate can be obtained by using the equation of classical Poiseuille flow with the calculated effective channel height.

4 Summary and Conclusions

For low Reynolds number pressure-driven flow through microchannels, the pressure drop over the microchannels is greatly increased by the existence of the three-dimensional surface roughness elements. The three-dimensional numerical simulations show the significant effects of the roughness height, size, spacing, and the microchannel height on the pressure drop per unit length. Nondimensional pressure gradient is found to be identical in the range of $0.001 < \text{Re} < 10$, however, the values depend on the geometry parameters of the rough channels. The results show that the pressure drop per unit length increases with the roughness height. The increasing protrusion of the roughness elements produces more stagnant liquid and hence the higher pressure drop per unit length. The pressure drop per unit length decreases as the channel height increases, but is still higher than the smooth channel with the same channel height. Keeping the spacing between the rough elements unchanged, the degree of the flow expansion and the flow compression grows larger when the rough elements size is increased. Therefore, the pressure drop per unit length increases as the roughness size increases. When the spacing between the rough elements increases the pressure drop per unit length decreases. This is mainly due to the decrease of the rough element density and the decrease of the flow expansion and the flow compression by enlarging the space between the rough elements.

A significant part of the pressure drop is used to provide a driving force for flow over the rough elements in the microchannel. The roughness elements act on the flow in at least two ways: causing the expansions and compressions of the streamlines, and obstructing the flow directly. For different roughness size, the relative contributions of the two effects are different. When roughness size is smaller than a certain value, the obstruction plays a bigger role, so that the symmetrical arrangement produces more energy losses due to more obstruction in one period. When roughness size is larger than a certain value, the periodical expansions and compressions become a major factor, so that the asymmetrical arrangement produces more energy losses due to more sudden expansions and compressions. These effects are summarized by a relationship between the relative channel height reduction and the characteristic parameters of the roughness elements and the channel height.

Acknowledgment

The authors are thankful for the financial support of the Institute for Polymer Research Dresden to Y. Hu and the support of a Research Grant of the Natural Sciences and Engineering Research Council of Canada to D. Li.

Nomenclature

H = the channel's height (m)
P = nondimensional pressure, $P = p/(\mu U_0/H)$
Re = Reynolds number, $\text{Re} = \rho U_0 H/\mu$
U,V,W = nondimensional velocity, $U = u/U_0$, $V = v/U_0$, $W = w/U_0$
U_0 = average velocity at the minimum cross section of the channel (m/s)
X,Y,Z = nondimensional coordinate variables, $X = x/H$, $Y = y/H$, $Z = z/H$
a = the size of the rough element's square-shaped base (m)
b = the distance between the center of the rough elements in x-direction (m)
c = the distance between the center of the rough elements in z-direction (m)
h = the rough element height (m)
p = pressure (Pa)
u,v,w = velocity components in x, y and z-direction, respectively (m/s)
x,y,z = coordinate variables (m)

Greek Symbols

ρ = density (kg/m^3)
μ = dynamic viscosity (kg/ms)
ν = kinematic viscosity (m^2/s)
ε = relative channel height reduction

References

[1] Mala, G. M., and Li, D., 1999, "Flow Characteristics of Water in Microtubes," Int. J. Heat Fluid Flow, **20**, pp. 142–148.
[2] Qu, W., Mala, G. M., and Li, D., 2000, "Pressure-Driven Water Flows in Trapezoidal Silicon Microchannels," Int. J. Heat Mass Transfer, **43**, pp. 353–364.
[3] Qu, W., Mala, G. M., and Li, D., 2000, "Heat Transfer for Water Flow in Trapezoidal Silicon Microchannels," Int. J. Heat Mass Transfer, **43**, pp. 3925–3936.
[4] Incropera, F. P., and DeWitt, D. P., 1996, *Introduction to Heat Transfer*, John Wiley and Sons, New York.
[5] Arulanandam, S., and Li, D., 2000, "Liquid Transport in Rectangular Microchannels by Electroosmotic Pumping," Colloids Surf., A, **161**, pp. 89–102.
[6] Yang, C., and Li, D., 1998, "Analysis of Electrokinetic Effects on the Liquid Flow in Rectangular Microchannels," Colloids Surf., A, **143**, pp. 339–353.
[7] Currie, I. G., 1993, *Fundamental Mechanics of Fluids*, McGraw-Hill, New York.

[8] Sparrow, E. M., Niethammer, J. E., and Chaboki, A., 1982, ''Heat Transfer and Pressure Drop Characteristics of Arrays of Rectangular Modules Encountered in Electronic Equipment,'' Int. J. Heat Mass Transfer, **25**, pp. 961–973.
[9] Jubran, B. A., Swiety, S. A., and Hamdan, M. A., 1996, ''Convective Heat Transfer and Pressure Drop Characteristics of Various Array Configurations to Simulate the Cooling of Electronic Modules,'' Int. J. Heat Mass Transfer, **39**, pp. 3519–3529.
[10] Patankar, S. V., Liu, C. H., and Sparrow, E. M., 1977, ''Fully Developed Flow and Heat Transfer in Ducts Having Streamwise-Periodic Variations of Cross-Sectional Area,'' ASME J. Heat Transfer, **99**, pp. 180–186.
[11] Amano, R. S., 1985, ''A Numerical Study of Laminar and Turbulent Heat Transfer in a Periodically Corrugated Wall Channel,'' ASME J. Heat Transfer, **107**, pp. 564–569.
[12] Patankar, S. V., 1980, *Numerical Heat Transfer and Fluid Flow*, Hemisphere, New York.
[13] Chou, H.-P., Spence, C., Schere, A., and Quake, S., 1999, ''A Microfabricated Device for Sizing and Sorting DNA Molecules,'' Proc. Natl. Acad. Sci. U.S.A., **96**, pp. 11–13.

Frictional Performance of U-Type Wavy Tubes

Ing Youn Chen

Yee Kang Lai

Mechanical Engineering Department,
National Yunlin University of Science and Technology,
Yunlin, Taiwan 640

Chi-Chuan Wang

Energy & Resources Laboratories,
Industrial Technology Research Institute,
Hsinchu, Taiwan 310

Measurements of the pressure drops for water flowing in small diameter tubes having U-type wavy configuration are presented. The inner diameters of the test copper tubes (D) are 3.43, 5.07, and 8.29 mm, whereas the curvature ratios (2R/D) and spacer length (L/D) span from 3.75 to 7.87 and 1.93 to 7.0, respectively. The test range of the Reynolds number for water is about 200<Re<18000. The measured pressure loss in U-type wavy tube includes the loss in U-bends and the loss caused by the distorted flow in the downstream straight tube. Thus, an equivalent friction factor, f_B, is then defined. For both laminar and turbulent flow the bend friction factor increases with the decrease of dimensionless curvature ratio and spacer length. The test results indicate that the recent reported correlations by Popiel and Wojkowiak (2000) and Wojkowiak (2000) do not accurately predict the data. A simple friction factor equation is developed based on the experimental data with characterizing parameters like curvature ratio and spacer length, new Dean number, and the Reynolds number. A good agreement with a mean standard deviation of 5.6% is observed between the proposed correlation and the existing data, which includes the test results of this study and those from Popiel and Wojtkowiak (2000). [DOI: 10.1115/1.1601259]

Introduction

Flow in curved channels has been utilized in many heat exchangers and flow transmitting devices. The curved channels can be in the forms of helical or spiral coils, and U-type return bends. In curved pipes, the centrifugal force drives the more rapid fluid toward the concave part of the curve channel while the fluid in the convex part is slowing down causing a secondary flow at right angle in the main flow, [1–3]. The magnitude of the secondary flow increases with a decreasing bend radius and increasing fluid velocity. The distorted flow condition by the induced secondary flow persists at a downstream distance of more than 50*D* for single-phase flow, [4], and of more than 70*D* for two-phase flow, [3]. As expected, the curved channel will cause a much higher friction loss than that of the corresponding straight tube for laminar flow, [5], and turbulent flow, [4]. Recently, Cho and Tae [6,7] investigated the effects of oil on the condensation and evaporation heat transfer coefficients for R-22 and R-407C inside a microfin tube with a U-bend. Their results indicate that the local heat transfer coefficients of R-22 and R-407C for the condensation and evaporation at the downstream straight sections of 48*D* and 30*D* are larger than those of upstream straight sections by 33% and 21%, respectively, because of the disturbance, caused by the secondary flow in the U-bend, carried into the downstream straight section after the U-bend. In this regard, the increase of the friction resistance associated with the induced turbulence should be carefully considered in the design.

For typical HVAC&R application (heating, ventilation, air conditioning, and refrigeration), exploitation of the consecutive U-type wavy tubes (hairpins) is very common. The higher pressure drop in the consecutive U-type wavy tubes may significantly affect the refrigerant distribution in the refrigerant circuitry. As a consequence, the frictional performance of a U-type wavy tube with consecutive 180° return bends is very important for the design of air-cooled heat exchanger. There are some investigations relevant to this subject, but most of the previous studies are associated with helical coils and a single 180° return bend. For single-phase flow inside U-type undulated wavy pipes, the investigations by Popiel and Wojtkowiak [8] and Wojtkowiak and Popiel [9] are probably the most informative. Their friction factor data for single-phase flow in U-type wavy tubes (f_B) are observed to be much higher than those of straight tube (f_S). For turbulent flow the ratio of f_B/f_S is about 2 to 2.5, but for laminar flow the ratio can be as high as 6 at curvature ratio $2R/D=6.62$.

Recently, in the application of HVAC&R, small-diameter tubes have become very popular, [10], because of lesser refrigerant inventory, better air-side heat transfer performance, and smaller air-side drag are likely. The U-type wavy tubes in air-cooled heat exchangers usually have a spacer length (L) between two consecutive 180° return bends. Therefore, the purpose of this study is to investigate the influences of the ratio of curvature radius ($2R/D$) and the ratio of the spacer length to the tube diameter (L/D) on the single-phase flow frictional performance of consecutive U-type wavy tubes having small diameter tubes.

Experimental Method

Test Facility. A schematic of the test rig and the details of the test section are seen in Fig. 1. The water flow loop consists of a variable speed gear pump, flow meters, test section, pressure transducers, and a water tank reservoir to collect water flow. The mixer at the upstream of the test section is designed to provide better uniformity of the flow stream. The inlet water temperature was of 25°C. For the measurement of water flow, three very accurate magnetic flow meters (YOKOGAWA AE110MG) with different applicable ranges are installed at the downstream of the gear pump. Their accuracy is ±0.2% of the test span. The test range of the Reynolds number was about 200<Re<18,000. The test tubes were made of copper having inner diameters (D) of 3.43, 5.07, and 8.29 mm. A total of nine tubes are used for testing. Further relevant geometries like radius of the return bend (R), curvature ratio ($2R/D$), and spacer length (L) are tabulated in Table 1. Each test section has nine consecutive U-bends. During the manufacturing of the return bend, special care was taken to prevent significant distortion. Only those return bends having a distortion ratio, evaluated as $|D_{\max,o}-D_{\min,o}|/0.5(D_{\max,o}+D_{\min,o})\times 100\%$, less than 7% were used for the experiments. According to the study of Geary [11], the 7% distortion is a well accepted value for typical HVAC return bend. As seen in Fig. 1, a straight entrance length of 100*D* is located at the upper stream of the straight test section to have a fully developed flow condition for measurement. A differential pressure transducer is used to mea-

Contributed by the Fluids Engineering Division for publication in the JOURNAL OF FLUIDS ENGINEERING. Manuscript received by the Fluids Engineering Division Apr. 2, 2002; revised manuscript received Apr. 30, 2003. Associate Editor: M. W. Plesniak.

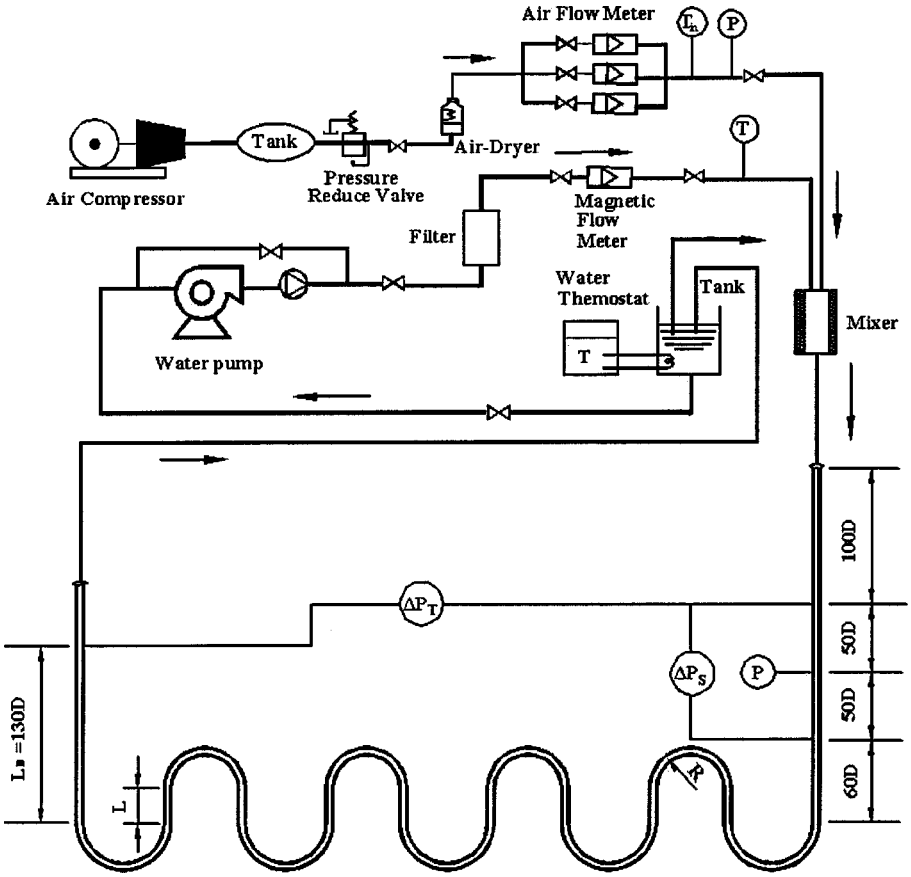

Fig. 1 Schematic of the test rig and the test section of wavy tube

sure the pressure drop (ΔP_S) across the upstream straight test section ($L_S=100D$) to serve as a reference for the comparison of the pressure gradient between the bend and the straight tube. Also, a straight length of $130D$ is directly connected to the bend outlet for the flow recovery. The other differential pressure transducer is used to measure the total pressure drop (ΔP_T), which includes the loss of the wavy section and the loss from the straight portions of the upstream ($L_U=160D$) and downstream ($L_D=130D$) straight tubes. Therefore, the total pressure loss due to the bending from the wavy tube can be calculated as: $\Delta P_B=\Delta P_T-(\Delta P_S/L_S)(L_U+L_L+L_D)$, where $L_L=8L$ is the total spacer length in the wavy tube and L is the single spacer length. Notice that the pressure drops were measured by YOKOGAWA EJ110 differential pressure transducers having an adjustable span of 1300 to 13,000 Pa. The holes of the pressure taps were drilled vertically to the test tubes with a hole diameter of 0.5 mm. Resolution of this pressure differential transducer is $\pm 0.5\%$ of the measurements.

The water temperatures were measured by resistance temperature device (Pt100Ω) having a calibrated accuracy of 0.1 K (calibrated by Hewlett-Packard quartz thermometer probe with quartz thermometer, model 18,111A and 2804A). Other relevant descriptions of the test apparatus can be found in a previous study, [10].

Data Reductions. The single-phase pressure drop of the wavy tube is calculated by subtracting the equivalent straight tube pressure drop having the length, $L_{ST}=L_U+L_L+L_D$, from the measured total pressured drop (ΔP_T). This leads to the definition of the equivalent friction factor, f_B, in the U-type section of the wavy tube. Thus,

$$f_B=\frac{\left(\Delta P_T-\dfrac{4(L_{ST})}{D}f_S\dfrac{\rho U_m^2}{2}\right)}{\dfrac{4L_C}{D}\dfrac{\rho U_m^2}{2}} \tag{1}$$

where $L_C=9\pi R$ is the total axial length of the nine U-bends, R is the radius of center line of the U-bend, U_m is the mean axial velocity in the tube, ρ is the fluid density, and the friction factor for the straight tube, f_S, is obtained from the measured data. Uncertainties in the reported value of the friction factor f are estimated by the method suggested by Moffat [12]. The range of uncertainties is from 1.3% to 6.4% with 95% confidence level. The highest uncertainties are associated with the lowest Reynolds number.

Table 1 Geometric parameters of the test sections and the test points

D (mm)		3.43±0.1			5.07±0.1			8.29±0.1	
R (mm)	6.5±0.2	10.5±0.2	13.5±0.2	10±0.2	13±0.2	17.5±0.2	20±0.2	25±0.2	30±0.2
L (mm)		24±0.5		30±0.5	24±0.5	22±0.5	18±0.5	16±0.5	24±0.5
$2R/D$	3.79	6.12	7.87	3.94	5.13	6.90	4.83	6.03	7.24
L/D		7.00		5.92	4.73	4.34	2.17	1.93	2.90
Data points	28	38	38	20	20	20	22	22	22

Notice that all the test sections have nine consecutive U-bends as shown in Fig. 1.

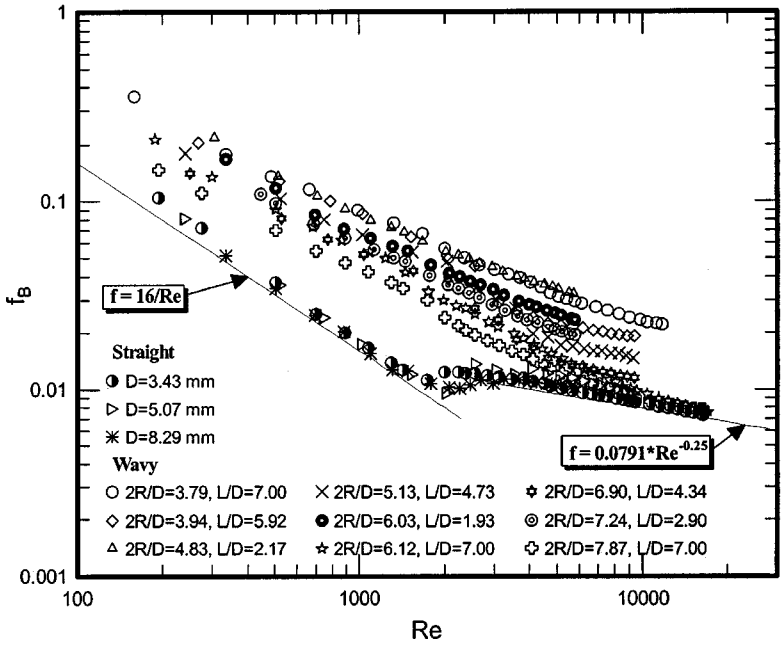

Fig. 2 Friction factor for straight tube and U-type wavy tubes

Results and Discussion

The test results of f_B and f_S are plotted in Fig. 2 presenting friction factor versus the Reynolds number. The base lines are the Fanning friction factor for laminar tube flow ($f_S = 16/\mathrm{Re}$) and the well-known Blasius equation for turbulent tube flow ($f_S = 0.0791\,\mathrm{Re}^{-0.25}$). As it is seen, the straight tube experimental data, f_S, agree favorably with the base lines. The good agreement shown for straight tube data in Fig. 2 illustrates the accuracy of the instrumentation and the experimental apparatus. The effects of curvature ratio $(2R/D)$ and dimensionless spacer length (L/D) on the data of f_B are also shown in Fig. 2. An abrupt change is seen in the slope of f_S at the interception of laminar flow and turbulent flow for a straight tube. However, the relation of f_B and Re is relatively smooth for wavy tubes in Fig. 2. The results may imply the strength of vortical motions caused by the secondary flow which may elongate and exceed the relevant transition between laminar flow and turbulent flow. Analogous results were also reported for flow in wavy tubes, [8,9], and for flow in helical tubes, [13].

The comparisons of the ratio of f_B/f_S for the nine wavy tubes are shown in Figs. 3, 4, and 5 for the tube diameters of 3.43, 5.07, and 8.29 mm, respectively. The ratio of f_B/f_S considerably increases with the decrease in curvature ratio of $2R/D$. This increase is mostly caused by the secondary flow, which increases the disturbance in flow in the curved tubes. For turbulent flow, the ratio of f_B/f_S is rising from about 3 to a value that is slightly

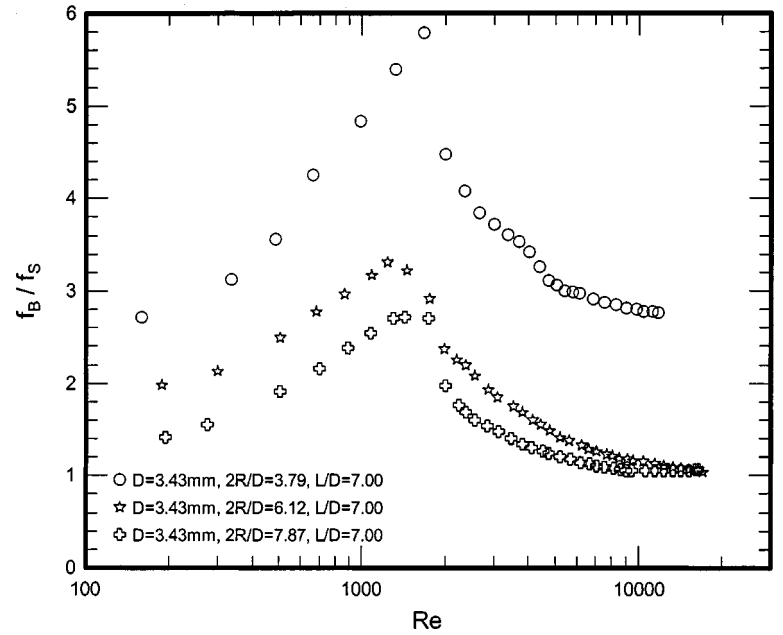

Fig. 3 The ratio of f_B/f_S for $D = 3.43$ mm

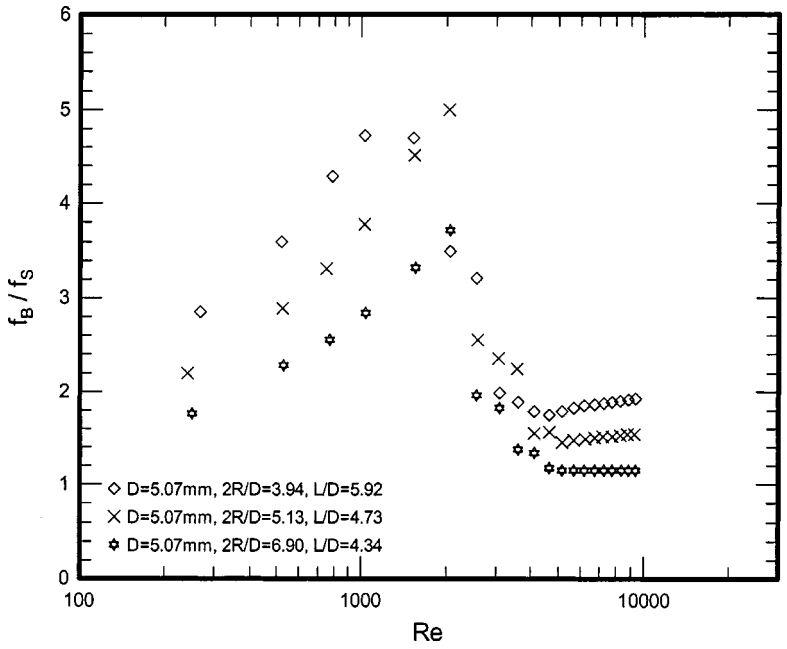

Fig. 4 The ratio of f_B/f_S for $D=5.07$ mm

greater than 1.0 at higher Re; for laminar flow the ratio of f_B/f_S is up to 5 at the measured transition region to turbulent flow in the straight tubes. As shown in Fig. 3, at values of Re>10,000, the f_B/f_S values are approximately equal one for the data of $D=3.43$ mm, $L/D=7.0$, $2R/D=6.12$ and 7.87. It shows that the f_B data are very near the line of Blasius equation. A similar result was obtained and explained by Popiel and Wojtkowiak [8] as the superimposed effects of the secondary vortex flow and the developed turbulent mixing. An explanation of this result may be attributed to the larger spacer length ($L/D=7$) for $D=3.43$ mm. A larger spacer length may relax the strength of the vortical motion of the swirled flow passing the return bend.

Popiel and Wojtkowiak [8] investigated the pressure losses in U-type undulated pipe flow with $L/D=0$. The results of the friction factor were presented for a wide range of curvature ratio ($2R/D=6.62\sim27.85$) and of Reynolds number (Re $=500\sim20000$). A Darcy friction factor equation was proposed to correlate their data by introducing a new Dean number (Dn $=\mathrm{Re}/(2R/D)$, i.e.,

$$\ln(f_D\,\mathrm{Re}/64)=a+b(\ln(\mathrm{Dn}))^2 \tag{2}$$

where $a=0.021796$, $b=0.0413356$. Figure 6 compares all the present data and the data of [8] with the predictions of Eq. (2).

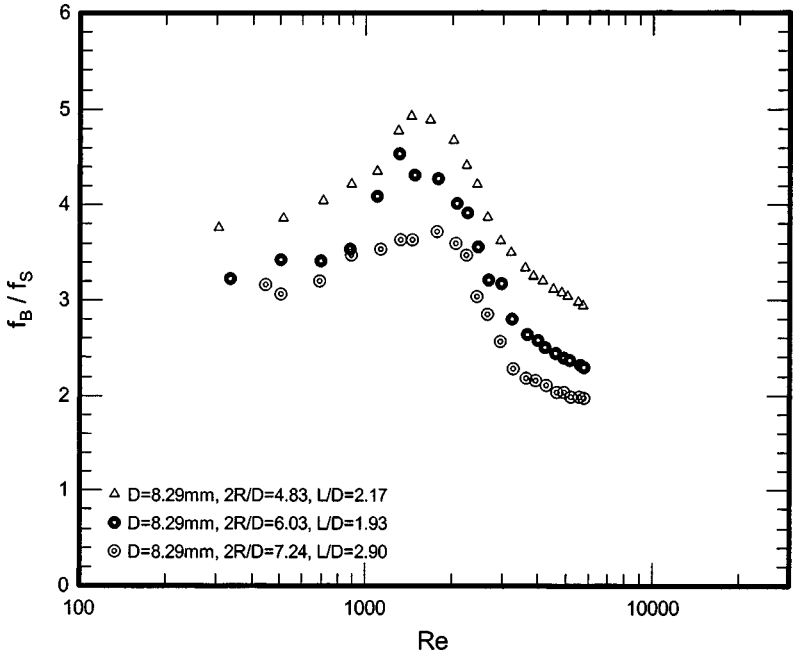

Fig. 5 The ratio of f_B/f_S for $D=8.29$ mm

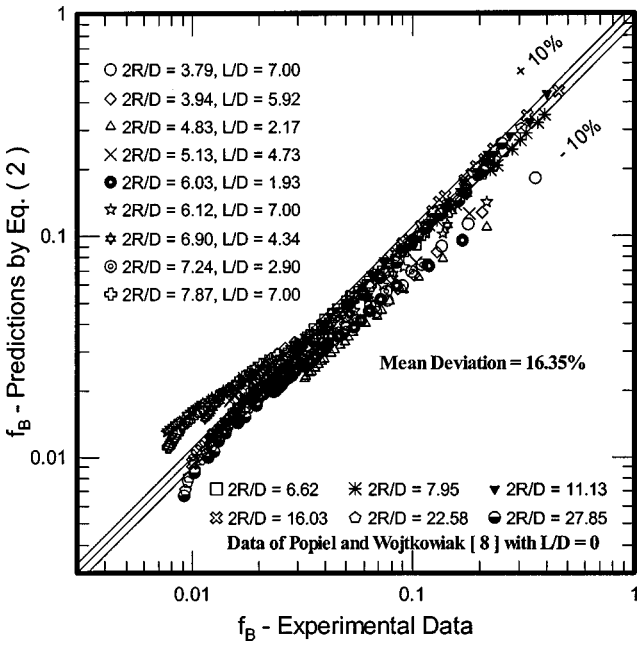

Fig. 6 Comparison of the experimental data and the predictions by Popiel and Wojtkowiak's correlation, [8]

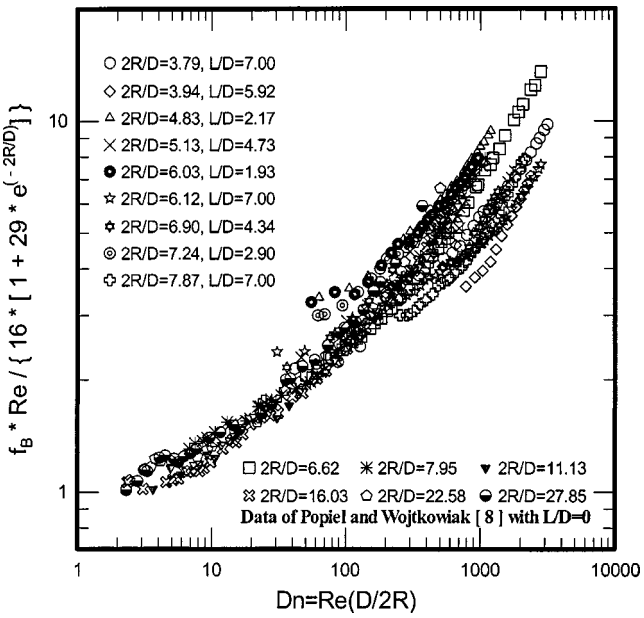

Fig. 8 Modified friction factor versus new Dean number

Their correlation gives a mean standard deviation of 5% for their data, 23.2% for the present data, and 16.35% for all the data combined. The higher deviation of the present data occurs because Eq. (2) does not include the influence of the spacer length between the consecutive U-bends for the present tested wavy tubes.

Wojtkowiak and Popiel [9] also conducted tests of measuring the pressure drop in two U-type wavy tubes having a fixed curvature ratio ($2R/D=6.62$) and two dimensionless spacer lengths ($L/D=0$ and 39.7). For $L/D=39.7$, their data clearly indicate that the equivalent friction factor approaches that of a straight tube at larger Reynolds numbers. This is expected because the strength of the swirled flow is reduced at large L/D. A Darcy friction factor correlation for adiabatic flow in U-type wavy tubes was recently corrected by Popiel [14] and is given as

$$f_D = a + b\ln(\mathrm{Dn}) + c/\mathrm{Dn} \tag{3}$$

where $a=0.121433-0.00182313(L/D)$, $b=-0.010311+0.0001936(L/D)$, $c=16.68855-0.16757(L/D)$. A comparison of the predictions by Eq. (3) against the present data, as well as the data of Wojtkowiak and Popiel [9], is shown in Fig. 7. In order to compare the f_B data obtained in the present study, the friction factor values calculated from the correlations by [8,9] were all divided by 4 as shown in Figs. 6 and 7. A very good agreement of 1.1% mean standard deviation with the data of Wojtkowiak and Popiel [9] is shown. However, the mean standard deviation for the present data is 36%. It is obviously shown in Fig. 7 that Eq. (3)

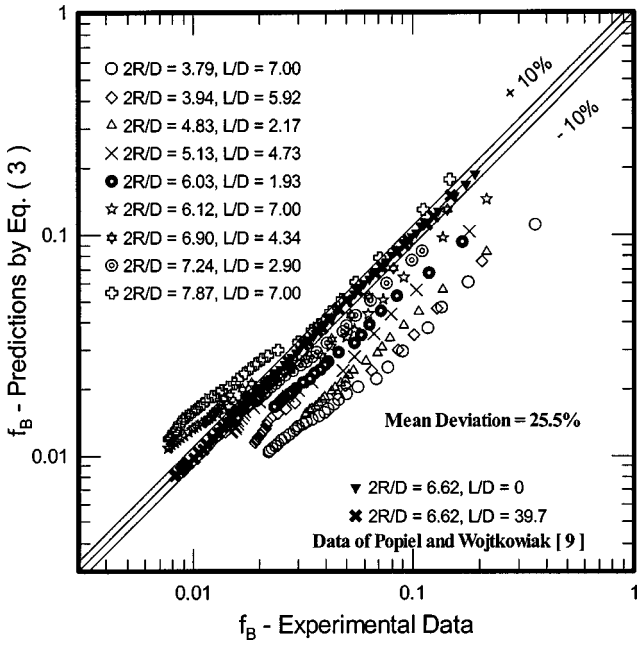

Fig. 7 Comparison of the experimental data and the predictions by Wojtkowiak and Popiel's correlation, [9]

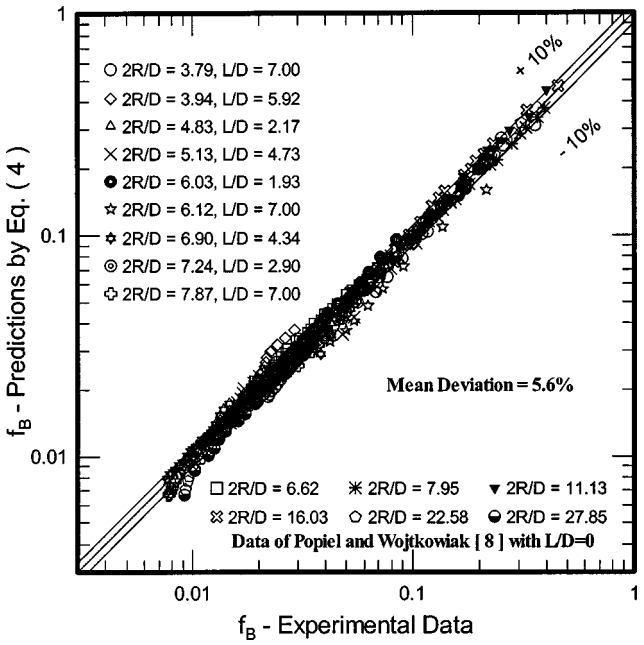

Fig. 9 Comparison between the predictions of the proposed correlation and the experimental data

underpredicts most of the present data, except the data sets of $D=3.43$ mm, $L/D=7.0$, $2R/D=6.12$ and 7.87 at higher values of Re. The deviation occurs because the definition of their Darcy friction factor for a U-type wavy tube, where $f_D=\Delta P_T/(0.5L_T\rho U_m^2/D)$, is not the same as the definition of f_B in Eq. (1). In addition, their data did not fully include the effect induced by the secondary flow to the downstream because their pressure taps were located at the distance of $5D$ before entering the first bend and at the distance about $20D$ after the last bend.

As depicted in Figs. 3–7, the Reynolds number, curvature ratio and spacer length are very significant in the frictional performance of the U-type wavy tubes. Therefore, it would be more rational to develop a correlation by introducing the dimensionless parameters of Re, $2R/D$, and L/D to reflect their influences to the friction loss. In Fig. 8, the data of the present study (for $L/D=1.93\sim7.0$) and the data of Popiel and Wojtkowiak [8] (for $L/D=0$) are presented in a form as $f_B\times(\mathrm{Re}/16)/(1+29\times e^{-2R/D})$ versus Dn. The data sets do not fall into one line perfectly, because of the effect of the dimensionless spacer length. At the fixed values of Re and $2R/D$, the friction factor decreases when L/D increases because the vortical strength of the disturbed flow in the recovery region (region after the return bend) decreases when L/D increases. Therefore, when L/D increases, the overall flow in the recovery region becomes more uniform leading to a lower friction factor in the system. A recent article by Chen et al. [15], who performed a flow visualization of the two-phase flow pattern of the air-water across the return bend, clearly identified this phenomenon.

For correlating all the data in Fig. 8, the relevant influence of dimensionless parameters ($2R/D$, Re, L/D, Dn) and their interactions are examined. A selection of the appropriate form is carried out based on the minimum mean deviation criterion. The proposed correlation is based on the correlation form by Popiel and Wojtkowiak [8] with an appropriate correction form to include the influence of spacer length, i.e.,

$$f_B=\frac{16}{\mathrm{Re}}[1+29e^{(-2R/D)}]e^{\{0.07+0.04\ln(\mathrm{Dn})^2+(L/D)[0.36-0.035\ln(\mathrm{Re})^{0.9}-0.0145(L/D)^{2.5}+0.005(L/D)^3]\}}. \quad (4)$$

Figure 9 represents the comparison between the predictions of Eq. (4) with the present data and the data of Popiel and Wojtkowiak [8]. Generally, this proposed correlation gives a very good agreement with all the experimental data with a mean standard deviation of 5.6%. A slight underprediction of the correlation is seen for data possessing a larger value of $2R/D$ and a higher Reynolds number because the increase of $2R/D$ makes the influence of the return bend less pronounced. The applicable range of the proposed correlation is as follows:

Re: 300–20000.
Dn: 2–3000.
$2R/D$: 3–28.
L/D: 1.93–7.0.

Concluding Remarks

Measured pressure drops for water flow in small diameter U-type wavy tubes are presented. Results of this study are summarized as

1. the nearly smooth transition of the friction factor f_B curves from laminar to turbulent region indicates that the effect of secondary flow at this transition is much greater than the developing turbulent flow in straight tubes.
2. the ratio of f_B/f_S considerably increases with the decrease in curvature ratio of $2R/D$ and the decrease of the spacer length L/D.
3. the correlation of Wojtkowiak and Popiel [9] can not accurately predict the present data because the influence of the spacer length is not fully shown.
4. an empirical friction factor correlation with the parameters of curvature ratio and spacer length, new Dean number and Reynolds number is proposed that gives a good agreement with a mean standard deviation of 5.6% with the present data, as well as the test results of Popiel and Wojtkowiak [8].

Acknowledgment

The finical supports by National Science Council (NSC 90-2212-E-224-006) and Energy Commission of the Ministry of Economic Affairs of Taiwan are gratefully acknowledged. The valid information provided by Prof. Popiel, C. O. is also gratefully appreciated by the authors.

Nomenclature

D = internal diameter of tube (m)
Dn = new Dean number (Re/($2R/D$))
f = Fanning friction factor
f_D = Darcy friction factor
L = spacer length (m)
L_C = total axial length of the nine U-bends, $L_C=9\pi R$ (m)
L_D = length of the downstream straight section of the tested wavy tube, $L_D=130D$ (m)
L_L = total spacer length (m)
L_S = straight tube length in the upstream for pressure drop measurement, $L_S=100D$ (m)
L_{ST} = total straight tube length in the test section (m)
L_T = total axial length of the tested wavy tube (m)
L_U = length of the upstream straight section of the tested wavy tube, $L_U=160D$ (m)
ΔP_S = pressure drop across the test straight tube section (Pa)
ΔP_T = total pressure drop across the test wavy tube section (Pa)
R = radius of center line of bend (m)
Re = Reynolds number ($\rho U_m D/\mu$)
U_m = mean axial velocity (m/s)

Greek Letters

ρ = density (kg/m^3)
μ = viscosity (Ns/m^2)

Subscripts

B = U-bend
D = downstream
S = straight tube
U = upstream

References

[1] Dean, W. R., 1927, "Note on the Motion of Fluid in a Curved Pipe," Philos. Mag., **4**, pp. 208–695.
[2] Barua, S. N., 1963, "On Secondary Flow in Stationary Curved Pipes," Q. J. Mech. Appl. Math., **16**, pp. 61–70.
[3] Cheng, K. C., and Yuen, F. P., 1987, "Flow Visualization Studies on Secondary Flow Patterns in Straight Tubes Downstream of a 180-deg Bend and in Isothermally Heated Horizontal Tubes," ASME J. Heat Transfer, **109**, pp. 49–61.
[4] Ito, H., 1960, "Pressure Losses in Smooth Pipe Bends," ASME J. Basic Eng., **82**, pp. 131–143.

[5] Manlapaz, R. L., and Churchill, S. W., 1980, ''Fully Developed Laminar Flow in a Helical Coiled Tube of Finite Pitch,'' Chem. Commun. (Cambridge), **7**, pp. 57–58.
[6] Cho, K., and Tae, S. J., 2000, ''Evaporation Heat Transfer for R-22 and R-407 Refrigerant-Oil Mixture in a Microfin Tube With a U-Bend,'' Int. J. Refrig., **23**, pp. 219–231.
[7] Cho, K., and Tae, S. J., 2001, ''Condensation Heat Transfer for R-22 and R-407 Refrigerant-Oil Mixtures in a Microfin Tube With a U-Bend,'' Int. J. Heat Mass Transfer, **44**, pp. 2043–2051.
[8] Popiel, C. O., and Wojtkowiak, J., 2000, ''Friction Factor in U-Type Undulated Pipe,'' ASME J. Fluids Eng., **122**, pp. 260–263.
[9] Wojtkowiak, J., and Popiel, C. O., 2000, ''Effect of Cooling on Pressure Losses in U-Type Wavy Pipe Flow,'' Int. Commun. Heat Mass Transfer, **27**, pp. 169–177.
[10] Chen, I. Y., Yang, K. S., and Wang, C. C., 2001, ''Two-Phase Frictional Pressure Drop of Air-Water in Small Horizontal Tubes,'' J. Thermophys. Heat Transfer, **15**(4), pp. 409–415.
[11] Geary, D. F., 1975, ''Return Bend Pressure Drop in Refrigerating Systems,'' ASHRAE Trans., **81**(1), pp. 250–265.
[12] Moffat, R. J., 1988, ''Describing the Uncertainties in Experimental Results,'' Exp. Therm. Fluid Sci., **1**, pp. 3–17.
[13] Mishra, P., and Gupta, S. H., 1979, ''Momentum Transfer in Curved Pipes. 1. Newtonian Fluids,'' Ind. Eng. Chem. Process Des. Dev., **18**(1), pp. 130–137.
[14] Popiel, C. O., private communication with I. Y. Chen and C. C. Wang.
[15] Chen, I. Y., Yang, Y. W., and Wang, C. C., 2002, ''Influence of Horizontal Return Bend on the Two-Phase Flow Pattern in a 6.9-mm Diameter Tube,'' Can. J. Chem. Eng., **80**(3), pp. 478–484.

An Expermentally Validated Model for Two-Phase Pressure Drop in the Intermittent Flow Regime for Noncircular Microchannels

Srinivas Garimella[1]
e-mail: srinivas.garimella@me.gatech.edu

Jesse D. Killion

John W. Coleman

George W. Woodruff School
of Mechanical Engineering,
Georgia Institue of Technology,
Atlanta, GA 30332-0405

This paper reports the development of an experimentally validated model for pressure drop during intermittent flow of condensing refrigerant R134a in horizontal, noncircular microchannels. Two-phase pressure drops were measured in six noncircular channels ranging in hydraulic diameter from 0.42 mm to 0.84 mm. The tube shapes included square, rectangular, triangular, barrel-shaped, and others. For each tube under consideration, pressure drop measurements were taken over the entire range of qualities from vapor to liquid at five different refrigerant mass fluxes between 150 kg/m^{2}s and 750 kg/m^{2}s. Results from previous work by the authors were used to select the data that correspond to the intermittent flow regime; generally, these points had qualities less than 25%. The pressure drop model previously developed by the authors for circular *microchannels was used as the basis for the model presented in this paper. Using the observed slug/bubble flow pattern for these conditions, the model includes the contributions of the liquid slug, the vapor bubble, and the transitions between the bubble and slugs. A simple correlation for nondimensional unit-cell length was used to estimate the slug frequency. The model successfully predicts the experimentally measured pressure drops for the noncircular tube shapes under consideration with 90% of the predictions within ±28% of the measurements (average error 16.5%), which is shown to be much better than the predictions of other models in the literature. The effects of tube shape on condensation pressure drop are also illustrated in the paper.* [DOI: 10.1115/1.1601258]

Introduction

Heat transfer coefficients and pressure drop for condensation inside tubes are strongly dependent on the different flow patterns that are established at different regions of the condenser as the fluid undergoes a transition from vapor to liquid along the length of the tube. Accurate heat transfer and pressure drop predictions require an approach that accounts for the flow pattern. Circular and noncircular microchannel tubes are being used in a variety of applications because of the extremely high heat transfer coefficients that these geometries offer. Coleman and Garimella [1–3] demonstrated in studies of two-phase flow of air-water mixtures and refrigerant R134a through small diameter circular and noncircular geometries that flow regime transitions in such geometries are different from those observed in larger diameter circular tubes for which flow regime maps such as those of Mandhane [4] and Taitel and Dukler [5] are valid. One significant conclusion was that as the tube diameter decreases, the range of conditions that exhibit intermittent flow broadens while the stratified regime is suppressed. The differences in the flow regimes are due to the significant differences in the relative magnitudes of gravity, shear, and surface tension forces as tube diameter is reduced. Thus, extrapolation of large round tube correlations to smaller diameters and noncircular geometries could introduce substantial errors into pressure drop and heat transfer predictions.

Limited research has been conducted on addressing pressure drop and heat transfer coefficients during condensation in the hydraulic diameter range considered here. Garimella et al. [6] presented an experimentally validated model for the pressure drop in circular tubes ranging in diameter from 0.5 mm to 4.91 mm for the intermittent flow regime. In this paper, this model is further extended to several noncircular tube shapes. The relatively few other studies on two-phase flow in small diameter round tubes have primarily used isothermal air-water mixtures, [1,7–9], or boiling refrigerants, [10], and have only considered round tubes. Coleman and Garimella [2,3] studied the influence of tube miniaturization on the flow patterns during condensation of refrigerant R134a in a 4.91-mm-round tube and four square tubes with hydraulic diameters ranging from 1 mm–4 mm but did not report pressure drop or heat transfer coefficients.

In the present study, the work of Coleman and Garimella [2,3] and Garimella et al. [6] was extended to investigate pressure drop during condensation of refrigerant R134a in small diameter noncircular tubes. Two-phase pressure drops in six different noncircular (square, rectangular, triangular, and other shapes) tubes of hydraulic diameters ranging from 0.424 mm to 0.839 mm were measured by the present authors over a range of flow rates that covered each of the flow regimes described above. However, the focus of the present work is the measurement and modeling of two-phase pressure drop during condensation in the *intermittent* flow regime in these tubes.

Experimental Approach

The test facility used by Coleman and Garimella [2,3] for the R134a phase-change flow visualization studies was also used in the present study. The experimental approach used in the present study to determine the frictional pressure drop for condensing R134a flow was described in detailed by Garimella et al. [6]. A

[1]To whom correspondence should be addressed.

Contributed by the Fluids Engineering Division for publication in the JOURNAL OF FLUIDS ENGINEERING. Manuscript received by the Fluids Engineering Division April 2, 2002; revised manuscript received April 30, 2003. Associate Editor: M. W. Plesniak.

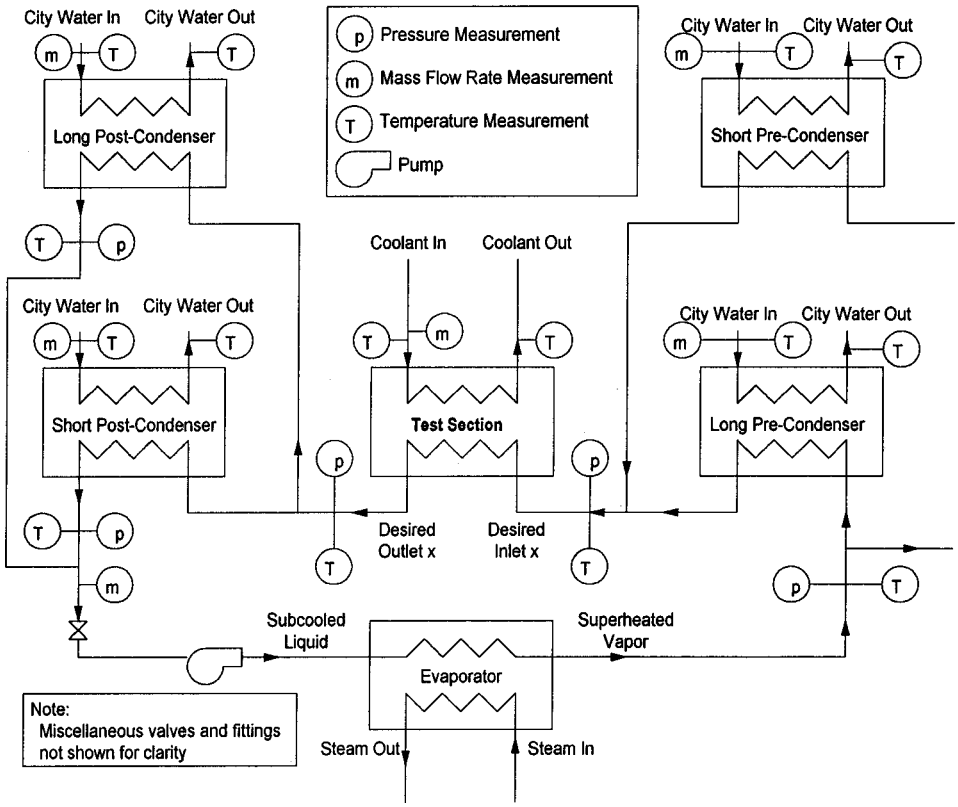

Fig. 1 Test facility schematic

detailed description of the facility and the experimental techniques used was also provided in those papers. A brief summary of the experimental approach is presented here. A schematic of the test loop is shown in Fig. 1. Subcooled liquid refrigerant flows through a coriolis mass flowmeter and is then pumped through a tube-in-tube evaporator to boil and superheat the refrigerant. The superheated state is ensured by a combination of a sight glass, temperature, and pressure measurements. The superheated vapor enters one of two pre-condensers to partially condense the vapor. The measured conditions at the superheated state, the heat duty of the pre-condenser, and the measured pressure at the pre-condenser outlet determine the thermodynamic state at the inlet to the test section. The outlet state of the test section was calculated in an analogous, but independent, manner starting from the measured subcooled state at the post-condenser outlet and using the heat duty required to completely condense and subcool the refrigerant. The measured pressure drop in the test section is characteristic of the average quality and mass flux in the test section.

The noncircular geometries tested in this study are shown in Fig. 2. The test sections were fabricated as flat tubes with multiple extruded parallel channels with the exception of the W29 tubes, which were formed by brazing a W-shaped insert inside a flattened tube. The designations for each tube are based on the shape of the extruded channel and its nominal hydraulic diameter; for instance S30 has square channels with a hydraulic diameter of 0.030 in. Similarly, B32 is ''barrel-shaped,'' N21 is ''N-shaped,'' RK15 is rectangular, T33 is triangular, and W29 has a ''W-shaped'' insert which forms roughly triangular channels. Note that two different W29 tubes were tested; these are labeled W29a and W29b, respectively. Three tubes were brazed together, as shown in Fig. 3, with refrigerant flowing through the center tube, and coolant flowing in counterflow through the top and bottom tubes. It should be noted that while water was used as the coolant for the pre- and post-condensers, air was used as the coolant in the test section. The low thermal capacity and heat transfer coefficients of air maintained low condensation rates and small changes in quality in the test section, which in turn enabled the measurement of the pressure drop variation as a function of quality with high resolution. This small quality change across the test section also minimized the likelihood of flow regime transitions within the test section for any data point. For all test sections, the outer tubes carrying the coolant had 16 rectangular channels of 0.986-mm hydraulic diameter. Using multiple parallel channels ensured that the refrigerant flow rates used were large enough to be adequately controlled and measured, with accurate heat balances around the test loop. The accuracy of the instrumentation and the resulting uncertainty in the test results were described by Garimella et al. [6]. For each of the test sections investigated in this study, single-phase tests were first conducted to calculate the single-phase fric-

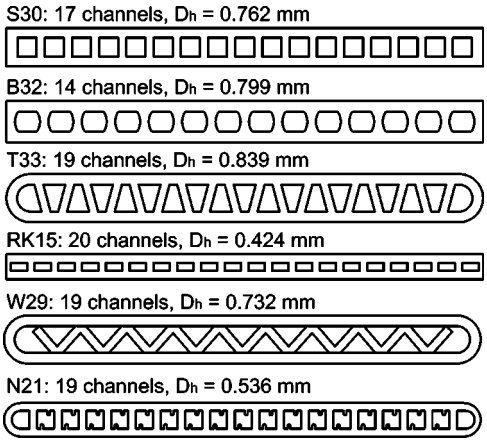

Fig. 2 Noncircular tubes investigated in the present study

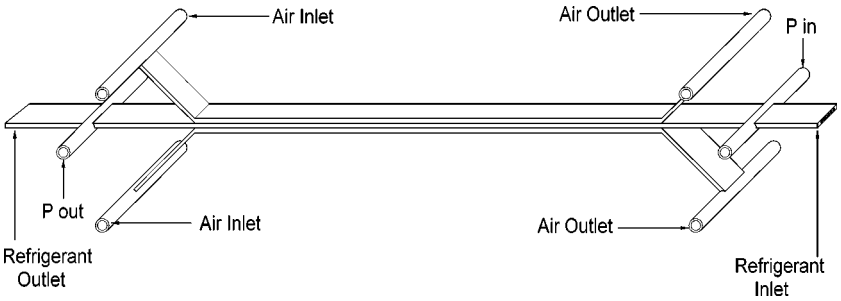

Fig. 3 Test section schematic

tion factors; the details of this procedure are given in [6]. Both single-phase liquid and single-phase vapor data were taken to span a wide range of conditions in the laminar, transition, and turbulent flow regimes. Contraction and expansion losses at the inlet and outlet were subtracted from the total measured pressure drop using the appropriate loss coefficients. The residual frictional component of the pressure drop was compared with the values predicted by the Churchill [11] correlation. The roughness values needed to match the Churchill [11] correlation values were within the range of roughnesses for such tubes, which validates the approach used in this study.

Data Analysis

Quality and Pressure Drop Calculation. The method of determining the average quality within the test section was described in [6]. Representative uncertainties for the range of mass flux and qualities studied are as follows:

$G = 150\ \text{kg/m}^2\text{-s}$:

$x_{avg} = 0.13 \pm 0.032 \quad x_{avg} = 0.50 \pm 0.027 \quad x_{avg} = 0.91 \pm 0.021$

$G = 450\ \text{kg/m}^2\text{-s}$:

$x_{avg} = 0.12 \pm 0.045 \quad x_{avg} = 0.48 \pm 0.014 \quad x_{avg} = 0.88 \pm 0.026$

$G = 750\ \text{kg/m}^2\text{-s}$:

$x_{avg} = 0.11 \pm 0.039 \quad x_{avg} = 0.51 \pm 0.022 \quad x_{avg} = 0.74 \pm 0.035$

The average saturation pressure for all the tests was 1396 kPa (202.5 psi) which corresponded to a saturation temperature of 52.3°C (126.1°C); the saturation temperature was within ±3°C of this for all the data points. For each data point, the measured pressure drop data can be represented by

$$\Delta P_{\text{measured}} = \Delta P_{\text{frictional}} + \Delta P_{\text{expansion+contraction}} + \Delta P_{\text{deceleration}} \quad (1)$$

where the expansion and contraction losses are due to the headers at both ends of the test section, and the pressure change due to deceleration is a result of the changing vapor fraction as condensation takes place. The portion of the total pressure drop (change) attributable to deceleration/acceleration of the fluid was estimated from void fraction and momentum change analyses; contraction/expansion losses at the inlet and outlet of the test section were estimated using two-phase ''minor loss'' models available in the literature. This process is described in detail by Garimella et al. [6]. These estimates were validated using pressure drop measurements on a ''near-zero'' length test section and tests conducted with and without condensation in the test section as described by [6]. Excellent agreement was obtained between these data and the models.

Flow Regime Determination. Experiments on the noncircular tubes under consideration were conducted over a nominal quality range of 5% to 95% for each of the mass fluxes of interest. However, the focus of the present study is the intermittent flow regime; therefore, only data points belonging to this regime were included for this pressure drop model. The transition criteria developed by Coleman and Garimella [3] from flow visualization studies and further described by Garimella et al. [6] were used to identify the data points with conditions that would lead to intermittent flow patterns. Intermittent flow occurs at low vapor qualities, with this flow regime persisting at higher qualities as the mass flux decreases, [3,6]. A total of 96 pressure drop data points from the six noncircular tubes tested were identified as belonging to the intermittent regime for model validation using these criteria. It should be noted that experimental observations of the flow patterns, which form the basis for these transition criteria, were made on circular, square, and rectangular channels. In the absence of other valid transition criteria for phase-change flow in small hydraulic diameter noncircular channels, these criteria were also assumed to apply for the different shapes of the tubes considered here, at equivalent hydraulic diameters.

Model Development. A model that predicts the pressure drop of two-phase flow in the intermittent flow regime through circular tubes from 0.5 to 4.91-mm diameter was presented in Garimella et al. [6]. The model was developed based on the flow patterns observed in these tubes when condensing R134a experienced intermittent (slug/bubble) flow; photographs of the plug/slug flow were previously presented in Garimella et al. [6]. These showed that solitary bubbles travel as long, nearly cylindrical shapes between slugs of liquid with virtually no vapor entrainment, especially in the 1-mm tube. Figure 4 shows a schematic of the assumed flow pattern which was also proposed by Suo and Griffith [7] and Fukano et al. [9]. Essentially, a long, cylindrical bubble of vapor with a uniform annular film of liquid surrounding it is assumed. The literature suggests that the cylindrical bubbles flow approximately 20% faster than the liquid slugs which bound it on either end, [7,9]; the annular film flows very slowly compared to both the bubble and the slug. Thus liquid is continually shed into

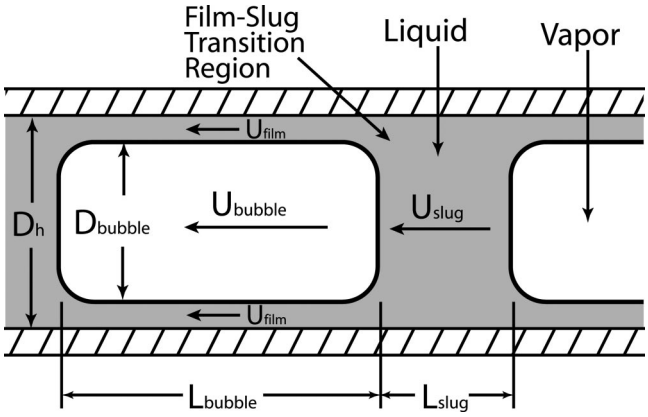

Fig. 4 Cross section of assumed flow pattern for model unit cell

the film from the posterior of the slug and picked up from the film at the anterior of the slug. The liquid slugs are assumed to contain no entrained vapor, and the bubbles are assumed to be uniform and constant throughout the test section. The total pressure drop due to this flow mechanism is the sum of the frictional pressure drop in the slug and film/bubble regions and the losses associated with the flow between the film and the slug.

The equations for pressure drop in the slug and film/bubble regions were presented in the previous paper, [6], and remain the same for the case of noncircular tubes also. To address the noncircular shapes, the concept of hydraulic diameter, $D_h = 4A/P$, is employed. For noncircular tubes with intermittent flow, this analogy is not ideal because the bubble is likely to deviate from a circular shape, and the film may not be uniform in thickness. Nevertheless, similar challenges of nonuniform thickness, shear stress, and velocity profiles exist in single-phase flow where the hydraulic diameter concept has proven to be very effective. Using the hydraulic diameter allowed for uniformity and consistency between the models for circular and noncircular tubes. Enhancements were made to the model to improve its simplicity and ease of solution, without significantly affecting the results. These include the use of the Churchill equation for friction factor instead of the Blasius equation (which does not account for surface roughness and is not smooth in the transition region.) Also, a control volume analysis was used to remove the need for the slug-length correlation by Fukano et al. [9]. The model can be summarized by the following equation set, where the hydraulic diameter (or radius), local two-phase quality, temperature, pressure, and total mass flux are the required inputs:

$$j_L = \frac{(1-x)G}{\rho_L} \tag{2}$$

$$j_V = \frac{xG}{\rho_V} \tag{3}$$

$$U_{\text{slug}} = j_V + j_L \tag{4}$$

$$\text{Re}_{\text{slug}} = \frac{\rho_L U_{\text{slug}} D_h}{\mu_L} \tag{5}$$

$$\left(\frac{dP}{dx}\right)_{\text{slug}} = f(\text{Re}_{\text{slug}}, \varepsilon/D_h)\frac{\rho_L U_{\text{slug}}^2}{2D_h}. \tag{6}$$

The friction factor, f, in Eq. (6) is calculated using the more comprehensive Churchill equation, [11], which is a function of Reynolds number, Re, and relative roughness, ε/D_h, instead of the Blasius equation used by Garimella et al. [6]. The Churchill equation, [11], is as follows:

$$f(\text{Re}, \varepsilon/D_h) = 8\left\{\left(\frac{8}{\text{Re}}\right)^{12} + \left(\left[2.457\ln\left(\frac{1}{(7/\text{Re})^{0.9} + 0.27\varepsilon/D_h}\right)\right]^{16} + \left(\frac{37530}{\text{Re}}\right)^{16}\right)^{-1.5}\right\}^{(1/12)}. \tag{7}$$

From the work of Fukano et al. [9], Suo and Griffith [7], and Dukler and Hubbard [8] the ratio between bubble and slug velocity is approximately 1.2:

$$\frac{U_{\text{bubble}}}{U_{\text{slug}}} = 1.2 \tag{8}$$

$$\text{Re}_{\text{film}} = \frac{\rho_L U_{\text{film}}(D_h - D_{\text{bubble}})}{\mu_L} \tag{9}$$

$$\text{Re}_{\text{bubble}} = \frac{\rho_V (U_{\text{bubble}} - U_{\text{interface}}) D_{\text{bubble}}}{\mu_V}. \tag{10}$$

The film flow was assumed to be laminar and driven by the combination of the pressure gradient in the film/bubble region and shear at the film/bubble interface. The velocity profile for combined Couette-Poiseuille flow through an annulus where the inner surface moves at the interface velocity, $U_{\text{interface}}$, is represented by the superposition of the pressure-driven and the shear-driven components, [12,13]. By applying a shear stress balance at the interface, the following relationships can be derived:

$$U_{\text{interface}} = \frac{-(dP/dx)_{f/b}}{4\mu_L}(R_{\text{tube}}^2 - R_{\text{bubble}}^2) \tag{11}$$

$$U_{\text{film}} = U_{\text{interface}}/2. \tag{12}$$

The pressure drop per unit length in the bubble/film region is

$$\left(\frac{dP}{dx}\right)_{f/b} = f(\text{Re}_{\text{bubble}}, \varepsilon/D_h)\frac{\rho_V (U_{\text{bubble}} - U_{\text{interface}})^2}{4R_{\text{bubble}}} \tag{13}$$

where the friction factor, f, is again calculated from the Churchill equation, [11]. From continuity over a control volume (the volumetric flow rate through any plane must be constant over a small length).

$$U_{\text{slug}} = U_{\text{bubble}}\left(\frac{R_{\text{bubble}}}{R_{\text{tube}}}\right)^2 + U_{\text{film}}\left(1 - \left(\frac{R_{\text{bubble}}}{R_{\text{tube}}}\right)^2\right). \tag{14}$$

It should be noted that the use of this control volume does not violate conservation of mass in any way; however, mathematical statements of the conservation of mass do not lead as directly to useful relationships between the variables of interest here since the mass flow rate through any cross section depends on the void fraction at that location which is not a single constant for this intermittent flow pattern. The above equations can be solved simultaneously given the model inputs to generate predictions of the contribution of the slug and bubble/film regions to the total pressure drop. For the conditions of interest here, these calculations yield $0.89 \leqslant R_{\text{bubble}}/R_{\text{tube}} \leqslant 0.91$; thus the predicted bubble diameter is about 90% of the tube diameter.

Instead of using the measurements of Fukano et al. [9] to predict the relative slug length as presented in Garimella et al. [6], a control volume analysis was again employed. The difference between the two methods was remarkably small, so the control volume method is preferable for consistency. Since the bubble defines the location of the unit cell, and the bubble is assumed to carry the total volumetric flow rate of the vapor, vfr_V:

$$vfr_V = \frac{Gx}{\rho_V}\frac{\pi D_h^2}{4} = U_{\text{bubble}}\frac{\pi D_{\text{bubble}}^2}{4}\frac{L_{\text{bubble}}}{L_{\text{unit cell}}} \tag{15}$$

or

$$\frac{L_{\text{bubble}}}{L_{\text{unit cell}}} = \frac{GxD_h^2}{U_{\text{bubble}}D_{\text{bubble}}^2\rho_V} \tag{16}$$

which is simply a function of inputs to, or values calculated in, the model. By definition,

$$L_{\text{unit cell}} = L_{\text{bubble}} + L_{\text{slug}}. \tag{17}$$

Thus the pressure drop due to frictional losses is known:

$$\frac{\Delta P_{\text{friction only}}}{L} = \left[\left(\frac{dP}{dx}\right)_{f/b}\left(\frac{L_{\text{bubble}}}{L_{\text{slug}} + L_{\text{bubble}}}\right) + \left(\frac{dP}{dx}\right)_{\text{slug}}\left(1 - \frac{L_{\text{bubble}}}{L_{\text{slug}} + L_{\text{bubble}}}\right)\right]. \tag{18}$$

For the conditions tested, this value is typically about 65% of the total measured pressure drop. Figure 5 illustrates how the calculated values of $\Delta P_{\text{friction only}}$ from both the slug and bubble/film regions compare with the total measured pressure drop.

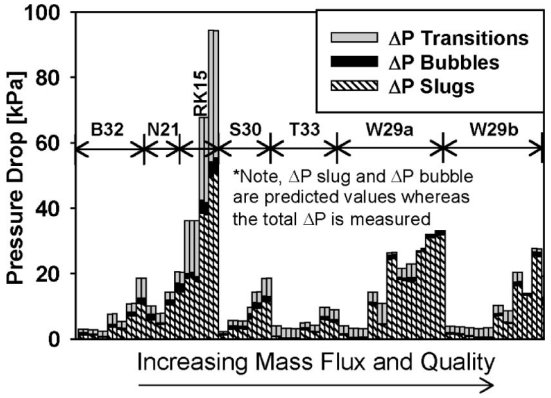

Fig. 5 Contribution of each pressure drop mechanism to total pressure drop for each test point

The remaining contribution to the total pressure drop is the loss associated with the flow of liquid between the film and the slug. This transition loss was taken from the expression proposed by Dukler and Hubbard [8]:

$$\Delta P_{\text{one transition}} = \rho_L \left(1 - \left(\frac{R_{\text{bubble}}}{R_{\text{tube}}}\right)^2\right) \frac{(U_{\text{slug}} - U_{\text{film}})(U_{\text{bubble}} - U_{\text{film}})}{2}. \quad (19)$$

The total pressure loss from these transitions can be expressed as

$$\Delta P_{\text{film/slug transitions}} = N_{UC} \cdot \Delta P_{\text{one transition}}. \quad (20)$$

The number of unit cells in a particular length of tube, N_{UC}, must be determined for the evaluation of this expression. Knowing the length or frequency of the unit cells would be sufficient to determine N_{UC} for any test section. Most of the work on predicting slug frequency in intermittent flow has been performed with larger tubes (20–50-mm diameter) using mixtures of air or another gas and water, [8,14–16]. Many of these works are reviewed by Tronconi [17]. Garimella et al. [6] proposed a correlation of the form

$$N_{UC}\left(\frac{D_h}{L_{\text{tube}}}\right) = \left(\frac{D_h}{L_{UC}}\right) = a(\text{Re}_{\text{slug}})^b = \omega \frac{D_h}{U_{\text{bubble}}} \quad (21)$$

with the following coefficients: $a = 2436.9$, $b = -0.5601$ for circular tubes with $0.5 \leq D_h \leq 4.91$ mm. ω is the slug frequency (Hz). In addition to this model, the slug frequency models developed by Tronconi [17] and Gregory and Scott [15] were also considered. The model by Tronconi [17] was developed from the measurements of several other researchers using different test configurations and frequency measurement techniques. The model itself is based on the Lockhart-Martinelli, [18], parameter, X. Since this work is based on larger tubes, the assumed flow pattern in the bubble/film region is stratified where the liquid film rests at the bottom of the tube beneath the vapor. The two phases assume complementary shapes with the interface defined by a horizontal line through the tube at a height characteristic of the flow conditions. Using the definition of the parameter, X, the dimensionless vapor height, H_V^*, and velocity, U_V^*, can be calculated from implicit relationships as shown by Taitel and Dukler [5] and Govier and Aziz [19]. From these parameters, the correlation proposed by Tronconi [17] is simply

$$\Omega = 0.61 \frac{U_V^*}{H_V^*} = \omega \frac{\rho_L D_h}{\rho_V j_V}. \quad (22)$$

The model proposed by Gregory and Scott [15] is particularly simple:

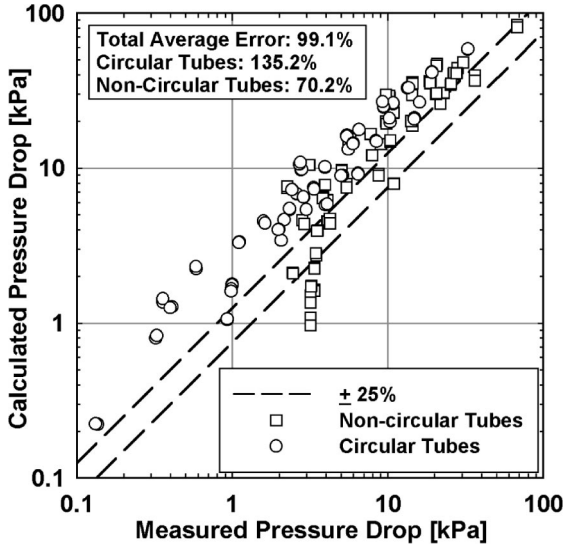

Fig. 6 Comparison of total predicted pressure drop based on frequency model of Tronconi [17] with measured data

$$\omega = 0.0226\left(\frac{j_L}{gD_h}\left[\frac{19.75}{U_{\text{slug}}} + U_{\text{slug}}\right]\right)^{1.2} \quad (23)$$

and it can also be expressed as a function of the Froude number. Figure 6 through Fig. 8 show a comparison of the predicted total pressure drop versus the measured pressure drop for all the test conditions and tubes considered here *and* the circular tubes considered by Garimella et al. [6] using the slug frequency models from Tronconi [17], Gregory and Scott [15], and Garimella et al. [6] (Eq. (21)), respectively. It should be noted that for the triangular tubes only, the frequency model of Garimella et al. [6] does not provide a good fit. These tubes seem to follow a trend that is significantly different than that of the other tube shapes including circular tubes. Therefore, for the triangular tubes (T33 and W29), the following correlation for the number of unit cells was developed:

$$N_{UC}\left(\frac{D_h}{L_{\text{tube}}}\right) = \left(\frac{D_h}{L_{UC}}\right) = a \exp(b\ \text{Re}_{\text{slug}}) = \omega \frac{D_h}{U_{\text{bubble}}} \quad (24)$$

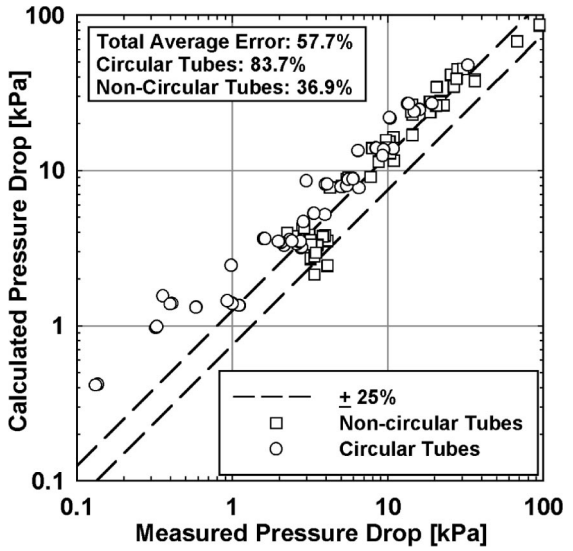

Fig. 7 Comparison of total predicted pressure drop based on frequency model of Gregory and Scott [15] with measured data

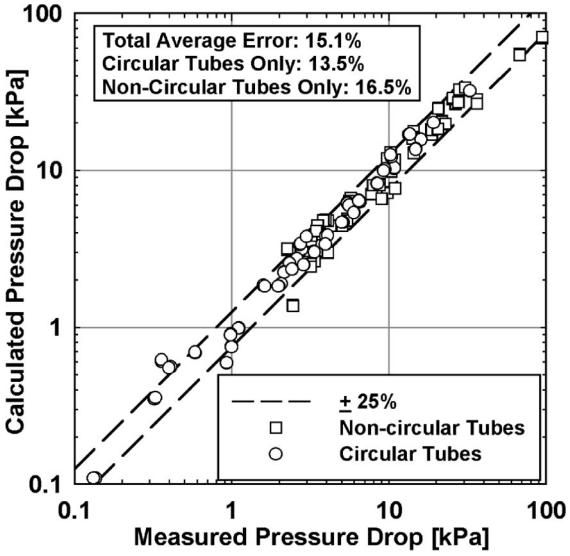

Fig. 8 Comparison of total predicted pressure drop based on frequency model of Garimella et al. [6], Eq. (21), and Eq. (24) with measured data

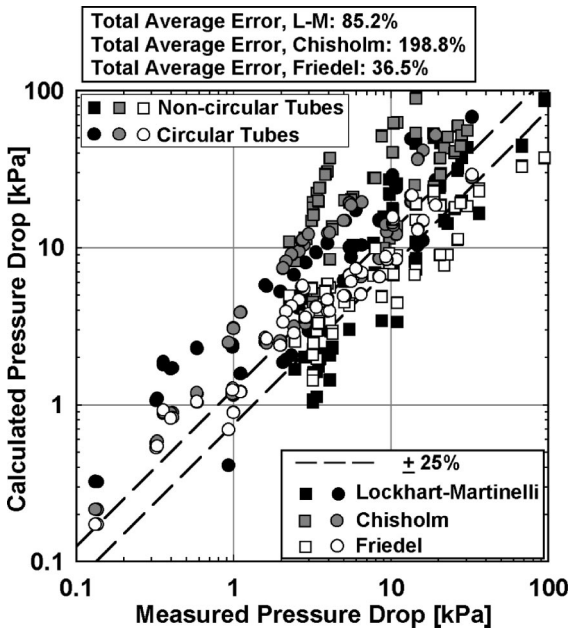

Fig. 10 Comparison of Lockhart-Martinelli, Chisholm, and Friedel two-phase pressure drop models, [22], with measured data

where $a=996.5$ and $b=-8.33\times10^{-4}$. This correlation, along with the earlier correlation (Eq. (21)) for other tube shapes, is shown in Fig. 9. The plot shown in Fig. 8 uses the above correlation for the triangular tubes and the correlation of Garimella et al. [6] for all other tube shapes. It is clear from Figs. 6–8 that the correlation by Garimella et al. [6] with the above modification for the triangular tubes fits the measured pressure drop significantly better than the models of Tronconi [17] and Gregory and Scott [15]. Their models generally predict higher slug frequencies and overpredict the total pressure drop when used with this model. This may be due to the significant differences between the thermophysical properties of the air-liquid combinations used in their work and those of the pure refrigerant used here. Additionally the range of tube diameters used in their work lead to stratified intermittent flow whereas the tubes used in the present work do not exhibit stratification in this regime, [2,3]. Thus Eq. (21) and Eq. (24) are recommended for the range of parameters considered here. The average error for the circular tubes using the recommended model is 13.5% (the value of 13.4% stated in [6] was before the friction factor and slug length calculations were changed as described above), for the noncircular tubes it is 16.5%. 90% of the predicted circular and noncircular tube results fall within 28% of the measured values.

The widely used two-phase flow pressure-drop models from Lockhart-Martinelli [18], Chisholm [20], and Friedel [21] were also compared with the measured values. These results can be seen in Fig. 10. Clearly the scatter is much greater with these correlations, but of the three, the Friedel correlation is closest, perhaps because it is the only one that attempts to account for surface tension. The average error using the Friedel correlation for the all the tubes (circular and noncircular) is 36%, with a max error of 158% (which is still considerably higher than the errors resulting from the present model). The Chisholm correlation generally overpredicts the measured results and has an average error of nearly 200% and a maximum of over 800%; the Lockhart-Martinelli correlation yields an average error of 85% with a maximum error of over 400%.

The effect of hydraulic diameter on pressure drop for circular tubes was predicted using this model in Garimella et al. [6]. However, the effect of the noncircular shapes can be both through changing the effective hydraulic diameter, and the roughness ratio (ε/D), which was determined experimentally for each tube using single-phase tests as described above. In addition, the triangular tubes follow a significantly different trend. Figure 11 shows a comparison of pressure drops for a representative tube with an $L/D_{h,\text{nominal}}=500$ (i.e., 375-mm-long tube) for the tube shapes considered in this study assuming the free flow area of all the shapes to be equal to that of a 0.75-mm circular tube. The noncircular shapes were nondimensionalized and scaled to obtain the appropriate hydraulic diameter for this flow area. The roughness ratios assumed were the same as those based on single-phase measurements (see Table 1). To incorporate the effect of tube roughness, the Churchill [11] equation for friction factor was used in place of the simpler Blassius equation in Eq. (6) and Eq. (13) as stated above. The combination of hydraulic diameter and relative roughness for each shape made the results unique to each tube shape and different than the corresponding circular tube. The noticeable slope changes in some of the curves are due to the independent transitions from laminar to turbulent flow in the liquid slug and the vapor bubble (for the conditions pictured, the film Reynolds number never exceeds 300). These single-phase transi-

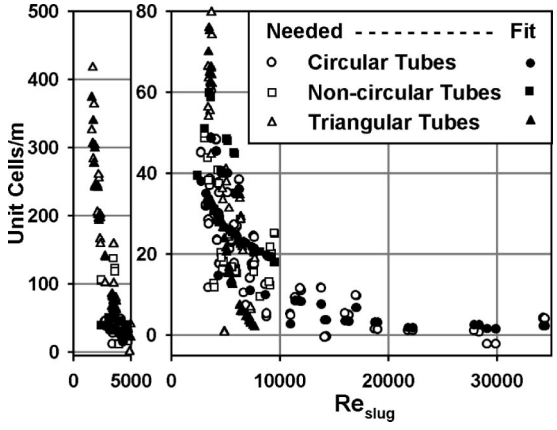

Fig. 9 Number of unit cells per meter derived from measured data as a function of slug Reynolds number, comparison with model: Eq. (21) and Eq. (24)

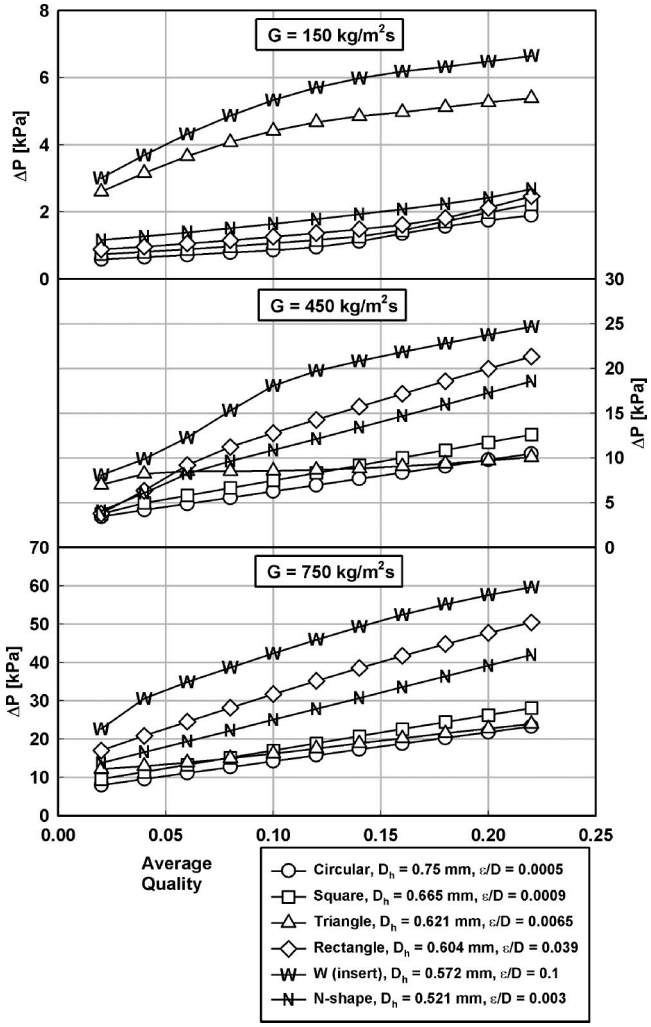

Fig. 11 Predicted effect of tube shape for nominal flow area equivalent to 0.75-mm diameter circular tube, $L/D_{h,\text{nominal}}=500$

tions generally occur between a Reynolds number of 2000 and 3000. At the two higher mass fluxes shown, the slope changes seen in Fig. 11 are the result of the laminar-turbulent transition within the vapor bubble. For instance, at a mass flux of 450 kg/m^{2}s and a quality of 0.1, the bubble Reynolds number is about 2700 for the W-tube and there is a visible slope change here; similarly at a mass flux of 750 and quality of 0.04, the bubble Reynolds number is about 2900 for the W-tube. At the lowest mass flux shown, 150 kg/m^{2}s, a more gradual slope change can be observed, which is due to the laminar-turbulent transition within the slug. It should be noted that the transitions for each tube shape do not occur at the same combination of quality and mass flux because the hydraulic diameter is different for each tube. In addition, the change in slope is related to the relative roughness, which is different for each tube; so some transitions appear more drastic than others. Figure 11 also shows that the triangular tubes are predicted to behave significantly differently than the other tubes at low mass fluxes (low slug Reynolds number). The reasons for this behavior are not fully understood although it can be seen from Fig. 9 that the number of unit cells per meter at these low slug Reynolds numbers are much higher for the triangular tubes than for the other circular and noncircular tubes. Moreover, there are more measured data available for the triangular tubes at these conditions than for the other tubes (see inset, Fig. 9). Certainly the W-tube is unlike any of the others due to its method of fabrication and may therefore be more likely to have features such as nonconstant passage geometry than the other tubes (note also the higher relative roughness values for the W-tube in Table 1), but with the extruded triangular tube, this difference does not exist.

Table 1 Hydraulic diameter and relative roughness values used in parametric study of effect of tube shape

Tube Shape	D_h (mm)	Roughness (ε/D_h)
Circular	0.750	0.0005
Square	0.665	0.0009
Triangle	0.621	0.0065
Rectangle	0.604	0.0390
W-insert (triangle)	0.572	0.1000
N-shaped	0.521	0.0030

Note: length of all tubes=375 mm

Conclusions

An experimentally validated pressure drop model for intermittent flow of condensing refrigerant R134a in noncircular horizontal tubes with hydraulic diameters from 0.42 to 0.84 mm was developed based on the observed flow patterns. The model includes the pressure drop due to the slug, the film/bubble region, and the transitions between them. The experimental work presented here in conjunction with prior flow visualization studies of condensing refrigerant flows provided an accurate set of measured pressure drop data for intermittent flow that was used for model validation. The model developed by Garimella et al. [6] was enhanced and extended using the concept of hydraulic diameter. A simple correlation for nondimensional unit-cell length based on slug Reynolds number was developed with two sets of coefficients, one for triangular tubes and one for all other tubes considered. Besides tube dimensions and thermophysical properties, the only inputs required for the model are the quality and mass flux of the refrigerant. The results of this model were within $\pm 16.5\%$ of the measured data on average for all noncircular tubes, with 90% of the predicted results within $\pm 28\%$ of the 96 measured data points. The results were also compared with predictions using two slug frequency models from the literature and predictions of generalized two-phase flow pressure drop correlations. The slug frequency models of Tronconi [17] and Gregory and Scott [15] were shown to generally overpredict the pressure drop contribution of the film-to-slug transitions. The more commonly used two-phase pressure drop models of Lockhart-Martinelli [18], Chisholm [20], and Friedel [21] were also not able to predict the measured data with acceptable errors. It was shown that the model proposed here predicts the measured results much more accurately than any of the other models. Finally, the model was used to characterize the effect of tube shape, mass flux, and quality on pressure drop in a systematic way.

Acknowledgments

This study was supported through a research grant from Modine Manufacturing Company, Racine, WI.

Nomenclature

A = cross-sectional area (m^2)
a, b = variable constants
D = diameter (m) (or (mm) as noted)
d = ordinary differential operator
ΔP = pressure drop (kPa)
dP/dx = pressure drop per unit length (kPa/m)
g = gravitational constant (m/s^2)
G = mass flux (kg/m^{2}s)
H = height (mm)
j = superficial velocity (m/s) (see Eq. (2) and Eq. (3))
L = tube length (m)
N_{UC} = number of unit cells

R = radius (m)
Re = Reynolds number
U = velocity (m/s) cross-sectional average
x = vapor quality
X = Lockhart-Martinelli parameter

Greek Symbols

α = void fraction
ε = surface roughness
ρ = mass density (kg/m^3)
μ = dynamic viscosity (Ns/m^2)
τ = shear stress (N/m^2)
ω = slug frequency (Hz)

Subscripts

avg = average within test section
f/b = film/bubble region
h = hydraulic diameter of tube
L = liquid
UC = unit cell
V = vapor

References

[1] Coleman, J. W., and Garimella, S., 1999, ''Characterization of Two-Phase Flow Patterns in Small Diameter Round and Rectangular Tubes,'' Int. J. Heat Mass Transfer, **42**(15), pp. 2869–2881.
[2] Coleman, J. W., and Garimella, S., 2000, ''Visualization of Refrigerant Two-Phase Flow During Condensation,'' *Proceedings of the 34th National Heat Transfer Conference*, ASME, New York.
[3] Coleman, J. W., and Garimella, S., 2000, ''Two-Phase Flow Regime Transitions in Microchannel Tubes: The Effect of Hydraulic Diameter,'' *Proc. ASME Heat Transfer Division—2000*, ASME, New York, Orlando, FL, HTD-Vol. 366-4, pp. 71–83.
[4] Mandhane, J. M., Gregory, G. A., and Aziz, K., 1974, ''A Flow Pattern Map for Gas-Liquid Flow in Horizontal Pipes,'' Int. J. Multiphase Flow, **1**, pp. 537–553.
[5] Taitel, Y., and Dukler, A. E., 1976, ''A Model for Predicting Flow Regime Transitions in Horizontal and Near Horizontal Gas-Liquid Flow,'' AIChE J., **22**(1), pp. 47–55.
[6] Garimella, S., Killion, J. D., and Coleman, J. W., 2002, ''An Experimentally Validated Model for Two-Phase Pressure Drop in the Intermittent Flow Regime for Circular Microchannels,'' ASME J. Fluids Eng., **124**(1), pp. 205–214.
[7] Suo, M., and Griffith, P., 1964, ''Two-Phase Flow in Capillary Tubes,'' J. Basic Eng., **86**, pp. 576–582.
[8] Dukler, A. E., and Hubbard, M. G., 1975, ''A Model for Gas-Liquid Slug Flow in Horizontal and Near Horizontal Tubes,'' Ind. Eng. Chem. Fundam., **14**(4), pp. 337–347.
[9] Fukano, T., Kariyasaki, A., and Kagawa, M., 1989, ''Flow Patterns and Pressure Drop in Isothermal Gas-Liquid Concurrent Flow in a Horizontal Capillary Tube,'' *ANS Proceedings 1989 National Heat Transfer Conference*, American Nuclear Society, La Grange Park, IL, **4**, pp. 153–161.
[10] Tran, T. N., Chyu, M.-C., Wambsganss, M. W., and France, D. M., 2000, ''Two-Phase Pressure Drop of Refrigerants During Flow Boiling in Small Channels: An Experimental Investigation and Correlation Development,'' Int. J. Multiphase Flow, **26**(11), pp. 1739–1754.
[11] Churchill, S. W., 1977, ''Friction Factor Equation Spans All Fluid Flow Regimes,'' Chem. Eng. (Rugby, U.K.), **84**(24), pp. 91–92.
[12] White, F. M., 1990, *Viscous Fluid Flow*, McGraw-Hill, New York.
[13] Berker, A. R., 1963, ''Intégration des équations du Mouvement d'un Fluide Visqueux Incompressible,'' *Encyclopedia of Physics*, S. Flügge, ed., Springer, Berlin, pp. 1–384.
[14] Heywood, N. I., and Richardson, J. F., 1979, ''Slug Flow of Air-Water Mixtures in a Horizontal Pipe: Determination of Liquid Holdup by Γ-Ray Absorption,'' Chem. Eng. Sci., **34**, p. 17.
[15] Gregory, G. A., and Scott, D. S., 1969, ''Correlation of Liquid Slug Velocity and Frequency in Horizontal Cocurrent Gas-Liquid Slug Flow,'' AIChE J., **15**(6), pp. 933–935.
[16] Kago, T., Saruwatari, T., Ohno, S., Morooka, S., and Kato, Y., 1987, ''Axial Mixing of Liquid in Horizontal Two Phase Slug Flow,'' J. Chem. Eng. Jpn., **20**, p. 252.
[17] Tronconi, E., 1990, ''Prediction of Slug Frequency in Horizontal Two-Phase Slug Flow,'' AIChE J., **36**(5), pp. 701–709.
[18] Lockhart, R. W., and Martinelli, R. C., 1949, ''Proposed Correlation of Data for Isothermal Two-Phase, Two-Component Flow in Pipes,'' Chem. Eng. Prog., **45**(1), pp. 39–48.
[19] Govier, G. W., and Aziz, K., 1972, *The Flow of Complex Mixtures in Pipes*, Van Nostrand Reinhold, New York.
[20] Chisholm, D., 1983, *Two-Phase Flow in Pipelines and Heat Exchangers*, George Godwin of Longman Group Limited, New York.
[21] Friedel, L., 1979, ''Improved Friction Pressure Drop Correlations for Horizontal and Vertical Two Phase Pipe Flow,'' *European Two Phase Flow Group Meeting, Ispra, Italy, Paper E2*.
[22] Carey, V. P., 1992, *Liquid-Vapor Phase Change Phenomena*, Hemisphere Publishing, Washington, DC.

Out-of-Plane Motion Effects in Microscopic Particle Image Velocimetry

Michael G. Olsen
Assistant Professor,
Department of Mechanical Engineering,
Iowa State University,
3025 H. M. Black Engineering,
Ames, IA 50011
e-mail: mgolsen@iastate.edu

Chris J. Bourdon
Senior Member Technical Staff,
Engineering Sciences Center,
Thermal, Fluids and Aero Experimental Sciences,
Sandia National Laboratories,
P.O. Box 5800, MS 0834,
Albuquerque, NM 87145
e-mail: cjbourd@sandia.gov

In microscopic particle image velocimetry (microPIV) experiments, the entire volume of a flowfield is illuminated, resulting in all of the particles in the field of view contributing to the image. Unlike in light-sheet PIV, where the depth of the measurement volume is simply the thickness of the laser sheet, in microPIV, the measurement volume depth is a function of the image forming optics of the microscope. In a flowfield with out-of-plane motion, the measurement volume (called the depth of correlation) is also a function of the magnitude of the out-of-plane motion within the measurement volume. Equations are presented describing the depth of correlation and its dependence on out-of-plane motion. The consequences of this dependence and suggestions for limiting its significance are also presented. Another result of the out-of-plane motion is that the height of the PIV signal peak in the correlation plane will decrease. Because the height of the noise peaks will not be affected by the out-of-plane motion, this could lead to erroneous velocity measurements. An equation is introduced that describes the effect of the out-of-plane motion on the signal peak height, and its implications are discussed. Finally, the derived analytical equations are compared to results calculated using synthetic PIV images, and the agreement between the two is seen to be excellent. [DOI: 10.1115/1.1598989]

Introduction

The rapid development of microfluidic MEMS devices has resulted in researchers developing experimental techniques to investigate fluid flow within these devices. One recently developed experimental microfluidic technique is microscopic particle image velocimetry, [1–3].

Particle image velocimetry (PIV) is a well-established technique used to obtain instantaneous velocity fields, typically in wind or water tunnels, [4]. In a typical PIV experiment, small tracer particles are illuminated by a double-pulsed sheet of light, and the images of these particles are recorded by a CCD camera. Then, instantaneous velocity fields are determined from the images using a cross-correlation technique. If the depth-of-focus of the camera is made larger than the thickness of the laser sheet, all of the illuminated particles will be in focus in the recorded image, and the depth of the measurement volume will be defined by the thickness of the laser sheet.

Microscopic PIV (microPIV) is an extension of PIV to study flows at the microscale. A diagram of a microPIV system is shown in Fig. 1. The microfluidic device of interest is placed beneath the objective of an epi-fluorescent microscope (or in the case of an inverted microscope, above the objective). The light beam from a double-pulsed Nd:YAG laser is expanded before entering the microscope through an aperture in the back of the microscope. After being redirected towards the microfluidic device by a prism, the laser light is focused onto a small region of the sample by the microscopic objective.

Because of the small length scales involved in microPIV, it is not possible to illuminate only a thin slice of the flowfield with a laser sheet. Instead, the entire flowfield is illuminated, and the depth over which the particle images are obtained is determined by the optical parameters of the microscope objective, not the thickness of a laser sheet. The intensity and size of an individual particle's image will be dependent on the particle's distance from the object plane of the microscope objective. Those particles very near the object plane will form small, bright images, and those particles away from the object plane will form larger, dimmer images.

The objective of the work presented here is to determine the effect of out-of-plane particle motion on microPIV interrogation. Out-of-plane motion may cause the image formed by each seed particle to vary between the PIV images to be cross-correlated, and this variation may affect the measurement volume and the PIV signal peak. The work presented here seeks to quantify these effects.

Particle Image Intensity Function

The diameter of an image formed by a particle as a function of distance from the microscope objective object plane can be estimated as the sum of a geometric optics term and a diffraction term. Olsen and Adrian [5] estimated the diameter as

$$d_e = \left(M^2 d_p^2 + 5.95(M+1)^2 \lambda^2 f^{\#2} + \frac{M^2 z^2 D_a^2}{(s_0+z)^2} \right)^{1/2}. \quad (1)$$

Equation (1) assumes that both the geometric optics term and the diffraction term can be approximated as Gaussian. In any microscopic measurement, $s_0 \gg z$, and the image diameter grows as $d_e \propto (\text{const.} + z^2)^{1/2}$, which is a hyperbola. Note that in microscopic applications, the numerical aperture is often used in place of the focal number. For large focal numbers and with air as the imaging medium, and making a paraxial approximation, the relation between numerical aperture and focal number is simply $NA = 1/2f^{\#}$. This approximation can break down for large numerical aperture objectives and for immersion lenses. Meinhart and Werely [6] have derived a more general relationship between $f^{\#}$ and numerical aperture that is valid for all numerical apertures and immersion media, and this can be used in place of the above relationship in cases where the paraxial approximation breaks down.

Olsen and Adrian [5,7] derived the following equation that describes the image formed by a particle in microscopic PIV:

Contributed by the Fluids Engineering Division for publication in the JOURNAL OF FLUIDS ENGINEERING. Manuscript received by the Fluids Engineering Division Apr. 23, 2002; revised manuscript received Apr. 14, 2003. Associate Editor: A. K. Prasad.

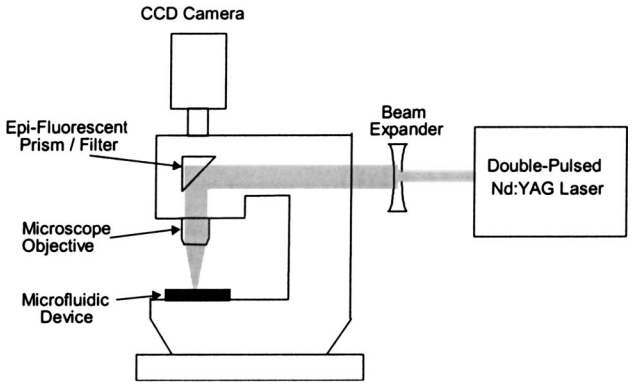

Fig. 1 Diagram of a microscope-based microPIV system

$$\hat{J}_0 = \frac{A}{d_e^2(s_0+z)^2}\exp\left(\frac{-4\beta^2\mathbf{X}^2}{d_e^2}\right) \tag{2}$$

where

$$A = \frac{(J_p/I_0)D_a^2\beta^2}{4\pi}.$$

Cross-Correlation Analysis

For an interrogation using cross-correlation analysis, two images are taken of the flowfield at times t_1 and $t_2 = t_1 + \Delta t$. As in Keane and Adrian [8–10], the two images to be cross-correlated can be represented by

$$I_1(\mathbf{X}) = W_{I1}(\mathbf{X}-\mathbf{X}_1)\int I_{01}(\mathbf{x})\hat{J}_0(\mathbf{X}-M\mathbf{x};z)g(\mathbf{x},t_1)d\mathbf{x} \tag{3}$$

$$I_2(\mathbf{X}) = W_{I2}(\mathbf{X}-\mathbf{X}_2)\int I_{02}(\mathbf{x}')\hat{J}_0(\mathbf{X}-M\mathbf{x}';z)g(\mathbf{x}',t_2)d\mathbf{x}' \tag{4}$$

where

$$g(\mathbf{x},t) = \sum_i \delta(\mathbf{x}-\mathbf{x}_i(t)) \tag{5}$$

indicates the Lagrangian position $\mathbf{x}_i(t)$ of each particle in the flow at time t. It is convenient to decompose t into mean and fluctuating parts, such that

$$g(\mathbf{x},t) = C(\mathbf{x},t) + \Delta g(\mathbf{x},t). \tag{6}$$

The local spatial cross-correlation of the two images can be estimated by the convolution integral

$$R(\mathbf{s}) = \int I_1(\mathbf{X})I_2(\mathbf{X}+\mathbf{s})d\mathbf{X}. \tag{7}$$

$R(\mathbf{s})$ can be decomposed into three components, such that

$$R(\mathbf{s}) = R_C(\mathbf{s}) + R_F(\mathbf{s}) + R_D(\mathbf{s}) \tag{8}$$

where $R_C(\mathbf{s})$ is the convolution of the mean intensities and is a broad function of $\mathbf{s}$ with a diameter of the order of the interrogation spot diameter, $R_F(\mathbf{s})$ is the fluctuating noise component due to the correlation of mean intensity with the fluctuating image intensity, and $R_D(\mathbf{s})$ is the displacement component of the correlation function. $R_D(\mathbf{s})$ gives the particle image displacement from time t_1 to t_2, and thus contains the information necessary to calculate the velocity vector for the interrogation volume (i.e., it is the PIV signal peak). Solving for $R_D(\mathbf{s})$ results in

$$R_D(\mathbf{s}) = \int d\mathbf{X}\int W_{I1}(\mathbf{X}-\mathbf{X}_1)\Delta g(\mathbf{x},t_1)I_{01}(\mathbf{x})\hat{J}_0(\mathbf{X}-M\mathbf{x};z)d\mathbf{x} \times \int W_{I2}(\mathbf{X}-\mathbf{X}_2+\mathbf{s})\Delta g(\mathbf{x}',t_2)I_{02}(\mathbf{x}')\hat{J}_0 \times(\mathbf{X}-M\mathbf{x}+\mathbf{s};z')d\mathbf{x}'. \tag{9}$$

Statistical Formulation

In each pair of PIV images to be cross-correlated, the particle locations are random, and this randomness causes variations in the correlation fields (even for two interrogation volumes with identical velocity fields). It is therefore appropriate to deal with averages of the correlation estimate. Indeed, this is exactly the interrogation technique that is used in many microscopic PIV experiments in order to maximize the spatial resolution, [2]. Also, by taking a large ensemble, the conditional average of $R_F(\mathbf{s})$ approaches zero, and can thus be neglected. Furthermore, the contribution of $R_C(\mathbf{s})$ is to create a plateau above which the signal peak rises. All the information necessary to determine velocity can be derived from the signal peak, $R_D(\mathbf{s})$. The conditional average of $R_D(\mathbf{s})$ for a given velocity field is

$$\langle R_D(\mathbf{s})|\mathbf{u}(\mathbf{x})\rangle = \int d\mathbf{X}\int W_{I1}(\mathbf{X}-\mathbf{X}_1)I_{01}(\mathbf{x})\hat{J}_0(\mathbf{X}-M\mathbf{x};z)d\mathbf{x} \times \int W_{I2}(\mathbf{X}-\mathbf{X}_2+\mathbf{s}) \times\langle\Delta g(\mathbf{x},t_1)\Delta g(\mathbf{x}',t_2)|\mathbf{u}(\mathbf{x})\rangle I_{02}(\mathbf{x}') \times\hat{J}_0(\mathbf{X}-M\mathbf{x}'+\mathbf{s};z')d\mathbf{x}'. \tag{10}$$

Adrian [11] showed that

$$\langle\Delta g(\mathbf{x},t_1)\Delta g(\mathbf{x}',t_2)|\mathbf{u}(\mathbf{x})\rangle = C(\mathbf{x},t_1)\delta(\mathbf{x}'-\mathbf{x}-\mathbf{u}(\mathbf{x},t)\Delta t). \tag{11}$$

Substituting Eq. (11) into (10) and simplifying results in

$$\langle R_D(\mathbf{s})|\mathbf{u}(\mathbf{x})\rangle = \int d\mathbf{X}\int W_{I1}(\mathbf{X}-\mathbf{X}_1)I_{01}(\mathbf{x})C(\mathbf{x},t)\hat{J}_0(\mathbf{X}-M\mathbf{x};z) \times W_{I2}(\mathbf{X}-\mathbf{X}_2+\mathbf{s})I_{02}(\mathbf{x}+\Delta\mathbf{x}) \times\hat{J}_0(\mathbf{X}-M\mathbf{x}-M\Delta\mathbf{x}+\mathbf{s};z+\Delta z)d\mathbf{x}, \tag{12}$$

the accuracy of the particle image intensity function and the convolution integrals describing microPIV interrogation has been investigated experimentally, [12]. These experiments were performed for microPIV systems with magnifications and numerical apertures of 11.5× and 0.29 and 23.5× and 0.38, respectively. For all of the cases investigated, the results of these experiments agreed with the analytical descriptions within 5%.

Out-of-Plane Motion Effects

The effect of out-of-plane motion on the cross-correlation signal peak in microscopic PIV can be determined by integrating Eq. (12). In doing this, it is first assumed that the entire interrogation volume is illuminated with equal laser intensity, and the intensity of both of the laser pulses is the same.

One effect of the out-of-plane motion is that the two images formed by an individual particle may not be the same. If the particle moves toward the object plane between laser pulses, then the second image will be brighter and have a smaller diameter, and if the particle moves away from the object plane between laser pulses, then the second image will be dimmer and have a larger diameter. The purpose of this analysis is to determine the effect of this variation in particle image intensity and diameter due to out-of-plane motion on the microPIV measurement.

The distance traversed in the z-direction by a particle from t_1 to t_2 can be denoted by Δz, where $\Delta z = u_z(\mathbf{x})\Delta t$. The particle's diameter at t_1 and t_2 will then be $d_e(z)$ and $d_e(z+\Delta z)$, respec-

tively, and these diameters can be determined using Eq. (1). Equation (2) can then be used to describe the particle image intensity function of the particle during both the first and second laser pulses. Substituting the particle image intensity functions into Eq. (12) with the previously stated assumptions results in

$$\langle R_D(\mathbf{s})|\mathbf{u}(\mathbf{x})\rangle = I_0^2 A^2 \int\int W_{I1}(\mathbf{X}-\mathbf{X}_1) W_{I2}(\mathbf{X}-\mathbf{X}_2) C(\mathbf{x},t) \times \frac{1}{d_e^2(z)(s_0+z)^2} \frac{1}{d_e^2(z+\Delta z)(s_0+z+\Delta z)^2} \times \exp\left(\frac{-4\beta^2\mathbf{X}^2}{d_e^2(z)}\right) \times \exp\left(\frac{-4\beta^2(\mathbf{X}+\mathbf{s}-M\Delta\mathbf{x})^2}{d_e^2(z+\Delta z)}\right) d\mathbf{X}d\mathbf{x}. \quad (13)$$

This can be integrated with respect to $\mathbf{X}$, yielding

$$\langle R_D(\mathbf{s})|\mathbf{u}(\mathbf{x})\rangle = \frac{\pi I_0^2 A^2}{4\beta^2} \int\int W_{I1}(\mathbf{X}-\mathbf{X}_1) W_{I2}(\mathbf{X}-\mathbf{X}_2) C(\mathbf{x},t) \times \left(\frac{1}{d_e^2(z)+d_e^2(z+\Delta z)}\right) \times \left(\frac{1}{(s_0+z)^2(s_0+z+\Delta z)^2}\right) \times \exp\left(\frac{-4\beta^2(\mathbf{s}-M\Delta\mathbf{x})^2}{d_e^2(z)+d_e^2(z+\Delta z)}\right) d\mathbf{x} \quad (14)$$

Equation (14) describes the size and shape of the cross-correlation signal peak in a microscopic PIV experiment with out-of-plane particle motion. Examination of this equation reveals that one effect of out-of-plane motion is to widen the signal peak and to reduce the peak height. This can have significant consequences in a microPIV experiment, because if the signal peak height becomes too low, then it may be difficult to identify the signal peak from the random noise peaks, resulting in erroneous velocity measurements.

The measured velocity is defined by the location where $\partial R_D/\partial \mathbf{s}=0$. Differentiating Eq. (14), and solving for $\mathbf{u}_0$, where $\mathbf{u}_0$ is the measured velocity, results in

$$\mathbf{u}_0 = \int \frac{\mathbf{u}(\mathbf{x}) C(\mathbf{x},t) W_{I1}(M\mathbf{x}-\mathbf{X}_1) W_{I2}(M(\mathbf{x}+\Delta\mathbf{x})-\mathbf{X}_2)}{(s_0+z)^2(s_0+z+\Delta z)^2(d_e^2(z)+d_e^2(z+\Delta z))^2} \times \exp\left(\frac{-4\beta^2(\mathbf{s}-M\Delta\mathbf{x})^2}{d_e^2(z)+d_e^2(z+\Delta z)}\right) d\mathbf{x} \times \left(\int \frac{C(\mathbf{x},t) W_{I1}(M\mathbf{x}-\mathbf{X}_1) W_{I2}(M(\mathbf{x}+\Delta\mathbf{x})-\mathbf{X}_2)}{(s_0+z)^2(s_0+z+\Delta z)^2(d_e^2(z)+d_e^2(z+\Delta z))^2} \times \exp\left(\frac{-4\beta^2(\mathbf{s}-M\Delta\mathbf{x})^2}{d_e^2(z)+d_e^2(z+\Delta z)}\right) d\mathbf{x} \right)^{-1} \quad (15)$$

where $\Delta\mathbf{x}=\mathbf{u}(\mathbf{x})\Delta t$. Equation (15) is implicit in $\mathbf{u}(\mathbf{x},t)$ because $\mathbf{u}$ appears in both sides of the equation, and as such, the measured velocity $\mathbf{u}_0$ will be a weighted average of $\mathbf{u}$ throughout the interrogation volume. However, although $\mathbf{u}(\mathbf{x},t)$ may vary within the interrogation volume, so long as the variation is not too great, then $\mathbf{s}_0 - M\Delta\mathbf{x} \cong 0$, and the exponential terms in Eq. (15) will be approximately equal to 1. With this approximation, Eq. (15) can be expressed as

$$\mathbf{u}_0 = \frac{\int \mathbf{u}(\mathbf{x},t) W(\mathbf{x}) d\mathbf{x}}{\int W(\mathbf{x}) d\mathbf{x}} \quad (16)$$

where $W(\mathbf{x})$ is the weighting function

$$W(\mathbf{x}) = \frac{C(\mathbf{x},t) W_{I1}(M\mathbf{x}-\mathbf{X}_1) W_{I2}(M(\mathbf{x}+\Delta\mathbf{x})-\mathbf{X}_2)}{(s_0+z)^2(s_0+z+\Delta z)^2(d_e^2(z)+d_e^2(z+\Delta z))^2}. \quad (17)$$

The weighting function gives the relative contribution to the cross-correlation signal peak as a function of particle position. As was done in Olsen and Adrian [5] for the case of microscopic PIV in the absence of out-of-plane motion, the weighting function can be used to define a boundary on the interrogation volume in the z-direction by defining a distance from the object plane beyond which particles no longer significantly contribute to the correlation function. The contribution of a particle to the correlation function can be assumed to be insignificant when the ratio of its weighting function to the weighting function of a particle at $z=0$ (i.e., a particle on the object plane) falls below some threshold. This threshold can be defined by the parameter ε. If the concentration of seed particles is assumed to be constant throughout the interrogation volume, then to find this distance (designated by z_{corr}) we first assume that $s_0 \gg z$ and then solve the equation

$$\varepsilon = \frac{(d_e^2(0)+d_e^2[(\Delta z)^2])^2}{(d_e^2(z_{\text{corr}})+d_e^2(z_{\text{corr}}+\Delta z))^2} \quad (18)$$

which results in

$$z_{\text{corr}} = \left[\left(f^{\#2} d_p^2 + \frac{5.95(M+1)^2 \lambda^2 f^{\#4}}{M^2} \right) \left(\frac{1-\sqrt{\varepsilon}}{\sqrt{\varepsilon}} \right) + \frac{1}{4} \left(\frac{4-\sqrt{\varepsilon}}{\sqrt{\varepsilon}} \right) (\Delta z)^2 \right]^{1/2} + \frac{\Delta z}{2}. \quad (19)$$

For $\Delta z = 0$, Eq. (19) reduces to the same equation for z_{corr} that was derived in Olsen and Adrian [7], as one would expect. Equation (19) can be used to determine the *depth of correlation*, an experimental parameter that defines the depth over which particles significantly contribute to the measured velocity. The depth of correlation defines the depth of the measurement volume in microscopic PIV and is simply $2z_{\text{corr}}$.

Equation (19) suggests that the depth of correlation is dependent on the local out-of-plane velocity component. This has serious implications in a microscopic PIV experiment in a three-dimensional velocity field. The measurement volume is not only dependent on particle size and optical parameters, which remain fixed for a given experiment, but also on the hydrodynamics of the flowfield. In a three-dimensional flowfield with large spatial variations in the z-velocity, the measurement volume will vary throughout the flowfield and can lead to difficulties in interpreting the experimental results.

Equation (19) shows that the effect of the out-of-plane motion is to increase the depth-of-correlation compared to an experiment without out-of-plane motion. The term outside the square root is due to the uncertainty in determining a particle's z-position due to out-of-plane motion, i.e., a particle that begins at $z=-\Delta z/2$ will end at $z=\Delta z/2$, effectively stretching the depth of correlation by distance Δz. The term inside the square root is because out-of-plane motion has the effect of making the image of a particle larger for one of the laser pulses than for the other. This broadening of the image, and the consequential diminishing of peak particle image intensity, will dilute a particle's contribution to the correlation function. This dilution will be greatest for particles near the object plane, because a small growth in their image diameter due to out-of-plane motion will have a larger relative effect then the effect of out-of-plane motion on particles far from the object plane, which have large image diameters to begin with and are less affected by a change in image diameter due to out-of-plane motion.

Table 1 Depth of correlation as a function of out-of-plane motion

OBJECTIVE	$\Delta z=0$ μm	$\Delta z=1$ μm	$\Delta z=2$ μm	$\Delta z=4$ μm
10×, $NA=0.25$ $d_p=1$ μm	38.0μm	39.5 μm	42.0 μm	49.5 μm
20×, $NA=0.5$ $d_p=1$ μm	10.5μm	13.2 μm	18.3 μm	31.1 μm
40×, $NA=0.6$ $d_p=1$ μm	7.7μm	10.9 μm	16.7 μm	30.1 μm

The depth of correlation for various microscope objectives and degrees of out-of-plane motion is summarized in Table 1. As these data demonstrate, the stretching of the depth of correlation can be significant even in the case of very small out-of-plane motion. Out-of-plane motion of only 1 μm stretches the depth of correlation by over 25% for a 20× objective. The stretching effect becomes more pronounced as the magnitude of the out-of-plane motion increases. For very small Δz, the term outside of the square root dominates the stretching of z_{corr} in Eq. (19), but as Δz increases, the term inside the square root grows in prominence until it is the dominant term in the stretching of z_{corr}. It would therefore be improper, except in cases of very small Δz, to estimate the depth of correlation by simply adding the out-of-plane motion to the depth of correlation determined without out-of-plane motion.

The data in Table 1 also show that the stretching of the depth of correlation due to out-of-plane motion becomes more significant if higher magnification, higher numerical aperture objectives are used. For these objectives, particle image diameter can vary greatly for even small changes in a particle's z-position. Thus, even seemingly small out-of-plane motion can affect a particle's image greatly, in turn significantly affecting the depth of correlation.

Equation (19) can be expressed in dimensionless form by normalizing both sides of the equation by z_{corr} for $\Delta z=0$ and expressing z_{corr} as a function of $\xi=\Delta z/2z_{corr}(0)$ (i.e., as a function of the ratio of Δz to depth of correlation for $\Delta z=0$). This results in

$$\frac{z_{corr}(\xi)}{z_{corr}(0)}=\left[1+\frac{1}{4}\left(\frac{4-\sqrt{\varepsilon}}{\sqrt{\varepsilon}}\right)(2\xi)^2\right]^{1/2}+\xi \tag{20}$$

where

$$z_{corr}(0)=\left[\left(f^{\#2}d_p^2+\frac{5.95(M+1)^2\lambda^2 f^{\#4}}{M^2}\right)\left(\frac{1-\sqrt{\varepsilon}}{\sqrt{\varepsilon}}\right)\right]^{1/2}.$$

The ratio $z_{corr}(\xi)/z_{corr}(0)$ is a stretching parameter that describes the change in z_{corr} as a function of the out-of-plane velocity component. The ratio $z_{corr}(\xi)/z_{corr}(0)$ as a function of ξ is plotted in Fig. 2.

Great care must be taken in interpreting microscopic PIV data in three-dimensional flowfields because of possible variations in the depth of correlation due to out-of-plane motion. To ease data interpretation, Eq. (19) can be used to assist in designing experiments such that variations in depth of correlation are insignificant. If the maximum out-of-plane velocity is known a priori, and if one sets a limit on the maximum tolerable stretching of the depth of correlation, denoted by ϕ, then one can set

$$z_{corr}(\Delta z_{max})=(1+\phi)z_{corr}(0) \tag{21}$$

and then solve for Δz_{max} using Eq. (19). From Δz_{max}, the experimenter can determine the maximum laser pulse separation Δt that can be used to keep the stretching of the depth of correlation within the desired limit. Of course, this can lead to other difficulties, as it may require that Δt be so small that particle motion within the object plane is also very small. Since the error associated with a PIV measurement is inversely proportional to the magnitude of particle motion within the object plane, selecting too small of a Δt can result in measurement errors that are undesirably large. Thus designing a microscopic PIV experiment for a flowfield with out-of-plane motion may require striking a balance between data interpretation and experimental uncertainty.

Another effect of the out-of-plane motion is to reduce the height of the correlation signal peak relative to the PIV noise peaks, which can result in difficulties in identifying the signal peak. Equation (14) shows that the contribution of a particle located at z to the signal peak height is proportional to

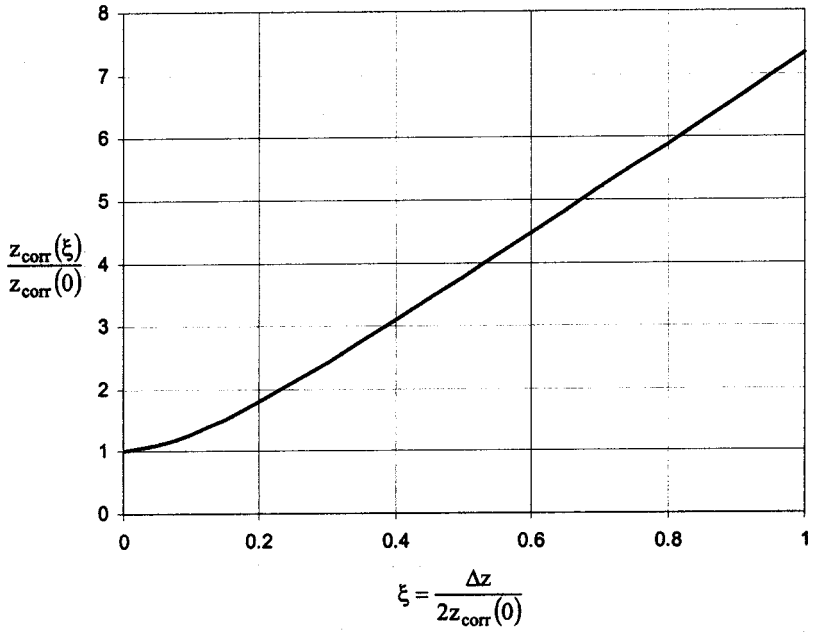

Fig. 2 Depth of correlation as a function of out-of-plane particle motion

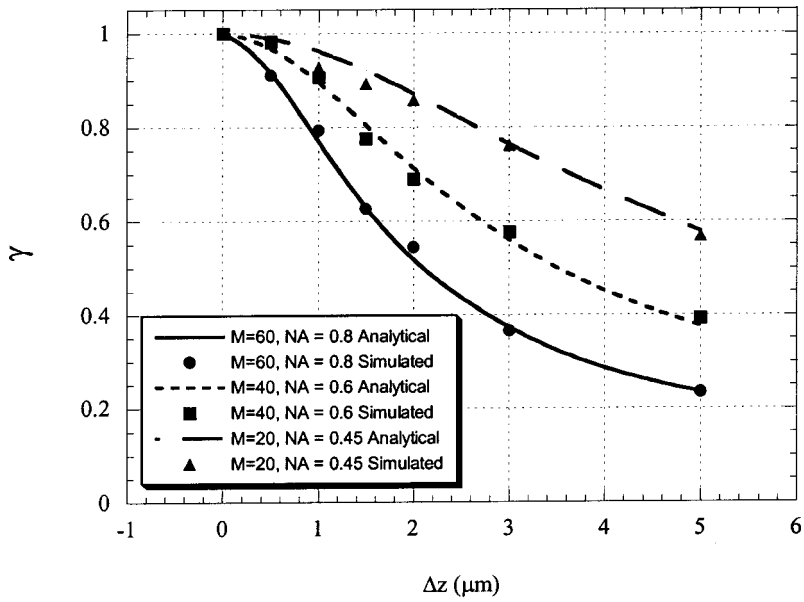

Fig. 3 Decrease in correlation signal peak height as a function of out-of-plane motion for 0.5 μm seed particles and various microscopic objectives

$$\frac{1}{d_e^2(z)+d_e^2(z+\Delta z)} \tag{22}$$

so that as Δz increases, the contribution of each individual particle to the signal peak height will decrease, making the total peak height smaller. This decrease in signal peak height can be quantified by taking the ratio of the contribution to the signal peak height of a particle with out-of-plane motion to the contribution to signal peak height in the absence of out-of-plane motion. Letting $\gamma(z)$ be this ratio, this ratio can be found to be

$$\gamma(z)=\frac{2d_e^2(z)}{d_e^2(z)+d_e^2(z+\Delta z)}. \tag{23}$$

This represents the ratio of the contributions at only one z-location. However, the total peak height will result from the contributions to signal peak height from particles from all z-locations. We can estimate the cumulative effect of out-of-plane motion on the total signal peak height by integrating Eq. (22) both with and without out-of-plane motion over z, and taking the ratio of the two integrals. This results in

$$\gamma=\left(\frac{M^2d_p^2+5.95(M+1)^2\lambda^2f^{\#2}}{M^2d_p^2+5.95(M+1)^2\lambda^2f^{\#2}+\dfrac{M^2(\Delta z)^2}{4f^{\#2}}}\right)^{1/2}. \tag{24}$$

Equation (24) is an estimate of the ratio of signal peak height with out-of-plane motion to signal peak height in the absence of out-of-plane motion. The noise peaks will not be affected by out-of-plane motion, and thus Eq. (24) can be used to estimate the change in the signal peak height relative to the random noise peaks for various degrees of out-of-plane motion. Equation (24) is plotted in Fig. 3 for various microscopic objectives for an experiment using 0.5 μm seed particles.

Equation (24) can be used to estimate the largest allowable Δz such that the signal peak height will not drop below a certain level. For example, if one desires for the signal peak height for an experiment with out-of-plane motion to be no less than $1/\sqrt{2}$ of the signal peak height of an experiment without out-of-plane motion, then the maximum allowable Δz can be estimated to be

$$\Delta z_{\max}=\left(\frac{4(M^2d_p^2f^{\#2}+5.95(M+1)^2\lambda^2f^{\#2})}{M^2}\right)^{1/2}. \tag{25}$$

Computational Methodology and Results

In order to verify the accuracy of the analytical findings presented in the previous section, a series of computational experiments has been performed. Synthetic image sets were generated with known in- and out-of-plane displacements between the two images. The initial particle centers were randomly located by a Monte-Carlo-based scheme within a 300-micron cube. The final particle positions were specified by simply adding the in- and out-of-plane motions to the initial particle position. Approximately 24,000 particles were placed in each volume, or approximately 1 particle per 10-micron cube. Although this number seems prodigious, over 85% of these particles are far enough removed from the focal plane (located midway through the depth of the cube) that they are essentially contributing only to the background glow of the image. Both the cube size and number of particles chosen here were arbitrary, and different numbers were implemented garnering identical results. The intensity field generated from each individual particle was represented in the image by the relationship given in Eq. (1). Each particle was projected in succession onto a two-dimentional digital image of 1000 by 1000 pixels in size. A sample synthetic and an actual microPIV image at similar magnification and particle size are presented in Fig. 4.

Each synthetic particle image pair was interrogated using a standard PIV cross-correlation algorithm, with a 32-pixel square interrogation region. Analysis was also completed with interrogation regions of 16×16 pixels and 64×64 pixels in size to establish that the results were independent of the interrogation region size. Since there was no background noise level added to the images, and all of the ambient light in the frames was directly contributed from individual particles, no pre-processing (such as background subtraction or spatial filtering) was performed on the raw images. A 900-correlation field average was generated from the individual correlation fields of each separate interrogation region for each image pair and recorded to disk. No post-processing or correlation optimization routines were used in this analysis. The peak height

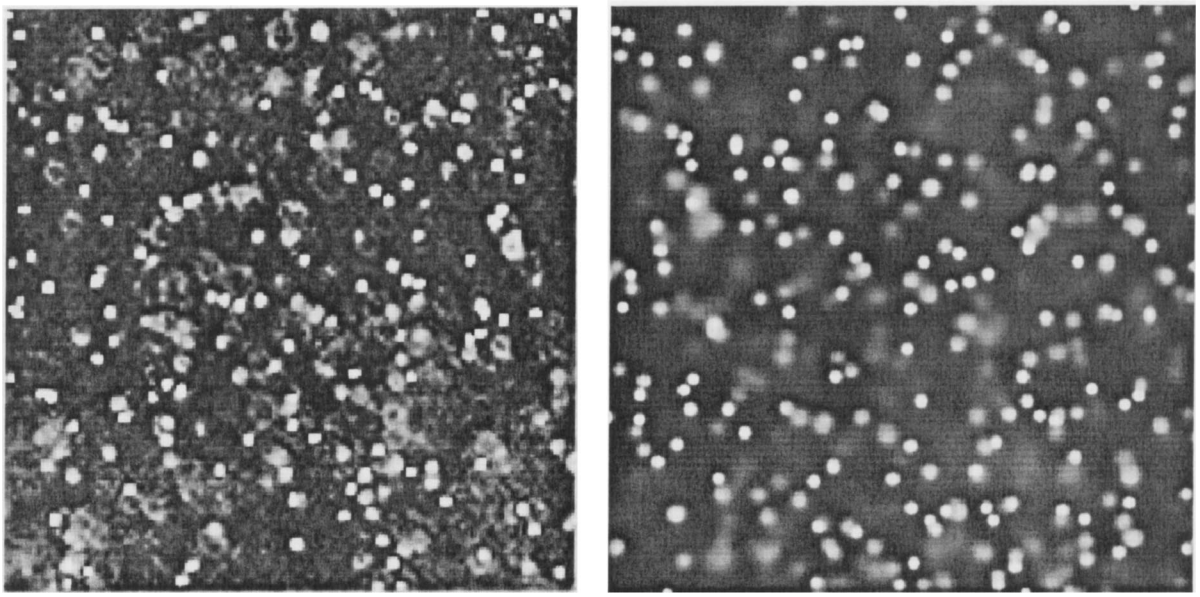

Fig. 4 Actual (left) and synthetic (right) microPIV images for the same specified conditions

above the background, normalized by the peak height for no out-of-plane motion can then be compared directly with the analytical solution for the same experimental parameters.

Synthetic images were generated for six out-of-plane displacements between 0.5 and 5 microns in depth for magnifications of 20, 40, and 60x. The normalized, averaged correlation peak heights are presented as symbols in Fig. 3. The agreement between the analytical solution and the computational results generated from the synthetic images is quite good, within 5% for all of the cases examined.

Summary and Conclusions

Out-of-plane motion can have significant effects in microscopic PIV experiments, and these effects are discussed here for the first time. One effect of the out-of-plane motion is that it will increase the depth of correlation. Because the out-of-plane velocity may vary throughout the flowfield, this will result in different measurement volume depths throughout the microscopic PIV velocity vector field. An equation was derived that described the depth of correlation as a function of optical parameters and the magnitude of the out-of-plane motion. With careful experimental design, stretching of the depth of correlation can be kept to a minimum, but such a limitation may also result in an increase in the experimental uncertainty of the measured velocity vectors.

Another effect of the out-of-plane motion is to reduce the height of the signal peak in the cross-correlation plane. Since the random noise peaks in the correlation plane will be unaffected by the out-of-plane motion, this can result in difficulties in identifying the signal peak from the surrounding noise peaks, leading to erroneous velocity measurements. An equation was derived that describes this reduction in signal peak height due to out-of-plane motion. These analytical results were compared directly with synthetic experiments, and the agreement was quite good, within 5% for all of the cases examined. Suggestions for the use of this equation have been made.

Acknowledgment

This work was supported by the National Science Foundation under grant number CTS-0134469. Additionally, a portion of this work was funded by Sandia Engineering Sciences Research Funds. Sandia is a multiprogram laboratory operated by Lockheed-Martin Company, for the United States Department of Energy under contract DE-AC04094AL85000.

Nomenclature

C = mean concentration of seed particles
δ = Dirac delta function
Δz = out-of-plane particle motion
d_e = particle image diameter
d_p = particle diameter
D_a = aperture diameter
ϕ = maximum tolerable stretching of the depth of correlation
$f^{\#}$ = focal number
I_i = PIV images for cross-correlation
I_0 = intensity of illuminating laser beam
$\hat{J}_0$ = particle image intensity function
J_p = flux of light from a particle
λ = wavelength of emitted light
M = magnification
NA = numerical aperture
R = spatial cross-correlation function
$\mathbf{s}$ = position vector in the correlation plane
s_0 = distance from lens to object plane
$\mathbf{u}$ = fluid velocity
$\mathbf{u}_0$ = measured fluid velocity
W_{Ii} = interrogation window function
$\mathbf{x}$ = position vector of particle
$\mathbf{X}$ = position vector in the image plane
ξ = dimensionless out-of-plane motion
z = distance from object plane
z_{corr} = distance from object plane to extent of measurement volume
$2z_{\mathrm{corr}}$ = depth of correlation

References

[1] Santiago, J. G., Wereley, S. T., Meinhart, C. D., Beebe, D. J., and Adrian, R. J., 1998, "A Particle Image Velocimetry System for Microfluidics," Exp. Fluids, **25**, pp. 316–319.
[2] Meinhart, C. D., Wereley, S. T., and Santiago, J. G., 1999, "PIV Measurements of a Microchannel Flow," Exp. Fluids, **27**, pp. 414–419.
[3] Meinhart, C. D., Wereley, S. T., and Santiago, J. G., 1999, "Micro-Resolution

Velocimetry Techniques,'' *Developments in Laser Techniques and Applications to Fluid Mechanics*, Springer, Berlin.
[4] Adrian, R. J., 1991, ''Particle-Imaging Techniques for Experimental Fluid Mechanics,'' Annu. Rev. Fluid Mech., **23**, pp. 261–304.
[5] Olsen, M. G., and Adrian, R. J., 2000, ''Out-of-Focus Effects on Particle Image Velocimetry and Correlation in Microscopic Particle Image Velocimetry,'' Exp. Fluids, **27**, pp. S166–S174.
[6] Meinhart, C. D., and Wereley, S. T., ''The Theory of Refraction-Limited Resolution in Microscopic Particle Image Velocimetry,'' Meas. Sci. Technol., to appear.
[7] Olsen, M. G., and Adrian, R. J., 2000, ''Brownian Motion and Correlation in Particle Image Velocimetry,'' Opt. Laser Technol., **27**, pp. 621–627.
[8] Keane, R., and Adrian, R. J., 1990, ''Optimization of Particle Image Velocimeters: I, Double Pulsed Systems,'' Meas. Sci. Technol., **1**, pp. 1202–1215.
[9] Keane, R., and Adrian, R. J., 1991, ''Optimization of Particle Image Velocimeters: II, Multiple Pulsed Systems,'' Meas. Sci. Technol., **2**, pp. 963–974.
[10] Keane, R., and Adrian, R. J., 1992, ''Theory of Cross-Correlation of PIV Images,'' Appl. Sci. Res., **49**, pp. 191–215.
[11] Adrian, R. J., 1986, ''Statistical Properties of Particle Image Velocimetry Measurements in Turbulent Flow,'' *Applications of Laser Anemometry to Fluid Mechanics*, Ladoan, Lisbon.
[12] Bourdon, C. J., Olsen, M. G., and Gorby, A. D., 2003, Proceedings of the 2003 ASME International Mechanical Engineering Congress and RD&D Exposition, Washington, DC, Nov. 15–21.

Modeling of the Onset of Gas Entrainment Through a Finite-Side Branch

M. Ahmed[1]

I. Hassan[2]
e-mail: hassan@me.Concordia.ca

N. Esmail

Department of Mechanical and Industrial Engineering,
Concordia University,
Montreal, Quebec H3G 1M8, Canada

A theoretical investigation has been conducted for the prediction of the critical height at the onset of gas entrainment during single discharge from a stratified, two-phase region through a side branch with a finite diameter. Two different models have been developed, a simplified point-sink model and a three-dimensional finite-branch model. The two models are based on a new criterion for the onset of gas entrainment. The results of the predicted critical heights at the onset of gas entrainment showed that the finite-branch model approaches the physical limits at low Froude numbers. However, as the values of the Froude number increased, the predictions of both models eventually converged to the same value. Based on the results of the models, the critical height corresponding to the onset of gas entrainment was found to be a function of Froude number and fluid densities. The results of both models are compared with available experimental data. The comparisons illustrate a very good agreement between the measured and predicted values.
[DOI: 10.1115/1.1601256]

1 Introduction

The research and development of experimental correlations and theoretical models of the onset of gas and liquid entrainments during discharge from a stratified, two-phase region through branches of finite diameter have gained great importance in recent literatures due to their relevance in several industrial applications; some of which include nuclear reactor safety during postulated loss-of-coolant accidents and two-phase distribution systems, where a certain incoming stream is fed into a larger header, as found in a shell-and-tube heat exchanger. Knowledge of the flow phenomena involved, the mass flow rate, as well as the quality of all discharging streams is essential for the design and/or performance prediction of such systems.

For the case of single discharge from a large, stratified flow channel, Zuber [1] stated that two distinct phenomena may occur, depending on the location of the gas-liquid interface relative to the branch. If the horizontal interface is located below the branch, liquid may be entrained in the predominating gas flow through the branch (onset of liquid-entrainment phenomenon). On the other hand, if the interface is located above the branch, gas can be entrained by a vortex or vortex-free motion into predominantly liquid flow through the branch (onset of gas-entrainment phenomenon). Zuber developed simplified correlations for the onsets of these phenomena in terms of pertinent system parameters and branch orientation (top, bottom or side). Later, detailed experimental data and correlations were obtained for the onset of gas and liquid entrainments, as well as the two-phase mass flow rates and quality between the two onsets, during single discharge (with or without main flow) through a single branch having different orientations (e.g., Smoglie and Reimann [2], Schrock et al. [3], Yonomoto and Tasaka [4,5], Micaelli and Memponteil [6], Parrott et al. [7], and Hassan et al. [8,9]). As an example for the prediction of the critical height at the onset of gas entrainment, for the case of single discharge from a side branch, Smogile and Reimann [2] experimentally developed the following correlation as a function of Froude number and branch diameter:

$$\frac{H_{\mathrm{OGE}}}{d} = 0.681 \ \mathrm{Fr}^{0.4},$$

where

$$\mathrm{Fr} = \frac{v_d}{\sqrt{gd\dfrac{\Delta\rho}{\rho_1}}}.$$

Parrott et al. [7] also experimentally investigated the onset of gas entrainment during single discharge from a large, stratified two-phase region. Using the least-square method, they developed the following correlation between the critical height at the onset of gas entrainment and the corresponding Froude number:

$$\frac{H_{\mathrm{OGE}}}{d} = 0.425 \ \mathrm{Fr}^{0.529} \quad \frac{H_{\mathrm{OGE}}}{d} \leqslant 1.15,$$

$$\frac{H_{\mathrm{OGE}}}{d} = 0.508 \ \mathrm{Fr}^{0.435} \quad \frac{H_{\mathrm{OGE}}}{d} \geqslant 1.15.$$

Recently, Hassan et al. [9] further investigated the single-side discharge from a large, stratified two-phase region through small branches and developed a similar correlation:

$$\frac{H_{\mathrm{OGE}}}{d} = 0.57 \ \mathrm{Fr}^{0.4}.$$

The reported theoretical investigations published to date in this area are essentially related to the prediction of the onset of liquid entrainment during single or dual discharge from a large, stratified region (e.g., Soliman and Sims [10], Hassan et al. [11] and Maier et al. [12]). The objective of the present work is to extend these theoretical investigations to the phenomenon of the onset of gas entrainment, as the second step towards the theoretical prediction of the mass flow rate and quality in the two-phase discharge region corresponding to $H_{\mathrm{OGE}} \geqslant H \geqslant H_{\mathrm{OLE}}$. Two models will be developed, a simplified point-sink model and a finite-branch model, which will include a new criterion for the onset of gas entrainment. The present analysis applies to any two immiscible fluids, with the term ''gas entrainment'' referring to the appearance of the lighter fluid in predominantly heavier-fluid flow through the branch.

[1]Present address: Mechanical Engineering Department, Assiut University, Egypt.
[2]To whom correspondence should be addressed.

Contributed by the Fluids Engineering Division for publication in the JOURNAL OF FLUIDS ENGINEERING. Manuscript received by the Fluids Engineering Division Feb. 1, 2002; revised manuscript received Mar. 27, 2003. Associate Editor: Y. Matsumoto.

2 Theoretical Analysis

The configuration considered in the present analysis is shown in Fig. 1, and consists of stratified layers of two immiscible fluids, with densities ρ_1 and ρ_2, contained in a large reservoir, with equilibrium of the interface being controlled by a balance of inertia and gravity. In the present analysis, the surface tension is ignored and the liquid flow is considered invicid, irrotational, incompressible, and quasi-steady. Therefore, the problem is governed by a single physical parameter: the Froude number. Quasi-steady-potential flow is assumed in the heavier fluid, while the lighter fluid is considered stagnant.

2.1 The Criterion of the Onset of Gas Entrainment. During single discharge from a stratified two-phase region through a side branch, if the interface level (H) well above the branch, the branch will be flowing liquid only, and the interface will be flat. As H is lowered and approaches H_{OGE}, a "dimple" begins to form in the interface. This dimple depression becomes more pronounced and cone-like until the bottom of the cone suddenly extends to the branch; this is the onset of gas entrainment (Hassan et al. [9]). As H is reduced below H_{OGE}, the branch will be flowing two-phase mixture. With decreasing H, the liquid stream to the branch becomes thinner until the flow of liquid into the branch ceases when $H=H_{OLE}$; this is called the onset of liquid entrainment. For $H<H_{OLE}$, the branch will be flowing gas only. The objective of the present paper is to simulate the onset of gas entrainment phenomenon, as shown in Fig. 1. The criterion used in for the prediction of the onset of gas entrainment is the equality between the acceleration of the liquid above the branch and the acceleration of gravity, at point B. Any further increase of liquid acceleration at point B above the acceleration of gravity will cause instability to the flow. This instability results in a catastrophic change in the free surface shape, which quickly extends the formed dip to the branch exit. This criterion is based on the study made by Taylor [13] to determine the onset of instability of inviscid liquid surfaces accelerated vertically. Taylor stated that the initial stability of the upper surface of a liquid would pass over into instability if the liquid were given a downward acceleration greater than that of gravity. Moreover, Taylor reported in his analysis that the amplitude of a two-dimensional disturbance accelerated downwards at acceleration a is given by

$$\frac{\eta}{\eta_o}=\cosh\left\{\sqrt{\frac{4\pi s(a-g)(\rho_1-\rho_2)}{\lambda a(\rho_1+\rho_2)}}\right\},$$

where η/η_o is the ratio of the amplitude of the disturbance at any time to its initial value, λ is the wavelength of the disturbance amplitude, s is the downward distance of the moving surface, a is the downward acceleration of the liquid surface, and g is the acceleration of gravity. Based on this equation, it is clear that if the acceleration a of the fluid surface is greater than the acceleration of gravity g the fluid surface would be unstable. Lewis [14] also investigated experimentally the instability of various liquids accelerating vertically downward. The instability criterion observed under a wide variety of experimental conditions has been analyzed, and good agreement between experiment and the theory of Taylor, mentioned above, was found. Furthermore, Zhou and Graebel [15] indicated that when the downward acceleration of the center of the free surface exceeds the gravitational acceleration, a dip appears in the free surface. Zhou and Graebel reported that the dip formation was due to the instability of the free surface, analogous to Rayleigh-Taylor instability.

2.2 Equilibrium of the Interface. In order to derive the interfacial equation along each side of the interface, the Bernoulli equation between point A and point B, shown in Fig. 1, can be written as follows:

For the heavier fluid region:

$$p_A+\frac{1}{2}\rho_1 v_A^2+\rho_1 gH=p_B+\frac{1}{2}\rho_1 v_B^2+\rho_1 gh. \tag{1}$$

Since v_A is finite, Eq. (1) can be written as

$$p_A+\rho_1 gH=p_B+\frac{1}{2}\rho_1 v_B^2+\rho_1 gh. \tag{2}$$

For the lighter, stagnant fluid region,

$$p_A+\rho_2 gH=p_B+\rho_2 gh. \tag{3}$$

From Eqs. (2) and (3), the velocity of the liquid at point B is given as

$$v_B^2=2g\frac{\Delta\rho}{\rho_1}[H-h]. \tag{4}$$

2.3 Point-Sink Analysis. In this analysis, the side branch shown in Fig. 1 is simulated as a point-sink with strength M, where the relation between the strength M and the mass flow rate $\dot{m}$ is given by

$$\dot{m}=2\pi\rho M.$$

The presence of the lighter, stationary fluid is ignored when developing the velocity field in the heavier fluid. Therefore, the flow field is treated as a semi-infinite medium extending over $-\infty\leqslant x\leqslant\infty$, $-\infty\leqslant y\leqslant\infty$, and $0\leqslant z\leqslant\infty$. The potential function of this three-dimensional flow field is given by Schetz and Fuhs [16] as follows:

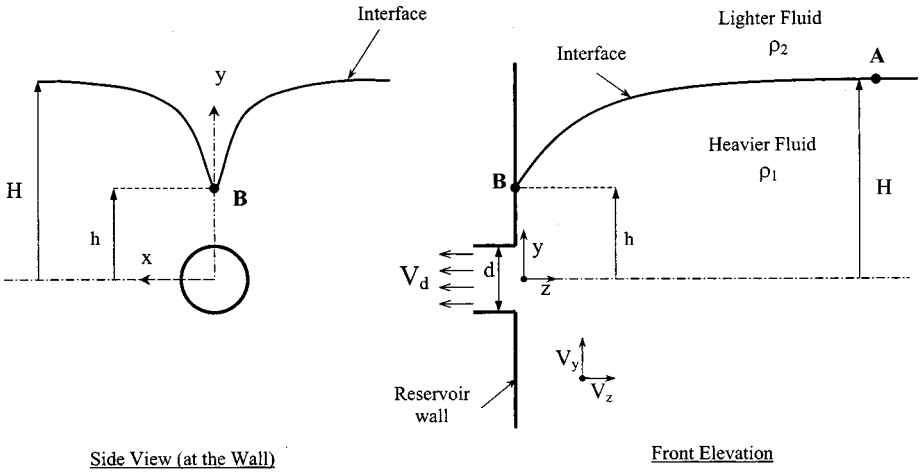

Fig. 1 Geometry and the coordinate system

$$\Phi = \frac{M}{\sqrt{x^2+y^2+z^2}}. \tag{5}$$

The criterion of the onset of gas entrainment is given by

$$[a]_B = g \tag{6}$$

where

$$[a]_B = -\left[\frac{\partial \Phi}{\partial y}\right]\left[\frac{\partial^2 \Phi}{\partial y^2}\right]_{B(x=z=0,y=h)}, \tag{7}$$

$$\left.\frac{\partial \Phi}{\partial y}\right|_{B(x=z=0,y=h)} = -\frac{M}{h^2},$$

$$\left.\frac{\partial^2 \Phi}{\partial y^2}\right|_{B(x=z=0,y=h)} = \frac{2M}{h^3}. \tag{8}$$

Substituting Eqs. (7) and (8) into (6), we get

$$h = \left(\frac{2M^2}{g}\right)^{0.2}. \tag{9}$$

From Eqs. (9) and (4) with $v_B = \partial\Phi/\partial y|_{x=z=0,y=h}$, the critical height at the onset of gas entrainment could be determined as

$$\frac{H_{\mathrm{OGE}}}{d} = \mathrm{Fr}^{0.4}\left[\frac{1}{2}\left(\frac{\Delta\rho}{\rho_1}\right)^{0.2} + \frac{1}{8}\left(\frac{\rho_1}{\Delta\rho}\right)^{0.8}\right]. \tag{10}$$

In the case of the lighter fluid having an infinitesimally small density with respect to the heavier fluid's density, Eq. (10) will become

$$\frac{H_{\mathrm{OGE}}}{d} = 0.625\ \ \mathrm{Fr}^{0.4}. \tag{11}$$

2.4 Finite-Branch Analysis. In the finite-branch analysis, the heavier fluid is also considered to be incompressible, homogenous, and irrotational. Furthermore, the presence of the lighter, stationary fluid is again ignored. As a result, the heavier fluid is considered to be a semi-infinite medium extending over $-\infty \leqslant x \leqslant \infty$, $-\infty \leqslant y \leqslant \infty$, and $0 \leqslant z \leqslant \infty$. The flow is caused by the discharge from a side branch, located at $y=x=z=0.0$. The continuity equation, in Cartesian coordinates, can be written in dimensionless form as follows:

$$\frac{\partial V_x^*}{\partial x} + \frac{\partial V_y^*}{\partial y} + \frac{\partial V_z^*}{\partial z^*} = 0.0, \tag{12}$$

where V_x^*, V_y^*, and V_z^* are the dimensionless velocity component in the x^*, y^*, and z^* directions, respectively. Introducing a dimensionless scalar potential function Φ^* such that

$$V_x^* = \frac{\partial \Phi^*}{\partial x^*}, \quad V_y^* = \frac{\partial \Phi^*}{\partial y^*}, \quad \text{and} \quad V_z^* = \frac{\partial \Phi^*}{\partial z^*}. \tag{13}$$

Therefore, Eq. (12) can be written as follows:

$$\nabla^2 \Phi^* = \frac{\partial^2 \Phi^*}{\partial x^{*2}} + \frac{\partial^2 \Phi^*}{\partial y^{*2}} + \frac{\partial^2 \Phi^*}{\partial z^{*2}} = 0.0, \tag{14}$$

with the following boundary conditions:

(i) At $z^*=0.0$,

$$\frac{\partial \Phi^*}{\partial z^*} = -1 \quad -\sqrt{1-y^{*2}} \leqslant x^* \leqslant +\sqrt{1-y^{*2}}$$

$$-1 \leqslant y^* \leqslant +1$$

$$= 0.0 \quad \text{for other values of } x^* \text{ and } y^*.$$

(ii) At $x^*=0.0$,

$$\frac{\partial \Phi^*}{\partial x^*} = 0.0 \quad \text{at all values of } y^* \text{ and } z^*.$$

(iii) At $x^* \to \pm\infty$, $y^* \to \pm\infty$, $z^* \to +\infty$, Φ^* is finite, where

$$x^* = \frac{x}{r_o}, \quad y^* = \frac{y}{r_o}, \quad z^* = \frac{z}{r_o},$$

$$V_x^* = \frac{V_x}{V_d}, \quad V_y^* = \frac{V_y}{V_d}, \quad V_z^* = \frac{V_z}{V_d}, \quad g^* = \frac{g r_o}{V_d^2}, \quad \nabla\Phi^* = \frac{\nabla\Phi}{V_d}.$$

The solution of Eq. (14), subjected to the boundary conditions given by (i), (ii), and (iii), could be obtained using the method of separation of variables as follows:

By applying the boundary conditions (ii) and (iii), the following equation was obtained:

$$\Phi^*(x^*,y^*,z^*) = \int_0^\infty \int_0^\infty [A_1(\lambda,\beta)\cos(\beta y^*) + A_2(\lambda,\beta)\sin(\beta y^*)]\cos(\lambda x^*) e^{-z^*\left(\sqrt{\lambda^2+\beta^2}\right)} \times d\lambda\, d\beta \tag{15}$$

where $A_1(\lambda,\beta)$ and $A_2(\lambda,\beta)$ are constants of integration and satisfy the boundary condition (i). To calculate the values of $A_1(\lambda,\beta)$ and $A_2(\lambda,\beta)$, we first take the partial derivative of Eq. (15) with respect to z^*, while setting $z^*=0$. We then apply the boundary condition (i), and using Fourier cosine and Fourier sine transformations the final values of $A_1(\lambda,\beta)$ and $A_2(\lambda,\beta)$ could be defined as

$$A_1(\lambda,\beta) = \frac{2}{\pi^2 \lambda \sqrt{\lambda^2+\beta^2}}\left[\int_{-1}^{1} \sin\left(\lambda\sqrt{1-(y^{*2})}\right)\cos(\beta y^*)\, dy^*\right], \tag{16}$$

and

$$A_2(\lambda,\beta) = \frac{2}{\pi^2 \lambda \sqrt{\lambda^2+\beta^2}}\left[\int_{-1}^{1} \sin\left(\lambda\sqrt{1-(y^{*2})}\right)\sin(\beta y^*)\, dy^*\right]. \tag{17}$$

Therefore, the final form of the solution can be written as

$$\Phi^*(x^*,y^*,z^*) = 2\int_0^\infty \int_0^\infty \frac{\cos(\beta y^*)\cos(\lambda x^*) e^{-z^*\sqrt{\lambda^2+\beta^2}}}{\pi^2 \lambda \sqrt{\lambda^2+\beta^2}} \times \left[\int_{-1}^{1} \sin\left(\lambda\sqrt{1-y^{*2}}\right)\cos(\beta y^*)\, dy^*\right] d\lambda\, d\beta + 2\int_0^\infty \int_0^\infty \frac{\sin(\beta y^*)\cos(\lambda x^*) e^{-z^*\sqrt{\lambda^2+\beta^2}}}{\sqrt{\lambda^2+\beta^2}} \times \left[\int_{-1}^{1} \sin\left(\lambda\sqrt{1-y^{*2}}\right)\sin(\beta y^*)\, dy^*\right] d\lambda\, d\beta. \tag{18}$$

The criterion for the onset of gas entrainment in dimensionless form is

$$[a^*]_B = -\left[\frac{\partial \Phi^*}{\partial y^*}\right]\left[\frac{\partial^2 \Phi^*}{\partial y^{*2}}\right]_{(x^*=z^*=0,y^*=h^*)} = g^*. \tag{19}$$

The values of the first and second derivatives of the stream function could be written in this form

$$\left.\frac{\partial \Phi^*}{\partial y^*}\right|_{x^*=z^*=0,y^*=h^*} = I_1[h^*] \tag{20}$$

and

$$\left.\frac{\partial^2\Phi^*}{\partial y^{*2}}\right|_{x^*=z^*=0,y^*=h^*} = I_2[h^*] \tag{21}$$

where

$$I_1[h^*] = -2\int_0^\infty\int_0^\infty \frac{\cos(\beta h^*)}{\pi^2\lambda\sqrt{\lambda^2+\beta^2}} \times\left[\int_{-1}^{1}\sin(\lambda\sqrt{1-y^{*2}})\cos(\beta y^*)dy^*\right]d\lambda d\beta + 2\int_0^\infty\int_0^\infty \frac{\sin(\beta h^*)}{\sqrt{\lambda^2+\beta^2}}\left[\int_{-1}^{1}\sin(\lambda\sqrt{1-y^{*2}}) \times\sin(\beta y^*)dy^*\right]d\lambda d\beta \tag{22}$$

$$I_2[h^*] = -2\int_0^\infty\int_0^\infty \frac{\cos(\beta h^*)}{\pi^2\lambda\sqrt{\lambda^2+\beta^2}} \times\left[\int_{-1}^{1}\sin(\lambda\sqrt{1-y^{*2}})\cos(\beta y^*)dy^*\right]d\lambda d\beta - 2\int_0^\infty\int_0^\infty \frac{\sin(\beta h^*)}{\sqrt{\lambda^2+\beta^2}}\left[\int_{-1}^{1}\sin(\lambda\sqrt{1-y^{*2}}) \times\sin(\beta y^*)dy^*\right]d\lambda d\beta. \tag{23}$$

Substituting Eqs. (20) and (21) into Eq. (19) will give

$$I_1[h^*]I_2[h^*] = -\left(\frac{1}{\mathrm{Fr}}\right)^2\left(\frac{\rho_1}{2\Delta\rho}\right). \tag{24}$$

Then the critical height at the onset of gas entrainment can be written as

$$\frac{H_{\mathrm{OGE}}}{d} = \frac{h^*}{2} + \frac{\mathrm{Fr}^2}{2}\{I_1[h^*]\}^2. \tag{25}$$

To calculate the critical height corresponding to the onset of gas entrainment, knowing the value of h^*, the Froude number is first calculated by solving Eq. (24). The values of $I_1[h^*]$ and $I_2[h^*]$ are calculated using numerical integration techniques as indicated by Stround [17] and Gradshteyn and Ryzhik [18]. Then, based on the values of h^* and Fr, the critical height is determined using Eq. (25).

3 Results and Discussion

In the present section, comparisons between the predicted critical heights, using the point-sink and finite-branch analyses, at the onset of gas entrainment during single discharge from a stratified two-phase region were made for different values of Fr. The objective of this comparison is to determine at which range of Fr number the values of H_{OGE}/d are not influenced by the point-sink assumption. Also, to better comprehend and provide a validation for the present analysis, comparisons between the experimental determinations of H_{OGE}/d, the available models in the literature, and the present computed results using the point-sink and finite-branch analyses will be provided in the following section. The experimental data used for these comparisons were found by Hassan et al. [9], Parrott et al. [7], and Smoglie and Reimann [2].

Figure 2 shows the behavior of H_{OGE}/d as a function of Fr number for both the finite-branch analysis and the point-sink analysis. The deviation present between the finite-branch and point-sink analyses is considerable when Fr$<$1, only to decrease in importance as the Fr number approaches 10, where it may be considered negligible beyond this point, and the prediction of the two models are identical. It is clear from Fig. 2 that the results of the finite-branch analysis converge to the physically appropriate limit of $H_{\mathrm{OGE}}/d=0.5$ when Fr=0. Figure 3 shows the deviation of the point-sink analysis (PSA) from the finite-branch analysis (FBA), where H_{PSA} refers to the value of (H_{OGE}/d) calculated from Eq. (10), and H_{FBA} refers to the value of (H_{OGE}/d) calculated from Eq. (25). The magnitude of this deviation is about 80% at Fr=0.01, 15% at Fr=1.0 and 3% at Fr=10.0. When Froude number approaches zero the deviation is 100%, since H_{PSA} approaches zero, based on Eq. (10), and H_{FBA} approaches the physical limits of $d/2$. Beyond Fr=10, which corresponds to $H_{\mathrm{OGE}}/d=1.5$, the error in using the point-sink analysis is negligible.

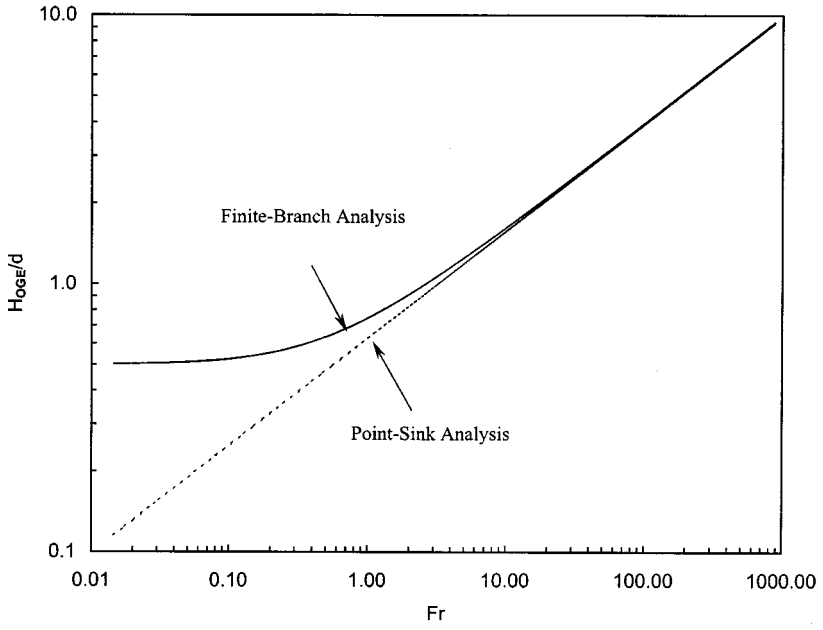

Fig. 2 Predictions of H_{OGE}/d with Fr

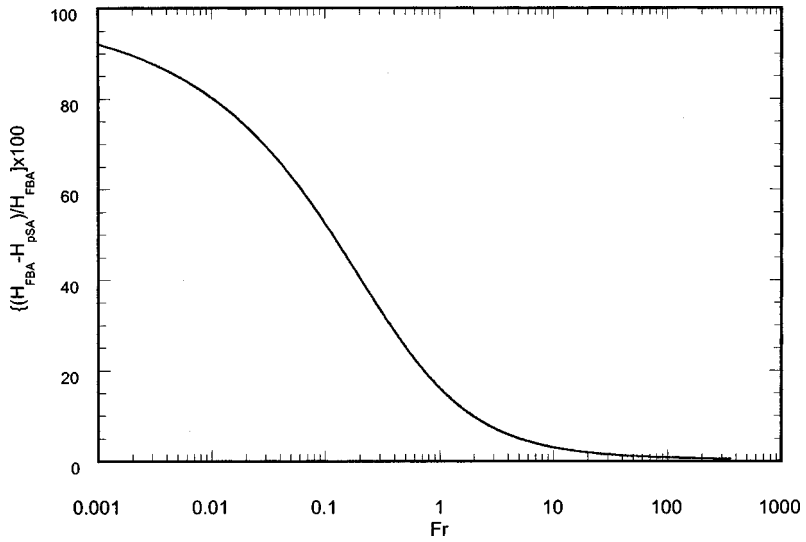

Fig. 3 Percentage deviation from the finite-branch analysis

Figure 4 shows the behavior of the ratio h/H_{OGE} and its corresponding Fr number. As illustrated, the results of the finite-branch analysis approach the physically appropriate limit of $h/H_{OGE}=1.0$ as the Froude number approaches zero. With increasing Froude number, the value of h/H_{OGE} converges to approximately 0.83, which also is very close to the constant value predicted by the point-sink analysis ($=0.80$).

A comparison between the present theoretical results, found using the point-sink and finite-branch analyses, and the experimental data found by Parrott et al. [7] and Hassan et al. [9] is shown in Fig. 5. The experimental data here were generated during single discharge through a 6.35 mm inner-diameter branch located on the sidewall of a large reservoir under stratified (air-water) conditions and different pressures ranging from 316 to 517 kPa. Despite the need for experimental data at lower Froude numbers ($Fr<1$), good agreement may be observed between the experimental data given and the point-sink and finite-branch analyses at $F>1$. Figure 6 quantifies the comparison between the experimental data in Fig. 5 obtained by Parrott et al. [7] and Hassan et al. [9] with the present analyses. At larger Froude numbers (>10), the deviation between the values of the critical height at the onset of gas entrainment found using the point-sink and finite-branch analyses, and the data given by Parrott et al. [7] is less than 2.5%. The finite-branch analysis predicts the data trend of Parrott et al. [7] very well over the whole range of Froude numbers. The experimental values found by Hassan et al. [9] are shown to be underpredicted by the two analyses by approximately 10%. It should be mentioned here that Parrott et al. [7] added the meniscus height (estimated to be 3.3 mm) to their values of the critical heights, while Hassan et al. [9] did not.

Figure 7 also demonstrates another comparison between the present theoretical results, found using the finite-branch and point-sink analyses, and the experimental results found by Smoglie and Reimann [2], for single discharge from a stratified region through a circular branch. Smoglie and Reimann performed their experiments using stratified air-water at 200 to 500 kPa in a horizontal

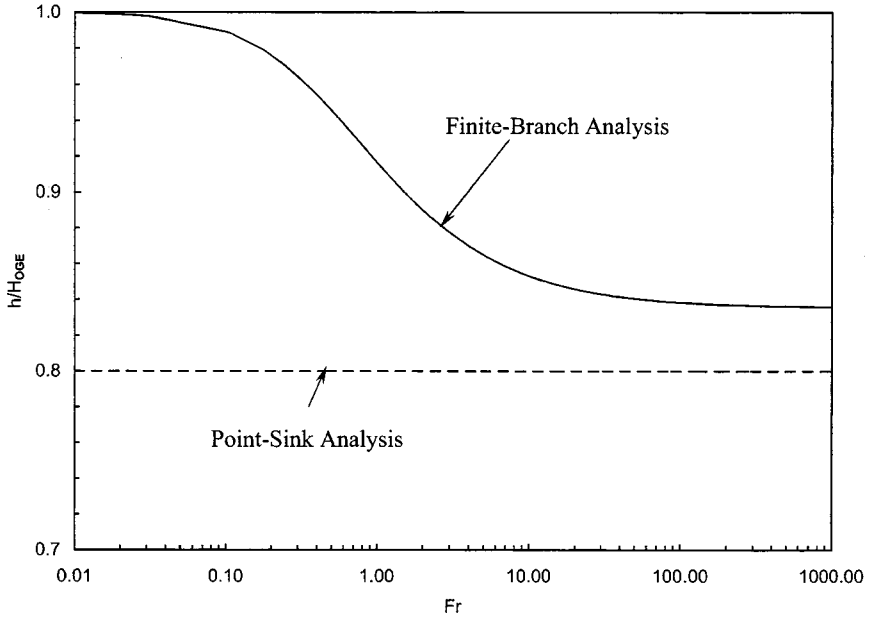

Fig. 4 Variations of h/H_{OGE} with Fr

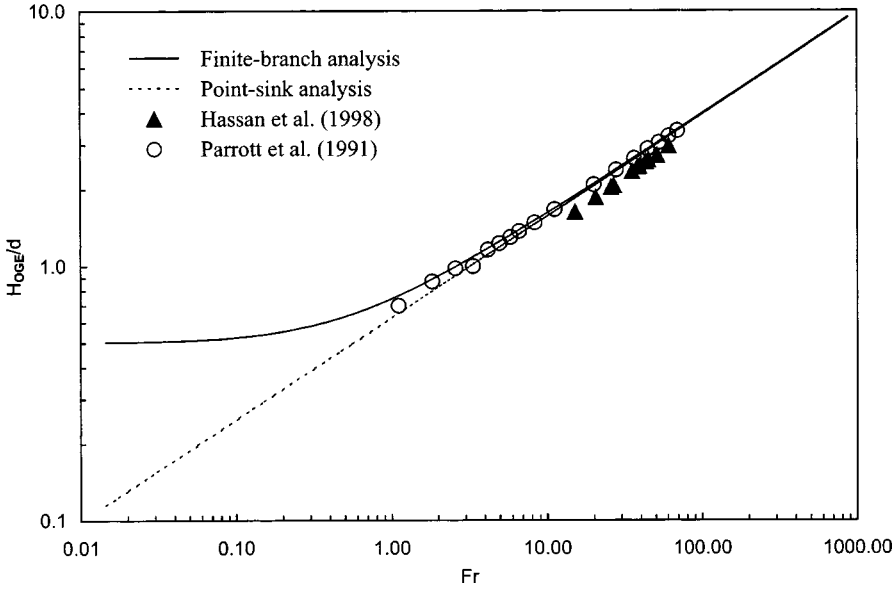

Fig. 5 Comparison between the present analysis and experimental data by Hassan et al. [9] and Parrott et al. [7]

pipe (20.6 cm in diameter) with different branch sizes ($d=6$, 8, 12, and 20 mm). The branch was simulated by pipe stubs (0.055 m in length) with sharp-edged entrances and the flow through the branch was controlled by a throttle valve. The onsets on entrainment were detected by the noise in the differential pressure signals across the branch. Once again, as shown in Fig. 7, the present analyses are proven to be in good agreement with the experimental data provided by Smoglie and Reimann [2].

The ability of the finite-branch model and the other available models in predicting the experimental data of H_{OGE} is shown in Fig. 8. The vertical axis of Fig. 8 is the critical Froude number, $Fr^*(=Q/4\pi\sqrt{gH^5})$, where Q is the volumetric flow rate, and the horizontal axis is $4Q/\pi\sqrt{gd^5}$. These coordinates were used here to facilitate the comparisons with the available models, which give their results as functions of Fr*. As shown in the figure, the present finite-branch model was able to predict the data trend fairly well, particularly at low values of $4Q/\pi\sqrt{gd^5}$. The models of Lubin and Springer [19], Zhou and Graebel [15], Miloh and Tyvand [20] and Xue and Yue [21], as well as the present point-sink analysis give a constant value of Fr* and fail to predict the correct trend of the data at low values of $4Q/\pi\sqrt{gd^5}$. In all of these models, the branch was simulated as a point sink and the potential flow theory was used, with different numerical and analytical techniques. Xue and Yue [21] used the mixed-Eulerian-Lagrangian boundary integral equation scheme in modeling the three-dimensional flow field of a sidewall submerged point-sink; the critical Froude number obtained out of this analysis is 0.193. This value is almost in agreement with the value obtained by the present point-sink analysis, which is about 0.202. Miloh and Tyvand [20] found that the critical Froude number Fr* is 0.258 using small time perturbation analysis and a bottom-oriented point-sink geometry. Lubin and Springer [19] first studied the problem ex-

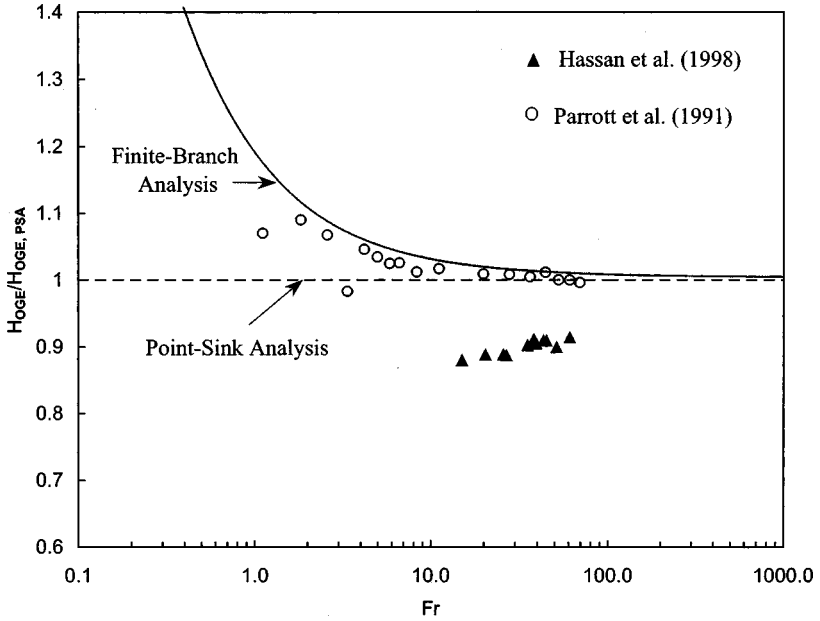

Fig. 6 Percent deviation from the point-sink model

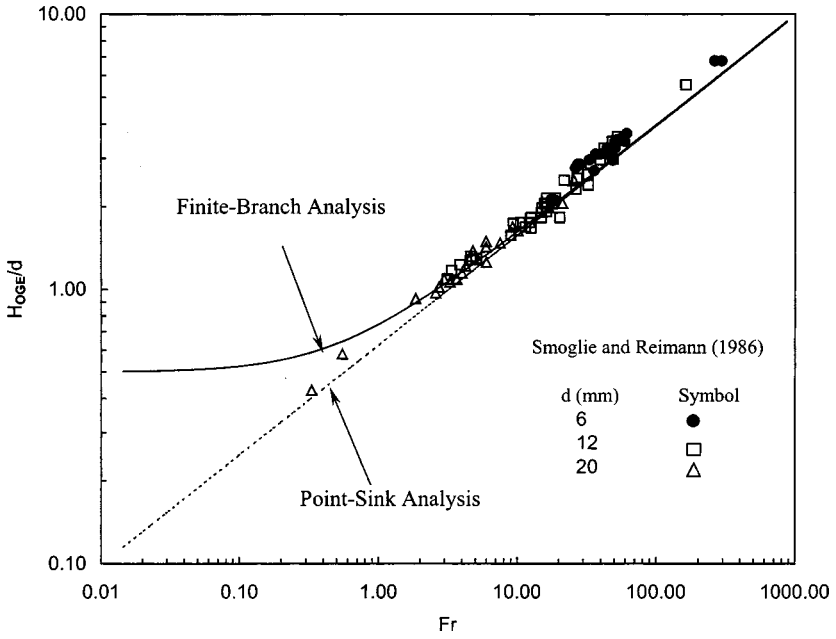

Fig. 7 Comparison between the present analysis and experimental data by Smoglie and Reimann [2]

perimentally using also a bottom-oriented point-sink, based on their observations, performed a simple analysis using the Bernoulli equation, which enabled them to find the critical Froude number Fr* corresponding to the onset of gas entrainment, which was 0.202. Once again the present finite-branch model, where the finite branch size was accounted, proves to be more accurate in predicting the experimental data over the whole range of $4Q/\pi\sqrt{gd^5}$ number.

It should be noted here that the experimental data is restricted in the sense that only data at higher Froude numbers (Fr>1) is available. Thus, it is difficult to deduce the effect of neglecting the viscous force and surface tension in the present analyses. Since these forces are expected to have an influence on the results of H_{OGE}/d at low values of Fr number (Fr<1); at higher values of Fr number the inertia forces are dominant and the effect of viscous force and surface tension may be neglected. Future experimental measurements of the critical heights at low values of Froude numbers would greatly help model validations.

4 Conclusions

The onset of gas entrainment during single discharge from a stratified two-phase region through a side branch was theoretically investigated. A new criterion for the onset of gas entrainment was developed based on the onset of instability of vertically accelerated fluids. Based on this criterion a simplified point-sink analysis and a three-dimensional finite-branch analysis were developed in order to predict the critical heights at the onset of gas entrainment.

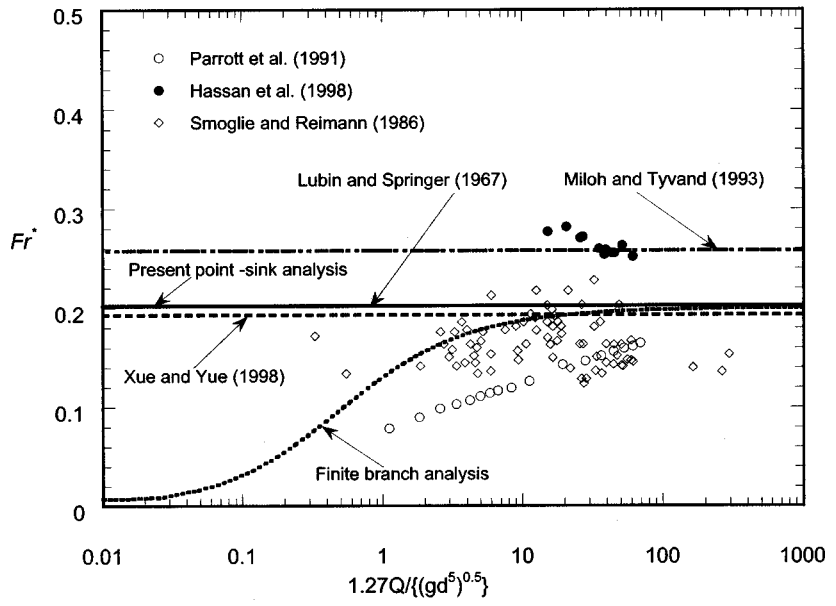

Fig. 8 Comparison between measured and predicted values of different models

The results of the predicted critical height at the onset of gas entrainment demonstrated that the finite-branch model is to be recommended at lower Froude numbers (Fr<10), as the model approaches the physical limits in this range. At higher Froude numbers, no noticeable deviation occurred to the predicted critical heights of both models. The critical heights were found to be a function of the Froude number and the density ratio of interfacing fluids, provided that the assumption of negligible viscous and surface tension forces are valid at low values of Fr number (Fr<1). Finally, the following modeling efforts are to be considered, the model may include the effect of wall inclination, to simulate different geometries (i.e., side, inclined, and bottom branches). As well as, experimental measurements of critical heights at low values of Froude numbers would greatly help model validations.

Nomenclature

a = downward acceleration of fluid surface, (m/s^2)
a^* = dimensionless downward acceleration of fluid surface, $[ar_o/V_d^2]$
d = branch diameter, (m)
Fr = Froude number
g = gravitational acceleration, (m/s^2)
g^* = dimensionless gravitational acceleration, $[gr_o/V_d^2]$
H_{OGE} = critical height corresponding to the onset of gas entrainment, (m)
H_{OLE} = critical height corresponding to the onset of liquid entrainment, (m)
$H_{OGE,PSA}$ = critical height corresponding to the onset of gas entrainment, obtained by the point-sink analysis, (m)
h = distance above the branch hole, as defined in Fig. 1, (m)
h^* = dimensionless height, (h/r_o)
$I_1[h^*]$, and $I_2[h^*]$ = arbitrary functions defined by Eqs. (22) and (23)
M = strength of point-sink, (m^3/s)
$\dot{m}$ = mass flow rate, (kg/s)
P_1 = static pressure of the interface from the side of heavier fluid, (N/m^2)
P_2 = static pressure of the interface from the side of lighter fluid, (N/m^2)
r_o = branch radius, (m)
V_x, V_y, V_z = velocity components in x, y, and z-directions, (m/s)
V_x^*, V_y^*, V_z^* = dimensionless velocity components in x^*, y^*, and z^*-directions, $(V_x/V_d, V_y/V_d, V_z/V_d)$
V_d = discharge velocity of the branch
x, y, z = Cartesian coordinate system as defined in Fig. 1
x^*, y^*, z^* = dimensionless variables, $(x/r_o, y/r_o, z/r_o)$

Greek Letters

ρ_1 = density of heavier fluid, (kg/m^3)
ρ_2 = density of lighter fluid, (kg/m^3)
$\Delta\rho$ = density difference between two fluids, $(\rho_1-\rho_2)$, (kg/m^3)
λ, β = constants
Φ = potential function, (m^3/s)
Φ^* = dimensionless potential function, $(\Phi/V_d r_o^2)$

References

[1] Zuber, N., 1980, "Problems in Modeling of Small Break LOCA," Nuclear Regulatory Commission Report, NUREG-0724.
[2] Smoglie, C., and Reimann, J., 1986, "Two-Phase Flow Through Small Branches in a Horizontal Pipe With Stratified Flow," Int. J. Multiphase Flow, **12**, pp. 609–625.
[3] Schrock, V. E., Revankar, S. T., Mannheimer, R., Wang, C. H., and Jia, D., 1986, "Steam-Water Critical Flow Through Small Pipes From Stratified Upstream Regions," *Proc. 8th Int. Heat Transfer Conf.*, San Francisco, CA, Hemisphere, Washington, DC, **5**, pp. 2307–2311.
[4] Yonomoto, T., and Tasaka, K., 1988, "New Theoretical Model for Two-Phase Flow Discharged From Stratified Two-Phase Region Through Small Break," J. Nucl. Sci. Technol., **25**, pp. 441–455.
[5] Yonomoto, T., and Tasaka, K., 1991,"Liquid and Gas Entrainment to a Small Break Hole From a Stratified Two-Phase Region," Int. J. Multiphase Flow, **17**, pp. 745–765.
[6] Micaelli, J. C., and Memponteil, A., 1989, "Two-Phase Flow Behavior in a Tee-Junction: The CATHARE Model," *Proc. 4th Int. Topical Meeting on Nuclear Reactor Thermalhydraulics*, G. Braun, Karlsruhe, Germany, **2**, 1024–1030.
[7] Parrott, S. D., Soliman, H. M., Sims, G. E., and Krishnan, V. S., 1991, "Experiments on the Onset of Gas Pull-Through During Dual Discharge From a Reservoir," Int. J. Multiphase Flow, **17**, pp. 119–129.
[8] Hassan, I. G., Soliman, H. M., Sims, G. E., and Kowalski, J. E., 1996, "Discharge From a Smooth Stratified Two-Phase Region Through Two Horizontal Side Branches Located in the Same Vertical Plane," Int. J. Multiphase Flow, **22**, pp. 1123–114.
[9] Hassan, I. G., Soliman, H. M., Sims, G. E., and Kowalski, J. E., 1998, "Two-Phase Flow From a Stratified Region Through a Small Side Branch," ASME J. Fluids Eng., **120**, pp. 605–612.
[10] Soliman, H. M., and Sims, G. E., 1992, "Theoretical Analysis of the Onset of Liquid Entrainment for Orifices of Finite Diameter," Int. J. Multiphase Flow, **18**, pp. 229–235.
[11] Hassan, I. G., Soliman, H. M., Sims, G. E., and Kowalski, J. E., 1999, "The Onset of Liquid Entrainment During Discharge From Two Branches on an Inclined Wall," Can. J. Chem. Eng., **77**(3), pp. 433–438.
[12] Maier, M. R., Soliman, H. M., Sims, G. E., and Armstrong, K. F., 2001, "Onsets of Entrainment During Dual Discharge From a Stratified Two-Phase Region Through Horizontal Branches With Centrelines Falling in an Inclined Plane: Part 1—Analysis of Liquid Entrainment," Int. J. Multiphase Flow, **27**(6), pp. 1011–1028.
[13] Taylor, G. I., 1950, "The Instability of Liquid Surfaces When Accelerated in a Direction Perpendicular to Their Planes," Proc. R. Soc. London, Ser. A, **201**, pp. 192–196.
[14] Lewis, D. J., 1950, "The Instability of Liquid Surfaces When Accelerated in a Direction Perpendicular to Their Planes, II," Proc. R. Soc. London, Ser. A, **202**, pp. 81–96.
[15] Zhou, Q. N., and Graebel, W. P., 1990, "Axisymmetric Draining of a Cylindrical Tank With a Free Surface," J. Fluid Mech., **221**, pp. 511–532.
[16] Schetz, J. A., and Fuhs, A. E., 1996, "Handbook of Fluid Dynamics and Fluid Machinery," *Fundamentals of Fluid Mechanics*, **1**, John Wiley and Sons, New York.
[17] Stround, A. H., 1971, *Approximate Calculation of Multiple Integrals*, Prentice-Hall, Englewood Cliffs, NJ.
[18] Gradshteyn, I. S., and Ryzhik, I. M., 2000, *Table of Integrals, Series and Products*, Sixth Ed., Academic Press, San Diego, CA.
[19] Lubin, B. T., and Springer, G. S., 1967, "The Formation of a Dip on the Surface of a Liquid Draining From a Tank," J. Fluid Mech., Part 2, **29**, pp. 385–390.
[20] Miloh, T., and Tyvand, P. A., 1993, "Nonlinear Transient Free Surface Flow and Dip Formation Due to Point Sink," Phys. Fluids A, **5**(6), pp. 1368–1375.
[21] Xue, M., and Yue, D. P., 1998, "Nonlinear Free Surface Flow Due to an Impulsively Started Submerged Point Sink," J. Fluid Mech., **364**, pp. 325–347.

Air Entrainment Processes in a Circular Plunging Jet: Void-Fraction and Acoustic Measurements

H. Chanson
Reader,
Fluid Mechanics, Hydraulics and Environmental Engineering,
Department of Civil Engineering,
The University of Queensland,
Brisbane QLD 4072, Australia
e-mail: h.chanson@uq.edu.au

R. Manasseh
Senior Research Scientist,
CSIRO Thermal and Fluid Engineering,
P.O. Box 56,
Highett VIC 3190, Australia
e-mail: richard.manasseh@dbce.csiro.au

Circular plunging jets were studied by both void fraction and acoustic techniques. There were two aims: to measure the structure of the jet flow and its regimes as a function of jet speed and free-jet length; and to develop and validate the acoustic measurement technique in the developing flow. Void fractions and bubble count rates were measured in the developing shear layer of a large-size plunging jet ($d_1 = 25$ mm). The data compared well with a solution of an advective diffusion equation and showed an increased air entrainment rate with increasing free-jet length for $x_1/d_1 \leqslant 12$. The acoustic data were processed by a novel technique to extract both bubble count and bubble size data. Three plunging jet flow regimes were noted. Near inception, acoustic pulses are isolated and indicate individual bubble entrainment as observable visually. Above a characteristic jet velocity, the number of the bubble pulses increases sharply although bubbles are still produced intermittently. At higher velocities, bubble production becomes quasi-continuous. The study suggests that an acoustic technique calibrated through detailed laboratory measurements can provide useful, absolute data in high-void fraction flows. The robust acoustic sensor can then be used in hostile industrial or environmental flows where more delicate instruments are impractical. [DOI: 10.1115/1.1595672]

Introduction

Plunging jet entrainment is a highly efficient mechanism for producing large gas-liquid interfacial areas. Applications include minerals-processing flotation cells, waste-water treatment, oxygenation of mammalian-cell bioreactors, riverine re-oxygenation weirs and the understanding of plunging ocean breakers, [1–3]. While detailed air-water flow measurements were conducted in a two-dimensional plunging jet, [4–6], most studies of air entrainment processes at circular plunging jets have been qualitative (Table 1, [2,7,8]). It is understood that plunging jet entrainment takes place when the jet impact velocity exceeds a critical velocity, [9,10]. For larger jet velocities, the developing region of plunging jet flow is subjected to strong interactions between the entrained air bubbles and the momentum transfer mechanism, [11].

While intrusive probe measurements (e.g., conductivity and optical probes that pierce the bubble) give local flow properties including void fraction and bubble count rate, the acoustic technique may provide useful information on the bubble size distribution, the onset of bubble entrainment and the entrainment regime. Bubbles generate sounds upon formation and deformation, [12,13], that are responsible for most of the noise created by a plunging jet. Most underwater acoustic sensors are made from robust piezoelectric crystals and a key advantage is their robustness for use in the field and in hostile environments.

This study is based upon a comparison of conductivity probe and acoustic measurements in the developing flow region of a large plunging jet system. Although the present acoustic technique was originally calibrated against precision laboratory photographs of rapidly produced bubbles, [14], comparisons with intrusive measurement techniques are limited. Furthermore, there are serious questions in interpreting acoustic signals when void fractions are high or bubbles form a fine cloud, [15]. The present work takes further steps towards an acoustic signature technique for characterizing the performance of a bubbly flow system with large void fractions in which both acoustics and intrusive properties of a bubbly shear flow are accurately documented.

Experimental Apparatus and Methods

The experimental apparatus (Fig. 1) consisted of a fresh water circular jet issuing from a 0.025 m diameter nozzle. The receiving channel was 0.3 m wide and 1.8 m deep with glass side walls 10 mm thick. The nozzle was made of aluminum with a 1/2.16 contraction ratio designed with an elliptical profile. Upstream of the nozzle, water was supplied by a straight circular pipe (0.054 m internal diameter, 3.5 m long). The jet and pipe were vertical to within ± 0.5 deg. The water supply (Brisbane tap water) was provided by a constant-head tank with a water level about 12.9 m above the nozzle. The apparatus provided nozzle velocities between 0.3 and 7 m/s. Further information were presented by Manasseh and Chanson [16].

Instrumentation. The discharge was measured with an orifice meter (British Standards design) calibrated on-site with a volume-per-time technique. The error on the discharge measurement was less than 1%.

All measurements were taken on the jet diameter through the centerline. The displacement of the probes in the flow direction and in the direction normal to the jet centerline was controlled by fine adjustment travelling mechanisms and measured with two Lucas Schaevitz Magnarules Plus MRU-012 and MRU-036. The error in the probe position was less than 0.1 mm in each direction.

In the free-falling jet, clear water jet velocities and turbulent velocity fluctuations were measured using a Prandtl-Pitot tube (diameter 3.3 mm) and a conical hot-film probe system. The Prandtl-Pitot tube was connected to a Validyne pressure transducer scanned at 500 Hz. The miniature hot-film probe (Dantec 55R42, 0.3 mm size) was scanned at 40 kHz. It was initially calibrated

Contributed by the Fluids Engineering Division for publication in the JOURNAL OF FLUIDS ENGINEERING. Manuscript received by the Fluids Engineering Division Oct. 16, 2001; revised manuscript received Mar. 10, 2003. Associate Editor: L. Mondy.

Table 1 Experimental flow conditions of circular vertical plunging jets. x_1: longitudinal distance between the nozzle and the free-surface pool; Tu_1: jet turbulence intensity at impact; Tu_o: turbulent intensity measured at jet nozzle; (—): information not available; N/a: not applicable.

Ref. (1)	Run (2)	x_1 m (3)	V_1 m/s (4)	d_1 m (5)	Tu_1 (6)	Comments (7)
Lin and Donelly [40]		0.020	0.8 to 2.04	0.002 to 0.008	—	Liquids: water, oil, glycol
Ervine et al. [9]		up to 5	0.8 to 9	—	—	$d_o=0.006$ to 0.025 m. $Tu_o=0.3$ to 8%
McKeogh and Ervine [29]		—	2.5 to 3.3	0.009	—	Fig. 6 ($Tu_o=5\%$), Fig. 8 ($Tu_o=1\%$) & Fig. 9 ($Tu_o=1\%$)
Van de Donk [41]		0.20	4.47 to 10.2	0.0057	—	Fig. 3.22 and 3.23
Detsch and Sharma [28]		—	1 to 7	—	—	$d_o=0.0015$ to 0.002 m. Liquids; water, salt water, ethanol, ethylene glycol solutions
Bonetto and Lahey [27]		0.01 and 0.03	5.3 to 7.9	0.0051	—	Figs. 11, 13, and 16
Elhammoumi [21]		0.29	3.1 and 3.7	0.0073 & 0.012	—	$Tu_o=0.0001$ to 0.0028%
Present study						$d_o=0.025$ m. Tap water ($\sigma=0.055$ N/m).
	BM013	0.005	0.52	0.0224	0.012	Onset of air bubble entrainment
	BM08	0.023	0.87	0.0200	0.0098	Onset of air bubble entrainment
	BM09a	0.10	1.58	0.0171	0.0047	Onset of air bubble entrainment
	BM09b	0.20	2.10	0.0145	0.004	Onset of air bubble entrainment
	BM03	0.02	1.27 to 5.85	N/a	N/a	Observations of bubble penetration depth
	BM01	0.1	1.68 to 5.01	N/a	N/a	Observations of bubble penetration depth
	BM04	0.2	2.24 to 5.85	N/a	N/a	Observations of bubble penetration depth
	RM3	0.005	0.94 to 5.0	N/a	N/a	Acoustic measurements. Hydrophone location: $r/d_1=0.5$ & 1.5, $x-x_1=0.02$ & 0.05 m.
	RM1	0.02	5.0	—	0.0035	Acoustic measurements. Hydrophone location: $r/d_1=0.5$ & 1.5, $x-x_1=0.02$ & 0.05 m.
	RM12	0.1	1.69 to 4.32	N/a	N/a	Acoustic measurements. Hydrophone location: $r/d_1=0.5$, $x-x_1=0.02$ m.
	RM20	0.3	4.57 to 4.75	N/a	N/a	Acoustic measurements. Hydrophone location: $r/d_1=0.5$, $x-x_1=0.02$ m.
	BM31_1	0.005	3.1	0.0249	0.0034	Resistivity probe measurements
	BM4_1	0.005	3.9	0.0250	0.0034	
	BM44_1	0.005	4.4	0.0250	0.0031	
	BM5_1	0.005	4.96	0.0250	0.0032	
	BM5_2	0.02	4.99	0.0249	0.0035	
	BM35_1	0.1	3.5	0.0239	0.0039	
	BM4_2	0.1	4.1	0.0242	0.0046	
	BM44_2	0.1	4.4	0.0243	0.0095	
	JV5	0.1	5	0.02455	0.0095	
	JV6	0.1	6	0.0247	—	
	BM5_3	0.2	4.986323	0.0240	0.0079	

with the Pitot tube data and the velocity distribution was checked with the measured flow rate (within 2%) for jet velocities ranging from 1 to 5 m/s.

A single-tip resistivity probe (inner electrode 0.35 mm and outer electrode 1.42 mm) was used to measure void fraction and bubble count rates in the plunging jet flow. The probe was excited by an air bubble detector (Ref. AS25240) with a response time less than 10 μs. Measurements were recorded with a scan rate of 5 kHz for 180 s.

Underwater acoustics were measured with a hydrophone (Brüel and Kjær type 8103) connected to a charge amplifier (Brüel and Kjær type 2635). The hydrophone was located at $r/d_1=0.5$ and $x-x_1=0.02$ m for most experiments (Table 1, column 7), where r is the radial distance measured from the jet centerline, d_1 is the jet diameter at impact, x is the longitudinal distance, and x_1 is the free jet length (Fig. 1(*a*)). A digital audio tape (DAT) recorder (Sony TCD-D7) digitized the signal at 44.1 kHz, implying an alias frequency of about 22 kHz. The range of jet conditions caused a difference in acoustic signal power of up to 20 dB (a factor of 10 in amplitude) between experiments. Since all data recorded on tape should have similar magnitudes to avoid distortion or loss of dynamic range, the charge amplification was set for each experiment to deliver optimal recorded quality and corrected for during the signal processing. DAT recordings were processed with a HP35670A dynamic signal analyzer. Fast Fourier transforms (FFTs) were taken. Each experimental dataset was subsampled into 500 sets 15.6 ms long to give a frequency span of 0–25.6 kHz. The data were also processed by a bubble-acoustic software StreamTone, [17].

Experimental Errors. The error on the void fraction C was estimated as $\Delta C/C\sim 3\%$ for $C\geqslant 5\%$ and $\Delta C/C\sim 0.5\%/C$ for $C\leqslant 5\%$. The minimum detectable bubble chord length is about 0.3 mm with the resistivity probe and also with the acoustic analysis. The accuracy of clear-water velocity V was about $\Delta V/V=1\%$. For the acoustic data, 95% confidence limits were calculated for the averaged spectrum for each run. At low speeds ($V_1<2.5$ m/s where V_1 is the jet velocity at impact), the acoustic signal was very intermittent. Although the representativity of these runs could not be checked, their averaged spectrum appeared statistically stationary within 500 samples. At higher speeds, statistical stationarity was easily obtained within 500 samples, while the StreamTone software gave an error in repeatability of less than 1% on bubble size, which was less than the 95% statistical confidence interval on the mean.

Experimental Flow Conditions. The flow conditions are summarized in Table 1, showing the flow rate Q_w, the free-jet

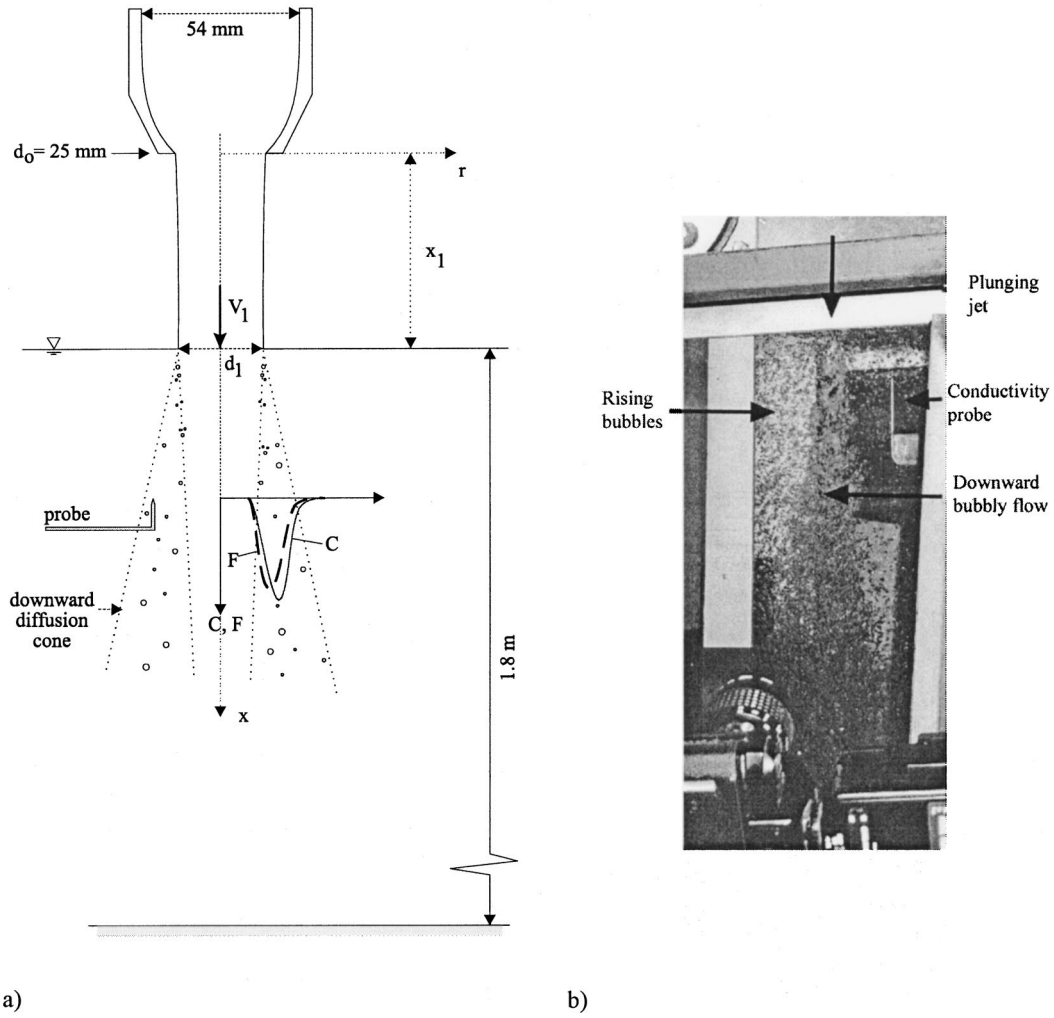

Fig. 1 Vertical circular plunging jet apparatus. (*a*) Sketch of the apparatus, (*b*) high-speed photograph for V_1=3.3 m/s, x_1=0.1 m.

length x_1, the impact flow velocity V_1, and diameter d_1. For each test, the water jet was extremely smooth and transparent. No air entrainment was visible upstream of the impingement point. Velocity and velocity fluctuation distributions, performed 5 mm downstream of the jet nozzle, were uniform for nozzle velocities ranging from 0.5 to 5 m/s. In the present study, the free-jet lengths ranged from 0.005 up to 0.3 m, and the impingement velocities were between 0.5 and 6 m/s.

The turbulence intensity of the water jet core was measured on the centerline at the impingement point. The data suggest that the turbulence level decreased with increasing jet speed for a given jet length (Table 1, column 6). For a constant plunge velocity, the turbulence increased gradually with the free-jet length for $0.2 \leqslant x_1/d_1 \leqslant 8$.

Physical Modeling and Scale Effects. In a physical model, the flow conditions are said to be similar to those in the prototype if the model displays similarity of form, similarity of motion, and similarity of forces. Dynamic similarity of plunging jet flows is, however, complex because of a variety of factors such as flow aeration, interactions between entrained bubbles and developing mixing layer, and others. In a geometrically similar model, true dynamic similarity is achieved only and only if each dimensionless parameter (or Π-terms) has the same value in both model and prototype. For example, for small facilities, bubble entrainment is strongly dependent on the scale of the experiment, [2,18,19]. For civil and environmental engineering applications, the latter recommended the use of model scales ranging from 10/1 to 1/10 to avoid significant scale effects, [2]. Conversely experimental results obtained in a large size facility cannot be down-scaled. In the context of this study, a large-size plunging jet facility (d_1 = 25 mm, pool depth: 1.8 m) was used to minimize scale effects when the results are upscaled to larger industrial facilities.

Air Bubble Entrainment Regimes

In a plunging jet, air bubbles start to be entrained when the jet impact speed V_1 exceeds a critical value. McKeogh [20] showed that the inception speed decreases with increasing jet turbulence for a given jet configuration.

In the present study, inception of bubble entrainment is defined as the threshold at which one bubble is entrained during a 3-minute period. Results are presented in Tables 1 and 2. Air bubble entrainment was detected visually and photographically for V_1 between 0.55 and 2.1 m/s while acoustic measurements were made up to 5.0 m/s. The data show that the inception velocity increases with increasing free-jet height x_1 which corresponds to a decrease in jet turbulence intensity (Table 1). The result is consistent with previous observations, [9,10,21], although it does not follow a conceptual model of increased free-jet surface roughness, [22,23].

For $V_1 > 0.7$ m/s, visual and photographic observations suggest three entrainment regimes, summarized in Table 2. In Regime I (i.e., for impact speeds slightly greater than the inception speed),

Table 2 Characteristic jet impact velocity V_1 (m/s) for the transitions between three entrainment regimes

x_1 (m) (1)	Inception (2)	V_1 (m/s) RI–RII (3)	RII–RIII (4)
0.005	0.52	1.0	3.5–5
0.023	0.87	—	—
0.10	1.58	1.7	2.5
0.20	2.10	—	—

fine individual bubbles are irregularly entrapped. The time interval between successive entrapment events may reach up to few minutes, as previously observed by Cummings and Chanson [10] for a plane jet. The entrapment process is distinctly audible using the hydrophone. Although some bubble trajectories are vertical, most entrained bubbles tend to follow a slightly helicoidal trajectory, consistent with previous studies, [24–26]. Note that void fraction measurements were inaccurate in Regime I because the void fraction was less than 0.1%.

With an impact speed of about 1.0 m/s for $x_1=5$ mm, an unstable air cavity starts to develop at one point along the impingement perimeter (Regime II). The air cavity position changes with time in an apparently random manner. Larger air packets are entrained below the air cavity with the stretching and breakup of the cavity tip.

At larger speeds (above about $V_1=3.5$ to 5 m/s for $x_1=5$ mm), the air cavity develops all around the perimeter and most air is entrained by elongation, stretching and breakup of the ventilated cavity (Regime III). Bonetto and Lahey [27], Cummings and Chanson [4], and Chanson and Brattberg [11] elaborated on this regime. Visually most entrained air bubbles/packets tend to follow a somewhat helicoidal trajectory. The rotation direction fluctuates irregularly at a low frequency (less than 0.5 Hz). Similar bubble trajectory rotation fluctuations were studied in detail by Yoshida et al. [25]. Furthermore, the direction seems related to the rotation sense of the free-surface vortex. Detsch and Sharma [28] reported a similar effect. Regime III is common in industrial processes.

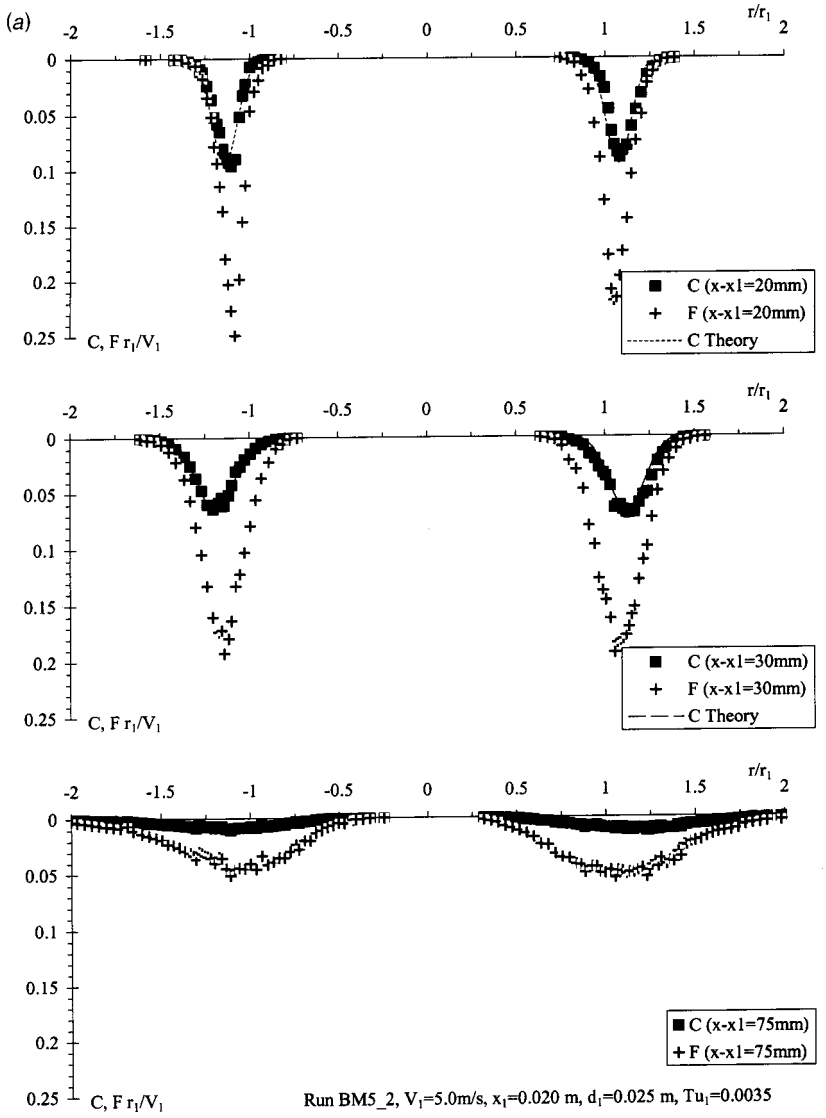

Fig. 2 Dimensionless distributions of void-fraction and bubble count. Dashed line is solution of Eq. (1). Tu_1 is turbulence intensity based on longitudinal velocity fluctuations at jet impact. *(a)* **Jet height, $x_1=20$ mm, jet velocity $V_1=5.0$ m/s, $Tu_1=0.35\%$.** *(b)* **Jet height $x_1=100$ mm, jet velocity $V_1=3.5$ m/s, $Tu_1=0.39\%$.**

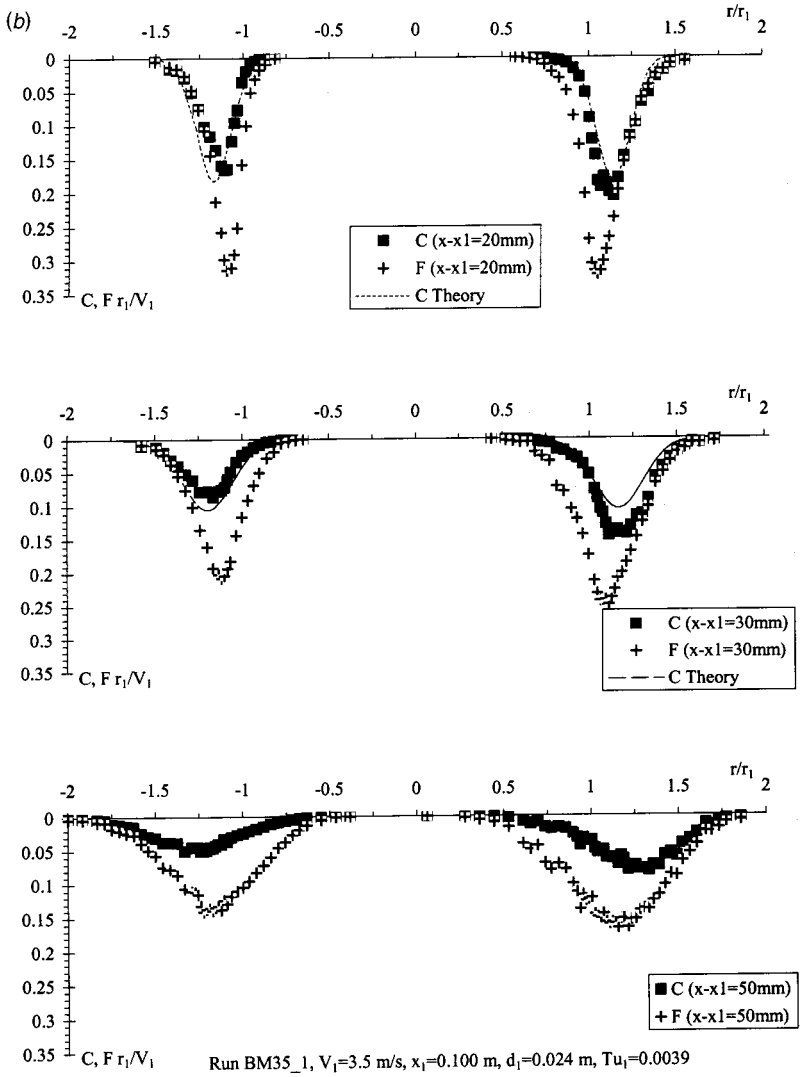

Fig. 2 (***continued***)

Spatial Distributions of Void Fraction and Bubble Count Rate

Void-fraction measurements show the advective dispersion of the entrained air bubbles in the developing flow region. Void fraction and bubble count rate data are presented in Fig. 2, for two impact flow velocities ($V_1=5.0$ and 3.5 ms) and free-jet lengths ($x_1=0.02$ and 0.1 m, respectively). Results for other velocities and free-jet lengths show similar curves and can be found in Manasseh and Chanson [16].

The distributions of void fraction are consistent with the earlier studies by McKeogh and Ervine [29] and Bonetto and Lahey [27] with 9 mm and 5.1 mm circular jets, respectively. The data compare favorably with a simple analytical solution of the advective diffusion solution,

$$C=\frac{Q_{\text{air}}}{Q_w}\frac{1}{8D^{\#}X}\exp\left(-\frac{R^2+1}{8D^{\#}X}\right)I_o\left(\frac{R}{4D^{\#}X}\right), \qquad (1)$$

where Q_{air} is the quantity of entrained air, Q_w is the water jet flow rate, $D^{\#}=2\,D_t/(V_1 d_1)$, D_t is the advective diffusion coefficient, $X=(x-x_1)/d_1$, $R=2\,r/d_1$, x is the distance along the flow direction measured from the jet nozzle, r is the radial distance from the jet centerline, and I_o is the modified Bessel function of the first kind of order zero, [2]. For each run, the values of Q_{air}/Q_w and $D^{\#}$ were determined from the best fit of the data to Eq. (1). Note that the data were best fitted by assuming $R=2\,(r+\delta r)/d_1$ where $\delta r>0$ increases with increasing distance x for a given experiment. For very low entrainments rates (e.g., Fig. 6(*a*)), void fraction distributions exhibited some dissymmetry which might be attributed to a feedback mechanism between the probe and developing vortices. It is hypothesized that the probe support interfered with the developing shear region, preventing the development of helicoidal vortical structures. In turn air entrapment was affected and found to be lesser on one side or another.

Bubble count rates were also measured at each point. Typical distributions are shown in Fig. 2. For a given void fraction and velocity, the bubble count rate is inversely proportional to the bubble diameter and proportional to the specific interfacial area, [30,31]. It provides additional information on the bubbly flow structure.

In the developing flow region, the void fraction distribution exhibits a peak ($C=C_{\max}$) at $r=r_{C_{\max}}$ at a given cross section (x constant). The distributions of bubble count rate F also show a maximum ($F=F_{\max}$) in the developing flow region, but at $r=r_{F_{\max}}$, where $r_{C_{\max}}$ and $r_{F_{\max}}$ are significantly different. For $(x-x_1)/d_1<8$ and all jet lengths, the bubble count peak was consistently on the inside of the void-fraction peak: i.e., $r_{F_{\max}}<r_{C_{\max}}$. The result is consistent with the observations of Brattberg and Chanson [6] for a plane jet.

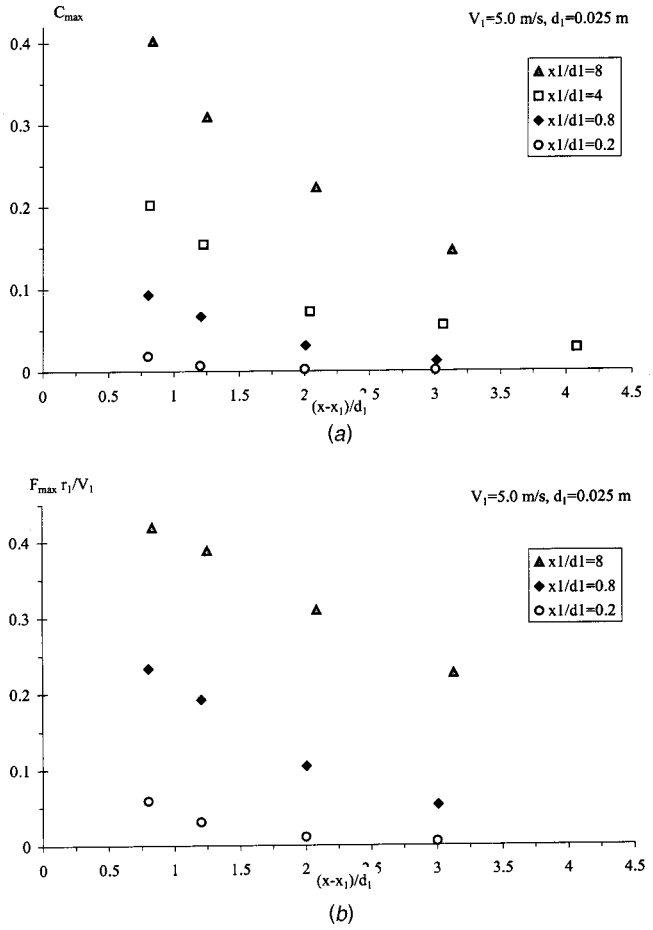

Fig. 3 Effect of the free jet length on the maximum void-fraction and bubble count. (*a*) Maximum void fraction, (*b*) maximum dimensionless bubble count.

Figure 3 illustrates the effect of the free-jet length x_1 on the maximum void fraction and bubble count. The data were recorded for an identical impact velocity V_1 at several vertical depths. The results show that the air entrainment rate increases with increasing jet length. It is proposed that short jet lengths (e.g., $x_1/d_1<0.2$ to 0.8) prohibit the development of large vortical structures with scale comparable to the jet diameter, hence preventing the development of free-jet turbulence favorable to bubble entrainment at the plunge point. For long free-jets, Van de Sande and Smith [32] suggested that interfacial aeration of the free-jet may contribute significantly to an increase in air entrapment. During the present study, the free-jet was visually transparent for $x_1/d_1<40$ and all investigated jet velocities.

Although the maximum void fraction and count rate become small for $(x-x_1)/d_1>5$ to 7 (Fig. 3), individual bubbles were seen at much greater depths (Fig. 1(*b*)). Millimetric bubbles were seen at depths of $(x-x_1)/d_1=30$ to 75 for free-jet lengths x_1 increasing from 5 to 200 mm, respectively. For the longest jet length, the observation was close to the results of Clanet and Lasheras [33]. However, fine bubbles (sizes less than 0.5 to 1 mm) were consistently observed at deeper depths for impact velocities greater than the onset velocity. Visual observations showed that tiny bubbles could be trapped in large vortical structures for several minutes, before being ejected to another vortical structure or toward the free surface. Some bubbles could stay near the flume bottom more than five minutes.

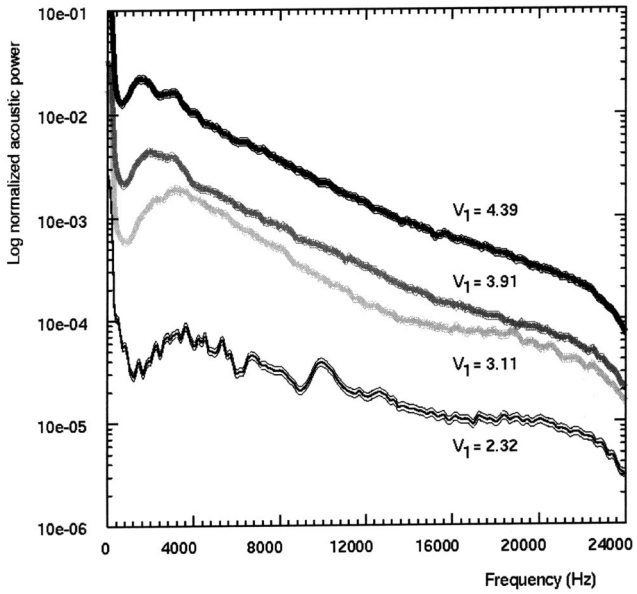

Fig. 4 Acoustic spectra, jet height $x_1=5$ mm after [16]

Acoustic Analysis of Entrainment Regimes

Acoustic Spectrum and Bubble Size Measurements. The acoustic data were analyzed following principles detailed elsewhere, [13,17]. Two techniques were used: a continuous, spectral analysis following Pandit et al. [34], and a discrete, pulse-wise analysis following the ''first-period'' method of Manasseh et al. [17]. The spectral analysis utilizes all bands of the signal, offering an overall ''signature'' of the system. However, the conversion to bubble-size spectra relies on a questionable assumption: that bubbles of different sizes are perturbed to the same proportional extent. The pulse-wise analysis can give greater accuracy on the true bubble frequencies, and offers the benefit of bubble count-rates, giving the Sauter-mean diameter of practical interest. However, in correcting the pulse-wise distributions to account for the greater amplitude of large bubbles, exactly the same questionable

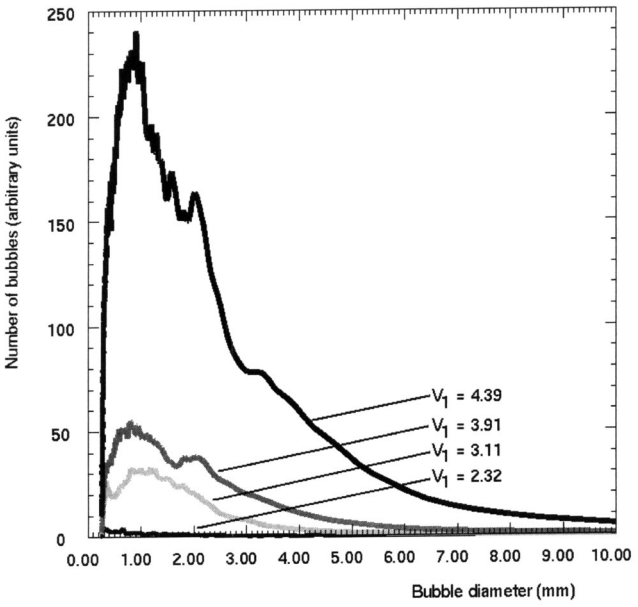

Fig. 5 Bubble-size spectra, jet height $x_1=5$ mm after [16]

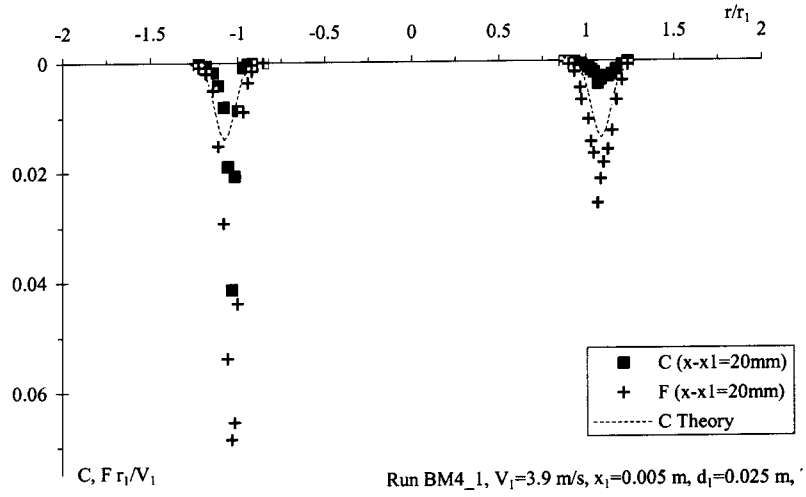

(*a*)

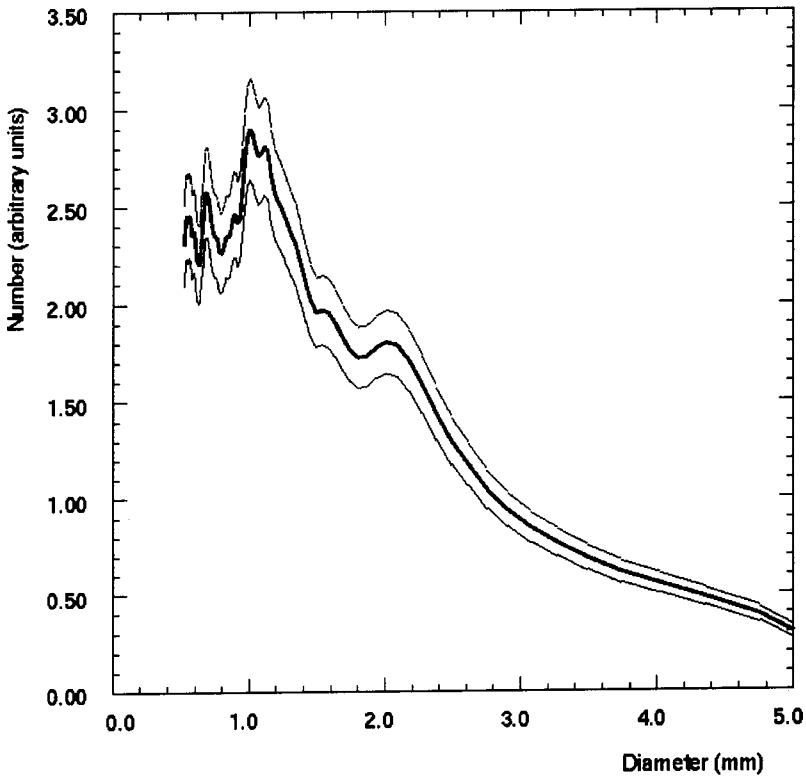

(*b*)

Fig. 6 Void-fraction, bubble count, and detailed bubble size spectrum, jet height $x_1 = 5$ mm, speed $V_1 = 3.9$ m/s. Dashed line in (*a*) is solution of Eq. (1). Tu_1 is turbulence intensity based on longitudinal velocity fluctuations; (*b*) after [16].

assumption on bubble excitation must be made. Both techniques also assume the bubble do not interact acoustically. Aspects of the techniques relevant to the present study are detailed in the Appendix.

Typical acoustic spectra are shown in Fig. 4 for the same geometric conditions ($x_1 = 0.005$ m, $x - x_1 = 0.020$ m, $d_1 = 0.025$ m) as in Fig. 6(*a*), and for several jet velocities. Each spectrum was normalized to its integral. Since different amplifications were used for some experiments, the normalized spectra were shifted in the vertical to account for the amplification used during each experiment, ensuring that comparisons between experiments with different amplifications were valid.

In Fig. 4, the ordinate is a logarithmic scale and fine lines bracketing the central lines indicate the bounds of 95% statistical confidence intervals. High-velocity experiments exhibit higher acoustic energy, illustrating a louder underwater noise. Each spectrum shows a minimum in energy at roughly 400 Hz, indicating that low-frequency noise probably due to background turbulence is below 400 Hz. In Regime II (e.g., $V_1 = 2.32$ m/s), individual bubble signals were very clear to the ear (in other words, a time series of the sound would show a series of clearly separated pulses); and a broad peak was centered around $f = 3.6$ kHz. Such a frequency corresponds to bubbles around 1.8 mm in diameter (Appendix Eq. (4)). With increasing jet speed, the frequency peak

shifted to lower frequencies. For the highest jet speed in Regime III, (i.e., $V_1=4.4$ m/s, Fig. 4), the peak was at about $f=1.7$ kHz, corresponding to bubbles about 3.8 mm in diameter. Since all peak frequencies were greater than the low-frequency noise found below 400 Hz, no high-pass filtering was required.

The bubble-size spectra may be derived from the acoustic spectra. Figure 5 presents the bubble-size spectra for the acoustic data shown in Fig. 4. (Figure 6(*b*) shows one of the curves of Fig. 5, for $V_1=3.9$ m/s, in better detail.) A major difference is the large number of bubbles in Regime III ($V_1=4.4$ m/s). For all acoustic experiments, the bubble-size spectra show a distinctive peak in the production of bubbles around 1 mm in diameter. Chord-length data for related two-dimensional flows showed also a peak around 1 mm, [5]. The aliasing frequency of the equipment of 22 kHz implies a cutoff to bubbles below 0.3 mm in diameter. Since the peaks in Fig. 4 fall off well before 0.3 mm, it is believed that they are genuine peaks subject only to the uncertainties of the assumptions in the analysis.

In Fig. 5, there is a second peak around 2.0 mm diameter for the larger-velocity data (i.e., $V_1=4.4$ and 3.9 m/s), while there is a smaller but significant third peak at about 1.6 mm in the $V_1=4.4$ m/s data. The corresponding ratio 2.0/1.6 is about the cube root of two. It could be inferred that, in Regime III, pairs of 1.6 mm bubbles are coalescing to form 2.0 mm bubbles, or alternatively that 2.0 mm bubbles are breaking up, [10,35]. However Cummings and Chanson [35] never observed bubble coalescence for $x-x_1<0.2$ m in a planar plunging jet. Both video and still photographs highlighted breakage only. Figure 6 shows acoustic and void-fraction data for one experiment: that is, $V_1=3.9$ m/s (Regime III). The resistivity probe data are shown in Fig. 6(*a*) while acoustic data are shown with 95% statistical confidence intervals in Fig. 6(*b*).

The spectral method of measuring bubble size has a number of disadvantages, [17]. Among these is the absence of data on bubble counts, readily provided by the resistivity probe. A quantity of practical interest to chemical engineers is the Sauter mean diameter:

$$D_{32}=\frac{\Sigma_{i=1}^{n}D_i^3}{\Sigma_{i=1}^{n}D_i^2} \tag{2}$$

where D_i is the diameter of a bubble and n is the total number of bubbles detected. In industry, D_{32} has traditionally been calculated by sampling individual bubbles and measuring them optically. A technique based on measurements of individual bubbles, rather than overall spectra, would be compatible with industrial experience, since it would enable the Sauter-mean diameter to be calculated and compared with optical measurements where those are available. Manasseh et al. [17] proposed an alternative ''first-period'' method providing the distribution of bubble sizes based on the identification of individual bubble pulses. The data can be used to infer bubble count rates and the Sauter mean diameter as well as a size distribution (Appendix).

The acoustic bubble count rate was calibrated based upon the count rates measured by the resistivity probe for identical flow conditions. The similar cutoff bubble size of 0.3 mm may help to match the two techniques. A typical distribution is shown in Fig. 7; its features are reproducible in multiple samples of data from the same settings. The trigger levels were scaled by the amplification used during each experiment. The location of the peaks in the corrected distributions (e.g., Fig. 7) are consistent with the frequency spectra (e.g., Fig. 6). (The distribution cuts off below 0.5 mm and above 3.3 mm owing to the windowing process by which the pulses were processed.) Figure 7, however, provides more details which may stem from the greater accuracy of the first-period method, [14]. The peak around 1 mm is in fact a double peak with subpeaks at 0.80 and 1.04 mm. Since the ratio of these sizes is close to the cube root of two, there may be a tendency for the 1.04 mm bubbles to split into two equal daughter bubbles, [10,35].

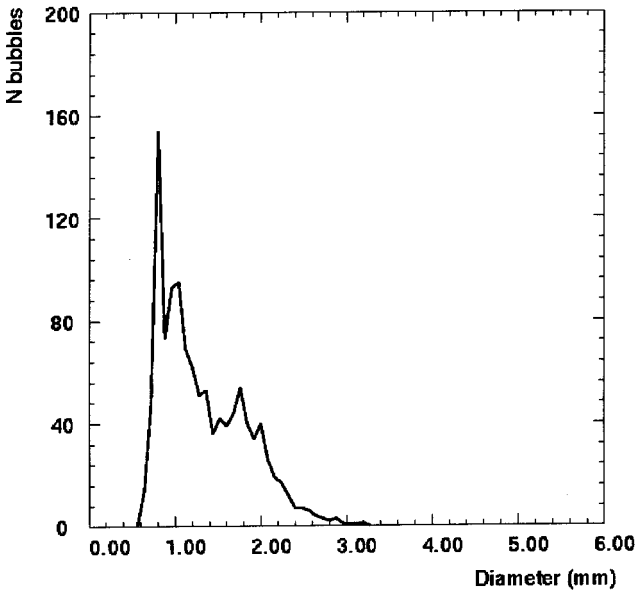

Fig. 7 Bubble-size distribution, jet height $x_1=5$ mm, speed $V_1=3.9$ m/s (acoustic data after [16])

The variations of bubble count rate F, mean corrected bubble size D_1, and Sauter mean diameter D_{32} are shown in Fig. 8 as functions of the jet velocity at impact. Each acoustic data point is based on the analysis of four minutes of data. The vertical error bars represent 95% statistical confidence intervals on the acoustic measurement. The bubble count rate data highlight the transition from Regime II to Regime III, with a sudden increase in bubble production (i.e., bubble count rate) at around $V_1=2.5$ m/s. This is heard as a change from individual ''plinking'' sounds to a ''rushing'' sound. The bubble count rate appears to be maximum around $V_1=3$ m/s (Fig. 8).

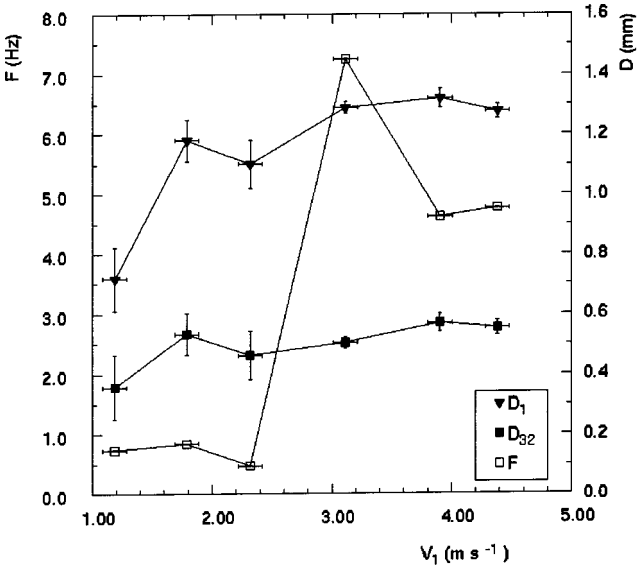

Fig. 8 Bubble count rates and diameters as a function of jet speed V_1, jet height $x_1=5$ mm (acoustic data)

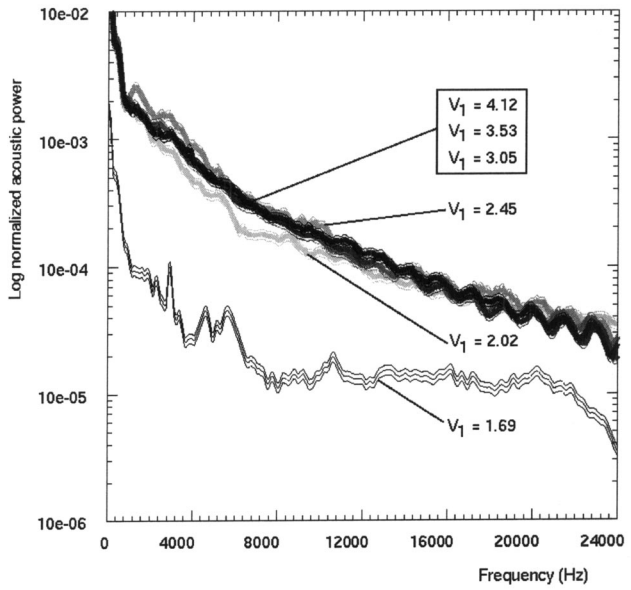

Fig. 9 Acoustic spectra, jet height $x_1 = 100$ mm

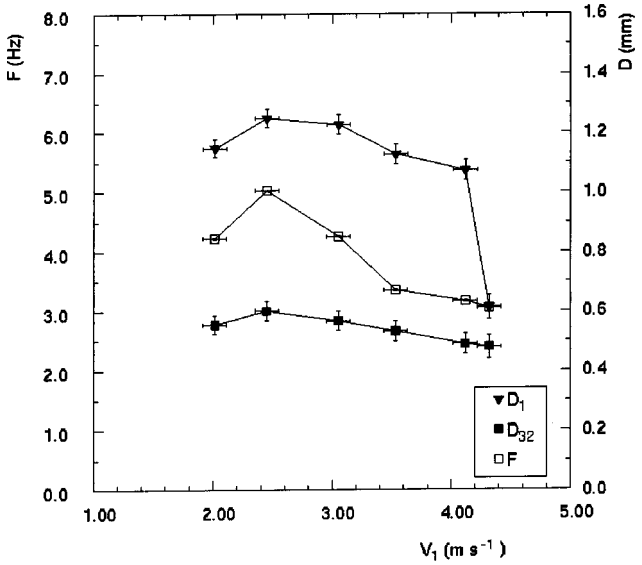

Fig. 11 Bubble count rates and diameters as a function of jet speed V_1, jet height $x_1 = 100$ mm

Effect of Jet Height on Acoustic Data. The above results were focused on experiments with a constant jet height x_1. Figure 9 presents data for a larger jet height of $x_1 = 0.1$ m. The data show that Regime II occurs at a lower jet velocity V_1 compared to the experiments with $x_1 = 0.005$ m (Table 2). The spectrum in Regime II has significantly less power than the spectra in Regime III (e.g., $V_1 = 3.9$ m/s) simply reflecting the fact that bubbles are not produced continually.

Although the boundary between Regime II and Regime III is detectable by ear between 2.0 and 2.4 m/s, there is little significant difference in the spectra for $V_1 > 2$ m/s. This is a marked contrast to the spectra for $x_1 = 0.005$ m, when increasing V_1 above the inception condition continues to increase the total sound power produced. The spectra also decay relatively monotonically.

In Fig. 9, there is some high-frequency noise in the system above about 14 kHz, the source of which is unknown. There might be aliased high-frequency energy in the data. It may be that, with the higher jet height of 100 mm, the bubble-size distribution becomes fixed (''saturated'') at a lower jet velocity. If this is the case, the effect of increasing the jet height is to decrease the importance of variations in the jet speed V_1, at least as far as the bubble-size distribution is concerned (Fig. 10). The bubble count rate F, mean corrected bubble size D_1 and Sauter-mean diameter D_{32} show a similar lessening of the importance of V_1 (Fig. 11): The sudden jumps in the curves at the low jet height no longer occur, since the transition from one regime to the next is not so marked at the high jet height.

The software measuring the bubble count rate based upon acoustic data can process up to 20 bubbles per second. It is unlikely that the maximum around six counts per second represents a saturation of the measurement system. An identical analysis protocol was used for each impact velocity V_1, with the straightforward correction for different amplifications during recording being the only variation. Since increasing the jet speed at a given height demands greater pumping costs, these results suggest that as long as the jet height exceeds a threshold, the jet speed could be fixed at a low level for the same aeration benefit.

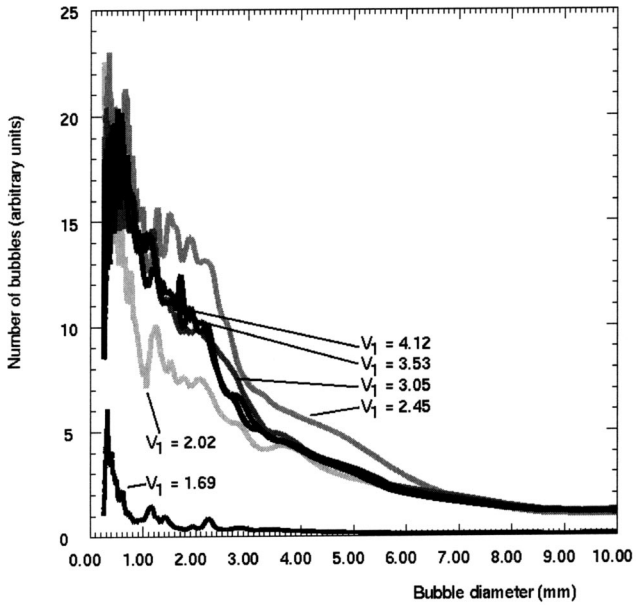

Fig. 10 Bubble-size spectra, jet height $x_1 = 100$ mm

Conclusions

Measurements in a large circular plunging jet flow show that there are three distinct regimes of air entrainment. These regimes are visually observable and boundaries between the second and third regimes are easily detectable acoustically. In the developing flow region, the spatial distributions of void fraction compares well with a solution of the advective diffusion equation (2) for all investigated flow conditions. Bubble count rate distributions exhibit a somehow different shape (Fig. 2) and there is a spatial offset in the peak of void fraction and bubble count, as with other two-dimensional plunging jet flows. The effects of the free-jet length were studied. The results showed an increased entrainment rate and increased dimensionless bubble count rate with increasing jet length for $x_1/d_1 \leqslant 12$.

Acoustic data reveal a bubble size population with a maximum probability around 1 mm in diameter, consistent with resistivity probe data. Since the acoustic bubble size measurements are measurements of true bubble volume, their distributions can be used to infer the presence of bubble breakup or coalescence. The results also suggest that, if the jet height is raised, the air bubble entrainment becomes insensitive to jet speed. The practical implication is

that in industrial systems, there is a threshold jet height above which pumping harder does not improve the aeration.

The acoustic technique can be accurately calibrated for a rapidly formed stream of bubbles precisely produced under laboratory conditions, [14]. The assessment of its accuracy is difficult in complex, high void-fraction flows, where the inherent bias towards large bubbles and acoustic interactions of bubble clouds can make interpretation of the signals in terms of fundamental theory problematic. Development of the acoustic technique as a semi-empirical signature method requires making comparative measurements using an alternative technique. The acoustic technique has so far yielded useful *relative* bubble size data, for example spatial differences in bubble size in a complex, high void-fraction flow. The present results suggest that an acoustic technique calibrated through detailed laboratory measurements can also yield useful, *absolute* data in high-void fraction flows. Moreover the robust acoustic sensor can then be used to make absolute measurements in hostile industrial or environmental flows where more delicate instruments are impractical.

Acknowledgments

The first writer acknowledges the assistance of his former students T. McGibbon, B. Bolden, T. Brattberg, and L. Toombes. He thanks Prof. C. J. Apelt, University of Queensland who supported this project since its beginning.

Nomenclature

C = air concentration defined as the volume of air per unit volume of air and water; it is also called void fraction
$C_{\max}$ = maximum void fraction in a cross section
D = bubble size (m)
D_1 = corrected mean bubble size (m)
D_{32} = Sauter mean diameter (m)
D_o = equilibrium (spherical) bubble diameter (m)
D_t = turbulent diffusivity (m^2/s)
$D^{\#}$ = dimensionless turbulent diffusivity: $D^{\#}=D_t/(V_1 r_1)$ for circular jet
d = jet diameter (m) measured perpendicular to the flow direction
d_1 = jet diameter (m) at the impact with the receiving pool of liquid
F = bubble count rate (Hz) defined as the number of detected bubbles per second
$F_{\max}$ = maximum bubble count rate (Hz) in a cross section
f = acoustic frequency (Hz)
g = gravity constant: $g=9.80\ m/s^2$ in Brisbane, Australia
I_o = modified Bessel function of the first kind of order zero
P = sound pressure (Pa)
P_∞ = absolute liquid pressure (Pa)
p = instantaneous sound pressure (Pa)
Q_{air} = air discharge (m^3/s)
Q_w = water discharge (m^3/s)
R = dimensionless radial distance: $R=2\,r/d_1$
r = radial distance (m) from the jet centerline
$r_{C_{\max}}$ = radial distance (m) where $C=C_{\max}$
$r_{F_{\max}}$ = radial distance (m) where $F=F_{\max}$
r_1 = jet radius (m) at impact
Tu = turbulence intensity defined as: $\text{Tu}=u'/V$
Tu_1 = turbulence intensity on the jet centerline measured at jet impact
Tu_o = turbulence intensity measured at jet nozzle
u = dimensionless variable
u' = root mean square of longitudinal component of turbulent velocity (m/s)
V = velocity (m/s)
V_1 = mean flow velocity (m/s) at jet impact
X = dimensionless longitudinal distance: $X=(x-x_1)/d_1$
x = distance along the flow direction (m) measured from the jet nozzle
x_1 = distance (m) between the jet nozzle and the impact flow conditions
γ = ratio of specific heats for the gas
θ, θ' = radial angular coordinate
ρ = liquid density (kg/m^3)
$\varnothing$ = diameter (m)

Subscripts

air = air flow
w = water flow
o = nozzle flow conditions
l = impact flow conditions

Appendix

Derivation of Bubble Sizes From Acoustic Data

Bubble Size Spectra. The relationship between bubble size and acoustic frequency is

$$f=\frac{1}{\pi D_o}\sqrt{\frac{3\gamma P_\infty}{\rho}} \tag{3}$$

where f is the frequency in Hz, P_∞ is the absolute liquid pressure, γ is the ratio of specific heats for the gas, ρ is the liquid density, and D_o is the equilibrium (spherical) bubble diameter, [12]. For these experiments, Eq. (3) becomes

$$f=\frac{6.58}{D_o}. \tag{4}$$

It is important to note that the acoustic frequency emitted by bubbles is essentially a function of the *cube root of bubble volume*. Severe distortions to the shape of the bubble (e.g., into a 4:1 ellipsoid) alter the frequency predicted by Eq. (4) by only 8%, [36]. Moreover bubbles tend to emit sounds when at their most spherical state, [14].

An acoustic spectrum of frequencies f may be inverted to give a spectrum of bubble sizes D_o. However, it is not correct to simply plot the sound power spectrum against the reciprocal of frequency, as Eq. (4) would suggest. Larger bubbles are louder and contribute more to the sound power. A spectral analysis would be biased unless a correction is introduced. Assumptions are required in comparing the relative excitation of bubbles. Pandit et al. [34] proposed a simple treatment. The instantaneous sound pressure produced by a single bubble, $p(t)$, is given by

$$p(t)^2=\frac{1}{f^2}\,\frac{3\gamma P_\infty^3}{4\pi^2\rho(\gamma(\gamma-1)r)^2}\,Y(t)^2 \tag{5}$$

where r is the distance from the bubble and the time-dependent factor $Y(t)$ is given by

$$Y(t)=\left(\frac{4}{3}-\gamma\right)\left(\frac{D_o}{D(t)}\right)^{3\gamma-1}+\frac{1}{3}\left(\frac{D_o}{D(t)}\right)^3 \tag{6}$$

for adiabatic compression of the bubble, where $D(t)$ is the instantaneous bubble diameter. This analysis does not, of course, consider the damping of the bubble, which gives rise to a broadening of the spectrum produced by any individual bubble. However, since time constants for the decay of a bubble pulse are significantly longer than the acoustic period, typically by a factor of 10–20 (e.g., typical pulses in Manasseh, [14,37]), the effect is not significant. For the simultaneous oscillations of n identical bubbles, the resultant summed sound pressure P, which would be measured by a hydrophone, is given by

$$P^2 = n\overline{p}^2 \tag{7}$$

where $\overline{p}$ is the rms value of $p(t)$. Using Eq. (5), this yields the corrected value of the frequency spectrum, N, as

$$N = P^2 f^2 K \tag{8}$$

where K is a function of the degree of excitation of the bubbles and of the distance between the bubbles and the hydrophone. Because sound power falls off as $1/r^2$, only bubbles close to the hydrophone contribute to the measured sound. The degree of excitation of the bubbles $(D_o/\overline{D})$ might differ with bubble sizes. In a plunging jet flow, it is likely that bubbles are excited both by their initial formation and by background turbulence, and it might be reasonable to assume $(D_o/\overline{D})$ being a constant. The overall factor K was assumed constant by Pandit et al. [34] and in the present work.

Bubble Size Distributions. The alternative ''first period'' method depends on an adjustable trigger level which will tend to bias the results towards larger bubbles, equivalent to the bias in the above spectrum-inversion approach. Assumptions are required to correct the distribution. Following the reasoning in Manasseh et al. [17], the use of a trigger means that only bubbles within a critical radius of the hydrophone get detected. This critical radius depends linearly on the bubble size. Assuming that the spatial distribution of bubbles is independent of their size, the number n_d of bubbles of a given size can be adjusted to the true number N_d, by equalizing the critical volumes:

$$N_d = n_d \left(\frac{D_{\text{ref}}}{D_o} \right)^3 \tag{9}$$

where D_{ref} is any reference bubble diameter. The distribution $N(D_o)$ is then normalized to ensure the total number of bubble counts is the same. The mean D_1 of a corrected distribution will generally be lower than the mean D_o of the raw distribution.

As noted above, in the plunging-jet context the pulse-damping time constant is likely to be an order of magnitude greater than the acoustic period, so spectral broadening is not likely to be significant. Nonetheless, it is worth noting that the use of the first period virtually eliminates effects of spectral broadening on the results.

In a complex bubbly flow, an additional phenomenon will result in a distortion of the measured bubble sizes away from the true sizes. It is well known that as bubbles are brought closer together, their acoustic emission frequency drops, [38,39]. The cloud of bubbles tends to behave as a continuum—one large composite bubble which has a lower frequency. In a flow where many bubbles are close together, the measured bubble sizes will be greater than the true sizes. This effect is not explicitly corrected for in the analyses presented in this paper. However, the underlying algorithm used to generate the bubble size distributions was introduced after noting that it gave more accurate results than conventional techniques when bubbles were closer together, [17]. The interaction effect is thus reduced, but cannot be eliminated entirely.

References

[1] Jameson, G. L., 1995, ''Bubbly Flows and the Plunging Jet Flotation Column,'' *Proceedings of 12th Australasian Fluid Mechanics Conference*, R. W. Bilger, ed., Sydney, Australia, **2**, pp. 735–742.

[2] Chanson, H., 1997, *Air Bubble Entrainment in Free-Surface Turbulent Shear Flows*, Academic Press, London.

[3] Kolani, A. R., Oguz, H. N., and Prosperetti, A., 1998, ''A New Aeration Device,'' *Proceedings ASME Fluids Eng. Summer Meeting*, June 21–25, Washington, D.C., **257**, pp. 111–145.

[4] Cummings, P. D., and Chanson, H., 1997, ''Air Entrainment in the Developing Flow Region of Plunging Jets. Part 1: Theoretical Development,'' ASME J. Fluids Eng., **119**(3), pp. 597–602.

[5] Cummings, P. D., and Chanson, H., 1997, ''Air Entrainment in the Developing Flow Region of Plunging Jets. Part 2: Experimental,'' ASME J. Fluids Eng., **119**(3), pp. 603–608.

[6] Brattberg, T., and Chanson, H., 1998, ''Air Entrapment and Air Bubble Dispersion at Two-Dimensional Plunging Water Jets,'' Chem. Eng. Sci., **53**(24), pp. 4113–4127; Errata: 1999, **54**(12), p. 1925.

[7] Bin, A. K., 1993, ''Gas Entrainment by Plunging Liquid Jets,'' Chem. Eng. Sci., **48**(21), pp. 3585–3630.

[8] Ervine, D. A., 1998, ''Air Entrainment in Hydraulic Structures: a Review,'' Proceedings of Institute of Civil Engineers, *Water, Maritime & Energy*, UK, **130**, pp. 142–153.

[9] Ervine, D. A., McKeogh, E. J., and Elsawy, E. M., 1980, ''Effect of Turbulence Intensity on the Rate of Air Entrainment by Plunging Water Jets,'' Proceedings of the Institute of Civil Engineering., Part 2, June, pp. 425–445.

[10] Cummings, P. D., and Chanson, H., 1999, ''An Experimental Study of Individual Air Bubble Entrainment at a Planar Plunging Jet,'' Chem. Eng. Res. Des., **77**(A2), pp. 159–164.

[11] Chanson, H., and Brattberg, T., 1998, ''Air Entrainment by Two-Dimensional Plunging Jets: The Impingement Region and the Very-Near Flow Field,'' *Proc. 1998 ASME Fluids Eng. Conf.*, FEDSM'98, Washington, DC, June 21–25, FEDSM98-4806.

[12] Minnaert, M., 1933, ''On Musical Air Bubbles and the Sound of Running Water,'' Philos. Mag., **16**, pp. 235–248.

[13] Leighton, T. G., 1994, *The Acoustic Bubble*, Academic Press, London.

[14] Manasseh, R., 1997, ''Acoustic Sizing of Bubbles at Moderate to High Bubbling Rates,'' *Proc. 4th World Conference on Experimental Heat Transfer, Fluid Mechanics and Thermodynamics*, Brussels, 2–6, June.

[15] Boyd, J. W. R., and Varley, J., 2001, ''The Uses of Passive Measurement of Acoustic Emissions From Chemical Engineering Processes,'' Chem. Eng. Sci., **56**, pp. 1749–1767.

[16] Manasseh, R., and Chanson, H., 2001, ''Void-Fraction and Acoustic Characteristics of Gas Bubbles Entrained by a Circular Plunging Jet,'' *Proc. 4th Intl Conf. Multiphase Flow*, ICMF'01, E. E. Michaelides, ed., New Orleans, LA.

[17] Manasseh, R., LaFontaine, R. F., Davy, J., Shepherd, I. C., and Zhu, Y., 2001, ''Passive Acoustic Bubble Sizing in Sparged Systems,'' Exp. Fluids, **30**(6), pp. 672–682.

[18] Esslingen, 1984, ''Scale Effects in Modelling Hydraulic Structures,'' *Proceedings of the International Symposium on Scale Effects in Modelling Hydraulic Structures*, H. Kobus, ed., IAHR, Esslingen, Germany.

[19] Wood, I. R., 1991, ''Air Entrainment in Free-Surface Flows,'' *IAHR Hydraulic Structures Design Manual No. 4, Hydraulic Design Considerations*, Balkema, Rotterdam.

[20] McKeogh, E. J., 1978, ''A Study of Air Entrainment Using Plunging Water Jets,'' Ph.D. thesis, Queen's University of Belfast, UK.

[21] El-Hammoumi, M., 1994, ''Entraînement d'Air par Jet Plongeant Vertical. Application aux Becs de Remplissage Pour le Dosage Pondéral,'' Ph.D. thesis, INPG, Grenoble, France (in French).

[22] Oguz, H. N., 1998, ''The Role of Surface Disturbances in the Entrainment of Bubbles by a Liquid Jet,'' J. Fluid Mech., **372**, pp. 189–212.

[23] Zhu, Y., Oguz, H., and Prosperetti, A., 2000, ''On the Mechanism of Air Entrainment by Liquid Jets at a Free Surface,'' J. Fluid Mech., **404**, pp. 151–177.

[24] Lunde, K., and Perkins, R. J., 1996, ''A Method for the Detailed Study of Bubble Motion and Deformation,'' *Multiphase Flow 1995, Proceedings of the 2nd Int. Conference on Multiphase Flow*, A. Serizawa, T. Fukano, and J. Bataille, eds., pp. 395–405.

[25] Yoshida, S., Manasseh, R., and Kajio, N., 1998, ''The Structure of Bubble Trajectories Under Continuous Sparging Conditions,'' *Proceedings, 3rd International Conference on Multiphase Flow*, Lyon, France.

[26] Manasseh, R., Yoshida, S., and Kajio, N., 1998, ''Bubble Trajectory Bifurcations in Cross Flow,'' *Proceedings, 13th Australasian Fluid Mechanics Conference*, Monash University, Melbourne, Dec. 13–18, pp. 1013–1018.

[27] Bonetto, F., and Lahey, R. T., Jr., 1993, ''An Experimental Study on Air Carryunder due to a Plunging Liquid Jet,'' Int. J. Multiphase Flow, **19**(2), pp. 281–294.

[28] Detsch, R. M., and Sharma, R. N., 1990, ''The Critical Angle for Gas Bubble Entrainment by Plunging Liquid Jets,'' Chem. Eng. J., **44**, pp. 157–166.

[29] McKeogh, E. J., and Ervine, D. A., 1981, ''Air Entrainment Rate and Diffusion Pattern of Plunging Liquid Jets,'' Chem. Eng. Sci., **36**, pp. 1161–1172.

[30] Moursali, E., Marie, J. L., and Bataille, J., 1995, ''An Upward Turbulent Bubbly Boundary Layer Along a Vertical Flat Plate,'' Int. J. Multiphase Flow, **21**(1), pp. 107–117.

[31] Chanson, H., 2002, ''Air-Water Flow Measurements With Intrusive Phase-Detection Probes. Can we Improve Their Interpretation?'' J. Hydraul. Eng., **128**(3), pp. 252–255.

[32] Van de Sande, E., and Smith, J. M., 1973, ''Surface Entrainment of Air by High Velocity Water Jets,'' Chem. Eng. Sci., **28**, pp. 1161–1168.

[33] Clanet, C., and Lasheras, J. C., 1998, ''Depth of Penetration of Bubbles Entrained by a Plunging Water Jet,'' Phys. Fluids, **9**(7), pp. 1864–1866.

[34] Pandit, A. B., Varley, J., Thorpe, R. B., and Davidson, J. F., 1992, ''Measurement of Bubble Size Distribution: An Acoustic Technique,'' Chem. Eng. Sci., **47**(5), pp. 1079–1089.

[35] Cummings, P. D., and Chanson, H., 1998, ''Individual Air Bubble Entrapment at a Planar Plunging Jet With Near-Inception Flow Conditions,'' *Proceedings, 13th Australasian Fluid Mechanics Conference*, Monash University, Melbourne, Australia, Dec. 13–18.

[36] Strasberg, M., 1953, ''The Pulsation Frequency of Nonspherical Gas Bubbles in Liquid,'' J. Acoust. Soc. Am., **25**, pp. 536–537.

[37] Manasseh, R., Yoshida, S., and Rudman, M., 1998, ''Bubble Formation Processes and Bubble Acoustic Signals,'' *Proc 3rd Intl. Conf. Multiphase Flow*, ICMF98, J. Bataille, ed., Lyon, France.
[38] Lu, N. Q., Prosperetti, A., and Yoon, S. W., 1990, ''Underwater Noise Emissions From Bubble Clouds,'' IEEE J. Ocean. Eng., **15**(4), pp. 275–281.
[39] Nicholas, M., Roy, R. A., Crum, L. A., Oguz, H., and Prosperetti, A., 1994, ''Sound Emissions by a Laboratory Bubble Cloud,'' J. Acoust. Soc. Am., **95**(6), pp. 3171–3182.
[40] Lin, T. J., and Donnelly, H. G., 1966, ''Gas Bubble Entrainment by Plunging Laminar Liquid Jets,'' AIChE J., **12**(3), pp. 563–571.
[41] Van de Donk, J., 1981, ''Water Aeration With Plunging Jets,'' Ph.D. thesis, TH Delft, The Netherlands.

Journal of Fluids Engineering

Technical Briefs

Capturing the Pinch-Off of Liquid Jets by the Level Set Method

Y. Pan

K. Suga[1]
e-mail: k-suga@mosk.tytlabs.co.jp

Toyota Central R&D Labs, Inc., Nagakute,
Aichi, 480-1192, Japan

Full three-dimensional dynamic simulations of forced liquid jets flowing into and pinching off in ambient of another liquid were performed by using the level set method for tracking the interface between the immiscible materials. The simulations were performed for jets with viscosity ratios between the inner and outer fluids of 0.17 and 1.7. The jets were forced at Strouhal number of 4.0. The Reynolds, Froud, and Bond numbers based on the conditions at the nozzle exit were 34–35, 0.2, and 6.1, for both cases. The numerical results are compared with the data from the experiment made by Longmire et al. (2001). The comparisons were made for (1) flow images of one complete pinch-off cycle and (2) the axial and radial profiles of the instantaneous velocities around the region of jet disintegration. The feasibility and accuracy of using the level set method in multiphase problems involving interface breakup/coalescence is explored and accessed by simulating such relatively low speed, low density-ratio two-phase flows. Although the level set method is quite promising, due to the surface tension model, it requires very fine grid resolution (the Weber number based on the grid spacing is smaller than 10^{-2}) even for capturing the laminar surface phenomena.
[DOI: 10.1115/1.1598986]

Introduction

Round liquid jets flowing into a second immiscible liquid have been investigated by many researchers (Cohen et al. [1], Wilkes et al. [2], and Zhang et al. [3]) due to their fundamental simplicity as well as their importance in a number of industrial systems. The experiments demonstrated that for low flow rates (and Reynolds number), droplets form at and detach from the jet outlet. As the flow rate is increased, the injected fluid forms a jet that develops axis-symmetric instabilities and pinches off at a finite length. Above a Reynolds number associated with the maximum length, three-dimensional instabilities and eventually direct atomization occur. The Reynolds number range corresponding to each flow mode depends significantly on the other system parameters, including the fluid properties. From the viewpoint of practical application, the break up of a continuous jet into discrete droplets is closely related to the liquid fuel injection/spray, which provides the fine atomization needed for rapid mixing of liquid and gas phases during combustion processes. People are interested in the behavior of liquid jets and the mechanism of jet breakup at the very initial stage right after the injector exit, i.e., dense spray region. In such a region, a liquid jet undergoes topological transitions associated with very small length and time scales, which are difficult to observe and characterize, particularly in flows with significant inertia such as a liquid jet into air. It challenges the continuum-based numerical simulations by posing singularities caused by small length and time scales accompanying transitions. In one of the most recent experimental studies on the pinchoff of liquid/liquid jet, Longmire et al. [4] employed a PIV technique to measure the full two-dimensional instantaneous velocity and vorticity field on both sides of a liquid/liquid interface. Their results thus provide realistic yet geometrically simple flow cases that can be used to assess numerical models.

In the present paper, we performed full three-dimensional dynamic simulations of a round liquid jets flowing into a second immiscible liquid of the same fluid properties and flow parameters as used by Longmire et al. [4]. In order to simulate directly the flows with material interface, one has to track the interface with reasonable accuracy. As is well known, there are several methods for expressing the moving interface between two fluids, such as the VOF method, the level-set method, and the front-tracking method. The VOF and level-set methods are categorized as a front capturing method, which tracks the movement of volume and finds the interface in an indirect way. One of the advantages of the front capturing methods is that topological transitions, i.e., collision and break up of interfaces, are easily treated. In this study, we have been using the level set method (Chang et al. [5]) as the interface tracking methodology. This method has been used by other investigators successfully for solving many multiphase problems, which contain interfaces between immiscible materials of different physical properties. Most of these studies deal with low speed, low density-ratio between the materials and had been limited to two-dimensional problems (Osher and Fedkiw [6]). Recently several efforts have been made to apply the level set method to engineering problems. Son et al. [7] carried out a numerical simulation of bubble generation and merger process on a single nucleation by the level set method. They included the phase change at the interface and incorporated the heat flux from the thin liquid film that forms underneath a growing bubble attached to the wall. Their simulations were two-dimensional and the comparisons with experiments were qualitative. The level set method is also used by Chung [8] to simulate the compressible flow with moving solid boundary for the problem of two trains passing by each other in a tunnel. Despite wide application of the level set method in various physical and industrial problems, detailed assessment by comparison, quantitative in particular, with experimental data is lacking in the literature.

[1]To whom correspondence should be addressed.

Contributed by the Fluids Engineering Division for publication in the JOURNAL OF FLUIDS ENGINEERING. Manuscript received by the Fluids Engineering Division Aug. 21, 2002; revised manuscript received Mar. 28, 2003. Associate Editor: S. Balachandar.

For the present simulations, we incorporate the numerical scheme of the level set method by Sussman et al. [9] and Chang et al. [5] into a finite-volume package, CFDLIB, developed by Los Alamos National Laboratory (Kashiwa and Rauenzahn [10] and Kashiwa et al. [11]). The surface tension force is treated as a body force by adopting the continuum surface force (CSF) model by Brackbill et al. [12]. Detailed comparisons are made, both qualitatively and quantitatively, to serve the purpose of assessment and validation of the level set method. Notice that such assessment is necessary for applying this method in various two-phase problems of practical interests.

Numerical Methods

We consider the fluid motion of a liquid injected into a space, which is initially filled with another liquid of different density and viscosity. Two liquids are immiscible to each other. The interface between the two liquids remains throughout the motion and a surface tension exists at the interface. The flow motion is governed by the Navier-Stokes equation,

$$\rho\left(\frac{\partial \mathbf{u}}{\partial t}+\mathbf{u}\cdot\nabla\mathbf{u}\right)=-\nabla p+\nabla\cdot(2\mu\mathbf{S})+\sigma\kappa(\theta)\nabla\theta\delta(\theta)+\rho\mathbf{g}. \tag{1}$$

No turbulence model is included since the flow is laminar. The third term on the right-hand side of the above equation represents a model, called the continuum surface force (CSF) model proposed by Brackbill et al. [12], for approximating the surface tension forces. In this model, the effect of surface tension can be expressed in terms of a singular source function which is defined by an indicative function, here the level set function, θ.

The level set method (Chang et al. [5]) is used to capture the interface between two fluids of different densities and viscosities. A level set function, say, θ, is a distance function about the interface. It has positive values outside the interface and negative inside the interface. At the interface θ keeps a value of zero. The magnitude of the level set function at any location represents the distance from this location to the interface. The level set function, like any passive scalar variables, moves with the fluid, and it follows that

$$\frac{\partial\theta}{\partial t}+\mathbf{u}\cdot\nabla\theta=0, \tag{2}$$

which moves the zero level of θ exactly as the actual interface. The density and viscosity are calculated through out the computational domain depending on the value of θ, by

$$\rho=\begin{cases}\rho_i\\ (\rho_i+\rho_o)/2\\ \rho_o\end{cases}\quad\text{and}\quad\mu=\begin{cases}\mu_i & \theta<0\\ (\mu_i+\mu_o)/2 & \text{for } \theta=0.\\ \mu_o & \theta>0\end{cases} \tag{3}$$

The Direac function δ is regularized by

$$\delta_\varepsilon(\theta)=\begin{cases}\frac{1}{2}(1+\cos(\pi\theta/\varepsilon))/\varepsilon & \text{if } |\theta|<\varepsilon,\\ 0 & \text{otherwise,}\end{cases} \tag{4}$$

and the corresponding regularized Heaviside function H_ε is defined as

$$H_\varepsilon(\theta)=\begin{cases}0 & \text{if } \theta<-\varepsilon,\\ (\theta+\varepsilon)/(2\varepsilon)+\sin(\pi\theta/\varepsilon)/(2\pi) & \text{if } |\theta|\leq\varepsilon,\\ 1 & \text{if } \theta>\varepsilon.\end{cases} \tag{5}$$

Using the regularized Heaviside function H_ε, we can define the corresponding regularized density function ρ and the regularized viscosity μ as

Table 1 Nondimensional flow parameters based on the nozzle exit diameter and velocity

Parameters	Case I	Case II
$\mathrm{Re}=\rho_i U_e D/\mu_i$	34	35.2
$\mathrm{Fr}=U_e(\rho_i/gD\Delta\rho)^{1/2}$	0.2	0.21
$\mathrm{Bo}=gD^2\Delta\rho/\sigma$	6.1	6.1
ρ_i/ρ_o	1.19	1.18
μ_i/μ_o	0.17	1.72
$\mathrm{St}=fD/U_e$	4	3.9

$$\rho_\varepsilon(x)=\rho_i+(\rho_o-\rho_i)H_\varepsilon(\theta(x)) \tag{6}$$

$$\mu_\varepsilon(x)=\mu_i+(\mu_o-\mu_i)H_\varepsilon(\theta(x)). \tag{7}$$

In our computations, we use $\varepsilon=\Delta x$. We denote ε as the prescribed ''thickness'' of the interface.

The nature of the level set method being a signed normal distance function from the interface has essentially to be kept all the time throughout the simulation. A procedure of re-initialization and re-normalization (Sussman et al. [9]) is therefore performed at every time step during the simulation to pertain such a property. This is achieved by solving the following equation to a steady state:

$$\frac{\partial\theta}{\partial t}=\mathrm{sgn}(\theta_0)(1-|\nabla\theta|) \tag{8}$$

with an initial condition

$$\theta(\mathbf{x},0)=\theta_0(\mathbf{x}) \tag{9}$$

where $\theta_0(\mathbf{x})$ is the level function before the re-normalization. By the above procedure we build a distance function $\theta(\mathbf{x})$ whose zero set is the same as $\theta_0(\mathbf{x})$.

In CFDLIB [10,11], the time-step Δt is adjusted at every cycle of the numerical integration. The criterion for the selection of the time-step is a multidimensional generalization of the well-known Courant-Friedrichs-Levy (CFL) condition. For one-dimensional, explicit, Eulerian hydrodynamics, the CFL condition is

$$\max\left[\frac{(|\mathbf{u}|+c)\Delta t}{\Delta x}\right]<1 \tag{10}$$

where c is the sound speed. The maximum is taken over the entire problem domain. In simple terms the CFL condition represents the restriction that a signal carried by the largest characteristic speed in the problem cannot travel more than a single grid in a single time-step.

Results and Discussions

The cases examined represent a parameter set where the fluid properties as well as inertia, gravity, and surface tension are all significant. The flow conditions can be characterized by a set of dimensionless parameters. The values of these parameters for the two cases are given in Table 1. Under the chosen flow conditions, gravitational effects cause the jet to accelerate and contract immediately after exiting the nozzle. In the absence of forcing, the above conditions yield a smooth jet column that travels all the way to the downstream fluid interface without developing any significant waves or instabilities. When the flow is forced with a sinusoidal velocity perturbation, however, instabilities are enhanced, and pinchoff occurs within the layer of surrounding fluid. Figure 1 shows typical instantaneous shapes of jets and droplets in the computational domain. The effect of the viscosity ratio on the evolving jet flow and droplet shapes can be clearly observed. The less gravitational acceleration within the jet fluid, yielded by higher viscosity ambient, results in a broader cone shape upstream and more rounded drops downstream of the pinchoff zone, with weak oscillations in shape, as shown by Fig. 1(*a*). On the other hand, a narrower cone shape, flatter drops and strong oscillations

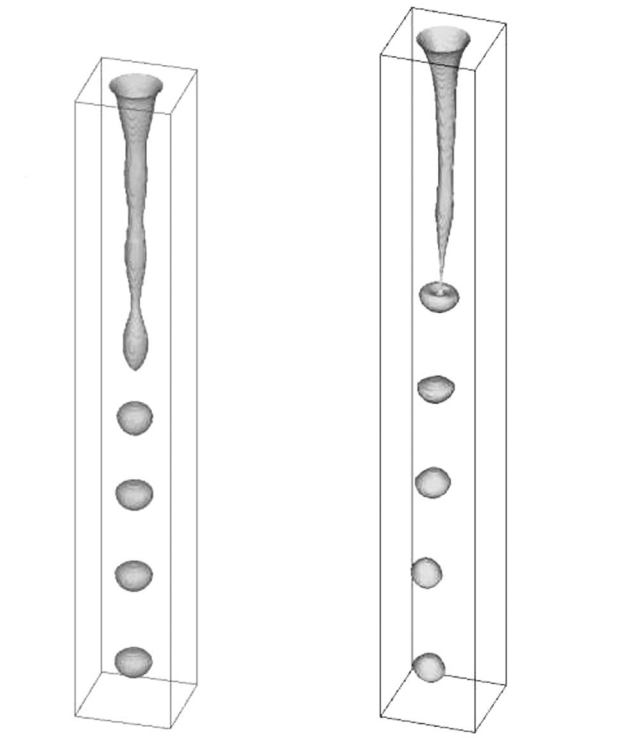

Fig. 1 The iso-surface of liquid density from instantaneous flow field by numerical simulations. Mesh: $\Delta x/D=\Delta y/D=\Delta z/D=3.125\times10^{-2}$; domain: $52\Delta x\times52\Delta y\times400\Delta z$. The jet diameter D is resolved by 32 grid points. (*a*) Case I ($\mu_i/\mu_o=0.17$, Re=34) (*b*) Case II ($\mu_i/\mu_o=1.72$, Re=35.2).

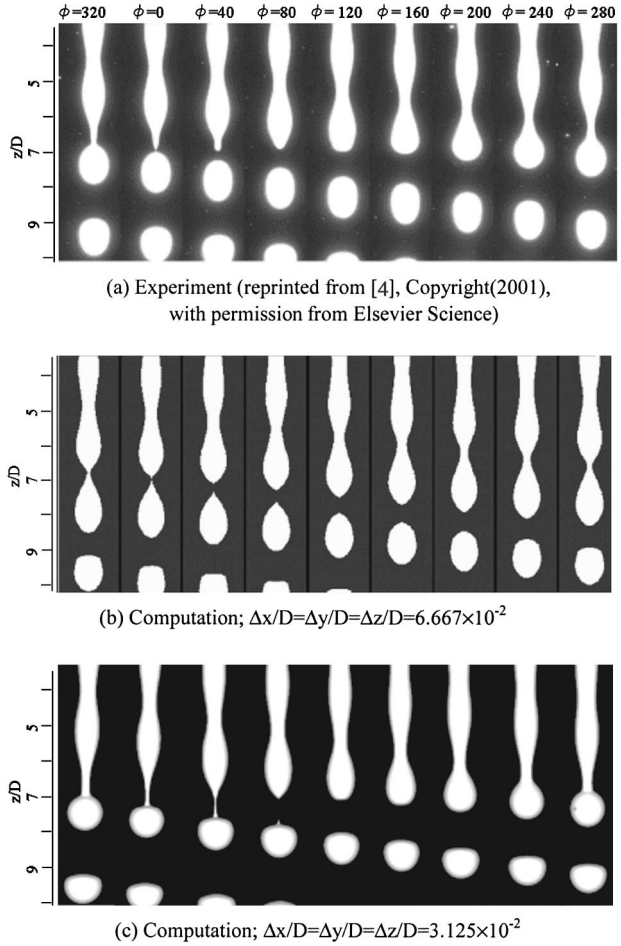

Fig. 2 One cycle of jet disintegration for Case I ($\mu_i/\mu_o=0.17$, Re=34). The time interval between the images is 1/9T. The pinchoff ($t=0$) is the second in each series. The images from computation show the iso-surface (three-dimensional) of zero level set function $\theta=0$. (*a*) Experiment (reprinted from [4], copyright(2001), with permission from Elsevier Science). (*b*) Computation: $\Delta x/D=\Delta y/D=\Delta z/D=6.667\times10^{-2}$. (*c*) Computation: $\Delta x/D=\Delta y/D=\Delta z/D=3.125\times10^{-2}$.

including inverted curvature with the droplets are observed in the case of lower viscosity ambient, i.e. Fig. 1(*b*). Notice that the instantaneous flow fields for building Fig. 1 are arbitrarily taken from the simulations. Some unsteadiness still exists in the flow, particularly for the case of low viscosity ratio. The location of pinchoff can be controlled by adjusting the forcing amplitude such that increasing the amplitude moves the pinchoff location upstream. For the experimental cases, the flow was forced at the laser pulsing frequency of 10 Hz yielding a Strouhal number, St, of about 4. Under the chosen conditions, one drop formed during each forcing cycle at a location approximately seven diameters downstream of the nozzle exit. In the present numerical simulation, this condition is achieved by setting a time-dependent velocity condition at the nozzle exit. The amplitude of the velocity fluctuation is adjusted such that a droplet is pinched off at the same downstream location as in the experiments. In particular, the section mean velocity at the nozzle exit is implemented as

$$\overline{u}=U_e(1+\alpha\cos(2\pi ft)), \tag{11}$$

in which α and f are the amplitude and frequency of the velocity fluctuation, respectively. The values of α are 0.8 and 0.15 for Case I and II, respectively. The spatial distribution of the velocity at the nozzle exit is resolved as a parabolic function. Due to the fact that a Cartesian, uniform mesh system is used in this simulation, the circular shaped nozzle exit is also approximated by the square-shaped grids.

Figures 2 and 3 serve the purpose of qualitative comparison with experiments, where one cycle of jet disintegration is manifested for Case I, and II, respectively. The images from experiments were taken from [4]. To check the grid dependence, the simulations were performed on two different mesh systems. The grid size of one simulation is about the half of the other. One can see that, for both cases, the numerical results match with the experimental ones reasonably well. Notice that, for Case II, due to the lower viscosity, the ambient fluid offers less resistance to the inner jet fluid, and hence the jet accelerates to a higher velocity and develops a more complex shape of the evolving jet tip than in Case I. Specifically, the jet tip develops a small spherical structure before the wide part of a wave approaches (shown by the 6th and 7th images from the left of Fig. 3(*a*)). The simulations, both the coarse and the finer ones, did not catch such small spherical structure, as one can see from Figs. 3(*b*) and 3(*c*). In the experiment, there is a local concavity lying within the newly formed drop, as shown in Fig. 3(*a*). This concavity recovers a convex shape of curvature under the action of surface tension force. In the simulation of coarse grid as shown by Fig. 3(*b*), one can observe that the drop recovers the spherical shape more slowly than it does in the experiment. This discrepancy is mainly due to the CSF model, [12], in which the surface tension force is evaluated by the curvature of the interface with a finite thickness and imposed on this layer. As indicated by Eqs. (4)–(7), the thickness of the interface is proportional to ε and typically ε is set to be the local grid spacing. Obviously the computations are not able to capture any curvature higher than $O(1/\Delta x)$. Therefore the calculated surface tension force is weaker and less concentrated in the simulation than in the experiment. A remedy would require a finer mesh to

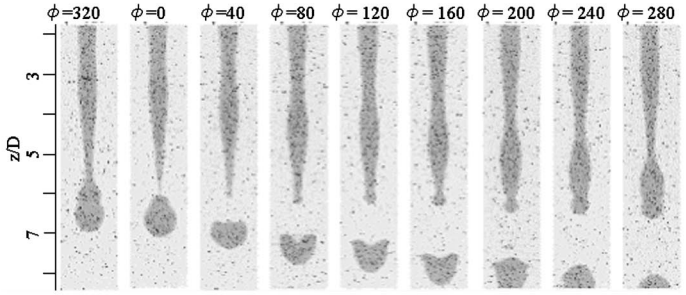

(a) Experiment (reprinted from [1], Copyright(2001), with permission from Elsevier Science)

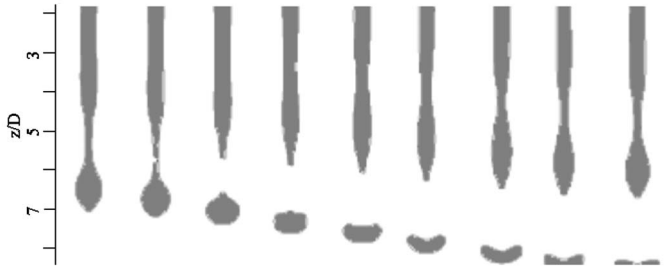

(b) Computation; $\Delta x/D=\Delta y/D=\Delta z/D=6.667\times10^{-2}$

(c) Computation; $\Delta x/D=\Delta y/D=\Delta z/D=3.125\times10^{-2}$

Fig. 3 One cycle of jet disintegration for Case II ($\mu_i/\mu_o=1.72$, Re=35.2). The time interval between the images is 1/9*T*. The pinchoff ($t=0$) is the second in each series. The plots from computation show the contours (two-dimensional) of zero level set function $\theta=0$ projected onto an azimuthal plane cutting through the axis of the jet. (*a*) Experiment (reprinted from [4], copyright (2001), with permission from Elsevier Science). (*b*) Computation: $\Delta x/D=\Delta y/D=\Delta z/D=6.667\times10^{-2}$. (*c*) Computation: $\Delta x/D=\Delta y/D=\Delta z/D=3.125\times10^{-2}$.

get a thinner interface. Indeed, the situation is significantly improved when a finer mesh is used. As shown by Fig. 3(*c*), the restoration of drop's upstream side to a convex curvature catches up quite closely with the experimental observations. From Fig. 2(*b*), one can also notice that a ''tear drop'' shaped droplet is formed immediately after the disintegration whereas the experimental results show that a more round-shaped droplet is formed there. Again numerical results are largely improved by simply using a mesh system with doubled resolution in each direction, as shown in Fig. 2(*c*). Note that the Weber number based on the finer grid spacing and jet exit velocity is 8.1×10^{-3} which indicates the surface tension force dominant regime. Generally, if the largest curvature appearing in the experiment is κ_0, one needs a grid size of $1/(3\kappa_0)$ to resolve the corresponding scales. More complicated and transitional phenomena appear in the pinchoff experiment when satellite droplets of various sizes are generated between the primary drops. In such a situation, the grid size is to be determined by the typical size of satellite droplets.

The quantitative comparisons are made on the axial velocity component. The numerical results used by comparison are extracted from simulations with grid size of $\Delta x/D=0.06667$. Figure 4 shows the vertical velocity along the jet axis at different time instant during one disintegration cycle for Case I. Figure 5 shows the radial profiles of the vertical velocity at a fixed axial location at different time instants during one disintegration cycle for Case I. Figure 6 shows the similar comparisons for Case II. One can see that better agreement is achieved in the case of higher ambient viscosity, i.e., Case I ($\mu_i/\mu_o=0.17$). In general, the wavelengths of the velocity variation match with the experiments. The comparisons on the magnitude of velocity are satisfactory as well. The discrepancies are most likely caused by the finite thickness of the jet and the drop surfaces resulting in an inner fluid of lighter weight than the real one. If one assumes the Stokes flow around a pinched-off drop, it can be readily estimated that the effective density caused by the finite thickness of the interface will induce an error in the magnitude of velocity up to 17% when a mesh of $\Delta x/D=0.06667$ is used. However, since our cases are quite beyond the Stokes regime, the difference between the data and the simulated results is much smaller than this value as can be seen in Figs. 4, 5, and 6. Notice that the Reynolds number, based on the viscosity of the outer liquid and the drop diameter, for both cases are much larger than one. Again a mesh system with finer resolu-

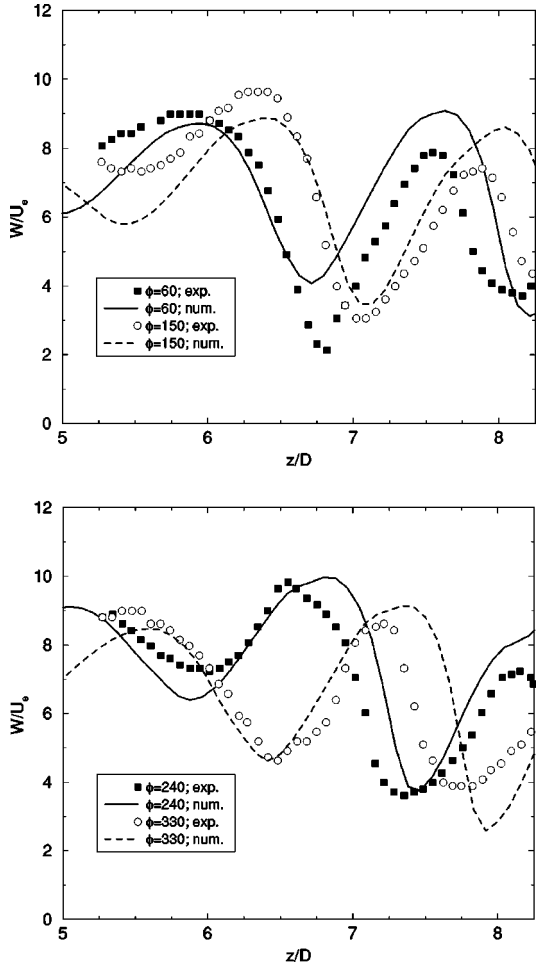

Fig. 4 The axial velocity along the centerline of the jet for Case I (μ_i/μ_o=0.17, Re=34), at different time during one cycle of disintegration. Symbols and lines represent the experimentally measured data and numerically calculated values, respectively. The phase corresponds to pinch is ϕ=0.

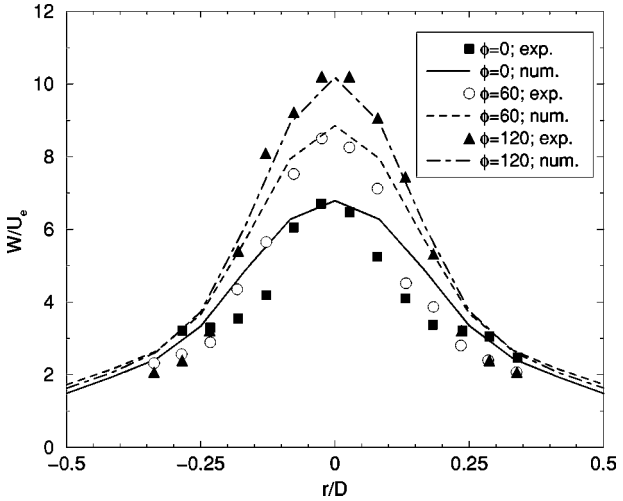

Fig. 5 The radial profiles of axial velocity at an axial location (z/D=6.15) for Case I (μ_i/μ_o=0.17, Re=34) at different time during one cycle of disintegration. Symbols and lines represent the experimentally measured data and numerically calculated values, respectively. The phase corresponds to pinch is ϕ=0.

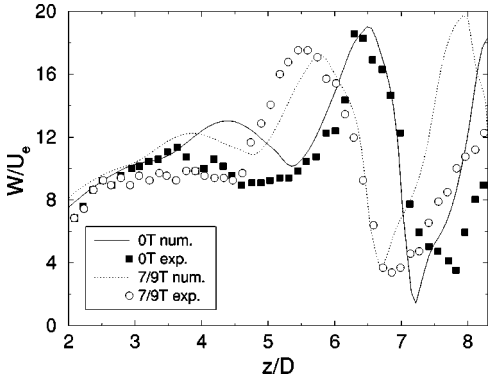

Fig. 6 The axial velocity along the centerline of the jet for Case II (μ_i/μ_o=1.72, Re=35.2), at different time during one cycle of disintegration. Symbols and lines represent the experimentally measured data and numerically calculated values, respectively. The time corresponds to pinch is t=0 and the phases 0T, 7/9T, respectively, correspond to ϕ=0, 280.

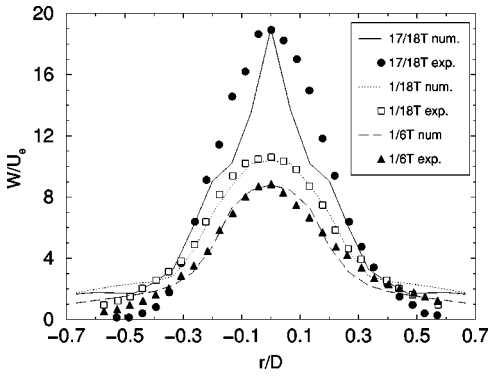

Fig. 7 The radial profiles of axial velocity at a axial location (z/D=6) for Case II (μ_i/μ_o=1.72, Re=35.2) at different time during one cycle of disintegration. Symbols and lines represent the experimentally measured data and numerically calculated values, respectively. The time corresponds to pinch off is t=0 and the phases 17/18T, 1/18T, 1/6T, respectively, correspond to ϕ=340, 20, 60.

tion would definitely help to improve the situation. Figure 7 compares the radial profiles of the instantaneous axial velocity for Case II. Good agreement is achieved around the core region, i.e., $|r/D|<0.4$. The measured value of velocity diminishes faster than the calculated one, outwards the core region, i.e., $|r/D|>0.4$. Similar phenomena are also observed in Fig. 5. We believe this is due to the relatively smaller computational domain in comparing the large experiment setup used in [4]. In this particular case, the flow is confined in a computational box of five jet diameters in the transverse direction. Obviously, at the same distance from the source of disturbances, here the jet, a smaller domain would result in larger values of velocity than the larger one does, due to the requirement of conserving total momentum and mass.

Conclusions

The comparisons between the numerical results and the experimental data show that the simulation based on the level set method is able to handle the three-dimensional problems with interface breakup quite well. The quantitative predictions of velocities are also satisfactory. The results demonstrated that the viscosity ratio had a significant effect on the evolving jet flow, the pinchoff process, and the resulting drop shapes. In general, the simulation gives more accurate prediction in the case of high-

viscosity ratio than in the case of low-viscosity ratio. Although the flow is laminar, sufficiently fine grid spacing (the Weber number based on the grid spacing is smaller than 10^{-2}) is required for capturing the surface phenomena reasonably.

Nomenclature

D = jet diameter: 1.0 cm
t = time
T = period of jet disintegration
U_e = velocity of inner liquid at the jet exit
W = axial component of fluid velocity
$\mathbf{S}$ = fluid strain rate, a tensor variable
$\mathbf{u}$ = fluid velocity vector
f = frequency of jet forcing
g = gravitational constant
p = pressure
r = radial distance from the jet axis
z = streamwise distance from the jet exit
$\delta(\ )$ = Dirac delta function
ϕ = phase of one cycle of jet disintegration, $360t/T$
κ = curvature of interface
ρ = density
μ = dynamic viscosity
σ = surface tension coefficient
$\Delta\rho$ = density difference, $\rho_i - \rho_o$

Subscripts

i = inside jet
o = outside jet

References

[1] Cohen, I., Brenner, M. P., Eggers, J., and Nagel, S. R., 1999, ''Two Fluid Drop Snap-Off Problem: Experiments and Theory,'' Phys. Rev. Lett., **83**(6), pp. 1147–1150.

[2] Wilkes, E. D., Phillips, S. D., and Basaran, O. A., 1999, ''Computational and Experimental Analysis of Drop Formation,'' Phys. Fluids, **11**(12), pp. 3577–3598.

[3] Zhang, W., and Lister, J. R., 1999, ''Similarity Solution for Capillary Pinch-Off in Fluids of Differing Viscosity,'' Phys. Rev. Lett., **83**(6), pp. 1151–1154.

[4] Longmire, E. K., Norman, T. L., and Gefroh, D. L., 2001, ''Dynamics of Pinch-Off in Liquid/Liquid Jets With Surface Tension,'' Int. J. Multiphase Flow, **27**, pp. 1735–1752.

[5] Chang, Y. C., Hou, T. Y., Merriman, B., and Osher, S., 1996, ''A Level Set Formulation of Eulerian Interface Capturing Methods for Incompressible Fluid Flows,'' J. Comput. Phys., **124**, pp. 449–464.

[6] Osher, S., and Fedkiw, R. P., 2001, ''Level Set Methods: An Overview and Some Recent Results,'' J. Comput. Phys., **169**, pp. 463–502.

[7] Son, G., Ramanujapu, N., and Dhir, V. K., 2002, ''Numerical Simulation of Bubble Merger Process on a Single Nucleation Site During Pool Nucleate Boiling,'' ASME J. Heat Transfer, **124**, pp. 51–62.

[8] Chung, M., 2001, ''A Level Set Approach for Computing Solutions to Inviscid Compressible Flow With Moving Solid Boundary Using Fixed Cartesian Grids,'' Int. J. Multiphase Flow, **36**, pp. 373–389.

[9] Sussman, M., Smereka, P., and Osher, S., 1994, ''A Level Set Approach for Computing Solutions to Incompressible Two-Phase Flow,'' J. Comput. Phys., **114**, pp. 146–464.

[10] Kashiwa, B. A., and Rauenzahn, R. M., 1994, ''A Multi-Material Formulation,'' *Numerical Methods in Multiphase Flows*, ASME, New York, ASME-FED-**185**, pp. 149–157.

[11] Kashiwa, B. A., Padial, N. T., Rauenzahn, R. M., and VanderHeyden, W. B., 1994, ''A Cell-Centered ICE Method for Multiphase Flow Simulations,'' ASME, New York, ASME-FED-**185**, pp. 159–167.

[12] Brackbill, J. U., Kothe, D. B., and Zemach, C., 1992, ''A Continuum Method for Modelling Surface Tension,'' J. Comput. Phys., **100**, pp. 335–354.

On the Water-Entry-Induced Cavity Closure for a Wide Range of Entry Speeds

M. Lee
Associate Professor, Department of Mechanical Engineering, Sejong University, 98 Kwangjin-Gu Kunja-Dong, Seoul 143-747, Korea.
e-mail: mlee@sejong.ac.kr
Mem. ASME

One of the important research areas in the water-entry problem is the cavity dynamics. A theoretical analysis is presented to predict the dynamics of water-entry cavity up to the first cavity closure, which is generated by a solid body entering a semi-inifinite free surface of water at a wide range of entry speed. Two types of cavity closure, which are surface closure and the deep closure, depending on the magnitude of ambient atmosphere pressure and entry speed are described by the proposed theory. The time of surface closure at the relatively low-speed entry regime is estimated and compared with published experimental data. Currently no experimental data are available for the high-speed entry case.

Introduction

A theoretical analysis is presented in this paper to predict the dynamics of water entry cavity up to cavity closure, which is generated by a solid body entering a semi-infinite free surface of water at a wide range of entry speed. The occurrence of two types of cavity closure, which are the surface closure and the deep closure, depending on the magnitude of ambient atmosphere pressure and entry speed, is described by the proposed theory. The time of surface closure, which is one of the important data, is estimated and compared with published experimental data.

The problem of a solid body entering a semi-infinite free surface of water is a classical one and several interesting phenomena are discussed by Gilbarg and Anderson [1], Abelson [2], May [3], and Gaudet [4]. Of particular interests are physical events that occur at various stages of the entry that not only influence the solid motion but also the nature of induced ballistic waves in water, [5,6]. Especially, the dynamics of the water-entry cavity is one of the important phenomena since the water-entry cavity controls the environment in which the entering solid body (missile) travels. The cavity dynamics is discussed exclusively in the Philosophical Transactions of the Royal Society, [7]. Recently, the dynamics of the high-speed water-entry cavity is studied analytically and numerically, [5]. Gaudet [4] proposed a simulated solution for the entry of a circular disk, which has also been investigated by several researchers.

Due to the highly transient characteristics of water entry process, the evolution of the water entry cavity must be explained by considering the entry speed, shape of the solid body, atmosphere pressure, and cavity pressure as the primary variables. This is because forces generated from the physical properties of the solid body, gas combined with gravity, and inertia determine the transient entry phenomena, [8]. It is known that the primary mechanism governing the cavity formation is the kinetic energy transfer from the solid body to the cavity. Later on, potential energy, which is the pressure difference between the surrounding fluid and inside cavity, becomes effective and causes the fluid to return to

Contributed by the Fluids Engineering Division for publication in the JOURNAL OF FLUIDS ENGINEERING. Manuscript received by the Fluids Engineering Division Sept. 12, 2002; revised manuscript received Mar. 31, 2003. Associate Editor: A. K. Prasad.

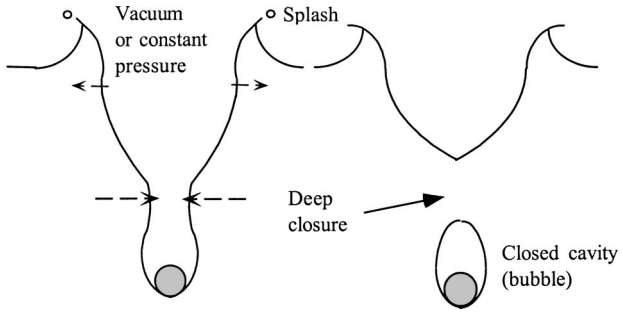

Fig. 1 Deep closure

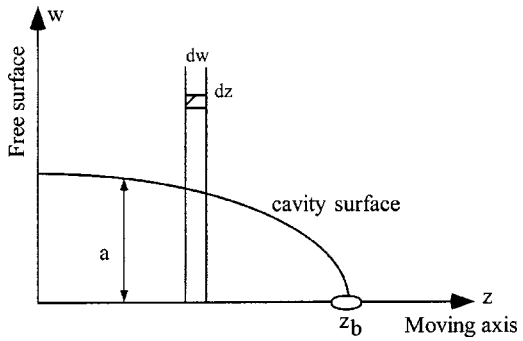

Fig. 2 Cavity evolution model

its undisturbed location. Hence, balance between the two energies mainly governs the dynamics of the water-entry cavity growth and collapse.

Due to the complexities involved in the water entry event, mathematical analysis of the dynamics of water-entry cavity is relatively little developed. Descriptions of the cavity dynamics in full life cycle cannot even be achieved in detail. It is the first cycle up to the closed cavity (bubble) that we are interested in analyzing. Some available theoretical models, [9,10] have different ranges of validity, which are related to the physical properties (e.q., entry speeds, ambient atmosphere pressure). Nevertheless, a current theoretical analysis would assist in clarifying the behavior of water-entry cavity and in removing some of the present difficulties. In general, the gravitational effect is negligible since it will take place long after the cavity has closed either at the water surface or below the surface. The main difficulty analyzing this water-entry cavity, which is discussed in this paper, is the determination of inside cavity pressure since the cavity is open during the entering process, causing airflows into the cavity. Different regimes of entry speed are also discussed. This is due to the fact that the location of cavity closure occurs either at the water surface or below the surface depending on the entry speed and atmosphere pressure.

Cavity Closure Locations

The entry speed Birkhoff and Zarantonello [11] examined is mostly below 50 m/s. Both surface closure and deep closure were observed depending on the entry speed. According to the classification of the entry speed proposed by Birkhoff and Zarantonello [11] and Lee et al. [5], there are four different regimes: very low-speed regime, low-speed regime, transient regime, and high-speed regime.

For *very low-speed entry* from an atmosphere pressure ($20<\mathrm{Fr}<70$), the airflow filling the induced cavity is relatively so fast that the pressure drop inside the cavity is negligible. Here, $\mathrm{Fr}=U_i^2/gD$, where g is gravitational acceleration, U_i is entry speed, and D is the characteristic length of an entering body (e.g., the diameter of a sphere). That is, the inside cavity pressure can be assumed to be constant at the atmosphere pressure. There is also a special case, entry from a vacuum, where the cavity pressure is constant. In these cases, the cavity closure occurs below the water surface (deep closure), as shown in Fig. 1.

In order to examine the cavity closure phenomena, a theory for the cavity dynamics is described below. Consider a solid body impulsively accelerated at $t=0$ to an initial U_i moving into a semi-infinite fluid medium. For consistency, the same symbols and notations to denote various quantities in the previous article, [5], will also be used here. For the convenience of discussion, the geometry of the problem is sketched in Fig. 2. Since the solid body is decelerated by the drag, the dynamics of a moving solid is governed by the kinetic energy loss, [12],

$$m_s\frac{d^2z}{dt^2}=m_s\frac{dU}{dt}=m_sg-\frac{1}{2}\rho_wA_oC_dU^2 \tag{1}$$

where the properties are the mass of the solid m_s, moving axis z, time t, solid moving velocity U, fluid density ρ_w, projected area of the solid A_o, and velocity-dependent drag coefficient C_d, which accounts for the shape of the solid body.

Now, the influence of solid-body motion on the formation of the cavity is estimated here. The fluid is assumed to be irrotational everywhere such that the solid body can be approximated as a moving source (Fig. 2). The local fluid radial velocity is then related to source strength $\zeta(\xi,t)$ and radial distance w as

$$u=\frac{2}{w}\cdot\zeta(\xi,t) \tag{2}$$

where ξ is the instantaneous location of the solid. In order to determine the source strength, it is assumed that the loss of the kinetic energy E_p of a solid body is deposited to the kinetic energy and potential energy in the fluid section, [11]. The energy balance equation can then be expressed as

$$\left[\frac{dE_p}{dz}\right]dz=[4\pi\rho_wN\zeta^2+\pi(P_0-P_c)a(z)^2]dz \tag{3}$$

where P_o and P_c are the surrounding fluid and cavity pressures, respectively, and a is the cavity radius as a function of depth. The two terms on the right-hand side of Eq. (3) represent the kinetic and potential energies, respectively. $N=\ln(\Omega/a)$ is an empirical constant. Here it is assumed that the kinetic energy of the fluid is only calculated within a finite radius Ω. The range Ω/a is usually assigned a value in the rage of 15–30, [11]. By defining $P_g=(P_o-P_c)$ and introducing two terms,

$$[A(z)]^2=\frac{1}{\pi P_g}\left[\frac{dE_p}{dz}\right],\quad [B(z)]^2=\frac{P_g}{\rho_wN}, \tag{4}$$

the source strength is obtained as

$$\zeta=\pm\frac{1}{2}B(z)\sqrt{[A(z)]^2-[a(z)]^2}. \tag{5}$$

Another boundary condition applied is the kinematic boundary condition at the cavity wall.

$$\zeta=\frac{1}{2}a(z)\dot{a}(z) \tag{6}$$

Finally, from Eqs. (5), (6) an equation of cavity dynamics is obtained,

$$a(z)\dot{a}(z)=\pm B(z)\sqrt{[A(z)]^2-[a(z)]^2}. \tag{7}$$

Equation (7) can now be easily integrated with the moving source arrival time $t_b(z)$ (Eq. (1)) at each depth,

$$a(z)=\sqrt{[A(z)]^2-[A(z)-B(z)(t-t_b)]^2},\quad t>t_b. \tag{8}$$

Equation (8) states that at each depth the cavity continues to expand until pressure difference between the surrounding fluid and inside cavity balances the induced inertia effects. Then it starts to collapse and leads to a cavity closure. Using this equation, the time of cavity collapse is estimated. Since each location of the cavity along the depth has different collapse time, the time of cavity closure is determined by the minimum value. Hence, cavity closure occurs at the depth where the time of cavity closure is minimum. As discussed previously, the balance between the inertia and potential energy controls the evolution of the cavity, and each effect becomes of major significance at different situations. Since the potential energy due to the pressure difference between the cavity and surrounding fluid is not a function of depth at this regime, the only important parameter governing the extent of cavity growth along the depth is the inertia from the moving solid. It is evident that maximum cavity inertia is deposited near the surface, so that it results in deep closure. Complete details of results cannot be given here since it is well described in the previous work, [5].

As the entry speed increases for roughly Fr>150 (*low-speed regime*), note that no upper limit is proposed in the late 1950s, a pressure drop inside the cavity starts to be observed causing significant pressure difference between the outside ambient and inside cavity pressures, at least near the cavity neck during the closure process. Now, the first closure occurs near the free surface (surface closure). That is, deep closure is *preceded* by a surface closure. The two major forces leading to the surface closure are the underpressure caused by the flow of air into the cavity behind the entry body, referred to as the Bernoulli effect, and surface tension. The air rushing into the cavity causes a local underpressure inside the cavity, frequently estimated by the air density (related to atmosphere pressure) and entry speed. This underpressure causes the neck to contract until a complete surface closure occurs. Hence to explain the surface closure phenomena, at least the cavity pressure near the surface should be less than any other locations in the cavity (maximum potential energy), in spite of the maximum deposition of inertia here. Surface tension is neglected with an assumption that the surface tension may start to play a role when the cavity is about to close at a very late stage. This might cause an error in the estimation of the time of surface closure, especially for a small cavity. Another factor that is difficult to model is the extent of the dome-like splash. In many cases the surface closure occurs slightly above the undisturbed free surface, [13]. As discussed here, the complexity of the water-entry-induced cavity results from all these variables and phenomena. It can also be noted that a reduction in ambient pressure has the same effect as an increase in hydrostatic pressure and the interplay with inertia is what governs the surface and deep closure.

There were a series of *low-speed entry* tests in the late 1940s. They found that the time of surface closure decreases with entry speed. A subset of Gilbags' data, [14], for the formation and collapse of the cavity (surface closure) is compared with the current predictions. The assumption for the present model is that the pressure drop at least in the splash neck is equal to $1/2\rho_a U_i^2 \cdot n$, where n is a constant determined from experimental data, and ρ_a is the air density. This is based on the measurement that the cavity pressure drop is an order of magnitude greater than the general assumption, $1/2\rho_a U_i^2$, [15]. Figure 3 displays the time of surface closure for the entry of a 1-in. sphere from the reduced atmosphere pressure of 0.25 atm. The experimental data are also displayed for a verification purpose. The correlated value of n here is 300. If the model presented here is adequate, then the time of surface closure for different entry cases should be represented by the same parameters. Figure 4 shows the time of surface closure (T_s) for the entry of spheres from the reduced atmosphere pressures. The experimental data for low-speed entry, [14], are also displayed. For different atmosphere pressures, the model predictions compare well with the experimental results.

The possible scaling for the time of surface closure, T_s, is investigated using the current model. If the pressure drop at the cavity neck is constant and determined by the Bernoulli effects, we can then obtain the following result, [5]. This is the same result given by Birkhoff and Issacs, [9].

$$\frac{\rho_a U_i T_s}{D} = \text{constant} \tag{18}$$

For the correlated value of n, the cavity pressure becomes vacuum pressure at the entry speed of 51 m/s. As the entry speed increases further for roughly Fr>10000 (*transient regime* through *high-speed regime*), the pressure inside the cavity remains the vapor pressure with no further decrease. It is then no longer a time-dependent variable. Hence, the time of surface closure starts to increase. This is due to the fact that as the entry speed increases a momentum deposition from the body into the cavity increases while the cavity pressure remains vacuum with no further pressure drop. Since the surface closure is delayed, possibly from some entry speed the deep closure occurs prior to the surface closure. That is, the closure occurs again below the water surface, as was observed in case of the very low-speed regime. Currently, no experimental data is available for the high-speed entry case.

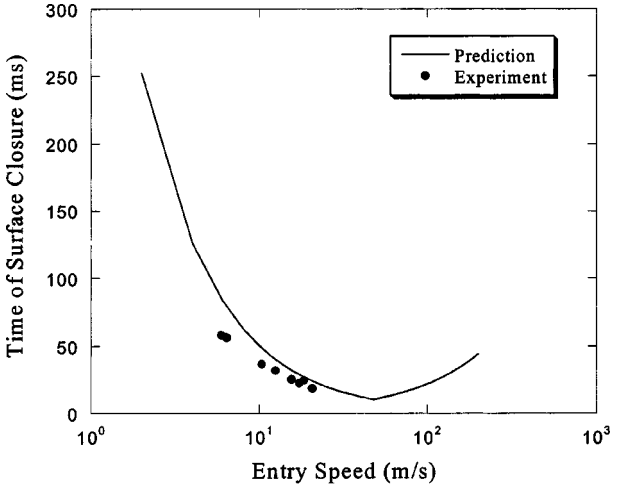

Fig. 3 Comparison of time of surface closure at atmosphere pressure of 0.25 atm

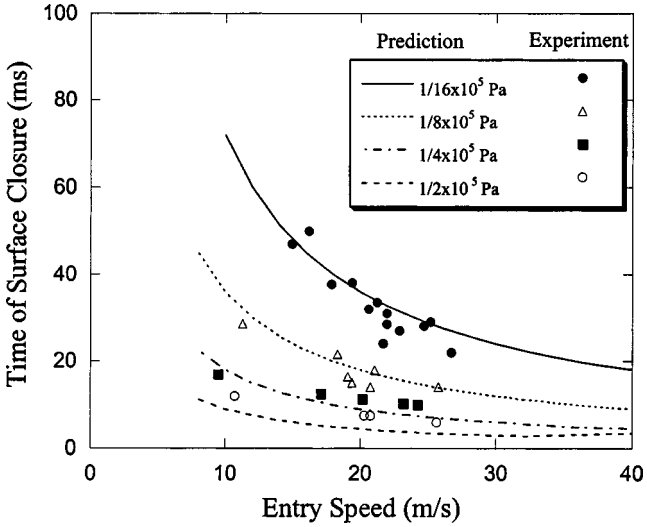

Fig. 4 Time of surface closure versus entry speed, 0.5-in. sphere at reduced atmosphere pressure, data from Gilbarg et al. [14]

Acknowledgment

This work was supported by Korea Ministry of Science and Technology (M20106000050-02B0500-04010).

References

[1] Gilbarg, D., and Anderson, R. A., 1948, ''Influence of Atmospheric Pressure on the Phenomena Accompanying the Entry of Spheres Into Water,'' J. Appl. Phys., **19**(2), pp. 127–139.
[2] Abelson, H. I., 1969, ''The Behavior of the Cavity Formed by a Projectile Entering the Water Vertically,'' Ph.D. thesis, The University of Maryland.
[3] May, A., 1970, ''Review of Water-Entry Theory and Data,'' J. of Hydronautics, **4**, pp. 140–142.
[4] Gaudet, S., 1998, ''Numerical Simulation of Circular Disks Entering the Free Surface of a Fluid,'' Phys. Fluids, **10**(10), pp. 2489–2499.
[5] Lee, M., Longoria, R. G., and Wilson, D. E., 1997, ''Cavity Dynamics in High-Speed Water Entry,'' Phys. Fluids, **9**(3), pp. 540–550.
[6] Shi, H. H., and Kume, M., 2001, ''An Experimental Research on the Flow Field of Water Entry by Pressure Measurements,'' Phys. Fluids, **13**(1), pp. 347–349.
[7] 1997, ''Violent Surface Motion,'' Philos. Trans. R. Soc. London, Ser. A, **355** (1724 15).
[8] Waugh, G., and Stubstad, G. W., 1972, *Hydroballistics Modeling*, Naval Underwater Center, San Diego, CA.
[9] Birkhoff, G., and Isaacs, R., 1951, ''Transient Cavities in Air-Water Entry,'' NAVORD Report No. 1490.
[10] Metzger, M. A., 1981, ''A Computer Program for Modeling Water Entry Cavity Performance and Comparison of Predicted With Observed Cavities,'' Naval Surface Weapons Center, Silver Springs, MD, Report No. NSWC/TR-81-59, Feb.
[11] Birkhoff, G., and Zarantonello, F. H., 1957, *Jets, Wakes, and Cavities*, Academic Press, New York.
[12] Lundstrom, E. A., 1971, ''Fluid Dynamic Analysis of Hydraulic Ram,'' Naval Weapons Center, China Lake, CA, NWC TP 5227, July.
[13] Shi, H., Itoh, M., and Takami, T., 2000, ''Optical Observation of the Supercavitation Induced by High-Speed Water Entry,'' ASME J. Fluids Eng., **122**, pp. 806–810.
[14] Gilbarg, D., and Anderson, R. A., 1948, ''Influence of Atmospheric Pressure on the Phenomena Accompanying the Entry of Spheres Into Water,'' J. Appl. Phys., **19**(2), pp. 127–139.
[15] Abelson, H. I., 1970, ''Pressure Measurements in the Water-Entry Cavity,'' J. Fluid Mech., **44**(1), pp. 129–144.

Journal of Fluids Engineering

Book Review

Perspectives in Fluid Dynamics: A Collective Introduction to Current Research, edited by G. K. Batchelor, H. K. Moffatt, and M. G. Worster. Cambridge University Press, New York, 631 pp.

REVIEWED BY THOMAS R. OSBORN[1]

This volume strives to counter the trend towards specialized texts in advanced fluid mechanics and to showcase the breadth of topics for research in fluid mechanics with a selection of 11 different topics. The articles are designed to provide an introduction to the topics assuming a general knowledge of fluid mechanics but not expertise on the specific subject. The titles give a good idea of the subjects covered and the clear progression from small scales to large scales.

- Interfacial Fluid Dynamics–S. H. Davis
- Viscous Fingering as an Archetype for Growth Patterns–Y. Couder
- Blood Flow in Arteries and Veins–T. J. Pedley
- Open Shear Flow Instabilities–P. Huerre
- Turbulence–J. Jiménez
- Convection in the Environment–P. F. Linden
- Reflections on Magnetohydrodynamics–H. K. Moffatt
- Solidification of Fluids–M. G. Worster
- Geological Fluid Mechanics–H. H. Huppert
- The Dynamic Ocean–C. Garrett
- On Global-Scale Atmospheric Circulation–M. E. McIntyre

[1]Department of Earth and Planetary Sciences, The Johns Hopkins University, Baltimore, MD.

Each of these topics already fills many books. To distill into the 50 pages of each chapter a coherent introduction of the subject is very hard work. Nevertheless, the appeal of having the range of subjects in one volume is irresistible.

What a challenge to the reader! You can start by reading a review in your own field (e.g., oceanography) and perusing the related fields (turbulence, atmospheric circulation, shear flow, and convection). But then you are drawn to the chapter on blood flow—a pulsating flow in flexible tubes. The interfacial regime is of interest for bubbles, droplets, and lubrication. That chapter draws one on to the viscous fingering and growth patterns. The spectacular color plates of solidification and geological phenomena catch one's eye and draw you to the text. It is the hot fluid in the center of the earth that enables the terrestrial magnetic field via magnetohydrodynamics. It is a book one uses like a supermarket—something from here, something else from there, you can't take it all at once—yet the open shelves lead one to look at new items and ideas.

The breadth and variety of topics and techniques make this a useful book for teaching an advanced course. The book displays the tremendous range of practical problems, environmental phenomena, industrial applications as well as research topics that involve fluid mechanics. This paperback version of the book is handsomely prepared with Jupiter's red spot on the cover, nice quality printing and a pleasant layout for reading.

This book was conceived by Professor Batchelor as a sequel to his *Introduction to Fluid Mechanics* and is dedicated to his memory by H. K. Moffatt and M. G. Worster. It is a very fitting tribute.

